BINDING SERVICES
Tel +44 (0)29 2087 4949
Fax +44 (0)29 20371921
e-mail bindery@cardiff.ac.uk

A STUDY OF THE TIME-DEPENDENT BEHAVIOUR AND ITS PREDICTION IN CONCRETE AND CONCRETE STRUCTURES

Richard Howells M.Eng. (Hons)

Thesis submitted to the University of Wales in
candidature for the degree of Doctor of Philosophy

September 2004

School of Engineering
University of Wales, Cardiff

ProQuest LLC
789 East Eisenhower Parkway
P.O. Box 1346
Ann Arbor, MI 48106-1346

ACKNOWLEDGEMENTS

I would like to thank my two tutors, Professor Ben Barr and Dr. Bob Lark, firstly for giving me the opportunity to carry out this research, and secondly for their invaluable help, support, guidance and friendship whilst this research was undertaken.

I am very grateful to the Engineering department at Cardiff University, the Engineering and Physical Sciences Research Council (EPSRC) and Tarmac Ltd. for jointly funding this research.

Special thanks are due to Professor Jan Vitek at Metrostav in Prague whose patience, help and assistance using the DOMO98 computer code was invaluable and most appreciated.

I would like to extend my gratitude to the technical staff, Des, Brian, Len, Mal, Carl and Andy for their advice and assistance throughout this project, especially when I was unable to carry out many normal tasks due to a broken ankle. Their help and friendly banter made a difficult time far easier.

Thanks are also due to all the friends and family who gave me encouragement and moral support over the last three years (has it really been that long?!) There are too many of you to thank individually but you know who you are. The good humoured teasing can finally stop – my tax-dodging, freeloading lifestyle has finally come to an end!

Finally, and most importantly, I would like to thank my parents, William and Carol, for their love and support, both financial and moral, not only over the last three years but throughout my life. Without you, this would not have been possible and I thank you from the bottom of my heart.

SUMMARY

The main objective of this study was to bring together two areas of research; the first being a laboratory study of the time-dependant properties of concrete; while the second is a study of the time-dependant behaviour of two prestressed concrete structures – the Grangetown and Cogan Viaducts.

A study of the influence of shrinkage and creep on a range of normal to high strength concretes in the laboratory found that as concrete strength increased, drying and total shrinkage also increased while the rate at which creep developed decreased. It was shown that autogenous shrinkage is more prevalent in high strength concrete, and the inclusion of pfa in concrete reduces the amount of total shrinkage.

The benefits and limitations of using current shrinkage and creep prediction models were determined through a sensitivity study of their input parameters and through comparisons with shrinkage and creep strains determined in the laboratory. It was found that certain models are more sensitive to specific parameters than others. All models predicted strains which gave good to adequate agreement with the measured strains when the material parameters were within the ranges specified by the models, but the prediction was less reliable when the parameters used in the models exceeded the recommended values.

It was shown that the prediction of the time-dependant behaviour of the Grangetown and Cogan Viaducts using these models is inadequate due to influences not considered by the models such as prestressing forces and the construction sequence.

The influence of the construction sequence and prestressing data was investigated using a complex computer code in conjunction with these models, and while it was not possible to improve the efficiency of predicting reliable strain behaviour over time, an appreciation of the level of detail necessary to do this was gained. Finally, the influence of environmental conditions on the strain behaviour of these two structures was shown to be greater than anticipated.

List of Contents

LIST OF TABLES

Chapter 2

Chapter 3

Chapter 4

Chapter 5

Chapter 6

Chapter 7

LIST OF FIGURES

Chapter 2

Chapter 3

Chapter 4

Chapter 5

Chapter 6

Chapter 7

Chapter 1

Introduction

1.1 Introduction

One of the main aims of the study reported in this thesis was to bring together two parallel strands of research which have been pursued at Cardiff University over a number of years. The first, is the work which has been undertaken intermittently on the Grangetown and Cogan Viaducts which were instrumented by a team of researchers at Cardiff and Bristol University in the late 1980's. The second, is the study of the behaviour of medium and high strength concretes which has been carried out at Cardiff over the last decade. In bringing together these two fields of research, it is hoped to gain a better understanding of the time-dependant properties of medium and high strength concrete, and how these properties influence the behaviour of concrete structures.

A number of publications have already been prepared based on the extensive data obtained over the last 17 years for the Grangetown and Cogan Viaducts. Initial studies were undertaken by Vitek and Barr[1-3] who used a sophisticated computer program called DOMO[4] to accurately predict the strain behaviour of the Cogan Viaduct during construction and over the early service life of the structure, and this analysis was extended to the long-term behaviour of the structure by Barr *et al*[5] using an updated version of the DOMO code called DOMO98[6]. The results of this analysis were used by Lark *et al*[7] in a paper describing a study of possible condition monitoring techniques to assess the integrity of the two viaducts over time. This paper describes how the model might be extended to predict the future performance of such structures and how this could then be used as a template against which the actual performance could be monitored. Beygi[8] reported the behaviour of the instrumented segments in Grangetown and Cogan Viaducts prior to, during, and after construction, and Barr *et al*[9] investigated the seasonal shrinkage variation in the bridge segments. In 2000, dataloggers were installed in both viaducts allowing data to be recorded on a daily and hourly basis, and as part of this study the strain behaviour of both structures was examined over a two-year period.

Early work at Cardiff on medium to high strength concretes was concentrated in a number of areas with initial studies centred on strength, stiffness and fracture properties. Thereafter, work on medium to high strength concretes was extended to include the time dependant properties. The initial work was carried out on shrinkage properties by Hoseinian[10] and El-baden[11], in particular the effect of shrinkage on high strength concretes, with the latter also reporting on the shrinkage of steel fibre reinforced concrete. The initial work on the effect of creep in high strength concrete was carried out by Bush[12], with whom the author of this thesis became involved when investigating the time-dependant properties of high strength concrete as part of a MEng dissertation (Howells[13]). Further details of the MEng Project study are reported in Chapter 5.

The overriding factor that links together these two separate areas of research is the time-dependant properties of concrete. The initial findings of these two areas of research have thus been extended in the program of work reported here.

1.2 Objectives of the Present Study

The overall aim of this study was to investigate the time-dependant behaviour of medium to high strength concrete, including the factors that influence the strains associated with this behaviour, and also the methods used to predict this behaviour both in the material on its own, and as part of a 'real-life' structure. This was pursued by linking a short-term laboratory study of the creep and shrinkage of concrete with long-term strain data obtained from two precast, post-tensioned, segmental concrete viaducts. The main objectives of the current investigation were:

- To undertake a short-term laboratory study to determine the effect of creep and shrinkage on a range of medium to high strength concretes made from previously established concrete mixes as well as a concrete mix similar to that used in the construction of the Grangetown and Cogan Viaducts.

- To determine whether it was possible to accurately predict the behaviour associated with these time-dependant effects using the most recent creep and shrinkage prediction models and in doing so verify which was the more reliable.

- To ascertain why certain models predict strains of different magnitudes for the same concretes, by investigating the influence of the individual model input parameters in the form of a sensitivity analysis.

- To investigate the influence of seasonal environmental effects on the time-dependant strains observed over a two-year period in the Grangetown and Cogan Viaducts.

- To determine whether it was possible to accurately predict the long-term, time-dependant strain behaviour recorded in the Cogan Viaduct using the same creep and shrinkage prediction models used in the laboratory study, and in doing so verify which was the more reliable.

- To use the DOMO98 computer code to establish whether the amount of information used in the original analysis of the Cogan Viaduct undertaken by Vitek and Barr[1-3] and Barr *et al*[5], could be simplified in order to produce a relatively quick and easy method of strain prediction in such structures.

- To update the creep and shrinkage function within the DOMO98 computer code to include the models used in the laboratory and subsequent field study.

- To determine which of these models when used in conjunction with the DOMO98 computer code, predicts strains which give the closest agreement with the strain behaviour recorded in the viaduct.

Following this study, it is hoped that a better understanding of the time-dependant behaviour and its prediction in concrete and concrete structures will be obtained, and better predictions of the behaviour of concrete structures will be possible allowing more efficient design in the future.

1.3 Layout of the Thesis

This thesis has been divided up into nine chapters including this one. Chapter 2 presents a review of relevant literature concerned with the material side of this study. The composition of concrete, and in particular high performance concrete, is detailed along with the related fresh and hardened state properties associated with the material. The factors which influence the time-dependant properties of concrete are discussed and current methods of predicting the time-dependant behaviour are investigated.

Chapter 3 presents background information on the Grangetown and Cogan Viaducts used in this study. The type of structure and its construction is detailed, and an in depth description of the design, manufacture and construction of the two structures is given. The findings of previous studies on the two structures are also reported.

Chapter 4 reports the findings of a sensitivity study on the influence that the input parameters used in a selection of recent prediction models have on the strains each model predicts.

Chapter 5 reports details of the laboratory shrinkage and creep study including concrete composition, experimental setup, identification of the shrinkage and creep effects for the different concretes, and comparisons with strains predicted using the creep and shrinkage prediction models reported in Chapters 2 and 4.

Chapter 6 reports the findings of a seasonal study on the effect of changing environmental conditions on the strain behaviour in the two viaducts over a two-year period.

Chapter 7 reports on the attempt to predict the long-term strain behaviour of the Cogan Viaduct. Comparisons between the recorded strains and strains predicted using the standard creep and shrinkage prediction models are made, and details of the simplification of the original DOMO analysis are presented along with comparisons between the predicted strain behaviour made using the original analysis and the simplified analysis. The DOMO98 computer code is updated to include the prediction model creep and shrinkage functions used throughout this research, and further comparisons are made between the recorded strain behaviour and the strain behaviour predicted using the updated DOMO98 computer code with the new creep and shrinkage functions.

Chapter 8 presents a summary of the main conclusions made throughout this study. Recommendations for future study are also detailed.

Chapter 2
Literature Review

2.1 Introduction

Concrete is a man-made composite material, made from cement paste and aggregate. It is one of the oldest construction materials, with various forms being found dating back to 5000 BC in parts of modern day Europe. The actual composition of concrete varies widely depending on the application, but will contain cement, water, aggregate and other specialist materials. Sometimes additional materials called admixtures are added to the concrete during mixing in order to modify one or more properties in the fresh or hardened states. [14,15]

Concrete is subject to time-dependant deformations caused by shrinkage, creep and variations in temperature. Shrinkage of concrete is caused by loss of water through evaporation or hydration of cement, and also by carbonation. Creep of concrete occurs when the concrete is subjected to stress over time. The phenomenon of shrinkage and creep form the basis for this research, in particular the effect on high performance concrete, and the accuracy of current methods of prediction.[15,16]

2.2 Normal Strength Concrete

Normal strength concrete (NSC) is one of the most important civil engineering materials. The tonnage consumed far exceeds that of steel, wood, and polymers combined and it is an essential ingredient in some of the largest structures built in the last century.[17]

A review of existing literature indicates that NSC has a 28-day compressive strength in the range of 7.5-60MPa. However, concrete is generally no longer defined in terms of strength alone. The most recent design standard BS 8110: Part 1: 1997[18], places greater emphasis on design for durability. The concrete specification in the standard emphasises the need for a nominal cover for specific exposure conditions for this purpose and this is specified in terms of maximum free water/cement (w/c) ratio, minimum cement content and lowest grade of

concrete. These three values are such that specifying the grade of concrete will ensure that the other two specifications are met, which in turn ensures that the target workability of the mix is achieved. Testing plays an important role in the specification as it provides confirmation of workability, w/c ratio and compressive strength. Testing the latter by means of the 28-day cube compression test will give an indication that the durability requirements of the mix are satisfied.[19]

2.2.1 Concrete Materials

It is necessary to provide background information on the concrete constituents. The effect they have on fresh and hardened properties will be discussed later.

2.2.1.1 Cement

The predominant modern cement used throughout the world today is Portland cement, which was developed and patented by Joseph Aspdin in 1824. BS 12: 1996[20] defines cement as a hydraulic binder, a finely ground inorganic material which, when mixed with water, forms a paste which sets and hardens by means of hydration reactions and processes and which, after hardening, retains its strength and stability even under water. New European Standards for cement have recently been published in the UK as British Standard BS EN 197–1: 2000[21], which is the new harmonised standard for common cements. The different types of Portland cement and their respective BS 12 and BS EN 197–1 equivalent classifications are shown in Table 2.1, while their American equivalents are shown in Table 2.2. As ordinary Portland cement (OPC) is suitable for most types of work and thus the most widely used, OPC will be used in this research project.[21-24]

The four main compounds of cement are tricalcium silicate (C_3S), dicalcium silicate (C_2S), tricalcium aluminate (C_3A), tetracalcium aluminoferrite (C_4AF) (where C represents CaO, S represents SiO_2, A represents Al_2O_3, and F represents Fe_2O_3 in the conventional shorthand used in concrete technology.) Their composition and abbreviation are shown in Table 2.3. The silicates and aluminates form hydration compounds which in time harden to form the hardened cement paste (hcp). The cement compounds contribute very differently to the strength of concrete over time as shown in Figures 2.1 and 2.2. The microcrystalline hydrate $C_3S_2H_3$ also produced during hydration is often described as calcium silicate hydrate or C-S-H. Figure 2.3 shows typical time-dependent heat evolution and strength development during hydration, while Figure 2.4 shows the development of the microstructure in hydrating cement paste over time.[14,16,23-27]

2.2.1.2 Aggregate

Aggregates make up the largest constituent of concrete occupying 70-80% of the absolute volume for normal weight natural aggregates. According to BS 882[28], coarse aggregates are generally crushed rocks or gravels, particles of which are larger than 5mm diameter, and fine aggregates are generally sands or crushed gravels, particles of which are smaller than 5mm diameter. The main aggregate properties that influence fresh or hardened concrete are shape and grading, porosity and absorption, specific gravity, elasticity, strength and surface characteristics affecting the bond of the aggregate to the hardened cement paste (hcp). Shape and grading are particularly important as they affect the workability of the mix.[14,16,23,24,29]

2.2.1.3 Water

Water used in concrete, in addition to reacting during hydration causing it to set and harden, is necessary for mixing, placing and compacting fresh concrete. It is also used for washing the aggregates and for curing purposes. In fresh concrete, water is essential for workability, while in hardened concrete, strength is influenced by the amount of water in the mix.[14,16,23,24]

2.2.1.4 Admixtures

Admixtures are chemicals that are added to the concrete immediately before or during mixing and significantly change its fresh, early age or hardened state to advantage. Only small quantities are required, typically 1 to 2% by weight of cement. Commonly used admixtures generally fall into one of four main categories: air-entraining agents, accelerators, water-reducers (plasticizers), and retarders. Other constituents termed 'mineral admixtures' are *cement replacement materials* which are not admixtures but will be noted here for completeness. They are powders of fineness similar to cement itself, but hydrate slower than Portland cement making useful long-term contributions to the strength and impermeability of concretes. Examples commonly used are ground granulated blastfurnace slag (ggbs) and pulverised-fuel ash (pfa). Dhir *et al* (2000)[30] found that the strength of concrete at a given age increased with the inclusion of conditioned pfa, and hydration studies indicated that conditioned pfa may actively contribute to the reactions in cementitious systems. This was reinforced by Siddique (2004)[31] who found that while the inclusion of high volumes of pfa in concrete resulted in decreased 28-day compressive, tensile and flexural strength and elastic modulus, each of these strength properties showed continuous and significant improvement at 3-months and 1 year.[14,16,23,24]

2.2.2 Mix Proportions

Clearly there is no single concrete which is ideal for all applications: the purpose for which the concrete is required will dictate the properties needed, while the nature of available materials will determine the mix proportions necessary to achieve them. Generally, mix specifications are based on strength and durability requirements. Shirley[15] suggests typical degrees of workability, aggregate/cement (a/c) ratios at given w/c ratios, and aggregate proportions for typical NSC mixes, in Tables 2.4-2.6.[15,23]

2.3 High Performance Concrete

High performance concrete (HPC) is often referred to as high strength concrete (HSC). However, while the term HSC places emphasis directly on its superior strength to that of NSC, it has many other properties that stem directly or indirectly from this, and the term HPC is intended to encompass this concept. There have been numerous attempts to define HPC since its introduction into the industry. Russell[32] states the definition of HPC given by the American Concrete Institute (ACI), as concrete meeting special combinations of performance and uniformity requirements that cannot always be achieved routinely using conventional constituents and normal mixing, placing, and curing practice. Table 2.7 shows the criteria developed by the Strategic Highway Research Program (SHRP) for HPC. There are many alternative definitions, but each agrees that HPC is a concrete in which certain characteristics are developed for a particular application and environment. Ease of placement; compaction without segregation; early age strength; long-term mechanical properties; impermeability; density; heat of hydration; toughness; volume stability and long life in severe conditions are examples of such characteristics.[22,32,33]

HPC is often considered to be a relatively new material. However, a report by the ACI[34] indicates that as far back as the 1950's, concrete with compressive strengths in excess of 34MPa have been produced. Development of HPC has continued gradually over the years with concrete with compressive strengths of 41 and 52MPa being used commercially in the 1960's, rising to 62MPa in the 1970's. During the last decade concrete with compressive strengths in excess of 140MPa has been used in the construction of cast-in-place buildings.[32]

As with the development of HPC in terms of increasing compressive strength, the range of application has also increased. During its initial development, HPC was restricted for use in few locations. In recent years the application of HPC has been extended worldwide. This growth can be attributed to the increased development in material technology, and increased

demand for HPC. Breitenbücher[35] has demonstrated the advantages of using HPC columns in terms of the amount of reinforcement required, and column dimensions.

2.3.1 Concrete Materials

Similarly to NSC, HPC consists of cement, water and aggregate. However, HPC also contains certain types of admixtures. Background information on the concrete constituents is provided here, and the effect they have on fresh and hardened properties will be discussed later.

2.3.1.1 Cement

HPC does not require a special cement and so OPC is generally used. If a high early strength is required e.g. in the case of prestressed concrete, then rapid hardening Portland cement may be used. These cements are classified in Tables 2.1 and 2.2.[22-24,34]

2.3.1.2 Aggregate

Aggregate used in the mix of HPC must be carefully chosen to achieve high strength. Aggregate size must be smaller than that used in NSC, the maximum size in HPC is usually between 10 and 14mm diameter. There are two reasons for this. With a smaller maximum size aggregate, the differential stresses at the aggregate-cement paste interface are smaller, and the possibility of microcracking is reduced. Also, smaller aggregate particles are stronger than larger ones due to the fact that the comminution of rock removes the largest flaws, which control strength.[33]

2.3.1.3 Water

The requirements for water in HPC are no more stringent than for NSC, and it serves much the same purpose. However, in order to achieve increased strength by reducing the w/c ratio, the amount of water added to the mix is less. The ratio of the mass of water to the total mass of cementitious material is known as the water/binder (w/b) ratio.[24,33,34]

2.3.1.4 Admixtures

Achieving these low w/c ratios and therefore obtaining concretes of increasing strength, is possible due the inclusion of certain admixtures in the mix. The inclusion of silica fume in the mix improves packing by reducing the number of voids in the mix and so improving the

strength, while the inclusion of a superplasticizer ensures that the mix retains sufficient workability. These admixtures will now be discussed in detail.[36,37]

Silica Fume

Silica fume (SF) is a recent arrival among cementitious materials. It was first introduced as a pozzolan, but due to its reactive nature it is also beneficial in other areas. SF is also referred to as microsilica or condensed silica, and it is a by-product of the manufacture of silicon metal. SF contains more than 90% silicium dioxide (SiO_2) and the particles are about 100 times finer than those of cement.[24,35]

The strength improvement in concrete due to the use of SF relies on various effects. The very small particles of SF can enter the fine pores which can be located in close proximity to the aggregate particles at the aggregate-cement interface. This zone is known to be a source of weakness in concrete due to the 'wall effect' that prevents the particles of Portland cement from packing tightly against the surface of the aggregate. The SF particles are used to fill this void and sufficient packing is achieved. The fineness of SF particles is such that mixing can prove difficult without the use of a superplasticizer. Silica is generally supplied in the form of a slurry in which the water content is about 50% by mass. Also, SF reacts with calcium hydroxide, which is produced during cement hydration in a pozzolanic reaction to form calcium silicate hydrates (C-S-H). These C-S-H are responsible for the strength in concrete. These effects lead to an extremely dense microstructure and hence an increased strength. [24,34,35,37]

Furthermore, due to its high fineness, SF reduces bleeding so that no bleeding water is trapped underneath coarse aggregate particles. The effect of this is that the porosity of the interface zone is reduced, and further chemical reactions of the SF mean that the interface zone is no longer weak in terms of strength or porosity. Also, the bond between mortar and the aggregate is improved significantly by silica fume as shown in Figure 2.5. In normal concrete, the bond areas are weakened by calcium hydroxide and ettringite, which form especially in these areas. By the addition of SF, the weak calcium hydroxide is converted into strong calcium silicate hydrate, so that only a few small faults remain in the bond. [24,35,37-38]

Superplasticizers

In the 1970's, water reducing agents and superplastizers (SP) were introduced into concrete production. SP are admixtures which allow a significant amount of water reduction. They are classified as 'water-reducing, high range' admixtures.[34,35]

SP are water-soluble organic polymers which are synthesised using a complex polymerisation process, to produce long molecules of high molecular mass. These long molecules wrap themselves around the cement particles and in doing so, give the cement particles a highly negative charge so that they repel each other. This results in deflocculation and dispersion of cement particles resulting in an improvement in workability. This improvement in workability means that concrete can be produced with either a very high workability, or a very high strength. Put simply, the effect of SP is the reduction of the water content of the concrete mix, thus reducing the w/c ratio whilst retaining the desired workability and increasing the compressive strength, or alternatively, improving workability at a given w/c ratio. [24,34,35]

In order to achieve even higher concrete strengths, further improvements can be utilised. To acquire these higher strengths, the w/c ratio needs to be reduced further, and an optimum value of about 0.25 is desirable. In order to do this while keeping the workability sufficient, extremely effective SP known as High Water Reducing Agents (HWRA), are used. Phelan[39] stated that Type A water-reducing admixtures allow water reduction of 5-7%, mid-range water-reducing admixtures allow water reduction of 7-9%, and Type F or G high-range water-reducing admixtures allow water reduction of 10-30%, with normal or retarded setting times. Figure 2.6 shows the relationship between compressive strength and w/c ratio for different concrete strengths over the last 50 years. It can be seen that compressive strengths in excess of 100 MPa cannot be achieved by simply reducing the w/c ratio. To achieve these strengths, SF must also be added to the concrete as discussed previously. The inclusion of SF in the concrete mix necessitates the use of a SP. However, the type of SP to be used must be compatible with the Portland cement to be used. Not every SP is compatible with every type of Portland cement as reported by Neville and Aïtcin[30] and Agarwal *et al*[40]. [24,34,35,39]

2.3.2 Mix Proportions

At present, there exists no standard to provide information on mix proportions for HPC. However, there is a wealth of information available regarding typical mix proportions for HPC, each varying depending on the properties of individual ingredients and on the desired properties of the concrete in service. Neville[24] selected details of actual mixes used in practice, in Table 2.8.

A report by Taylor *et al*[41] specifies that in order to achieve 28-day strengths in the range of 90 to 120MPa, typical cement contents of 450 to 500 kg/m^3 are suitable, although amounts which vary significantly above and below these values have been successfully used. W/b ratios varying between 0.25 and 0.35 are common although lower values have been used. Similarly, the proportions of SF and SP used vary. SF is usually about 10% of the weight of

cement, while the SP appears to vary far more widely. Sand contents range from about 35 to 45% of the total aggregate (but are sometimes much less), depending on sand grading amongst other factors. Table 2.9 summarises mix proportions for a range of typical mixes.[41,42]

2.4 Concrete Properties

The properties of concrete must be considered when the concrete is fresh, and when the concrete has hardened.

2.4.1 Fresh Properties

The properties of fresh concrete need to be considered during and just after mixing when the concrete is still fluid. They generally fall into two categories, workability and stability, both of which are largely related to the setting time of the concrete.

2.4.1.1 Workability

Workability depends on a number of interacting factors: w/c ratio, aggregate type and grading, a/c ratio, presence of admixtures and fineness of cement. The main factor is the water content of the mix since by simply adding water, the interparticle lubrication is increased. Furthermore, evaporation of any excess water from the cement paste, leaves voids in the paste structure which are unlikely to become filled. The lower the proportion of these voids, the greater the chance that the concrete will develop properties such as strength, impermeability and durability. Drying shrinkage will also be minimised. Figure 2.7 shows the relationship between compressive strength at various ages and w/c ratio. However, to achieve optimum conditions for minimum voids, the influence of aggregate type and grading must be considered, with regard to size distribution and shape, and the porosity of the aggregate. For a constant w/c ratio, the workability increases as the a/c ratio is reduced because the amount of water relative to the total surface of solids is increased. The introduction of admixtures such as air-entraining agents reduces the water requirement for a given workability, while the fineness of cement has minor influence on workability but the finer the cement, the greater the water demand.[15,23,24]

Singh[43] found that for a constant w/c ratio, a concrete mix with a high aggregate/cement (a/c) ratio leads to higher strength as demonstrated in Figure 2.8. This can be explained when the total volume of voids in the concrete is considered. A concrete mix with a high a/c ratio means that the cement paste represents a smaller proportion of the volume than normal, lowering the total porosity of the concrete and increasing the strength.[23,24]

An ideal concrete is one which is workable enough to be fully compacted, but does not require an excessive water content to achieve that workability. Workability in HPC is mainly dependent on cement content, water/cement ratio and the dosage of SP used. Faroug *et al*[44] and Zain *et al*[45] have commented on the marked increase in workability and flowability of HPC containing SP, the former reporting that SP becomes more effective at lower w/c ratios. Generally, the inclusion of silica fume in HSC requires a complimentary amount of SP in order to attain the required workability. However, even with sufficient SP the useful workability received is limited to a maximum of one hour and in some cases extra dosage may be required due to the reduced setting times.[22,29,32]

2.4.1.2 Stability

Stability, or cohesiveness as it is also known, is the property whereby the concrete remains as a homogenous uniform mass, i.e. the constituents remain uniformly distributed in the concrete during mixing, compaction and beyond, until the concrete stiffens. A cement paste which is too greatly diluted (i.e. w/c > 1), may be excessively fluid, tending to drain particles away from the surface of the aggregate causing defects in the fresh concrete. Also, the greater the amount of excess water present in the paste, the greater the amount of bleeding, reducing the durability of the hardened concrete.[14,16,23,24]

There is a major difference in the cohesiveness of HPC relative to that observed for NSC with HPC showing a marked increase in cohesiveness. With the inclusion of silica fume there is a surplus of finer particles in the mix, which adversely affects the consistency and makes the concrete more 'sticky'. This increase in cohesiveness leads to a greater degree of stability in the mix and a reduction in the amount of bleeding during setting. One disadvantage of reduced bleeding is the problem of plastic shrinkage, which increases since evaporation of water from the setting concrete far exceeds the amount of bleeding. However, this can be overcome by applying proper curing measures to the concrete surface.[22,34,41]

2.4.2 Hardened State Properties

The properties of concrete in the hardened state relate to compressive and tensile strength, and the stiffness of the concrete. Strength is generally considered one of the most important properties of concrete, since the first consideration in structural design is that the structural elements must be capable of carrying the imposed loads. The preceding sections in this chapter deal with concrete properties that are directly or indirectly related to strength: constituent materials, water content, w/c ratio, a/c ratio and workability. Further factors which influence strength include the effect of age, temperature and humidity. The degree of

hydration increases with age, leading to the effect of age on strength which is apparent in Figure 2.7. Since hydration reactions are never complete, then in the presence of moisture, concrete will continue to gain strength for many years at an increasingly reducing rate. Higher temperature maintained throughout the life of a concrete will result in higher short-term but lower long-term strengths.[14,16,23,24,42,46]

2.4.2.1 Compressive Strength

Concrete resists compression better than any other type of stress, so the compressive strength of a concrete may be its most important property. The current compressive strength standard test in the UK (BS 1881: Part 116: 1983[47]) is based on the concrete cube. The cube test gives no direct information about the strength of the concrete in a member, but rather indicates the potential strength of the mix in question, providing an indication of the quality of the concrete as supplied.[14-16,23,24]

The compressive strength of HPC is directly affected by the amount of SF added to the mix as previously stated. Numerous authors have reported a significant increase in compressive strength of concrete containing SF.[48-51] A report by Kjellssen *et al*[49], investigated the effect of SF on the compressive strength development in HPC and paste. The results are shown in Table 2.10. What is noticeable is that the inclusion of SF increases the strength of the paste as well as the concrete.

2.4.2.2 Tensile Strength

Concrete is a comparatively brittle material which is relatively weak in tension. Direct testing of concrete in uniaxial tension is difficult because of problems associated with gripping and aligning the test specimens. BS 1881: Part 117: 1983[52] and BS 1881: Part 118: 1983[53] prescribe alternative methods of determining the tensile strength: in indirect tension (*cylinder splitting*) and in flexure (*modulus of rupture*). The tensile strength of concrete is usually taken to be about one-tenth of its compressive strength. This can vary depending on the method used for measuring tensile strength and the type of concrete. Figure 2.9 shows typical relationships between direct and indirect tensile and compressive strengths from which it can be seen that the modulus of rupture gives the highest apparent strength.[14,16,23,24,54]

Sabir[51] reported that the 7-day strength of NSC is approximately 60 to 70% of the 28-day strength, whereas HPC will attain strengths in the region of 86 to 93%. This rate in gain of strength cannot be found in the tensile strength; experimental results show that while for NSC the tensile strength achieved is about 10% of the compressive strength, for HSC the result was

nearer to 5%. This is an important issue since the tensile strength will be responsible for most structural failures, a problem that has not yet been accounted for in the design codes since it is generally accepted that concrete members are designed to take loads in compression. The compressive strength of HSC develops quicker than the tensile strength and there is evidence to suggest that the tensile strength reaches a plateau while the compressive strength in still increasing.[24,41,51]

2.4.2.3 Stiffness

The stiffness of a concrete member can be expressed by the term EI, where E is the modulus of elasticity of the material, and I is the second moment of area. Since I is governed by the sectional dimensions of the concrete, then if this is kept constant the stiffness will be determined by E value of concrete.

Figure 2.10 shows typical stress-strain (σ-ε) relationships for concrete of different strengths. The σ-ε line is nearly linear up to a stress-strength ratio of about 80% for HPC. After exceeding the ultimate load, the σ-ε response falls off rapidly, which is typical for a brittle material. Such a sudden failure in a structure can be prevented by using increased confinement reinforcement. In the structural design of reinforced concrete, the entire σ-ε curve must be considered. For this reason, the behaviour of concrete which has a very high strength is of especial interest. Such concrete develops a smaller amount of cracking than NSC during all stages of loading; in consequence, the ascending part of the σ-ε curve is steeper and linear up to a very high proportion of the ultimate strength. The descending part of the curve is also very steep so that the HPC is more brittle than ordinary concrete, and indeed explosive failure of specimens of HPC tested in compression has often been encountered. However the apparent brittleness of HPC is not necessarily reflected in the behaviour of reinforced concrete members made with such concrete.[24,35]

Corresponding to the steeper σ-ε line, Young's Modulus (E) of HPC is also higher than that of NSC. The increase in E, however, is less significant than the increase in compressive strength.[24,25,55] Gutierrez and Canovas[56] have observed that special aggregates can double or halve the E value of the same HPC while normal aggregates introduce differences of 30% or more. The type of aggregate can obviously affect the stiffness of HPC greatly and it is worth noting that BS 8110: Part 1: 1997[18] is the only standard that currently takes this into account.

2.5 Concrete Volume Change

Volume changes in concrete can be classified in terms of either water movement (shrinkage or swelling), or temperature variation (thermal strain). Such deformations are important because, in practice, if concrete is subjected to restraint there is the possibility of inducing tensile stress, which can lead to cracking, which impairs concrete durability and structural integrity.

2.5.1 Shrinkage and Swelling

The volume of a cement paste varies with its water content. Drying causes volume decrease or 'drying shrinkage' as it is known, while wetting causes volume increase or 'swelling'. Settlement of solids and loss of free water while the concrete is still plastic is known as 'plastic shrinkage', while a reduction in volume by the chemical combination of cement with water is known as 'autogenous shrinkage', and more specifically 'carbonation shrinkage' is a product of the reaction of CO_2 with hydrated cement. These are discussed in more detail in the following sections, as are the mechanisms of shrinkage and swelling. [17,23,24,57,58]

2.5.1.1 Plastic Shrinkage

Shrinkage which occurs before the concrete has set is known as *plastic shrinkage*. This occurs due to the loss of free water with, or even without, significant settlement of solids in the mix. Since evaporation usually accounts for a large proportion the water losses, plastic shrinkage is most common over large surface areas (i.e. slab construction) and is characterised by the appearance of surface cracks which can extend quite deeply into the concrete, therefore affecting the durability of the concrete while also being aesthetically undesirable. This is known as plastic shrinkage cracking and can be controlled by complete prevention of evaporation immediately after casting by making the mix more cohesive, and by covering concrete with wet hessian.[14,16,23,24,58]

A study by Samman *et al*[59] indicates that crack behaviour of NSC is much less severe than that of HPC even when the HPC is subjected to lower rates of evaporation. This is confirmed by Branch *et al*[60] and Hammer[61] who report a rapid development under-pressure of the pore water at the surface of the concrete on external drying, reflecting increasing tensile stress in the pore water. Thus the pore water pressure development at the surface may influence the tensile strain capacity.

2.5.1.2 Autogenous Shrinkage

Volume changes that occur after setting has taken place may be in the form of shrinkage or swelling. Continued hydration when a supply of water is present, leads to expansion. However, when no moisture movement to or from the paste is permitted, shrinkage occurs. This shrinkage is the consequence of withdrawal of water from the capillary pores by the hydration of the hitherto unhydrated cement, a process known as self-dessication. The menisci appearing in the capillary system create tensile stresses within the cement paste, which shrinks under these stresses. The resulting shrinkage of the concrete is called *autogenous shrinkage*. The contraction of the cement paste is restrained by the rigid skeleton of the already hydrated cement paste and also by the aggregate particles. In consequence, autogenous shrinkage of concrete is of a magnitude smaller than in neat cement paste.[24,62]

Both Tazawa and Miyazawa[46,47] and Lee *et al*[65] indicate that in contrast to drying shrinkage, autogenous shrinkage increases as the w/c ratio decreases and the microstructure of the cement paste becomes denser. Therefore, autogenous shrinkage is more significant for HPC, and at low w/c ratios autogenous shrinkage is almost the same as drying shrinkage. Work by Igarashi *et al*[66,67] and Miyazawa and Monteiro[68] found that restrained autogenous shrinkage at early ages results in a relatively high internal stress for low w/b ratio concrete, that sometimes causes premature cracking when the ratio between the restraining stress and the tensile strength approaches 50%. Aïtcin[62] suggests that it is possible to avoid or minimise autogenous shrinkage by water curing concrete using external sources of water. Interestingly, Persson[69] found that the occurrence of autogenous shrinkage in high performance concrete coincided with no loss of weight in the concrete specimens.

2.5.1.3 Drying Shrinkage

When hardened concrete, cured in water, is allowed to dry it first loses water from its voids and capillary pores and only starts to shrink during further drying when water is drawn out of its cement paste. This process is known as *drying shrinkage*. It is common, in practice, for concrete to undergo alternating periods of wetting and drying. Figure 2.11 shows moisture movement in concrete due to this pattern of alternative wetting and drying. It can be seen that maximum shrinkage occurs on first drying, a large proportion of which is irreversible. Further cycles of wetting and drying result in shrinkage that is reversible. Concrete subjected to wetting and drying in this manner approaches the same shrinkage level as that caused by complete drying. Furthermore, Figure 2.11 indicates that, in practice a range of possible shrinkage values may be taken depending on the condition of the specimen or structure.[14,16,23,24, 57,58,66]

Similarly to plastic shrinkage, when concrete is prevented from shrinking freely as it dries, tensile stresses develop which may be sufficiently large to initiate cracking. Numerous authors have shown that cracking increases with the use of HPC[50,58,70-73]. Wiegrink *et al*[80] have shown that cracking develops much faster and is significantly wider in HPC than NSC. Even though HPC had a higher tensile strength than NSC at all ages, its shrinkage cracking was substantially poorer, possibly due to higher free shrinkage, lower specific creep, higher E and lower aggregate interlock along the cracked faces.

2.5.1.4 Carbonation Shrinkage

Carbon dioxide (CO_2) from the air reacts, in the presence of moisture, with hydrated cement resulting in carbonation which can cause shrinkage of the concrete called *carbonation shrinkage*. Carbonation proceeds from the surface inwards at an extremely slow rate. The actual rate of carbonation depends on the permeability of the concrete, its moisture content, and on the CO_2 content and relative humidity of the ambient medium. It has been previously mentioned that the permeability of concrete is governed by the w/c ratio and the effectiveness of curing. Therefore, inadequately cured concrete at high w/c ratios will be more susceptible to carbonation. Carbonation of OPC concrete results in slightly increased strength, and reduced permeability. More importantly, carbonation neutralises the alkaline nature of the hydrated cement paste, leaving any steel reinforcement prone to corrosion.[23,24]

Figure 2.12 shows drying and carbonation shrinkage of mortar at different relative humidities. It can be seen that carbonation increases shrinkage at intermediate humidities but not at 100% or 25%. If the pores are full of water, the diffusion of CO_2 into the paste is slow, while if there is insufficient water in the pores within the cement paste, then CO_2 cannot form carbonic acid. As a result, carbonation is greater in concrete protected from direct rain but exposed to moist air, than concrete periodically washed by rain.[23,24]

Shrinkage studies by Persson[69,72] show that carbonation shrinkage of HPC is related to w/c ratio and SF content. At low w/c ratios (< 0.28) and high SF content (10%), no carbonation shrinkage was observed within four years. This is useful when using HPC since carbonation shrinkage can be more or less eliminated.

2.5.1.5 Swelling

Cement paste or concrete cured continuously in water from the time of placing exhibits a noticeably small but continuous swelling of the hcp as illustrated in Figure 2.11. The water content first increases due to absorption of water by the cement gel, to make up for the self-

dessication during hydration and to keep the paste saturated. Additional water is drawn into the C-S-H structure to cause the net increase in volume and also, this ingress of water reduces the surface tension of the gel and a further expansion takes place. This is characteristic of many gels, but in hcp the expansion is resisted by the skeletal structure so that the swelling is small compared to the drying shrinkage strains.[14,16,23,24,57]

The observed swelling of sealed concrete subjected to drying before sealing can be explained by the release of surface tension of capillary water due to the change in vapour pressure above the water menisci, as reported by Kovler.[75]

2.5.2 Mechanisms of Shrinkage and Swelling

This part of the review of literature draws heavily on a Chapter by Illston[14], in the book 'Construction Materials'. Although the book was published some 10 years ago, this Chapter dealing with shrinkage and swelling mechanisms, provides a good summary of the background information required for a basic understanding of the phenomenon. Four principal mechanisms have been proposed for describing shrinkage and swelling in cement pastes.

2.5.2.1 Capillary Tension

Free water surfaces in the capillary and larger gel pores will be in surface tension, and when the water starts to evaporate due to a lowering of the ambient vapour pressure, the free surface becomes concave and the surface tension increases, as shown in Figure 2.13. The tensile stress within the water near the meniscus must be balanced by the compressive stress in the surrounding solid. Hence the evaporation which causes an increase in the tensile stress will subject the hcp solid to increased compressive stress which will result in a decrease in volume, i.e. shrinkage.

The width of the meniscus cannot be smaller than that of the capillary, and the pore therefore empties at the corresponding vapour pressure. Hence on exposing cement paste to a steadily decreasing vapour pressure, the pores gradually empty according to size, the widest first. Higher w/c ratio pastes with higher porosities will therefore shrink more. As a pore empties, the imposed stresses on the surrounding solid reduce to zero, and hence a full recovery of shrinkage would be expected on complete drying. Since this does not occur, it is generally accepted that other mechanisms become operational at low humidities, and this mechanism only applies at relative humidities above 50%.[14,23,24]

2.5.2.2 Surface Tension

The surface of both solid and liquid materials will be in a state of tension due to the net attractive forces of the molecules within the material. Work therefore has to be done against this force to increase the surface area, and the surface energy is defined as the work required to increase the surface by unit area.

Surface tension forces induce significant compressive stresses in the material and in the hcp solids, whose average particle size is very small. Adsorption of water molecules on to the surface of the particles reduces the surface energy, hence reducing the balancing internal compressive stresses, leading to an overall volume increase, i.e. swelling. This process is also reversible.

There are differing opinions as to the importance of this effect and its contribution to overall shrinkage. As the greatest change in surface energy occurs when water molecules are adsorbed or desorbed on to dry or nearly dry surfaces, it is unlikely that this mechanism will be significant at lower vapour pressures.[14,23,24]

2.5.2.3 Disjoining Pressure

A typical gel pore is shown in Figure 2.14, narrowing from a wider section containing free water in contact with vapour to a much narrower space between the solid in which all the water is under the influence of surface forces. The two layers are prevented from moving apart by an interparticle force i.e. van der Waals bond. The adsorbed water forms a layer about 1.3 nm thick on the solid surface at saturation, which is under pressure from the surface attractive forces. In regions narrower than 2.6 nm, the interlayer water will be in an area of hindered adsorption. This results in the development of a swelling or disjoining pressure, which is balanced by a tension in the interparticle bond. On drying, the thickness of the adsorbed water layer reduces, as does the area of hindered adsorption, hence reducing the disjoining pressure. This results in an overall shrinkage.[14,23,24]

2.5.2.4 Movement of Interlayer Water

The previous mechanisms refer to free and adsorbed water only. The third type of evaporable water, the interlayer water, may also have a role to play. Its intimate contact with the solid surfaces and the tortuosity of its path to the open air suggest that a steep hygrometric gradient is needed to move it, but also that such movement is likely to result in significantly higher shrinkage than the movement of an equal amount of free or adsorbed water.[14,24]

2.5.3 Irreversible Shrinkage

Some of the shrinkage that occurs in the first cycles of drying and wetting (Figure 2.11) is irreversible. The irreversible shrinkage is associated with the formation of additional physical and chemical bonds in the cement gel when adsorbed water has been removed. The initial loss of free water from the voids and capillaries, as previously mentioned, induces humidity gradients within the cement paste structure so that with time, water molecules are transferred from the large surface area of the C-S-H into empty capillaries and out of the concrete causing the cement paste to contract. However, the reduction in volume is not equal to the volume of water removed because the initial loss of free water does not cause a significant volumetric contraction of the paste and because of internal restraint to consolidation by the C-S-H structure. Figure 2.15 shows the relationship between drying shrinkage and water loss. The change in slope with moisture losses at relative humidities of less than 10% implies that there is more than one mechanism of shrinkage. It is likely that the mechanism of movement of interlayer water is associated with the steeper slope of the graph at the lower relative humidities.[14,24,25]

Opinion is divided on the relative importance of the above mechanisms and their relative contribution to the total shrinkage. These differences of opinion are clear from Table 2.11, which shows the mechanisms proposed by four main authors, and the suggested humidity levels over which they act.

2.5.4 Factors Influencing Shrinkage

Since shrinkage of cement paste is related to water loss, all the factors that affect drying (i.e. humidity, temperature, and maturity) will also affect shrinkage. Shrinkage is also affected by aggregate content, specimen geometry and cement type.

2.5.4.1 Water

The large surfaces in the hydrated gel gives the hcp a considerable affinity for water, making its overall dimensions water-sensitive, i.e. loss of water results in shrinkage, which is largely recoverable on regain of water. This behaviour can be explained by considering the ways in which water is contained in the paste, and can be classified into different types depending on the degree of difficulty of removal, as shown in Figure 2.16 and explained as follows:[14,16,23,24,78]

Water vapour – If larger voids are only partially filled with water, then the remaining space will contain water vapour at a pressure in equilibrium with the relative humidity and temperature of the surrounding environment.

Capillary water – Bulk water, located in the capillary pores and gel pores larger than 5nm diameter, which is free from the influence of the attractive forces of solid surfaces. Water in voids larger than 50nm can be considered as free water and its removal will not constitute any overall volume change. However, water in voids smaller than 50nm is subject to capillary tension forces, and its removal at normal temperatures and humidities may result in shrinkage.

Absorbed water – Water that is close to solid surfaces and under the influence of surface attractive forces. This is the main contributor to drying shrinkage as a large proportion is lost on drying at 30% relative humidity.

Interlayer water – This water is contained in gel pores, under the influence of two surfaces and hence strongly held. It can be removed only by strong drying at elevated temperatures and/or relative humidities less than 10%, but its loss results in considerable shrinkage, the van der Waals forces being able to pull the solid surfaces closer together.

Chemically combined water – This is the water that has combined with the fresh cement during the hydration process and not lost on drying, but can be evolved when the paste is decomposed by heating to high temperatures in excess of 1000°C.

There is a considerable overlap between the removal of water of different states, resulting in a continuous loss of water and shrinkage as the relative humidity is reduced. The effect of w/c ratio on shrinkage is demonstrated in Figure 2.17. At earlier stages when the shrinkage rate is high, the w/c ratio has no significant effect on shrinkage. At later stages however, shrinkage decreases with the decrease in the w/c ratio, and stops at an earlier age for cements with low w/c ratios.[11,14,23,24,71] The shrinkage data can be expressed in terms of water-loss as shown in Figure 2.18. Shrinkage up to 28-days is essentially the same for all pastes, as expected, regardless of water lost. The amount of water lost from 28 to 365 days however, is nearly the same for all pastes while shrinkage varies considerably, increasing with the w/c ratio. This variation in shrinkage can be attributed to the way in which water is contained in the paste, as mentioned above. Water is initially lost from the larger pores (i.e. capillary pores) and only on more intensive drying do the smaller pores (i.e. gel pores) begin to empty. Therefore, the amount of water loss may cause different amounts of shrinkage when the ratio of gel to capillary water is not the same.[23,24]

Tazawa and Miyazawa[80] report that as the w/b ratio decreases, autogenous shrinkage increases. Therefore the decreasing shrinkage reported by other authors can be attributed to drying shrinkage. At a w/b ratio of 0.17, shrinkage can be completely attributed to autogenous shrinkage. El-baden[11] reports that HPC has a higher early rate of shrinkage but lower weight loss development than NSC, indicating a linear relationship between shrinkage and weight loss. This may be attributed to the lower porosity of the HPC caused by the reduction in w/b ratio and contribution of SF.

2.5.4.2 Aggregate

Drying shrinkage of concrete is less than that of neat cement paste (typically 10-30%) due to the restraining action of the aggregate which is generally dimensionally stable during changing moisture states. The amount of restraint depends on two main factors, the aggregate content (i.e. volume), and its modulus of elasticity (E) (stiffness).

Figure 2.19 shows the influence of aggregate content on the ratio of shrinkage of concrete to that of neat cement paste. The maximum size and grading of aggregate do not directly influence the magnitude of shrinkage in concrete at a given aggregate volume and a given w/c ratio. However, the use of larger aggregate permits the use of a leaner mix at a constant w/c ratio, such that larger aggregate leads to lower shrinkage. It can be seen from Figure 2.20 that for a given aggregate content, shrinkage of concrete is a function of w/c ratio. At a constant w/c ratio, shrinkage increases with an increase in the cement content because this results in a larger volume of hydrated cement paste which is liable to shrinkage. However, at a given workability (i.e. a constant water content), shrinkage is unaffected by an increase in the cement content, or may even decrease, because the w/c ratio is reduced and the concrete is therefore better able to resist shrinkage. This is demonstrated in Figure 2.21.[14, 23-25]

The effect of aggregate stiffness on concrete shrinkage is shown in Figure 2.22. Normal density aggregates have a higher E value and are therefore stiffer and provide more restraint than lightweight aggregates. Hence, lightweight aggregates tend to have a higher shrinkage than normal density concretes of similar volumetric proportions. Even within the range of ordinary aggregates, there is a considerable variation in shrinkage of the resulting concrete. Figure 2.23 shows shrinkage of concretes of fixed mix proportions, but made with different aggregates.

Miyazawa and Monteiro[68], reported that HPC in moist conditions had a higher decrease in volume than mortar containing the same aggregate volume fraction. This difference is

attributed to the higher porosity in the transition zone between the aggregate and the cement paste.

2.5.4.3 Relative Humidity and Temperature

Relative Humidity (RH) is the amount of water vapour within the air, relative to the maximum amount that would be held in saturated air at the same temperature. In effect, temperature affects the RH of the environment in which concrete is placed. The RH of the air surrounding concrete greatly affects the magnitude of shrinkage as shown in Figure 2.24. It can be seen that swelling in water at 100% RH, is six times smaller than shrinkage in air at 70% RH or eight times smaller than shrinkage in air at 50% RH. Thus as previously mentioned, concrete placed in a 'dry' (unsaturated) environment shrinks, while it swells in water or saturated air. This indicates that the vapour pressure within the cement paste is always less than the saturated vapour pressure, and it is logical to expect that there is an intermediate humidity at which the paste would be in hygral equilibrium.[23,24,86,87]

2.5.4.4 Specimen Geometry

The size and shape of a concrete specimen will influence the rate of moisture loss and the degree of overall restraint provided by the central core, which will have a higher moisture content than the surface. In general terms, the lower shrinkage of large members is due to the fact that only the outer part of the concrete is drying and its shrinkage is restrained by the non-shrinking core. The rate and amount of shrinkage, and the tendency for the surface zones to crack are therefore affected by geometry. The shape of the specimen will affect shrinkage, and is expressed as a function of the volume/surface ratio of the specimen. Longer moisture diffusion paths lead to lower shrinkage rates, e.g. a T beam has a high surface/volume ratio and will therefore dry and consequently shrink more rapidly than a beam with a square cross-section of the same area.[14,23,24]

Both Tazawa and Miyazawa[64] and Alumudaiheen and Hansen[89] have indicated that the effect of specimen size is negligible or even independent of drying shrinkage. However, Tazawa and Miyazawa[64] have observed that this is not the case with autogenous shrinkage. Size effects are noticeable not only with water-cured specimens, but also with concrete sealed immediately after placing. Work by Miyazawa and Monteiro[68] has demonstrated that small specimens swell, while large specimens shrink during the first two weeks of testing. This may be because the curing water can only permeate a small way into the surface of the concrete and so the inside of larger specimens is subjected to self-dessication, which leads to autogenous

shrinkage. El-baden[11] has shown this to be the same for HPC. Autogenous shrinkage increases as the specimen size increases, and the w/b ratio decreases.

2.5.4.5 Cement Type

A study of 199 different Portland cements in the USA[14], found that shrinkage of concrete specimens made with otherwise identical mixes varied between 150 and 400 microstrain after drying for eight weeks. It was determined that changes in C_3A and sulphate content were responsible for the greatest variations in shrinkage, but other variables such as alkali content and fineness also have a significant effect. This is a current problem in concrete mix design in that, mix proportions are specified for the cement that is readily available. However, as cement technology progresses rapidly, its composition varies slightly, but enough to alter important properties such as creep and shrinkage. Tazawa and Miyazawa[80] have found that the composition of a cement has a greater influence on autogenous shrinkage than on drying shrinkage. Furthermore, autogenous shrinkage increases with cements containing increasing C_3A and C_4AF content.

2.5.4.6 Admixtures

The introduction of admixtures into a concrete mix (i.e. as with high performance concrete) can have a marked effect on the shrinkage of concrete. The inclusion of SF has already been referred to regarding the control and elimination of carbonation shrinkage. It has also been observed that the presence of SF reduces shrinkage strains considerably, and this is accounted for by the much lower rate of weight loss, probably due to its much finer pore structure.[24,36,48,50,71,90] Jianyong and Yan[90] noted that the use of SF along with ultra fine ggbs can not only greatly reduce shrinkage by increasing packing, but can substantially promote the hydration of cement, increasing the amount of C-S-H in the cement paste giving the hardened concrete a stronger structure and higher resistance to deformation. However, Shah *et al*[70], have shown that cracking increases with the use of HPC, especially with SF addition. This may be attributed to increased brittleness, increased microcracking, and decreased creep relaxation.

Experimental work by Brooks[91], shows that the inclusion of water reducers (SP) in concrete can have a shrinkage reduction of around 20% compared with concrete of the same mix proportions but without admixtures. The use of specialist shrinkage reducing admixtures (SRA) has been found to significantly reduce drying shrinkage (and subsequently cracking), by nearly 50%, with a 2% addition of SRA by weight of cement.[70,92,93] Bentz *et al*[93] have concluded that SRA are beneficial to concretes with low w/c ratios that are undergoing self-

dessication. The SRA maintains a higher internal RH and reduces autogenous shrinkage. Lee *et al*[65] observed that the inclusion of pfa in concrete resulted in a decrease in autogenous shrinkage, as are some types of admixtures, such as surface tension reducing agents, water-repellent-treated powders and expansive admixtures.[80]

2.6 Creep

When a concrete specimen is subjected to loading, the specimen first shows an instantaneous deformation which is then followed by a further gradual deformation increase. This slow increase of deformation, discovered by Hatt in 1907, is called creep. As previously discussed, concrete specimens slowly deform in time even in the absence of applied loads by means of shrinkage. It is generally accepted that creep and shrinkage are independent of each other, and cumulative. However the two types of deformation should not be considered as additive, but interdependent; simultaneous shrinkage effectively increases the magnitude of creep.

2.6.1 Classification of Deformations

The relationship between stress and strain for concrete that occurs over time is due to creep. Creep is defined as the increase in strain under a sustained constant stress, taking into account other time-dependant deformations not associated with stress, such as shrinkage, swelling and thermal deformations. Since this increase in strain can be several times as large as the strain on loading, creep is of considerable importance in structures.

2.6.1.1 Creep

In its most general form, the behaviour of a material subjected to creep strain over time is shown in Figure 2.25. The strain at zero time is primarily elastic, but may include a non-elastic component. Thereafter, there are three stages of creep. In the primary creep range, the rate of creep decreases with time. If the material exhibits a minimum creep rate, the secondary creep range (sometimes referred to as stationary creep) designates the range of steady state creep. The straight line relationship of secondary creep may be a convenient approximation when the magnitude of this creep is large compared with primary creep. The tertiary creep component may not occur, depending on whether there is an increase in stress or not. For example, in concrete this may arise from an increase in creep due to microcracking at high stresses. For normal working levels of stress in concrete (typically 25-40% of the short-term strength), primary creep cannot be distinguished from secondary creep, and tertiary creep

does not exist. The stress and strain curves over time are shown in Figure 2.26, and creep is simply defined as the gradual increase in strain with time under a sustained stress.[14-17, 23-25,94]

The strain at loading is mainly elastic strain and corresponds to the static modulus of elasticity at the age at which load is first applied. It is important to note that since elastic modulus increases with time, the elastic strain decreases with time. Thus, creep should be regarded as strain in excess of the elastic strain at the time considered, and not in excess of the elastic strain at the time of application of load.[14-17, 23-25,94]

It is important to distinguish between creep of concrete under conditions of no moisture movement to or from the ambient medium (hygral equilibrium), known as *basic creep*, and the additional creep caused by drying, known as *drying creep*. This is illustrated in Figure 2.27. Basic creep is often used to describe creep of concrete stored in water. In such a case, when the swelling as measured on an unloaded specimen is small compared with creep under a compressive load, the conditions approximate to those of no moisture exchange. The combination of basic and drying creep is termed *total creep*. Shrinkage, elastic deformation and creep are expressed as strain i.e. dimensionless quantities. However, it is sometimes convenient to give the magnitudes of the elastic deformation and creep not for the actual stress applied (usually expressed as a proportion of the short-term strength) but per unit stress. Such values are called *specific elastic strain* and *specific creep*.[14-17, 23-25,94]

To date, there is little information available regarding the creep behaviour of HPC. Nagataki and Yonekuru[73] have shown that the specific creep of stressed HPC is approximately between a quarter and a fifth of NSC. Previous work by this author (Howells[13]) has found that the rate of gain in strain for HPC is greater than that of NSC, a property which is similar to shrinkage in HPC as found by El-baden[11].

2.6.1.2 Instantaneous Strain

The strain at loading is known as *instantaneous strain*, and depends on the rate of application of load, therefore making the demarcation between elastic and creep strains difficult, especially when comparing creep data from different sources. For practical purposes, the assumption that the elastic strain on loading is not distinguishable from the observed instantaneous deformation is convenient. The assumption makes it possible to separate out the two important types of deformation: that which occurs on application of load, and that which occurs with the passage of time while the load continues to act.[94]

2.6.1.3 Creep Recovery

It has so far been implied that a sustained stress, once applied, continues to act. This is the case when considering the self-weight of a member, but many other loads, although sustained, do not act indefinitely. When the stress is removed after some time, the strain decreases immediately by an amount equal to the elastic strain. This strain is generally smaller than the initial elastic strain because of the increase in the modulus of elasticity with age. The instantaneous recovery is followed by a gradual decrease in strain, termed *creep recovery*. Creep recovery is important when it is necessary to estimate stresses when relaxation occurs such as in prestressed concrete.[14-17, 23-25,94]

2.6.1.4 Relaxation

Under certain circumstances, the deformation of a concrete member may be kept constant or varied in a predetermined manner, the stress varying accordingly. Under conditions of constant strain, the manifestation of creep action is a lowering of the stress, which is defined as *relaxation*. Relaxation and creep are closely connected, physically.[14-17, 23-25,94]

2.6.2 Mechanisms of Creep

An understanding of the mechanism of creep is difficult to attain since no theory exists to provide a singularly accurate and concise explanation. Numerous hypotheses have been put forward, each of which can explain a number of observations and accords fully with certain experimental results. It is likely that the actual mechanism of creep involves a combination of two or more of these proposed mechanisms, which will now be discussed. As creep is partly reversible, it can be considered that it may consist of a partly visco-elastic movement (consisting of a purely viscous phase and a purely elastic phase) and also a non-reversible plastic deformation. An *elastic* deformation is always recoverable on unloading. A *plastic* deformation is never recoverable, can be time-dependent, and there is no proportionality between plastic strain and the applied stress, or between stress and rate of strain. A *viscous* deformation is never recoverable on unloading, is always time-dependent, and there is always proportionality between the rate of strain and the applied stress, and hence between stress and strain at a given time. These various types of deformation can be summarised as shown in Table 2.12, and provide a basis for some of the following hypotheses, which have been summarised from work by Neville *et al*[94] and Ali and Kesler[95].

2.6.2.1 Plastic Deformations

Plastic deformations include inter crystalline slips and local rupture of the hardened cement paste, and possibly the aggregate. As previously mentioned, such deformations would be irrecoverable, non-linear with the applied stress and occur after a limiting stress is exceeded. Creep of concrete does have an irrecoverable part, but there is no apparent threshold of stress below which there is no creep. Strain at any instant is practically in linear proportion to the sustained stress up to stress levels as high as 50% of the ultimate. The great sensitivity of creep to moisture and moisture movement cannot be explained in terms of the plastic deformation mechanism. Such deformations might contribute significantly only at stress levels near the ultimate.

2.6.2.2 Delayed Elasticity

The behaviour of concrete under load can be attributed to internal stresses induced as a result of the change in the form of the capillary structure of cement paste due to load. It is assumed that under a compressive stress, the capillaries are deformed and the water meniscus displaced outward to a point where the capillary diameter is larger, so that the tension under which the capillary water is held is decreased. This reduces the induced compressive stress and partially offsets the applied external stress. However, hygral equilibrium is upset with the result that the water will evaporate from the capillaries until the vapour pressure is reduced to the ambient value. The tension in the capillary water rises, and compression in the solid phase increases such that equilibrium is maintained. The resultant deformation constitutes creep.

2.6.2.3 Viscous Flow

Hardened cement paste may be considered as a viscous fluid, surrounding the loose and relatively rigid aggregate particles. The concept offers plausible explanations for the linearity of creep strain with stress, the absence of a limiting stress for creep to occur, stress relaxation at a constant deformation, and the sensitivity of creep to temperature. It cannot, however, explain either wholly or partially certain observed characteristics of creep. These include creep recovery on removal of the applied stress, volume change during creep, the progressive reduction of the creep rate with time and the marked sensitivity of creep to moisture exchange.

2.6.2.4 Visco-elastic Flow

The morphology of hydrated cement indicates the presence of both crystalline and noncrystalline components of colloidal size with associated absorbed moisture. Under load, the gel could presumably behave as a composite body consisting of more or less elastic and viscous phases which could interact, resulting in delayed elastic behaviour. Creep of concrete exhibits such behaviour, but to a rather limited extent. This mechanism cannot offer a convincing explanation of the observed influence of moisture exchange on creep.

2.6.2.5 Seepage of Gel Water

Hardened cement paste has been considered as a limited swelling gel, whose equilibrium with its solid skeleton and external load is determined by the vapour pressure of the gel water. The seepage theory envisages a disturbance of such equilibrium under applied load and its gradual re-establishment by exchange of moisture with the environment. The volume change accompanying the resulting moisture movement is identified with creep. Such a process which describes the marked increase in creep under compression with simultaneous drying, may well be an appropriate description of the mechanism of drying creep.

An approach describing an abnormal deformation of concrete under drying creep as a sum of shrinkage-induced creep and creep-induced shrinkage was put forward by Kovler[96], in which the shrinkage-induced creep is linearly proportional to free shrinkage strain, and the creep-induced shrinkage is linearly proportional to basic creep, but should depend on the intensity of shrinkage. When drying creep is under tension, initially the creep-induced shrinkage is dominating, and the total time dependent strain is less than the sum of the basic creep and free shrinkage which is the opposite to its behaviour in compression. However, later on the creep-induced shrinkage becomes dominant, and the total strain becomes larger than the previous sum, which is similar to that in compression. Kovler[75,97], revised this approach suggesting that the abnormal behaviour of drying creep strain in the initial period of drying, when drying creep is contrary to load direction, indicates the possibility of additional swelling deformation of sealed concrete due to a release of surface tension of capillary water due to the change of vapour pressure above water menisci, similar to that of delayed elasticity.

2.6.2.6 Non-uniform Shrinkage

The presence of differential shrinkage stresses due to non-uniform drying, has occasionally been considered partly or wholly responsible for the phenomenon of creep in concrete. The validity of the assumptions involved in the concept that creep is entirely the result of

restrained shrinkage has been seriously challenged. Only a small part of the increase in creep with simultaneous drying, especially at high stresses, may be explained on this basis.

2.6.2.7 Intercrystalline Deformation

Imperfectly formed crystal lattices are known to suffer viscous deformation under sustained stress. Such disordered zones are likely to exist not only where the crystalline components of cement gel grow into each other, but also at the gel-aggregate interface. Although such deformations would be expected to progress very slowly, the almost constant rate of flow could result in sizeable deformations after a sufficiently long time.

2.6.3 Factors Influencing Creep

Creep is sensitive to many properties of concrete, the most influential of which will now be discussed.

2.6.3.1 Cement

Creep is affected by the type of cement in so far as it influences the strength of the concrete at the time of application of load. Neville and Brooks[23] have stated that on the basis of equality of the stress/strength ratio, most Portland cements lead to sensibly the same creep. On the other hand, on the basis of equality of stress, the specific creep increases (in the order of type of cement) as follows: high-alumina cement, rapid-hardening and ordinary Portland cement (OPC). The order of magnitude of creep of Portland blast-furnace, low-heat Portland cement and Portland-pozzolan cements is less clear, and so is the influence of partial replacement of cement by blast-furnace slag or by fly-ash (pfa) as the effect depends upon the storage environment. For example, when compared with OPC, for sealed concrete, creep decreases with an increase in the level of replacement of slag or of fly-ash but, when there is concurrent drying, creep is sometimes higher. When such concrete is to be used it is recommended that tests be undertaken to assess creep.[23,24,94,98,99]

The cement paste content of structural concrete nearly always lies within the range 28-40% by volume. Within this range, creep (for a given strength/stress ratio) can be assumed to increase at the approximate rate of 5% for each percent increase in the cement paste content. Creep of concrete is due to the deformations that occur in the cement paste, since aggregate does not creep under load; hence the increase in creep with cement paste content.[99]

2.6.3.2 Aggregate

As previously mentioned, in normal weight aggregate concrete, the source of creep is the hardened cement paste since the aggregate is not liable to creep at the level of stress existing in the concrete. Because the aggregate is stiffer than the cement paste, the main contribution of the aggregate is to restrain the creep in the cement paste, the effect depending upon the elastic modulus of the aggregate and its volumetric proportion. Hence, the stiffer the aggregate the lower the creep and the higher the volume of aggregate, the lower the creep. This can be seen in Figures 2.28 and 2.29 respectively. Porosity of aggregate has also been found to influence the creep of concrete, but since aggregates with a higher porosity generally have a lower modulus of elasticity, it is possible that porosity is not an independent factor in creep. However, aggregates with higher absorption tend to remove water from the cement paste, thereby reducing the capillary pore space and decreasing the creep potential of the cement paste, and this may be directly associated with creep.[23,24,94,98,99] Igarashi *et al*[67], confirmed that aggregate has a diluting effect on creep but the extent of the reduction is different at early ages. The effect is due to the development of stress induced by the restrained autogenous shrinkage.

2.6.3.3 Admixtures

There is varying information available regarding the effect that the inclusion of admixtures has on the creep of concrete. The effect of inclusion of SF in the mix, in particular, is the subject of conflicting reports. Brooks[91] reports a small reduction in creep for small quantities of SF, but beyond an approximate 16% dosage there is an increase in creep. Persson[55] found that for short-term and long-term creep, the creep rate was slightly reduced when 10% SF was used compared with 5% SF with the same amount of cement. A series of papers by Igarashi *et al*[66,67,100], have shown that the addition of SF increases the early age tensile creep of HPC compared to NSC of the same w/b ratio but containing no SF. This is useful as the enhanced creep provides a mechanism to relieve the restraining stress induced in the concrete by autogenous shrinkage. However, Wiegrink *et al*[50] have noted a reduction in specific creep with increasing SF content, while Jianyong and Yan[90] noted a decrease in creep with the addition of SF and ggbs, though this may be due to the ggbs and not the SF. Brooks[91] found that creep in HPC was reduced by 20% when a water reducer was included in the mix, and also by 20% with an increase in ggbs and fly ash.

2.6.3.4 Water/Cement Ratio

As previously mentioned in Section 2.4, the water/cement (w/c) ratio is the main factor influencing the strength of concrete. Thus the effect of a decrease in w/c ratio is to decrease creep. Figure 2.30 shows the range of results obtained for the effect of w/c ratio on the creep of concrete, relative to creep at a w/c ratio of 0.65. Furthermore, for a given aggregate/cement ratio, a decrease in w/c ratio decreases the cement paste content and hence the creep. Therefore it can be expected that creep and strength are related. Indeed, within a wide range of mixes, creep is inversely proportional to the strength of concrete at the age of application of the load. Moreover, for a given type of concrete, we can expect creep to decrease as the age at application of load increases because, of course, strength increases with age. This effect is depicted in Figure 2.31.[14,16,23-25,94,98,99] Two studies by Igarashi *et al*[66,67] have determined that for HPC, a decrease in w/b ratio results in a higher creep strain. This may confirm what was discussed in Section 2.6.3.3, i.e. that the inclusion of SF in the mix causes an increase in creep, which overrides the effect of lowering the w/b ratio.

2.6.3.5 Relative Humidity and Temperature

One of the most important external factors influencing creep is the relative humidity (RH) of the air surrounding the concrete, and the influence of RH on creep and on shrinkage is similar. Creep is generally higher the lower the RH, for a given concrete and for specimens cured at a relative humidity of 100 per cent, then loaded and exposed to different humidities as illustrated in Figure 2.32. Thus, even though shrinkage has been taken into account in determining creep, there is still an influence of drying on creep as previously discussed. This influence of relative humidity is much smaller or absent, in the case of specimens which have been allowed to dry prior to application of load so that hygral equilibrium with the surrounding medium exists under load; in this case, creep is much reduced. However, such a practice is not normally recommended as a means of reducing creep, especially for young concrete, because inadequate curing will lead to a low tensile strength and possibly to shrinkage-induced cracking.[14,16,23-25,94,98,99]

Creep is smaller when concrete is cured at a high temperature because strength is higher than when concrete is cured at normal temperature before heating and loading. If unsealed concrete is subjected to a high temperature at the same time as, or just prior to, the application of load, there is a rapid increase in creep as the temperature increases to approximately 50 °C (about 120 °F), then a decrease in creep down to about 120 °C (about 250 °F), followed by another increase in creep to at least 400 °C (about 750 °F) as shown in Figure 2.39. The initial

increase in creep is due to a rapid expulsion of evaporable water; when all of that water has been removed, creep is greatly reduced and becomes equal to that of pre-dried (desiccated) concrete.

2.6.3.6 Stress and Strength

In the discussion so far we have compared the influence of the various factors on creep on the basis of equality of stress. Of course, creep is affected by stress, and normally creep is assumed to be directly proportional to the applied stress up to about 40 per cent of the short-term strength, i.e. within the range of working or design stresses. Hence, we can use the term: specific creep, i.e. creep per unit of stress. Above 40 to 50 per cent of the short-term strength, microcracking contributes to creep so that the creep-stress relationship becomes non-linear, creep increasing at an increasing rate. Furthermore, it has been found that an alternating load with a given mean stress/strength ratio, leads to a larger time-dependant deformation than a static load corresponding to the same stress/strength ratio. For different concretes of the same cement paste content, creep is approximately proportional to the stress/strength ratio. Hence a concrete of characteristic strength 60 N/mm^2 stressed to 15 N/mm^2 would have approximately the same creep as another concrete of strength 40 N/mm^2 stressed to 10 N/mm^2 provided the two concretes have the same cement paste content. Figure 2.34 shows the increase in the rate of creep between specimens undergoing constant loading, and specimens of increasing stress/strength ratios.[14,16,23-25,94,98,99] Nagataki and Yonekura[73] confirmed that the specific creep of HPC is greatly influenced by unit cement paste volume and compressive strength. Sicard *et al*[101] determined that the intensity of compressive creep load on HPC, disturbs the orientation and density of surface microcracking due to dessication and that recovery after unloading induces surface microcracking, which is strongly oriented in a given direction.

2.6.3.7 Age at and Duration of Loading

The effect that duration of loading has on creep is summarised in Table 2.13. The effect on creep of age at loading is mainly due to the increase in strength of concrete with age. Since, for a given stress, creep is inversely proportional to strength, the effect of age at loading can be estimated provided the strength-age relationship is known. In terms of the structure of the cement paste, the degree of hydration increases with age. Therefore, as the concrete ages, the porosity of the cement paste decreases and the seepage of the adsorbed water becomes more difficult; hence the reduction in creep. Of course, the strength of concrete is also a measure of the degree of hydration; hence the possibility of relating creep to strength.[24,94,98,99]

2.6.3.8 Specimen Geometry

When drying occurs at a constant relative humidity, creep is smaller in a larger specimen; this size effect is expressed in terms of the volume/surface ratio of the concrete member as shown in Figure 2.35. If no drying occurs, as in mass concrete, creep is smaller and is independent of size because there is no additional effect of drying on creep.[23,24,94,98]

2.7 Temperature Effects

Laboratory testing of concrete is usually performed at a controlled temperature, and so the properties associated with fresh and hardened concrete are generally based on the behaviour of concrete at these temperatures. In reality, concrete is mixed at a wide range of temperatures depending on location and situation, while there is always the possibility of exposure to extreme temperatures if fire were to occur. Therefore, variations in temperature may cause problems for both fresh and hardened concrete.

2.7.1 Influence of Temperature on Fresh Concrete

A rise in the curing temperature of concrete speeds up the chemical reactions of hydration and thus affects beneficially the early strength of concrete without any ill effects on the later strength. Higher temperature during and following the initial contact between the cement and water reduces the length of the dormant period so that the overall structure of the hydrated cement paste becomes established very early. Although a higher temperature during placing and setting increases the very early strength, it may adversely affect the strength from about 7 days onwards. The explanation is that a rapid initial hydration does not give the hydration products sufficient time to diffuse throughout the cement paste matrix, hence leaving the interstitial space relatively open, and thus ensuring the hcp is more porous. An increase in pore volume causes the permeability of the concrete to increase and therefore a decrease in durability. This is the same for HPC.[21,40,102-106] Furthermore, increasing the temperature at curing causes earlier cracks to form and therefore a higher degree of plastic shrinkage.[104]

2.7.2 Influence of Temperature on Hardened Concrete

Numerous authors have commented on the reduction in compressive strength and Young's Modulus (E) in NSC and HPC when subjected to temperatures greater than 250°C.[102,105-109] This is closely related to the increased porosity of the hcp, resulting in increased permeability and a reduction in durability. However, it should be noted that the deterioration in durability occurs at lower temperatures than those at which the compressive strength decreases. The

inclusion of the admixtures, silica fume (SF) and pulverised fuel ash (pfa) in the mix have marked effect on the hardened properties of concrete at elevated temperatures. The effect of SF on concrete is to increase the strength, and this continues to be the case at high temperatures despite the reduction in strength caused by the temperature increase.[110,111] Furthermore, the inclusion of pfa results in an increase in compressive strength, tensile strength and flexural strength, which may be due to a delayed pozzolonic reaction.[112,113]

2.8 Creep and Shrinkage Prediction

Modern construction techniques enable concrete structures to be constructed rapidly. The loads occurring due to the construction process can be as large as the design service load. These construction loads can cause significant immediate deflections due to concrete cracking and its low early-age modulus. Due to the large stresses involved and also shrinkage, the time dependant deflections may be unacceptably large. These changes in the construction process, warrant a review of the validity of current creep and shrinkage provisions.

2.8.1 History

Bažant and Baweja[114] stated that realistic prediction of creep and shrinkage of concrete is a formidably difficult problem because the phenomenon is a result of several interacting physical mechanisms and is influenced by many variable factors. In view of this fact it is not surprising that improvements in prediction have been coming only slowly and gradually. No major breakthrough has occurred in the history of the research of this phenomenon; however, the accumulated advancement of knowledge since Ross[115] first proposed a creep prediction chart in 1937, and especially during the last two decades, has been enormous. It is now possible to formulate a much better prediction model than twenty years ago.

Over the last century, there have been numerous prediction models put forward, generally by the three main contributors; the American Concrete Institute (ACI), the Comité Euro-International du Béton (CEB), and Réunion Internationale des Laboratoires d'Essais et de recherche sur les Matériaux et les Constructions (RILEM). These organisations have each produced their own models, while also collaborating to create jointly produced models. The ACI Committee 209 was first organised in the 1930's, and have been producing models since, the most recent being the ACI Committee 209R-82[116] in 1982, and a revised version 209R-92[117] in 1992. The CEB, working in conjunction with the Fédération Internationale de la Précontraine with whom they have recently merged, first produced International Recommendations for Reinforced Concrete Structures in 1964[118] with a revised version in

1970[119]. The most recent contributions are the Model Codes for Concrete Structures, published in 1978[120] and 1990[121]. Guénot *et al*[122] found that CEB-FIP Model Code 1990[104] gives excellent early age results.

RILEM has been the most active by far in the development of prediction models over the past two decades. In 1978, Bažant and Panula[123] collaborated in the formation of a 'new' model for practical prediction of creep and shrinkage. The model was intended to provide large scope verification of test data. This model, which later became known as the BP model, was to a larger extent based on physical considerations and mathematical arguments than preceding models and proved to give much better predictions. This model relied heavily on several parameters pertaining to the composition of the concrete mix. For preliminary design purposes where the composition of the concrete to be used might not be known, a simpler model was desired, and so in 1980, Bažant and Panula[124] updated the BP Model to reflect this naming the updated model BP2. At the same time, both these models were deemed more complex than others, which some engineers found objectionable. Over a decade later, in 1991, Bažant and Panula worked again with Kim and Xi[125] to improve and update the original BP model. This model became known as the BP-KX model and was presented in a series of papers dealing with the prediction of shrinkage, basic creep, drying creep, temperature effects on basic and drying creep, the effects of cyclic stress and cyclic humidity. This model was deemed less complex than the BP model. However, the committees of engineering societies demanded a formula that was not only simple, but also short. Therefore, in 1993 Bažant, Xi and Baweja[126] presented a short form of the BP-KX model, known as the BP-KX+ model in which predictions were based on short-time measurements. Yet greater demand was present for simpler, better theoretically supported models which were as accurate as the previous models had proved to be. To this end in 1995, Bažant and Baweja[114] further refined the current prediction model, incorporating a theoretically derived formula rather than an empirical expression for the drying creep, and calibration of the model by an enlarged data set which included data published over the previous few years. This model was termed the B3 model. The most recent creep and shrinkage prediction model was presented in 1996, again by Bažant and Baweja[127]. This model was termed a short form version of the B3 model and is known as the B3+ model. This improved model is intended to remove the dependence of the model on the composition of the concrete mix, leaving only dependence on the strength and water content of the concrete mix.

Aside from these three main contributors, a number of independent models have been published in the ACI Materials Journal. In 1993, Gardner and Zhao[128] stated that due to the changes in modern construction techniques and materials, a review of the validity of creep

and shrinkage provisions was warranted, and so produced their own model which is now known as the GZ Model. A new version of this model was recently published in the ACI Materials Journal, in 2001 by Gardner and Lockman[129].

In the UK, BS 8110: Part 2: 1985[88] recommends a method of estimating shrinkage and swelling after periods of 6 months and 30 years, as well as ultimate creep, also at 30 years. BS 5400: Part 4: 1990[130], recommends alternative methods for determining creep and shrinkage deformations for steel, concrete and composite bridges. The method takes into account conditions particular to the structure itself and is based on the CEB-FIP International Recommendations 1970[119]. Similarly, the creep and shrinkage design provisions in the British Standard, Eurocode 2: Design of Concrete Structures DD ENV 1992-1-1: 1992[131] is also based heavily on the CEB-FIP International Recommendations 1990[121]. Since many of the models mentioned have either been revised (CEB-FIP, ACI, etc.), or are based on improving preceding models (RILEM, ACI, etc.), then only the more recent and relevant models will be considered in this research project. A brief overview of each will now be given, while complete versions are included in Appendix A. Table 2.14 provides a summary of the main parameters considered in the common prediction models.

2.8.2 BS 8110: Part 2: 1985

BS 8110: Part 2: 1985[88] gives values of shrinkage and swelling after periods of 6 months and 30 years for various relative humidities of storage and effective section thicknesses, as can be observed from Figure 2.36. The data applies to concretes made with high-quality, dense, non-shrinking aggregates and to concretes with an effective original water content of 8% of the original mass of concrete (corresponding to 190 l/m^3 of concrete). For concretes with different water contents, shrinkage may be regarded as proportional to water content within the range of 150 - 230 l/m^3.

The final (30 year) creep strain in concrete, ϵ_{cc}, for various relative humidities of storage and effective section thicknesses, can be predicted from:

$$\epsilon_{cc} = \frac{\text{stress}}{E_t} \times \phi \qquad (2.1)$$

where E_t is the modulus of elasticity of the concrete at the age of loading t, and ϕ is the creep coefficient which may be estimated from Figure 2.37. Parrott[132], whose work formed the basis for the standard, indicates that problems can arise when using Figure 2.37 because creep results from two components of strain, of which only one is affected by drying. The two previously mentioned components, basic and drying creep can be treated individually but, for

a simplified approach, Figure 2.37 should prove adequate when, if drying is prevented by immersion in water or by sealing, the creep factor should be determined on the assumption that the effective section thickness is equal to 600 mm. It can be assumed that about 40%, 60%, and 80% of the final creep develops during the first month, 6 months and 30 months under load respectively, when concrete is exposed to conditions of constant relative humidity. Furthermore, creep is partly recoverable with a reduction in stress. The final recovery after 1 year is approximately 0.3 × stress reduction/E_t.

2.8.3 BS 5400: Part 4: 1990

BS 5400: Part 4: 1990[130] predicts values of shrinkage and creep deformations based on information given in CEB-FIP International Recommendations 1970[119]. The shrinkage strain at any instant may be determined by the product of four partial coefficients:

$$\text{Shrinkage strain} = k_L k_c k_e k_j \tag{2.2}$$

where k_L depends on the environment, k_c depends on the composition of the concrete, k_e depends on the effective thickness of the member, and k_j depends on the development of shrinkage as a function of time. The coefficients can be estimated from Figures 2.38 - 2.41, respectively. In addition it is possible to add a coefficient for internal restraint, k_2, which depends on the geometric ratio of longitudinal reinforcement, ρ.

Similarly, the creep coefficient from Equation 2.1, when E_t is replaced by E_{28} (the secant modulus of elasticity at the age of 28 days, taken from Table 2.15) is equal to the product of five partial coefficients:

$$\phi = k_L k_m k_c k_e k_j \tag{2.3}$$

where k_L, k_c, k_e and k_j are as above and k_m depends on the hardening (maturity) of the concrete at the age of loading and can be estimated from Figure 2.42. For creep, values of k_L and k_e can be taken from Figures 2.43 and 2.44 respectively.

2.8.4 CEB-FIP Model Code 1990

The CEB-FIP Model Code 1990[121] gives the following expressions for predicting time dependent effects. The total strain $\epsilon_c(t)$ at time t (days) of a concrete member uniaxially loaded at time t_0 with a constant stress $\sigma_c(t_0)$ may be expressed as follows:

$$\varepsilon_c(t) = \varepsilon_{ci}(t_0) + \varepsilon_{cc}(t) + \varepsilon_{cs}(t) + \varepsilon_{cT}(t) \tag{2.4}$$

where $\epsilon_{ci}(t_0)$ is the initial strain at loading, $\epsilon_{cc}(t)$ is the creep strain at time $t > t_0$, $\epsilon_{cs}(t)$ is the shrinkage strain and $\epsilon_{cT}(t)$ is the thermal strain. The total shrinkage strain $\epsilon_{cs}(t,t_s)$ may be calculated from:

$$\varepsilon_{cs}(t,t_s) = \varepsilon_{cso}\beta_s(t-t_s) \tag{2.5}$$

where ϵ_{cso} is the notional shrinkage coefficient, β_s is the coefficient to describe the development of shrinkage with time, t is the age of concrete (days), and t_s is the age of concrete at the beginning of shrinkage or swelling i.e. at the end of curing (days). The value of ϵ_{cso} depends on the strength of the concrete, the cement type, the relative humidity of the ambient environment and the size of the concrete specimen. For a constant stress applied at time t_0, the creep strain $\epsilon_{cc}(t,t_0)$ may be calculated from:

$$\varepsilon_{cc}(t,t_0) = \frac{\sigma_c(t_0)}{E_{ci}}\phi(t,t_0) \tag{2.6}$$

where $\phi(t,t_0)$ is the creep coefficient and E_{ci} is the modulus of elasticity at the age of 28 days. The value of $\phi(t,t_0)$ depends on the strength of the concrete, the relative humidity of the ambient environment and the size of the concrete specimen. The thermal strain $\epsilon_{cT}(t)$ due to the thermal expansion of concrete, may be calculated from:

$$\varepsilon_{cT} = \alpha_T \Delta T \tag{2.7}$$

where ΔT is the change in temperature (K), and α_T is the coefficient of thermal expansion (K^{-1}) which for the purpose of structural analysis is generally taken as 10×10^{-6} K^{-1}.

2.8.5 Eurocode 2 1992

The Eurocode 2[131] (EC2) gives the following expressions for predicting time dependent effects. The total strain $\epsilon_{tot}(t,t_0)$ for concrete subjected to initial loading at time t_0 with a stress $\sigma(t,t_0)$ and subjected to subsequent stress variations $\Delta\sigma(t_i)$ at time t_i may be expressed as follows:

$$\varepsilon_{tot}(t,t_0) = \varepsilon_n(t) + \sigma(t_0)J(t,t_0) + \sum J(t,t_i)\Delta\sigma(t_i) \tag{2.8}$$

where $\epsilon_n(t)$ denotes an imposed strain independent of applied stress (e.g. shrinkage, temperature effects), and $J(t,t_0)$ is the creep function at time t. The total shrinkage strain $\epsilon_{cs}(t,t_s)$ may be calculated from:

$$\varepsilon_{cs}(t,t_s) = \varepsilon_{cso}\beta_s(t-t_s) \tag{2.9}$$

where ϵ_{cso} is the notional shrinkage coefficient, β_s is the coefficient to describe the development of shrinkage with time, t is the age of concrete (days), and t_s is the age of concrete at the beginning of shrinkage or swelling i.e. at the end of curing (days). The value of ϵ_{cso} depends on the strength of the concrete, the cement type, the relative humidity of the

ambient environment and the size of the concrete specimen. The creep function is given by the relationship:

$$J(t,t_0) = \frac{1}{E_c(t_0)} + \frac{\phi(t,t_0)}{E_{c28}} \tag{2.10}$$

where $\phi(t,t_0)$ is the creep coefficient, $E_c(t_0)$ is the modulus of elasticity at time t_0, and E_{c28} is the modulus of elasticity at 28 days. The value of $\phi(t,t_0)$ depends on the strength of the concrete, the relative humidity of the ambient environment and the size of the concrete specimen. The effect of temperature on the age of the concrete may be taken into account by modifying the age of loading t_0 in accordance with equation 2.11:

$$t_0 = t_{0,T}\left(\frac{9}{2+(t_{0,T})^{1.2}}+1\right)^{\alpha} \geq 0.5 \tag{2.11}$$

where $t_{0,T}$ is the temperature adjusted age of concrete at loading, and α is constant depending on the type of cement.

2.8.6 ACI Model 1992

The ACI Model 1992[117] gives the following expressions for predicting time dependent effects. The shrinkage strain $(\epsilon_{sh})_t$ at time t (days) from the end of the initial curing, may be calculated from:

$$(\varepsilon_{sh})_t = \frac{t^{\alpha}}{f+t^{\alpha}}(\varepsilon_{sh})_u \tag{2.12}$$

where $(\epsilon_{sh})_u$ is the ultimate shrinkage strain. For standard conditions, constants $\alpha = 1$ and $f = 35$ and 55 for moist and steam curing respectively, and $(\epsilon_{sh})_u = 780 \times 10^{-6}$. For non-standard conditions, the ultimate shrinkage may be calculated from:

$$(\varepsilon_{sh})_u = 780\gamma_{sh} \times 10^{-6} \tag{2.13}$$

where γ_{sh} represents the product of correction factors for loading age, differential shrinkage, curing period, ambient relative humidity, member size, temperature changes and concrete composition. The creep coefficient v_t (ratio of creep strain to initial strain) at time t (days) after loading, may be calculated from:

$$v_t = \frac{t^{\psi}}{d+t^{\psi}} v_u \tag{2.14}$$

where v_u is the ultimate creep coefficient. For standard conditions, constants $\psi = 0.6$ and $d = 10$, and $v_u = 2.35$. For non-standard conditions, the ultimate creep may be calculated from:

$$v_u = 2.35\gamma_c \tag{2.15}$$

where γ_c represents the product of correction factors for loading age, differential shrinkage, curing period, ambient relative humidity, member size, temperature changes and concrete composition. Any strains associated with changes in external temperature are incorporated in the non-standard shrinkage and creep coefficients, γ_{sh} and γ_c.

2.8.7 BP-KX Model 1991

The BP-KX creep and shrinkage prediction model 1991[125] gives the following expressions for predicting time dependent effects. The total strain $\epsilon(t)$ at time t (days) of a concrete member uniaxially loaded at time t' (days) with a constant stress σ may be expressed as follows:

$$\varepsilon(t) = J(t,t')\sigma + \varepsilon_{sh}(t) \tag{2.16}$$

where $\epsilon_{sh}(t)$ is the mean shrinkage strain, $\epsilon_{sh}(t,t_0)$, in the cross-section and may be calculated from:

$$\epsilon_{sh}(t, t_0) = \epsilon_{sh\infty} k_h S(\hat{t}) \tag{2.17}$$

where $\epsilon_{sh\infty}$ is the ultimate shrinkage strain, k_h is the humidity dependence function, and $S(\hat{t})$ is the time function for shrinkage, and t_0 is the age when drying begins (days). The creep strain may be characterised by the secant compliance function $J(t,t',\sigma) = \epsilon/\sigma$ where ϵ is the strain at time t caused by a sustained (constant) uniaxial stress σ applied at time t' (t represents the current age, t' is the age a loading, and t_0 is the age at the start of drying all in days). The compliance function includes the initial instantaneous strain at age t', represented by $J(t,t',\sigma)$. Therefore the total creep strain at time t caused by a unit sustained uniaxial stress applied at time t' may be calculated from:

$$J(t,t',\sigma) = q_1 + F(\sigma)\left[C_0(t,t') + C_d(t,t',t_0)\right] \tag{2.18}$$

where q_1 represents the initial instantaneous strain due to unit stress, $C_0(t,t')$ represents the basic creep compliance which takes into account the effect of temperature, $C_d(t,t',t_0)$ represents the additional creep due to simultaneous drying, while $F(\sigma)$ represents the non-linear dependence on stress.

2.8.8 BP-KX+ Model 1993

The short-form of the BP-KX creep and shrinkage prediction model, denoted BP-KX+ 1991[126], uses the same initial formulae for predicting the time-dependent deformations in concrete as the standard BP-KX Model[125] detailed in Section 2.8.7. The BP-KX formulae for predicting material parameters in the model are simplified by reducing the number of influencing factors taken into consideration, and as such can still be applied to structures that do not have a high sensitivity to creep or shrinkage.

2.8.9 GZ Model 1993

The Gardner-Zhao (GZ) Model 1993[128] gives the following expressions for predicting time dependent effects. The total strain ϵ of a concrete member uniaxially loaded at time t_0 with a constant stress σ may be expressed as follows:

$$\varepsilon = \varepsilon_{sh} + \frac{\sigma}{E_{cmto}} + \frac{\sigma\phi}{E_{cm28}} \tag{2.19}$$

where ϵ_{sh} is the shrinkage strain, E_{cmto} is the mean modulus of elasticity at loading, E_{cm28} is the mean modulus of elasticity at 28 days, and ϕ is the creep coefficient. The total shrinkage strain ϵ_{sh} may be calculated from:

$$\varepsilon_{sh} = \varepsilon_{shu}\beta(h)\beta(t) \tag{2.20}$$

where ϵ_{shu} is the notional ultimate shrinkage strain, $\beta(h)$ is the correction term for the effect of humidity on shrinkage, and $\beta(t)$ is the correction term for the effect of time t, on shrinkage. The value of ϵ_{shu} depends on the strength of the concrete and the cement type. The creep coefficient ϕ may be calculated from:

$$\phi = \left[\frac{7.27 + \ln(t - t_0)}{17.18}\right] \times \left[1.57 + 2.98 \times \left(\frac{f'_{cm28}}{f'_{cmt0}}\right) \times \left(\frac{25}{f'_{cm28}}\right)^{1/2} \times (1 - h^2) \times \left(\frac{t - t_0}{(t - t_0) \times 0.1 \times (V/S)^2}\right)\right] \tag{2.21}$$

where f'_{cm28} is the compressive strength at 28 days, f'_{cmt0} is the compressive strength at the age of loading t_0, h is the humidity, and V/S is the volume/surface ratio.

2.8.10 B3 Model 1995

The B3 creep and shrinkage prediction model 1995[114], gives the following expressions for predicting time dependent effects. The total strain $\epsilon(t)$ at time t (days) of a concrete member uniaxially loaded at time t' (days) with a constant stress σ may be expressed as follows:

$$\varepsilon(t) = J(t,t')\sigma + \varepsilon_{\mathrm{sh}}(t) + \alpha\Delta T(t) \tag{2.22}$$

$\epsilon_{\mathrm{sh}}(t)$ is the mean shrinkage strain, $\epsilon_{\mathrm{sh}}(t,t_0)$, in the cross-section and may be calculated from:

$$\varepsilon_{\mathrm{sh}}(t,t_0) = -\varepsilon_{\mathrm{sh}\infty} k_{\mathrm{h}} S(t) \tag{2.23}$$

where $\epsilon_{\mathrm{sh}\infty}$ is the ultimate shrinkage strain, k_{h} is the humidity dependence function, and $S(t)$ is the time function for shrinkage, and t_0 is the age when drying begins (days). The total creep strain at time t caused by a unit sustained uniaxial stress, σ, applied at time t' is characterised in Equation 2.22 by the secant compliance function $J(t,t')$ and may be calculated from:

$$J(t,t') = q_1 + C_0(t,t') + C_{\mathrm{d}}(t,t',t_0) \tag{2.24}$$

where q_1 represents the initial instantaneous strain, $C_0(t,t')$ represents the basic creep compliance, and $C_d(t,t',t_0)$ represents the additional creep due to simultaneous drying. The

final term from Equation 2.22 characterises deformation due to temperature effects where $\Delta T(t)$ is the temperature change from the reference temperature at time t and α is the thermal expansion coefficient.

2.8.11 B3+ Model 1996

The short-form of the B3 creep and shrinkage prediction model, denoted B3+ 1996[127], uses the same initial formulae for predicting the time-dependent deformations in concrete as the standard B3 Model[114] detailed in Section 2.8.10. The B3 formulae for predicting material parameters in the model are simplified by dropping the dependence of these parameters on the composition of the concrete mix, leaving only dependence on the strength and water content of the mix.

2.8.12 GL Model 2001

The Gardner-Lockman (GL) Model 2001[129] gives the following expressions for predicting time dependent effects. The total strain ϵ of a concrete member uniaxially loaded at time t_0 with a constant stress σ may be expressed as follows:

$$\varepsilon = \varepsilon_{sh} + \frac{\sigma}{E_{cmto}} + \frac{\sigma\phi_{28}}{E_{cm28}} \tag{2.25}$$

where ϵ_{sh} is the shrinkage strain, E_{cmto} is the mean modulus of elasticity at loading, E_{cm28} is the mean modulus of elasticity at 28 days, and ϕ_{28} is the creep coefficient. The total shrinkage strain ϵ_{sh} may be calculated from:

$$\varepsilon_{sh} = \varepsilon_{shu}\beta(h)\beta(t) \tag{2.26}$$

where ϵ_{shu} is the notional ultimate shrinkage strain, $\beta(h)$ is the correction term for the effect of humidity on shrinkage, and $\beta(t)$ is the correction term for the effect of time t, on shrinkage. The value of ϵ_{shu} depends on the strength of the concrete and the cement type. The creep coefficient ϕ_{28} may be calculated from:

$$\phi_{28} = \Phi(t_c)\left[2\left(\frac{(t-t_0)^{0.3}}{(t-t_0)^{0.3}+14}\right)+\left(\frac{7}{t_0}\right)^{0.5}\left(\frac{t-t_0}{t-t_0+7}\right)^{0.5}+2.5(1-1.086h^2)\left(\frac{t-t_0}{t-t_0+0.15(V/S)^2}\right)^{0.5}\right] \tag{2.27}$$

where $\Phi(t_c)$ is a term which takes drying before loading into account so reducing basic and drying creep, h is the humidity, and V/S is the volume/surface ratio.

Table 2.1. Classification of British Standard cements and their European equivalents (British Cement Association[22]).

British Standard		Cement	BS EN 197-1 cement notation	Clinker content, %	Content of other main constituents %
To be withdrawn	To co-exist				
BS 12*1	BS 4027	Portland cement	CEM I	95 – 100	-
-	BS 146*3	Portland-slag cement	CEM II/A-S	80 – 94	6 – 20
			CEM II/B-S	65 – 79	21 – 35
-	-	Portland-silica fume cement	CEM II/A-D	90 – 94	6 – 10
-		Portland-pozzolana cement	CEM II/A-P	80 – 94	6 – 20
			CEM II/B-P	65 – 79	21 – 35
			CEM II/A-Q	80 – 94	6 – 20
			CEM II/B-Q	65 – 79	21 – 35
BS 6588*1		Portland-fly ash cement	CEM II/A-V	80 – 94	6 – 20
			CEM II/B-V	65 – 79	21 – 35
-			CEM II/A-W	80 – 94	6 – 20
			CEM II/B-W	65 – 79	21 – 35
-		Portland-burnt shale cement	CEM II/A-T	80 – 94	6 – 20
			CEM II/B-T	65 – 79	21 – 35
-		Portland-limestone cement	CEM II/A-L	80 – 94	6 – 20
BS 7583*1			CEM II/A-LL	80 – 94	6 – 20
-			CEM II/B-L	65 – 79	21 – 35
			CEM II/B-LL	65 – 79	21 – 35
-		Portland-composite cement	CEM II/A-M	80 – 94	6 – 20
			CEM II/B-M	65 – 79	21 – 35
-	BS 146*3	Blastfurnace cement	CEM III/A	35 – 64	36 – 65
BS 4246*2	-		CEM III/B	20 – 34	66 – 80
			CEM III/C	5 – 19	81 – 95
-	-	Pozzolanic cement	CEM IV/A	65 – 89	11 – 35
-	BS 6610		CEM IV/B	45 – 64	36 – 55
-	-	Composite cement	CEM V/A	40 – 64	36 – 60
			CEM V/B	20 – 39	61 - 80

*1. These three British Standards are withdrawn on 1st April 2002.
*2. This British Standard will be withdrawn to a time-scale dictated by the revision of BS 146.
*3. BS 146 to be revised to remove any conflict with BS EN 197-1 and to include BS 4246 cement.

Table 2.2. Classification of British Standard cements and their American equivalents (Neville and Brooks[23]).

British Classification		American Classification	
Description	**BS**	**Description**	**ASTM**
Ordinary Portland	12: 1991	Type I	C 150-92
Rapid-hardening Portland	12: 1991	Type III	C 150-92
Low-heat Portland	1370: 1979	Type IV	C 150-92
Modified cement	-	Type II	C 150-92
Sulphate-resisting Portland	4027: 1991	TypeV	C 150-92
Portland blastfurnace (slag cement)	146: 1991	Type IS Type IS(MS)	C 595-93
Low-heat Portland blastfurnace	4246: 1991	-	-
White Portland	12: 1989	-	C 150-92
Portland-pozzolan	6588: 1985 3892: 1993	Type IP Type P Type I(PM)	C 595-93

NB Cements Type I, IS, IP, I(PM), II, and III are also available with an interground air-entraining agent, and are then denoted by letter A, e.g. Type IA.

Table 2.3. Main compounds in Portland cement (Neville and Brooks[23]).

Name of compound	Oxide composition	Abbreviation
Tricalcium silicate	$3CaO.SiO_2$	C_3S
Dicalcium silicate	$2CaO.SiO_2$	C_2S
Tricalcium aluminate	$3CaO.Al_2O_3$	C_3A
Tetracalcium aluminoferrite	$4CaO.Al_2O_3.Fe_2O_3$	C_4AF

Table 2.4. Suggested degrees of workability for various applications (20mm aggregate concrete (Shirley[15]).

Degree of workability	Suitable for	Slump (mm)
Very low	Vibrated concrete in large sections	0-10
Low	Mass concrete compacted without vibration; Simple reinforced sections with vibration	10-25
Medium	Normal reinforced work without vibration; Heavily reinforced sections with vibration	25-75
High	Sections with congested reinforcement	65-135

Table 2.5. Typical total aggregate/cement ratios by weight required to give different degrees of workability at various free water/cement ratios (no admixtures) (Shirley[15]).

Workability required	Free w/c ratio desired	Aggregate/cement ratio by mass					
		Uncrushed aggregate of maximum size			Crushed aggregate of maximum size		
		40mm	20mm	10mm	40mm	20mm	10mm
Very low	0.4	5	4½	3½	4½	4	3
	0.5	7½	6½	5½	6½	5½	4½
	0.6	-	-	7½	-	7	6
	0.7	-	-	-	-	-	7
Low	0.4	4½	4	3	4	3½	-
	0.5	6½	5½	4½	5½	5	4
	0.6	7½	7	6	7	6	5
	0.7	-	8	7	8	7	6
Medium	0.4	4	3½	-	3½	3	-
	0.5	5½	4	3	5	4	3
	0.6	7	6	5	6	5	4½
	0.7	8	7	6	7	6	5½
High	0.4	3½	3	-	3	3	-
	0.5	5	4	3½	4½	4	3
	0.6	6½	5	4½	5½	4½	4
	0.7	7½	6	5½	6	5½	5

Table 2.6. Typical fine aggregate proportions in concrete of medium workability containing aggregate of 20mm maximum size (Shirley[15]).

Grading zone (BS 882)[28] in which fine aggregate falls	Quantity of fine aggregate (% by mass of total aggregate)
C	40 to 50
M	31 to 40
F	25 to 31

Table 2.7. High-performance concrete as developed by SHRP (Russell[32]).

HPC type	Minimum strength criteria	$w/(c+m)$	Minimum durability factor
Very Early Strength (VES)	14MPa in 6 hours	≤ 0.4	80%
High Early Strength (HES)	34MPa in 24 hours	≤ 0.35	80%
Very High Strength (VHS)	69MPa in 28 days	≤ 0.35	80%
Fibre Reinforced	HES + (Steel or Poly)	≤ 0.35	80%

N.B. $w/(c+m)$ is the water/cementitious material ratio, i.e. water/binder (w/b) ratio.

Table 2.8. Mix proportions of various high performance concretes* (Neville[24]).

Ingredient (kg/m³)	Mix *A*	*B*	*C*	*D*	*E*	*F*	*G*	*H*	*I*
Portland cement	534	500	315	513	163	228	425	450	} 460
Silica fume	40	30	36	43	54	46	40	45	
Fly ash	59	-	-	-	-	-	-	-	-
ggbs	-	-	137	-	325	182	-	-	-
Fine aggregate	623	700	745	685	730	800	755	736	780
Coarse aggregate	1069	1100	1130	1080	1100	1110	1045	1118	1080
Total water	139	143	150	139	136	138	175†	143	138
Water/cementitious material ratio	0.22	0.27	0.31	0.25	0.25	0.30	0.38	0.29	0.30
Slump, mm	255	-	-	-	200	220	230	230	110
Cylinder strength (MPa) at age (days)									
1	-	-	-	-	13	19	-	35	36
2	-	-	-	65	-	-	-	-	-
7	-	-	67	91	72	62	-	68	-
28	-	93	83	119	114	105	95	111	83
56	124	-	-	-	-	-	-	-	-
91	-	107	93	145	126	121	105	-	89
365	-	-	-	-	136	126	-	-	-

* Mix location: (A) United States; (B) Canada; (C) Canada; (D) United States; (E) Canada; (G) Morocco; (H) France; (I) Canada.
† It is suspected that the high water content was occasioned by a high ambient temperature in Morocco.

Table 2.9. Mix proportions and slump values for main mixes (Taylor *et al*[41]).

Nominal mean 28-day f_c (N/mm²)	Mix proportions by mass	w/c	Nominal cement content (kg/m³)	Superplasticizer (SP) (ml/kg of cement)	Slump (mm)
Limestone					
40	1: - : 2.00: 2.50: 0.56	0.56	400	-	200
60	1: - : 1.81: 2.81: 0.50	0.50	400	-	90
80	1: 0.11: 2.12: 3.50: 0.45	0.50	340	13.5	160
100	1: 0.11: 1.77: 2.97: 0.32	0.35	400	23.0	170
120	1: 0.11: 1.28: 2.13: 0.22	0.24	510	35.9	160
Gravel					
40	1: - : 2.00: 2.50: 0.56	0.56	400	-	200
60	1: - : 1.81: 2.81: 0.50	0.50	400	-	100
80	1: 0.11: 1.93: 3.21: 0.39	0.43	370	21.5	190
100	1: 0.11: 1.53: 2.53: 0.26	0.29	455	26.5	140
120	1: 0.11: 1.28: 2.13: 0.22	0.24	510	35.9	175

Table 2.10. Compressive strength development of HPC and paste at various w/b ratios and SF content (Kjellsen *et al*[38]).

Mix	Compressive Strength (MPa)												
	Concrete							Paste					
	1 day	7 days	28 days	90 days	9 months	2 years	4 years	1 day	7 days	28 days	90 days	9 months	2 years
w/b = 0.25	38.9	93.1	108.0	117.7	124.7	131.8	126.1	40.4	89.1	107.0	121.2	122.2	126.8
w/b = 0.25 5% SF	33.0	78.9	108.7	121.4	122.4	131.2	133.1						
w/b = 0.25 10% SF	35.5	98.2	130.2	142.6	139.5	152.5	147.4	33.5	92.7	123.2	144.6	139.5	146.5
w/b = 0.40	18.7	52.3	68.3	77.8	80.4	90.9	93.9	16.7	45.3	59.8	69.3	76.4	85.4
w/b = 0.40 10% SF	17.3	56.3	77.3	94.1	93.9	100.3	100.6	18.3	53.3	76.3	95.1	94.9	101.3

Table 2.11. Summary of suggested shrinkage mechanisms (Soroka[25]).

Source	Relative humidity (%)										
	0	10	20	30	40	50	60	70	80	90	100
Powers (1965)	Disjoining pressure										
							Capillary tension				
Ishai (1965)	Surface tension						Capillary tension				
Feldman and Sereda (1970)	Interlayer water					Capillary tension and surface tension					
Wittman (1968)	Surface tension						Disjoining pressure				

Table 2.12. Types of deformation (Neville[24]).

Type of deformation	Instantaneous	Time-dependent
Reversible	Elastic	Delayed-elastic
Irreversible	Plastic set	Viscous

Table 2.13. Effect of duration of loading on creep of concrete (Evans and Kong[99]).

Duration of loading	Percentage of long-term creep
28 days	40%
6 months	60%
1 year	75%
5 years	90%
10 years	95%
30 years	100%

Table 2.14. Parameters considered in the more recent common prediction models.

Description	BS 8110: Part 2: 1985[88]	BS 5400: Part 4: 1990[130]	CEB-FIP 1990[121]	Eurocode 2 1992[131]	ACI 209-R92[117]	BP-KX[125]	BP-KX+[126]	B3[114]	B3+[127]	GZ[128]	GL[129]
Humidity	√	√	√	√	√	√	√	√	√	√	√
Temperature			√	√	√	√		√			
Age at drying		√			√	√	√	√	√	√	√
Age at loading	√	√	√	√	√	√	√	√	√	√	√
Slump					√						
28-day strength	√	√	√	√	√	√	√	√	√	√	√
Elastic Modulus	√	√	√	√	√	√	√	√	√	√	√
w/c	√	√				√	√	√	√		
Cement content		√			√	√	√	√	√		
Cement type			√	√	√	√	√	√	√	√	√
Curing Regime					√	√	√	√	√		
Aggregate Content					√	√	√	√			
Size	√	√	√	√	√	√	√	√	√	√	√
Shape						√		√			

Table 2.15. Modulus of elasticity as specified by BS 5400: Part 4: 1990[130] and BS 8110: Part 2: 1985[88].

Compressive strength, f_{cu}	**Static modulus, E_c, BS 5400**		**Static modulus, E_c, BS 8110**	
	Mean value	Typical Range	Mean value	Typical Range
N/mm²	**kN/mm²**	**kN/mm²**	**kN/mm²**	**kN/mm²**
20	25	21 to 29	24	18 to 30
25	26	22 to 30	25	19 to 31
30	28	23 to 33	26	20 to 32
40	31	26 to 36	28	22 to 34
50	34	28 to 40	30	24 to 36
60	36	30 to 42	32	26 to 38

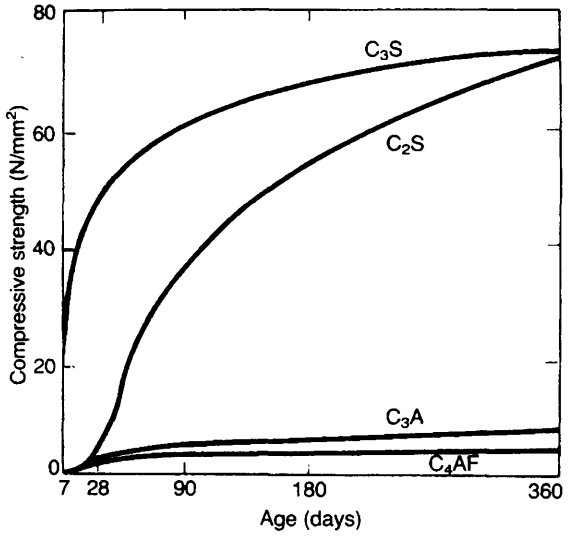

Figure 2.1. Development of strength of pure compounds in Portland cement (Bogue[26], 1955, from [14]).

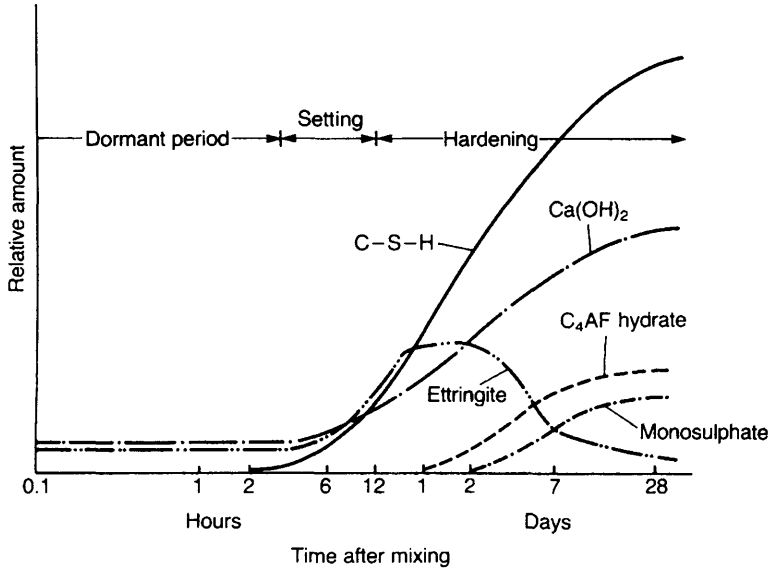

Figure 2.2. Typical hydration product development in Portland cement (Soroka[25], from [14]).

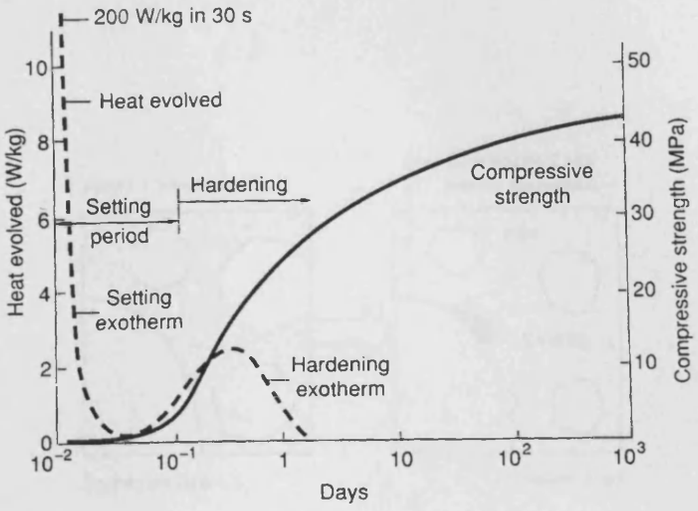

Figure 2.3. Time-dependent heat evolution and strength change during hydration (Weidmann *et al*[27], from [14]).

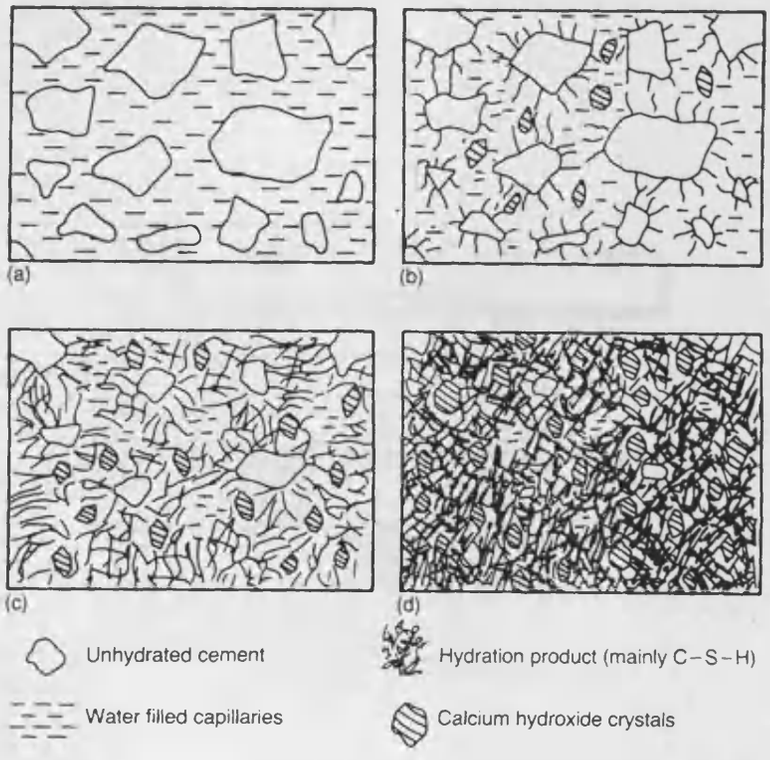

Figure 2.4. Schematic depicting the development of microstructure in hydrating cement paste: (a) fresh cement and water; (b) initial set – interlocking of weak C-S-H product, some $Ca(OH)_2$ crystals; (c) two to three days old – strength from denser C-S-H between unhydrated cement and capillary voids; (d) mature paste – denser C-S-H around $Ca(OH)_2$ crystals, residue of unhydrated cement and capillary voids (Illston[14], 1994).

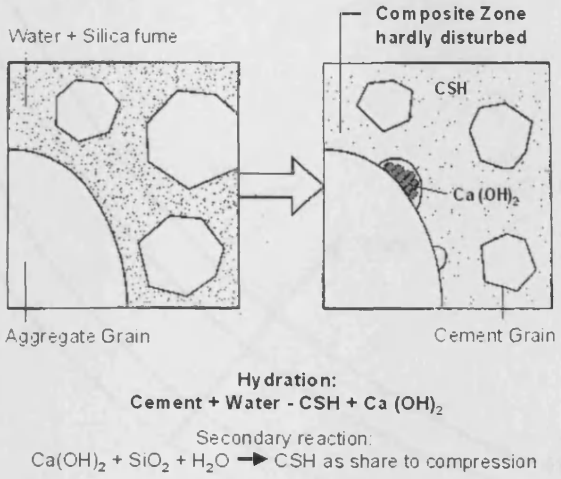

Figure 2.5. Improvement of bond behaviour between mortar and aggregates by silica fume (Breitenbücher[35]).

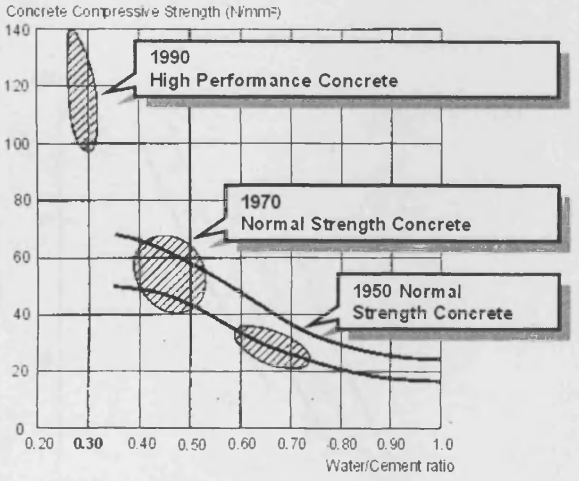

Figure 2.6. Development of concrete strength (Breitenbücher[35]).

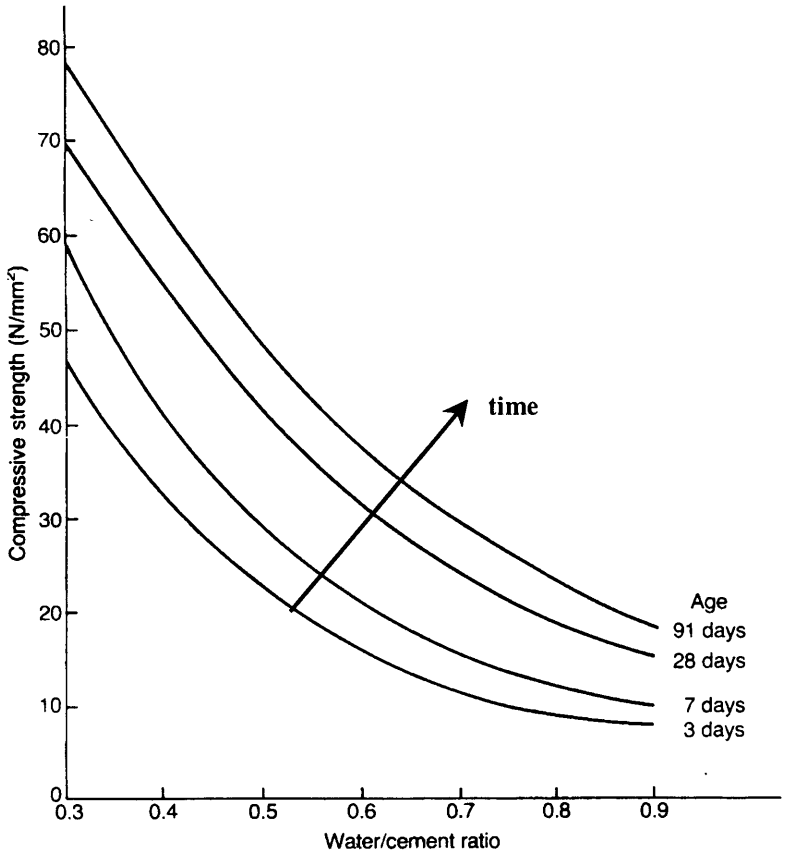

Figure 2.7. Typical effect of age and w/c ratio on concrete strength (Portland cement, uncrushed aggregate) (Teychenné[42], from [14]).

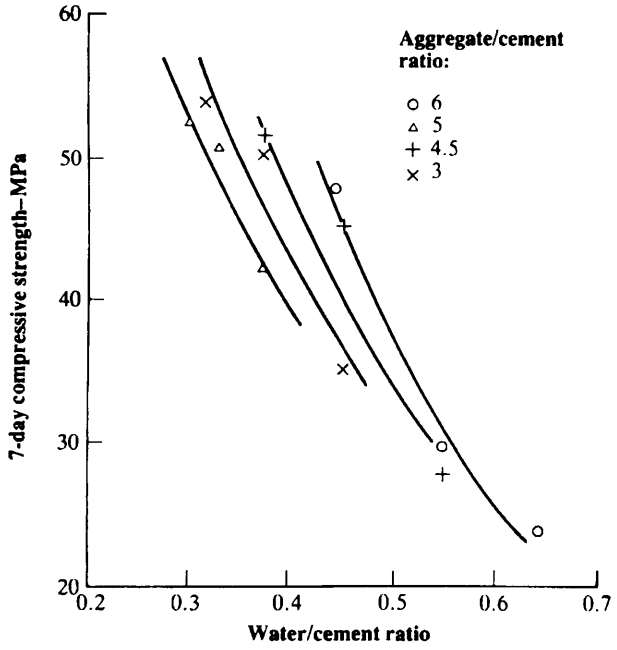

Figure 2.8. Influence of the aggregate/cement ratio on strength of concrete (Singh[43], from [23]).

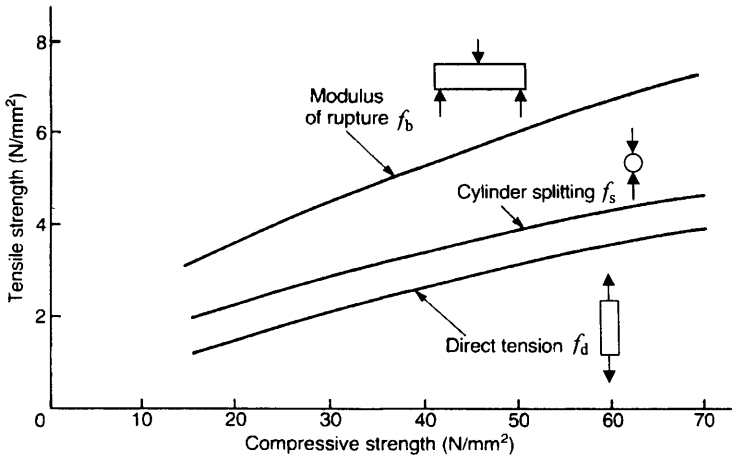

Figure 2.9. Typical relationships between tensile and compressive strengths of concrete (Carasquillo *et al*[54], from [14]).

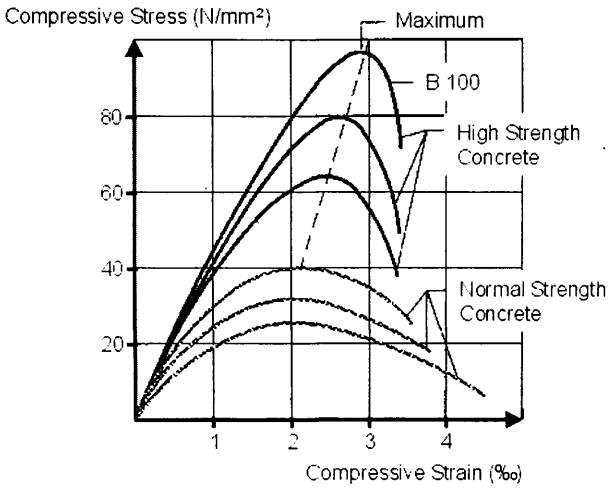

Figure 2.10. Stress-strain relationships for normal and high strength concrete (Breitenbücher[35]).

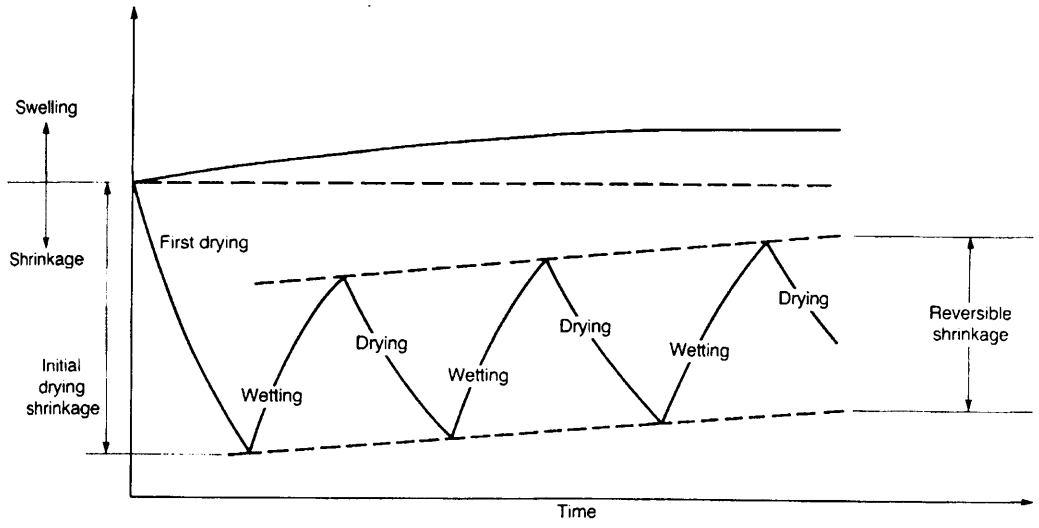

Figure 2.11. Volume changes in cement paste or concrete due to alternate cycles of drying and wetting (Illston[14]).

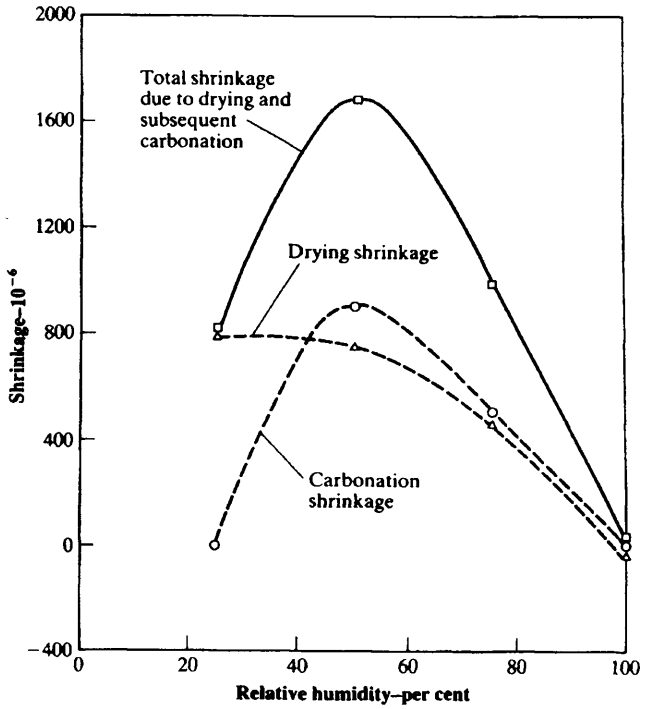

Figure 2.12. Drying and carbonation shrinkage of mortar at different relative humidities (Verbeck[74], from [24]).

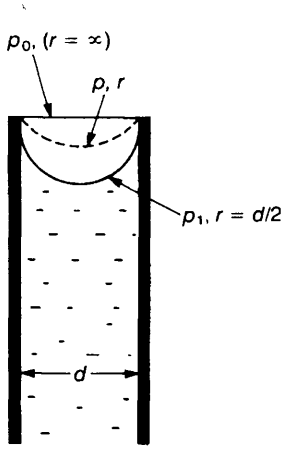

Figure 2.13. Capillary surface tension (Soroka[25]).

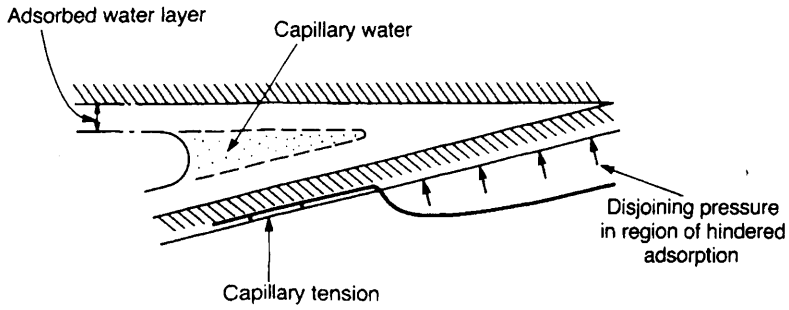

Figure 2.14. Water forces in a gel pore in hardened cement paste (Bazant[76], from [14]).

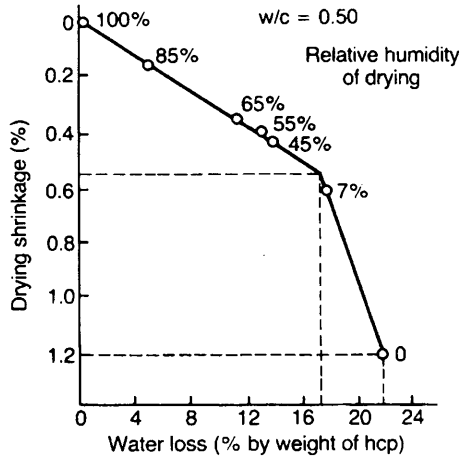

Figure 2.15. The effect of water loss on drying shrinkage of hardened cement paste (Verbeck and Helmuth[77], from [14]).

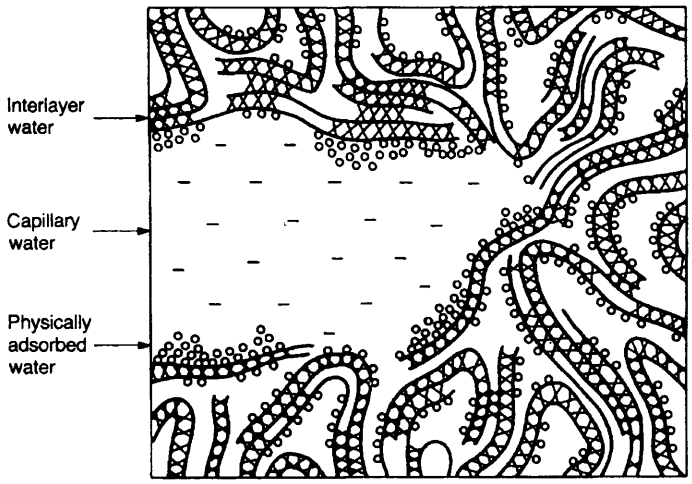

Figure 2.16. Schematic depicting types of water within calcium silicate hydrate (Feldman and Sereda[78], from [14]).

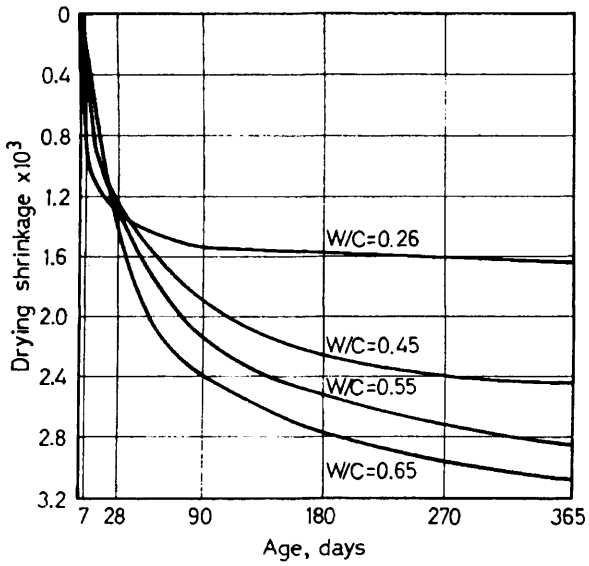

Figure 2.17. Effect of w/c ratio on shrinkage of cement pastes (Haller[79], from [25]).

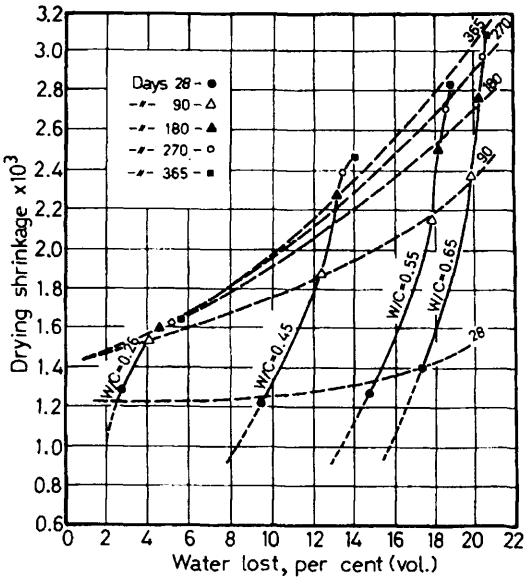

Figure 2.18. Effect of water-loss on shrinkage of cement pastes of different w/c ratios (Haller[79], from [25]).

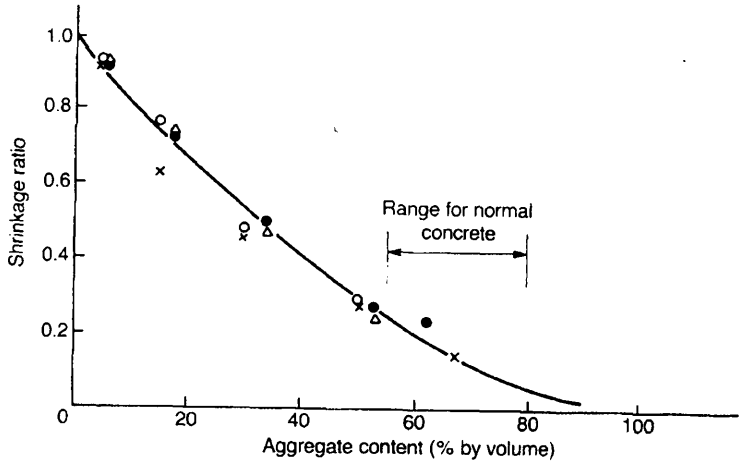

Figure 2.19. Influence of aggregate content in concrete on the ratio of concrete to that of neat cement paste (Pickett[81], from [14]).

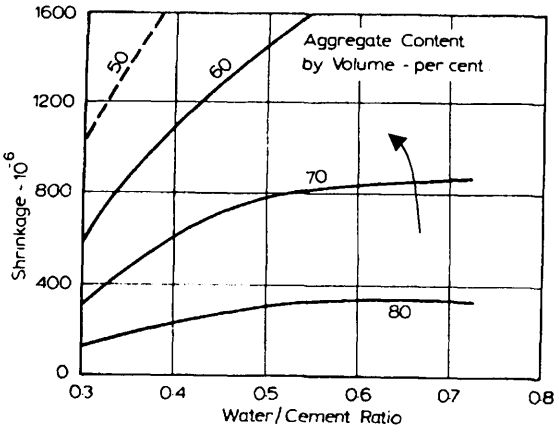

Figure 2.20. Influence of water/cement ratio and aggregate content on shrinkage (Ödman[82], from [24]).

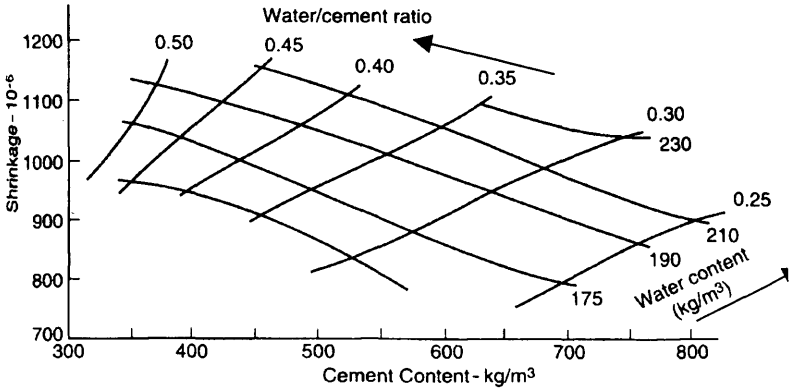

Figure 2.21. The pattern of shrinkage as a function of cement content, water content, and water cement ratio: concrete moist-cured for 28 days, thereafter dried for 450 days (Shoya[83], from [24]).

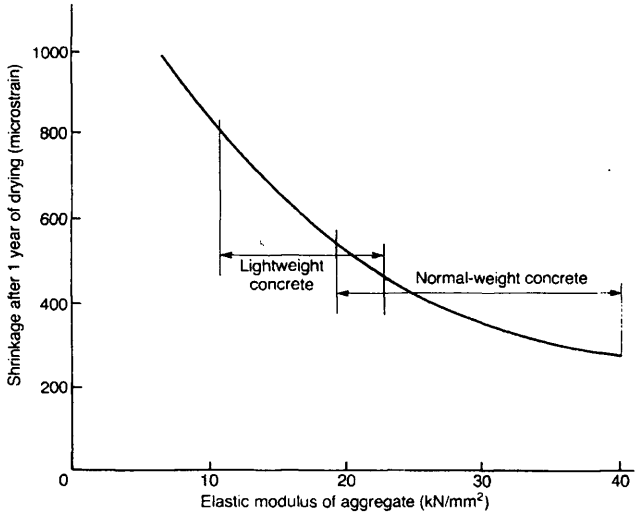

Figure 2.22. The effect of aggregate stiffness on concrete shrinkage (Mindess and Young[84], from [14]).

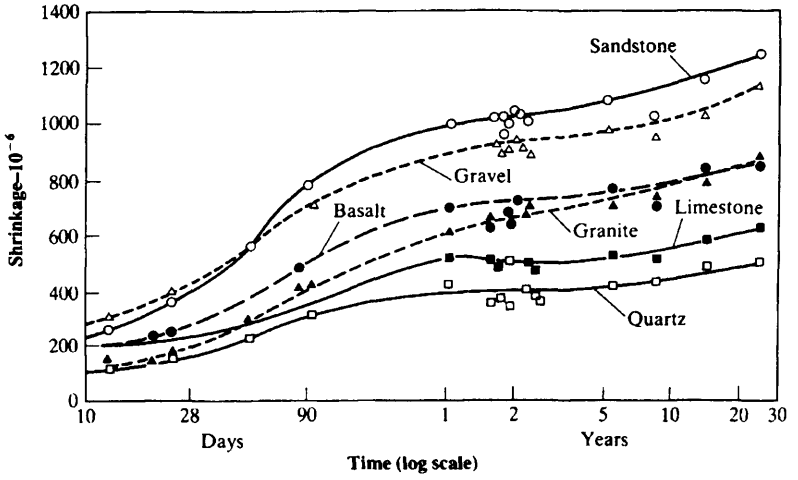

Figure 2.23. Shrinkage of concretes of fixed mix proportions but made with different aggregates, and stored in air at 21°C and a relative humidity of 50% (Troxell *et al*[85], from [24]).

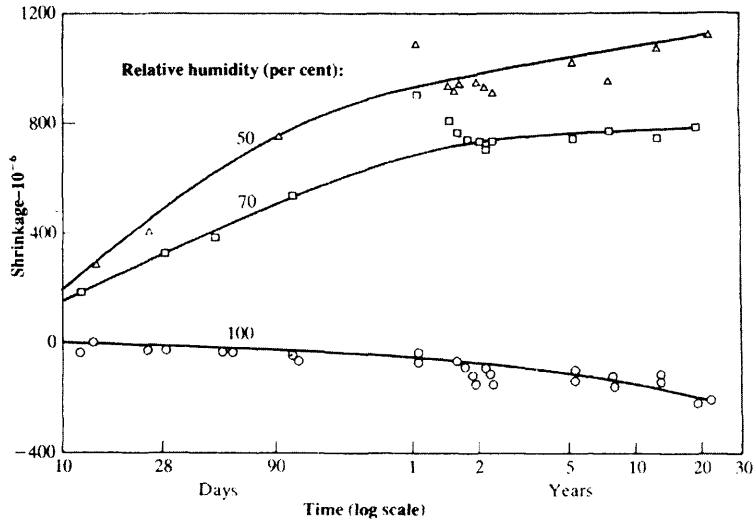

Figure 2.24. Relationship between shrinkage and time for concretes stored at different relative humidities (Troxell *et al*[85], from [24]).

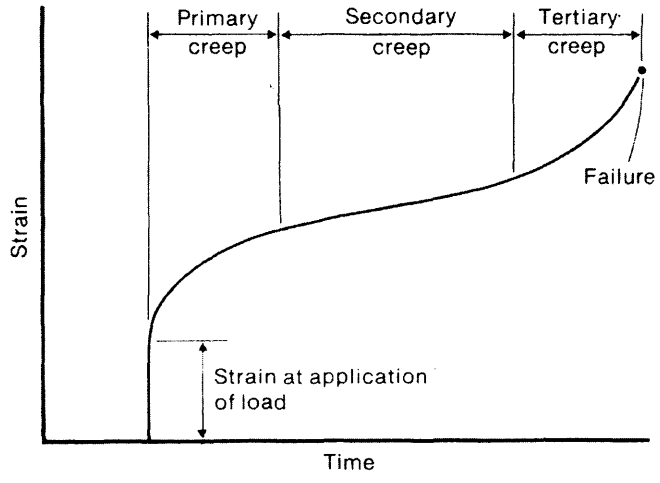

Figure 2.25. General form of the strain-time curve for a material subjected to creep (Neville *et al*[94]).

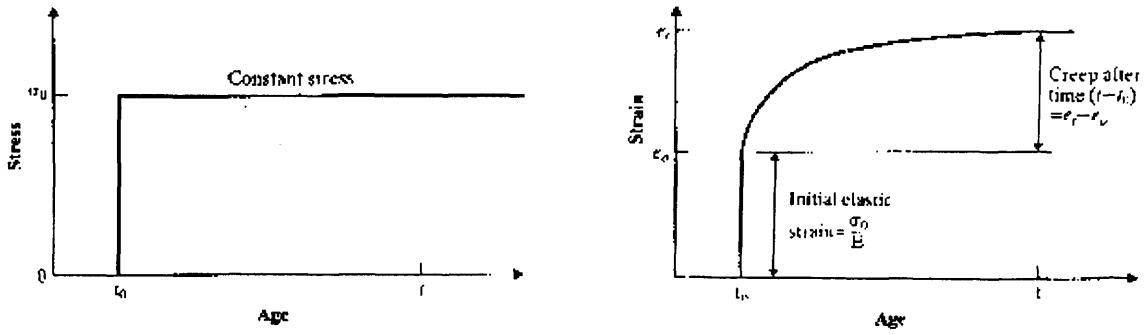

Figure 2.26. Definition of creep under constant stress (Neville and Brooks[23]).

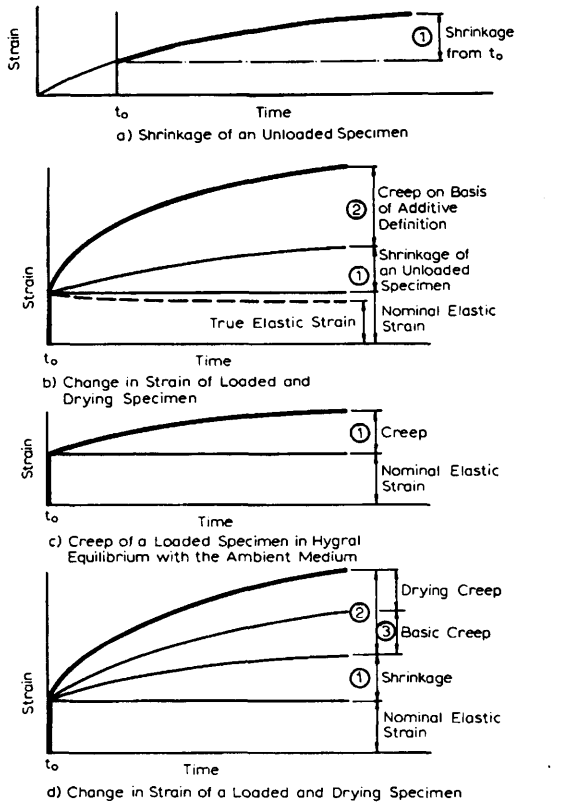

Figure 2.27. Time-dependent deformations in concrete subjected to a sustained load (Neville and Brooks[23]).

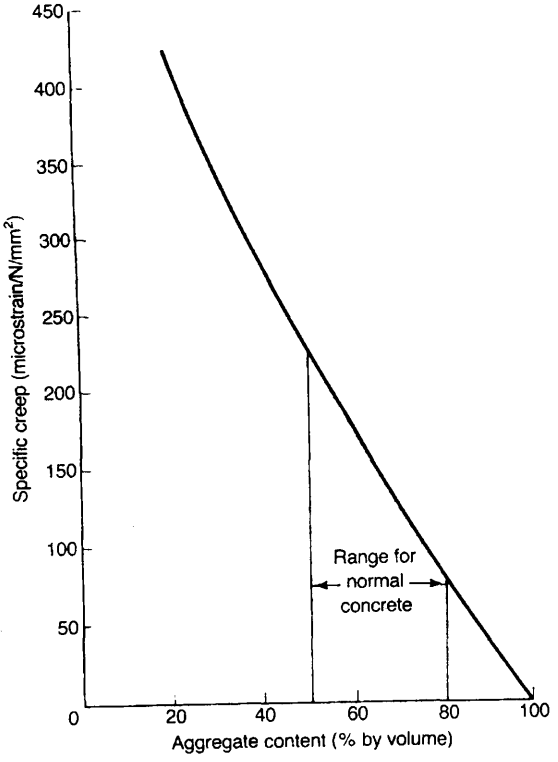

Figure 2.28. The effect of aggregate content of concrete on creep (Concrete Society, 1973, from [14]).

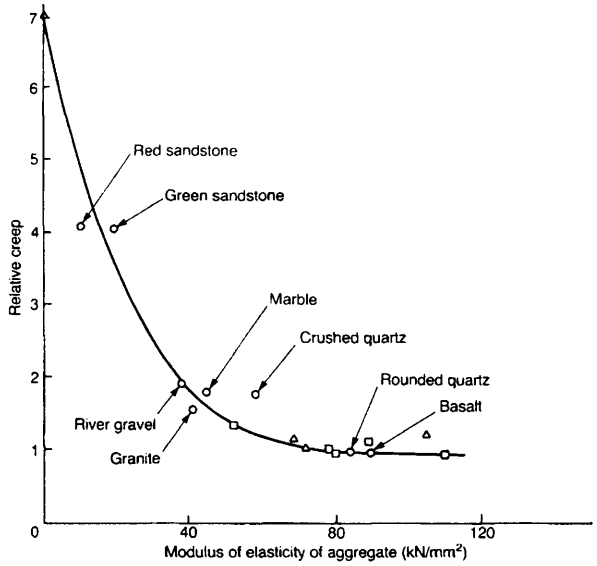

Figure 2.29. The effect of type of aggregate on relative creep of concrete (Concrete Society, 1973, from [14]).

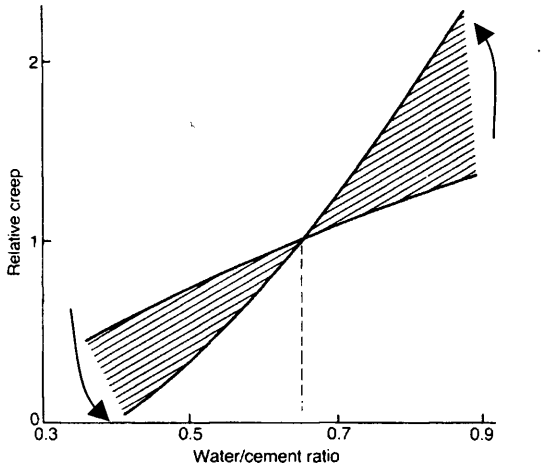

Figure 2.30. Range of results for effect of w/c ratio on creep of concrete relative to creep at a w/c ratio of 0.65 (Neville and Brooks[23], from [14]).

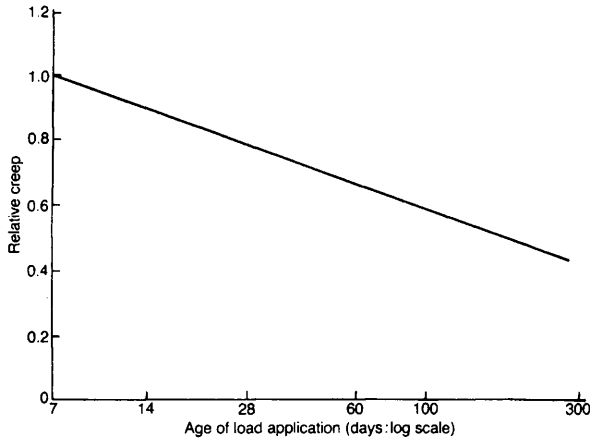

Figure 2.31. The effect of age at load application on creep of concrete stored at 75% relative humidity (L'Hermite, 1959, from [14]).

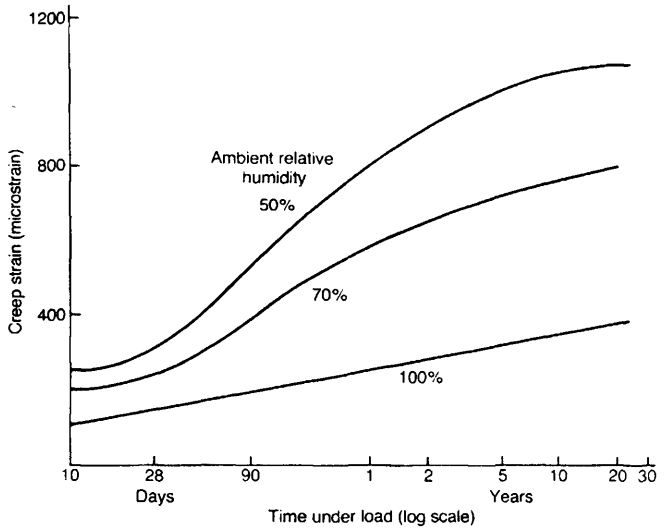

Figure 2.32. Creep of concrete moist-cured for 28 days, then loaded and stored at different relative humidities (Troxell *et al*[85], from [14]).

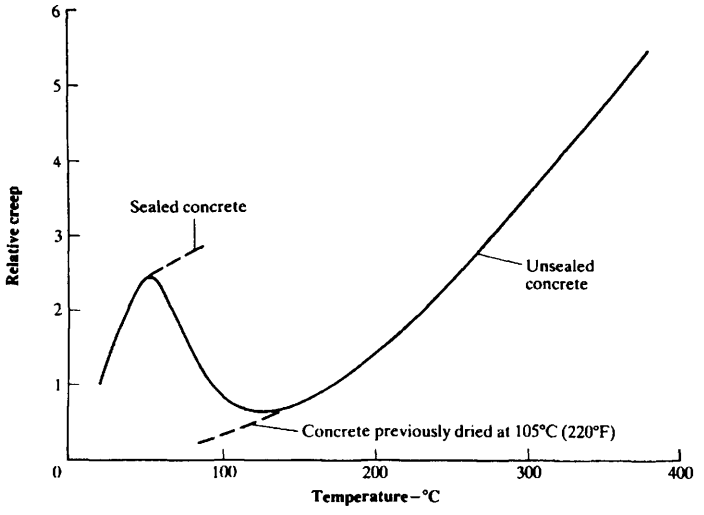

Figure 2.33. Influence of temperature on creep of unsealed concrete relative to creep at 20°C (Maréchal, 1969, from [23]).

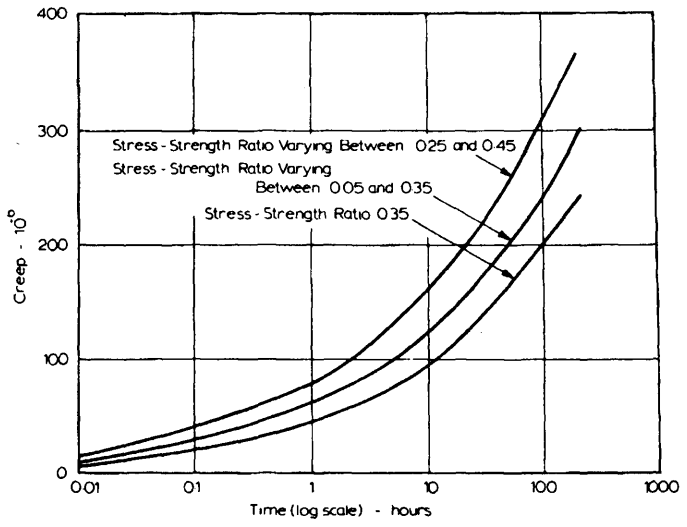

Figure 2.34. Creep under alternating and static loading (Neville and Brooks[23]).

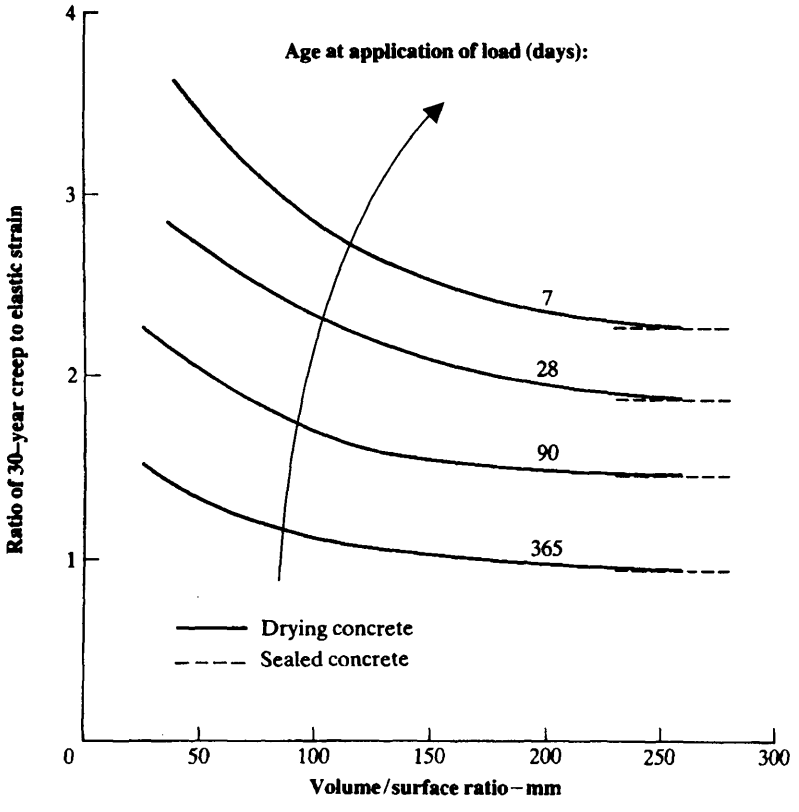

Figure 2.35. Influence of volume/surface ratio on the creep to elastic strain for sealed concrete and for drying concrete stored at a relative humidity of 60% (Neville and Brooks[23]).

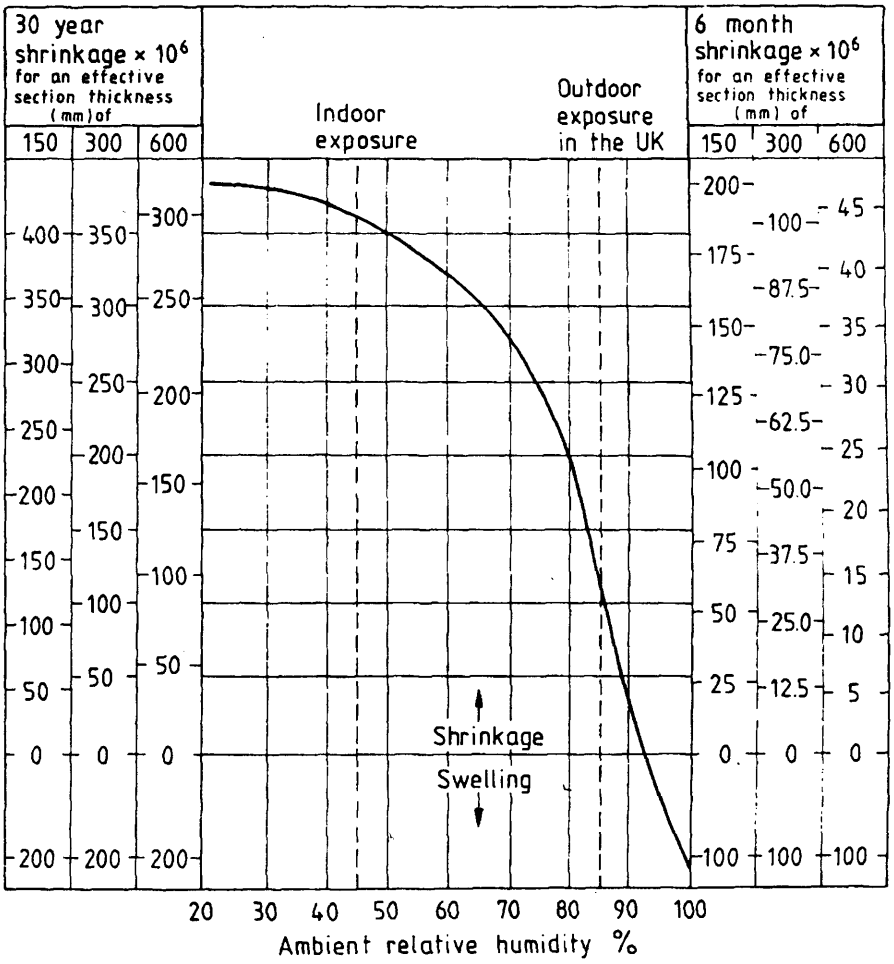

Figure 2.36. Drying shrinkage of normal-weight concrete (BS 8110: Part 2: 1985[88]).

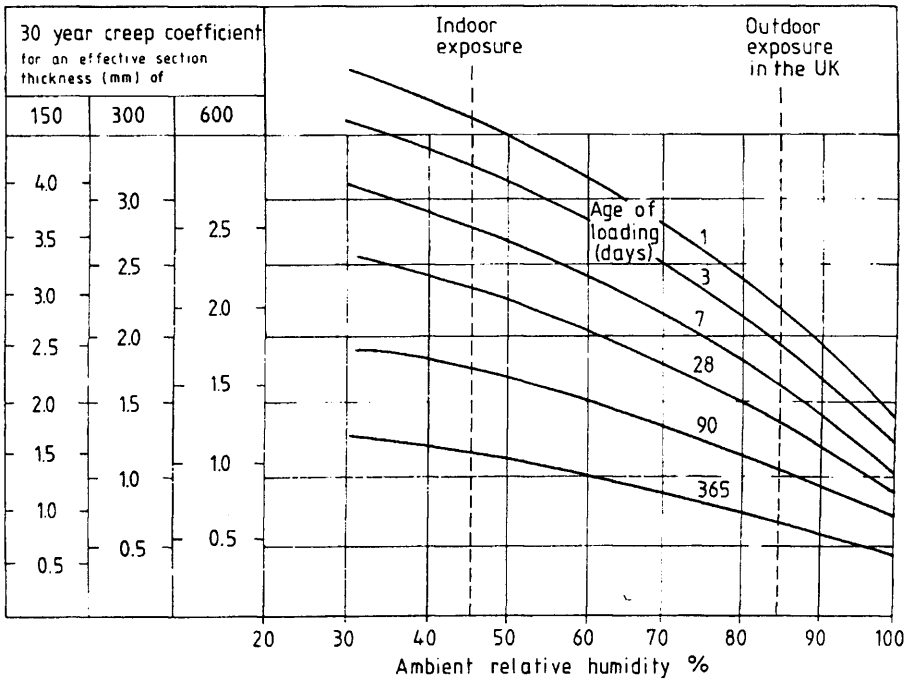

Figure 2.37. Effects of relative humidity, age of loading and section thickness upon creep factor (BS 8110: Part 2: 1985[88]).

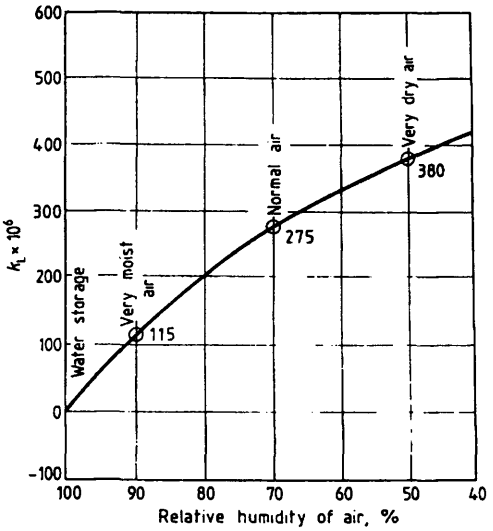

Figure 2.38. Coeffeicient k_L for relative humidity (BS 5400: Part 4: 1990[130]).

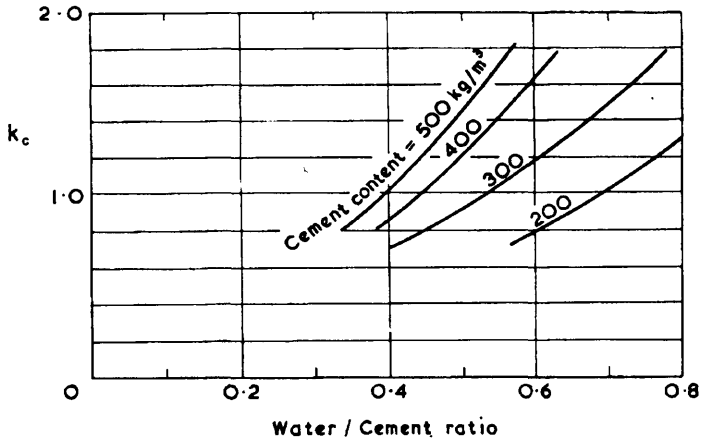

Figure 2.39. Coefficient k_c for cement content and w/c ratio (BS 5400: Part 4: 1990[130]).

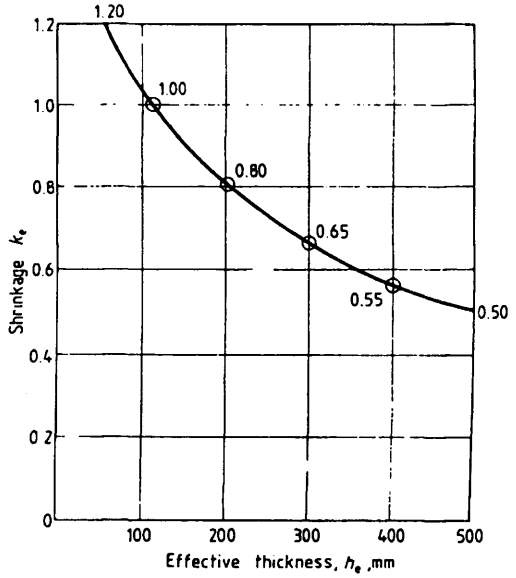

Figure 2.40. Coefficient k_e for effective thickness (BS 5400: Part 4: 1990[130]).

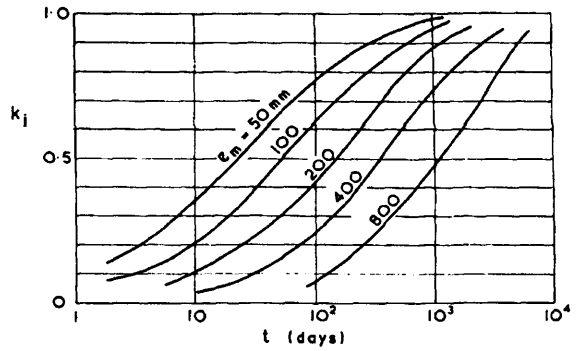

Figure 2.41. Coefficient k_i for duration t under load (BS 5400: Part 4: 1990[130]).

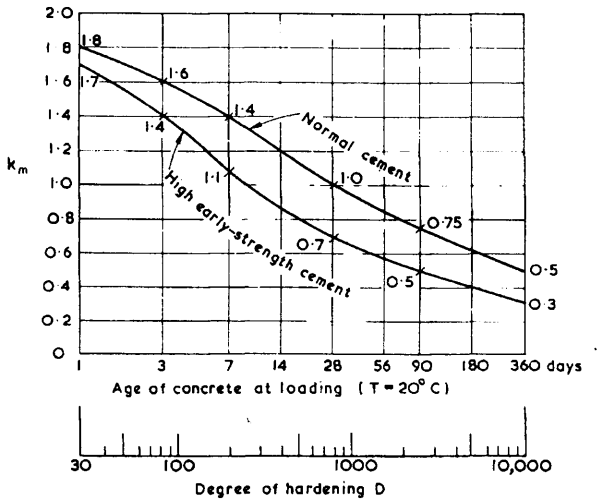

Figure 2.42. Coefficient k_m for age at loading (BS 5400: Part 4: 1990[130]).

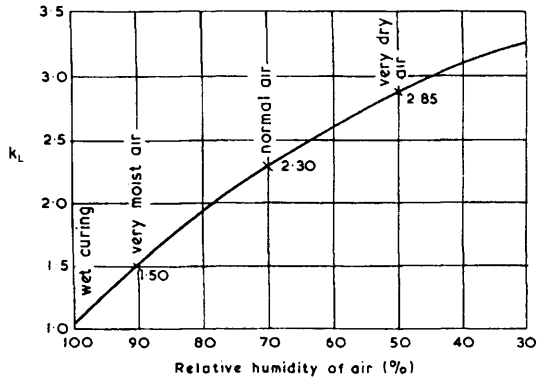

Figure 2.43. Coefficient k_l for relative humidity (BS 5400: Part 4: 1990[130]).

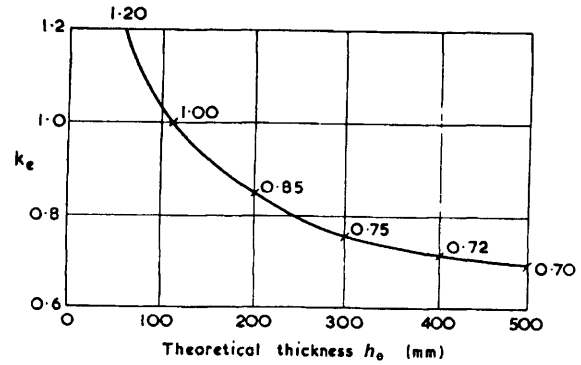

Figure 2.44. Coefficient k_e for effective thickness (BS 5400: Part 4: 1990[130]).

Chapter 3

Structural Applications

3.1 Introduction

Precast modular and segmental construction has been used with varying success in recent years. One of the great advantages of modular systems is the ability to improve quality and reduce construction times significantly, and in most cases this saving in time will result in an overall cost saving. The parallel programming possible with a modular approach means that work can be taking place on-site and off-site simultaneously. Off-site prefabrication of precast concrete elements can occur in a controlled factory environment, within which one can control quality and safety and minimise waste, while the site is being prepared and foundations developed. As soon as the site is ready, the modules can be delivered and it is possible in some cases to see a project appear overnight. The application of such methods is endless. Any structure imaginable could be created in such a way, from schools where storage cupboards can be cast as part of modular wall construction, to oil platforms where individual levels could be cast as modules which may be sealed off if damage were to occur.

A significant problem in employing modular construction methods is the detailing of the joints. In many cases the connections will have important structural requirements. Often the modular elements contribute to the structural performance of the project, placing specific demands on the joint. Even if the elements are non-structural, the connections have an important role to play in providing support or weatherproof external envelope. For overall success with modular construction, the practicalities of making the joint must be considered. Gaps between joints generally cannot be controlled effectively due to the effects of time-dependent deformations and differential movement. With the increased use of high strength concrete and the benefits of early strength gain and creep occurrence, modular units can now be constructed in a factory to a level of accuracy at which the largest tolerance that can be expected when placed on site is of the order of 1mm. Therefore the maximum gap that could be expected between two units would be 2mm. Compared to current values, this level of tolerance is very small. The advantage of this is that some form of high performance material

can be used to fill the joint due to the relatively small quantities involved, ensuring that relatively expensive jointing materials are affordable.

Concrete has adapted to the modular approach to construction with great ease. Coupled with the advances made in high performance concrete technology, such an approach would satisfy the three most important aspects of any project; time and cost whilst retaining quality.

The estimation of time dependent deformations within concrete structures is very difficult. From the information in the previous chapter, areas in which shrinkage, creep, and thermal strains will manifest themselves have become evident, however since the effect of these mechanisms only becomes noticeable after concrete has set, engineers have no way of knowing exactly to what scale they will occur. It is very well to carefully monitor the type and volume of the cement constituents but when a structure is in the process of being built, these deformations will not be noticeable until the structure has been completed at which time there is little that can be done about the problem and hence, if there is great damage or even failure due to these mechanisms, then a great deal of money will have been wasted. Therefore, it is vital that the full extent and effect that these deformations will have on concrete structures, in particular those made from high-performance concrete, is understood and where possible steps can be taken to reduce or even eliminate their effect. It is the aim of this research to provide such an understanding.

3.2 Segmental Bridge Construction

The first segmentally constructed bridge was a 68.5m span structure completed in 1930 in Rio de Peixe, Brazil. Twenty years later, German engineers improved the technique of segmental construction by adding post-tensioning to cast-in-place concrete. Of major importance was the development of cast-in-place cantilever segmental construction. In the 1960's, French engineers further improved the technique with the introduction of precast balanced cantilever, segmental construction which has been used throughout the world for the construction of multispan bridges and viaducts.[133]

Segmental post-tensioned concrete bridges have been popular due to their suitability for use for medium to long spans. However, concern has mounted for the safety of these structures since the sudden and unexpected collapse of the Ynys-y-Gwas segmental post-tensioned concrete bridge in Port Talbot, South Wales, in 1985 after only 32 years of service. The failure was attributed to corrosion of the tendons due to inadequate protection of the tendons at the segmental joints. The result caused concern about the condition of other post-tensioned concrete bridges in which tendons pass through joints.[134]

Further concern has been shown in recent years regarding the allowances made for long-term creep, shrinkage and environmental influences on such bridges. Current methods which make allowances for these mechanisms rely on data obtained from short-term studies of small scale laboratory specimens, and assumptions that the structure will experience average environmental conditions. However, little information exists regarding the long-term performance of the structure, and since failure is most likely to occur in the long-term, such data is vital for a complete study.

3.2.1 Advantages

The advantages of segmental construction are numerous and have been summarised by Beygi[8], as follows:

1. Cantilever segmental construction is an efficient and economical method for medium to long spans of between 50 and 120 metres.

2. The effects of concrete deformations, in particular creep and shrinkage, may be substantially reduced. This is due to the maturity of precast segments, at the time of erection, which have already gained significant strength, while the greater part of shrinkage has already taken place.

3. The precast method of construction saves time. While the substructure is under construction, segments may be manufactured in the factory or casting yard. Hence, segments are ready for assembly as soon as the piers are in place. Therefore, the speed of construction of the bridge deck is greatly increased, by starting simultaneous erection of cantilevers at both ends of the bridge superstructure. Consequently, savings in the total cost of the structure are achievable.

4. Factory casting conditions allow better and easier quality control, and therefore HPC may be used. As a result, cross-section size may be reduced.

5. The precast segmental construction method can accommodate changes in horizontal or vertical curvature with only small variations in the precasting operation.

6. Compared with alternate schemes such as deck truss, steel arch, and steel box girder, generally segmental concrete construction offers savings of between 10 and 20%, although this figure depends on the economic climate at the time.

7. Box girder prestressed concrete bridges can be aesthetically pleasing structures.

3.2.2 Construction Method

Segmental construction techniques are usually categorised according to the methods of casting and erection of segments. The most common methods in use today include:

1. *Span-by-span method*, which features a superstructure constructed in one direction, one span at time, incorporating either precast or cast-in-situ segments, as demonstrated in Figure 3.1.

2. *Balanced cantilever method*, which consists of building a bridge deck from a succession of segments which can either be precast or cast-in-situ. Each segment is integrated with the previous one as soon as the concrete gains sufficient strength; it then becomes self-supporting and, in its turn, forms the base for a new segment. The integrity of the resulting cantilever is secured at each step of construction by prestressed cables which are set within the box section, as shown in Figure 3.2.

3. *Progressive placing method*, used when it is preferable to build asymmetrically from the piers. This may be achieved by either using a single temporary support pier, or several, as construction progresses, cantilevering segments outward from only one side of the pier whilst the side span is concreted on falsework to act as a counterweight, counter-loading or anchoring one cantilever span whilst building the adjacent span, or progressive construction with cable-staying, as demonstrated in Figure 3.3.

4. *Incremental launching method*, which is based on the manufacture of units under factory conditions involving repetitive cycles, and sliding the units forward over the piers into its final position.[135]

3.3 Project History

In 1975, the idea of a Peripheral Distributor Road (PDR) for Cardiff was first approved in principle by the then South Glamorgan County Council. The PDR formed a fundamental part of the Transport Policies for the County. Traffic congestion in and around the city of Cardiff gave rise to the requirement for improved access to the principal industrial areas from the M4 motorway to the west and east of the city, and access on to a primary road system from each sector of Cardiff whilst avoiding the main population areas. The objective of the PDR was to significantly reduce traffic, particularly commercial vehicles, on the City's existing roads and so improve road safety, public transport and the environment.[136,137]

Figure 3.4 shows the scheme plan. The scheme commences in the west from a previously completed embankment at the eastern end of the Ely Link Contract, which was completed in 1982. The route connects the Ely Link with the Grangetown Link, crossing and connecting to the Leckwith Interchange and continuing to run eastwards following the course of the River Ely, connecting the Grangetown Link with the Butetown Link and the Eastern Bay Link at the Ferry Road interchange. The scheme has been divided into individual links in this manner due to the size of the undertaking, and each link includes a major viaduct; the Ely Link comprises the Ely River Viaduct, the Grangetown Link comprises the Grangetown Viaduct, The Eastern Bay Link comprises the Cogan Viaduct, and the Butetown Link comprises the Taff Viaduct, hence the term 'a family of glued segmental bridges'. During construction of the Grangetown and Cogan Viaducts, Cardiff University in conjunction with Bristol University, instrumented segments close to the support (segment no.1), at quarter-span (segment no.6), and at mid-span (segment no. 11/12 respectively). It is worth noting that the Taff Viaduct was instrumented by Strainstall Engineering Services on behalf of Cardiff County Council, and detailed strain data is available for analysis upon request. However, since there is little information available on the construction of the Taff Viaduct, it was decided to limit research into the time-dependent deformations of this type of structure to the Grangetown and Cogan Viaducts.[5,7,9,136-138]

3.4 Bridge Description

Each bridge is similar in size and shape but there are variations, not only between bridges but also between the segments in each bridge. Therefore, it is necessary to provide some background information on each bridge.

3.4.1 Grangetown Viaduct

The twin trapezoidal box deck is made up of a total of 641 segments (weighing between 43.5 and 74 tonnes) of lengths 3.165m and 3.255m for the eastbound and westbound carriageways respectively. Table 3.1 shows the arrangement and lengths of the 17 spans of each carriage-way but due to the run-on spans at both abutments, actual continuous bridge deck lengths are 992.81m and 1014.15m. The longitudinal elevation of the main decks has been designed so that the standard 2.8m deep section appears continuous through the 4 transition segments to the 3.5m deep pier segment (see Figure 3.5). Expansion and contraction in the main deck is catered for by multi-element mechanical expansion joints which each allow a maximum of 360mm of movement. Run-on spans were built into each end abutment. [7,9,136-138]

Each 'balanced cantilever', supported by a single 3m diameter column, consists of 21 segments, 10 either side of a pier segment, which was then connected to the previous completed deck section by an in-situ concrete joint. At each abutment support a further 2 or 4 segments, depending on the carriageway, are attached to ensure that uplift does not occur at the bearings. Between the abutments each deck is supported by 14 circular columns varying in height from 8.5m to 18m, with each column springing from a hexagonal pile cap founded on 7 no. 1300mm diameter piles extending up to 30m below ground level.[136]

3.4.2 Cogan Viaduct

The second post-tensioned glued segmental viaduct on the contract varies considerably from the Grangetown Viaduct in that the deck is based on a rectangular box section made necessary by the curved soffit of the 95m main span, which also provides a 15m navigable clearance to the River Ely at high tide. Table 3.2 shows the arrangement and lengths of the 6 spans for each of the twin boxes, which required a total of 300 segments approximately 2.5m long and weighing between 43 and 117 tonnes. The pier segments to the main span are 6m deep reducing in a graceful curve to 3m deep at the centre of this span and at each approach support (see Figure 3.6). This section depth is kept constant in all the remaining spans. Expansion joints are again multi-element mechanical at both abutments allowing movements of 180mm and 240mm.[5,7,9,136-139]

The arrangement of the spans produces considerable variety in the balanced cantilevers. Supports 2, 3, 4 and 5, counting from the Grangetown abutment, carry a pier segment and 11 further segments in each cantilever. Support 5, the eastern support to the main span, carries a further 7 segments out of balance to reach the closure joint and each balanced cantilever to support 6 consists of 18 segments either side of the pier segment. There are minor variations, particularly in the end spans where the cantilevers go out of balance to reach the abutments. Between abutments, each deck is supported by 5 columns varying in height from 10.8 to 17m and designed to use the Grangetown Viaduct circular section but split in half with 1.5m straights in the transverse direction. The pile caps are carried on piles extending up to 40m below ground level, except for support 6 which is a conventional pad footing and, similarly, Cogan abutment.[136,139]

3.5 Design and Manufacture

The design and manufacture of the bridge segments were similar for each viaduct.

3.5.1 Design

Due to the required horizontal and vertical road alignment and the frequency and spacing of obstacles, the choice of viaducts was a logical solution. A careful feasibility study for Grangetown Viaduct, including comparison of costs for the different construction materials and forms available, showed that the post-tensioned glued segmental balanced cantilever method of construction would provide an economic and aesthetically pleasing structure.[136,139]

The use of twin structurally independent continuous boxes enabled the piers to be positioned to accommodate the skew angles at which the various obstacles needed crossing. Both viaducts were designed to carry the Department of Transport's H.A. loading and checked for 45 units of H.B. loading. The design loading was higher than usual for a principal road so that the needs of the docks and future development areas were met.[136,139]

3.5.2 Concrete Mix

All concrete design work was undertaken in accordance with BS 5400 which relates the quantity of Ordinary Portland Cement (OPC) to concrete type (i.e. plain, reinforced or prestressed), exposure conditions, aggregate size, and control of the maximum water cement ratio. The main overriding factor was the attainment of the specified 28-day cube strength. This was obtained by the inclusion of Pulverised Fuel Ash (pfa) which produced concrete with initially a slower strength gain, but which comfortably exceeded the 28-day strength requirement. The concrete, C52.5, should, according to the design assumption, have a characteristic cube strength of 52.5 N/mm^2 and a Modulus of Elasticity of 34.5 kN/mm^2. The measured compressive strength at 28 days was 49 N/mm^2 and the Modulus of Elasticity was 38 kN/mm^2, which indicated that the concrete was of a higher quality than expected. The mix composition was the same for both Grangetown and Cogan Viaducts, and mix proportions are shown in Table 3.3. White cement was used for aesthetic reasons and the concrete was supplied by an on-site batching plant located adjacent to the precast factory. Plasticizers were added to the mix and during cold weather the water to be used in the mix was heated to a max temperature of 65°C to aid workability.[1,136,139]

3.5.3 Segment Manufacture

The precast deck segments were manufactured on site by the short-line (casting cell) match cast method. By this method the form-work remains stationary whilst the segment moves from the casting position to the match cast position where, prior to being moved to storage, it acts as joint formwork for the next segment to be cast and, therefore, ensures a perfect surface

match between adjacent segments. The segment manufacture sequence is shown in Figure 3.7. A factory was erected on-site to manufacture the segments. The factory consisted of three casting bays, each capable of producing 1 unit per day. The concrete was supplied by an adjacent batching plant in truck mixers.[5,136]

Each casting bay contained 2 formwork jigs of the casting cell, an instrument station and target and the casting cell itself. This consisted of a base pallet, 2 side shutters, 1 removable stop end for the pier segments, a retractable and collapsible core and a rigidly fixed stop end (bulkhead) shutter. The side shutters were rail mounted as was the base pallet, which in addition was self propelled. Manufacture typically commenced with the casting of a pier segment, which was then moved clear of the casting cell. A base pallet and trolley was positioned and set to the required level onto which was then placed the appropriate reinforcement cage. The pier segment was then brought up to the match-cast position where fine adjustments were made to it to reflect the desired alignment into the next segment to be cast. The side shutters were moved into position against seals on both the bulkhead and match-cast segment. Final adjustments, such as concrete cover, were made to the reinforcement cage, etc. at this stage after which the core shutter was inserted and expanded against seals on the bulkhead and match-cast segment. Very precise survey and alignment procedures were employed with the aid of a pile founded survey station and target tower to provide a consistent horizontal and vertical datum such that adjustments could be made to provide for all variations in crossfall, vertical and horizontal curves. Once the segment had gained sufficient strength so that it could be moved (generally the following day), the pier segment was moved out of the factory, turned around and set up to repeat the process. The match casting sequence was then repeated in two bays until a full cantilever of segments was complete.[5,136]

3.6 Construction

The viaducts were constructed segmentally in balanced cantilever, as described in Section 3.1.2, and demonstrated in Figure 3.8. Segment erection proceeded outwards in the form of a pair of balanced cantilevers from each pier. Initially, the pier segment was placed on the permanent bearings and packs at each corner of the unit. Lateral and longitudinal restraint was provided by locking devices which connected the pier segment to the column. The first span segment was lifted to within 500mm of the face of the pier segment and an epoxy adhesive was applied by hand over the previously grit blasted mating faces. The segment was then brought into contact with the pier segment and temporarily stressed into place by Dywidag bars, which provided a uniform pressure over the glued joint. A prop system in the form of

previously erected jacks on military trestles was then constructed under the first span segment to provide stability. This process was repeated for the balancing segment, after which the packs beneath the pier segment were removed. It was then possible to proceed with the threading and stressing of the permanent tendons for the first 3 segments. After stressing, surplus strand was cut off and the deck was then ready for the standard erection cycle of lifting, gluing and stressing into place the remaining segments to complete a balanced cantilever. Permanent stressing was carried out after each pair of balancing segments were in place.[5,136]

Once a balanced cantilever was completed an additional segment was placed under temporary stress on the leading face of the previous balanced cantilever. Minor corrections to the alignment of the recently completed balanced cantilever were carried out at this stage to optimise any error. The adjacent completed cantilevers were separated by a gap approximately 300mm wide, across which the ducts for the continuity tendons through mid-span were placed and the gap concreted. The ends of the cantilevers were then locked together by inserting temporary packs across the joint and stressing against them by means of temporary Dywidag bars. Stressing of the permanent continuity tendons ensued. Deck erection could now proceed at the next pier. The final operation and the most important for durability of the structure was the grouting of the ducts, which was carried out after the closure joint had been completed.[136]

The speed of assembly was generally two segments per day, (one segment on either side of the cantilever) and all construction times relative to this research, are relating to the casting of segment one, i.e. time zero. The most important events during construction relating to this research for the Cogan Viaduct along with comparative dates for the Grangetown Viaduct, are presented in Table 3.4.[5]

3.7 Prestressing System

Both Grangetown and Cogan Viaducts were post-tensioned by means of tendons comprising 8 no. low relaxation 7 wire compact stabilised strands. The strands were fitted into the galvanised ducts by strand pushers and all 8 strands making up a tendon were simultaneously stressed by ram jacks. The specified jacking force was either 2130kN (70% UTS) or 2280kN (75% UTS) and was measured by both the pump pressure gauge and a load cell located in the head of the jack. This was the primary load measuring device having a rated accuracy of ±0.5%. Tendon extensions were also monitored and were found to correlate well with predicted values with a tendency to be greater than calculated. Tendon lengths up to 40m were generally single end stressed unless their extensions fell 5% below the predicted value

when along with tendons over 40m long they were double end stressed. Stressing was alternated end-to-end and side-to-side to ensure an even stress distribution throughout the deck.[136]

The design required a balanced pair of segments to be permanently stressed prior to erecting the next pair. This is generally achieved by a single tendon commencing over each web, but where the design dictated double (and at times on Cogan Viaduct triple) tendons were required. An ancillary prestressing system was used in the end spans of Grangetown Viaduct comprising Macalloy bars stressed to 910kN.[136]

3.8 Instrumentation

As previously mentioned, three specific segments (support, quarter-span and mid-span) in the Grangetown and Cogan Viaducts were instrumented in 1986 by Vitek and Barr[1-3], as part of a research project to investigate early shrinkage and creep in concrete structures. It was decided that in order to measure strains, vibrating wire gauges would be embedded into the bridge during construction. This type of gauge was chosen due to its robustness during installation and casting, and also because, unlike electrical gauges, its readings are not affected by disconnection. Since there was no provision for re-calibrating the gauges, a redundant approach was taken where more gauges were installed than required. Hence, 92 vibrating wire strain gauges type TES/5.5 (Figure 3.9) were embedded at select locations within segment numbers 1, 6, and 11 in Cogan Viaduct, and segment numbers 1, 6, and 12 in Grangetown Viaduct. These segments were chosen since they were located at specific points: as close to the point of maximum hogging moment without being over a support, at quarter-span, and at the point of maximum sagging moment i.e. mid-span, respectively. This can be seen in Figures 3.10 and 3.11, while Figure 3.12 and 3.13 show the locations of the strain gauges within each segment. The gauges are oriented longitudinally in order to measure longitudinal strains (i.e. creep), while a number of rosettes were included in order to measure transverse strains (i.e. shrinkage). Furthermore, in order to measure variations in temperature, a type K thermocouple was installed within segment no. 6 of each structure, its selection based again on its robustness and stability over long periods of time. The instrumentation was deemed successful as only 2 gauges failed to respond after placing the concrete in the segments, both in the Grangetown Viaduct.[5,7,138,139]

The measurement of strain readings is a lengthy process when performed manually due to the number of gauges involved. Therefore it was deemed economical to automate readings by means of a data logger, which could be programmed to take readings at specified intervals and then store the data for collection. Thus visits to the bridge could be minimised and need

only occur on a quarterly basis. A standalone, battery powered, Datataker 600 data logger was employed for this task. However, the data logger has a limited capacity for the number of gauges which it may record. The data logger can record up to 10 differential/30 analog channels at any one time. Each gauge takes up 1 channel and since there are roughly 90 gauges in each bridge, the operator must be selective as to what data is needed and when.

3.9 Previous Studies

Due to the unique position that Cardiff University is in, having instrumented two of the bridges and being responsible for subsequent data acquisition while also having access to the Taff Viaduct data, numerous studies have been undertaken since the construction of the bridges, by both staff and students. This section will summarise the studies carried out so far and the main conclusions each has produced.

A summary of the existing creep and shrinkage data for the Cogan Viaduct was made in the report by Barr *et al*[5]. The results recorded indicate a rapid increase in strain in the top flange during the period of cantilever construction, followed by fluctuations in strain at a decreasing rate as continuity cables in adjacent spans were stressed. Using Bažants double power law for the prediction of creep in concrete, which was a precursor to the BP Model[123], and the CEB-FIP Model Code 1990[121] for predicting shrinkage in concrete, an analysis of the structure was carried out using DOMO98, a computer program developed by Vitek[6] specifically written to facilitate the analysis of modern prestressed concrete bridges (details of the DOMO program provided by Vitek[6] are detailed in Appendix G). Predicted values for long-term strains were shown to compare favourably with the observed values and indicated that the structure was still behaving as predicted after 12 years of service.[1-3,5,7,139]

Nikolaides[140] studied the prediction of creep and shrinkage of Cogan Viaduct using different prediction models, in order to evaluate how accurate such prediction can be when compared to real values of creep and shrinkage for the long-term performance of the structure. The models that were considered that are relevant to this research are BS 5400: Part 4: 1990[130], CEB-FIP Model Code 1990[121], and the B3 Model[114]. It was determined that each of these models gave adequate agreement with the actual strains obtained for the period prior to segment erection, and each could realistically be used to obtain reliable predictions of the short-term shrinkage of concrete structures. However, a comparison of the experimental and predicted strains after segment erection indicated a significant overestimation of the actual total strains. The CEB-FIP Model Code 1990 was deemed the most reliable for prediction of long-term shrinkage, giving agreement to within 10% of the actual strains. The B3 Model overestimated strains by approximately 40% but the strain behaviour was unlike that

interpreted from the real site data, while BS 5400: Part 4: 1990[113] overestimated strains by approximately 50% but the behaviour was similar to that obtained.
Beygi[8], studied the behaviour of the instrumented sections in Grangetown and Cogan Viaducts prior to, during, and after construction. It was determined that the most important factors in the build up of strain during erection and afterwards, were the magnitude of the prestressing force, the weight of the segments and the time-dependent deformations, the most important and uncertain being the magnitude of the prestressing force.

Barr *et al*[9] investigated seasonal shrinkage variation in bridge segments using the strain gauges embedded within the Cogan and Grangetown Viaducts. An extensive programme of monitoring was undertaken in order to determine the relationship between seasonal environmental conditions and concrete shrinkage effects.

The segments for the Cogan Viaduct were cast in the Spring, while the segments of the Grangetown Viaduct were cast in late Summer. Although the concrete mix used for all segments in both bridges was similar, the shrinkage strains observed for the segments of the two bridges have a completely different character. It was concluded that the difference in shrinkage strains for the two bridges was due to varying seasonal effects. To further investigate this variation in shrinkage behaviour, average humidity and temperature data for the Cardiff area for the periods following casting of the segments was obtained from the Meteorological Office. As the relative humidity was much higher at night, two sets of data were calculated; the average daily relative humidity for the day only (between the hours of 9.00 a.m. and 6.00 p.m.), and the total average daily relative humidity, which includes an assumed night average humidity of 90%. It was observed that the relative humidity of the air is very variable and that the strains in the concrete could not follow the rapid changes. However, the strains in the concrete were able to follow the more significant longer term trends in humidity changes.[9]

Another aspect of the research was to test the accuracy of current prediction models to see whether they accurately predict shrinkage behaviour under the same environmental conditions. It was decided to use a simplified form of the BP model[123] which shared the same basic shrinkage formula as the CEB-FIP Model Code 1990[121], the ACI Committee 209 recommendations[117], and the Eurocode 2 for design of concrete structures[131].

Due to the monitoring system used and the early morning measurements, the humidity effects were dominant and the variation in temperature did not significantly influence the measured strains. Hence the effect of temperature was neglected. Since shrinkage strains vary in the individual parts of the cross section (the top flange is exposed to the effects of the weather,

while the bottom flange may be close to the earth), the shrinkage strains measured in the webs were considered the most suitable for this investigation. The shrinkage analysis was carried out assuming two humidity variations for each set of results. The first variation was based on a variable humidity as described by the data obtained from the Meteorological Office, while the second analysis assumed that the humidity remained constant throughout construction.[9]

The results obtained indicted that the assumption of variable humidity gave a predicted shrinkage curve that corresponded very well with the measured results for both bridges, while the assumption of constant humidity produces shrinkage curves that are not quite as accurate, but give satisfactory results which provide a suitable basis for use in design.[9]

Table 3.1. Span lengths for Grangetown Viaduct (County of South Glamorgan[136]).

	Eastbound Carriageway	Westbound Carriageway
Leckwith Abutment	13.00m	12.17m
	38.22m	45.85m
	13×70.00m	7×72.00m
	44.59m	71.00m
		2×70.00m
		71.00m
		2×72.00m
		39.30m
Grangetown Abutment	29.20m	20.29m
Total	1035.01m	1046.61m

Table 3.2. Span lengths for Cogan Viaduct (County of South Glamorgan[136]).

	Eastbound Carriageway	Westbound Carriageway
Grangetown Abutment	37.5	40.0
	3×60.0	3×60.0
	95.0	95.0
Cogan Abutment	57.7	60.0
Total	370.0	375.0

Table 3.3. Mix proportions for Grangetown and Cogan Viaducts (Vitek and Barr[1]).

Ingredient	
Ordinary Portland cement	330 kg/m^3
pfa	170 kg/m^3
20mm aggregate	746 kg/m^3
10mm aggregate	320 kg/m^3
Sand	710 kg/m^3
Water	149 l/m^3
Plasticizer (Complast 211)	1.6 l/m^3

Table 3.4. Important project dates for the Cogan and Grangetown Viaducts (Barr *et al*[5], and Vitek and Barr[1]).

Cogan Viaduct		Grangetown Viaduct	
Time (days)	Construction Stage	Time (days)	Construction Stage
0	Segment No.1 – cast (05/03/87)	0	Segment No.1 – cast (20/08/86)
9	Segment No.6 – cast (14/03/87)	9	Segment No.6 – cast (29/08/86)
20	Segment No.12 – cast (25/03/87)	15	Segment No.11 – cast (04/09/86)
112	Pier segment on pier No. 2		
150	Erection of Segment No. 1		
155	Erection of Segment No. 6		
161	Continuity stressing, span 1		
165	Erection of Segment No. 12		
169	Pier segment on pier No. 4		
206	Continuity stressing, span 2, 1st stage		
231	Pier segment on Pier No. 5		
243	Continuity stressing, span 3, 1st stage		
260	Pier segment on Pier No. 6 Continuity stressing, span 2, 2nd stage		
273	Continuity stressing, span 3, 2nd stage		
281	Continuity stressing, span 4		
347	Continuity stressing, span 6		
379	Continuity stressing, span 5		
433	Additional dead load applied		
535	Loading test (21/08/88)		

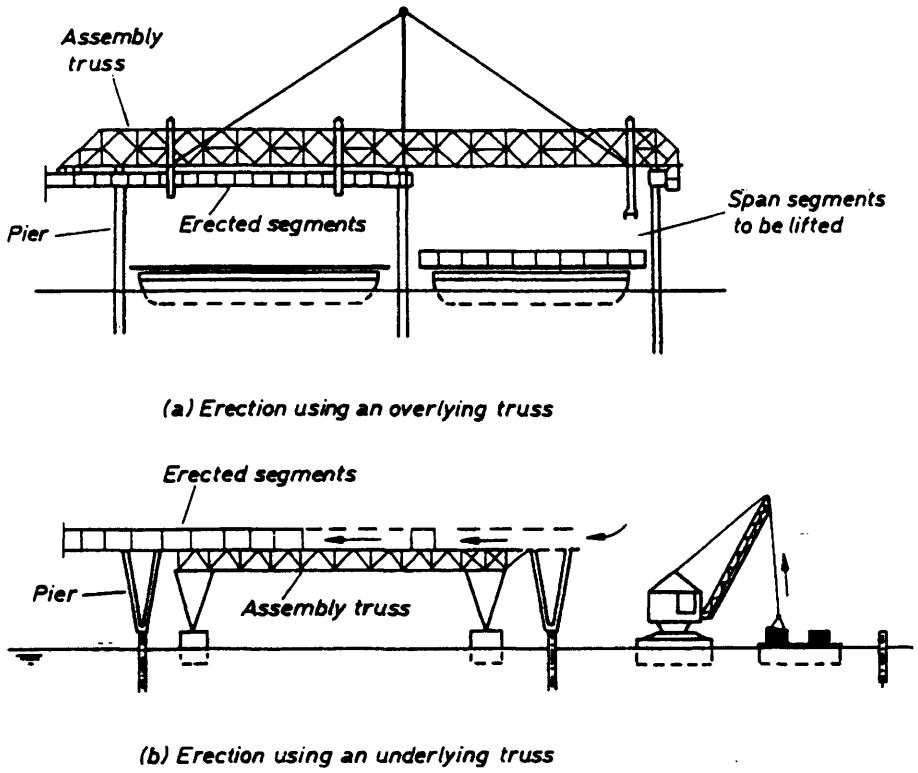

Figure 3.1. Construction using span-by-span method (Ziadat and Waldron[135]).

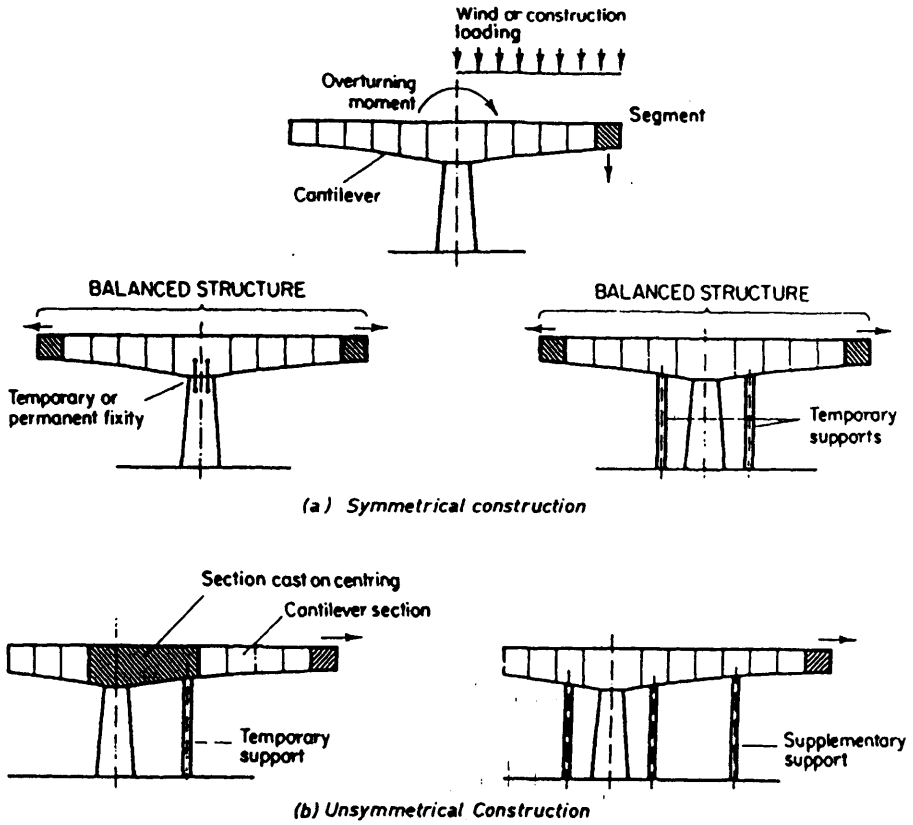

Figure 3.2. Balanced cantilever construction (Ziadat and Waldron[135]).

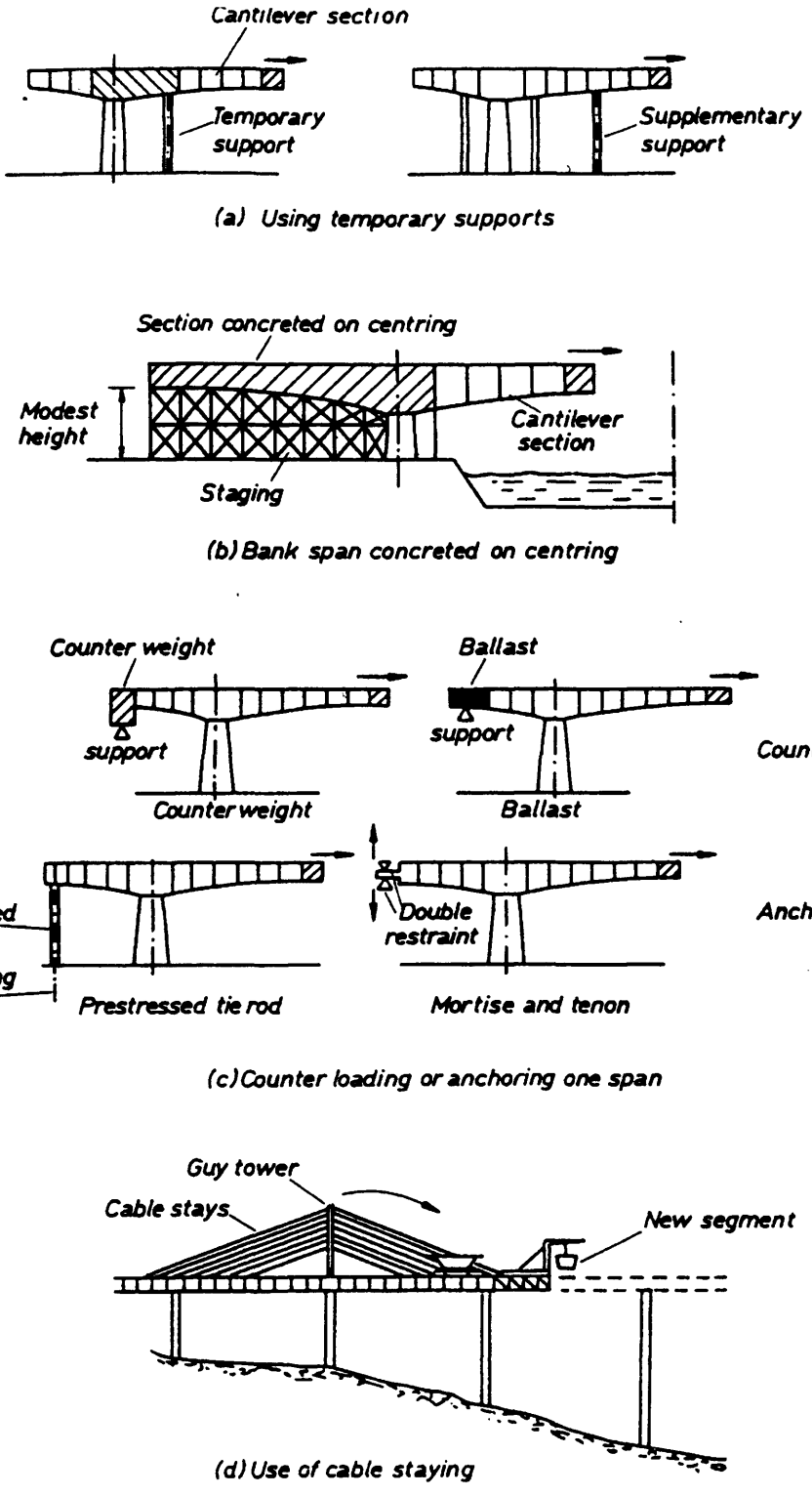

Figure 3.3. Progressive placing techniques (Ziadat and Waldron[135]).

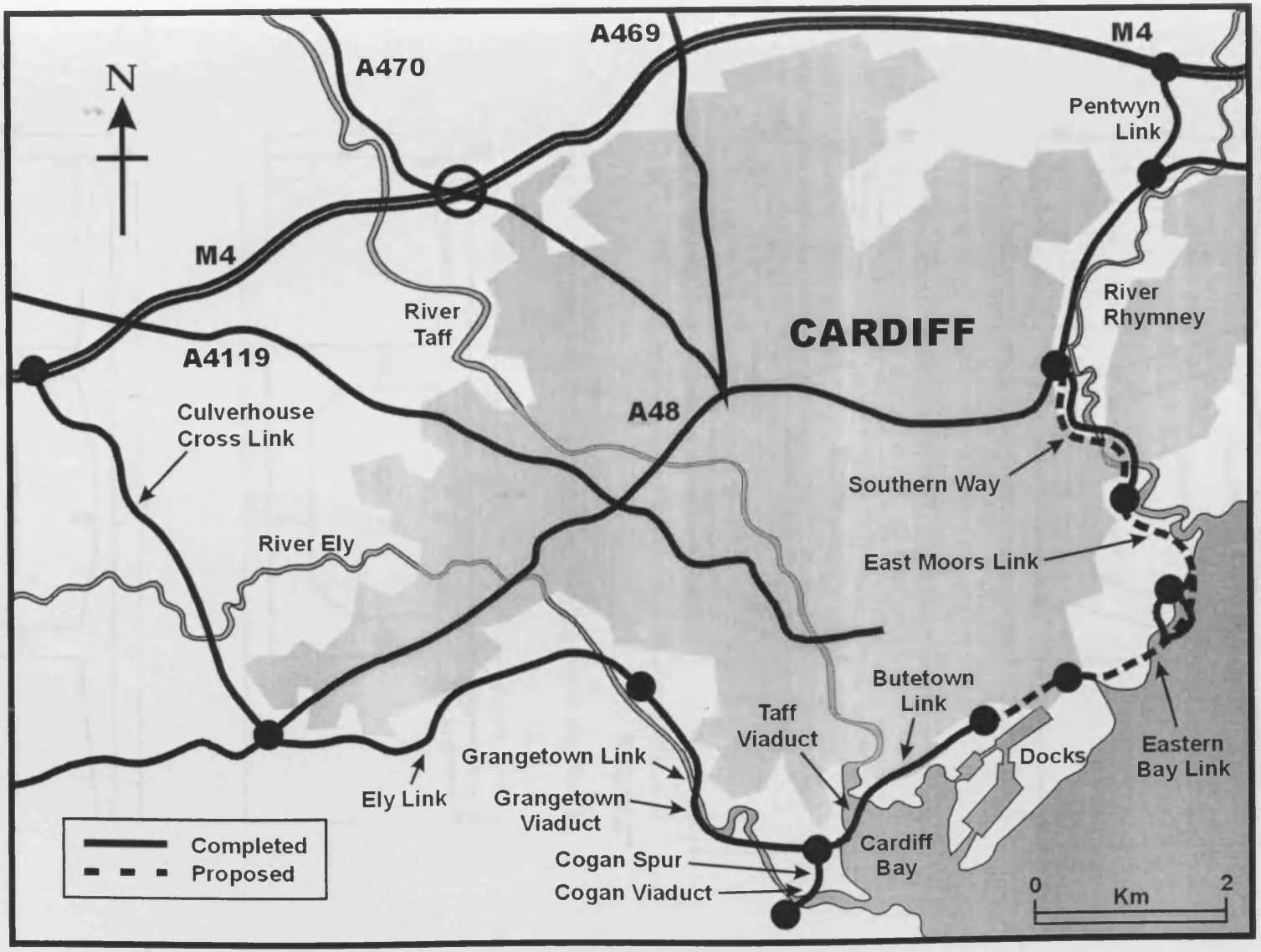

Figure 3.4. Scheme plan

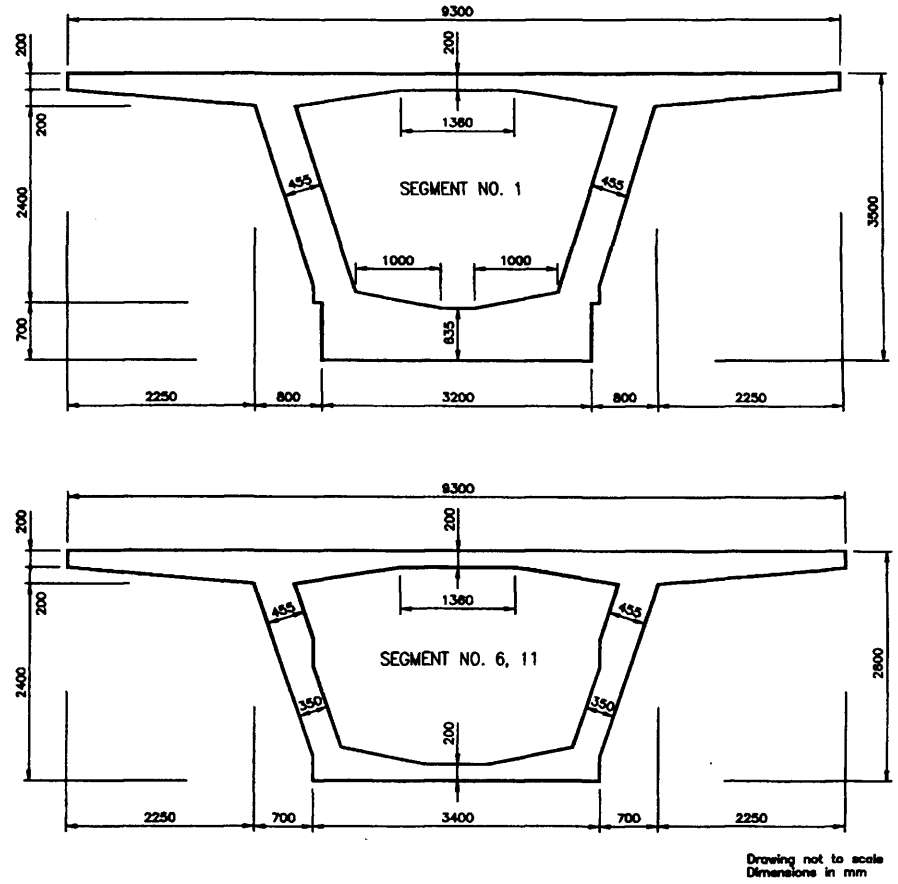

Figure 3.5. Segment geometry, Grangetown Viaduct (Vitek and Barr[1]).

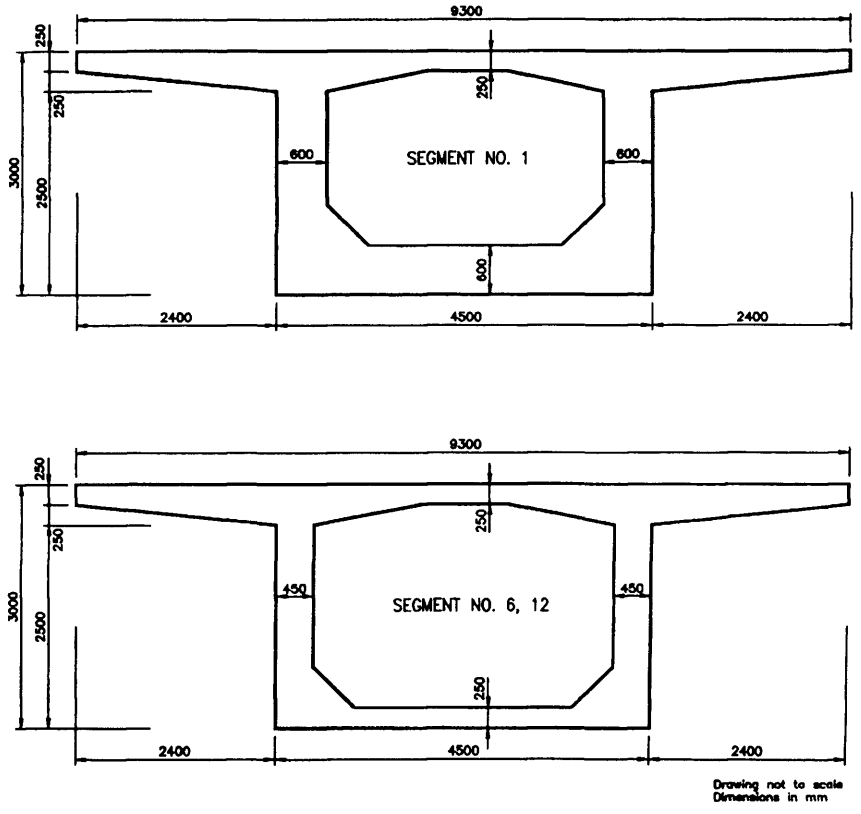

Figure 3.6. Segment geometry, Cogan Viaduct (Vitek and Barr[1]).

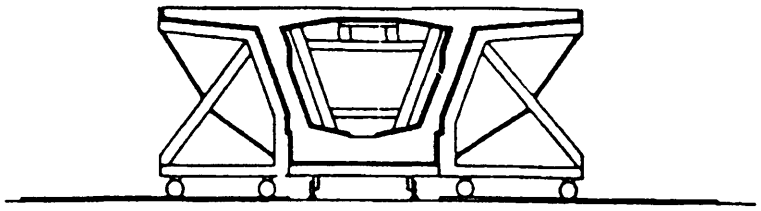

Diagrammatic section showing side shutters and base pallet on rails and core shutter in place ready for concreting.

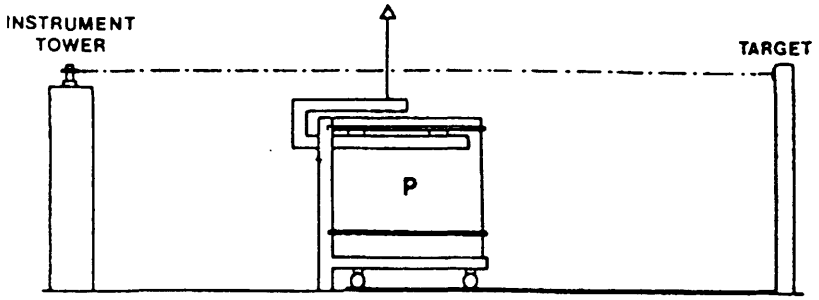

a.

1. Align base pallet.
2. Place reinforcement.
3. Position side shutters.
4. Insert core shutter.
5. Concrete

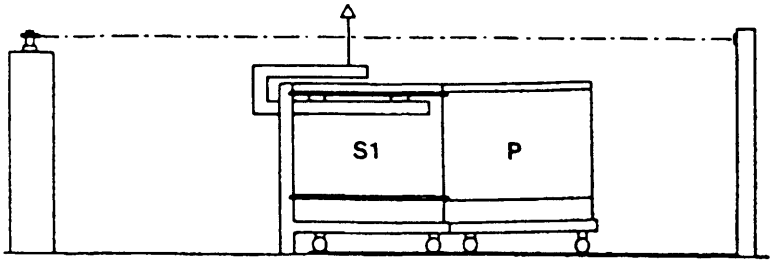

b.

1. Strip shutters.
2. Move pier to match cast position and align.
3. Repeat stage **a**.

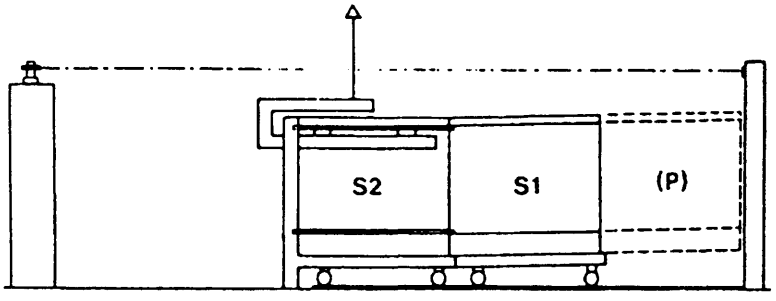

c.

1. Pier unit to store.
2. S1 to match cast position.
3. Repeat stage **a**.
4. Repeat to complete cantilever.

Figure 3.7. Manufacture sequence for match casting of segments (Ramezankhani *et al*[139]).

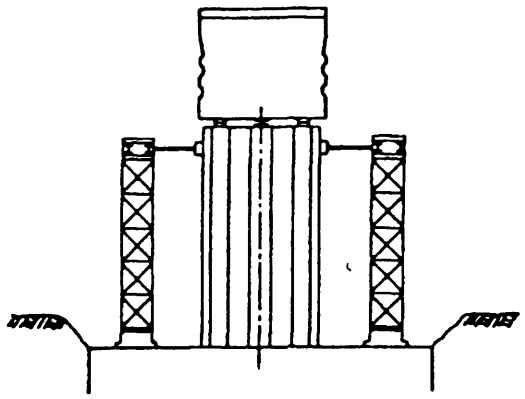

a

1. Bearings set to line and level then grouted.
2. Pier segment placed on bearings and packs.

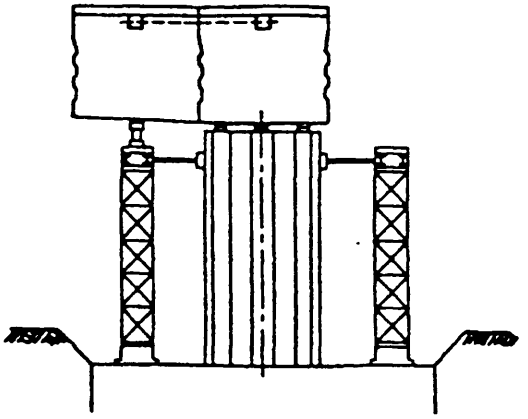

b

1. First span segment glued and temporarily stressed into place.
2. Jacks raised to support segment.
3. Crane detached.

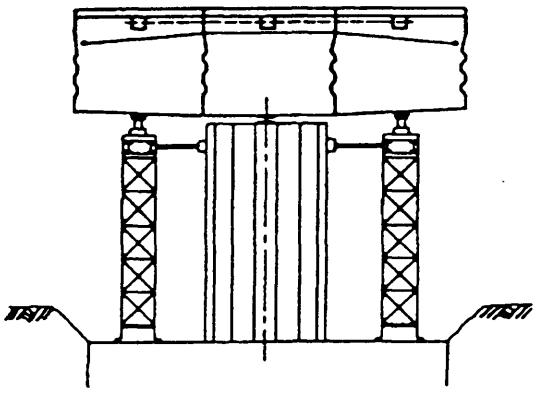

c

1. Second span segment glued and temporarily stressed into place.
2. Jacks raised to support segment.
3. Crane detached and packs removed.
4. Thread and stress permanent tendons.
5. Remove temporary stressing.

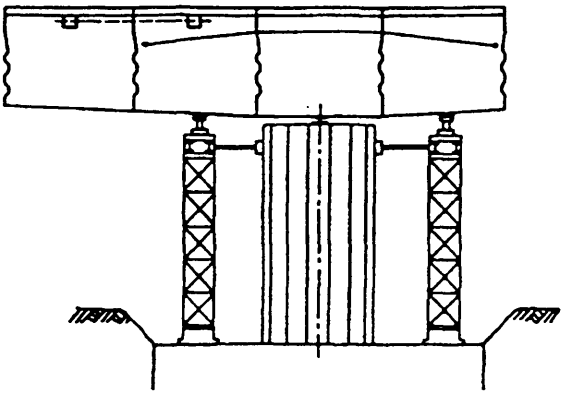

d

1. Next span segment glued and temporarily stressed into place.
2. Crane detached.
3. Repeat 1 and 2 to achieve balance.
4. Thread and stress permanent tendons.

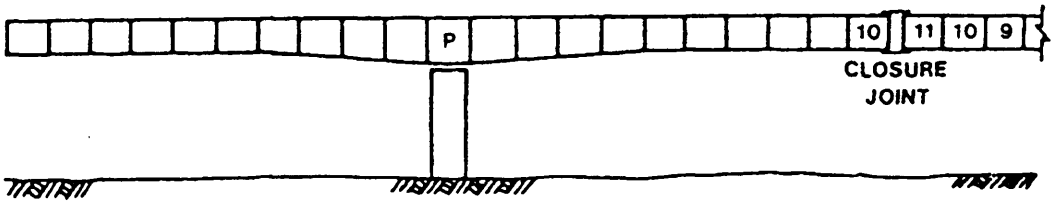

e

1. Repeat stage **d** to complete balanced cantilevers.
2. Erect out of balance segment to previous cantilever.
3. Concrete closure joint to make continuous.
4. Thread and stress continuity tendons.

Figure 3.8. Sequence of balanced cantilever construction (Ramezankhani *et al*[139]).

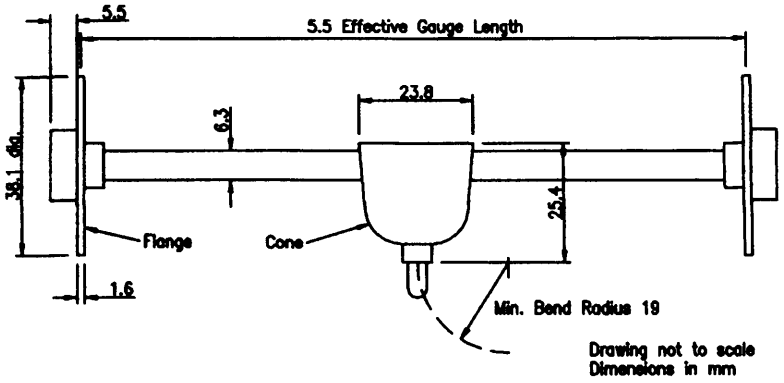

Figure 3.9. Vibrating wire stain gauge (Ramezankhani *et al*[139]).

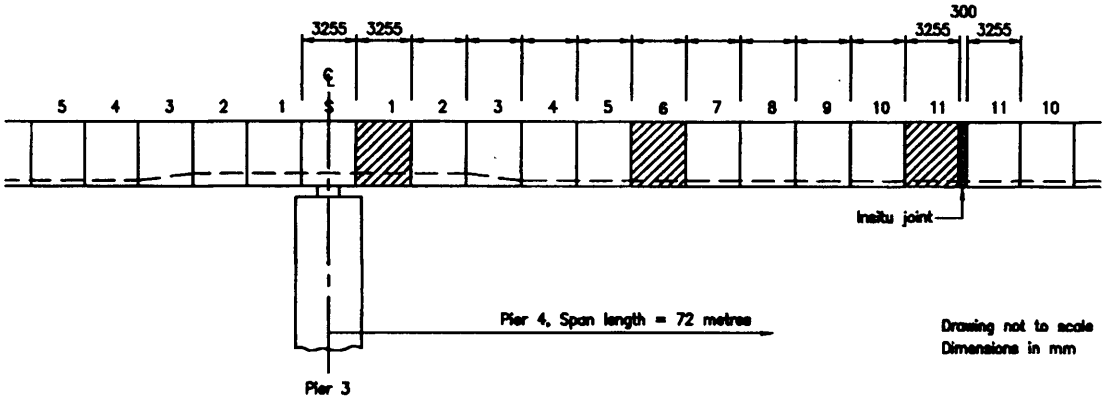

Figure 3.10. Instrumented segments within cantilever right of pier 3, Grangetown Viaduct.

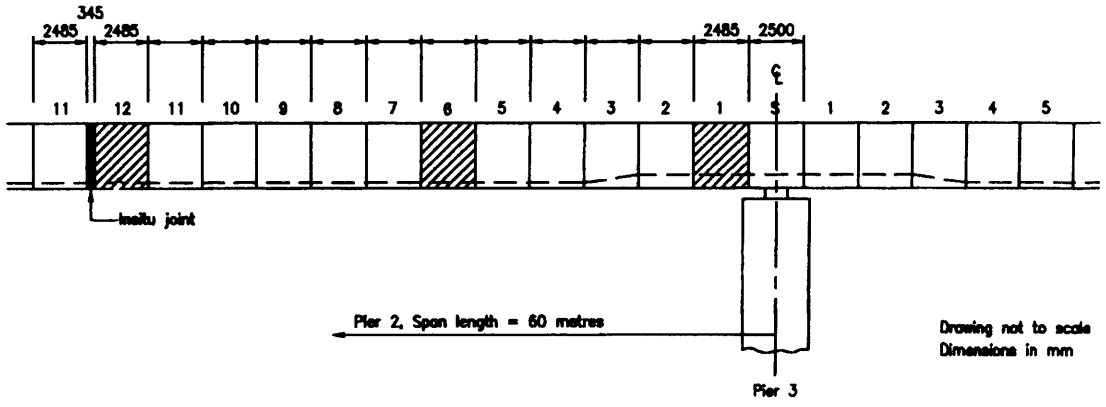

Figure 3.11. Instrumented segments within cantilever left of pier 3, Cogan Viaduct (Ramezankhani *et al*[139]).

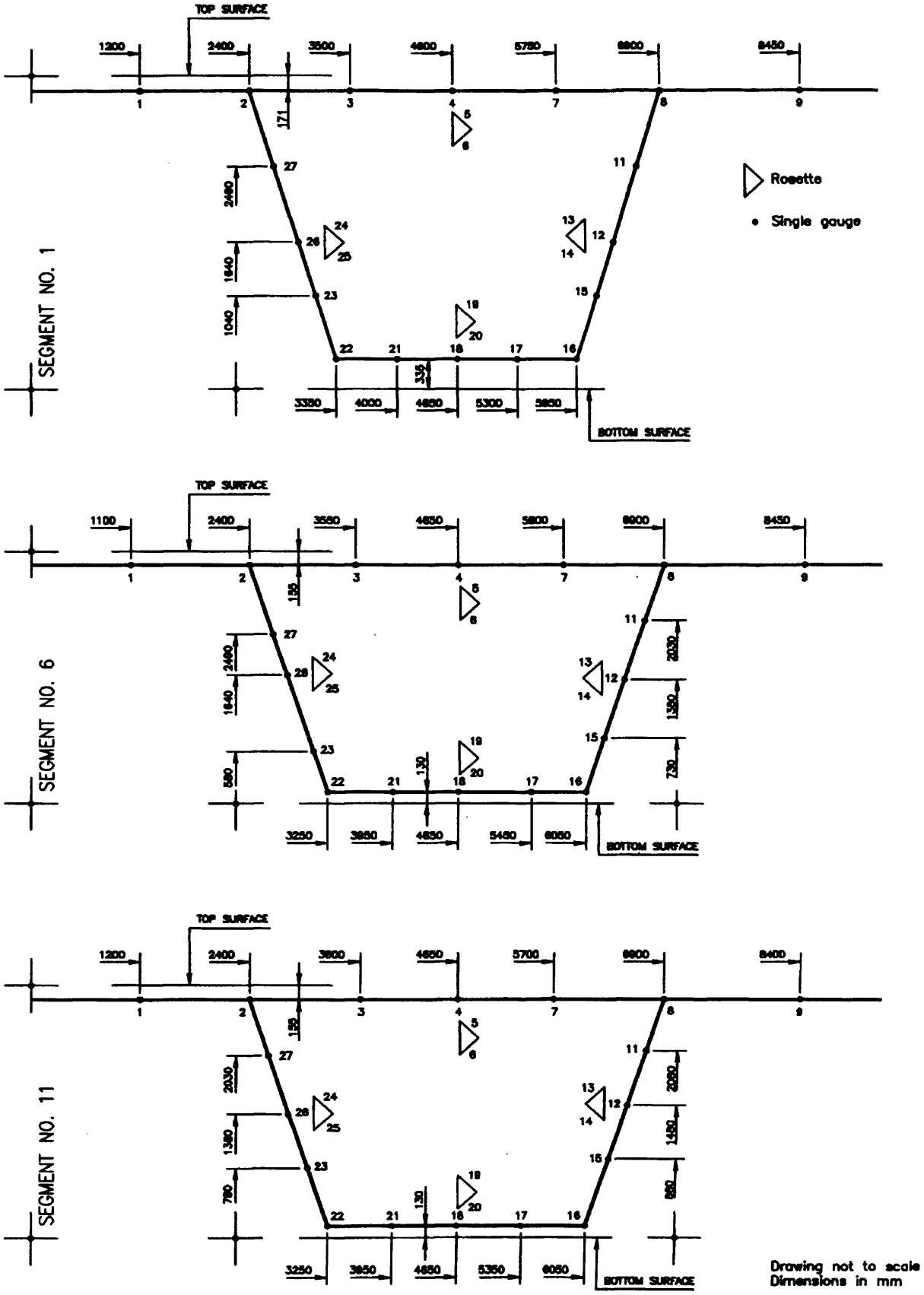

Figure 3.12. Location of strain gauges, Grangetown Viaduct (Vitek and Barr[1]).

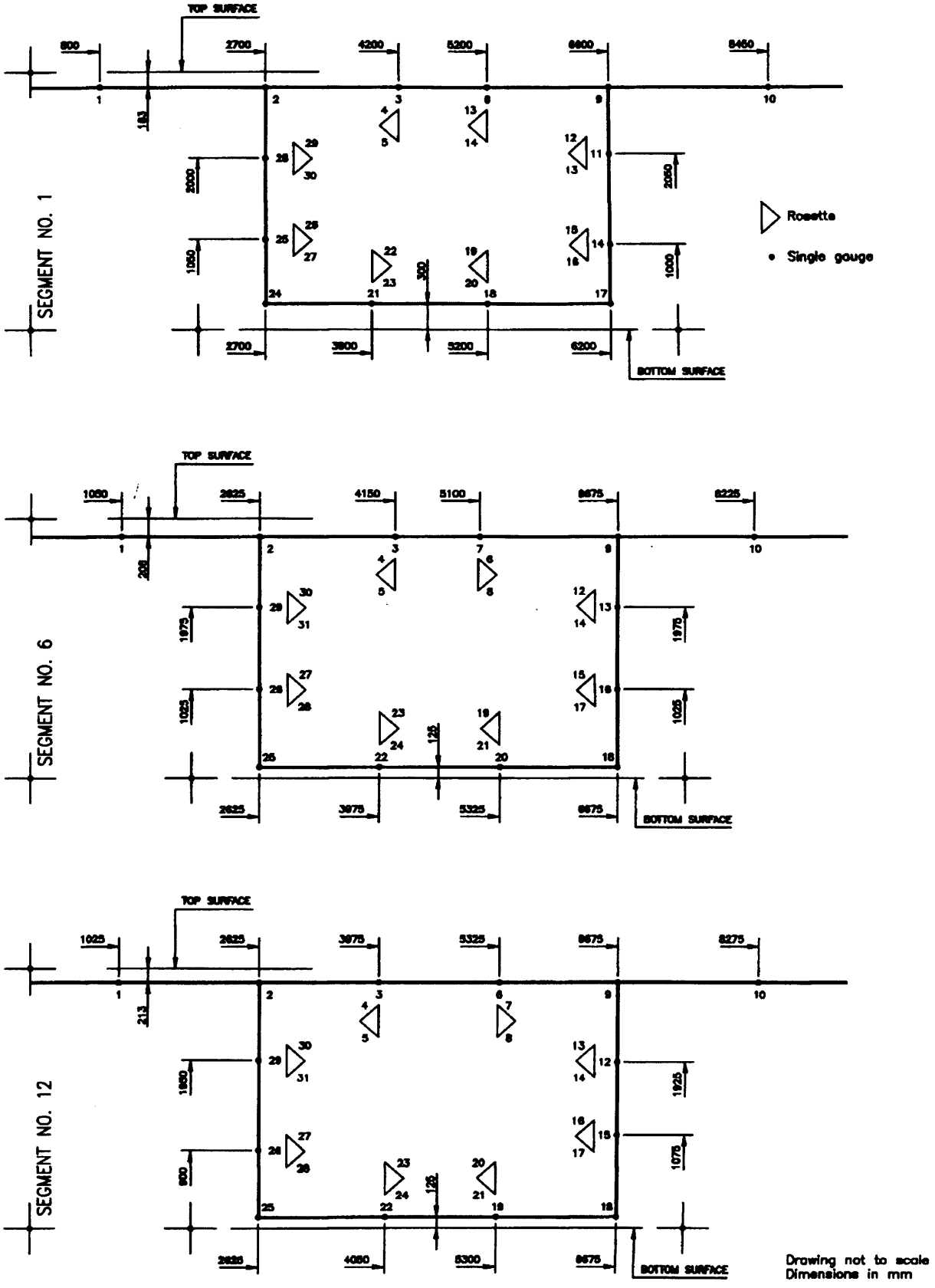

Figure 3.13. Location of strain gauges, Cogan Viaduct (Vitek and Barr[1]).

Chapter 4

Prediction Model Sensitivity Study

4.1 Introduction

With so many different models available for the prediction of time-dependent properties, and the manner in which they do so differing between models, it is difficult to know which is best suited for a given purpose. Indeed, some are more complex than others requiring large amounts of input data such as fresh and hardened concrete properties, environmental conditions, specimen size and shape, and loading conditions.

The aim of this study was to determine how sensitive these prediction models are to the individual input parameters that constitute the input data. In order to do this, the problem was addressed in two parts. Firstly, the sensitivity of changes in the predicted strain to different input data were investigated at a given time, which in this case was 6 months, and secondly, the variation of this sensitivity over time i.e. between 6 months and 2 years, was explored.

4.2 Model Parameters

The models used to predict shrinkage and creep strains in this study are detailed in Chapter 2 and Appendix A. In summary, they are the CEB-FIP Model Code 1990[121] (CEB-FIP), the ACI-92R Model[117] (ACI) the BP-KX Model 1991[125] (BP-KX), the short-form BP-KX Model 1993[126] (BP-KX+), the GZ Model 1993[128] (GZ), the B3 Model 1995[114] (B3), the short-form B3 Model 1996[127] (B3+) and the GL Model 2001[129] (GL). Table 2.14 shows a list of the parameters that were considered in each model. Each of these variables was examined, and in order to do this, a range of values was adopted for use in the study. For compressive strength, the change in the predicted strains was recorded when the 28-day compressive strength was increased from 40 N/mm^2 to 120 N/mm^2. The compressive strength of concrete is dependent upon the mix proportions, in particular the water content and to a lesser degree the cement content. Many of the prediction models considered here take these factors into account and so it is not always a case of simply changing the compressive strength, but also changing the

water, cement, fine and coarse aggregate contents, and even the slump. For the models that take these additional parameters into account (shown in Table 2.15), the mix proportions that were used were as specified by Taylor *et al*[41]. The decision to use these two concrete strengths was due to the fact that normal strength 40 N/mm^2 concrete may be considered as a typical strength for use in the construction of concrete structures, while with the advancement of concrete technology, the use of high strength 120 N/mm^2 concrete is becoming prevalent. Furthermore, a large amount of data was available from earlier and parallel studies, carried out in the same laboratory, on these two concretes.

When changing the compressive strength from normal to high strength concrete, the stiffness of the concrete is also expected to increase. Therefore, changing the Young's Modulus from 30 kN/mm^2 to 60 kN/mm^2 accounts for a wide range of stiffness values found in modern concretes, although the compressive strength was not changed in order to assess the effect of increasing the stiffness alone.

Certain models take into account the effect of cement type and curing regime and hence the cement type was changed from type I to types II and III, while the curing regime was changed from water curing to steam curing and specimens sealed during curing (where appropriate). The curing time was varied from 2 days to 7 days, and also from 7 days to 28 days. The reason for this was to assess the influence of the duration of curing on the shrinkage strain. Also, the time ratio from 2 to 7 days is almost identical to that from 7 to 28 days, and the change in strain over these periods could therefore be analysed in order to determine how sensitive shrinkage is to the length of curing. Following the introduction of a time element to the study, the effect that the age of concrete at loading has on the time-dependent properties was also investigated. In the laboratory creep tests (detailed in Chapter 5), concrete specimens were loaded after 3 months so that the concrete had sufficient time to develop the majority of its compressive strength. This is not always necessary since concrete used in construction has generally attained a desired strength level after 28-days. Therefore, the effect that loading at 28-days had on the strains developed as opposed to loading after 3-months was analysed. Obviously, in the case of shrinkage, loads are not applied to the concrete and hence it was decided to see how the shrinkage strains developed would change if shrinkage testing began in parallel with loading at these two times.

A very important influence on strain, in particular shrinkage strains due to moisture transfer with the environment, is the effect of varying relative humidity (RH). The RH parameter was therefore increased from 45% to 75%, reflecting the range of humidities that a real life structure may experience from changes in environmental conditions.

Finally, the effect that specimen geometry has on the development of strains was addressed. This involved two different factors, namely specimen size and specimen shape. Varying the specimen size affects the shrinkage strains developed because the central core of larger specimens provides a greater restraint to shrinkage, and therefore the amount of shrinkage is reduced. Creep is also reduced in larger specimens because the effects of drying creep are reduced for the same reason. In changing the size of a specimen (with each dimension changed by the same ratio), the effective thickness and volume/surface (v/s) ratio change. A prism of size 600 × 150 × 150 mm having a v/s ratio of 37.5 mm was adopted as the control specimen, since laboratory work on creep has previously shown that this size of specimen yields good creep results[25]. Such a specimen is typical of real life construction, but much larger sizes are also often employed and hence it was decided to see how the predicted strains would change when the specimen size was increased by a factor of 5 i.e. a prism or column type member of size 3000 × 750 × 750 mm, having a v/s ratio of 187.5 mm. Varying the specimen geometry will effect the shrinkage strains developed because specimens with longer moisture diffusion paths will have lower shrinkage rates, although size should have less effect on creep. Some models also allow the shape to be specified in the calculations, however, in changing the shape of a specimen the effective thickness and v/s ratio also change, so altering the shape can effectively be incorporated into all models by changing these values. The two obvious choices for alternative shapes were cylinders and slabs, both of which are used extensively in construction. While the shape was changed, it was important to keep the volume of concrete the same. Therefore, in the case of the cylinder, the cross-sectional area was also kept the same. However, the dimensions of the slab had to be altered significantly in order to make it precisely that, a slab. It was decided to make the slab 50mm thick and hence the cross-sectional area was calculated from the volume since it had to be the same as that of the prism. It is appreciated that this is unusually thin for a slab but it was deemed sufficient for the proposed sensitivity study. A summary of each of these parameters and their values is shown in Table 4.1.

4.3 Magnitude of Change in Strain

Changes in shrinkage strain after 6 months between the aforementioned parameter values are shown in Figures 4.1 and 4.2, while changes in creep strain at the same time are shown in Figures 4.3 and 4.4. The parameters are split over two charts for clarity, and to distinguish between increasing and decreasing changes in strain. It is widely recognised that certain parameters have a more pronounced effect on the time-dependent properties of concrete than others. As a result, all the parameters detailed in this study were grouped according to their influence i.e. they were categorised as major or negligible. In order to ascertain how sensitive

each model is when a particular parameter is varied, the effect that that variable has on the time dependent properties was considered.

4.3.1 Major Influencing Factors (at 6 months)

These factors are those parameters which generally caused a change in strain of the order of 100 με or more and includes those related to environmental effects such as relative humidity, material properties such as compressive strength and stiffness, size effects such as specimen geometry, and time effects such as the age of the concrete when loaded in the case of creep. This limiting value of 100 με is arbitrary and is open to debate.

4.3.1.1 Relative Humidity

When the RH of the environment surrounding the concrete is increased, it is anticipated that shrinkage will decrease because the moisture content in the air is increased and hence, the moisture differential between the concrete and the environment is decreased. This influence is similar for creep. At some point, as the RH of the environment approaches 100%, hygral equilibrium will be reached and the shrinkage and creep strains that occur due to the effect of RH should stop. In increasing the RH from 45 to 75% in this study, the change in shrinkage and creep strains should be significant. This was found to be the case with most of the models predicting changes in shrinkage strain in the range 80 to 190 με and changes in creep strain in the range 140 to 310 με. The one exception to this was the GZ model which unexpectedly exhibited virtually no change in creep strain (-1 με).

4.3.1.2 Compressive Strength

When the compressive strength is increased, both shrinkage and creep are expected to decrease because in order to increase the strength of concrete the water content used in the concrete mix had to be reduced. Therefore, decreasing the amount of water in the concrete should result in less drying shrinkage and drying creep. In this study, in order to increase the strength of concrete by such a large margin from 40 to 120 N/mm^2, the water content had to be significantly reduced from 224 to 122 kg/m^3 and hence the change in shrinkage and creep strains was expected to be quite large. This was certainly the case with most models giving changes in shrinkage strains in the range 120 to 380 με, although the ACI model predicted a smaller change of only 50 με. The models gave differing results with regard to the change in creep strains. The CEB-FIP, EC2, B3 and B3+ models exhibited changes in the range 320 to 460 με, while the BP-KX and BP-KX+ models displayed changes of approximately 800 με.

The ACI model predicted a small change of approximately 50 με while the GZ and GL models suggested that there would be virtually no change whatsoever, which was unexpected. In changing strength, it is inevitable that other factors which also influence shrinkage and creep such as the mix proportions must also be changed. In this study, such a wide variation in predicted strains due to changes in the compressive strength was somewhat surprising, and is an indication of how difficult it is to isolate one parameter such as strength in the prediction models.

4.3.1.3 Young's Modulus

Increasing the Young's Modulus should have no effect on the shrinkage of concrete because it does not change the way in which water is removed from the material, as was the case with all of the models. However, it should have an effect on creep. Young's Modulus is a measure of a material's resistance to deformation, so it can be anticipated that increasing the Young's Modulus will cause an increase in the stiffness of the concrete, which means that the concrete will have a higher resistance to deformation due to the applied load and hence the creep strain should decrease. In increasing the Young's Modulus from 30 to 60 kN/mm^2, the output from the models differed by the magnitude of the change in creep strain. The BP-KX, BP-KX+, B3 and B3+ models predicted changes in creep strains in the range 130 to 220 με, while the CEB-FIP, EC2, ACI, GZ and GL models exhibited more significant changes in the range 420 to 600 με.

4.3.1.4 Size

When the size of the concrete member is increased, the volume/surface (v/s) ratio increases and it might be expected that shrinkage and creep will decrease, with the effect being more pronounced in the short-term. The size of a concrete specimen will influence the rate of moisture loss and the degree of overall restraint provided by the central core, which will have a higher moisture content than the surface. Therefore, as the member size is increased, shrinkage should reduce due to the fact that only the outer part of the concrete is drying and its shrinkage is restrained by the non-shrinking core. Obviously over time the core will also dry out, although this will be a gradual process and will not cause the same rapid effect witnessed in the short-term. Also, if no drying occurs as in very large concrete members, creep is smaller and is independent of size because there is no additional effect of drying on creep.

When the specimen size is increased from a v/s ratio of 37.5 to 187.5 mm, all models exhibited the expected decrease in shrinkage strain but differed in the magnitude by which the shrinkage strain changed. The BP-KX, BP-KX+, B3 and B3+ models indicated a decrease in the range 150 to 190 με, the CEB-FIP, EC2, ACI and GZ models suggested a decrease in the range 240 to 300 με, while the GZ model predicted a decrease of approximately 400 με.

Similarly, for the same increase in specimen size all models with the exception of the GZ model predicted the expected decrease in creep strain but differed in the magnitude by which the shrinkage strain changed. The GZ model showed a negligible 3 με increase in creep strain, which was somewhat surprising. The CEB-FIP, EC2, ACI and GL models exhibited a decrease in the range 220 to 280 με, while the B3 and B3+ models predicted a large decrease in the range 1050 to 1080 με, and the BP-KX and BP-KX+ models exhibited an even larger decrease in the range 1442 and 1310 με respectively.

4.3.1.5 Shape

The effect of changing the concrete specimen shape from a prism to either a cylinder or slab varies significantly depending on the shape and the v/s ratio of the specimen. Longer moisture diffusion paths lead to lower shrinkage rates, e.g. a T-beam has a high surface/volume ratio and will therefore dry and consequently shrink more rapidly than a beam with a square cross-section of the same area. The same principle applies with drying creep. Therefore, since the cylinder had the same cross-sectional area as the prism, the v/s ratio was also very similar and there should be very little difference in the shrinkage and creep strains between these two shapes, with the cylinder possibly having lower shrinkage strains due to the geometry of the cross-section. However, the effect of changing the shape from a prism to a slab of the same volume of concrete should have been much greater since, while the depth of the specimen was decreased from 600 to 50 mm, the cross-sectional area was increased from 22500 to 270000 mm^4, and therefore the v/s ratio was increased from 37.5 to 129.9 mm. The minimum moisture diffusion path length in the prism was 75 mm whereas in the slab the minimum length was 25 mm. Therefore, shrinkage and drying creep should occur far more rapidly with much lower strains, and the difference in strain should be large.

When the shape is changed from a prism to a cylinder, all models exhibited either the expected negligible decreases or unexpected but negligible increases in shrinkage strain of up to 25 με. All models indicated the expected negligible decreases in creep strain of up to 30 με. When the shape is changed from a prism to a slab the changes in the time-dependent strains were much larger. All models exhibited an expected decrease in shrinkage strain of 100 to

343 με. Similarly, all models showed the expected decrease in creep strain but differed in the magnitude by which the creep strain changed. The GZ model indicated a negligible 3 με decrease in creep strain which was somewhat surprising, the CEB-FIP, EC2, ACI and GL models suggested a decrease in the range 160 to 220 με, while the RILEM models indicated a surprisingly large decrease in the range 1000 to 1384 με.

4.3.1.6 Age at Loading

The effect that changing the age at which the concrete is loaded has on the time dependant deformations of concrete applies to the creep strains only, since the application of load only affects the magnitude of creep. If concrete is loaded after 3 months as opposed to 28 days, it was expected that the magnitude of the creep strains should be less as the concrete will have hydrated for longer, so allowing more C-S-H to develop, and strength and stiffness to increase so providing a greater resistance to deformation. Therefore, the magnitude of the change in creep strain should be greater in the short-term for the concrete loaded at 28-days, as it is still gaining strength, as opposed to the concrete loaded at 3 months which will have gained the majority of its strength.

This is a slightly unfair comparison as the concrete will be a different age depending on when it was loaded. The ACI and GZ models indicated an increase in creep strain with loading ages of 5 and 91 με respectively, which is contrary to what was expected. All other models gave the expected decrease in creep strain, but the magnitude of the change in strain differed. The CEB-FIP, EC2 and B3 models all showed deceases in strain in the range 80 to 100 με, while the BP-KX, BP-KX+, B3+ and GL models suggested deceases in strain in the range 200 to 270 με.

4.3.2 Negligible Influencing Factors (at 6 months)

These factors are those parameters which generally caused a change in strain of the order of approximately 100 με or less and includes those related to material composition such as cement type, and those related to the hydration process such as the curing regime and duration. This range of strain variation (0 to 100 με) is arbitrary and is open to debate.

4.3.2.1 Cement Type

It was anticipated that the effect of changing the cement type from Ordinary Portland Cement (OPC) (Type I) to either slowly hardening cement (Type II) or rapid hardening cement (Type

III) would be more pronounced within the first three months. With slowly hardening cement, the rate of gain in compressive strength of the concrete will be slower than in OPC, while with rapid hardening cement, the rate of gain in compressive strength of the concrete will be much quicker. However, after six months most of the compressive strength of the concrete will have developed for each of the cement types and the differences in shrinkage and creep strains should be minimal. If there were any differences at this time, there should be an increase in shrinkage and creep strains when the cement type is changed from OPC to rapid hardening and a decrease when it is changed from OPC to slowly hardening.

When the cement type was changed from OPC to slowly hardening cement, all models which considered this parameter exhibited the expected decrease in shrinkage strain in the range 50 to 70 με, with the exception of the GZ and GL models which suggested changes of 120 and 220 με respectively. The same models showed either the expected increase or an unexpected decrease in creep strain in the range 30 to 80 με. When the cement type was changed from OPC to rapid hardening, all relevant models indicated an expected increase in shrinkage strain in the range 25 to 140 με, while the ACI model showed no change. However, unexpectedly all models suggested an unexpected decrease in creep strain in the range 25 – 100 με.

4.3.2.2 Curing Regime

In a similar fashion to the effect of changing the cement type, the effect of changing the curing regime from water curing to steam curing or sealing the concrete during curing is more pronounced in the short-term. When concrete is cured in steam, the curing temperature is increased and the development of calcium silicate hydrate (C-S-H) gel within the cement paste during hydration becomes more rapid, so increasing the rate of strength gain and the stiffness of the concrete. Since hydration occurs at a quicker rate, it finishes earlier and hence there is less water held in the concrete, and therefore shrinkage and drying creep is reduced. However, after six months most of the compressive strength of the concrete will have developed and the differences in shrinkage and creep strains should be minimal. When concrete is sealed during curing, the concrete is denied water, hydration comes to a halt sooner and so there should be a noticeable increase in shrinkage over the early life of the concrete. Similarly, since hydration comes to a halt, the development of the concrete strength is reduced and since the compressive strength is reduced, the creep strain should increase.

When the curing regime was changed from water to either steam or sealed curing, all models in which this parameter could be varied exhibited negligible changes in shrinkage and creep

strains as expected with the exception of the BP-KX and BP-KX+ models which predicted unexpected and surprisingly large decreases in creep strain in the range 150 and 210 με.

4.3.2.3 Duration of Curing

It is anticipated that in the short-term, the effect that increasing the curing time has on the time dependant deformation of concrete will become more noticeable the longer the period of initial curing. When concrete is placed under a controlled curing regime, as the curing time increases more cement becomes hydrated and the volume of unhydrated cement particles reduces. Obviously, the longer the concrete is cured, the more C-S-H is developed within the paste and the greater the strength and stiffness of the concrete that results. Curing concrete for 2 days would mean that the concrete is still very weak and therefore the creep strain would be high because of this. After 7 days, the concrete would be well cured and adequate strength and stiffness would have developed, so the creep strain should be less. Similarly, after 28 days the concrete will have cured further, the strength and stiffness of the concrete will be larger still and the creep strain will further reduce. However, since hydration is most rapid between 2 and 7 days, then the change in shrinkage and creep strains between 7 and 28 days is expected to be only marginally larger than the corresponding change in strain between 2 and 7 days.

When the curing time was changed from 2 days to 7 days and from 7 to 28 days, all models showed a negligible change in shrinkage strain with the exception of the ACI and GZ models which for the former exhibited decreases of 100 and 130 με. Likewise, all models showed negligible changes in creep strain indicating that what is important is the percentage change in time rather than the actual duration when predicting strains.

4.4 Magnitude of Change in Strain over Time

It was also important to see how the predicted strains made by the models, change over time when the parameters are varied. Figures 4.5 and 4.6 show the changes in shrinkage strain after 2 years, while Figures 4.7 and 4.8 show the changes in creep strain after 2 years. As can be seen, certain parameters show increases in the magnitude of the change in strains from 6 months to 2 years while some parameters show decreases. Tables 4.2 and 4.3 show the magnitude of the changes and also the percentage change (in italics) in shrinkage and creep strains over this period. It is important to note that positive values of the percentage change show an increase in the *magnitude* of the change in strain while negative values show a decrease. It is also important to look at the magnitude of the change in strain as well as the

percentage change because whereas the percentage change in strain is very large in some cases (much greater than 100%), the actual change in the magnitude of strain is often very small (less than 50 με). The effect that changing these parameters has on the predicted strains over time will now be discussed.

4.4.1 Major Influencing Factors over Time

These are factors that still had a pronounced effect on the time dependent properties of concrete after 6 months and 2 years, such as relative humidity, compressive strength, stiffness and specimen geometry.

4.4.1.1 Relative Humidity

It has already been noted that the relative humidity of the environment surrounding the concrete might be expected to have a marked effect on the time-dependant strains in concrete. The effect should still be noticeable in the change in shrinkage strain after 6 months, but the change in creep strain over the same period due to the influence of drying creep can be expected to be even greater. All models (with the exception of the ACI and GZ models) were found to be moderately sensitive to changes in RH over time, predicting changes in shrinkage strain in the range 40 to 70 με, while the ACI model predicted a smaller change of 28 με and the GZ model showed no change which was somewhat surprising. Similarly, all models (with the exception of the ACI, GZ and B3 models) suggested the same noticeable change in creep strain in the range 60 to 130 με, while the B3 model indicated a large change of 261 με with a percentage change over time of 84%. The ACI model predicted a small change of 32 με, and the GZ model showed no change in creep strain, which was again unexpected.

4.4.1.2 Compressive Strength

The effect that changing the compressive strength of the concrete has on the time dependent deformations should also be significant due to the fact that increasing the compressive strength means reducing the water content causing the majority of both creep and shrinkage to occur far earlier in the life of the concrete. All models (with the exception of the ACI and GZ models) demonstrated that this was the case, predicting changes in shrinkage strain in the range 75 to 120 με, while the ACI and GZ models predicted much smaller changes in the range 9 to 22 με, which were somewhat smaller than those anticipated. Similarly for creep, the ACI model predicted a negligible change in creep strain between 6 months and 2 years of 15 με while the GZ and GL model showed no change in creep strain, which was again

surprising. The CEB-FIP and EC2 models, which incidentally have shown almost identical shrinkage and creep strains throughout this study due to the fact that they are based on similar prediction formulae, indicated a change in creep strain of 81 με, while the B3 and B3+ models exhibited larger changes in the range 150 to 170 με, and the BP-KX and BP-KX+ models exhibited changes of 260 and 310 με. Percentage changes in creep strain were also relatively small for all models (less than 45%) indicating that the sensitivity to change over time is relatively low.

4.4.1.3 Young's Modulus

As previously mentioned, changing the Young's Modulus of the concrete should have no effect on the shrinkage strain and this was again the case for all models. Increasing the Young's Modulus should only have an effect at the time of load application when the instantaneous strain developed. Between the age of 6 months and 2 years, it is expected that there will be no further effect on the creep strain by changing this parameter, and the change in strain should be negligible. This was certainly the case for the BP-KX, BP-KX+, B3 and B3+ models where there was no change at all, while the GZ model exhibited a negligible change of 13 με. However, the CEB-FIP, EC2, ACI and GL models showed changes in creep strain in the range 80 to 100 με, which was unexpected.

4.4.1.4 Size

The effect that changing the size of the specimen has on the predicted strains over time was expected to be very similar to changing the specimen shape from a prism to a slab since the v/s ratio is similar. There should be a marginal change in the shrinkage strain and this was the case with all models showing changes in shrinkage strain of less than 100 με. Again it might have been expected that there would be a noticeable change in creep strain over time due to the fact that drying creep should still be occurring in the prism while it should have finished in the slab due to the larger v/s ratio and shorter moisture diffusion paths. The models predicted conflicting results when this change in creep strain over time is observed. The CEB-FIP, EC2, ACI and GL models all showed small, negligible changes in creep strain of up to 50 με, while the BP-KX, BP-KX+, B3 and B3+ models showed much larger changes in creep strain in the range 270 to 450 με. The GZ model again exhibited no change which was unexpected. Percentage changes in creep strain were also relatively small for all models indicating that the sensitivity to change over time is low.

4.4.1.5 Shape

When the specimen shape is changed from a prism to a cylinder, all models demonstrated a negligible change in shrinkage and creep strains which was as expected since the cross-sectional area and v/s ratio were very similar for the two different shapes. Since the majority of shrinkage will have taken place in the first 6 months, there is little change in shrinkage strain expected even when the specimen shape is changed from a prism to a slab. This was certainly the case with regard to the change in shrinkage strain with all models showing negligible changes in strain. However, since the majority of drying creep will have taken place within the slab over the first 6 months, a noticeable change in creep strain was expected when the specimen shape was changed from a slab to a prism since drying creep will still be occurring in the prism after this time due to the smaller v/s ratio. The models indicated conflicting results when this change in creep strain over time was observed. The CEB-FIP, EC2, ACI, GZ and GL models all depicted negligible changes in creep strain of up to 60 με which was unexpected, while the BP-KX, BP-KX+, B3 and B3+ models predicted much larger changes in creep strain in the range 250 to 430 με.

4.4.2 Negligible Influencing Factors over Time

As previously mentioned, the effect of changing certain parameters will have a more pronounced effect in the early life of the concrete when hydration is still occurring and the rate in gain of the compressive strength is at its most rapid. However, in the long term (6 months and onwards), the effect of these parameters on the shrinkage and creep of concrete should be minimal. These parameters include the cement type, length of curing and the curing regime, and the shape of the concrete specimen. Percentage changes in creep and shrinkage strain for the following parameters were often large, but because the magnitude of change was relatively small, it can be concluded that all models gave an adequate representation of the change in shrinkage and creep strains over time when the parameter in question was changed.

4.4.2.1 Cement Type

When the cement type was changed from OPC to either slowly hardening or rapid hardening, all models exhibited negligible changes in shrinkage and creep strain of less than 50 με.

4.4.2.2 Curing Regime

The CEB-FIP, EC2, GZ and GL models do not consider this parameter when predicting shrinkage and creep strains. When the curing regime was changed from water to steam, all other models showed a negligible change in shrinkage strain. Similarly, when the curing regime was changed from water to sealed all models again exhibited negligible changes for both shrinkage and creep, which was as expected.

4.4.2.3 Duration of Curing

Since the majority of curing will have taken place prior to six months regardless of how long the concrete was cured initially, it is anticipated that there will be little change in strain from 6 months to 2 years. All models showed the expected negligible change in shrinkage and creep.

4.4.2.4 Age at Loading

As previously mentioned the age at loading applies to the creep strains only. After 2 years, whether the concrete was loaded after 28 days or 3 months was expected to have little effect on the magnitude of the creep strain since hydration and the majority of strength development will have come to an end. However, it is probable that after 6 months there would still be some effect on the magnitude of creep strain and so there may be a small difference in the strain values. All models with the exception of the BP-KX model showed a negligible change in strain of less than 40 $\mu\varepsilon$, while the BP-KX model suggested an exceptional large change in creep strain of 234 $\mu\varepsilon$, which was somewhat surprising.

4.5 Conclusions

From this study of the CEB-FIP, EC2, ACI, BP-KX, BP-KX+, GZ, B3, B3+, and GL prediction models, it has been concluded that certain parameters have a much bigger influence on the time-dependent strains than others. It has been confirmed that the two most influential parameters on the shrinkage and creep of concrete are the relative humidity of the environment and the compressive strength of concrete, while the Young's Modulus of concrete has an effect on the creep strain, although to a lesser extent. The specimen geometry also has an influence on the shrinkage and creep behaviour although also to a lesser extent. An appreciation of these facts and the sensitivity level of these parameters as opposed to the negligible factors must therefore be taken into account when selecting a prediction model for the time-dependent analysis of concrete materials and structures.

It has been determined that each of these models is more sensitive to some parameters than others, with the parameters that are the most sensitive being dependant upon the model.

However, if the strains predicted by each model are even remotely similar over time then this would suggest that for any given model, any parameters that don't appear to indicate entirely accurate behaviour when changed may well counterbalance each other, and any errors are therefore cancelled out. This would suggest that no one model can be said to be more accurate, and when deciding which model to use when predicting shrinkage and creep strains, it is prudent to look at the individual parameters on which each model is dependant, and assess the sensitivity level of each of these parameters so that the most appropriate model for the specific circumstances can be selected.

On a final note, it has been noticed that the CEB-FIP Model Code 1990 and the Eurocode 2 1992 have predicted virtually identical strains for both creep and shrinkage for all varied parameters. This is unsurprising since the two models share exactly the same shrinkage formulae, and very similar creep formulae. In the following studies within this thesis where time-dependant strain prediction for concrete is considered, it has been deemed unnecessary to use both models and therefore the strains predicted by the CEB-FIP Model Code 1990 will be assumed to be the same for the Eurocode 2.

Table 4.1. Model parameter values.

Model Parameter	**Control**	**Alternative(s)**
Relative Humidity (%)	45	75
28-day Compressive Strength (N/mm^2)	40	120
Cement Content (kg/m^3)	400	510
w/c ratio	0.56	0.24
Water Content (kg/m^3)	224	122
Aggregate Content (kg/m^3)	1800	1739
Slump (mm)	200	160
Cement Type	I	II, III
28-day Young's Modulus (kN/mm^2)	30	60
Curing Regime	Water	Steam, Sealed
Curing Time (days)	28	2, 7
Age at Loading (days)	90	28
Size (mm)	$600 \times 150 \times 150$	$3000 \times 750 \times 750$
V/S ratio (mm)	37.5	187.5
Shape	Prism	Cylinder, Slab

Table 4.2. Change in shrinkage strain between 6 months and 2 years when model parameters are varied with percentage change in italics.

Model	Relative Humidity	28-day Compressive Strength	28-day Young's Modulus	Cement Type (I-II)	Cement Type (I-III)	Curing Regime (Water – Steam)	Curing Regime (Water – Sealed)	Curing Time (2 – 7 days)	Curing Time (7 – 28 days)	Size	Shape (Prism – Cylinder)	Shape (Prism – Slab)
CEB-FIP	-44	-118	0	-15	44	-	-	-	-	-18	12	11
	+31	*+31*	*0*	*+31*	*+31*	-	-	-	-	*+6*	*-45*	*-5*
EC2	-44	-118	0	-15	44	-	-	-	-	-18	12	11
	+31	*+31*	*0*	*+31*	*+31*	-	-	-	-	*+6*	*-45*	*-5*
ACI	-28	-9	0	-	0	0	-	-16	-15	-46	-2	-32
	+15	*+15*	*0*	-	*0*	*0*	-	*+15*	*+15*	*+15*	*+15*	*+15*
BP-KX	-71	-113	0	-29	20	-46	78	47	42	-74	7	-3
	+75	*+75*	*0*	*+75*	*+75*	*+61*	*+75*	*+266*	*+175*	*+39*	*+222*	*+2*
BP-KX+	-52	-82	0	-21	14	-35	57	3	13	5	26	49
	+56	*+56*	*0*	*+56*	*+56*	*+56*	*+56*	*+35*	*+31*	*-3*	*+2224*	*-39*
GZ	-15	-22	0	-15	17	-	-	-19	-10	95	6	93
	+15	*+15*	*0*	*+15*	*+15*	-	-	*+15*	*+15*	*-40*	*-71*	*-54*
B3	-64	-97	0	-26	18	-44	35	3	14	-57	20	-16
	+68	*+77*	*0*	*+68*	*+68*	*+68*	*+68*	*+144*	*-55*	*+23*	*+448*	*-26*
B3+	-55	-95	0	-23	15	-38	30	-30	-10	-35	7	27
	+74	*+74*	*0*	*+74*	*+74*	*+74*	*+74*	*+44*	*+39*	*+34*	*+228*	*+11*
GL	-60	-75	0	-53	27	-	-	0	0	-35	16	7
	+32	*+32*	*0*	*+32*	*+32*	-	-	*0*	*0*	*+9*	*-43*	*-2*

Table 4.3. Change in creep strain between 6 months and 2 years when model parameters are varied with percentage change in italics.

Model	Relative Humidity	28-day Compressive Strength	28-day Young's Modulus	Cement Type (I-II)	Cement Type (I-III)	Curing Regime (Water – Steam)	Curing Regime (Water – Sealed)	Curing Time (2 – 7 days)	Curing Time (7 – 28 days)	Age at Loading	Size	Shape (Prism – Cylinder)	Shape (Prism – Slab)
CEB-FIP	-58	-81	-96	12	-5	-	-	-	-	-21	-19	-2	-15
	+24	*+25*	*+16*	*+20*	*+21*	-	-	-	-	*+34*	*+7*	*+9*	*+7*
EC2	-57	-81	-96	12	-5	-	-	-	-	-21	-19	-2	-14
	+24	*+25*	*+16*	*+20*	*+21*	-	-	-	-	*+34*	*+7*	*+9*	*+7*
ACI	-32	-15	-78	-	-8	-10	-	0	0	-5	-50	-5	-45
	+23	*+23*	*+14*	-	*+14*	*+14*	-	*0*	*0*	*-1691*	*+23*	*+23*	*+23*
BP-KX	-84	-313	0	-35	-4	-60	92	-10	-16	234	-404	3	-386
	+44	*+39*	*0*	*+44*	*+10*	*+39*	*+44*	*+74*	*+328*	*-47*	*+28*	*-43*	*+28*
BP-KX+	-68	-260	0	-28	0	-67	75	1	2	33	-330	15	-313
	+37	*-33*	*0*	*+37*	*+1*	*+32*	*+37*	*+7*	*+5*	*-12*	*+25*	*-105*	*+25*
GZ	0	0	-13	1	-2	-	-	0	0	3	0	0	0
	+7	*+7*	*+3*	*+3*	*+3*	-	-	*0*	*0*	*+4*	*+7*	*+7*	*+7*
B3	-261	-155	0	33	-41	27	-34	21	18	-1	-445	6	-429
	+84	*+45*	*0*	*+72*	*+50*	*+483*	*+72*	*+43*	*+41*	*-1*	*+41*	*-35*	*+41*
B3+	-131	-172	0	0	-14	-18	0	1	5	0	-268	17	-256
	+54	*+37*	*0*	*0*	*+26*	*+26*	*0*	*+25*	*+22*	*0*	*+26*	*-59*	*+25*
GL	-71	0	-102	7	-18	-	-	2	11	-39	23	21	59
	+32	*0*	*+18*	*+18*	*+18*	-	-	*+29*	*+29*	*-22*	*+11*	*+533*	*-36*

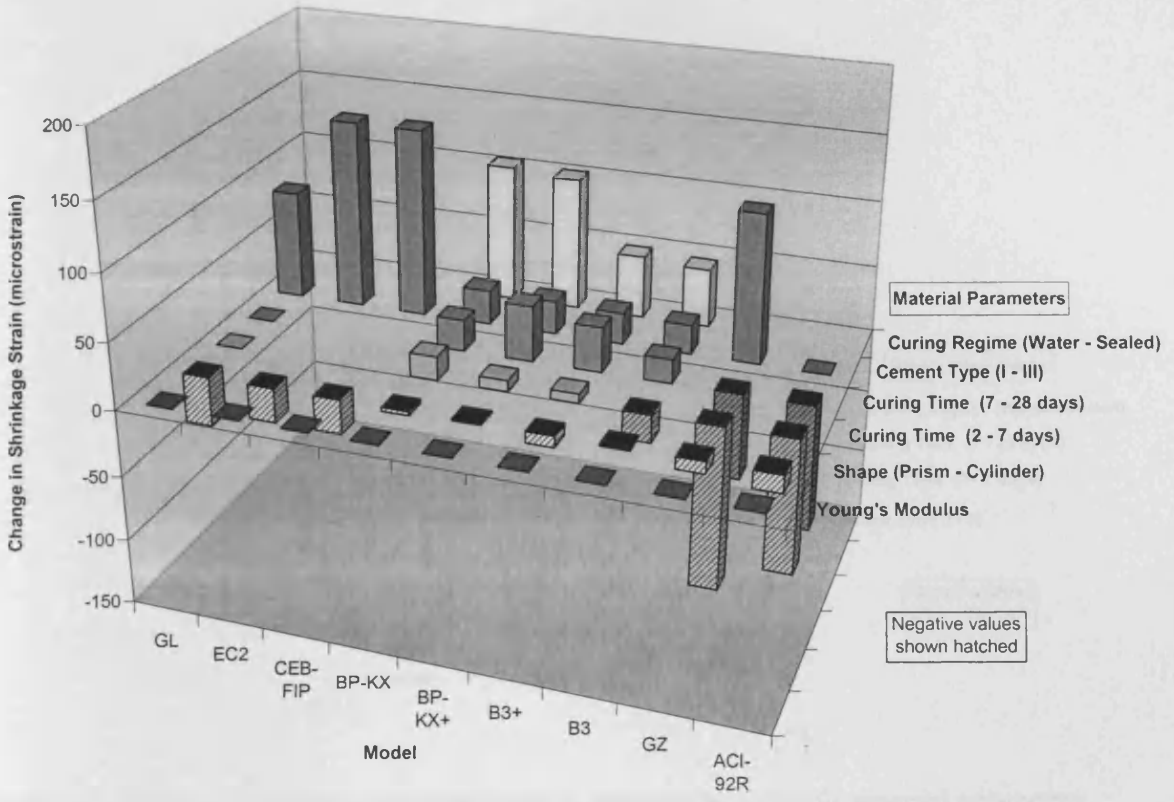

Figure 4.1. Change in predicted shrinkage strain after 6 months when specific material parameters are varied.

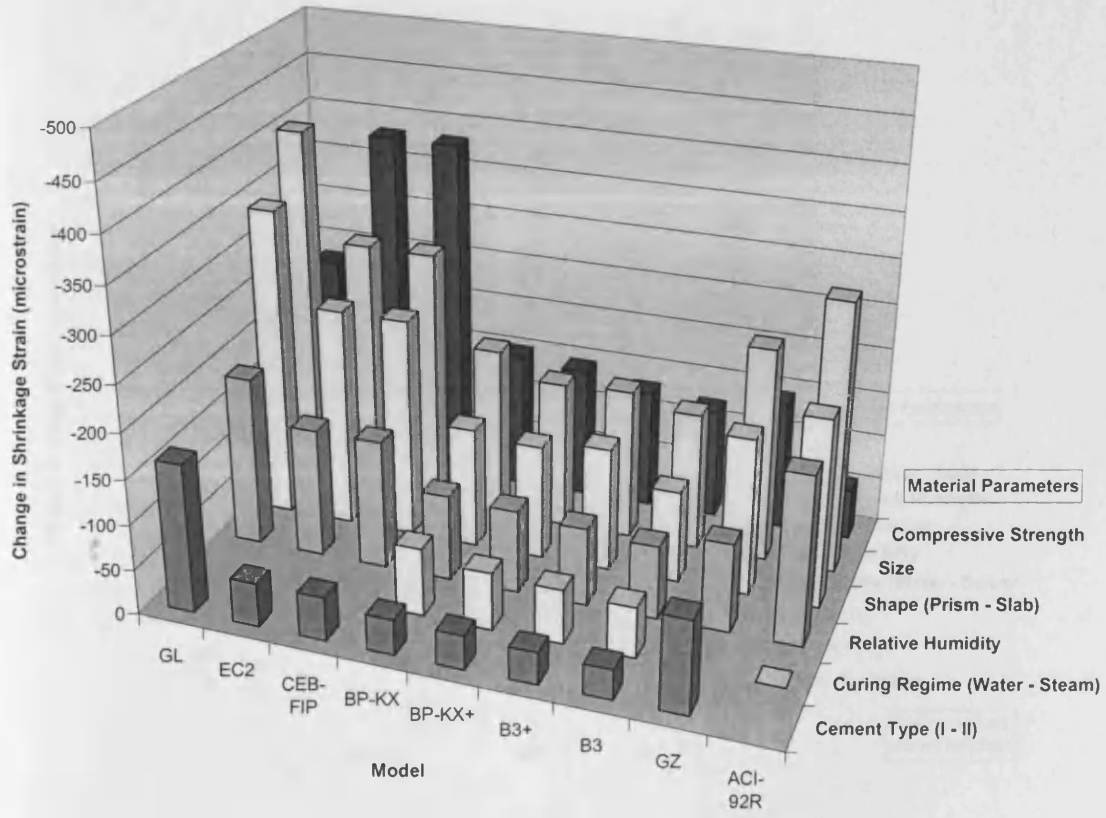

Figure 4.2. Change in predicted shrinkage strain after 6 months when specific material parameters are varied.

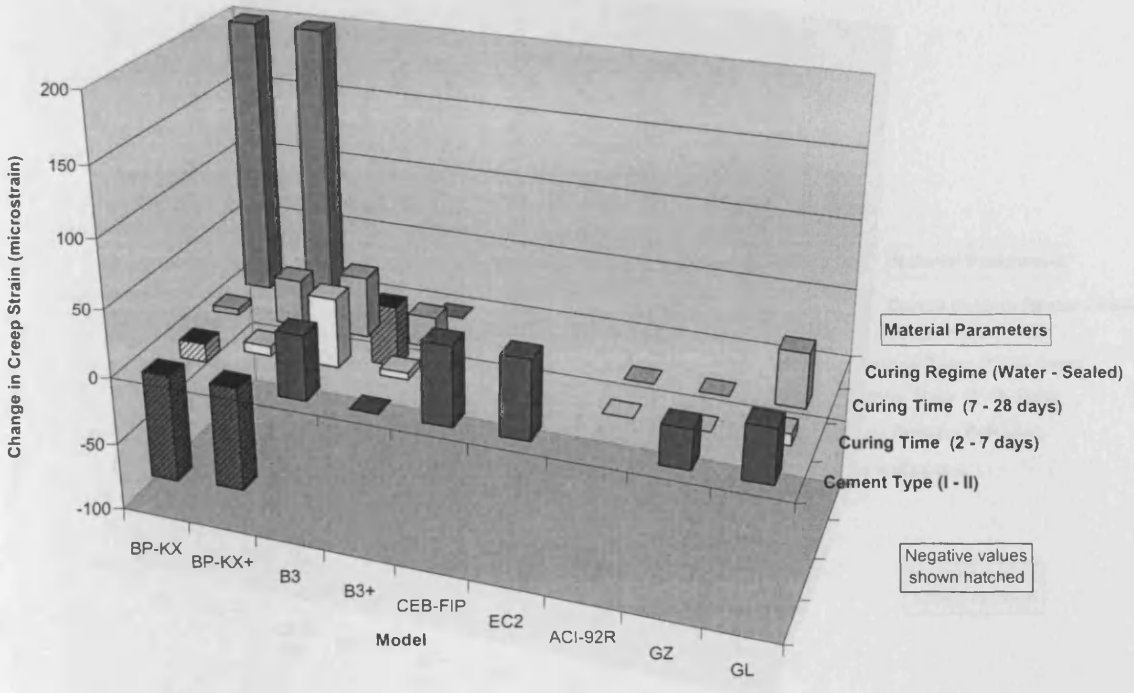

Figure 4.3. Change in predicted creep strain after 6 months when specific material parameters are varied.

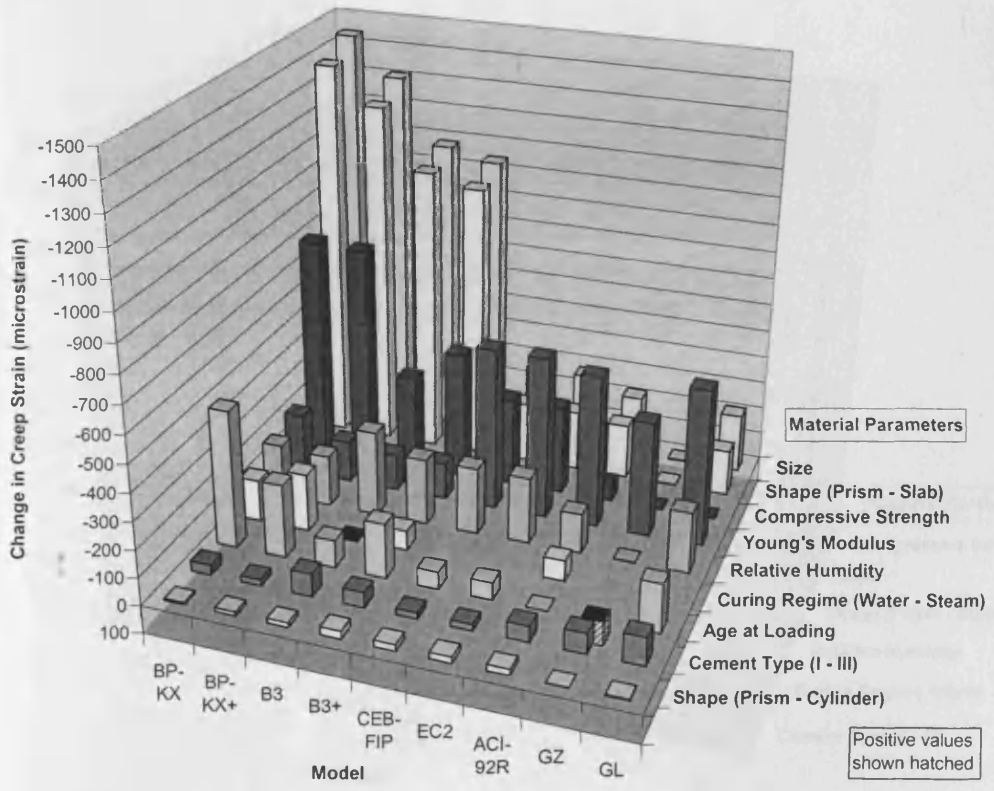

Figure 4.4. Change in predicted creep strain after 6 months when specific material parameters are varied.

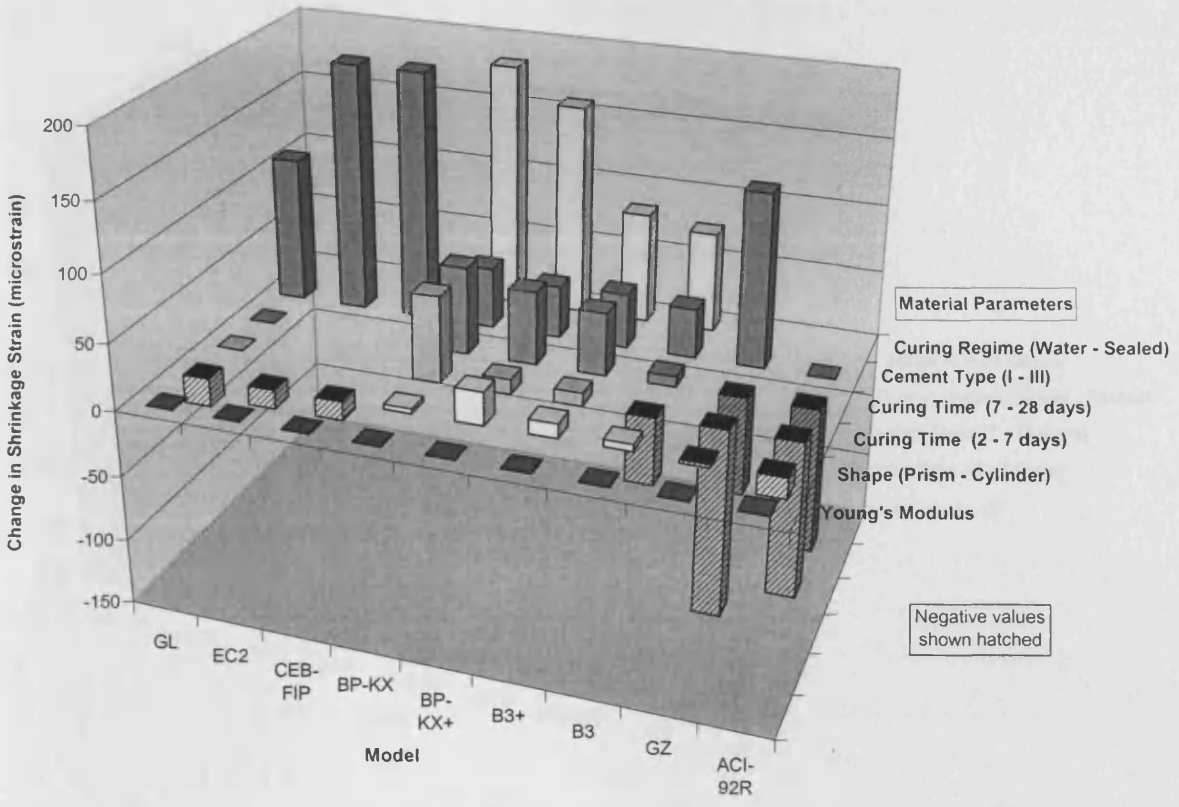

Figure 4.5. Change in predicted shrinkage strain after 2 years when specific material parameters are varied.

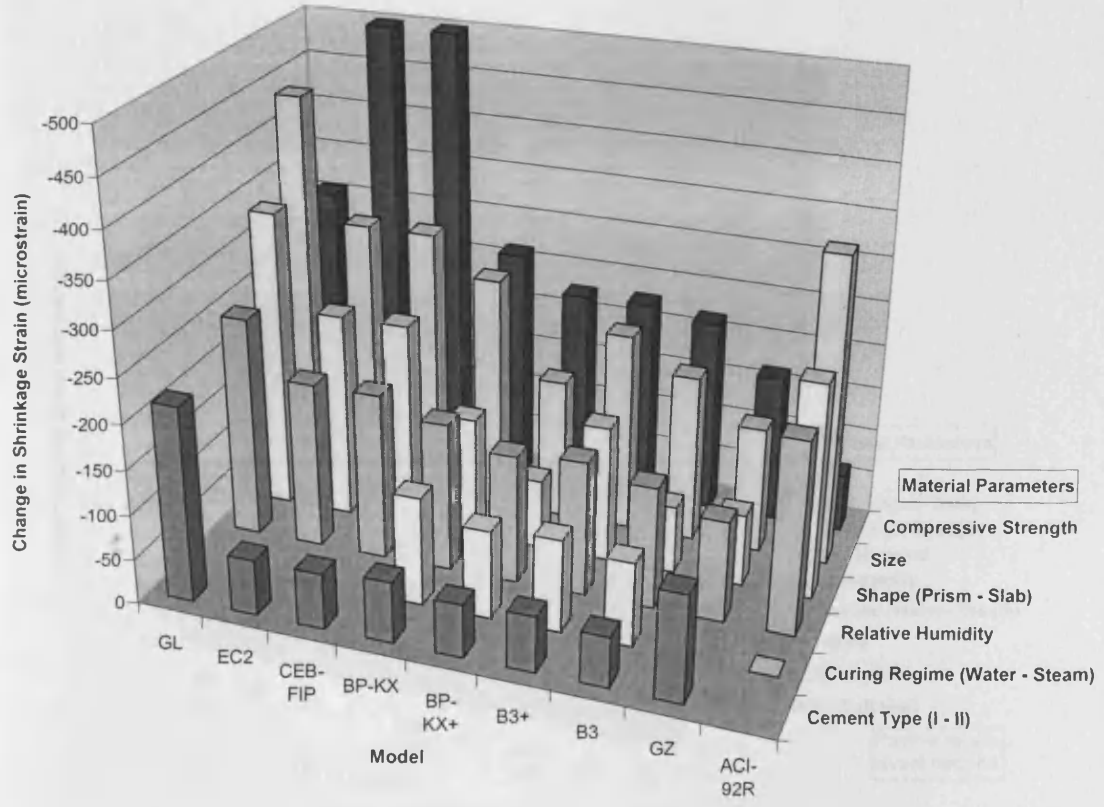

Figure 4.6. Change in predicted shrinkage strain after 2 years when specific material parameters are varied.

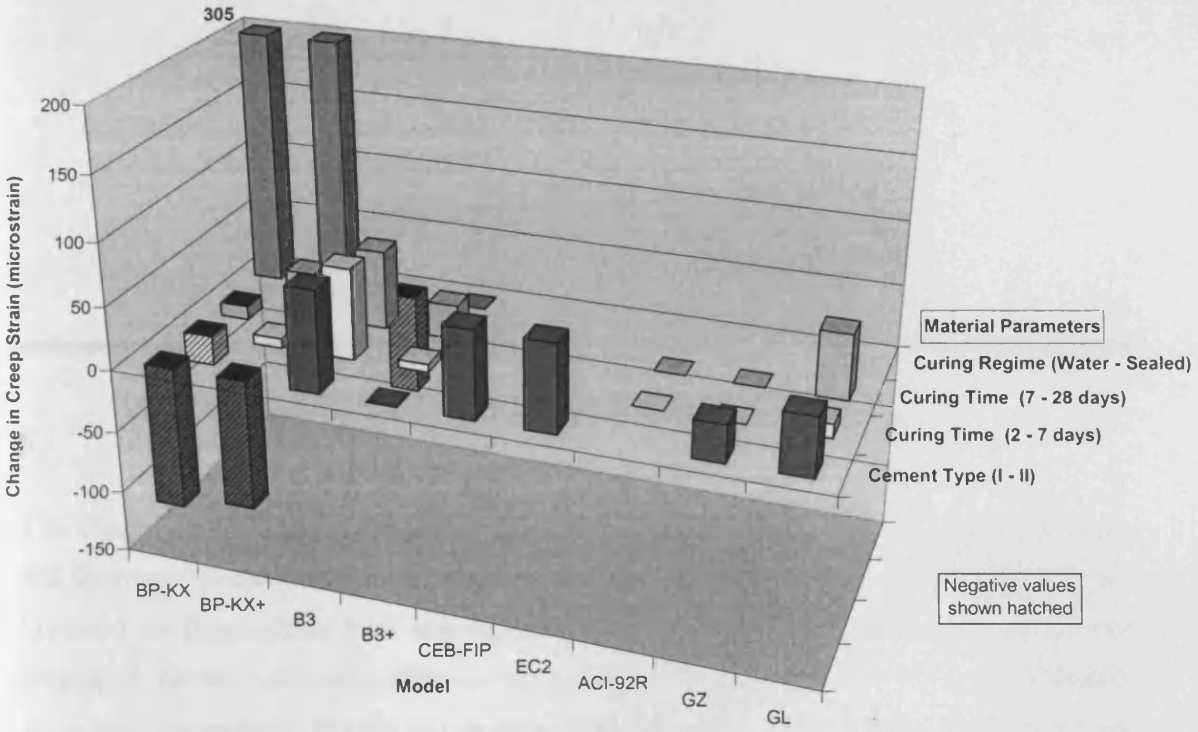

Figure 4.7. Change in predicted creep strain after 2 years when specific material parameters are varied.

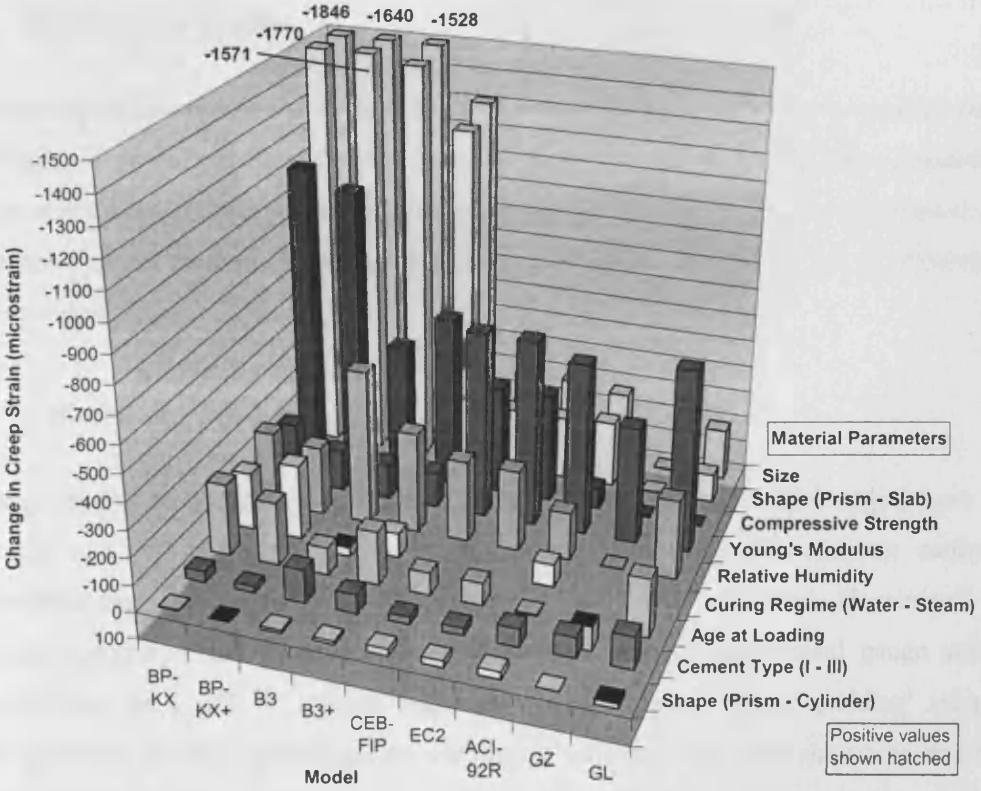

Figure 4.8. Change in predicted creep strain after 2 years when specific material parameters are varied.

Chapter 5

Laboratory Study

5.1 Introduction

This chapter outlines the experimental methods used in this study in investigating the creep and shrinkage of concrete. Previous studies on creep undertaken in the same laboratory are reviewed to demonstrate how the experimental procedure adopted for this study was developed. Furthermore, the quality and preparation of the main materials for each concrete grade, mix proportions, mixing and casting details and the curing regimes used during this study are reported here. In addition, standard and non-standard tests to characterise both the fresh and hardened concrete properties are also reported herein.

5.2 Preliminary Studies

The experimental procedure for determining creep and shrinkage in concrete detailed later in this Chapter is the culmination of a succession of studies on the time-dependent properties of concrete carried out at Cardiff University. This author had the opportunity to participate in the development of the method for determining creep and this development will be described in more detail in Section 5.2.2.

5.2.1 Shrinkage Studies

Shrinkage studies in concrete (including full scale studies in segmental bridges) have been undertaken at Cardiff University over the last decade, and a suitably accurate method of measurement has been developed, more notably by El-Baden[11] and Hoseinian[10]. For laboratory specimens, the method involves the attachment of mechanical gauge studs to opposing sides of a 300 × 150mm diameter cylinder using 'plastic padding' adhesive. Shrinkage strains are then determined for varying periods of time – both short-term and long-term. Generally, four specimens are cast for each grade of concrete, two of which are wrapped in industrial strength plastic film and fixed with sealing tape in order to measure

autogenous shrinkage, while two specimens are left unwrapped in order to measure drying shrinkage. A number of readings are taken for each set of gauge studs and an average is then taken.

5.2.2 Creep Studies

This author's final year undergraduate project (Howells[13]) investigated creep of high strength concrete. The testing system adopted was that specified in the American Standard Test Method designated C 512-87[141], which describes a 'test for creep of concrete in compression', as illustrated in Figure 5.1. Large loading frames which had been previously used in testing the creep of masonry columns and piers, were available for applying a large constant load to a creep test specimen and hence were used in this study. Three such rigs were available, the details of which will be discussed later in Section 5.6.3.1. The main results of this initial study showed that the rate of gain in creep strain is greater for high strength concrete than normal strength concrete, a conclusion which is similar to that observed for shrinkage in high strength concrete. This suggested that the design codes maybe out of date since they consider high strength concrete to behave in the same way as normal strength concrete.

In the above preliminary study three batches of concrete with nominal strengths of 40, 80 and 120MPa were investigated, and four 300 × 150 × 150mm specimens were produced from each mix. Each specimen was instrumented using a vibrating wire gauge on the front face, and mechanical gauge studs were attached on the two side faces. As shown in the ASTM method, the four specimens (of each mix) were stacked as a column in between two 150mm dummy cubes, and loaded to one third of their nominal 28-day strength (e.g. stress/strength ratio = 0.33) over a period of two months (following two weeks of water curing). It was initially decided to place a cork layer in between each specimen to minimise the lateral stresses caused at the interfaces. However, upon application of load, the column immediately began showing signs of horizontal deflection caused by the cumulative effect of non-uniform compression in the cork layers. In order to combat this, the column was unloaded and the cork pads were removed. As a replacement, 'plastic padding' adhesive was used and spread evenly over the cross-section of the column at the joints between test specimens while two cork pads were left at the very top and bottom of the column. Since the layer of plastic padding was very thin, no more lateral deflection problems were observed.

The basic creep results recorded (using the vibrating wire gauges and the mechanical gauges) for each grade of concrete are shown in Figures 5.2 – 5.4. The results show that the rate of gain in creep strain is greater for high strength concrete than normal strength concretes, a

response which is similar to shrinkage in high strength concrete. It should also be noted that the results obtained using the different types of gauges was somewhat variable. The mechanical gauge is not as accurate as the vibrating wire gauge as there are more sources of possible error with mechanical gauges.

Based on the development work reported above, a study on creep and shrinkage of concrete of various grades was initiated by an MPhil student (Khandri[142]). While spending a summer vacation working in the concrete laboratory at Cardiff University (in order to gain experience prior to starting research) the author of this thesis assisted in the development and setup of the improved creep testing methods which will now be detailed.

Due to the problems previously experienced with horizontal deflections (due to the joint material used to separate the test specimens) it was decided to reduce the number of joints, and hence the overall height of the column. Consequently, only one 600 × 150 × 150mm specimen was cast for three grades of concrete of nominal strengths of 60MPa, 120MPa, and a high strength pfa mix. These specimens were again placed in between two 150mm dummy cubes, the joints between which were again lined with plastic padding adhesive. Due to the problems previously encountered using a mechanical gauge as opposed to vibrating wire gauges, it was decided that four vibrating wire gauges would be attached to all four sides of the specimens. Furthermore, it was decided to use extended vibrating wire gauges where the vibrating wire length remains the same as that previously used (140mm or 5.5"), but the gauge length was increased up to 610mm or 24", giving greater accuracy when measuring the creep strain. This arrangement is shown in Figure 5.5. The specimens were cured in water for five days and then in air in a controlled environment for two days prior to testing. They were then loaded to one-third of their nominal 28-day strength for a period of six months.

Due to errors in the loading process of the C60 concrete specimens, the creep and shrinkage data for these specimens were discarded since the values obtained proved incomparable. The total creep results recorded for the other two grades of concrete can be seen in Figures 5.6 – 5.7 while shrinkage data for the same concrete mixes over the same time span, prepared as specified in Section 5.2.1, can be observed in Figures 5.8 – 5.9. The shrinkage data suggests similar values of total shrinkage for the C120 and pfa concretes of approximately 450 microstrain; however what is interesting is the proportions of the total shrinkage which represent drying and autogenous shrinkage. Approximately 85% of the total shrinkage in the pfa concrete is due to drying shrinkage, compared to only 75% in the high strength concrete. This supports the findings of Tazawa and Miyazawa[63,64] and Lee *et al*[65] who indicate that autogenous shrinkage increases as the w/c ratio decreases. The creep data again suggests similar values of total creep for both grades of concrete, with the high strength concrete

exhibiting slightly higher strains of approximately 1350 microstrain compared to 1250 microstrain in the pfa concrete. The rate of gain in strain is again more rapid than that observed for normal strength concretes. It is interesting to note the undulations in the pfa curve. These indicate that load relaxation occurs more readily in the pfa concrete than in the C120 concrete. This may mean that the inclusion of the pfa in the mix causes an increase in the stiffness of the hardened concrete, a property that will be further investigated later in this project. Examination of the C120 creep curve shows significant variations in the creep values obtained from gauges positioned on different sides of the specimen. These differences can be attributed to a load eccentricity in the specimen, which suggests that more care must be taken when positioning the specimens prior to application of the load.

Cubes cast using the pfa mix had a 28-day strength of 82.7 MPa. Creep comparisons with the C80 mix from the previous preliminary study (Howells[13]) can therefore be made, as well as comparisons between the two C120 mixes. This comparison is shown in Figure 5.10. It is immediately apparent that the curves obtained by loading four small specimens as a column are considerably less smooth than those obtained through loading one larger specimen, suggesting that the latter option is more suitable for observing creep behaviour. It is pleasing to see that the creep values of both C120 specimens are very close, which is as expected since the mix proportions for both were the same. The C80 pfa mix demonstrates creep development more similar to that of the high strength concretes than the plain C80 concrete, indicating that creep develops over a longer period of time when pfa is included in the mix.

It was observed during testing that the extended vibrating wire gauges were more prone to failure than the normal variety, since two of the gauges on the C60 strength specimen failed early in the loading period. Furthermore, it was deemed that the extended vibrating wire gauges were only marginally more accurate than the standard type, while costing a significant amount more. Therefore, it was decided to use the standard 5.5" gauges in future creep tests.

5.3 Materials Used

The materials used in the production of all test specimens will now be detailed.

5.3.1 Cement

The cement used was Ordinary Portland Cement (Class 42.5N) locally produced by Blue Circle Cement (with the typical composition shown in Table 5.1) conforming to BS 12: 1996[20]. Variations in cement type were not considered to be of any major significance in this study and, therefore, existing stocks of cement were used.

5.3.2 Aggregate

The coarse aggregate used was crushed limestone rock with a maximum aggregate size of 10mm, conforming to BS 882: 1992[28]. The aggregate was air dried for 24 hours immediately before use. Fine aggregates consisted of sea-dredged sand from the Bristol Channel also conforming to BS 882: 1992[28]. Similarly to the coarse aggregate, the sand was air dried for 24 hours prior to use.

5.3.3 Silica Fume

Fine silica fume was used in the Grades 80 and 100 concrete in order to attain the desired strength. The product (Elkam Emsac 500S) was used in a 50:50 water/powder slurry form. A description of its physical properties and chemical composition has been given earlier in Section 2.3.1.4.

5.3.4 Pulverised Fuel Ash

Class F pulverised fuel ash, conforming to BS 3892: Part 1: 1997[143], was used in the concrete mix which closely resembled that used in the construction of the Grangetown, Cogan and Taff Viaducts as described in Section 5.4.1.

5.3.5 Superplasticizer

A sulphonated napthalene type superplasticizer was used in the mixes that contained silica fume to give adequate workability. The superplasticizer used was 'Adoflow Extra' which complies with BS 5075: Part 3: 1985[144]. A description of its physical properties and chemical composition has been given earlier in Section 2.3.1.4. The dosage requirement was dependent on the amount of cement used; however individual adjustments were made to achieve the necessary workability in all cases.

5.4 Mix Details

Details of mix proportions, procedure, casting and control testing are reported in this Section.

5.4.1 Mix Proportions

As previously stated in Section 2.3.2, a detailed study (carried out in the same laboratory) of mix proportions for medium to high strength concrete was conducted by Taylor *et al*[41].

Consequently, the concrete mixes used in this project were based on the findings of this research which has been used by a number of researchers working in the same laboratory. Taylor devised mix proportions, by mass, to achieve 28-day compressive strengths of 40, 60, 80, 100 and 120 MPa as shown earlier in Table 2.9.

In this project, the 40MPa concrete is considered to be normal strength consisting of the basic constituents (cement, aggregate and water) only. The 80 and 100 MPa concretes are considered to be high strength concrete. Silica fume and superplasticizer have been used in these mixes to achieve the desired strength and workability. The amount of water was adjusted to take into account the additional water supplied by the 50:50 water and silica fume slurry. A concrete mix was also produced which was similar to that used in the construction of the Grangetown, Cogan and Taff Viaducts. The concrete composition of these structures has been detailed by Ramezankhani *et al*[139] and Vitek and Barr[1]. However, both these sources show different sets of mix proportions for the same mix. Based on the design assumption, this mix was intended to have a characteristic strength of 52.5MPa. However, the mix proportions given by Vitek and Barr[1] indicate a much higher characteristic strength a fact reflected in site correspondence which indicated that the mix design had been altered on site, such that a high early strength was achieved, and as such the characteristic strength was also changed but not documented. Furthermore the set of mix proportions quoted by Vitek and Barr[1] was a pump mix and the actual mix was slightly different. The three different sets of mix proportions are shown in Table 5.2. Hence it was decided that trial mixes should be made based on the three sets of mix proportions, and compression tests were carried out over 28-days to decide on which set of mix proportions to use. Since Cardiff University only uses one size of coarse aggregate, the 20mm and 10mm aggregate contents were added together. Since it is not possible to obtain Conplast 211 plasticizer anymore, Adoflow Extra superplasticizer of a similar composition was used, with a dosage level of 1.6 l/m^3. The development of compressive strength with time for all mixes is shown in Figure 5.11. It was very difficult to achieve sufficiently workable mixes using the specified mix proportions for all three trials and so the w/c ratio and the SP dosage was increased in all cases to achieve workability. All three mixes give similar rates of gain in compressive strength as well as 28-day strengths in the range 62 – 68 N/mm^2. Therefore, it was decided to use the mix proportions for trial mix no. 3 of strength 65 N/mm^2, in order to cast the test specimens since this mix was specified in site documentation (Table 5.2) and was deemed the most likely to have been used in the construction of the viaducts.

5.4.2 Mix Procedure

Each concrete batch was produced three months in advance of the time of testing due to time and labour constraints in the laboratory. The constituent materials were weighed in buckets to an accuracy of 0.05kg prior to mixing. Water and cementitious materials were the final constituents to be weighed.

Batch mixing took place in a Cumflow horizontal pan mixer with a capacity of approximately 250kg. The materials were added in alternate layers, starting with the coarse aggregate, the cementitious materials and finally the fine aggregate. The full mix was allowed to turn for approximately 2 minutes to allow the materials to distribute evenly. The water/superplasticizer mix was added after this initial 2 minutes and mixing continued for a further 3 minutes.

For those mixes containing silica fume and superplasticizer the process was identical except for two points. The silica fume slurry was added to the mix during the first 2 minutes of mixing and the superplasticizer was included at the final mixing stage, as recommended by Hsu *et al*[145] until the desired workability was achieved. For the mix containing pfa and superplasticizer, the pfa was added at the same time as the cement and aggregates, while the superplasticiser was gradually added with the water, since the addition of pfa causes the workability of the mix to develop over a longer period of time during mixing.

5.4.3 Casting

The required moulds for each type of mix were pre-oiled for ease of demoulding, following which the mix was placed directly into the moulds and compacted with the aid of a vibrating table. Casting was achieved in two equal layers for optimum compaction. After casting had taken place, the specimens were covered with damp hessian to limit the amount of overnight evaporation. The specimens were demoulded 24 hours later, prepared and placed in curing tanks for three months.

It was decided that specimens of the same dimensions as those developed in previous creep studies at Cardiff University would be used. Hence, it was intended to produce eight 150 × 150 × 600 mm beams in total for each mix, with the number of specimens produced at any one time dependent upon the capacity of each loading frame. In addition, for each mix, two 150 mm dummy cubes were produced to act as end blocks for the columns, while twelve 100 mm test cubes and twelve 200 mm × 100 mm diameter test cylinders were prepared to determine the rate of gain of strength and the modulus of elasticity of each mix at 28-days, at

loading after 84-days, and at unloading after 252-days, using standard and non-standard control tests.

5.4.4 Fresh Concrete Properties

The workability of each mix was measured indirectly using two standard tests; slump and Vebe time, immediately after the mixing process in accordance with BS 1881: Part 102[146] and Part 104: 1983[147]. Workability results for each mix are reported in Table 5.3.

It should be noted that the results for the slump and Vebe tests for all mixes demonstrate reasonably high levels of workability. This was to be expected since Taylor *et al*[41] designed the mixes for use with a high level of steel fibre additions.

5.5 Specimen Preparation

The manner in which the specimens were prepared and arranged prior to and during testing will now be discussed.

5.5.1 Gauge Setup

Immediately after demoulding, the cubes, beams and cylinders were placed in a water bath to cure at 20 °C until required for testing. Shrinkage and creep testing require the use of mechanical strain gauges with Demec gauge studs, and vibrating wire gauges respectively as detailed in Section 5.2. Mechanical gauges require gauge studs to be fixed to two opposite sides for the shrinkage cylinders while vibrating wire gauges were prepared in advanced of testing and fixed centrally to each face of each creep specimen. Connection to a logger and computer produced an efficient method of data collection.

Each gauge or gauge stud was fixed to the concrete with 'plastic padding' adhesive and positioned using standard reference bars. For mixes containing silica fume and superplasticizer a smooth layer had developed on the surface of the concrete, which had to be scraped off in order to produce a rough surface that the adhesive would adhere to.

5.5.2 Curing and Test Environment Details

Following demoulding, the creep specimens were placed in a 20 °C curing tank for a period of 82 days before being transferred to a controlled environment laboratory for a further 2

days. During the 'drying' period all vibrating wire gauges were positioned and fixed in place. The specimens were then transferred to a storage area to await testing.

As with the creep specimens, the shrinkage specimens were placed in a 20 °C curing tank for a period of 82 days after demoulding before being transferred to the controlled environment laboratory where, after the surface of the specimens had dried, demec gauge studs were positioned and fixed in place. After the gauge adhesive had been allowed to harden for approximately 30 minutes, the shrinkage specimens were returned to the curing tank for a further 2 days, at which time they were removed and weighed immediately. Two of the specimens were then wrapped in three or four layers of industrial strength plastic film fixed with packing tape, in order to evaluate autogenous shrinkage. A final layer of rubberised sealing tape was used to secure the edges; therefore, any moisture loss due to drying could be kept to a minimum. The specimens were then transferred to a storage area to await testing.

5.6 General Experimental Details

Testing arrangements and measurement details are reported in this Section.

5.6.1 Strain Measurement

5.6.1.1 Mechanical Gauges - Shrinkage

The measurement of shrinkage strains was achieved with the use of mechanical gauges with an accuracy equivalent to 10 microstrain per division. (N.B. gauges measure deflections rather than strain.) Initial readings were taken immediately after the specimens had been removed from the curing tank and wrapped if appropriate, these readings being assumed to be at a time of zero strain.

In order to reduce any anomalous variations in the readings taken, correct use of the gauge devices was critical. In this instance the demountable gauge was held in two hands with an even pressure being maintained at all times. While in place the gauge device was 'rocked' and the peak value was recorded. It was important that all subsequent readings were taken in an identical manner with the following of greatest concern: orientation of the specimen and gauge, conditions and storage. The specimen was placed horizontally between two semi-circular holding blocks such that the gauge was mounted perfectly level when the reading was taken. In between readings, the specimens remained in the controlled environment laboratory where the relative humidity and temperature remained relatively constant.

Changes in microstrain were calculated from the following equation given in the manual:

$$\varepsilon = (x_1 - x_2) \times G \times 10^6 \tag{4.1}$$

where:

ε is the strain value in microstrain,

x_1 is the initial dial gauge reading,

x_2 is the current dial gauge reading,

G is the gauge factor.

5.6.1.2 Vibrating Wire Gauges - Creep

The vibrating wire gauges used in this project were supplied by Gage Technique Ltd. Each gauge measured strain over a 5.5 inch length and worked to an accuracy of 1 microstrain. Prior to installation, the gauges were bolted to transport plates and the cable connected to a vibrating frequency meter. Gauge frequencies were set in accordance with Gage Techniques specifications and held in position with the locking collar.

Gauges were installed two days in advance of test in order for the gauge to settle in. Each gauge was removed from its transport plate and fixed to the concrete with plastic adhesive. As with the Demec gauges, the surface of each specimen was lightly keyed with a chisel to aid adhesion. When the adhesive had cured, the locking collars were released and the barrel was given 2-3mm of play between end blocks. Initial gauge readings were then taken. Datum readings were recorded immediately prior to loading, two days after the gauges had been installed.

All gauges were connected to a Datataker data logger which could be directly connected to a PC. Using Datataker software written especially for the logger, a program was written and stored in the logger memory ready for execution.

Calculation of strain from vibrating wire gauges was derived from the 'Vibrating Wire Equation' that is quoted in the manufacturer's product manuals[148]:

$$\varepsilon = \left[\frac{F_1^2}{1000} - \frac{F_2^2}{1000} \right] \times G \times 10^3 \tag{4.2}$$

$$G = 0.1 \times L^2 \times 10^3 \tag{4.3}$$

where:

ε is the strain in microstrain,

F_1 is the initial data frequency,

F_2 is the current measured frequency,

G is the gauge factor,

and L is the gauge length in inches.

5.6.2 Load Measurement

Since this research concentrated on the variation in creep strain due to various imposed stress levels as well as concrete strengths, accurate application of load was essential. Preliminary studies detailed in Section 5.2.3 indicated that each concrete strength should be loaded to stress/characteristic strength ratios of 0.25, 0.30, 0.35 and 0.40. Hence it was vital that the load be applied in such a way that it could be easily monitored and adjusted if necessary. Proving rings were chosen as the most effective method of providing long term load application while minimising maintenance. The mechanical dial gauges on each ring were used to indicate deflection which could then be converted into a load, and vice versa. Calibration curves were obtained prior to application of the load for each of the proving rings used and are given in Appendix B.

5.6.3 Load Application

The creep laboratory houses two types of specially constructed loading frames. Both rigs were designed with the intention of providing long-term stability of both load application and frame geometry. They are of two different sizes, one designed for tall slender specimens, while the other for smaller, more compact specimens. For stability and safety reasons, both types of frame had previously been bolted to the reinforced concrete floor of the laboratory. Since the specimens used in the research could fit either rig, both were used where appropriate. These rigs had previously been successfully used in testing the creep of masonry (Harvey[149]). Both frames will now be discussed in detail.

5.6.3.1 Large Creep Frame

Figure 5.12 shows the standard design and arrangement of the larger of the two loading frames. Two steel H-section girders of web and flange thickness 10 mm and having additional welded reinforcing plates, are fixed in position at either end of four threaded 50 mm mild steel guide columns. A third modified girder is used to evenly distribute load applied to the uppermost girder by a series of six 20 tonne hydraulic jacks, which are linked together by a

common hydraulic manifold supplied by a hand pump. The jack force is transmitted through this floating beam to a number of proving rings (the number depending on the load applied), which in turn transmit the load to a 50 mm thick spreader plate which acts on the concrete specimen. Loads are maintained by isolating the hydraulic pressure within the jack system using a hand operated valve, while the floating beam can be locked in place using threaded collars screwed downwards on the reaction bars, so preventing any upwards movement. The entire loading system can be moved vertically using these threaded collars within the range of the threaded section on the reaction bars, so allowing a variety of specimen lengths to be tested.

Figure 5.13 shows the concrete specimen arrangement within the large creep rig. Due to the length of the specimen in relation to the rig, 1 metre high steel plinths were utilised to bring the top of the specimen within the threaded area of the reaction bars. Before load was applied to the specimen a careful levelling regime was carried out, including the installation of shimming pieces to ensure intimate contact between the levelled spreader plate and the proving rings. It was possible in certain loading cases to test two specimens in the one rig at the same time, due to the size of the steel plinth. This approach was necessitated due to time constraints, and hence some of the lower strength specimens were tested in this way. Since testing was carried out over such a long period of time, some relaxation in the loading system was expected and hence the load was readjusted on a weekly basis.

5.6.3.2 Small Creep Frame

Figure 5.14 shows the standard design and arrangement of the smaller of the two loading frames. As with the larger frame, two substantial 50 mm steel plates are fixed in position at the top and base of the frame using a reaction bar, which in this case is a single centrally located 60 mm diameter bar, around which specimens can be orientated. A third 50 mm plate is used to evenly distribute load via four proving rings to the specimens. A maximum force of 80 tonnes is applied to the spreader plate through the proving rings, by means of a worm and screw arrangement operating through a substantial ball-race thrust bearing. Stability of the spreader plate is maintained by four 25 mm diameter guide bars, located at the corners of the rig. The entire loading system can be moved vertically using an electric motor within the range of the threaded section on the reaction bar, so allowing a variety of specimen lengths to be tested.

Figure 5.15 shows the loading arrangement for two test specimens within the small creep rig. The size of the loads applied and the nature of the arrangement dictated that only two specimens could be loaded at any one time. As a consequence, it was decided to remove the

front and back proving rings such that the load could be distributed more evenly using only the left and right proving rings. Since testing was carried out over such a long period of time, some relaxation in the loading system was expected and inspection of the proving ring dial gauges indicated that the load needed to be readjusted on a daily basis.

5.7 Method and Development

It was initially intended to load the C40 and pfa specimens in the smaller creep rigs, while the C80 and C100 specimens would be loaded in the larger rigs. Due to the discovery that the pfa mix was not a C52.5 'normal strength' concrete but a higher strength pfa concrete with a nominal strength of 65 N/mm^2, it was realised that the smaller rigs would not be able to apply the necessary loads to the specimens, and hence the pfa concrete would have to be loaded in the larger creep rigs. This presented a problem since there was not enough time to load all grades of concrete at all four load factors, before the designated end of this research project. Hence it was decided to reduce the number of proposed stress/strength ratios to three and where necessary, the number of specimens for each stress/strength ratio from two to one. It was decided to drop the 0.40 stress/strength ratio since in real life situations there is a greater scope for designing concrete members to withstand loads of up to one-third of its nominal strength than 40 percent. Therefore, the C80, C100 and pfa concrete specimens were loaded by load factors of 0.25, 0.30, and 0.35 of their nominal strength.

As previously mentioned the number of specimens under load at any one time depended upon the number and load capacity of the loading frames. Since it was planned to load two specimens of a given strength to each stress/strength ratio, the time constraints this imposed meant that certain creep specimens were loaded in pairs in the same rig with each pair being subjected to the same stress/strength ratio. However, for the higher strength concretes this was not always possible due to the limited load capacity of the rigs and as such the specimens were cast in two or more separate batches at different times and loaded individually. In all cases, the shrinkage specimens were cast with the first of the mixes.

5.8 Results

This section reports the results of the control tests, shrinkage and creep tests, and comparisons with predicted data.

5.8.1 Control Tests

As previously mentioned, the compressive strength, tensile strength and Young's Modulus of each mix was determined at 28 days, at loading (after 84 days) and at unloading (after 252 days). The tests used were the British Standard method for determination of compressive strength of concrete cubes (BS 1881: Part 116[47]), and the torsion test, developed at Cardiff University. The torsion test is a method that simply applies pure torsion to a concrete cylinder and effectively subjects the specimen to a uniform torque, from which the tensile strength and the Young's Modulus can be derived (Norris *et al*[150]). The torsion tests were conducted in an Avery-Dennison test rig while the cube tests were carried out in a Contest compression machine. Prior to testing, the samples were removed from the curing tanks, dried (to remove surface water) and their weight recorded. Tests were then conducted using the appropriate apparatus and the strength values recorded.

Compression test results for each grade of concrete are reported in Tables 5.4 – 5.10 while torsion test results are reported in Tables 5.11 – 5.17. Sample calculations for the torsion test are detailed in Appendix C. All grades of concrete attained 28-day compressive strengths which were lower than the mix design strength. However, after 3 months when testing began all grades had achieved compressive strengths either higher than or very close to the mix design strength. It can be seen that for both the C80 and C100 concrete, there is little increase in compressive strength between 28 days and 3 months, and even less between 3 and 9 months indicating that the majority of the compressive strength gain for high strength concrete had occurred within the first 28 days. However, there is an appreciable amount of compressive strength development after 9 months in both the low strength C40 concrete and the high strength pfa concrete, indicating that the rate of gain in compressive strength was far slower, as expected.

The concrete grades, made in multiple batches, displayed compressive strengths and elastic moduli which were within 10% of each other indicating that the specimens exhibited very similar properties despite being cast at different times and from different batches of concrete. It is interesting to note that both batches of the high strength C100 concrete were less stiff at the end of testing than when testing began. This phenomenon has been experienced by other researchers in the same laboratory and is currently being investigated separately.

5.8.2 C40 Test Results

Since the C40 concrete was the first to be tested, the results for that particular mix will be reported first. Subsequently, all other concrete strengths will be reported in a similar manner before comparisons are made between them.

Figure 5.16 shows the shrinkage results for the C40 concrete. The x-axis represents the time from the beginning of testing in days, while the y-axis represents the measured strain in microstrain ($\mu\varepsilon$). As previously mentioned, two shrinkage specimens were wrapped to measure autogenous shrinkage, while two specimens were left unwrapped to measure total shrinkage. The curves for total and autogenous shrinkage are average values taken from the two specimens. The drying shrinkage was calculated by subtracting the autogenous shrinkage values from the total shrinkage. Prior to testing, it was found that the temperature and relative humidity (RH) controls within the laboratory were not operating correctly. Nevertheless, because of the location of the laboratory, in the basement at the centre of the engineering building, it was decided that the influence of external weather conditions would be minimal and testing should continue as planned. However, each curve does display strain fluctuations indicating that changes in the temperature and RH did have some influence on the measured strains. Hence, Figure 5.16 also displays 'smoothed curves' for the total, drying and autogenous shrinkage curves for later basic creep calculations and prediction model comparisons. The actual and modified curves are identified on the legend. As expected, autogenous shrinkage was far smaller than drying shrinkage, just over 100 $\mu\varepsilon$ after 6 months which was approximately a third of the drying shrinkage strains. Furthermore, there was little increase in autogenous shrinkage after this time indicating that it was virtually complete. Drying shrinkage was still increasing at an appreciable rate after 6 months indicating that the shrinkage of C40 concrete after half a year is primarily caused by drying shrinkage.

Figures 5.17a and 5.17b show the relationship between shrinkage and weight loss for total shrinkage and autogenous shrinkage respectively. Each specimen was weighed at the time each reading was taken and the average percentage weight loss was then calculated. As can be seen, the total shrinkage specimens show far greater weight loss than the autogenous shrinkage specimens which is reflected in the magnitude of shrinkage in each case. Weight loss in the autogenous shrinkage specimens is unexpected since the specimens are sealed and therefore there should be no loss of water or weight. However, since the weight loss in the autogenous shrinkage specimens was approximately 15% of the total weight loss, this indicates that some water was lost through the points of contact between the demec gauge and gauge studs, indicating that the system of autogenous shrinkage measurement is not entirely

satisfactory. Furthermore, the correlation between total shrinkage and percentage weight loss is very good and the linear relationship is clear to see. However, the correlation between autogenous shrinkage and percentage weight loss is initially poor, although it becomes linear over time. It is likely that the autogenous shrinkage is far more sensitive to changes in the temperature and RH of the environment and any fluctuations would account for the poor correlation between strain and weight loss. Despite the fact that the autogenous specimens are sealed, due to moisture loss at the location of the gauge studs, some drying shrinkage will occur and the fact that the relationship suddenly became linear after 70 days could indicate that the effect of autogenous shrinkage becomes minimal far earlier than first thought, and any additional strain is mainly due to drying shrinkage.

Figure 5.18 presents curves of the total measured strain against time for the various stress/strength ratios. The x-axis represents the time under load, while the y-axis represents the recorded strain. The strain associated with each specimen is represented by a different line as indicated by the legend, and each strain is an average value taken for the four gauges on each specimen i.e. one on each face. For clarity, the strains shown are those recorded every second day. It was decided that in order to undertake accurate observations on the mechanism of creep, the effects of external influences should be minimised. To this end it was decided to isolate the basic and drying creep results in order to provide a basis for comparison segregated from the external influences connected with shrinkage. Hence, in order to isolate basic creep, the total shrinkage was subtracted from each of the creep strains. This is demonstrated for specimen 0.25A in Figure 5.19. The shrinkage strains were recorded less frequently than the creep strains. Hence linear interpolation was used to calculate the strains between recorded points.

The basic and drying creep strains for each specimen are shown in Figure 5.20 in the same manner as for total measured strain under load. The curve for each stress/strength ratio is typical of a standard concrete creep curve. It can be seen that each curve is not entirely smooth. This is due to some relaxation in the small creep frame which was unavoidable since it was not possible to lock the load in place, and so the load had to be reapplied at regular intervals during the initial stages of loading. The specimens loaded to the same design stress/strength ratio can be clearly defined since they exhibit similar strains which are within 5% for each specimen at the same ratio. In all instances, the rate of creep is more pronounced over the first 2 months although the rate at which strain develops is decreasing as expected. However, there is still an appreciable amount of strain development after 6 months under load (in the range of 58 – 67 $\mu\varepsilon$), indicating that the magnitude of the applied load may have some

influence on the rate of development of creep. This influence of applied load on the development of creep strain will now be discussed in more detail.

Closer scrutiny of Figure 5.20 shows a large difference in the magnitude of creep between the 0.30 and 0.35 stress/strength ratios. In order to determine whether this difference was due to the increase in applied stress/strength ratio, it was necessary to determine the actual stress/strength ratios (rather than the nominal stress/strength ratios) to which each specimen was subjected. During load application, strain readings were recorded at 30-second intervals in order to determine the magnitude of the instantaneous strain from the vibrating wire gauges. Using the elastic modulus at loading which was calculated from the torsion tests (Tables 5.11 – 5.17) with the instantaneous strain, it was possible to deduce the actual stress/strength ratio to which each specimen was subjected. These are shown in Table 5.18 along with the actual stress/strength ratios for all other concrete creep specimens. As can be seen in the case of the C40 concrete specimens, the stress/strength ratios are slightly greater than the intended values, and there is a wider spread. It can be seen that the difference between the creep strains that are developed in the concrete specimens loaded at the proposed 0.30 and 0.35 ratios is actually due to the fact that they were loaded to ratios of 0.31/0.33 and 0.40/0.44 which correspond to a ratio difference of approximately 0.1 as opposed to the intended 0.05.

Further examination of Figure 5.20 illustrates that the larger the stress/strength ratio, the steeper the creep curve. In order to assess the impact of increasing the stress/strength ratio on the rate at which creep strain develops, creep strains at 7 days, 28 days, 3 months and 6 months were compared with increasing stress/strength ratios as shown in Figure 5.21. The x-axis represents the stress/strength ratio while the y-axis represents the creep strain. Each series represents a different time at which the strain was recorded as depicted by the legend. As expected, the relationship between creep strain and stress/strength ratio is linear, as denoted by the lines of best fit which illustrate good correlation between the data sets. However, it can be observed that as the stress/strength ratio increases, the rate at which creep strain develops also increases. This is also expected since applying a larger load would correspond with increased deformation in the concrete, hence meaning that creep effects are more pronounced for longer at higher stress/strength ratios.

5.8.3 C80/C100/pfa Test Results

The shrinkage and creep results for the C80, C100 and pfa concrete specimens were analysed in the same manner as the C40 results detailed above. Measured shrinkage, total strain and basic creep curves for each type of concrete are reported in Appendix D.

The total shrinkage strain after 6 months for the C80 concrete is approaching 290 με. However, the strain behaviour changes significantly at approximately 40 days. During the first 40 days, the relationship between shrinkage and time is virtually linear and the rate at which shrinkage strains develop is rapid. After 40 days until the end of testing, the relationship between shrinkage and time is again virtually linear but the rate at which shrinkage strain develops is much lower. However it can be observed that after 6 months, shrinkage strains are still developing at the same rate indicating that for the 80 N/mm^2 concrete, an appreciable amount of shrinkage will still occur long after 6 months. The drying and autogenous shrinkage strains are very similar in magnitude and behaviour, with the autogenous strains only approximately 50 με less than the drying strains. The drying shrinkage accounts for 57% of the total shrinkage with autogenous shrinkage making up the remaining 43%.

The total shrinkage strain after 6 months for the C100 concrete is around 220 με. Up until 21 days the rate of total shrinkage strain development is very high, after which time it becomes more gradual and is continuously decreasing. Indeed, at 6 months the rate of gain in strain is quite small indicating that for high strength concrete (of nominal strength 100 N/mm^2), after 6 months increases in total shrinkage strain are minimal. At 6 months, autogenous shrinkage accounts for 81% of the total shrinkage strain and the rate of autogenous strain development is slightly larger than total strain development indicating that increases in shrinkage strain after this time will be mainly due to autogenous shrinkage. Drying shrinkage accounts for the remaining 19% of the total shrinkage although after 40 days the drying shrinkage strains reduce from 68 to 43 με, indicating that there is some discrepancy between the measured total and autogenous shrinkage strains from which the drying shrinkage strains are calculated. It is probable that this is due to some drying shrinkage occurring in the autogenous shrinkage specimens due to moisture loss at the points of contact between the demec gauge and gauge studs.

The total shrinkage strain after 6 months for the pfa concrete is around 140 με. The rate of total shrinkage strain development is initially very rapid, but becomes more gradual at a continuously decreasing rate. Indeed, after 98 days there is no further increase in the magnitude of the total shrinkage strain indicating that for concrete containing pfa, moisture movement is very rapid and shrinkage is over very early in the life of the concrete. Unfortunately, during the pfa shrinkage testing period the creep laboratory was subject to renovation activity which caused the environmental conditions to fluctuate. The autogenous shrinkage data recorded was significantly affected by this and it was not possible to interpret

the data in any meaningful way. Therefore, it was not possible to examine autogenous shrinkage and consequently drying shrinkage for the pfa concrete.

Figures 5.22a and 5.22b show the relationship between shrinkage and weight loss for total shrinkage and autogenous shrinkage respectively in the C80 concrete, whilst Figures 5.23a and 5.23b show the same relationships for the C100 concrete, and Figure 5.24 shows the relationship between shrinkage and weight loss for total shrinkage in the pfa concrete. The correlation between total shrinkage and weight loss is generally good in all cases, although the pfa concrete exhibits further weight loss once total shrinkage has stopped. As with the C40 specimens, there is weight loss in the autogenous shrinkage specimens where none should be occurring, since each autogenous shrinkage specimen is sealed. Weight loss in the C80 autogenous shrinkage specimens is approximately 15% of the total weight loss, similar to the C40 concrete, while weight loss in the C100 autogenous shrinkage specimens is approximately 30% of the total weight loss. Again this indicates that some water was lost through the points of contact between the demec gauge and gauge studs, indicating that the system of autogenous shrinkage measurement is not perfect. It is interesting to note that the weight loss in the C100 autogenous test specimens is twice that of the C40 and C80 specimens, especially since the w/c ratio in the C100 concrete is roughly half of the other two concrete strengths (0.26 compared with 0.56 in the C40 and 0.5 in the C80). The correlation between autogenous shrinkage and percentage weight loss is very good and a linear relationship is clear for both the C80 and C100 concretes. Surprisingly this was not as clear with the C40 concrete.

Figures 5.25 – 5.27 show the comparison between total, autogenous and drying shrinkage respectively over time for the different concretes under test. The x-axis represents the time (in days) from the start of testing, while the y-axis represents the shrinkage strain in $\mu\varepsilon$. Each concrete strength is represented by a different line on the chart as indicated on the legend. From examination of the total and drying shrinkage comparisons (Figures 5.25 and 5.27), it is apparent that as concrete strength increases, the amount of total shrinkage decreases as expected. The exception to this rule is the pfa concrete which has the lowest total shrinkage despite having a nominal concrete strength of 65 N/mm^2. However, it is likely that the inclusion of pfa within the mix has reduced the effect of total shrinkage, although it is difficult to determine why this is the case since it was not possible to examine autogenous and drying shrinkage in the pfa concrete because of the reasons mentioned previously. The autogenous shrinkage comparison (Figure 5.26) indicates that as the concrete strength increases (due to a reduction in w/c ratio), autogenous shrinkage also increases i.e. the reverse of total and drying shrinkage. Also it has already been mentioned that as the concrete strength

increases, the percentage of total shrinkage that is autogenous shrinkage increases while drying shrinkage decreases. These findings support the work of Tazawa and Miyazawa[46,47] and Mazloom *et al*[36] who also found that autogenous shrinkage increases as the w/c ratio decreases indicating that autogenous shrinkage is more significant for high strength concrete.

The basic creep strain after 6 months for the C80 concrete is in the range of 830 - 1240 με depending on the applied load. The specimens loaded to the same proposed stress/strength ratio can be clearly defined since they exhibit similar strains which are within 10% for each specimen at the same ratio. However, there are irregular differences in the magnitude of creep strain between specimens loaded to the design stress/strength ratios, as was found with the C40 concrete, and so the actual stress/strength ratios were again calculated. Hence, it was found that the large difference between the creep strains in specimen A loaded to a stress/strength ratio of 0.25 and specimen B loaded to a stress/strength ratio of 0.30, is because the actual stress/strength ratios are 0.30 and 0.37 respectively. It can be seen from Appendix Figure D3.1 that after an initial decrease in the rate of creep strain over the first 16 days, the rate of gain in strain is virtually constant up to 6 months and the relationship between creep strain and time appears to be linear in this range. This is obviously not the case since the rate will be continuously reducing until there is no further creep. Figure 5.28 shows the relationship between creep strain and stress/strength ratio for the C80 concrete. As with the C40 concrete, it can be seen that as the time increases the gradient of the line of best fit becomes steeper indicating that as the stress/strength ratio increases, the rate at which creep strain develops also increases.

The basic creep strain after 6 months for the C100 concrete is in the range of 680 - 1380 με depending on the applied load. Again it is easy to identify which specimens were loaded to the same design stress/strength ratio with the strains at 6 months for the designed 0.30 and 0.35 ratios within 10% for each specimen at the same ratio. However, there is a much larger difference in the creep strains at 6 months for the two specimens loaded to the nominal 0.25 ratio. It was found later that the two specimens were actually loaded to stress/strength ratios of 0.22 and 0.32, which explains the large difference. These two specimens were loaded in the same creep frame at the same time and it is likely that the difference is due to eccentricities in the applied load. As with the C80 concrete, it can be seen from Appendix Figure D3.2 that after an initial increase in the rate of creep strain over the first 16 days, the rate of gain in strain is virtually constant up to 6 months and the relationship between creep strain and time is again almost linear in this range. Figure 5.29 shows the relationship between creep strain and stress/strength ratio. Again it can be seen that as the stress/strength ratio increases, the rate at which creep strain develops also increases.

The basic creep strain after 6 months for the pfa concrete is in the range of 600 - 900 με depending on the applied load. In this case, only one specimen was loaded for each stress/strength ratio due to time constraints. As with the C80 and C100 concretes, it can be seen from Appendix Figure D3.3 that after an initial decrease in the rate of creep strain (over a shorter period of 6 days), the rate of gain in strain becomes virtually constant up to 6 months and the relationship between creep strain and time again is nearly linear in this range. Figure 5.30 shows the relationship between creep strain and stress/strength ratio. Again it can be seen that as the stress/strength ratio increases, the rate at which creep strain develops also increases, although the increase appears to be less in the pfa concrete than the previous two concretes.

Due to the wide variation in actual stress/strength ratios experienced by the creep specimens for all concrete strengths, it was necessary to select stress/strength ratios which are similar between the different concrete strengths for comparison. This was made possible by either using the strains from individual stress/strength ratio specimens, or averaging strains from two different stress/strength ratio specimens. Table 5.19 shows the selected stress/strength ratios used in this study. As can be seen, it is possible to compare strains recorded for all concrete strengths using two ratios, the 0.32 and 0.36, while it is also possible to compare strains between the C100 and pfa, and the C40 and C80 using other appropriate ratios. Figures 5.31 and 5.32 show the comparison of creep strain for concrete loaded to stress/strength ratios of 0.32 and 0.36 respectively for each concrete strength. It should be noted that there are problems associated with this method when representing and comparing creep strain in this manner as like is not compared with like. For example, at 6 months the C40 basic creep strain is approximately 1340με. Half of this value (670με) occurs after only 16 days. The same cannot be said for the other mixes. The basic creep for the C80 concrete at 6 months is approximately 1320με while half of that value occurs after only 5 days, and the basic creep for the C100 concrete at 6 months is approximately 1180με while half of that value occurs immediately following the instantaneous application of the load. Similarly, the basic creep for the pfa concrete at 6 months is approximately 930με while half of that value also occurs instantly. The C100 concrete attains the majority of its strength very early, while the C80 develops strength more slowly and the C40 develops slower again. The inclusion of pfa in the mix means the concrete strength will develop at an even slower rate. Unfortunately, there is nothing that can be done about this. It is impossible to test in such a way that strength develops at an equal rate for concrete of different strengths, so while the test method adopted is acceptable for testing for creep, the results for each concrete reported above are not strictly comparable. Hence, in the discussion of these results absolute values are not quoted but trends are identified.

It is immediately apparent that as concrete strength increases (due to a decrease in the w/c ratio), the rate at which creep strain develops also increases. In the case of the specimens loaded to a stress/strength ratio of 0.32 (Figure 5.31), during the first 70 days the C40 concrete creep strain is developing at a much slower rate than the C80 concrete creep strain which is similarly developing more slowly than the C100 concrete creep strain. After 70 days, the opposite is the case. The creep strains are still developing, but at a faster rate in the C40 than the C80, which in turn is faster than the C100. Because of this, the magnitude of the creep strain from 70 days onwards is larger the weaker the concrete is. It is interesting to note that the creep strains in the C40, C80 and C100 concrete are the same at exactly the same time i.e. 70 days. This is similar for the concrete loaded to the 0.36 stress/strength ratio (Figure 5.32) although due to the increased load, the different concrete strengths exhibit strains that are the same magnitude sooner, at 50 days. It is also interesting to note that the pfa concrete strains develop most rapidly, despite the fact that the pfa concrete is much weaker than both the C80 and C100 concretes indicating that the inclusion of pfa causes a reduction in creep.

5.9 Comparisons with Prediction Models

The models used to predict shrinkage and creep strains in this study are detailed in Chapter 2 and Appendix A. In summary, they are the CEB-FIP Model Code 1990[121] (CEB-FIP), the ACI-92R Model[117] (ACI) the BP-KX Model 1991[125] (BP-KX), the short-form BP-KX Model 1993[126] (BP-KX+), the GZ Model 1993[128] (GZ), the B3 Model 1995[114] (B3), the short-form B3 Model 1996[127] (B3+) and the GL Model 2001[129] (GL). The Eurocode 2 1992 (EC2) has also been investigated but this model uses the same formulae and therefore predicts the same strains as the CEB-FIP, and so any strains predicted by the CEB-FIP will be considered to be the same as the EC2. The input parameters used in the prediction models were selected to be as close to the actual parameters as possible in order to obtain predicted data that is directly comparable to the test data. Therefore, all mix proportions were as detailed in Section 5.4.1, all concrete properties were as measured and discussed in Section 5.8.1, specimen dimensions were as detailed in Section 5.4.3 and in order to obtain accurate environmental data, a relative humidity sensor was installed in the laboratory and an average value was taken over the duration of testing for use in the prediction models.

5.9.1 C40 Comparison

Figure 5.33 shows the comparison between the measured total shrinkage strains and the predicted total shrinkage strains obtained by using the aforementioned prediction models. The x-axis represents the time since testing began in days, while the y-axis represents the total

shrinkage strain in με. It can be seen that for the first 28 days, the CEB-FIP, ACI and GZ models predict strains which are virtually identical to the measured strains. After this period however, the measured strains continue to increase more rapidly than that given by either of these models and after 6 months are approximately 50 με larger than the CEB-FIP and ACI models and 130 με larger than the GZ model. The shape of the measured shrinkage strain curve is very similar to those given by the BP-KX, B3 and B3+ models, although the strains these models predict appear to be approximately 15% larger than the measured values. The strains predicted by the GL and BP-KX+ models are larger again, some 108 and 173 με greater respectively. This initial analysis suggests that the CEB-FIP, ACI, BP-KX, B3 and B3+ models predict strains which give good agreement with the test data, while the GZ and GL predict strains which give adequate agreement and the BP-KX+ strains give limited agreement.

Figures 5.34 – 5.38 show comparisons between the measured laboratory strains, and the predicted creep strains for the stress/strength ratios, 0.28, 0.32, 0.36, 0.40 and 0.43 respectively. It is immediately apparent that the measured strain curve in all instances increases rapidly after 28 days. During the first 28 days, the rate of creep is greater and so the load had to be reapplied at regular intervals. Unfortunately this was not always possible due to limited access during nights and weekends, and so the strains recorded during these periods are less than expected since the load was less. Therefore the graphs slightly under-estimate the strains during this period.

A comparison of the measured and predicted creep strains for the concrete loaded to a stress/strength ratio of 0.28 (Figure 5.34), show that up to 28 days the ACI model gives very good agreement with the measured strains while all other models overestimate strains. The CEB-FIP, B3, B3+ and GL models all give adequate agreement within 200 $\mu\epsilon$. Between 28 and 56 days the measured strain curve rises rapidly, as discussed previously, and the strain increase is quicker than predicted by any of the models. After 56 days, the B3 model predicts strains that are almost identical to the test data, while the CEB-FIP, B3+ and GL models give adequate agreement within 150 $\mu\epsilon$ after 6 months. The ACI model gives limited agreement after 6 months, under-predicting strains by 400 $\mu\epsilon$. Over the 6 month test period, the BP-KX and BP-KX+ models significantly over-predict strains of 700 and 375 $\mu\epsilon$ at 6 months, while the GZ model displays behaviour contrary to the test data and all other models, over-predicting strains up to 28 days and under-predicting strains from 28 days to 6 months, giving strains which are approximately 400 $\mu\epsilon$ lower than the test data at 6 months.

The pattern of strain agreement between the model predictions and the test data is similar for the other four stress/strength ratios and hence will only be summarised here. Generally the best agreement is between the B3 and B3+ models which predict strains which are within 30 – 210 and 90 – 280 $\mu\epsilon$ respectively after 6 months. The CEB-FIP and GL models give adequate agreement with the test data, predicting strains that are within 250 – 500 and 175 – 400 $\mu\epsilon$ respectively after 6 months. The ACI and GZ models significantly under-predict strains in the range of 500 – 900 and 600 – 1000 $\mu\epsilon$ respectively after 6 months. Conversely, the BP-KX model considerably over-predicts strains in the range of 700 – 1200 $\mu\epsilon$ after 6 months, while the BP-KX+ short form model also over-predicts strain but to a lesser extent of around 350 $\mu\epsilon$ for all stress/strength ratios, again after 6 months.

From examination of each figure, it can be seen that the measured creep strain curves become larger with increasing stress/strength ratio, at a quicker rate than the predicted strain curves. Earlier on in this chapter it was observed that as the stress/strength ratio increases, the rate of gain in creep strain also increases. Therefore for grade C40 concrete, it is apparent that while the prediction models do take this effect into account, they all underestimate the amount by which strain increases with increasing stress levels.

In order to highlight which models give the best prediction of the test data, the measured strains were plotted against the predicted strains for each model. Figures 5.39a – 5.46a show the creep comparison, Figures 5.39b – 5.46b show the shrinkage comparison, while Figures 5.39c – 5.46c show the total strain comparison. In each figure, the x-axis represents the predicted strain while the y-axis represents the measured strain (both in microstrain). The dashed line represents the equality line on which the majority of points should lie if good agreement between the measured and predicted strains exists. In the case of the creep and total strain figures (a and c respectively), there are five different comparative data sets each representing a different stress/strain ratio as depicted by the legend.

From inspection of the shrinkage comparison figures, it is apparent that the CEB-FIP model gives the best agreement with the test data, since the strains are almost identical and there is only slight divergence from the equality line at 6 months. The ACI model also gives very good agreement although the strain behaviour varies more than the CEB-FIP model. The GZ model shows good initial agreement up to 56 days after which there is a noticeable divergence which gets worse with time. The BP-KX and B3 models predict strains which give relatively good agreement with the test data, as does the B3+ model although there is an increasing divergence with time. The worst agreement is between the measured strains and the BP-KX+ and GL models which get increasingly worse over time.

It can be seen that for each basic creep (and hence total strain) comparison, the increase in strain after 28 days (discussed in Section 5.8.2) is immediately noticeable due to the kink in the curve in all figures. It can be seen that the B3 and B3+ models best predict the test data as demonstrated by the closeness of the data to the equality line, and because comparisons between the measured and predicted strains made using these two models reveal the smallest increase in strain after 28 days. The CEB-FIP, ACI and GL models predict similar strains to the test data up to 28 days after which point there is noticeable divergence which gets worse with time. The BP-KX and BP-KX+ models again show very poor agreement with the test data, while it is obvious that the strain behaviour predicted by the GZ model is the least representative of the test data.

Therefore, it can be concluded that for 'normal' strength concrete with a nominal strength of 40 N/mm^2, the models best suited for predicting shrinkage strains are the CEB-FIP and ACI models, while the models best used for predicting creep strains are the B3 and short form B3 models. Overall, the single model that predicts shrinkage, creep and total strains that give the closest agreement with the measured strains is the B3 model.

5.9.2 C80/C100/pfa Comparison

It should be noted that the majority of the models under investigation impose recommended restrictions on the input data. For example, the maximum 28-day compressive strength that is recommended for each model is, for the CEB-FIP model, 80 N/mm^2, for the BP-KX and BP-KX+, 62 N/mm^2, while for the B3 and B3+ it is 70 N/mm^2. It is appreciated that the concrete mixes used in this study go beyond these limits, but since these concretes are being used more regularly in the construction industry and also since there are no other methods of predicting the time-dependent deformations in higher strength concretes, it was decided to test their predictive capabilities for comparative purposes.

It was intended to use the same mix proportions in the pfa mix as those used in the construction of the Cogan and Grangetown Viaducts. Since each prediction model has a limited number of input parameters regarding mix proportions, and these do not include the addition of admixtures, the inclusion of pfa causes a certain amount of difficulty in the calculations. Since pfa is a finely ground material, its inclusion significantly increases the amount of fine particles in the concrete mix. It was decided to include the quantity of pfa as part of the cement content, also increasing the water content such that the w/c ratio remains the same. It was also decided to reduce the total amount of constituents by equal percentages to ensure that the final density was 2400 kg/m^3 which corresponded to the actual density of the concrete mix. The original and final mix proportions are shown in Table 5.20.

Comparisons between the measured and predicted shrinkage and creep strains for the C80, C100 and pfa concrete specimens can be found in Appendix D. The comparison was made in the same way as for the C40 concrete detailed above. For the C80 concrete, all models except the ACI and GL models predict shrinkage strains which give adequate agreement with the measured shrinkage strains. Over the first 36 days, all models over-predict the magnitude of the shrinkage strains, however, after 36 days the CEB-FIP and BP-KX models predict strains which are virtually identical to the test data as shown in Figures 5.47 and 5.48. Similarly, for the C100 concrete all models except the ACI and GL models predict strains which give adequate agreement with the measured shrinkage strains. The BP-KX, BP-KX+, B3 and B3+ models all give very good agreement with the measured strains, but the best fit is given by the GZ model which marginally over-predicts shrinkage strains over the first 70 days, but after this time predicts strains which are virtually identical to the test data as shown in Figure 5.49. All models over-predict shrinkage strains in the pfa concrete by some margin, between 100 and 400 με after 6 months. The closest agreement is given by the CEB-FIP model as shown in Figure 5.50.

A comparison of the measured and predicted creep strains for the C80 concrete loaded to a stress/strength ratio of 0.23 reveals that all models except the ACI and GZ models over-estimate (by some margin) the magnitude of the creep strains. The ACI model gives the best agreement with the predicted data, while the CEB-FIP model also predicts creep strains that are within 100 με at all times. The B3 and GZ models display behaviour that is contrary to the measured strains and all other predicted strains. Similar observations can be made for the C80 concrete loaded to a stress/strength ratio of 0.32, and for the concrete loaded to a stress/strength ratio of 0.37, with all models except the GZ over-predict strains at 6 months. Again the ACI model gives the closest agreement with the predicted basic creep and total strains as shown in Figures 5.51and 5.52 for basic creep and total strain respectively.

A comparison of the measured and predicted creep strains for the C100 concrete loaded to all stress/strength ratios (0.22, 0.32, 0.36, 0.41 and 0.43) shows that all models over-estimate the magnitude of the creep strains, in the range of 320 to 1230 με after 6 months depending on the applied load and model. The model that gives the best prediction of creep and total strains for all stress/strength ratios is the GZ model, although the model doesn't reflect the strain behaviour as accurately as the next best model, the CEB-FIP model which over-predicts strains by up to 500 με. This can be seen in Figures 5.53 and 5.54 for basic creep and total strain respectively.

A comparison of the measured and predicted creep strains for the pfa concrete loaded to all stress/strength ratios (0.23, 0.32 and 0.36) shows that (similar to the C100 concrete), all models over-estimate the magnitude of the creep strains, in the range of 125 to 1780 με after 6 months depending on the applied load and model. Again, the model that predicts the closest creep and total strains for all stress/strength ratios is the GZ model, although again the model does not reflect the creep strain behaviour as accurately as the next closest model, this time the ACI model which over-predicts strains by up to 500 με but more accurately reflects the creep strain behaviour as shown in Figure 5.55. However, with regard to the prediction of total strain, the GZ model gives by far the most accurate agreement with the test data indicating that any inaccuracies in the predicted shrinkage and creep strains seem to cancel out as shown in Figure 5.56.

Therefore it can be concluded that no one model is consistently more accurate when predicting shrinkage, creep and total strains for a given concrete strength. For the C80 concrete, the CEB-FIP model gives the best prediction of shrinkage strains, while the ACI model more accurately reflects creep and total strains. For the C100 concrete, the GZ model gives the best prediction of shrinkage strains, while the CEB-FIP model is better in relation to creep and total strain behaviour. For the pfa concrete, the CEB-FIP model estimates the shrinkage strains well, while the ACI model more accurately predicts the creep strain behaviour and the GZ model gives the best prediction of the total strains. However, using different models for different types of strain is not particularly practical and therefore a compromise must be reached to determine which model gives the best overall agreement with the measured strains for each concrete strength. Overall, the model that best predicts the shrinkage, creep and total strains of the test specimens for the C80 and C100 concrete is the CEB-FIP model, while the GZ model gives the best agreement for the pfa concrete as can be seen in Figures 5.57 – 5.59 respectively.

5.10 Conclusions

It can be concluded that shrinkage and creep is affected by the properties of concrete of varying composition and strength in the following ways:

- For the C40, C80 and C100 concretes, as concrete strength increases the amount of total and drying shrinkage decreases. However, the pfa concrete has the lowest shrinkage of all despite having a nominal strength of 65 N/mm^2, indicating that the inclusion of pfa within the mix results in a reduction of the total shrinkage.

- For the C40, C80 and C100 concretes, as concrete strength increases the percentage of total shrinkage that is autogenous shrinkage increases while drying shrinkage decreases, indicating that autogenous shrinkage is more prevalent in high strength concrete.

- A linear relationship between total shrinkage and percentage weight loss was observed for all concrete strengths, indicating that shrinkage is dependent upon water content. The same relationship was observed between autogenous shrinkage and percentage weight loss in the C80 and C100 concretes. Since there should be no weight loss in the autogenous test specimens it was concluded that some moisture transfer occurs at the contacts between the demec gauge and gauge studs indicating that this method of testing is subject to error.

- For the C40, C80 and C100 concretes, as concrete strength increases, the rate at which creep strain develops increases. Initially, the C40 creep strain develops at a slower rate than the C80 creep strain which in turn develops more slowly than the C100 creep strain. After some time, depending on the stress/strength ratio, the opposite is the case with the C40 creep strain developing more quickly than the C80 creep strain which in turn develops more quickly than the C100 creep strain. Therefore, with time creep strains are larger the weaker the concrete is.

- pfa concrete strains develop most rapidly, despite the fact that the pfa concrete is weaker than both the C80 and C100 concretes indicating that the inclusion of pfa reduces creep.

- A linear relationship exists between creep strain and stress/strength ratio. However, as the stress/strength ratio increases, the rate at which creep strain develops also increases indicating that creep effects will be more pronounced for longer at higher stress/strength ratios.

A study of the predicted shrinkage, creep and total strains obtained using a range of different prediction models when compared with actual strains observed in concrete of varying composition and strength has yielded the following conclusions:

- For a normal strength concrete of nominal strength 40 N/mm^2, the CEB-FIP and ACI models predict shrinkage strains which are in closest agreement with the measured shrinkage strains, while the B3 and short form B3 models predict creep and total strains which are in closest agreement with the measured creep strains. Overall, the one model that predicts shrinkage, creep and total strains that most closely agree with the measured strains is the B3 model.

- For high strength concrete of nominal strength 80 N/mm^2, the CEB-FIP model predicts shrinkage strains which are in closest agreement with the measured shrinkage strains, while the ACI model best predicts the measured creep and total strains. Overall, the one model that predicts shrinkage, creep and total strains that most closely agrees with the measured strains is the CEB-FIP model.

- For high strength concrete of nominal strength 100 N/mm^2, the GZ model gives the best prediction of the shrinkage strains while the CEB-FIP model best predicts the measured creep and total strains. Overall, the best model for predicting shrinkage, creep and total strains is the CEB-FIP model.

- For pfa concrete of nominal strength 65 N/mm^2, the CEB-FIP model gives the best prediction of the shrinkage strains, while the ACI model best predicts the measured creep strains and the GZ model best predicts the measured total strains. Overall, the best model for predicting shrinkage, creep and total strains is the GZ model.

- It can be concluded that all prediction models generally predict strains that give good to adequate prediction of the recorded strains for concrete when the material parameters are within the ranges specified by the models. When the concrete properties exceed the recommended values, then the agreement given between the predicted and measured strains becomes unreliable. Certain models will give good agreement whilst others will not and the user must be selective when choosing which to use, basing the selection on the concrete properties.

Table 5.1. Composition of cement supplied by Blue Circle.

Oxide	Compound	Composition %
SiO_2		20.1
Al_2O_3		4.3
Fe_2O_3		1.9
CaO		63.7
MgO		2.4
SO_3		2.8
Other		Trace
	C_3S	60.9
	C_2S	7.2
	C_3A	8.2
	C_4AF	5.8

Table 5.2. Compositions of the Grangetown, Cogan and Taff Viaduct concrete mixes (details from various sources).

Material	Ramezankhani *et al*[139]	Vitek and Barr[1]	Site Correspondence
Ordinary Portland cement	330 kg/m^3	330 kg/m^3	330 kg/m^3
pfa	170 kg/m^3	170 kg/m^3	170 kg/m^3
20mm aggregate	1245 kg/m^3	746 kg/m^3	870 kg/m^3
10mm aggregate		320 kg/m^3	373 kg/m^3
Sand	535 kg/m^3	710 kg/m^3	534 kg/m^3
Water	92 kg/m^3	149 l/m^3	138 l/m^3
Water/Cement ratio	0.28	0.45	0.42
Plasticizer (Conplast 211)	320 ml/kg	1.6 l/m^3	1.6 l/m^3

Table 5.3. Results of slump and Vebe tests.

Concrete Reference	Mix No.	Slump (mm)	Vebe (sec.)
40	1	55	2
pfa	1	54	7
80 (1)	1	15	3
80 (2)	2	36	6
80 (3)	3	31	5
100 (1)	1	56	8
100 (2)	2	120	-

Table 5.4. Compression test results C40 concrete.

Age of Concrete (days)	Cube No.	Load at failure (kN)	Compressive Strength (N/mm^2)	Average (N/mm^2)
28	1	370	37.0	**37.5**
	2	375	37.5	
	3	381	38.1	
84	1	471	47.1	**46.8**
	2	458	45.8	
	3	475	47.5	
252	1	568	56.8	**56.6**
	2	550	55.0	
	3	580	58.0	

Table 5.5. Compression test results for pfa concrete.

Age of Concrete (days)	Cube No.	Load at failure (kN)	Compressive Strength (N/mm^2)	Average (N/mm^2)
28	1	725	72.5	**72.2**
	2	708	70.8	
	3	734	73.4	
84	1	931	93.1	**91.4**
	2	872	87.2	
	3	938	93.8	
252	1	985	98.5	**99.3**
	2	1001	100.1	
	3	-	-	

Table 5.6. Compression test results for C80 concrete mix 1.

Age of Concrete (days)	Cube No.	Load at failure (kN)	Compressive Strength (N/mm^2)	Average (N/mm^2)
28	1	718	71.8	**70.7**
	2	699	69.9	
	3	705	70.5	
84	1	756	75.6	**77.3**
	2	779	77.9	
	3	784	78.4	
252	1	787	78.7	**80.3**
	2	806	80.6	
	3	816	81.6	

Table 5.7. Compression test results for C80 concrete mix 2.

Age of Concrete (days)	Cube No.	Load at failure (kN)	Compressive Strength (N/mm^2)	Average (N/mm^2)
28	1	684	68.4	**66.7**
	2	632	63.2	
	3	686	68.6	
84	1	732	73.2	**74.3**
	2	753	75.3	
	3	743	74.3	
252	1	745	74.5	**75.5**
	2	757	75.7	
	3	764	76.4	

Table 5.8. Compression test results for C80 concrete mix 3.

Age of Concrete (days)	Cube No.	Load at failure (kN)	Compressive Strength (N/mm^2)	Average (N/mm^2)
28	1	688	68.8	**71.2**
	2	735	73.5	
	3	-	-	
84	1	741	74.1	**75.4**
	2	766	76.6	
	3	-	-	
252	1	774	77.4	**78.1**
	2	788	78.8	
	3	-	-	

Table 5.9. Compression test results for C100 concrete mix 1.

Age of Concrete (days)	Cube No.	Load at failure (kN)	Compressive Strength (N/mm^2)	Average (N/mm^2)
28	1	893	89.3	**87.3**
	2	872	87.2	
	3	853	85.3	
84	1	1002	100.2	**100.7**
	2	1012	101.2	
	-	-	-	
252	1	1029	102.9	**102.8**
	2	1027	102.7	
	-	-	-	

Table 5.10. Compression test results for C100 concrete mix 2.

Age of Concrete (days)	Cube No.	Load at failure (kN)	Compressive Strength (N/mm^2)	Average (N/mm^2)
28	1	963	96.3	**98.1**
	2	978	97.8	
	3	1001	100.1	
84	1	1009	100.9	**104.7**
	2	1053	105.3	
	3	1079	107.9	
252	1	1051	105.1	**105.3**
	2	1054	105.4	
	3	-	-	

Table 5.11. Torsion test results for C40 concrete.

Age of Concrete (days)	Cylinder No.	Load at failure (kN)	Tensile Strength (N/mm^2)	Average (N/mm^2)	Young's Modulus (kN/mm^2)	Average (kN/mm^2)
28	1	2.37	3.02	**2.74**	40.74	**37.68**
	2	1.94	2.47		34.62	
	-	-	-		-	
84	1	2.13	2.71	**2.92**	38.08	**38.96**
	2	2.46	3.13		39.84	
	-	-	-		-	
252	1	2.48	3.16	**3.09**	44.25	**41.48**
	2	2.37	3.02		38.70	
	-	-	-		-	

Table 5.12. Torsion test results for pfa concrete.

Age of Concrete (days)	Cylinder No.	Load at failure (kN)	Tensile Strength (N/mm^2)	Average (N/mm^2)	Young's Modulus (kN/mm^2)	Average (kN/mm^2)
28	1	4.43	5.64	**4.95**	50.76	**53.89**
	2	3.72	4.74		53.29	
	3	3.52	4.48		57.62	
84	1	4.87	6.20	**6.08**	55.81	**54.72**
	2	4.68	5.96		53.63	
	3	-	-		-	
252	1	5.20	6.62	**7.06**	59.59	**63.21**
	2	5.89	7.50		66.83	
	3	-	-		-	

Table 5.13. Torsion test results for C80 concrete mix 1.

Age of Concrete (days)	Cylinder No.	Load at failure (kN)	Tensile Strength (N/mm^2)	Average (N/mm^2)	Young's Modulus (kN/mm^2)	Average (kN/mm^2)
28	1	2.80	3.57	**3.56**	43.32	**40.84**
	2	2.79	3.55		38.37	
	-	-	-		-	
84	1	2.79	3.55	**3.63**	43.16	**47.30**
	2	2.91	3.71		51.45	
	-	-	-		-	
252	1	3.18	4.05	**4.20**	52.06	**49.39**
	2	3.45	4.39		49.42	
	3	3.26	4.15		-	

Table 5.14. Torsion test results for C80 concrete mix 2.

Age of Concrete (days)	Cylinder No.	Load at failure (kN)	Tensile Strength (N/mm^2)	Average (N/mm^2)	Young's Modulus (kN/mm^2)	Average (kN/mm^2)
28	1	2.58	3.28	**3.11**	42.24	**47.59**
	2	2.18	2.78		41.63	
	3	2.57	3.27		58.90	
84	1	3.21	4.09	**3.65**	40.87	**48.06**
	2	2.30	2.93		52.71	
	3	3.09	3.93		50.58	
252	1	3.74	4.76	**4.58**	47.62	**48.52**
	2	3.45	4.39		49.42	
	3	-	4.58		48.52	

Table 5.15. Torsion test results for C80 concrete mix 3.

Age of Concrete (days)	Cylinder No.	Load at failure (kN)	Tensile Strength (N/mm^2)	Average (N/mm^2)	Young's Modulus (kN/mm^2)	Average (kN/mm^2)
28	1	3.53	4.49	**4.37**	48.74	**50.29**
	2	3.19	4.06		54.56	
	3	3.57	4.55		47.57	
84	1	3.96	5.04	**5.04**	54.67	**51.47**
	2	3.96	5.04		48.27	
	3	-	-		-	
252	1	3.97	5.05	**5.19**	49.93	**53.39**
	2	4.19	5.33		56.85	
	3	-	-		-	

Table 5.16. Torsion test results for C100 concrete mix 1.

Age of Concrete (days)	Cylinder No.	Load at failure (kN)	Tensile Strength (N/mm^2)	Average (N/mm^2)	Young's Modulus (kN/mm^2)	Average (kN/mm^2)
28	1	4.31	5.49	**5.36**	49.39	**46.80**
	2	4.05	5.16		46.41	
	3	4.28	5.45		44.59	
84	1	5.50	7.00	**6.44**	52.52	**52.82**
	2	4.88	6.21		55.92	
	3	4.80	6.11		50.00	
252	1	4.27	5.44	**6.01**	54.37	**51.87**
	2	5.17	6.58		49.37	
	-	-	-		-	

Table 5.17. Torsion test results for C100 concrete mix 2.

Age of Concrete (days)	Cylinder No.	Load at failure (kN)	Tensile Strength (N/mm^2)	Average (N/mm^2)	Young's Modulus (kN/mm^2)	Average (kN/mm^2)
28	1	4.56	5.81	**5.65**	58.06	**56.47**
	2	4.31	5.49		54.88	
	3	-	-		-	
84	1	5.41	6.89	**6.82**	56.36	**58.49**
	2	5.29	6.74		60.62	
	-	-	-		-	
252	1	5.82	7.41	**7.50**	55.58	**56.48**
	2	5.82	7.41		60.63	
	3	6.04	7.69		53.24	

Table 5.18. Determination of actual stress/strength ratios from instantaneous strains.

Concrete Type	Compressive strength at loading (N/mm^2)	Elastic Modulus at loading (N/mm^2)	Proposed stress/strength ratio	Specimen No.	Expected instantaneous strain ($\mu\epsilon$)	Actual instantaneous strain ($\mu\epsilon$)	Actual stress/strength ratio
C40	46.8	38960	0.25	A	300	334	0.28
	46.8	38960	0.25	B	300	346	0.29
	46.8	38960	0.30	A	360	402	0.33
	46.8	38960	0.30	B	360	376	0.31
	46.8	38960	0.35	A	420	479	0.40
	46.8	38960	0.35	B	420	525	0.44
	46.8	38960	0.40	A	480	557	0.46
	46.8	38960	0.40	B	480	520	0.43
C80	77.3	47300	0.25	A	441	446	0.28
	75.4	51470	0.25	B	366	401	0.27
	77.3	47300	0.30	A	529	551	0.37
	75.4	51470	0.30	B	439	518	0.36
	74.3	48060	0.35	A	541	676	0.44
	75.4	51470	0.35	B	513	503	0.37
C100	100.7	52820	0.25	A	477	418	0.22
	100.7	52820	0.25	B	477	617	0.32
	100.7	52820	0.30	A	572	647	0.32
	100.7	52820	0.30	B	537	637	0.36
	100.7	52820	0.35	A	627	774	0.43
	100.7	52820	0.35	B	627	730	0.41
pfa	91.4	54720	0.25	A	418	390	0.23
	91.4	54720	0.30	A	501	536	0.32
	91.4	54720	0.35	A	585	598	0.36

Table 5.19. Summary of actual stress/strength ratios.

Concrete Type	Stress/strength ratios					
C40		0.28	0.32	0.36	0.40	0.43
C80		0.27	0.32	0.36		
C100	0.22		0.32	0.36	0.41	0.43
pfa	0.23		0.32	0.37		

Table 5.20. Original and modified concrete mix proportions for use in model predictions.

Material	Original composition	Modified composition
Ordinary Portland cement	330 kg/m^3	480 kg/m^3
pfa	170 kg/m^3	
20mm aggregate	746 kg/m^3	1023 kg/m^3
10mm aggregate	320 kg/m^3	
Sand	710 kg/m^3	681 kg/m^3
Water	149 l/m^3	216 kg/m^3
Plasticizer	1.6 l/m^3	

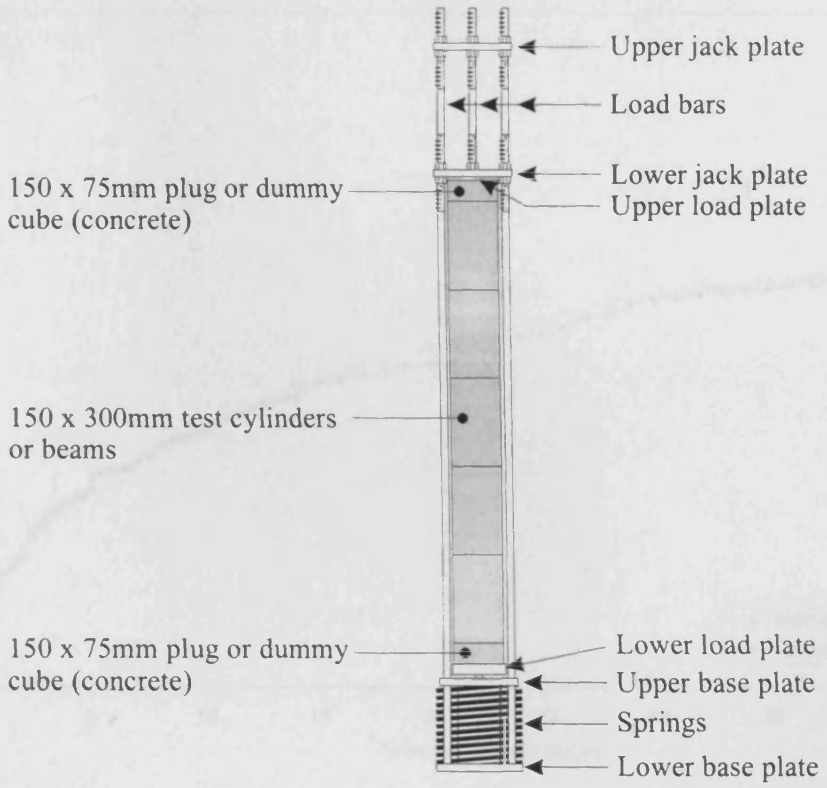

Figure 5.1. American Standard Test Method for creep of concrete in compression (ASTM C 512-87[141]).

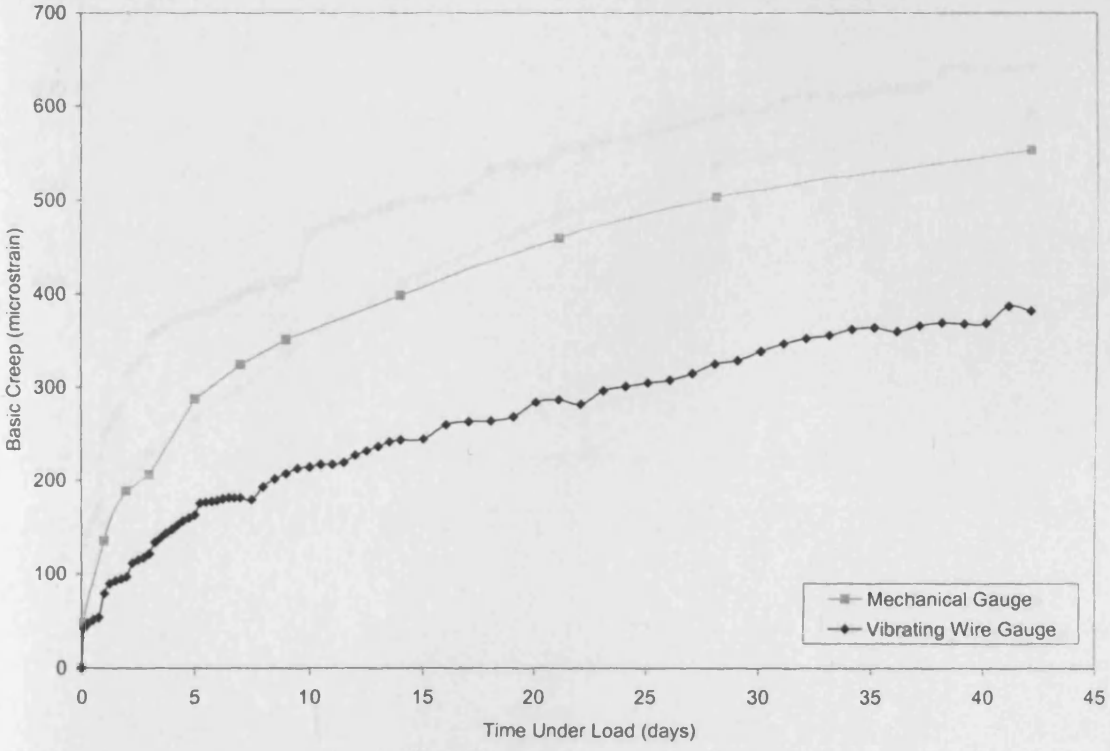

Figure 5.2. Test results for the creep of concrete of strength 40MPa (Howells[13]).

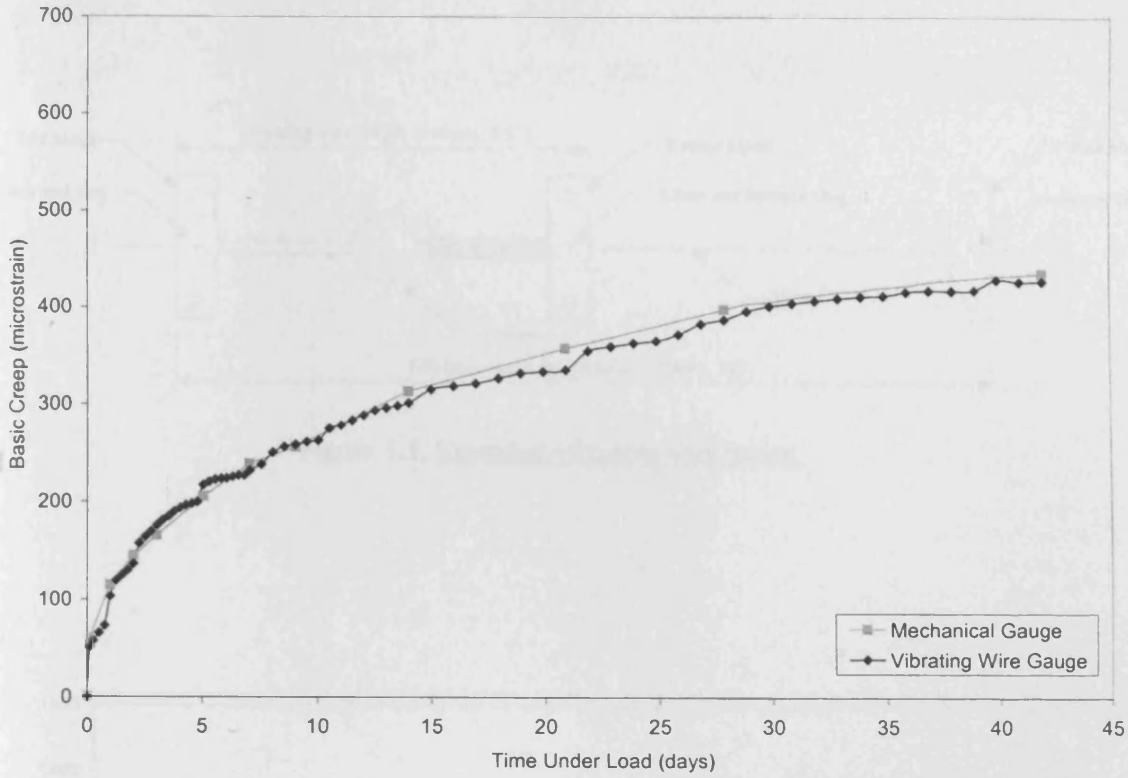

Figure 5.3. Test results for the creep of concrete of strength 80MPa (Howells[13]).

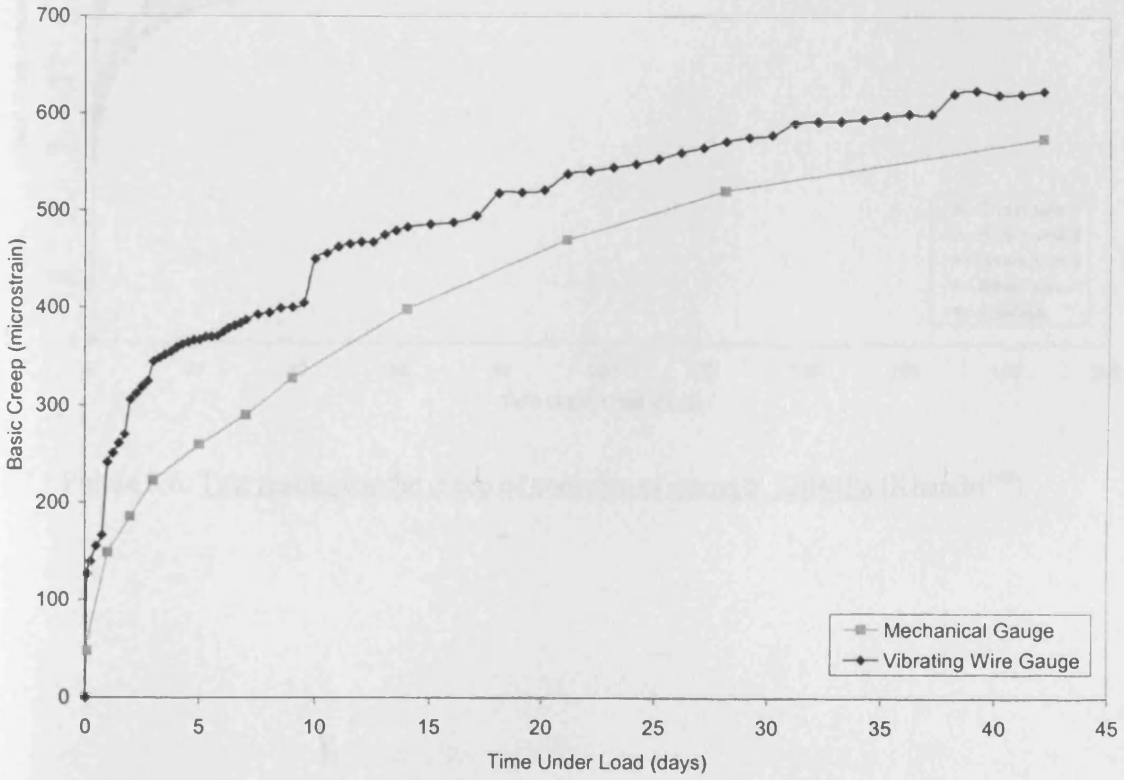

Figure 5.4. Test results for the creep of concrete of strength 120MPa (Howells[13]).

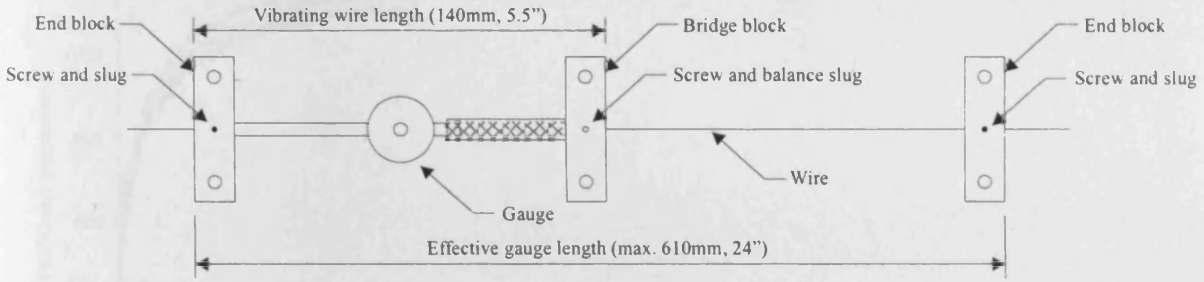

Figure 5.5. Extended vibrating wire gauge.

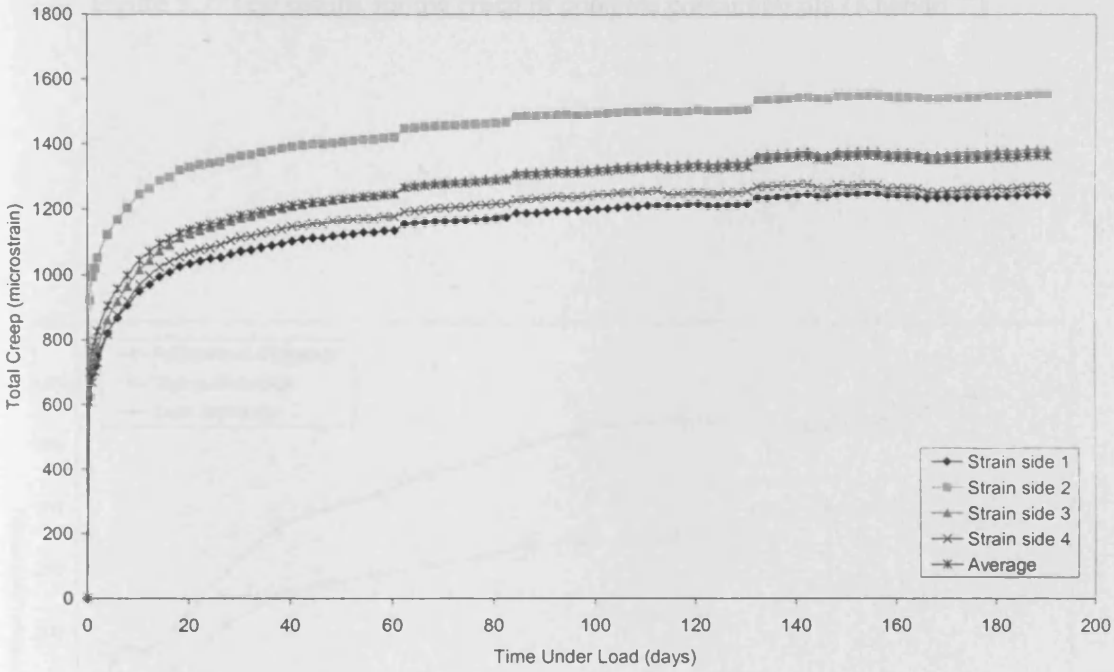

Figure 5.6. Test results for the creep of concrete of strength 120MPa (Khandri[142]).

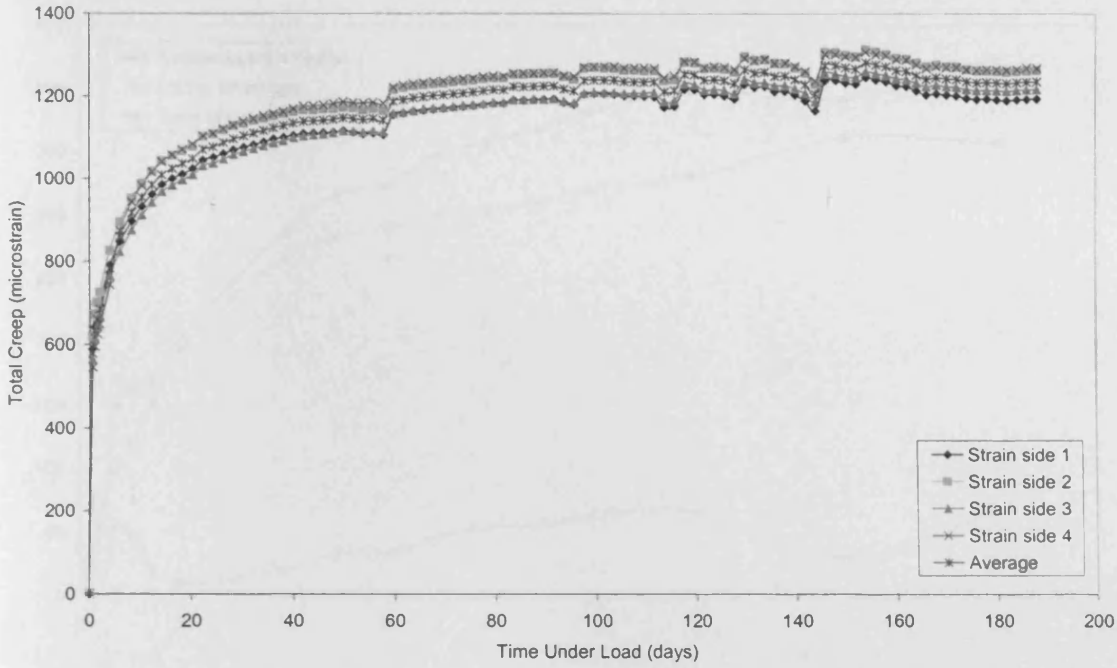

Figure 5.7. Test results for the creep of concrete containing pfa (Khandri[142]).

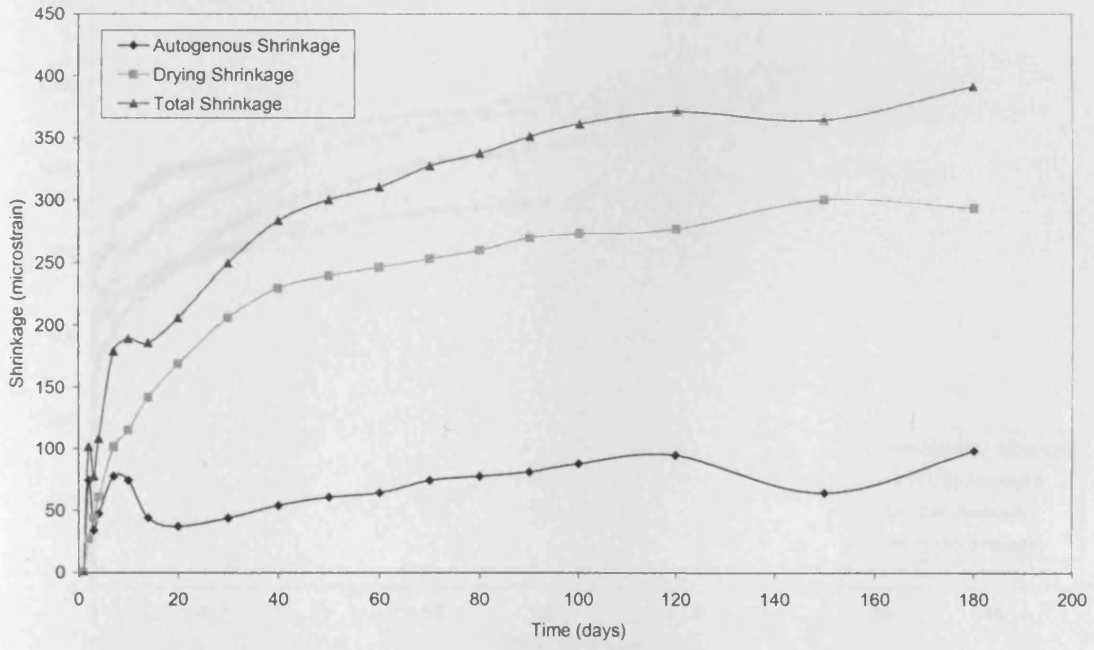

Figure 5.8. Test results for the shrinkage of concrete of strength 120 MPa (Khandri[142]).

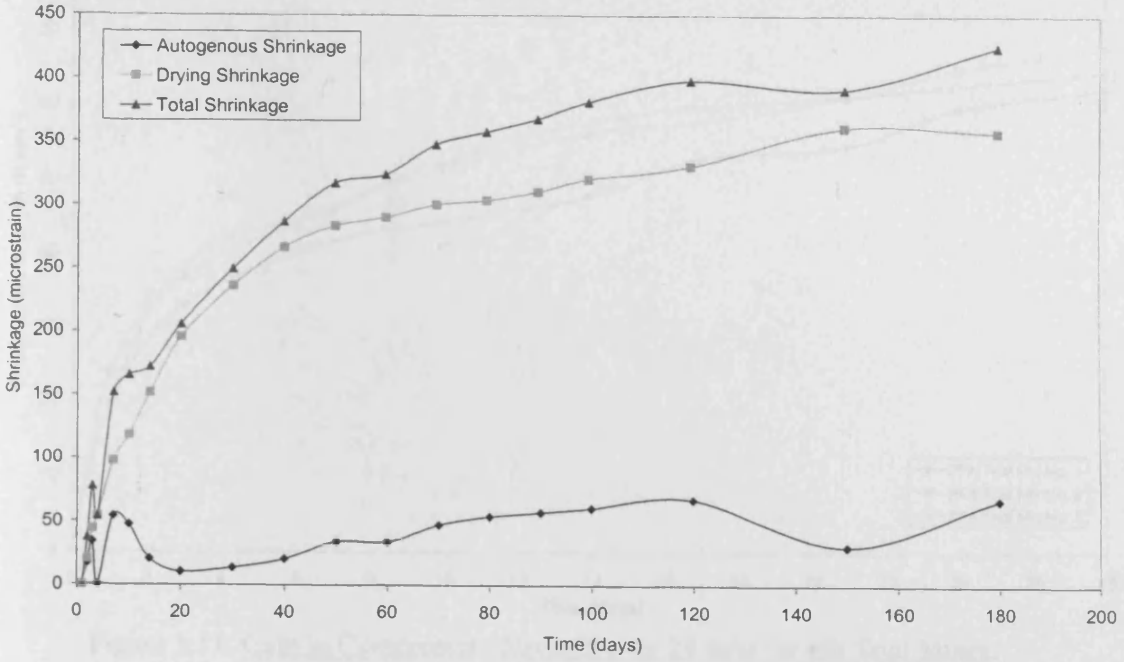

Figure 5.9. Test results for the shrinkage of concrete containing pfa (Khandri[142]).

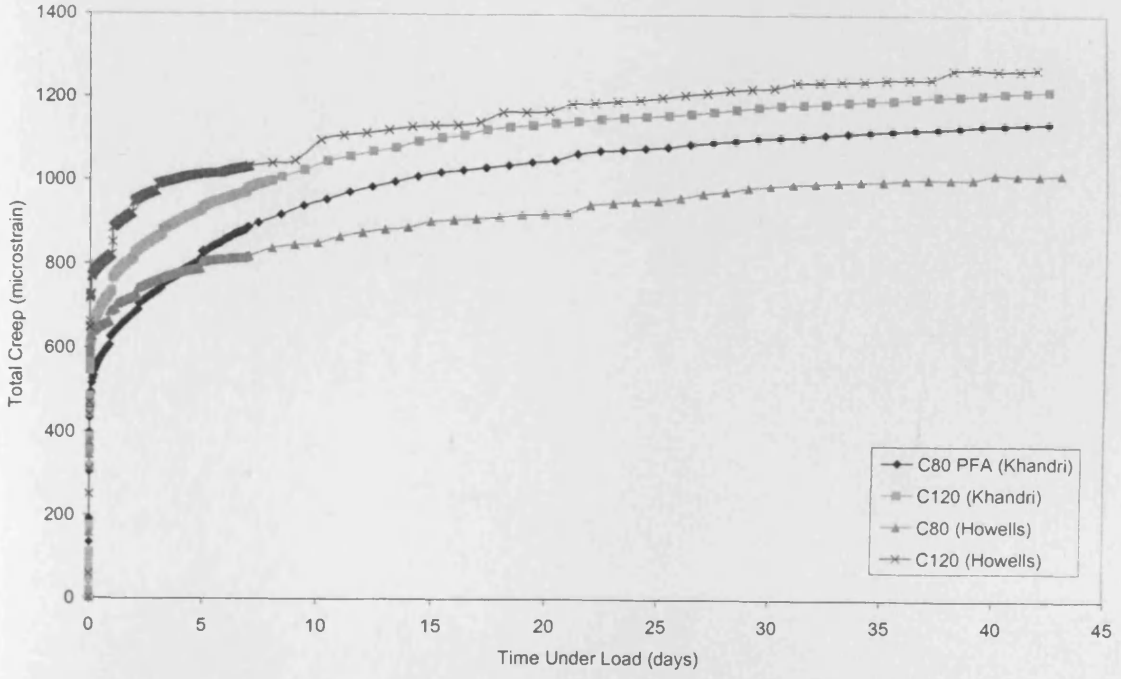

Figure 5.10. Comparison of creep data obtained from preliminary creep studies.

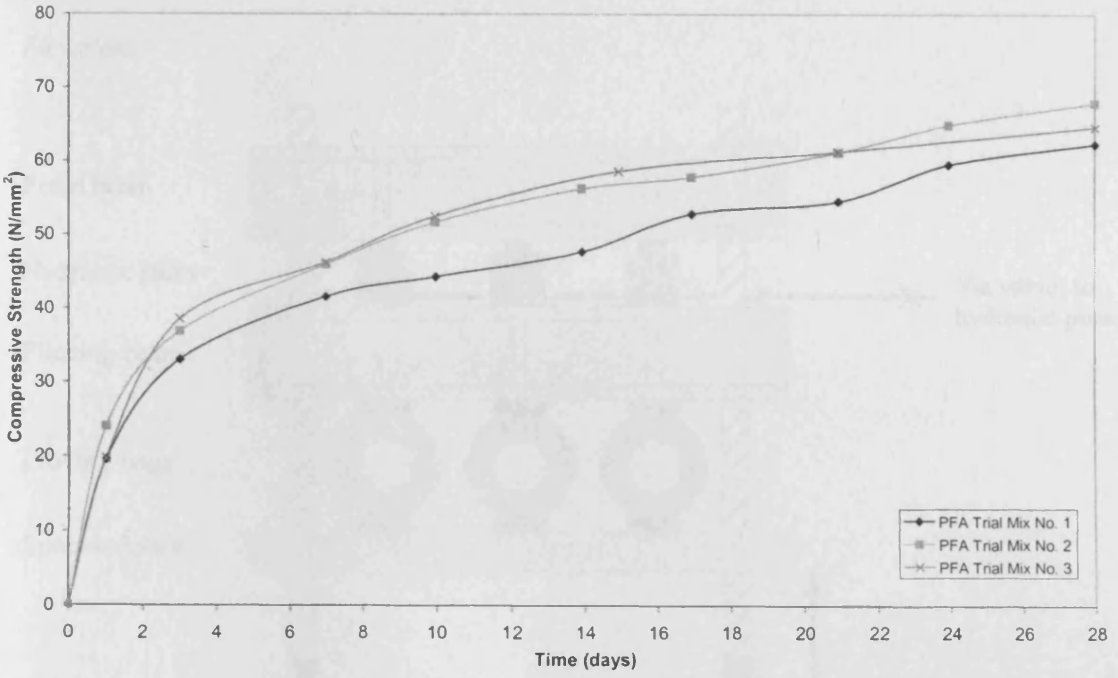

Figure 5.11. Gain in Compressive Strength over 28 days for pfa Trial Mixes.

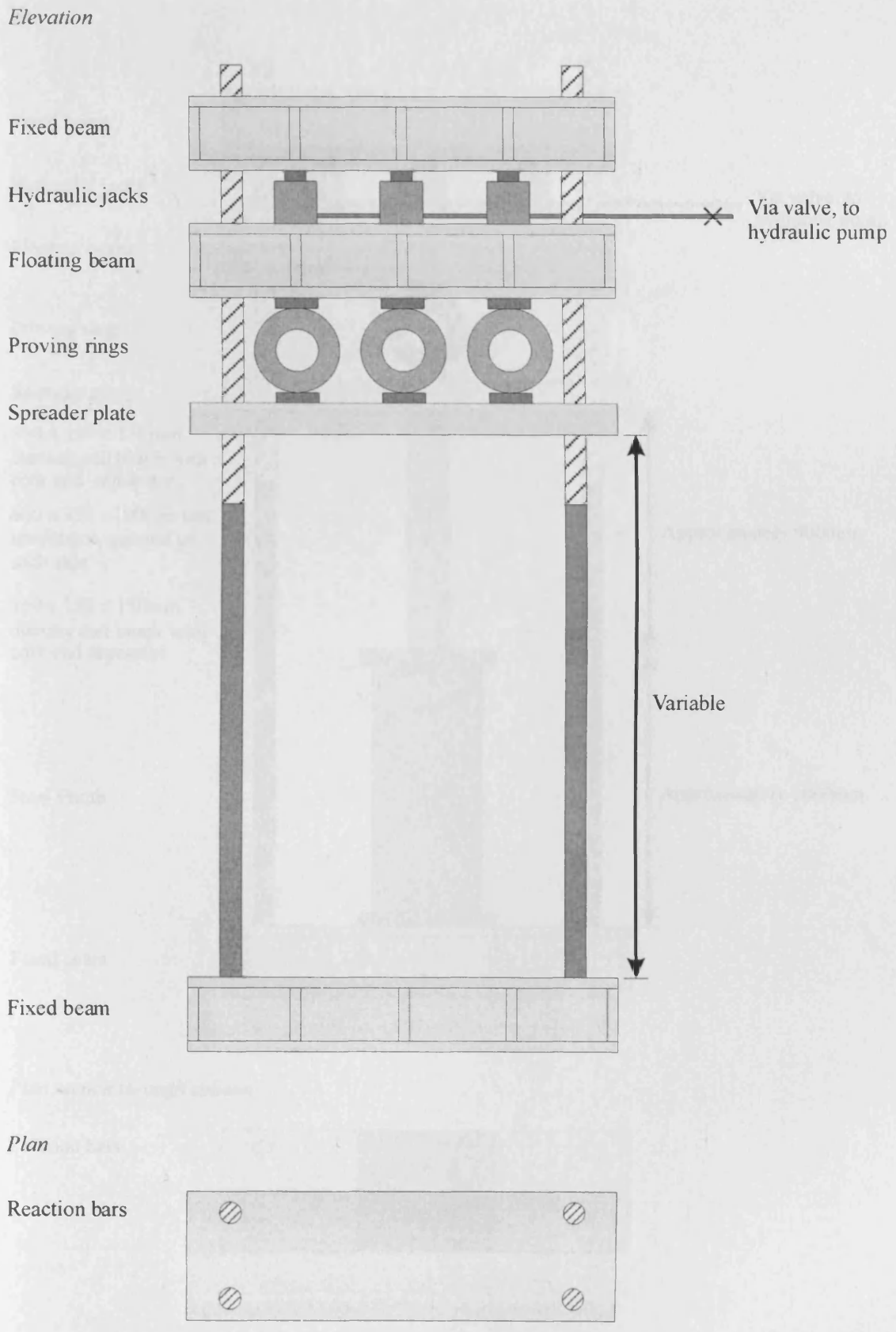

Figure 5.12. Large Creep Rig.

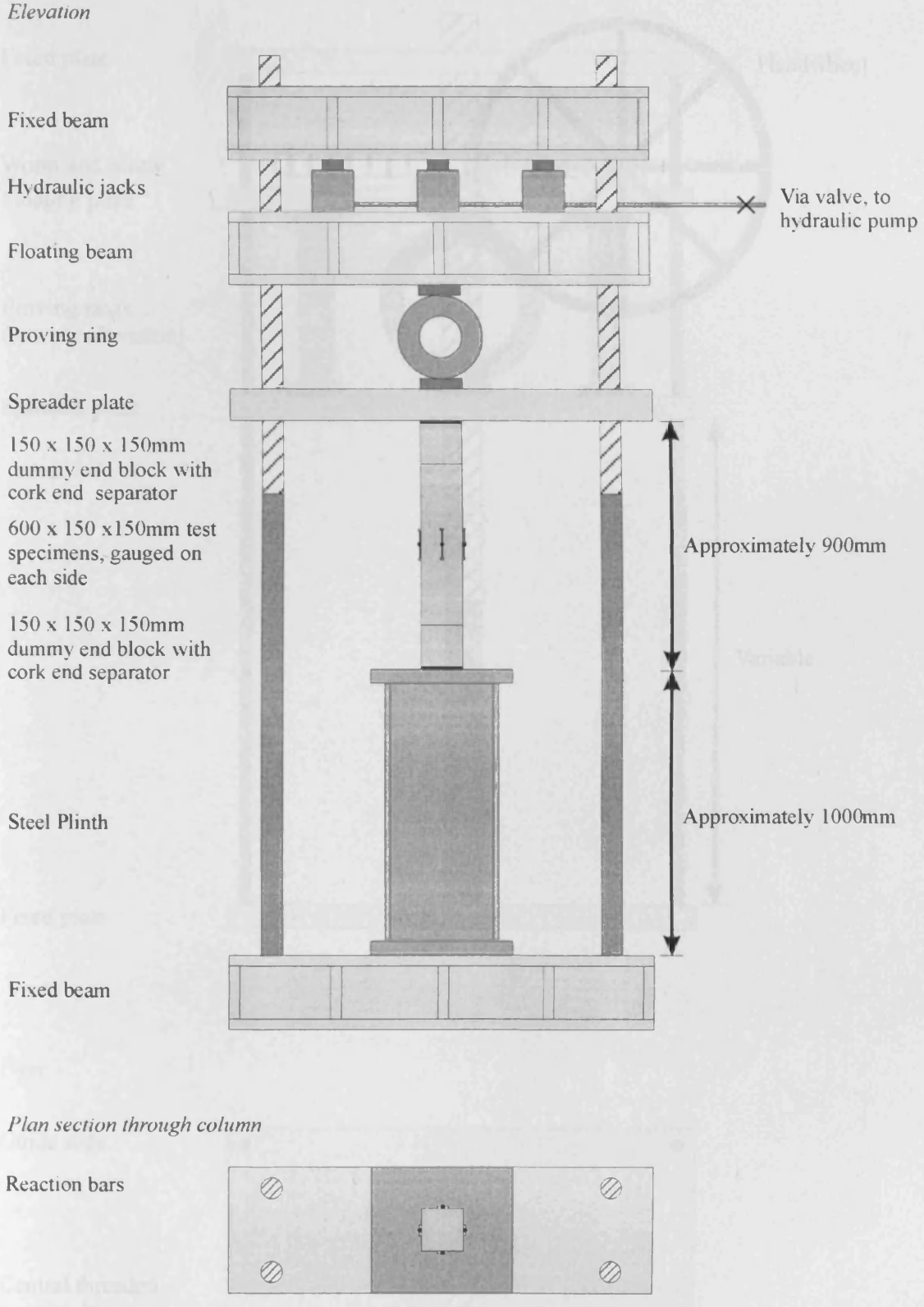

Figure 5.13. Specimen Arrangement in Large Creep Rig.

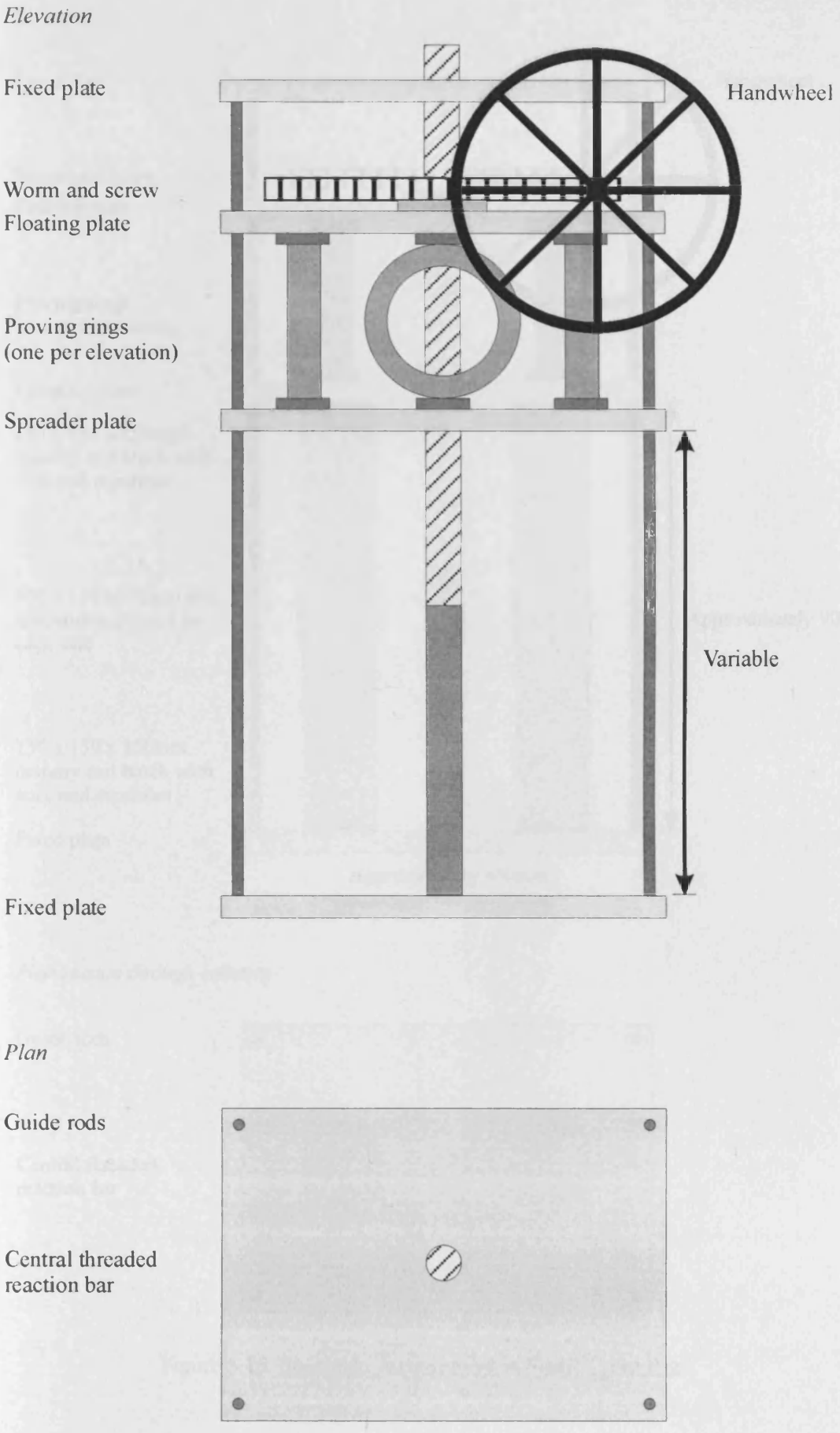

Figure 5.14. Small Creep Rig.

Elevation

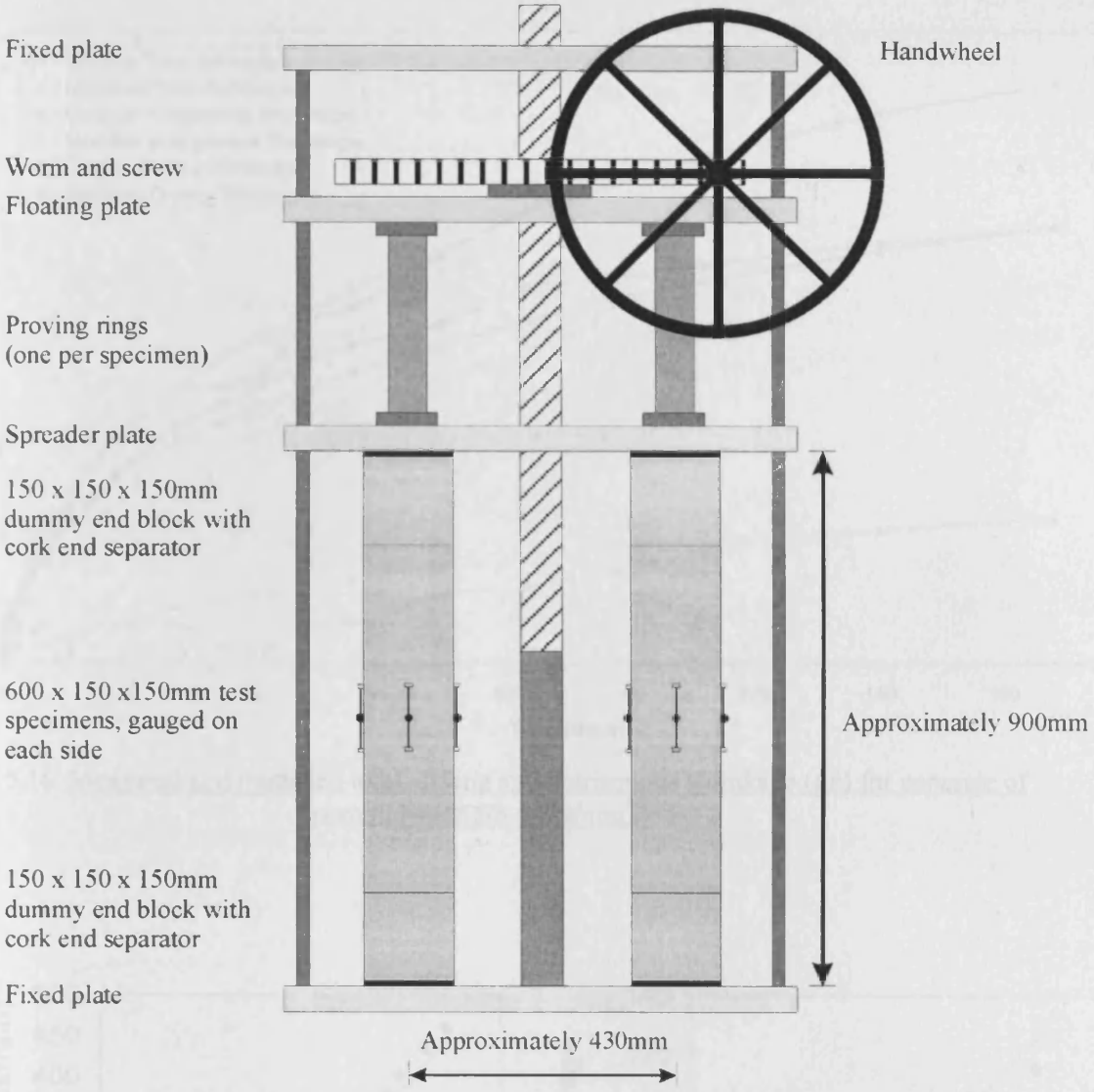

Plan section through columns

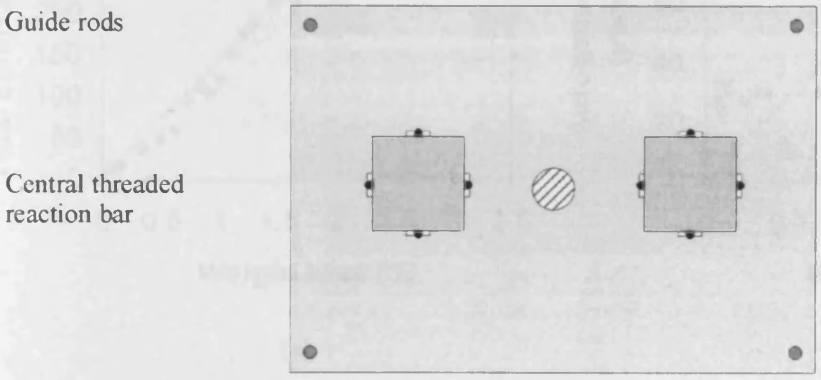

Figure 5.15. Specimen Arrangement in Small Creep Rig.

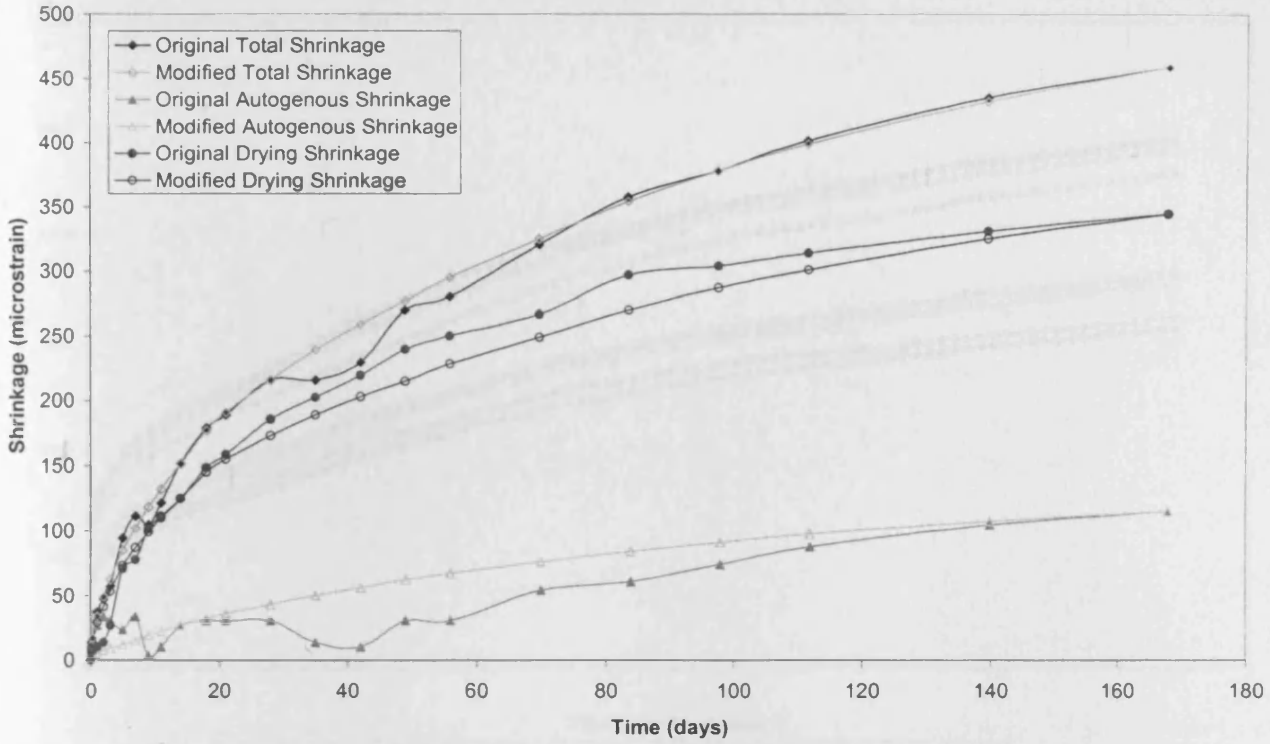

Figure 5.16. Measured and modified total, drying and autogenous shrinkage (με) for concrete of nominal strength 40 N/mm^2.

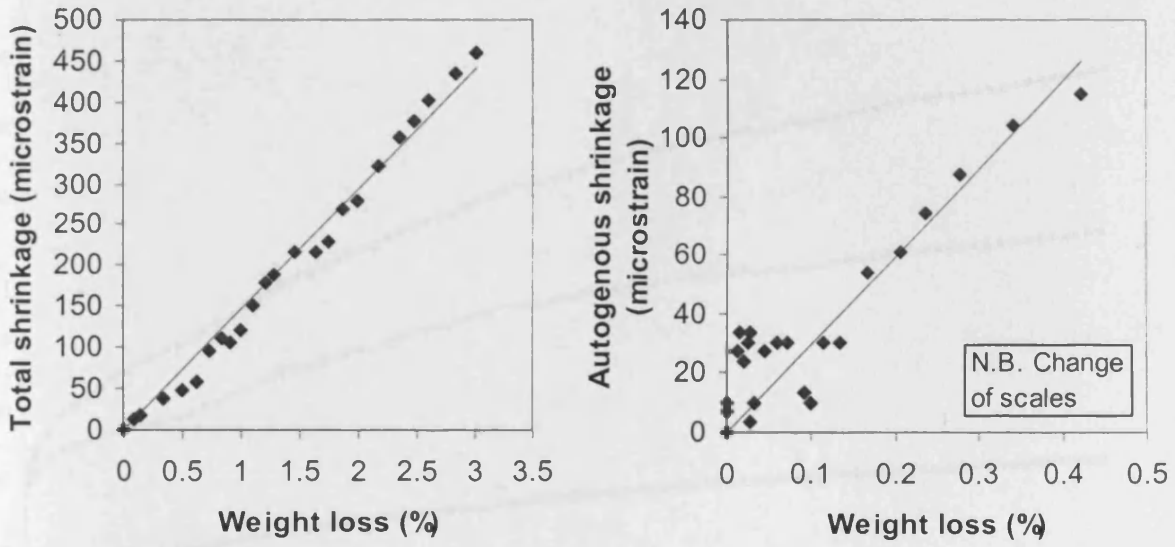

(a) (b)

Figure 5.17. Relationship between total/autogenous shrinkage (με) and percentage weight loss for concrete of nominal strength 40 N/mm^2.

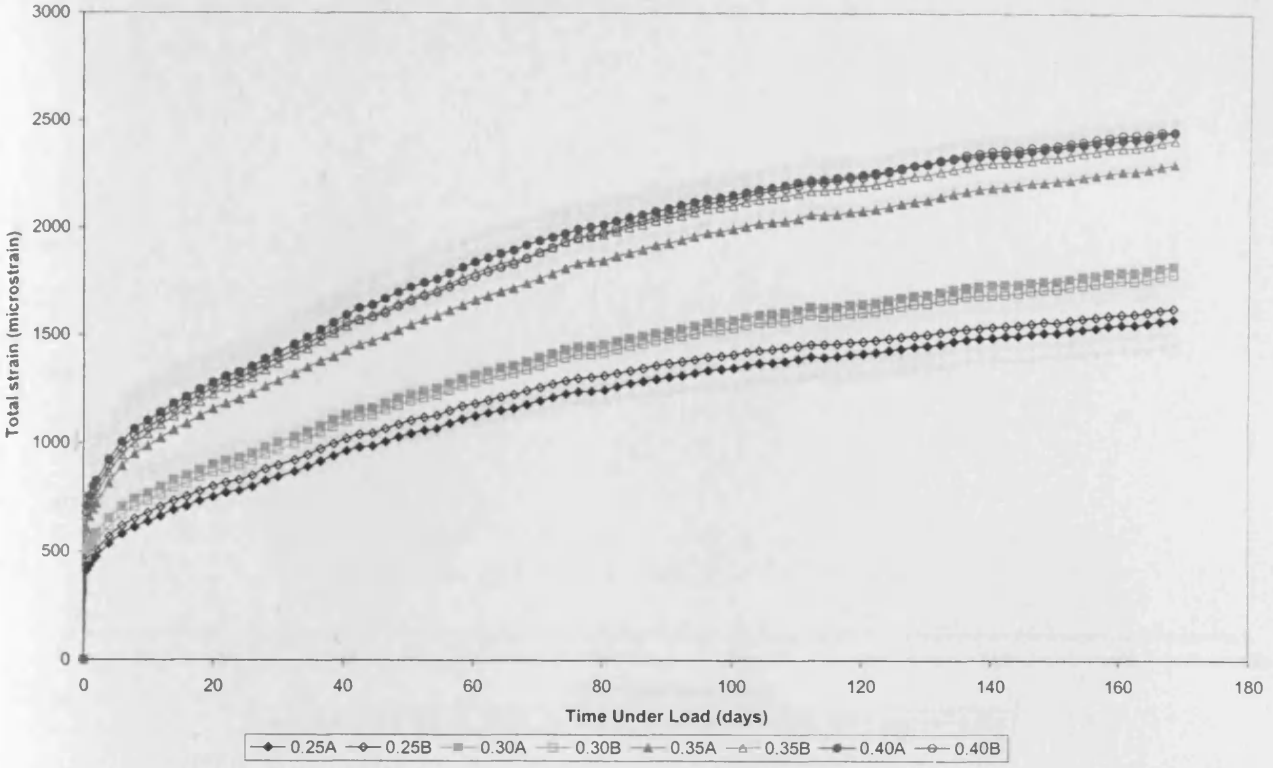

Figure 5.18. Measured total strain (με) under load for concrete of nominal strength 40 N/mm^2.

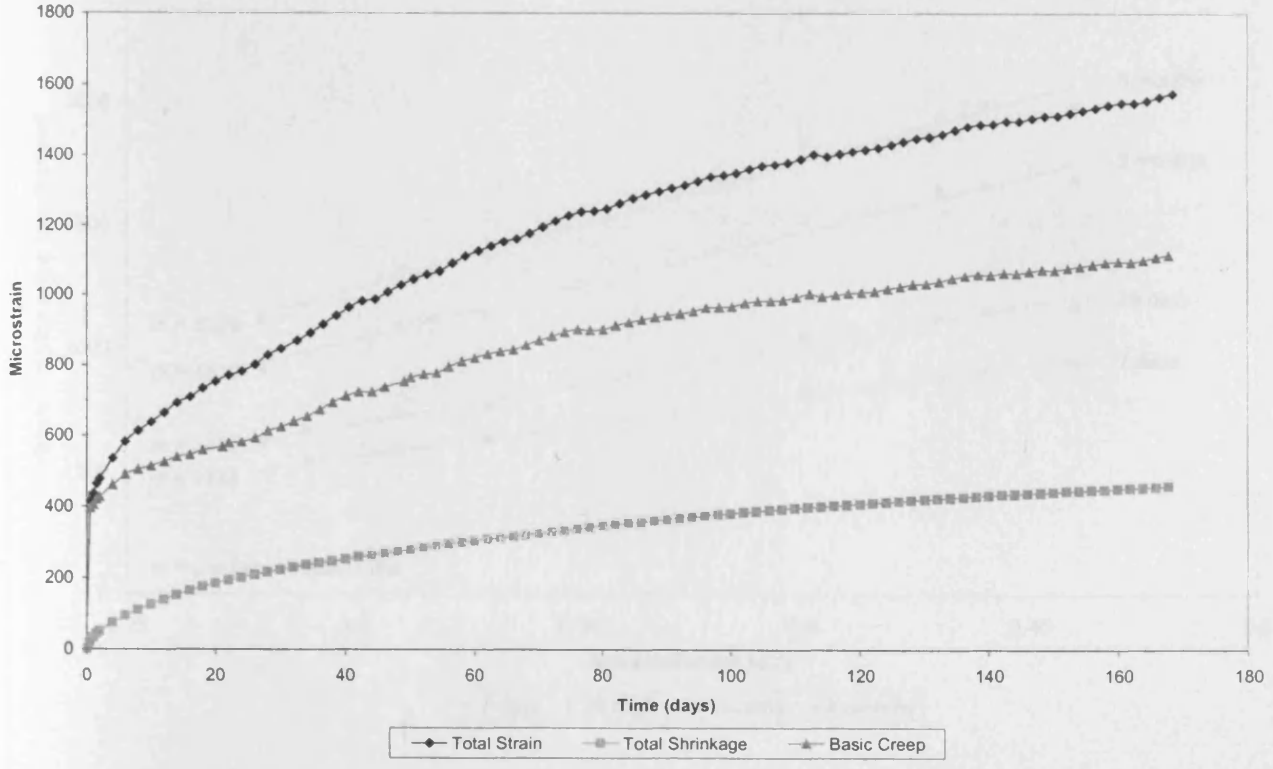

Figure 5.19. Determination of basic and drying creep strain (με) from measured total strain and total shrinkage strain values for creep specimen 0.25A of nominal strength 40 N/mm^2.

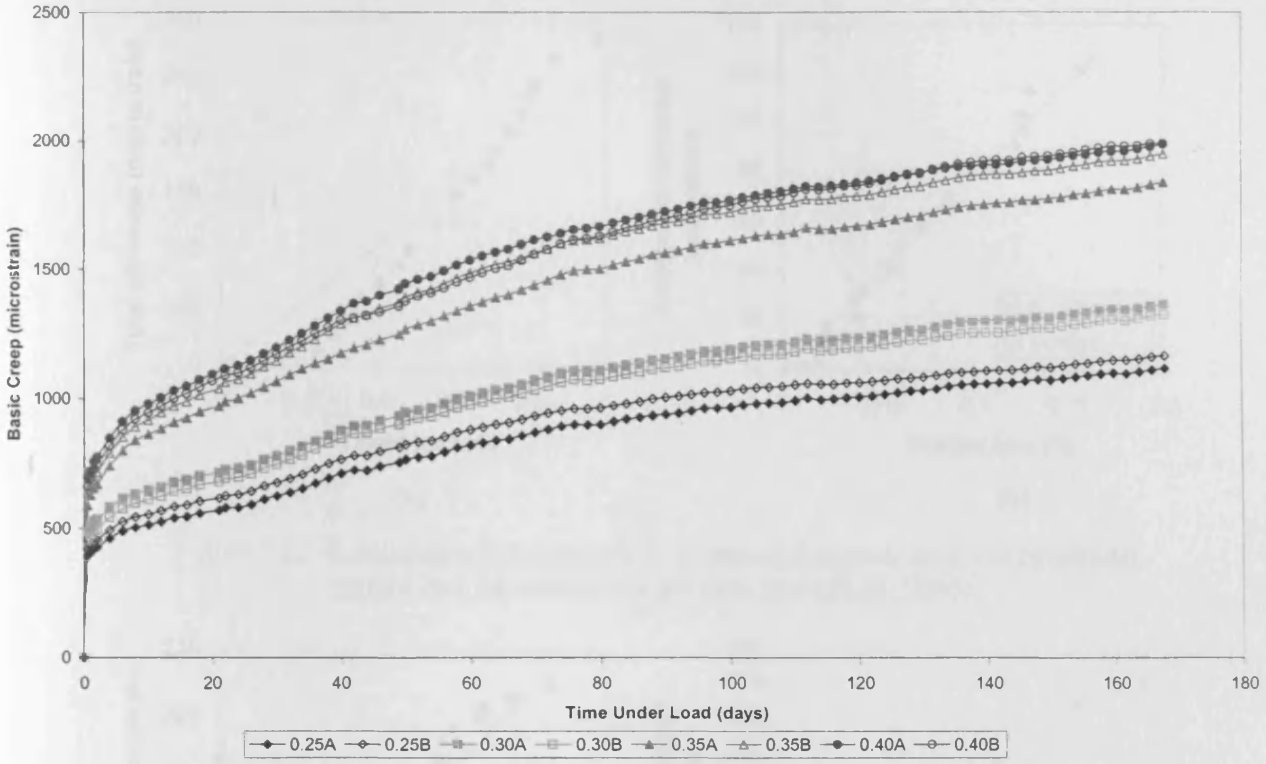

Figure 5.20. Calculated basic and drying creep strains (με) for concrete of nominal strength 40 N/mm^2.

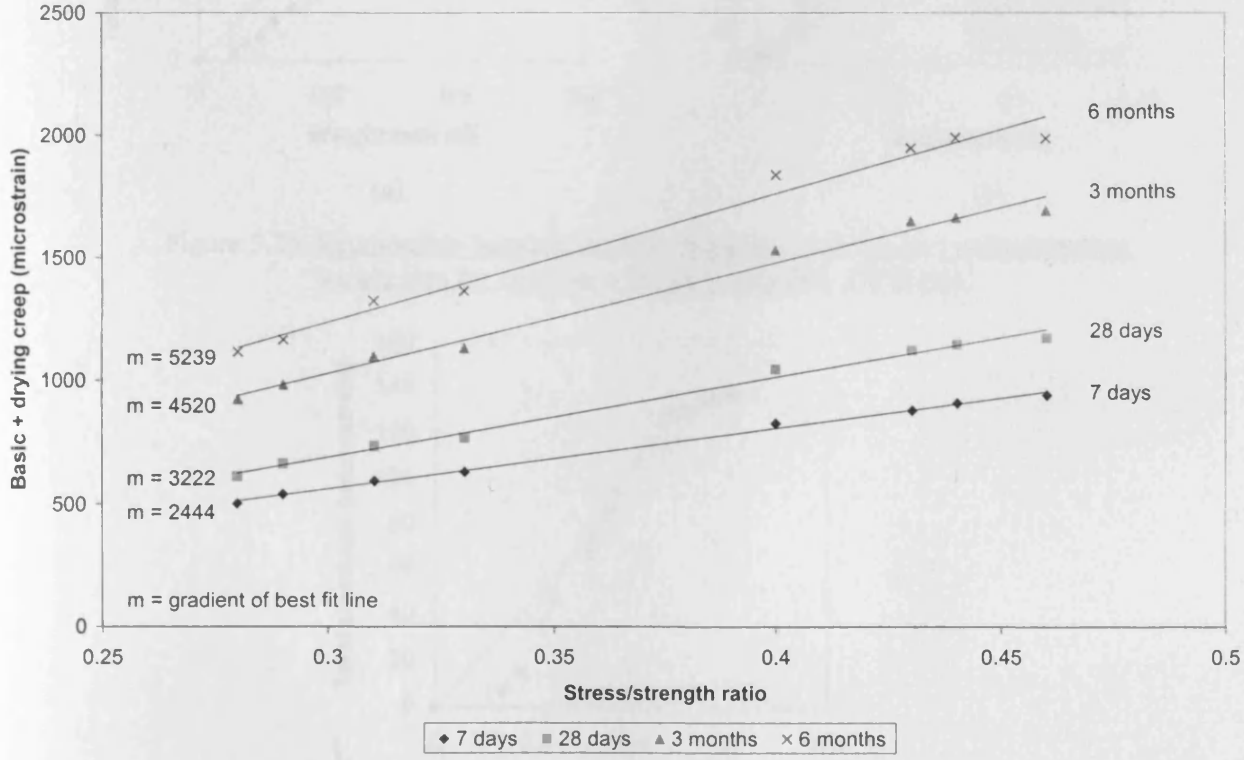

Figure 5.21. Relationship between creep strain (με) and stress/strength ratio over time for concrete of nominal strength 40 N/mm^2.

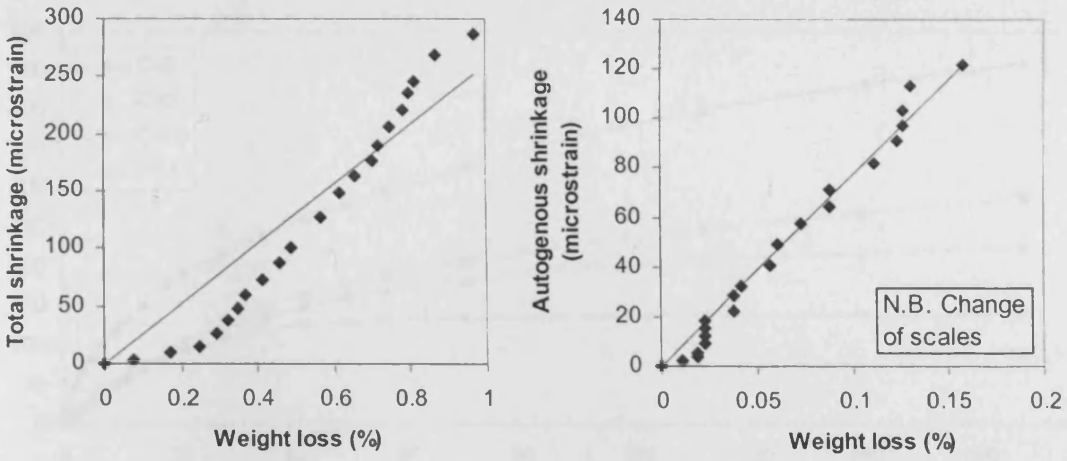

(a) (b)

Figure 5.22. Relationship between total/autogenous shrinkage (με) and percentage weight loss for concrete of nominal strength 80 N/mm^2.

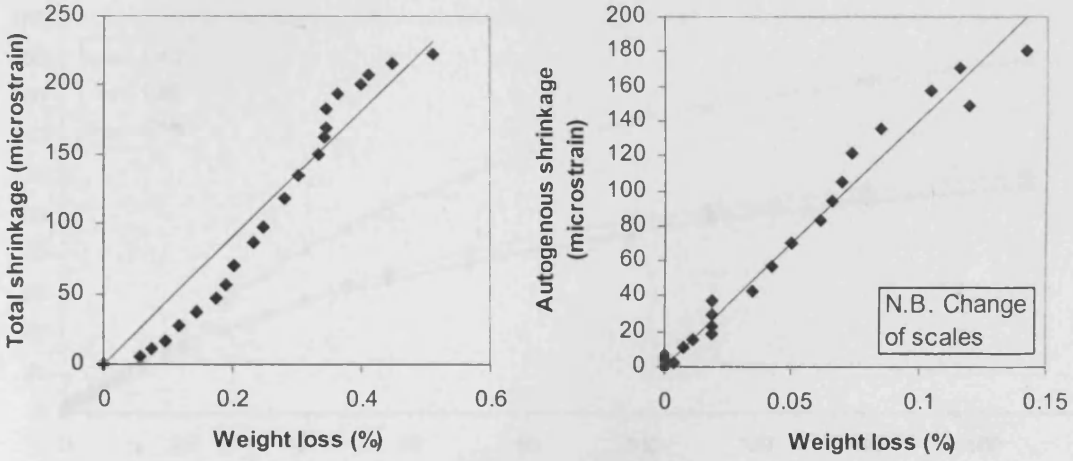

(a) (b)

Figure 5.23. Relationship between total/autogenous shrinkage (με) and percentage weight loss for concrete of nominal strength 100 N/mm^2.

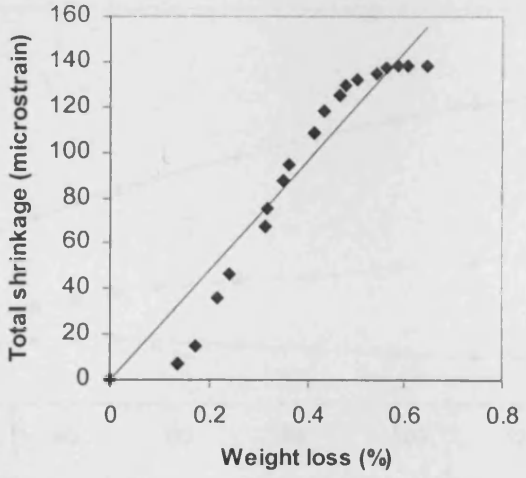

Figure 5.24. Relationship between total shrinkage (με) and percentage weight loss for pfa concrete of nominal strength 65 N/mm^2.

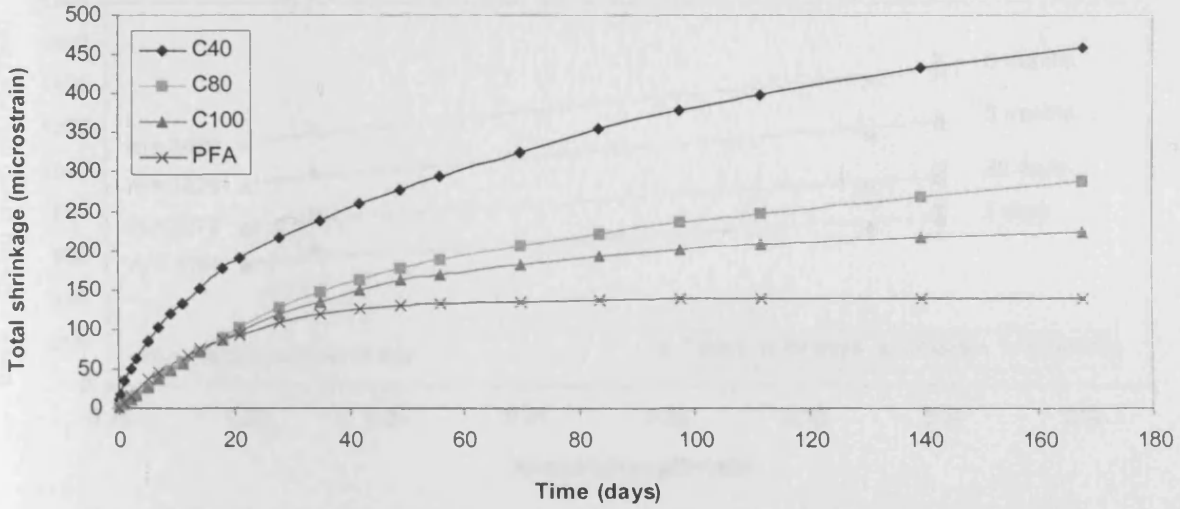

Figure 5.25. Comparison of total shrinkage strains for different concrete strengths.

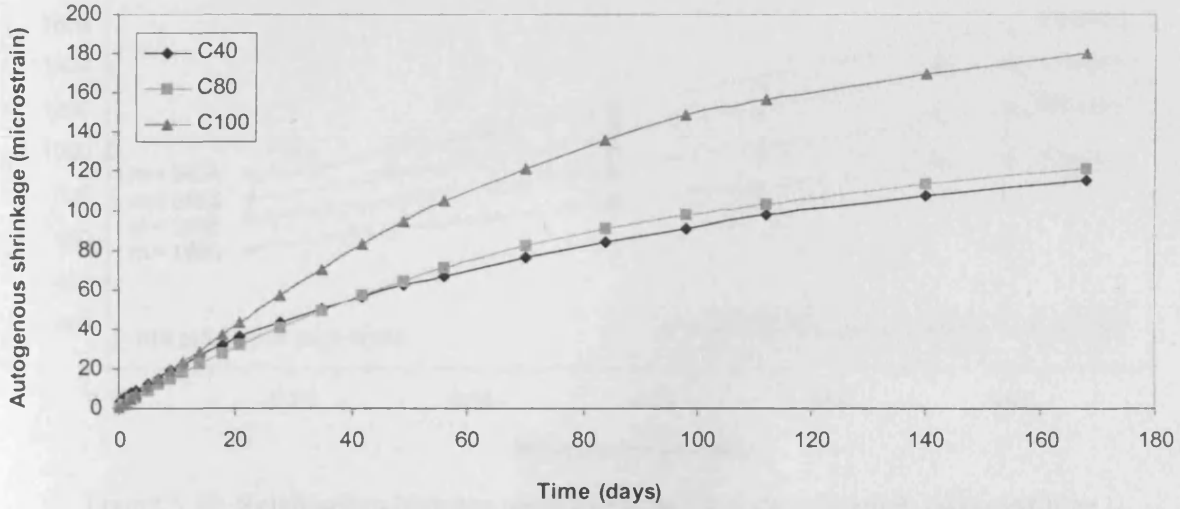

Figure 5.26. Comparison of autogenous shrinkage strains for different concrete strengths.

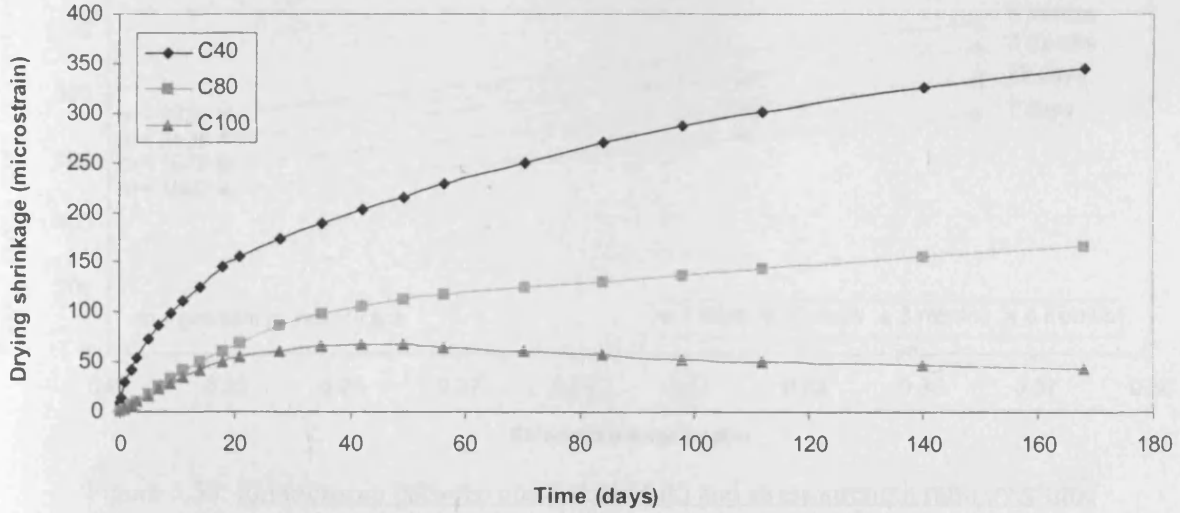

Figure 5.27. Comparison of drying shrinkage strains for different concrete strengths.

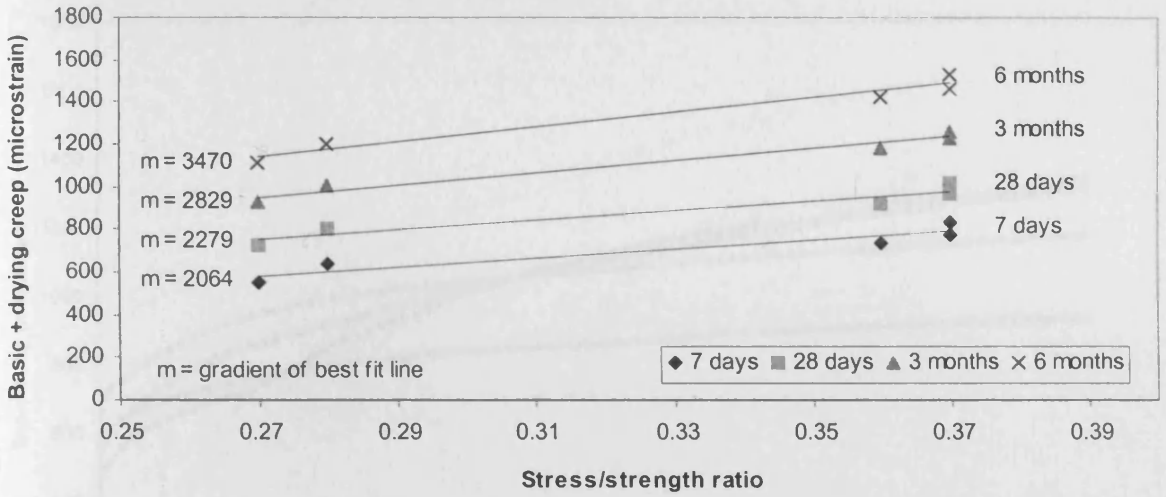

Figure 5.28. Relationship between creep strain (με) and stress/strength ratio over time for concrete of nominal strength 80 N/mm^2.

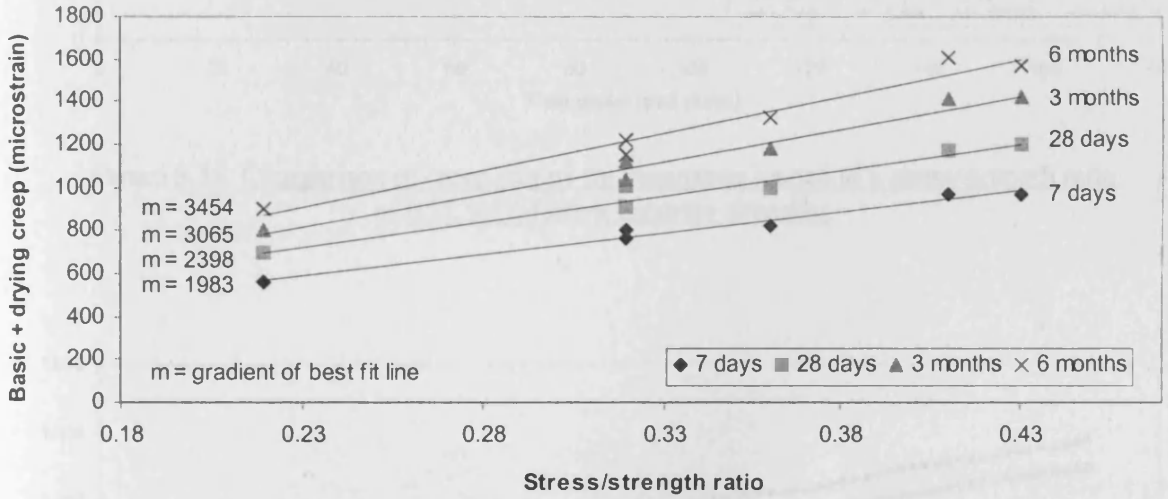

Figure 5.29. Relationship between creep strain (με) and stress/strength ratio over time for concrete of nominal strength 100 N/mm^2.

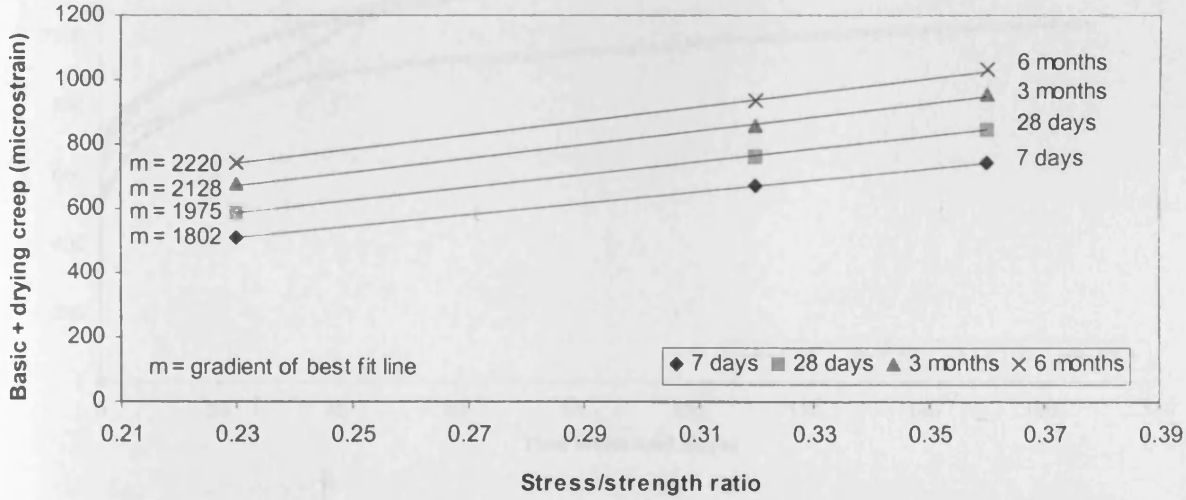

Figure 5.30. Relationship between creep strain (με) and stress/strength ratio over time for pfa concrete of nominal strength 65 N/mm^2.

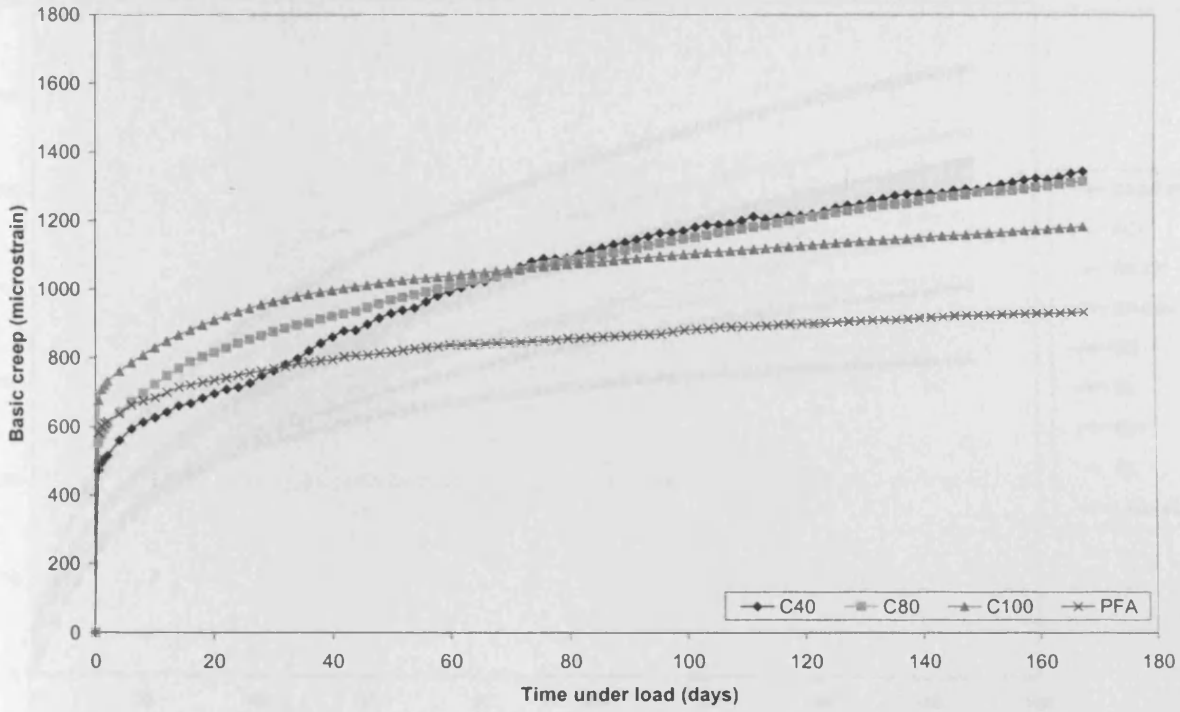

Figure 5.31. Comparison of creep strains for specimens loaded to a stress/strength ratio of 0.32 for different concrete strengths.

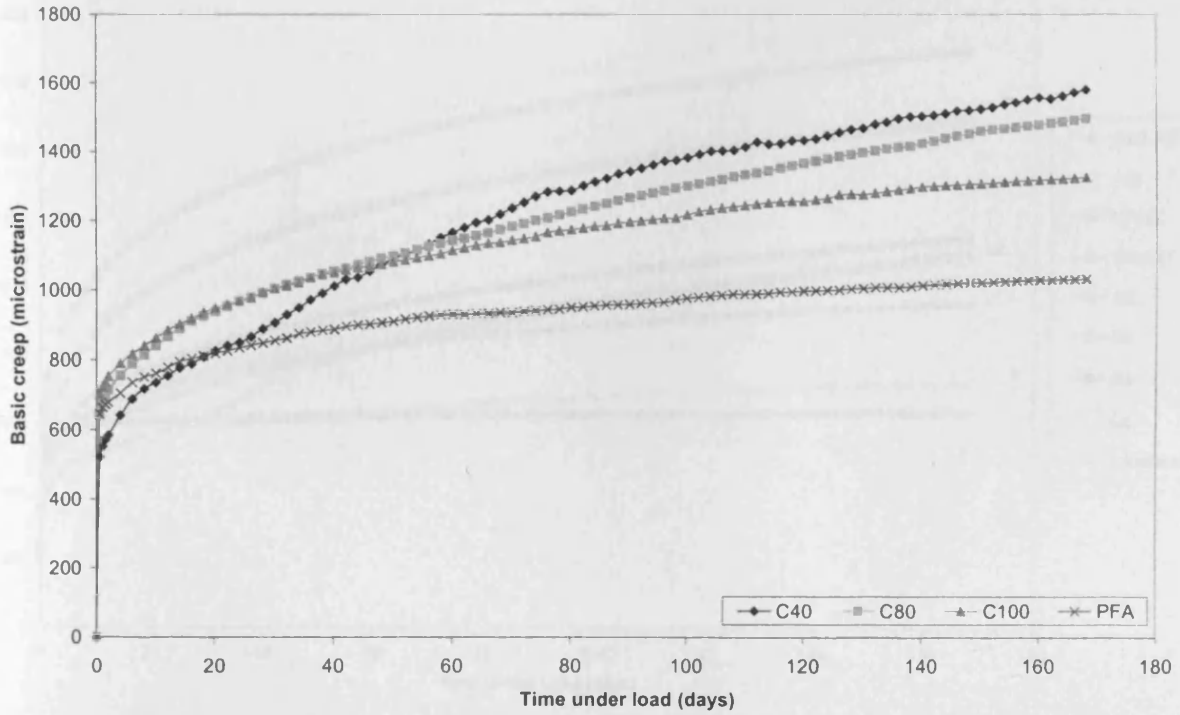

Figure 5.32. Comparison of creep strains for specimens loaded to a stress/strength ratio of 0.36 for different concrete strengths.

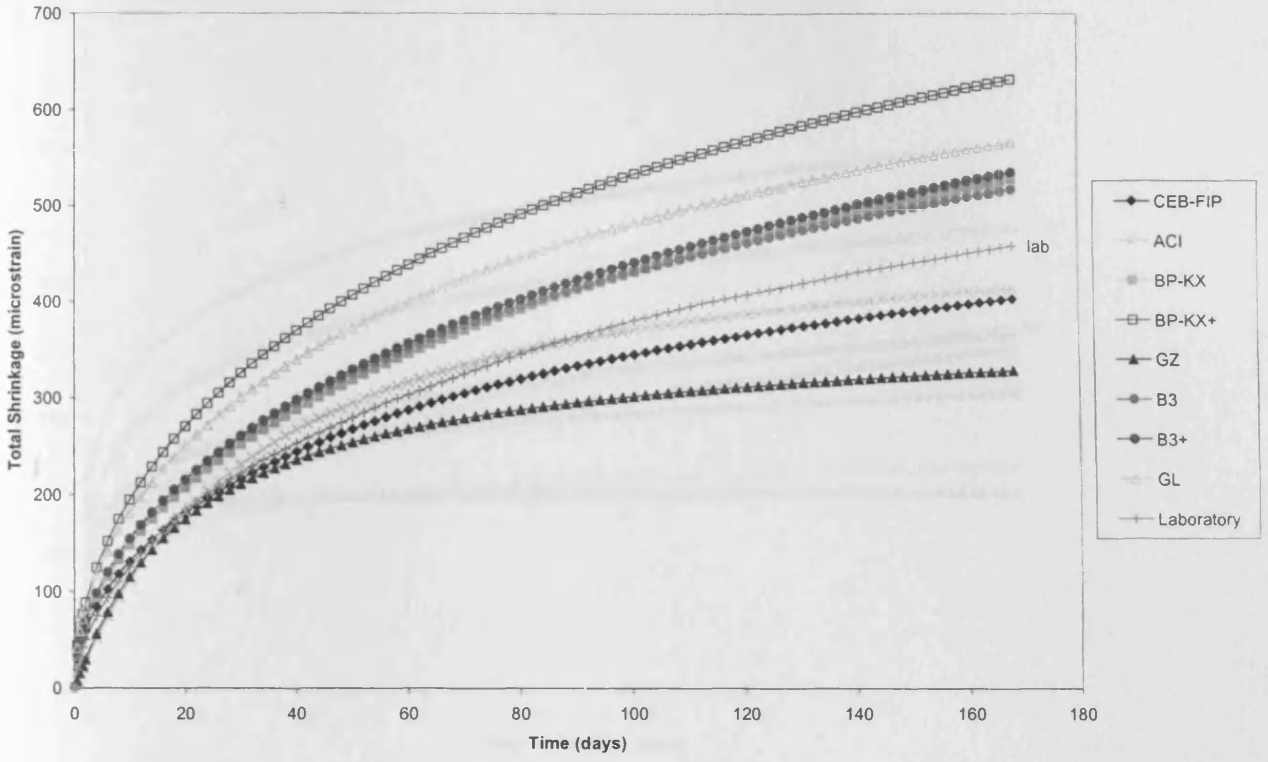

Figure 5.33. Comparison between experimental and predicted total shrinkage strains (με) for concrete of design strength 40 N/mm^2, using selected prediction models.

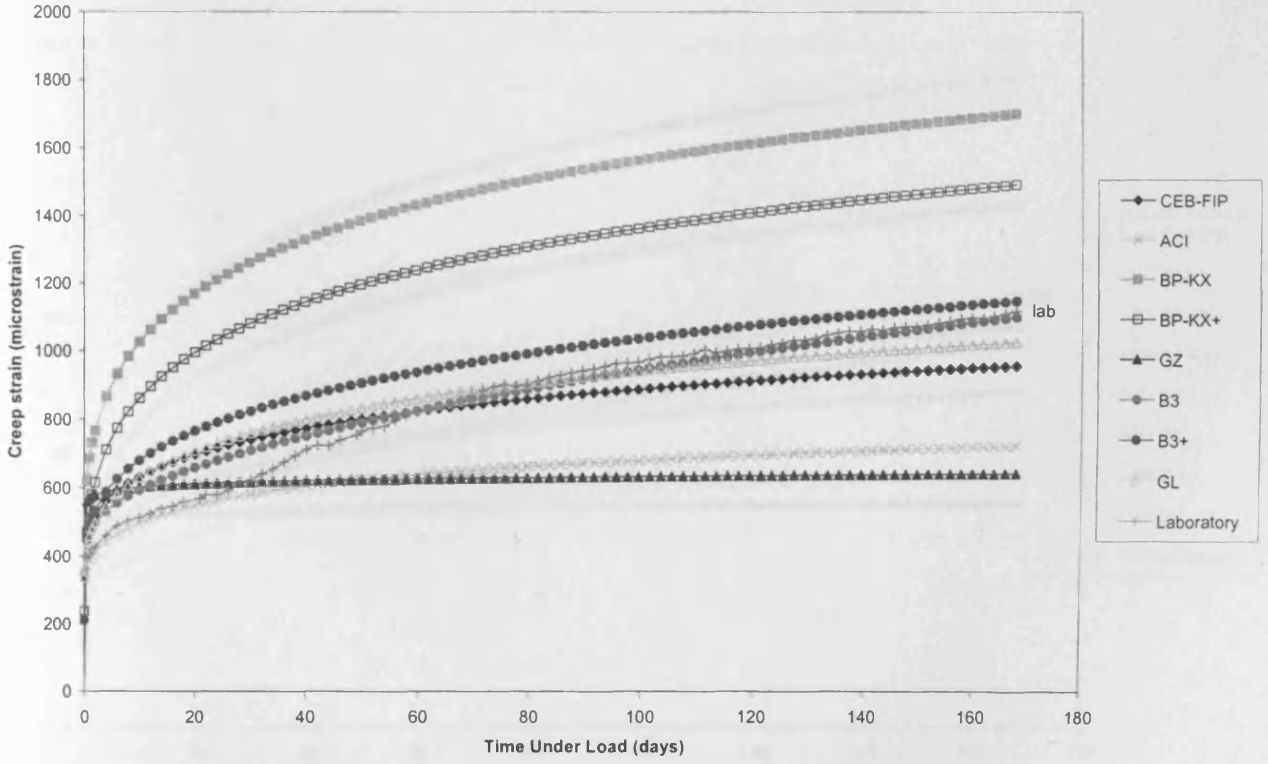

Figure 5.34. Comparison between experimental and predicted creep strains (με) for concrete of design strength 40 N/mm^2, loaded to a stress/strength ratio of 0.28 of the compressive strength at loading, using selected prediction models.

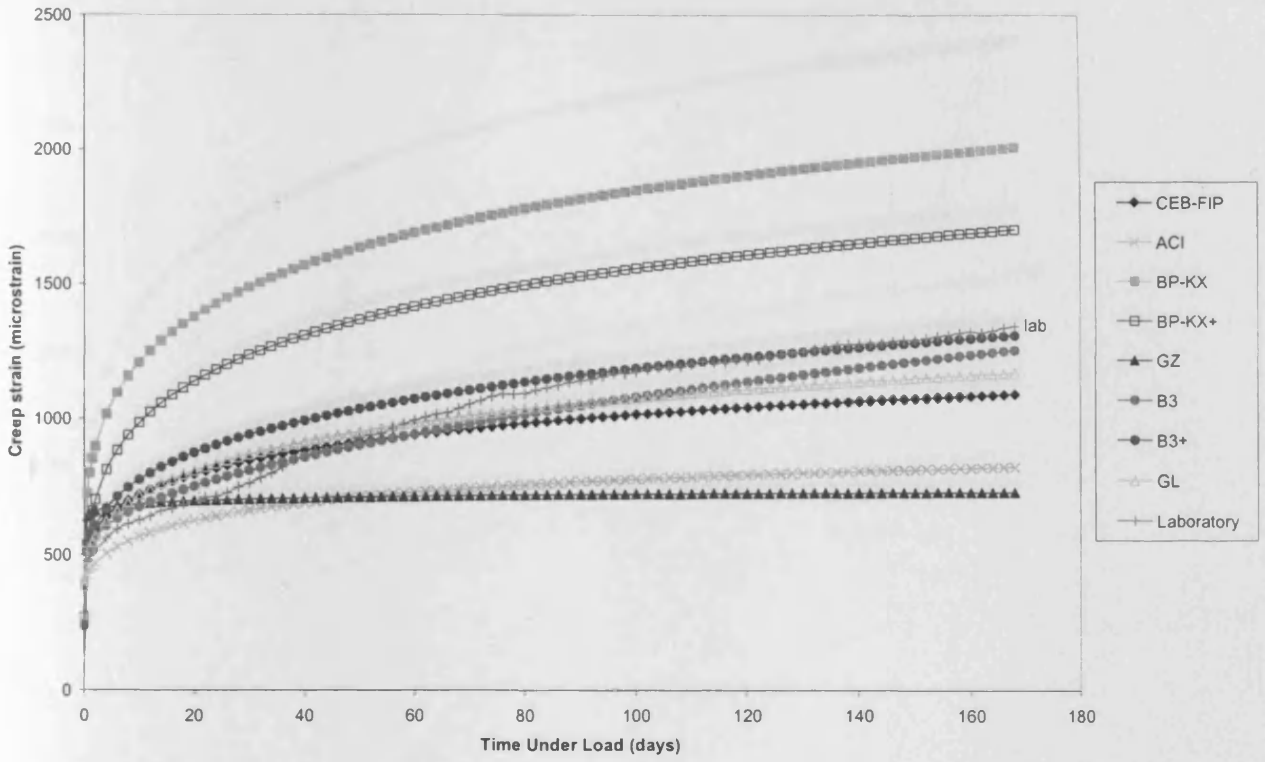

Figure 5.35. Comparison between experimental and predicted creep strains (με) for concrete of design strength 40 N/mm^2, loaded to a stress/strength ratio of 0.32 of the compressive strength at loading, using selected prediction models.

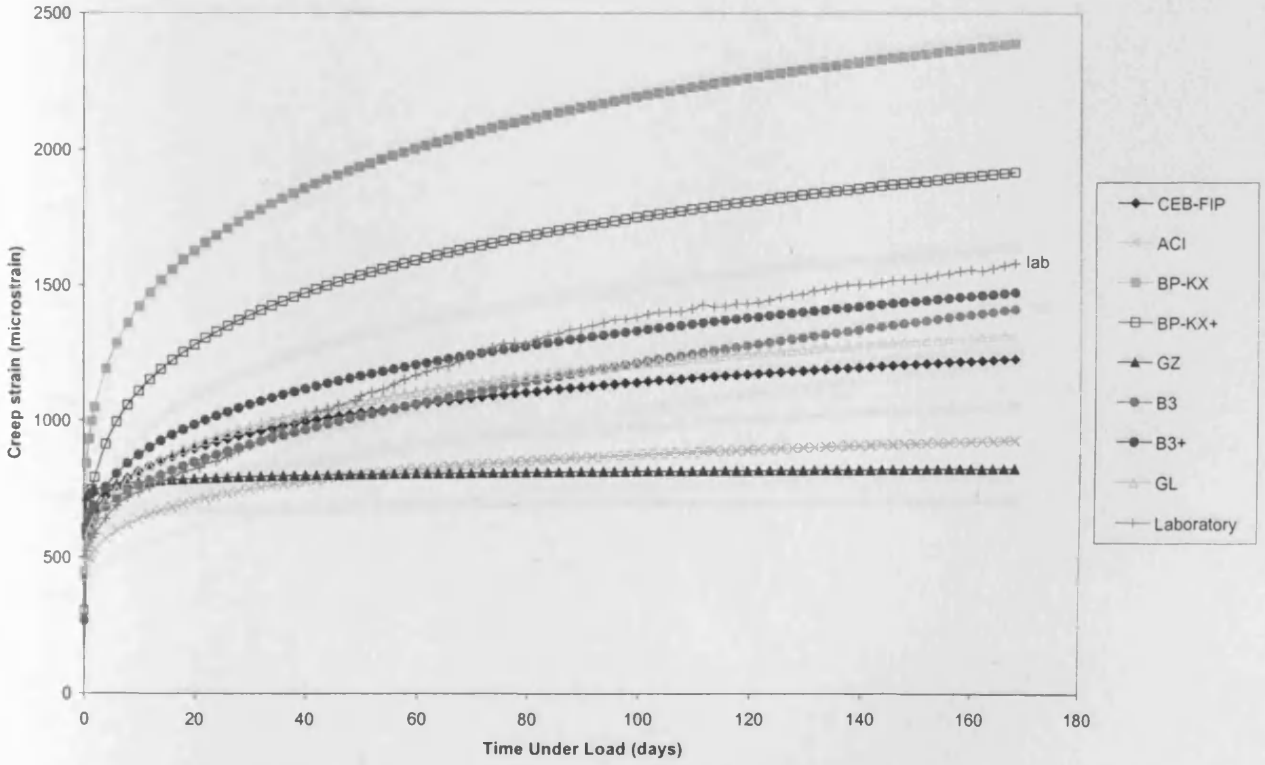

Figure 5.36. Comparison between experimental and predicted creep strains (με) for concrete of design strength 40 N/mm^2, loaded to a stress/strength ratio of 0.36 of the compressive strength at loading, using selected prediction models.

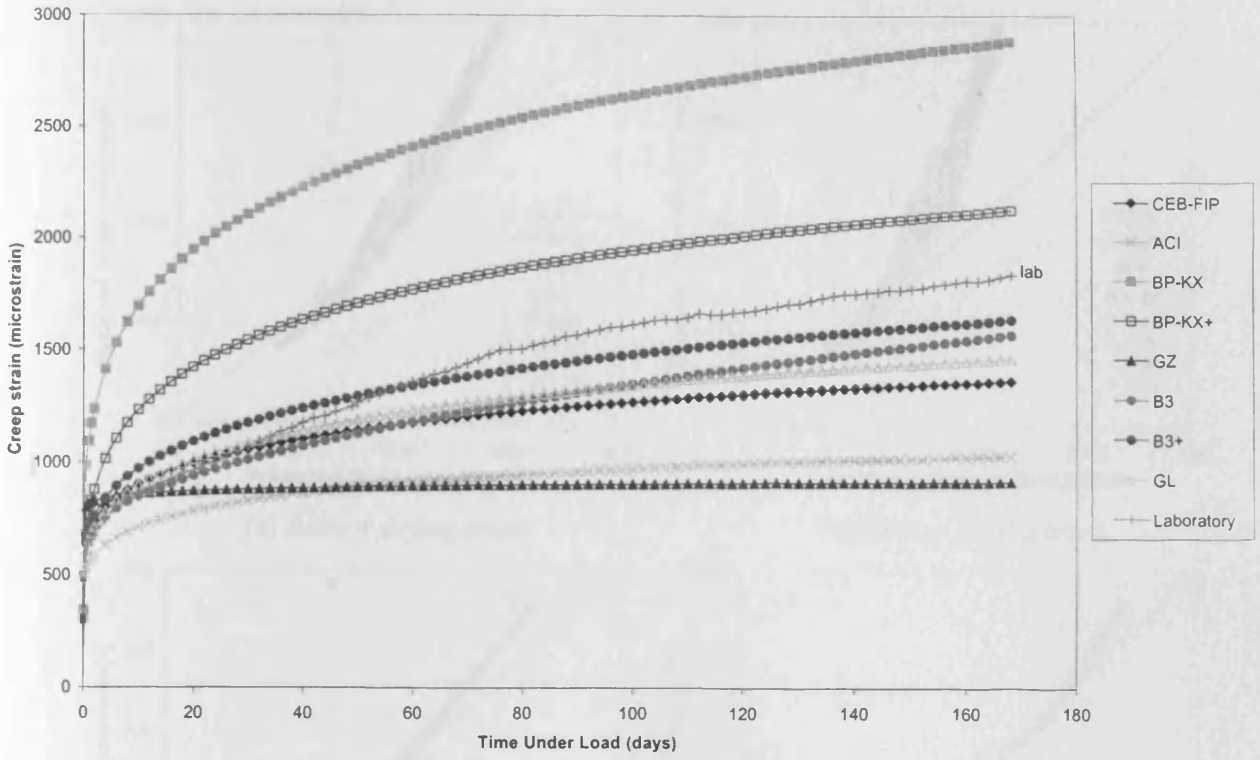

Figure 5.37. Comparison between experimental and predicted creep strains (με) for concrete of design strength 40 N/mm^2, loaded to a stress/strength ratio of 0.40 of the compressive strength at loading, using selected prediction models.

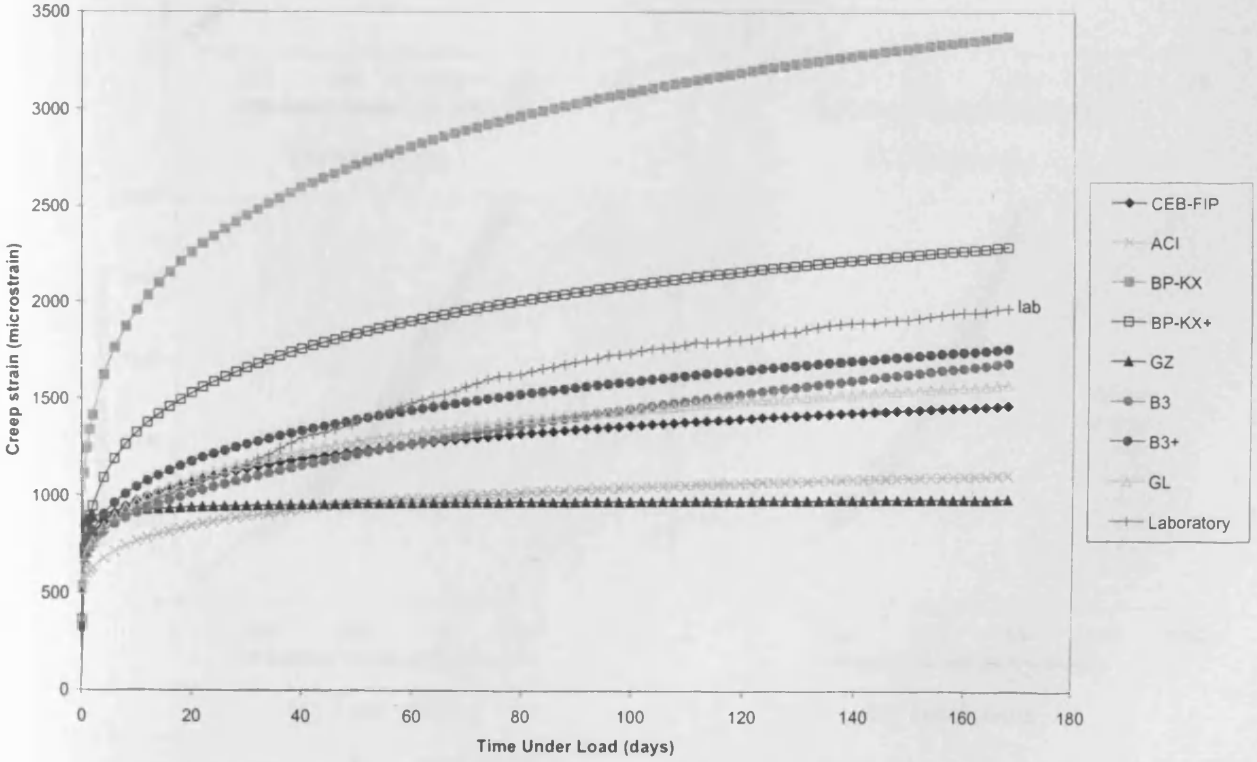

Figure 5.38. Comparison between experimental and predicted creep strains (με) for concrete of design strength 40 N/mm^2, loaded to a stress/strength ratio of 0.43 of the compressive strength at loading, using selected prediction models.

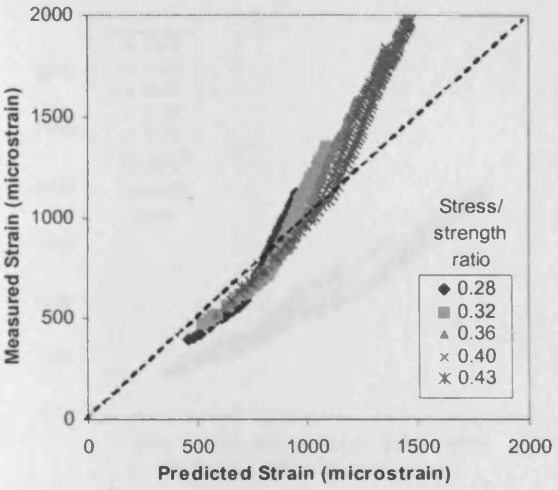

(a) Basic + drying creep

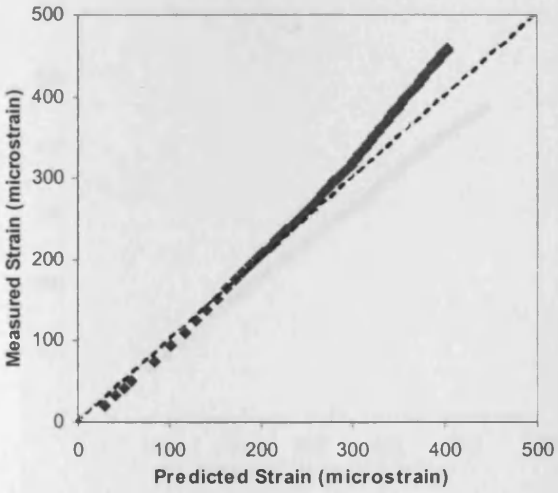

(b) Shrinkage

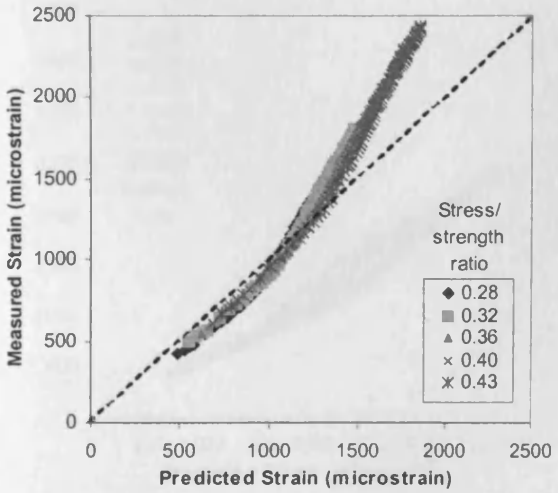

(c) Total strain

Figure 5.39. Comparison of measured and predicted strains for concrete of nominal strength 40 N/mm^2, using the CEB-FIP Model Code 1990.

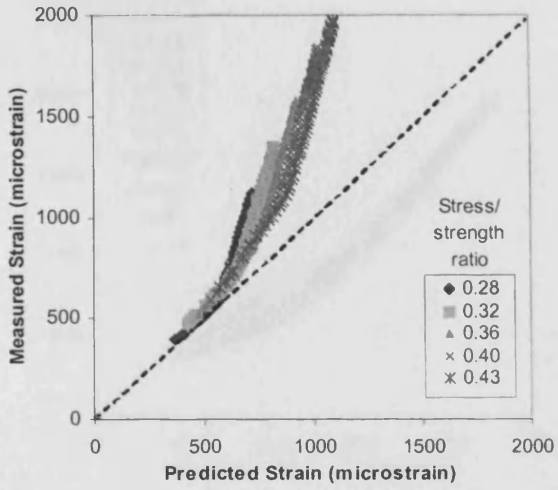

(a) Basic + drying creep

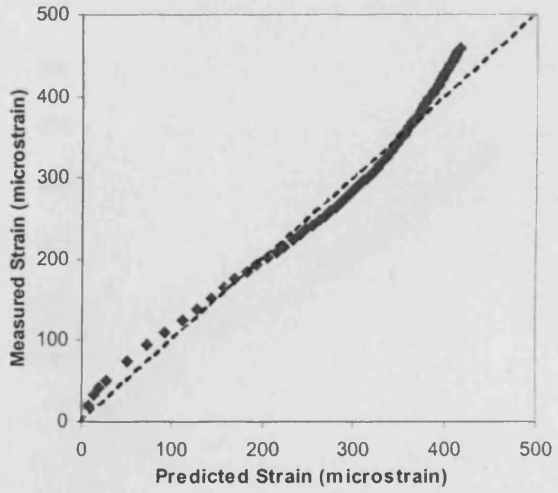

(b) Shrinkage

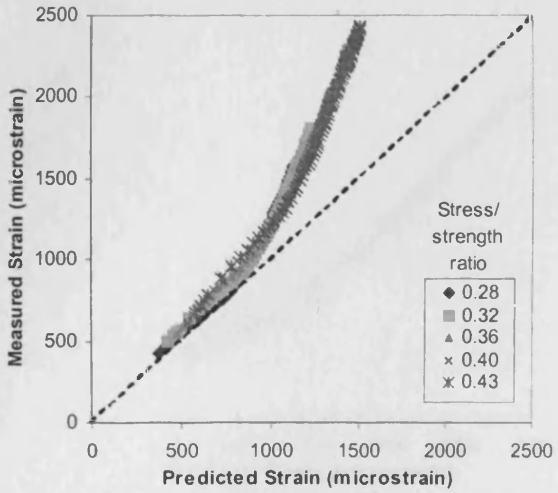

(c) Total strain

Figure 5.40. Comparison of measured and predicted strains for concrete of nominal strength 40 N/mm^2, using the ACI Model 1992.

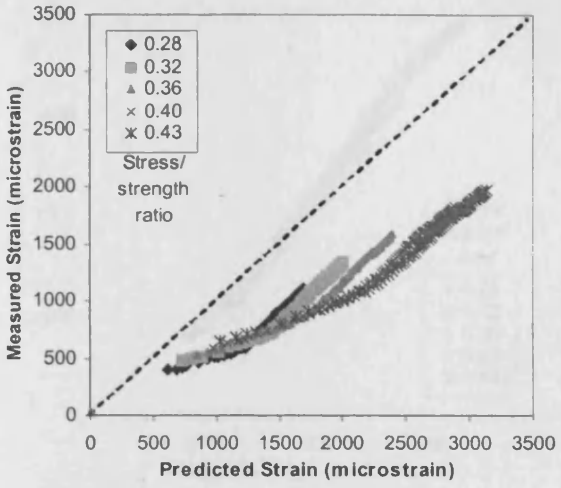

(a) Basic + drying creep

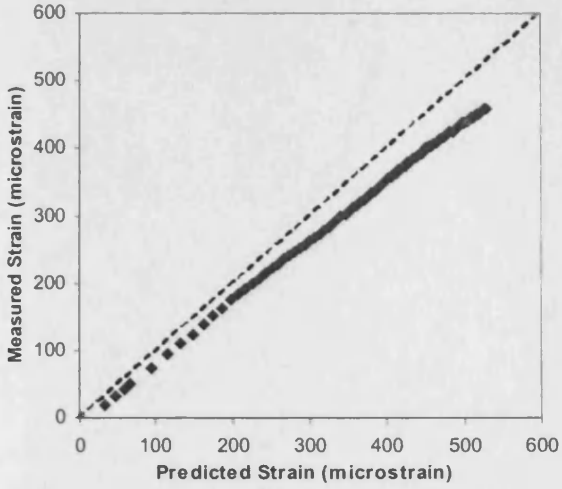

(b) Shrinkage

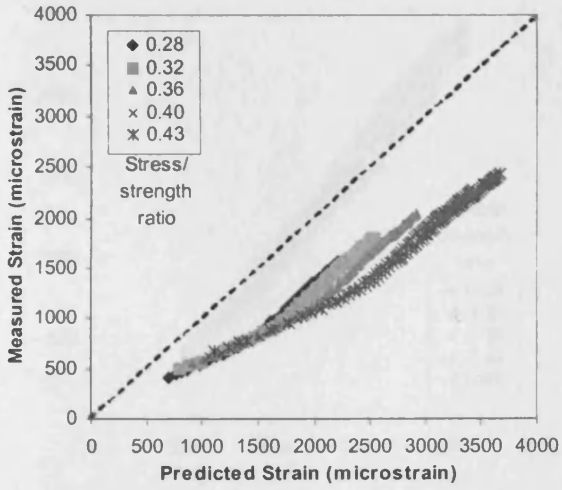

(c) Total strain

Figure 5.41. Comparison of measured and predicted strains for concrete of nominal strength 40 N/mm^2, using the BP-KX Model 1991.

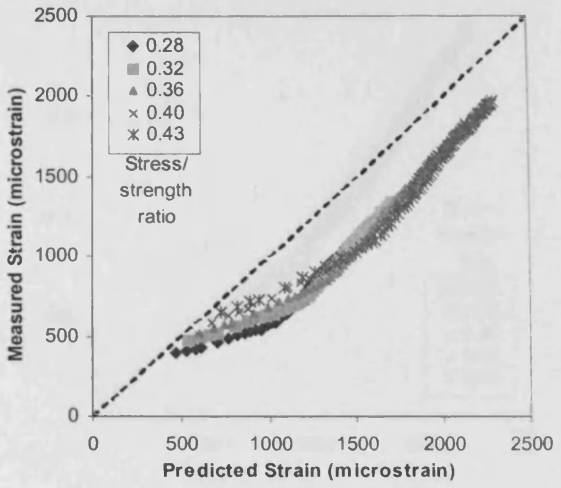

(a) Basic + drying creep

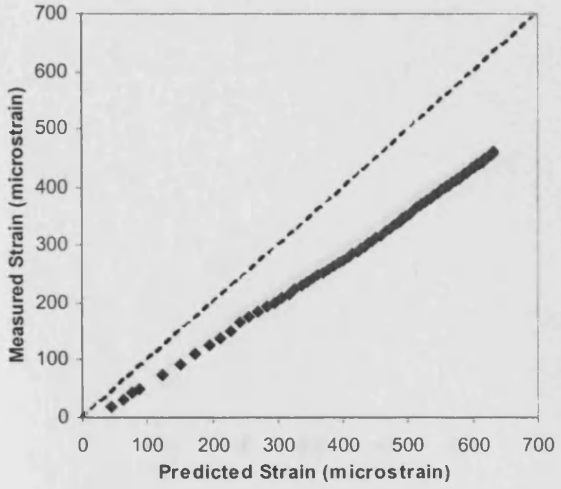

(b) Shrinkage

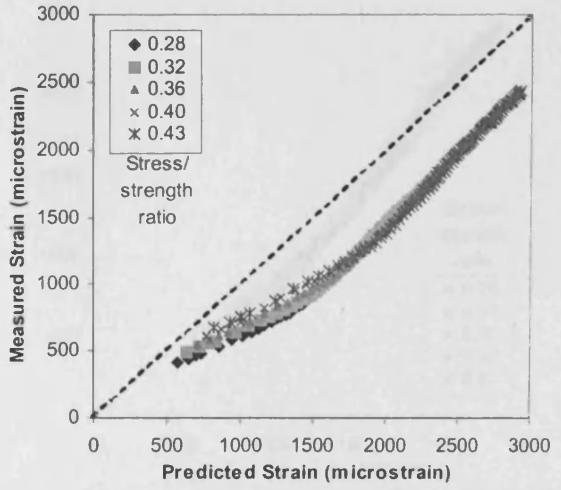

(c) Total strain

Figure 5.42. Comparison of measured and predicted strains for concrete of nominal strength 40 N/mm^2, using the short-form BP-KX Model 1993.

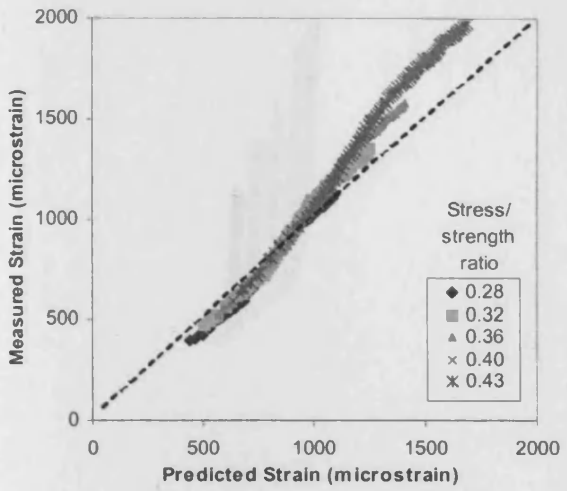

(a) Basic + drying creep

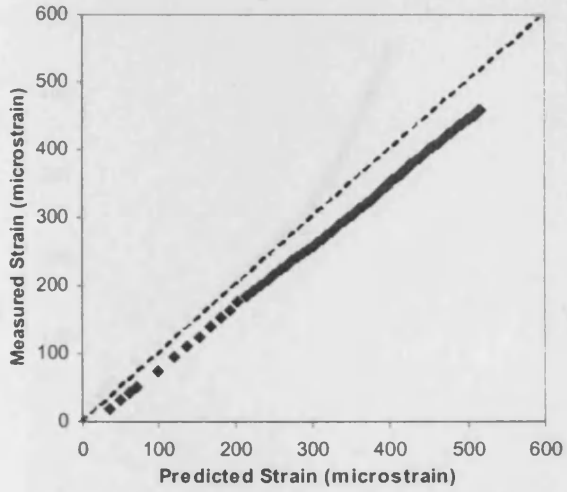

(b) Shrinkage

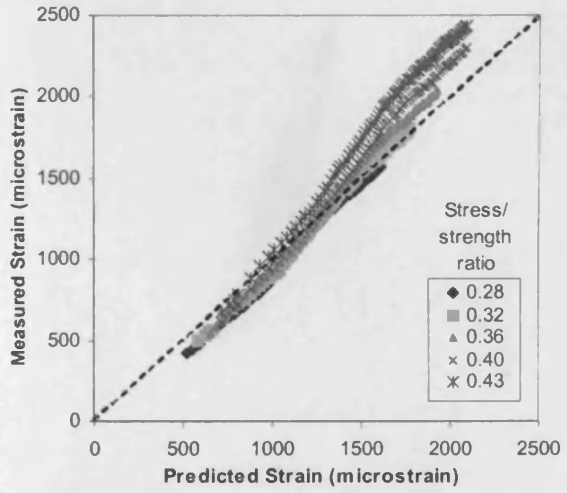

(c) Total strain

Figure 5.43. Comparison of measured and predicted strains for concrete of nominal strength 40 N/mm^2, using the B3 Model 1995.

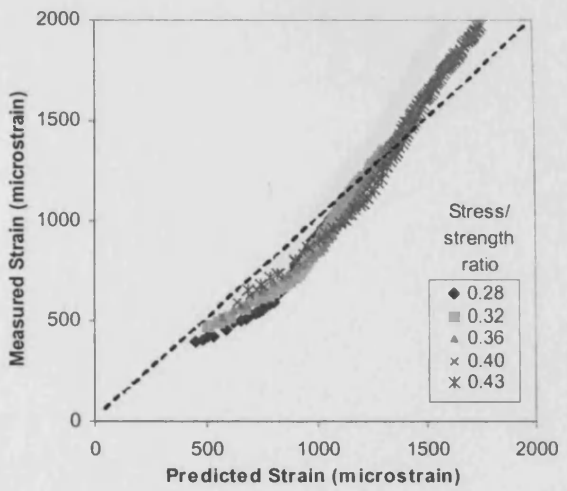

(a) Basic + drying creep

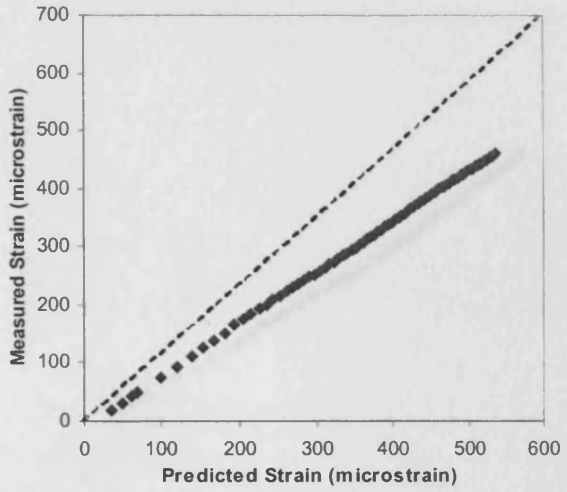

(b) Shrinkage

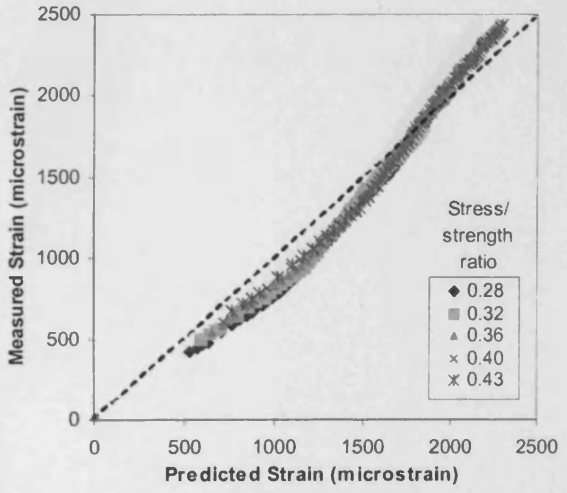

(c) Total strain

Figure 5.44. Comparison of measured and predicted strains for concrete of nominal strength 40 N/mm^2, using the short-form B3 Model 1996.

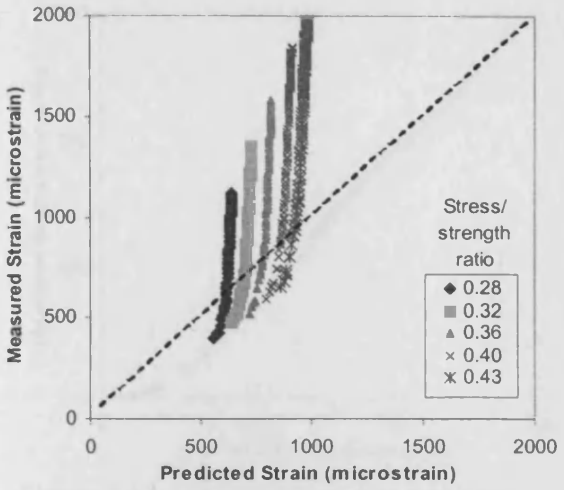

(a) Basic + drying creep

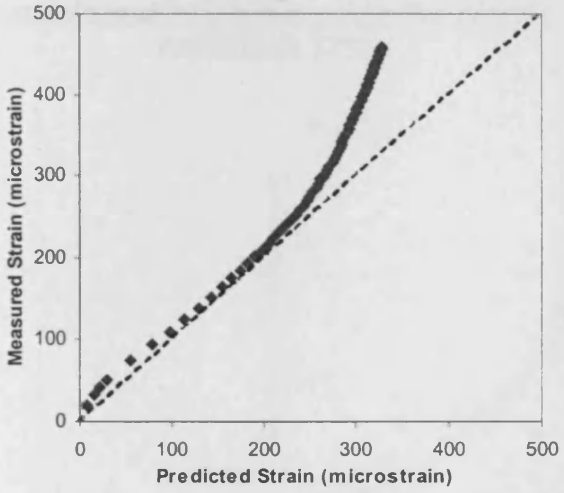

(b) Shrinkage

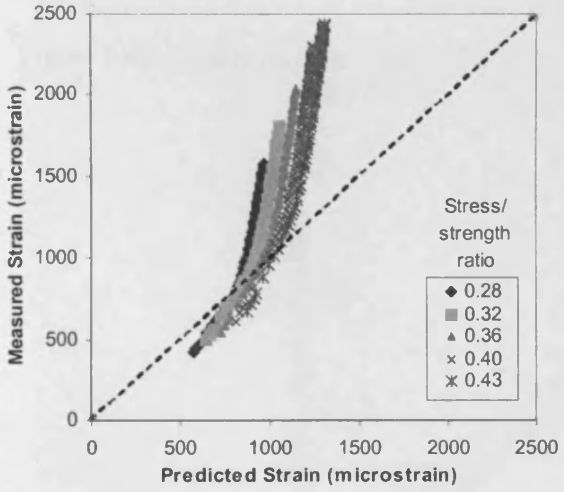

(c) Total strain

Figure 5.45. Comparison of measured and predicted strains for concrete of nominal strength 40 N/mm^2, using the GZ Model 1993.

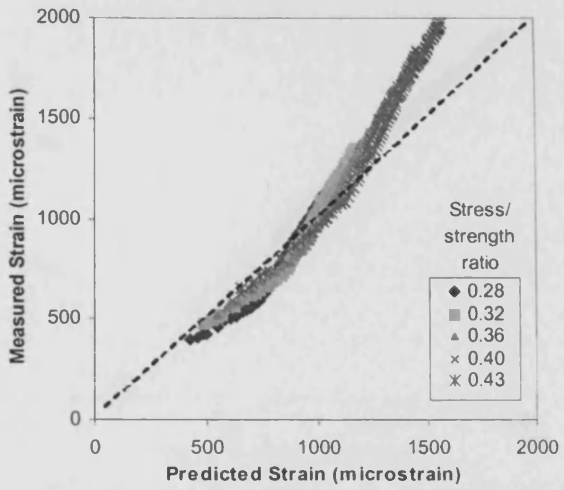

(a) Basic + drying creep

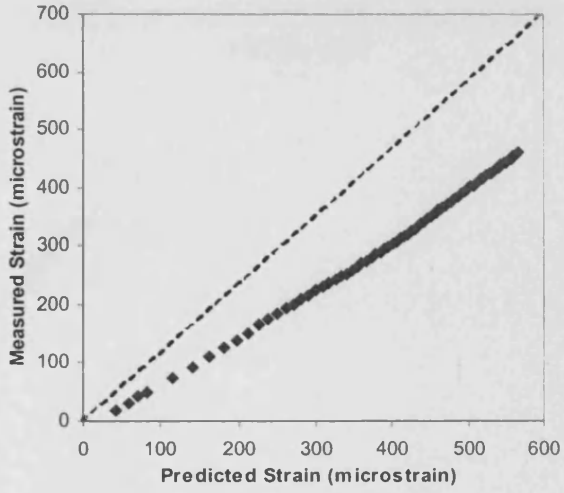

(b) Shrinkage

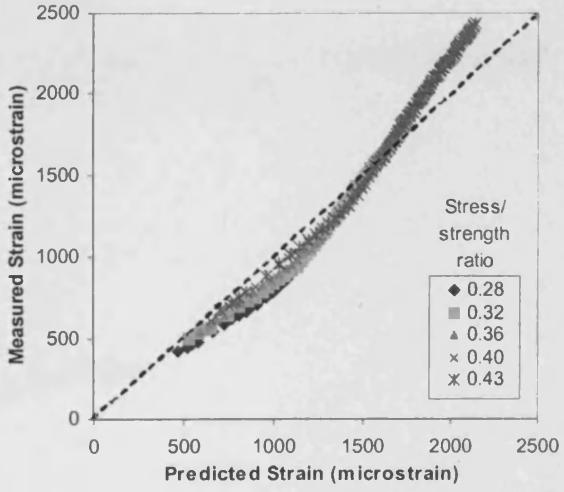

(c) Total strain

Figure 5.46. Comparison of measured and predicted strains for concrete of nominal strength 40 N/mm^2, using the GL Model 2001.

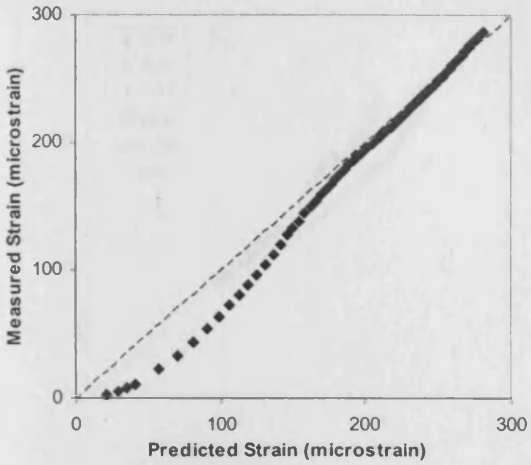

Figure 5.47. Comparison of measured and predicted shrinkage strains for concrete of nominal strength 80 N/mm^2, using the CEB-FIP Model Code 1990.

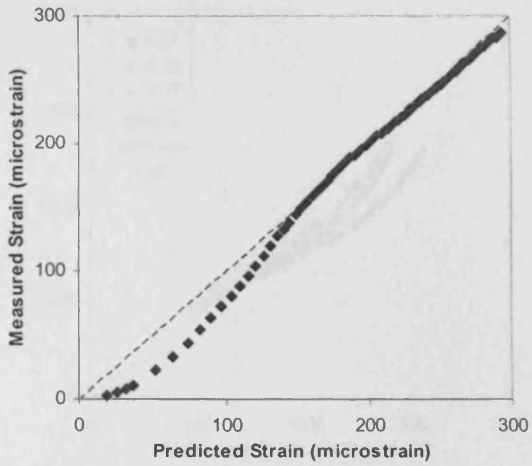

Figure 5.48. Comparison of measured and predicted shrinkage strains for concrete of nominal strength 80 N/mm^2, using the ACI Model 1992.

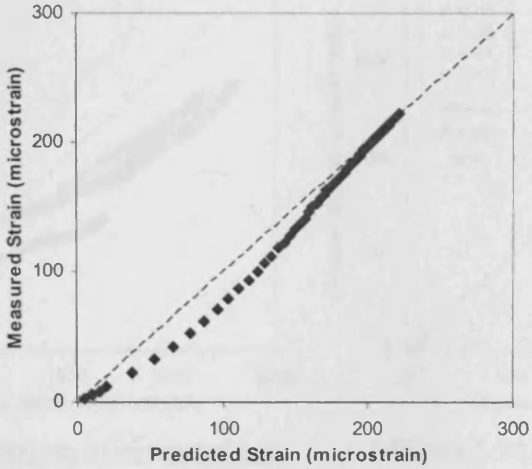

Figure 5.49. Comparison of measured and predicted shrinkage strains for concrete of nominal strength 100 N/mm^2, using the GZ Model 1993.

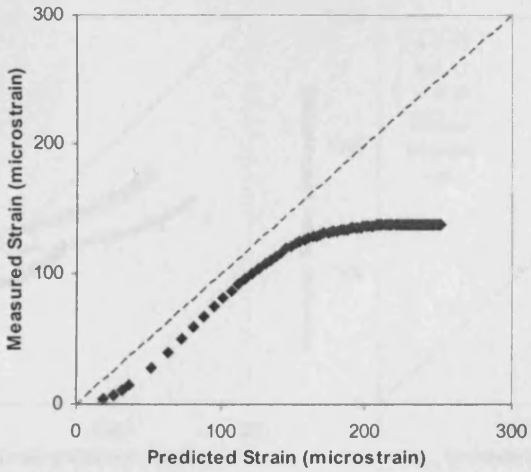

Figure 5.50. Comparison of measured and predicted shrinkage strains for pfa concrete of nominal strength 65 N/mm^2, using the CEB-FIP Model Code 1990.

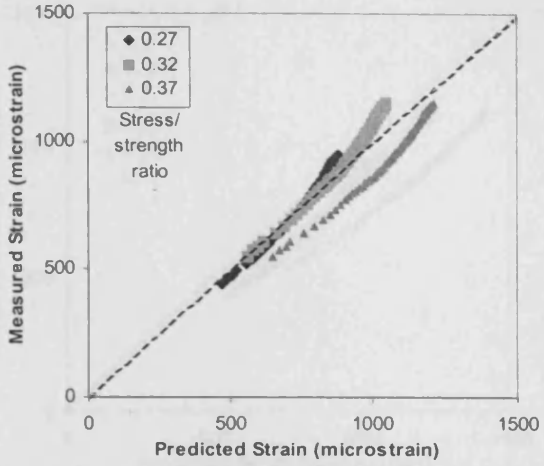

Figure 5.51. Comparison of measured and predicted basic creep strain for concrete of nominal strength 80 N/mm^2, using the ACI Model 1992.

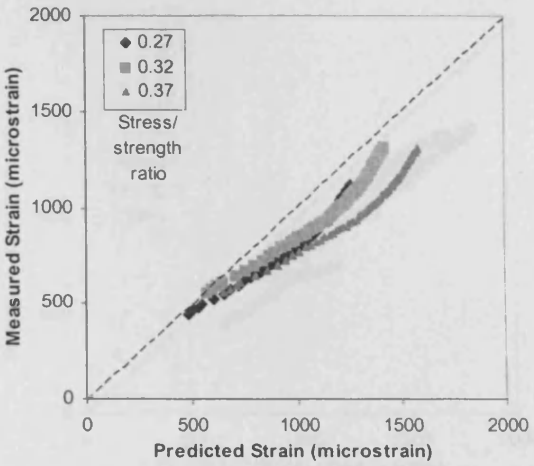

Figure 5.52. Comparison of measured and predicted total strain for concrete of nominal strength 80 N/mm^2, using the ACI Model 1992.

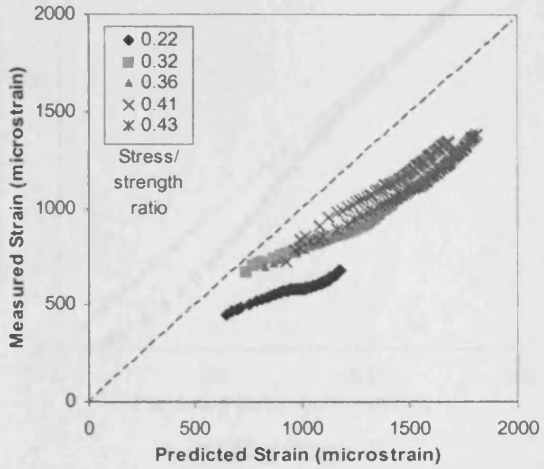

Figure 5.53. Comparison of measured and predicted basic creep strain for concrete of nominal strength 100 N/mm^2, using the CEB-FIP Model Code 1990.

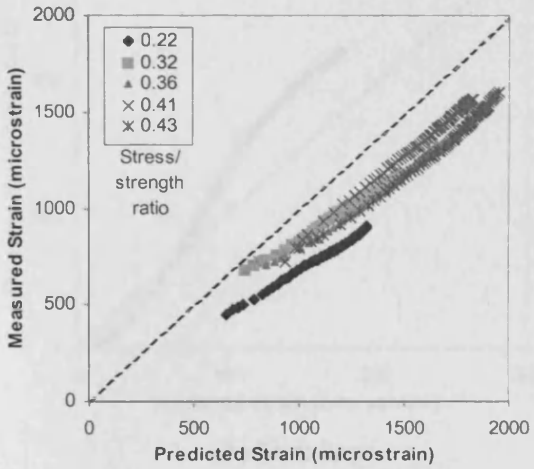

Figure 5.54. Comparison of measured and predicted total strain for concrete of nominal strength 100 N/mm^2, using the CEB-FIP Model Code 1990.

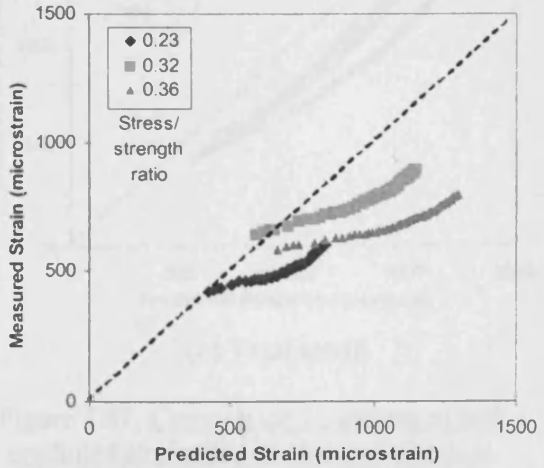

Figure 5.55. Comparison of measured and predicted basic creep strain for pfa concrete of nominal strength 65 N/mm^2, using the ACI Model 1992.

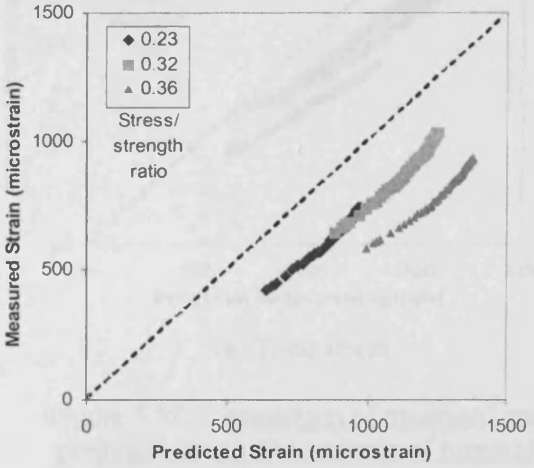

Figure 5.56. Comparison of measured and predicted total strain for pfa concrete of nominal strength 65 N/mm^2, using the GZ Model 1993

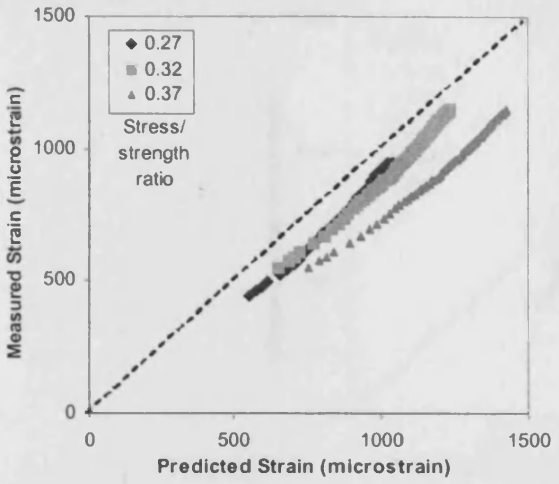

(a) Basic + drying creep

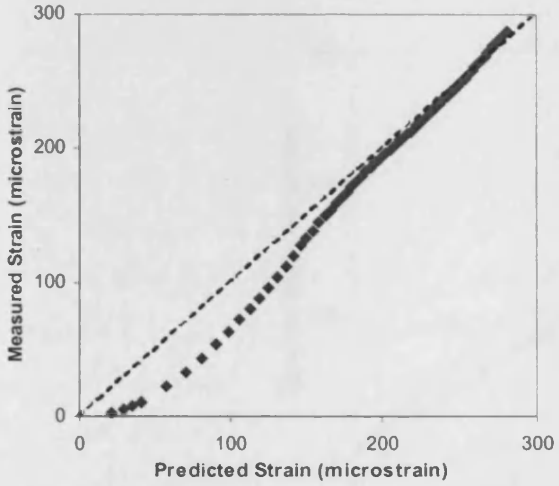

(b) Shrinkage

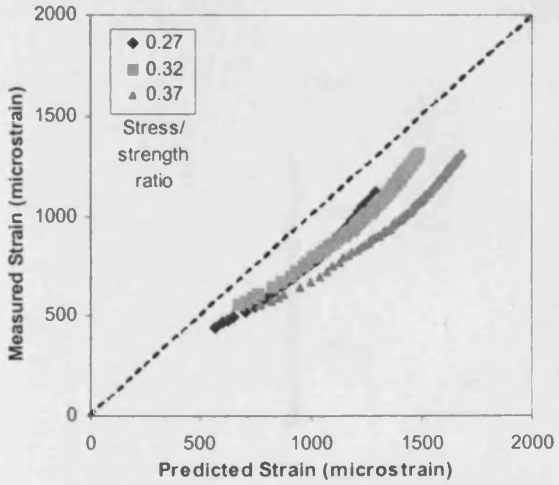

(c) Total strain

Figure 5.57. Comparison of measured and predicted strains for concrete of nominal strength 80 N/mm^2, using the CEB-FIP Model Code 1990.

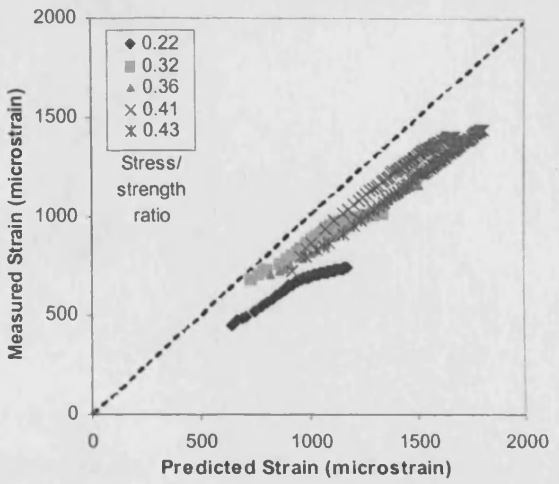

(a) Basic + drying creep

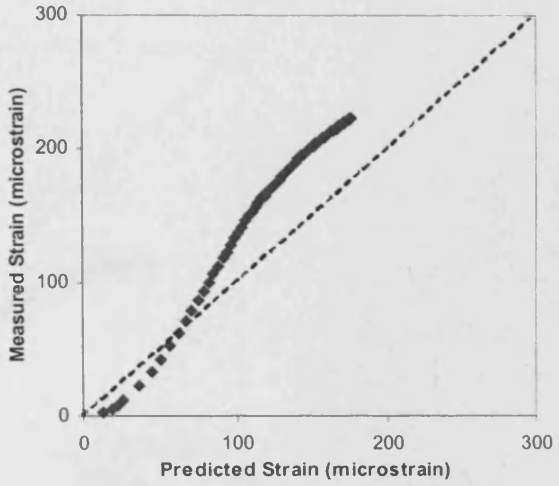

(b) Shrinkage

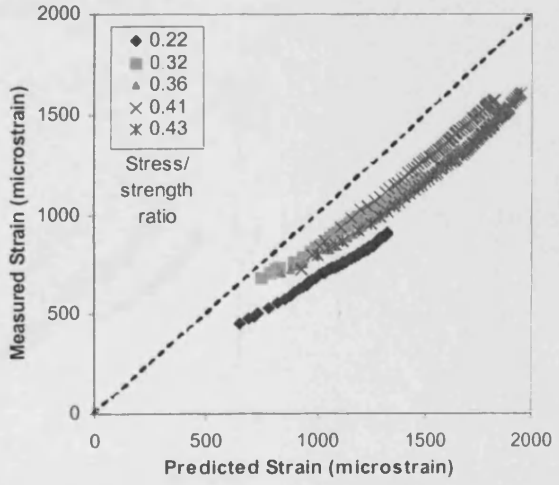

(c) Total strain

Figure 5.58. Comparison of measured and predicted strains for concrete of nominal strength 80 N/mm^2, using the CEB-FIP Model Code 1990.

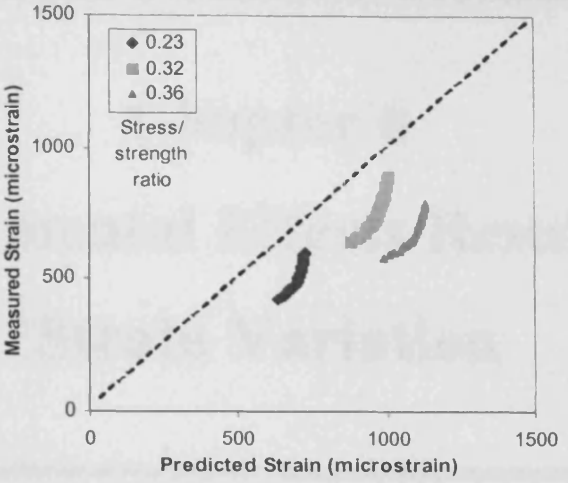

(a) Basic + drying creep

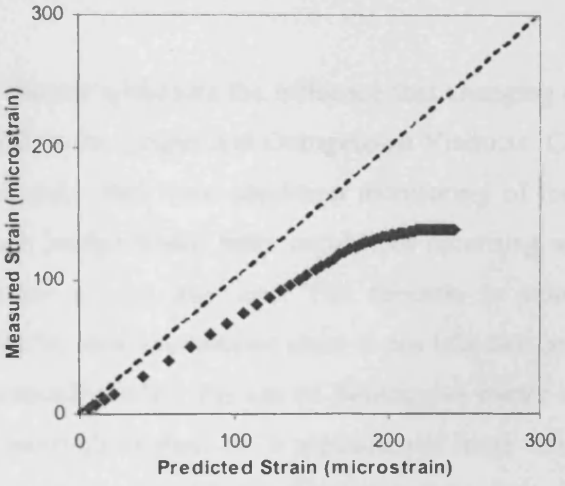

(b) Shrinkage

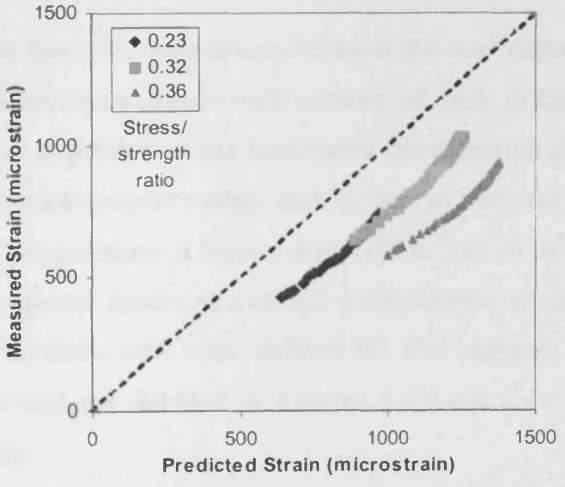

(c) Total strain

Figure 5.59. Comparison of measured and predicted strains for pfaconcrete of nominal strength 100 N/mm^2, using the GZ Model 1993.

Chapter 6
Environmental Effects Resulting in Strain Variation

6.1 Introduction

The study reported in this chapter addresses the influence that changing environmental effects have on the strains recorded in the Cogan and Grangetown Viaducts. Cardiff University was granted permission to undertake their own condition monitoring of the viaducts and hence installed dataloggers in each bridge which were capable of recording up to 30 gauges or 27 gauges and the thermocouple at any one time. The decision to automate readings using dataloggers was necessitated by time restrictions since it can take two people up to an hour to take one set of readings manually, while the use of dataloggers meant the readings could be taken at specified times at intervals as short as 15 seconds, and large volumes of data could be stored in the dataloggers memory for downloading at a later date. The downside is the restriction imposed on the number of gauges that can be monitored at any one time.

In order to provide a sound basis for comparison between the two viaducts, it was decided to try and ensure that gauge locations within each section of each bridge were as similar as possible, an objective which depended on the location of the defective gauges. It was decided from the outset to utilise thermocouples within each bridge so that recorded strains could be compared with changes in temperature, a feature reported by Barr *et al*[5]. In order to measure transverse strains, i.e. horizontal strains across the cross-section of the viaduct segments, opposing rosettes located in each web were utilised for this purpose. Gauges selected for monitoring and their locations are detailed in Figures 3.13 and 3.14 for Grangetown and Cogan Viaducts respectively.

Strain and temperature readings were taken daily over a two-year period for both Grangetown and Cogan Viaducts, using the embedded vibrating wire gauges detailed in Section 3.8. Unfortunately, due to problems with the datalogger installed in the Grangetown Viaduct, large

periods of strain data are missing over this two-year period and therefore a yearly study of the strain behaviour can only be made for the Cogan Viaduct. In addition to the daily recorded data, for four individual weeks over this 2-year period in which the weather was deemed to be representative of one of each of the four seasons of the year i.e. Spring, Summer, Autumn and Winter, the dataloggers were programmed to take readings at hourly intervals for the full week. It was possible in these instances to record hourly data for both viaducts, enabling seasonal strain comparisons to be made for both structures. Daily and hourly environmental data were obtained from the Met Office for Cardiff Weather Station, situated at National Grid Reference 3182E 1761N, which is located in a similar geographical situation some 1.7 miles from the Grangetown Viaduct and 2 miles from the Cogan Spur Viaduct, at 52m above sea level. Using this information, a comparison between changes in meteorological conditions and the bridge strains can be made.

6.2 Analysis of Environmental Data

The daily data obtained from the Met Office comprised daily mean air temperatures and daily mean average humidities. The main climatological hour in the United Kingdom is 0900 GMT and hourly temperature and humidity readings are taken over the period 0900 – 0900 GMT for a particular day. Temperature readings were recorded hourly using a dry bulb thermometer, while relative humidity readings were recorded using a humidity sensor. Hourly readings used in this study are as recorded, while the daily readings are averaged hourly readings over the space of a day. It has been shown by Barr *et al*[9] that there is a delay in the strain response of the bridges to changes in temperature and relative humidity. Since the external temperature and relative humidity can vary considerably over a 24-hour period, comparing actual temperature and relative humidities which have been recorded at the same time as that at which the strains are recorded would not be entirely accurate since the concrete is still responding to earlier changes in temperature and humidity. Therefore, when analysing the seasonal strain behaviour it was decided to use daily averages for the environmental data in order to provide the most realistic comparison. The hourly data obtained from the Met Office comprised actual air temperatures and humidities recorded at the same times as the hourly strains, such that the influence of environmental effects could be assessed in real time.

6.3 Strain Sensitivity

It should be noted at this point that the strain values and ranges reported in this study need to be treated with a certain degree of caution since they are not absolute values. There are many

external influencing factors aside from environmental effects which can influence the strain reading as it is recorded.

The largest of these is the influence of live loading. Any motor vehicle passing over a gauge location at the moment the reading is taken will have an influence on the recorded strain, the larger the vehicle, the bigger the influence. Unfortunately, this cannot be prevented if readings are to be logged at regular intervals. Live loading at other locations along the length of the structure can also marginally affect the strain. When a strain is recorded manually, the reading recorded is the period reading measured in seconds $\times 10^{-7}$, and is between 4 and 5 digits long. It can be noticed that the final digit is very sensitive and can alter by up to 5×10^{-7} seconds, due to the aforementioned influencing factors. It has been calculated that a change in one digit corresponds to a strain change of 0.6 $\mu\epsilon$, so a change of 5×10^{-7} seconds corresponds to a strain change of 3.0 $\mu\epsilon$. Changes in the temperature of concrete will cause some change in the temperature of the vibrating wire gauge itself. A temperature sensitivity study for vibrating wire gauges was undertaken and is detailed in Appendix E. It was found that a change in temperature of 10 °C can cause a change in strain of up to 1 $\mu\epsilon$. These changes in strain may appear to be very small, but it has been estimated that a combination of these factors could result in a change in strain of up to $\pm$ 10 $\mu\epsilon$ but a more realistic assessment is more of the order of $\pm$ 2 - 5 $\mu\epsilon$. Therefore for the changes in strain reported in this study, it is important to remember that while they can be considered to be accurate when related to one another, the variability discussed here means that they are absolute only within a tolerance of approximately $\pm$ 10 $\mu\epsilon$.

6.4 Annual Data

The period of investigation for the long-term study ran from 22/01/2002 to 28/02/2004. The raw logger data downloaded from the datataker in the Cogan Viaduct over this period was converted into microstrain ($\mu\epsilon$) for each of the selected gauges.

Figures 6.1 and 6.2 show typical comparisons between daily measured strains and daily average temperature in the top and bottom flanges respectively for segment 1, while Figures 6.3 and 6.4 show a typical comparison between the same strains and daily average relative humidity (RH) in the top and bottom flanges respectively of segment 1. Figures showing the comparisons of measured strains with temperature and RH for segments 6 and 12 can be found in Appendix E. Each figure is split into two halves, the top half showing either the average daily temperature in °C or the average daily RH (%), while the bottom half shows the recorded strain in $\mu\epsilon$. The date when each reading was taken is shown on the x-axis. It is

important to note that while the y-axis temperature/RH scale remains constant for each figure, the y-axis strain scale varies depending on gauge location within the segment and also segment location within the bridge, in order to fully demonstrate the relationship between changing temperature/RH and strain. It can be observed that while the temperature varies from 0 to 26 °C and the RH varies from 37 to 97%, the corresponding strain variations are of the magnitude of approximately 75 and 50 $\mu\epsilon$ in the top and bottom flanges of segment 1 respectively, indicating a greater variation in the top flange than the bottom. This fact is also noted in the other segments and will be discussed in more detail later in this chapter.

In order to fully appreciate the magnitude of the change in strain over the course of the 2-year period, the year was split into seasons. Thus, average strains, temperatures and humidities were calculated for each season. Season start and end dates were chosen to correspond with the rotation of the earth's axis, when weather conditions are most typical of each season i.e. the Winter solstice (22nd December), the vernal equinox (21st March), the Summer solstice (21st June) and the Autumnal equinox (22nd September). Hence it was possible to observe the corresponding change in average strain when the average temperature/humidity for a season changes from one season to the next. Figures 6.5 and 6.6 depict the change in average seasonal strain with change in average seasonal temperature in the top and bottom flanges of segment 1 respectively, while Figures 6.7 and 6.8 depict the change in average seasonal strain with change in average seasonal relative humidity for the same locations. For clarity and simplicity, an average strain value has been taken for corresponding gauges either side of the vertical centreline of each segment in both flanges i.e. gauges at the corner joints between the top flange and both webs have been averaged, as have gauges in the centre of the top and bottom flanges. These charts are again split into two halves with the upper half showing the variation in average seasonal temperature (°C) or RH (%), while the bottom half illustrates the variation in average seasonal strain ($\mu\epsilon$) with values of these three variables shown on the y axis. The x-axis shows the date and corresponding season. Again, the temperature/RH scale remains constant for each figure while the y-axis strain scale varies depending on gauge location. Values representing the calculated changes in temperature, RH and strain are shown next to the appropriate increase/decrease on the chart. It can immediately be seen that the pattern of temperature and RH variation after the first year repeats itself over the second year indicating that this method of seasonal averaging adequately reflects the temperature and RH behaviour observed over this period, and hence validates the decision to use this method in this study. Over the two-year period, it can be seen that the largest change in strain in any one year is from Winter 2003 to Summer 2003 and is the same for all gauges. The maximum strain changes and their locations within each flange and each segment are shown in Table 6.1, along with the corresponding changes in temperature and RH. This again confirms that

the influence of environmental effects is more pronounced in the top flange than the bottom, but also indicates that the influence is greater in the webs than the bottom flange, signifying a reducing influence with distance from the exposed top flange.

A more detailed analysis of the relationship between strain and environmental effects at these specific locations is thus warranted. Figures 6.9 – 6.16 show the change in temperature between seasons and the corresponding change in average seasonal strain for each gauge in the top flange of segment 1, the bottom flange of segment 1, the top flange of segment 6, the bottom flange of segment 6, the top flange of segment 12, the bottom flange of segment 12, the webs of segment 12, and the transverse strain, calculated using the rosettes in the webs of segment 12 respectively. Similarly, Figures 6.17 – 6.24 show the change in RH between seasons and the corresponding change in average seasonal strain for each gauge at the same locations. Consider Figure 6.9, which depicts the changes in temperature and strain in the top flange of segment 1. The x-axis shows the season change while the y-axis shows the magnitude of the change in temperature/strain. Consider the first season change, Winter 2002 – Spring 2002. The 1st bar represents the change in temperature, while the four subsequent bars represent the change in strain for each gauge in the following order: 2, 3, 6 and 9, as indicated adjacent to each bar on the chart. The same pattern is repeated for each subsequent season change, and also for all other figures of this type. It should also be noted that the scale is the same for all figures of this type.

From examination of the change in strain in each of these figures, it can again be observed that the influence that the varying environmental effects have on the strains is far greater in the top flange than in the bottom. Figure 6.9 shows the effect that changing temperature has on the average strains in the top flange of segment 1, while Figure 6.17 shows the effect that changing relative humidity has on the average strains. Immediately it can be seen that an increase in temperature gives an increase in strain. Similarly, in most cases a decrease in RH gives an increase in strain. There are some seasons where this is not the case, although in these instances the change in RH is very small. Furthermore, the largest changes in strain occur when the season changes from Winter to Spring when there are large increases in strain due to increasing temperatures, and from Summer to Autumn when there are large decreases in strain due to decreasing temperatures. In between these two periods, when the season changes from Spring to Summer, the change in strains are increasing although the magnitude is less than the Winter to Spring change, while when the season changes from Autumn to Winter, the change in strains are decreasing, although again the magnitude is less than the Summer to Autumn change. This shows that the strain behaviour is as expected – when the seasons change from Winter through Spring to Summer, temperatures rise, humidity generally

falls as the weather improves, and strains increase, while when the seasons change from Summer through Autumn to Winter, temperatures fall, humidity generally rises as the weather worsens, and strains decrease. Changes in strain for the Winter – Spring/Summer – Autumn season changes are in the range 15 – 35 $\mu\epsilon$, for temperature and RH increases/decreases in the ranges 3.6 – 8.8 °C and 7.2 – 8.9 %. Changes in strains for the Spring – Summer/Autumn - Winter season changes are in the range 10 – 25 $\mu\epsilon$, with corresponding increases/decreases in temperature and RH in the ranges 3.0 – 5.6 °C and 0.4 – 3.1 %.

Figure 6.10 shows the effect that changing temperature has on the average strains in the bottom flange of segment 1, while Figure 6.18 shows the effect that changing relative humidity has on the average strains. It can be seen that the magnitude of the changes in strain are much less than in the top flange, with changes in strain for the Winter – Spring/Summer – Autumn season changes in the range 5 – 15 $\mu\epsilon$ (compared to 15 – 35 $\mu\epsilon$), while changes in strain for the Spring – Summer/Autumn - Winter season changes are in the range 5 – 10 $\mu\epsilon$ (compared to 10 – 25 $\mu\epsilon$). Furthermore, the pattern of increasing/decreasing strains with seasonal weather change is far more varied in the bottom flange and it is difficult to accurately identify which seasonal change gives the greatest change in strain. This again indicates that the influence of environmental effects on strain variation is far less in the bottom flange.

Figures 6.11 and 6.19 illustrate the effect that seasonal average temperature and RH change respectively have on the strains in the top flange of segment 6, while Figures 6.12 and 6.20 depict the same effects in the bottom flange. As in the top flange of segment 1, the pattern of strain change shows the greatest increase for the Winter – Spring season change and the greatest decrease for the Summer – Autumn season change, both in the range 15 – 25 $\mu\epsilon$ which is slightly less than in segment 1. This was as expected since this segment is close to the point of contraflexure of the viaduct span where stresses are smaller. The strain changes due to the Spring – Summer/Autumn - Winter season changes are again increasing/decreasing in the range 10 – 15 $\mu\epsilon$ which are less than the strains due to the other season changes, again comparable to segment 1. The bottom flange of segment 6 again gives no obvious indication of which season change produces the biggest influence on strain variation, with all strain changes in the range 5 – 10 $\mu\epsilon$.

Figures 6.13 and 6.21 describe the effect that seasonal average temperature and RH change respectively have on the strains in the top flange of segment 12, while Figures 6.14 and 6.22 depict the same effects in the bottom flange. The same trends are present for the top flange although the magnitude of the larger strain change seasons (Winter – Spring/Summer – Autumn) is slightly greater than in segment 1, in the range 25 – 40 $\mu\epsilon$ as opposed to 15 – 35

$\mu\epsilon$ in segment 1. This is likely to be due to the smaller section thickness of segment 12 which is at mid-span as opposed to segment 1 which is at the pier. The strain changes due to the Spring – Summer/Autumn - Winter season changes are again lower than those associated with the Winter – Spring/Summer – Autumn season changes in the range 10 – 20 $\mu\epsilon$, and also smaller than the corresponding strain changes in segment 1 (10 – 25 $\mu\epsilon$). The bottom flange of segment 12 again gives no obvious indication of which season change produces the biggest influence on strain variation, with all strain changes in the range 2 – 12 $\mu\epsilon$, which are less than the corresponding strain changes in segment 1 (5 – 15 $\mu\epsilon$).

Figures 6.15 and 6.23 describe the effect that the variation of seasonal average temperature and RH change respectively have on the strains in the webs of segment 12, while Figures 6.16 and 6.24 depict the effect that the same environmental effects have on the transverse strains in the webs of segment 12, calculated using the rosettes in the webs. In this instance, the pattern of longitudinal and transverse strain behaviour is similar to that observed in the top flange segments, although there is no clear indication of which season change gives the greatest strain change, with longitudinal strains in the range 5 – 15 με, and transverse strains in the range 10 – 20 με. Because the transverse strains are measured across the bridge section rather than along it they are unrestrained, and therefore this observation simply confirms the complexity of strain behaviour in a continuous structure. It suggests that the restraint provided longitudinally is sufficient to ensure that the influence of environmental effects is reduced along the bridge, as opposed to across it, where there is less restraint.

In order to further determine the relationship between change in temperature/humidity and strain, Figures 6.25 and 6.26 show correlation plots of the change in average seasonal strain against change in average seasonal temperature in the top and bottom flanges respectively, while Figures 6.27 and 6.28 show correlation plots of the change in average seasonal strain against change in average seasonal RH in the top and bottom flanges respectively, for all gauges in all segments. Lines of best fit are also plotted for each segment. In the top flanges (Figure 6.25), there is good correlation between strain and temperature especially between the pier segment 1 and the mid-span segment 12 where the relationship is almost linear. The correlation for the quarterspan segment 6 is also good although not as good as for the other segments. This trend is similar for strain and RH (Figure 6.27) although both the Spring - Summer season changes and the Autumn 2002 – Winter 2003 season change do not reflect this indicating that the relationship between RH and strain is not linear, although this could be due to the fact that RH is considerably more variable than temperature. Neither of the comparisons with strain and temperature (Figure 6.26) or strain and RH (Figure 6.28) in the bottom flanges give meaningful trends, as was observed earlier in this chapter. In order to

understand why this is the case, the orientation of the structure and its geographical location must be analysed. The section of Cogan Viaduct in which the instrumented segments are located runs from northeast to southwest. This means that while the top flange is subjected to direct sunlight (including when there is cloud cover) all day long, the bottom flange is always in shade, and since sunlight is responsible for increased temperatures and generally, decreased humidity, this may account for the greater strain response in the top flange and the smaller response in the bottom flange. Furthermore, since it is the northern carriageway that is instrumented, it may be expected that the gauges on the outer bottom corner should be influenced to a certain extent, since they would be exposed to the path of the sun in the mid to late afternoon. However, the proximity of a hill to the west means that these gauges also get very little direct exposure and hence are generally unaffected by changes in temperature. In addition, the bottom flange retains a large amount of moisture during the day due to increased RH during the night and owing to the lack of direct sunlight exposure, the concrete in the bottom flange will be much cooler than the top flange, thus ensuring that any variations in strain are small.

6.5 Weekly Data

The periods of investigation for the weekly study were from 15:00 on 30/04/2003 – 14:00 on 07/05/2003 (Spring), 16:00 on 07/08/2003 – 15:00 on 14/08/2003 (Summer), 15:00 on 24/11/2003 – 14:00 on 01/12/2003 (Autumn), and 16:00 on 23/01/2003 – 15:00 on 30/01/2003 (Winter). For each of these periods the raw logger data was downloaded from the datalogger in both Cogan and Grangetown Viaducts, and was converted into microstrain ($\mu\epsilon$) for each of the selected gauges. It should be noted at this point that there is limited internal temperature data for the Cogan Viaduct in the Autumn, and none for the Winter due to a fault with the thermocouple. Also, there is no data for gauge CV1-G9 in the Winter due to gauge failure. Furthermore, due to power failure in the datalogger in Grangetown Viaduct, there is only ¾ of a week of data available for this viaduct in the Winter.

Because the first part of this study indicated that the predominant influencing environmental variable is temperature and not RH, the weekly study will focus solely on temperature effects. Figure 6.29 shows the strains in the top flange of segment 1 of Cogan Viaduct in the Spring, while Figure 6.30 shows the strains in the bottom flange of segment 6 of Grangetown Viaduct in the Summer. All other strains and temperature variations for every location within both structures, for all four seasons can be found in Appendix E. Each figure is split into two halves, the top half showing the external and internal air temperature in °C while the bottom half shows the recorded strain in $\mu\epsilon$. The date when each reading was taken is shown on the x-

axis. It is important to note that the y-axis temperature scale varies for each figure depending on the season, while the y-axis strain scale varies depending on gauge location within the segment and also segment location within the bridge. In Figure 6.29, it is apparent that there are two distinct patterns of strain variation which represent differences in gauge locations. The pair of gauges CV1-G2 and CV1-G9 although differing in magnitude, show virtually identical strain behaviour as do the other pair of gauges CV1-G3 and CV1-G6. This is because the former pair of gauges are located at either corner of the top flange at the junction with each web, while the latter pair of gauges are located in the centre of the top flange, demonstrating different strain behaviour depending on position within the flange. Figure 6.30 reinforces this fact and shows that the effect is not solely related to the vertical position within the section, longitudinal position within the structure, the structure itself, nor the season and hence the temperature. The pair of gauges GV6-G16 and GV6-G22 show matching strain patterns due to these two gauges being at either corner of the bottom flange, while gauge GV6-G18 shows slightly different strain behaviour, since it is located in the centre of the bottom flange. These figures were chosen to demonstrate this detail, since they demonstrate behaviour which is typical of all gauges within both structures, and also of each season. Hence in order to simplify this analysis, an average was taken for each pair of corresponding gauges within each flange (i.e. corners, centres, cantilevers). As mentioned at the beginning of this chapter, it is expected that there will be a time lag between temperature change and strain change. From closer scrutiny of the external and internal air temperature variation in Figures 6.29 and 6.30, qualitatively it is obvious that there is indeed a time lag which varies depending on the season, however, a quantitative relationship has not been established since it is beyond the scope of this study. It is apparent that this strain lag is a function of the variation in temperature, and is likely to be due to the response of mass concrete to these changes in temperature. It takes time for the concrete mass to heat up and cool down and so it is not surprising that it can take up to 24 hours in some cases for the strains measured to reflect temperatures associated with the previous day. It is also obvious that there is a time lag between the internal and external air temperatures, with it being noticeable that there is considerably less variation of the internal temperature than the external temperature. Since this study is concerned with the influence of environmental effects on strain, the variation of external temperature will be the primary focus of this analysis.

In order to determine the relationship between strain and temperature variation for each of the four seasons, it was decided to isolate five individual periods of notable temperature change over the space of the week in question. Figures 6.31 – 6.34 show the strain changes for varying locations in both Cogan and Grangetown Viaducts for each of the four seasons in question. The selected upper and lower temperature boundaries, between which the changes

in strain occur, are circled in Figures 6.31 – 6.34 (Spring, Summer Autumn and Winter respectively), with the temperature value alongside. The five temperature changes are designated a, b, c, d, e, and are also shown. It should be noted that the strain and temperature scales vary in each of these figures. Hence, for each of these changes in temperature, the subsequent strain for all measured strain locations in each bridge has been determined and the change in strain for the corresponding change in temperature has been calculated. The changes in strain for each location are shown in Appendix E while average changes in strain for each of the five temperature changes, for each season are presented in Table 6.2 in the case of Cogan Viaduct, and Table 6.3 in the case of Grangetown Viaduct. These changes are depicted graphically in Figures 6.35 – 6.41, for the top flange of segment 1, the bottom flange of segment 1, the top flange of segment 6, the bottom flange of segment 6, the top flange of segments 11/12, the bottom flange of segments 11/12, and the webs of segments 6/12, for Grangetown and Cogan Viaducts respectively.

Figure 6.35 shows the changes in strain in the top flange of segment 1. The x-axis shows the season while the y-axis shows the magnitude of the change in temperature/strain. Consider the 1st season (Spring 2003). The 1st bar represents the change in temperature, while the four subsequent bars represent the change in strain for each location, with the progression as indicated by the legend. The same pattern is repeated for each subsequent season change, and also for all other figures of this type. It should also be noted that the scale is the same for all figures of this type. Average external air temperature changes are approximately 8, 11, 6 and 6 °C for Spring, Summer, Autumn and Winter respectively. Immediately it can be seen from Figure 6.35 that there are two distinct magnitudes of strain change. The average Spring and Summer strain changes are very similar with changes in the range 16 – 27 $\mu\epsilon$ for Cogan Viaduct and 22 – 25 $\mu\epsilon$ for Grangetown Viaduct, while the Autumn and Winter strain changes are much lower in the range 5 – 10 $\mu\epsilon$ for both Cogan and Grangetown Viaducts. Furthermore, there is far less strain variation between the different locations in the latter seasons than the former, despite the fact that the average change in temperature over the space of a day is very similar in the Spring, Autumn and Winter (5.7 – 7.7 °C). The same split in the magnitude of strain change is observed in the bottom flange of both viaducts, although to a lesser extent as shown in Figure 6.36. The average Spring and Summer changes are again similar although lower than in the top flange with changes in the range 13 – 18 $\mu\epsilon$ for Cogan Viaduct and 11 – 13 $\mu\epsilon$ for Grangetown Viaduct, while the Autumn and Winter strain changes are again lower, around 5 $\mu\epsilon$ for both Cogan and Grangetown Viaducts. This again suggests that the influence of temperature is more pronounced in the top flange than the bottom as seen in the yearly study, although the observation is now based on more than one structure.

The average Spring and Summer changes in the top flange of segment 6 (Figure 6.37) are in the range 9 – 16 $\mu\epsilon$ for Cogan Viaduct and 15 – 24 $\mu\epsilon$ for Grangetown Viaduct, while the Autumn and Winter strain changes in the range 3 – 8 $\mu\epsilon$ for both Cogan and Grangetown Viaducts. There is a greater difference in the Spring/Summer strain changes between viaducts which may be because they are quarter span segments which are close to the point of contraflexure. The average Spring and Summer changes in the bottom flange of segment 6 (Figure 6.38) are in the range 5 – 12 $\mu\epsilon$ for Cogan Viaduct and 9 – 16 $\mu\epsilon$ for Grangetown Viaduct, while the Autumn and Winter strain changes in the range 2 – 6 $\mu\epsilon$ for both Cogan and Grangetown Viaducts, which is similar to segment 1.

Figure 6.39 shows the average changes in strain in the top flange of segments 12 (Cogan) and 11 (Grangetown), with Spring and Summer changes in the range 16 – 22 $\mu\epsilon$ for Cogan Viaduct and 21 – 30 $\mu\epsilon$ for Grangetown Viaduct, while the Autumn and Winter strain changes are in the range 6 – 11 $\mu\epsilon$ for both Cogan and Grangetown Viaducts. The magnitude of these changes in strain is very similar to segment 1, and slightly larger than segment 6 for the reasons given above. The average Spring and Summer changes in the bottom flange of segment 6 (Figure 6.40) are around 7 $\mu\epsilon$ for Cogan Viaduct and 13 $\mu\epsilon$ for Grangetown Viaduct, while the Autumn and Winter strain changes are in the range 4 – 6 $\mu\epsilon$ for both Cogan and Grangetown Viaducts, which is very similar to the other two segments in both viaducts.

Figure 6.41 shows the average changes in strain in the webs of segments 12 (Cogan) and 6 (Grangetown), with longitudinal Spring and Summer changes in the range 11 – 15 $\mu\epsilon$ for Cogan Viaduct and 16 – 18 $\mu\epsilon$ for Grangetown Viaduct, while the Autumn and Winter longitudinal strain changes are in the range 3 – 5 $\mu\epsilon$ for Cogan Viaduct and 4 – 7 $\mu\epsilon$ for Grangetown Viaduct. The differences between the two viaducts are due to the strain locations being in different segments (at mid span for Cogan, and at quarter span for Grangetown). Transverse Spring and Summer changes are around 6 $\mu\epsilon$ for both Cogan and Grangetown Viaducts, while the Autumn and Winter longitudinal strain changes are around 3 $\mu\epsilon$ for both Cogan and Grangetown Viaducts. Therefore, for the three different locations along the span of both viaducts (pier, quarter span and mid span), the same difference in the magnitude of change in strain between the Spring/Summer and Autumn/Winter is observed. Furthermore, the changes in strain in the top flange are noticeably larger and more variable than in the bottom flange. This reinforces the conclusions drawn from the annual study reported earlier. Bearing in mind that the tolerance of the strain measurements on which these observations are based is believed to be of the order of $\pm$ 2 - 5 $\mu\epsilon$, it is clear that some of these differences are very small. Nevertheless, the trends reported are quite distinct and would seem to properly describe the response of the viaducts to environmental effects.

In order to try and quantify the relationship that exists between strain and temperature, the five temperature changes and corresponding strain changes detailed in Tables 6.2 and 6.3 for the Cogan and Grangetown Viaducts respectively were compared. It has been shown that while the changes in strain are greater in the top flange than the bottom, these changes are very similar for both viaducts. Hence, it was decided to compare changes in strain with changes in temperature for each flange of both viaducts simultaneously. Figures 6.42 – 6.45 show the relationship between the change in temperature and strain in the top flanges of all instrumented segments for the Spring, Summer, Autumn and Winter respectively, while Figures 6.46 – 6.49 show the relationship between the change in temperature and strain in the bottom flanges of all instrumented segments for the same seasons. Figure 6.42 depicts the changes in temperature and strain in the top flanges in the Spring. The x-axis represents the change in temperature in °C, while the y-axis represents the change in strain in microstrain. The location at which the change in strain is observed is denoted by a marker as indicated by the legend, and lines of best fit represent the average change in strain for each flange in either viaduct, again as indicated by the legend. The same representation has been adopted for all other figures of this type, and the scale is the same in all cases in order to fully appreciate the changing patterns in the temperature/strain relationship.

Examination of the change in strain with temperature over the four seasons in the top flange (Figures 6.42 – 6.45) shows that the correlation for each location is generally good, particularly in the Summer and Autumn. There is a slightly wider spread for the Spring results with the strains in the top corner of segment 1, Grangetown Viaduct, exhibiting unexpected behaviour. Likewise, the spread of the Winter strains is also significant. The spread of strains for each location is due to the fact that each data set represents a different location along or through the bridge, with each location bringing with it a certain degree of variability i.e. gauge depth and cover, flange thickness etc. The poor spread in the Winter is most likely due to the fact that daily changes in temperature and strain are so much smaller in the Winter than the other three months, bringing another degree of variability to the measured strains and so the data is unable to demonstrate what the relationship actually is. However, the averages for each flange which are represented by the lines of best fit show very similar behaviour between all flanges in both viaducts, again suggesting that there may be a linear relationship between strain and temperature. This argument is strengthened by the fact that each line of best fit intercepts the x and y-axis very close to zero in both cases. However, comparing the flange averages from one season to the next it becomes apparent that the relationship changes depending on the season. In the Spring, the gradient of the lines of best fit for the average strain in each flange varies between 1.2 and 3.1. This reduces slightly in the Summer to between 1.0 and 2.0, decreasing again in the Autumn to between 0.6 and 1.4, and reducing

further still in the Winter to between 0 and -0.8. This occurs despite the average temperature changes being very similar for the Spring, Autumn and Winter as mentioned previously.

The relationship between strain and temperature for each of the four seasons in the bottom flange is shown in Figures 6.46 – 6.49. Again, the correlation for each location is very good for the Summer and Autumn, with a slightly wider spread for the Spring. The strains in the top corner of segment 1, Grangetown Viaduct, in the Spring again exhibit unexpected behaviour, whilst the spread of the Winter strains is again significant for the reasons mentioned above. In fact, the bottom flange behaviour is virtually identical to that of the top flange, with the averages for each flange (represented by the lines of best fit) showing a very similar trend in all flanges in both viaducts, with intercepts with the x and y-axis which are again very close to the origin. The gradients and the pattern in each season are also similar, reducing slightly each time from Spring 2003 to Winter 2004. In the Spring, the gradient varies between 0.4 and 2.0, reducing slightly in the Summer to between 0.8 and 1.5, decreasing again in the Autumn to between 0.4 and 0.7, and reducing further still in the Winter to between 0 and -0.3. These values are slightly lower than the equivalent values in the top flange, indicating that the influence of temperature is slightly reduced.

Therefore, the seasonal study has confirmed what was first identified in the annual study i.e. that a relationship does exist between temperature and strain, although the effect is more dominant in the top flange. The fact that it is more noticeable in the top flange than the bottom can be attributed to the temperature differential that exists between the top and bottom flanges, since the top flange experiences greater direct exposure to the environment than the bottom flange. As in the yearly study, the decline in the gradient of the relationship between temperature and strain, for each subsequent season from Spring to Winter in both flanges, is apparent. This change in gradient of the relationship between temperature and strain from season to season can also be attributed to the differential temperature effects since the differential temperature profile also varies from season to season. This confirms that the response of the structure to changes in temperature is not solely due to the expansion and contraction of the concrete, but is also influenced by these differential temperature profiles. This is obviously the case since the restraint provided in a continuous bridge deck will induce stresses in the material which in turn affect the strain behaviour. The true nature of these differential temperature profiles is unknown and the facility to monitor them in this study was not available. However, as noted above they will vary from season to season and although not quantified, this is evident from the results presented in this section as is the observation that the effect of temperature change on strain variation in these two structures is the major influencing environmental factor.

6.6 Comparative Influence of Temperature and Relative Humidity

The findings of the previous sections have indicated that while the effect of temperature is by far the most influential of the environmental variables, it would be unwise to dismiss the effect that relative humidity (RH) has on strain behaviour without further investigation. It was decided to examine the hourly RH data obtained from the Met Office for each season to determine whether there were instances where the RH was of similar value, for different seasons. Figure 6.50 shows a comparison of the RH for the recorded week of each season. The x-axis shows the time in days, starting at zero when recording began, while the y-axis shows the RH in percent. It was decided to identify similar RH between each season over a small range RH, in order to examine the change in temperature and strain for a minimal change in RH. Closer examination of Figure 6.50 indicates that a large amount of RH data for each season falls in the range 80 to 90%, as indicated by the two boundary lines on the chart. Hence it was decided to study temperature and strain behaviour at intervals between these two values.

RH's for each season as close as possible to 80, 82.5, 85, 87.5 and 90% were selected and the equivalent temperatures were determined as shown in Table 6.4. It should be noted that the values of RH for each season were deliberately chosen at different times of the week in order to provide a representation of the week as a whole, and not just individual days. This data is depicted graphically in Figure 6.51. The x-axis shows the selected RH's in percent, while the y-axis shows the equivalent temperature in °C. Lines of best fit illustrate the relationship between the two. Immediately it can be seen that despite the change in temperature between seasons, a 10% change in RH can be accompanied by little if any change in temperature, indicating that for small changes in RH, temperature can be considered to be independent of RH. Since it has been proposed previously in this chapter that temperature is linearly related to strain, then a comparison of equivalent strains and temperatures for each of these RH's should also show a linear relationship between the two.

In order to prove this is the case, it was desirable to look at strains at a location which has been shown to give the greatest change in strain with temperature. This is the case in the top flange in segments 1 and 12/11 in both viaducts, and so the top flange of segment 1 in Grangetown Viaduct was selected. Figure 6.52 shows the equivalent strains and temperatures for each selected RH in the 80 – 90 % range for this location. The x-axis shows the temperature in °C, while the y-axis shows the strain in $\mu\epsilon$. Each RH is represented by a different marker, as indicated by the legend. The correlation for each RH is generally good with the exception of three points. However, the lines of best fit for four out of the five RH's

are virtually parallel to each other while the other line (82.5%) is only thrown slightly off parallel by one of the previously mentioned wayward points. There are a number of reasons why there may be some variation, such as a large vehicle passing over the gauge location at the instant the reading was taken, as well as differential temperature effects. Thus if these points are ignored, these results confirm that for changes in RH of less than 10% changes in strain are primarily influenced by temperature, validating the observations made previously in this chapter. Furthermore, in this case it can be said that a change in temperature of around 15°C is responsible for an increase in strain of approximately 50 $\mu\epsilon$.

6.7 Conclusions

Over the period of a year, it has been shown that changes in temperature and RH influence the strain behaviour in Cogan Viaduct in the following ways:

- As the temperature increases and RH decreases, strain increases.

- A temperature variation of up to 26 °C and RH variation of 60% produces corresponding strain variations of up to 75 $\mu\epsilon$ in the top flange, and 50 $\mu\epsilon$ in the bottom flange for both the viaducts studied. This indicates a greater strain variation in the top flange than the bottom for these structures. In all instances, strain changes in the top flange are larger than strain changes in the bottom flange and webs. Similarly, strain changes in the webs are greater than strain changes in the bottom flange, indicating a decrease in strain change with increasing distance from the top surface of the bridge.

- Seasonal average changes in temperature of around 4°C, and in RH of approximately 1.5%, for the Winter to Spring and Summer to Autumn seasons produce the largest changes in strain (20 and 10 $\mu\epsilon$ in the top and bottom flanges respectively). These strains are inversely proportional to the change in temperature, i.e. an increase in the former is a as result of a decrease in the latter.

- Similarly, seasonal average changes in temperature of around 2.5°C and RH of around 2.5% for the Spring to Summer and Autumn to Winter seasons produce smaller but similar and inversely proportional changes in strain (10 and 5 $\mu\epsilon$ in the top and bottom flanges respectively).

- It was observed that a linear relationship exists between changes in average seasonal strain and average seasonal temperature/RH, for the top flange of Cogan Viaduct.

- These linear relationships differ slightly depending on the location of the segment along the span.

- No such relationship was observed in the bottom flange.

- Strain response depends on temperature which in turn is related to exposure to direct sunlight (including through cloud cover). Hence there is a temperature differential between the two flanges leading to a greater strain response in the top flange than the bottom.

The strain behaviour of Cogan and Grangetown Viaducts was studied over one week in each season of the year in which the weather was typical of each season. The following observations were made:

- A change in temperature results in a delayed change in strain of up to 24 hours.

- Internal air temperature variation was minimal when compared to external air temperature variation.

- Strain behaviour in each flange differs depending on the location of the recording gauge within the flange i.e. the magnitude and variation of strain is different at the centre of the flange than at the corners, i.e. at the connection with the webs.

- The average daily change in strain is of similar magnitude for the Spring and Summer (up to 15 $\mu\epsilon$ for both Viaducts) despite the equivalent average temperature change being different, 8°C in the Spring and 12°C in the Summer.

- The average daily strain change for the Autumn and Winter is also similar but much smaller (up to 5 $\mu\epsilon$ for both Viaducts) despite temperature variations of 7°C in the Autumn and 6°C in the Winter, which are very similar to the Spring value.

- A linear relationship again exists between strain and temperature for each season of the year. However, this relationship varies slightly according to the location at which the strain was measured in each segment, and also the location of the segment along the span.

- The gradient of the linear relationship is different for each season, indicating that the response of the structure to overall changes in temperature is not solely due to the direct expansion and contraction of the concrete. Indeed, it is almost certain that differential temperature effects will have a marked influence on the strain behaviour and the change in gradient representing the relationship between strain and temperature between seasons

is likely to be a reflection of the fact that the differential temperature profiles change from season to season.

- The change in gradient of the linear relationship also indicates that temperature is not solely responsible for changes in strain and other environmental factors will certainly apply e.g. RH, rainfall, wind speed, solar gain, frost etc. and a combined effect of any number of these factors.

- A linear relationship between strain and temperature was observed when RH is within the range 80 – 90% indicating that temperature is the dominant influencing factor in strain variation in structures such as these.

- The seasonal study has shown that a change in temperature of around 15°C can cause an increase in strain of approximately 50 $\mu\epsilon$.

Table 6.1. Maximum changes in average seasonal strains and their locations with equivalent change in temperature and RH between Winter 2003 and Summer 2003.

Segment No.	Flange	Gauge No.	Location	Change in Strain ($\mu\epsilon$)	Temperature Change (°C)	RH Change (%)
1	Top	CV1-G3	Centre	52	+11.6	-8.1
	Bottom	CV1-G24	Corner	27		
6	Top	CV6-G3	Centre	40		
	Bottom	CV6-G18	Corner	17		
12	Top	CV12-G9	Corner	61		
	Bottom	CV12-G25	Corner	22		
	Web	CV12-G29	Centre	30		

Table 6.2. Average strain changes (microstrain) with change in temperature (°C) for different seasons of the year – Cogan Viaduct.

		Segment 1				Segment 6				Segment 12				
		Top Flange		Bottom Flange		Top Flange		Bottom Flange		Top Flange		Bottom	Webs	
Season	Temp Change (°C)	Corner	Centre	Corner	Centre	Corner	Centre	Corner	Centre	Cantilever	Corner	Corner	Longitudinal	Transverse
Spring	7.7	15.8	25.4	18	13.2	15.2	8.6	5.2	10.4	20.6	15.6	6.2	11.2	5.6
Summer	11.4	19.4	27	17	17	15.8	7.8	7.4	11.6	22.4	16.8	7.2	15.4	6.2
Autumn	6.3	6.8	5.2	6.2	4.8	5.4	2.8	3.4	2.4	10	6.4	3.8	2.6	3.6
Winter	5.7	7.2	9.8	5.8	6.0	6.0	4.6	3.0	3.4	9.0	7.0	4.2	5.4	3.4

Table 6.3. Average strain changes (microstrain) with change in temperature (°C) for different seasons of the year – Grangetown Viaduct.

		Segment 1				Segment 6						Segment 11			
		Top Flange		Bottom Flange		Top Flange		Bottom Flange		Webs		Top Flange		Bottom Flange	
Season	Temp Change (°C)	Corner	Centre	Corner	Centre	Corner	Centre	Corner	Centre	Long.	Trans.	Cantilever	Centre	Corner	Centre
Spring	7.7	23.2	24.8	11.8	11.4	17.8	24.2	14.8	10.2	16	6.6	20.8	29.8	13.2	12.8
Summer	11.4	23	21.6	12.2	13	15	20.4	16.2	9	17.6	5.4	21.6	25.2	13.4	12.8
Autumn	6.3	6.8	5.8	4	4.8	5.6	6	2.4	4.2	3.6	3.4	10.6	7.4	2.2	2.6
Winter	5.7	5.5	8.8	3.3	6.0	6.0	8.0	6.0	3.0	6.5	2.5	11.0	11.0	6.0	5.0

Table 6.4. Selected relative humidities (%) and corresponding temperatures (°C) for each season.

	RH ≈ 80 %		RH ≈ 82.5 %		RH ≈ 85 %		RH ≈ 87.5 %		RH ≈ 90 %	
Season	RH (%)	Temp (°C)	RH (%)	Temp (°C)	RH (%)	Temp (°C)	RH (%)	Temp (°C)	RH (%)	Temp (°C)
Spring	80.1	9.5	82.6	7.5	84.9	11.1	87.3	10.6	90.0	8.1
Summer	79.9	20.6	82.6	20.9	84.6	19.3	87.5	19.4	89.3	19.2
Autumn	79.7	8.8	82.6	7.3	84.9	6.0	87.3	13.2	90.1	4.2
Winter	79.9	3.8	82.5	7.1	85.0	4.2	87.4	5.5	90.2	4.6
Average	79.9		82.6		84.9		87.4		89.9	

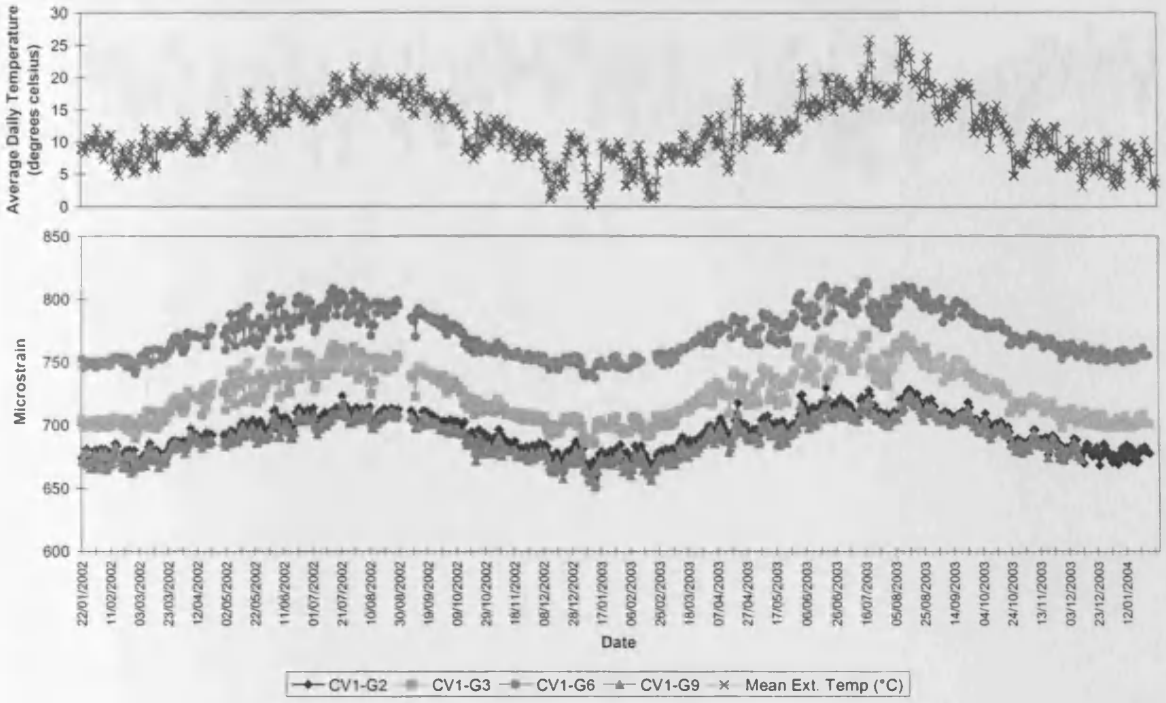

Figure 6.1. Comparison between daily measured strains and daily average temperature in the top flange of segment 1, Cogan Viaduct.

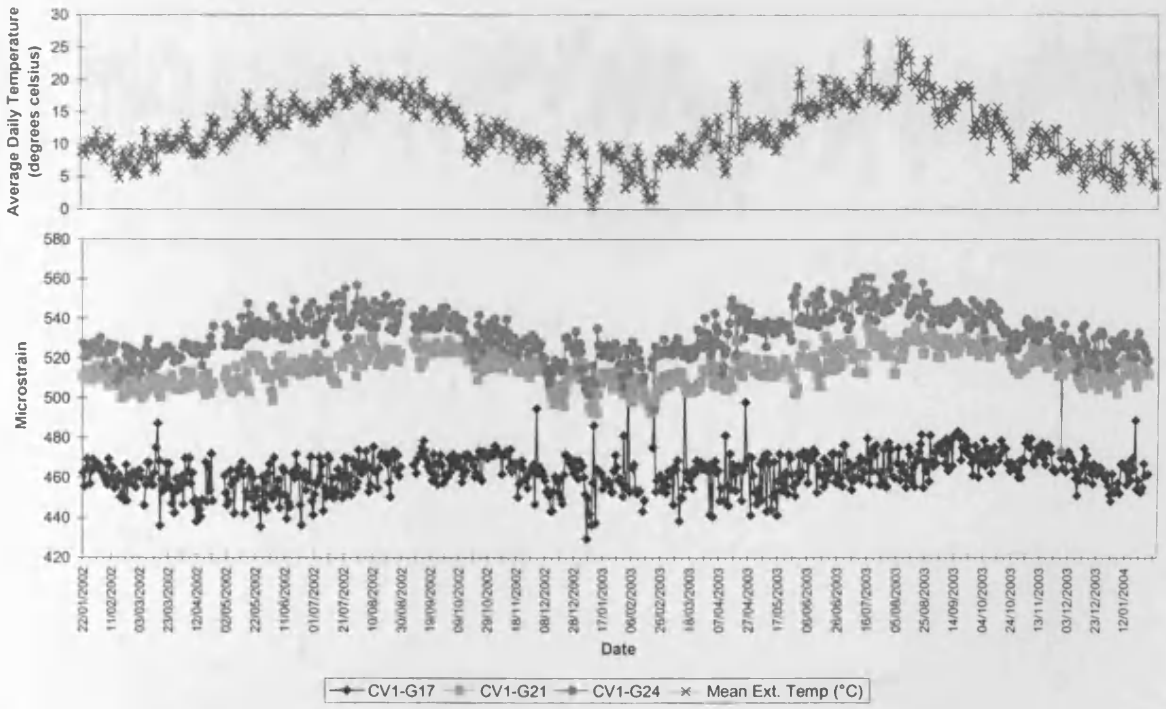

Figure 6.2. Comparison between daily measured strains and daily average temperature in the bottom flange of segment 1, Cogan Viaduct.

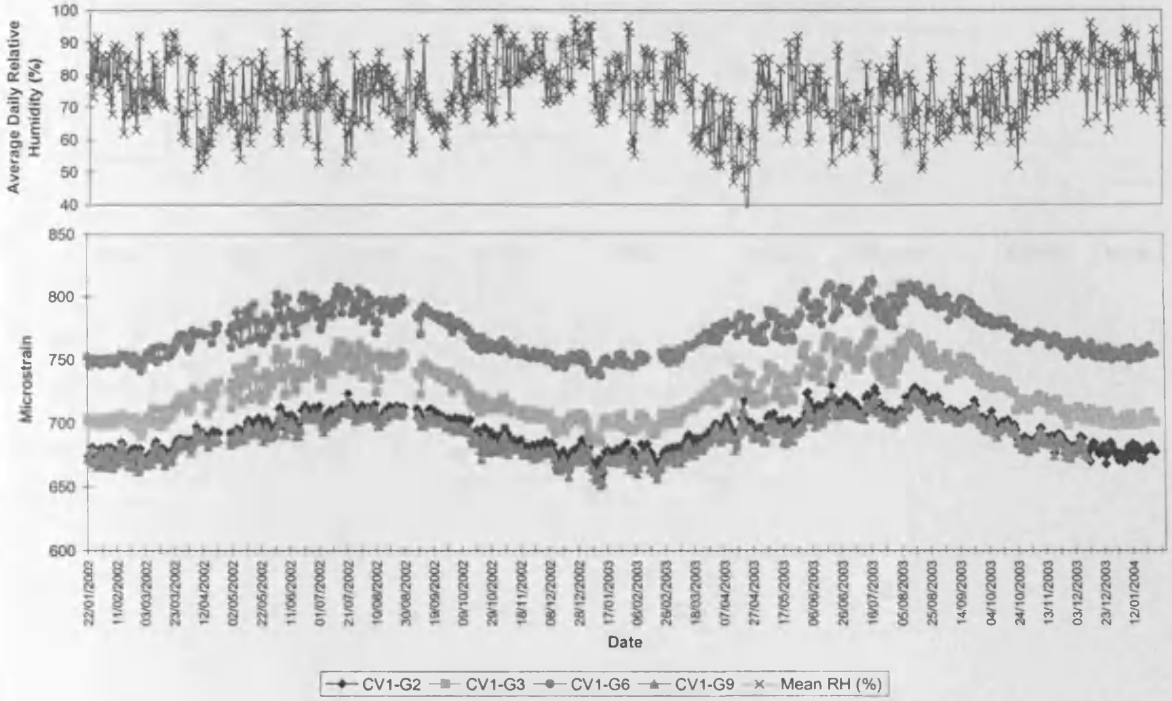

Figure 6.3. Comparison between daily measured strains and daily average relative humidity in the top flange of segment 1, Cogan Viaduct.

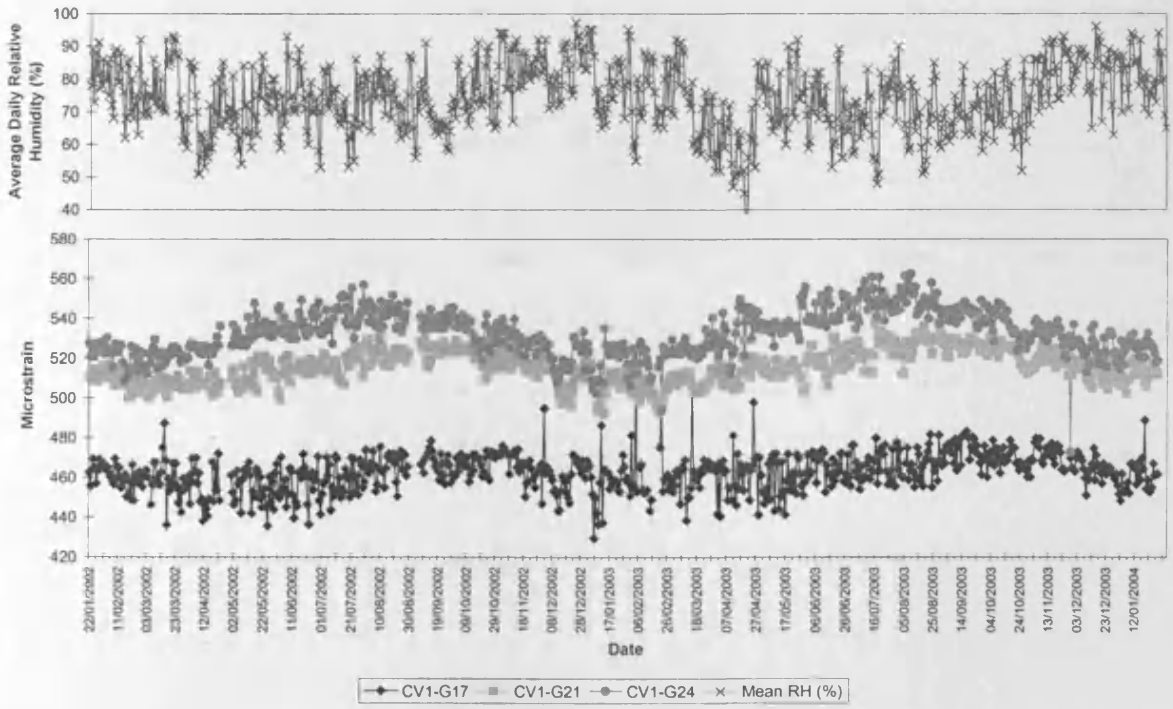

Figure 6.4. Comparison between daily measured strains and daily average relative humidity in the top flange of segment 1, Cogan Viaduct.

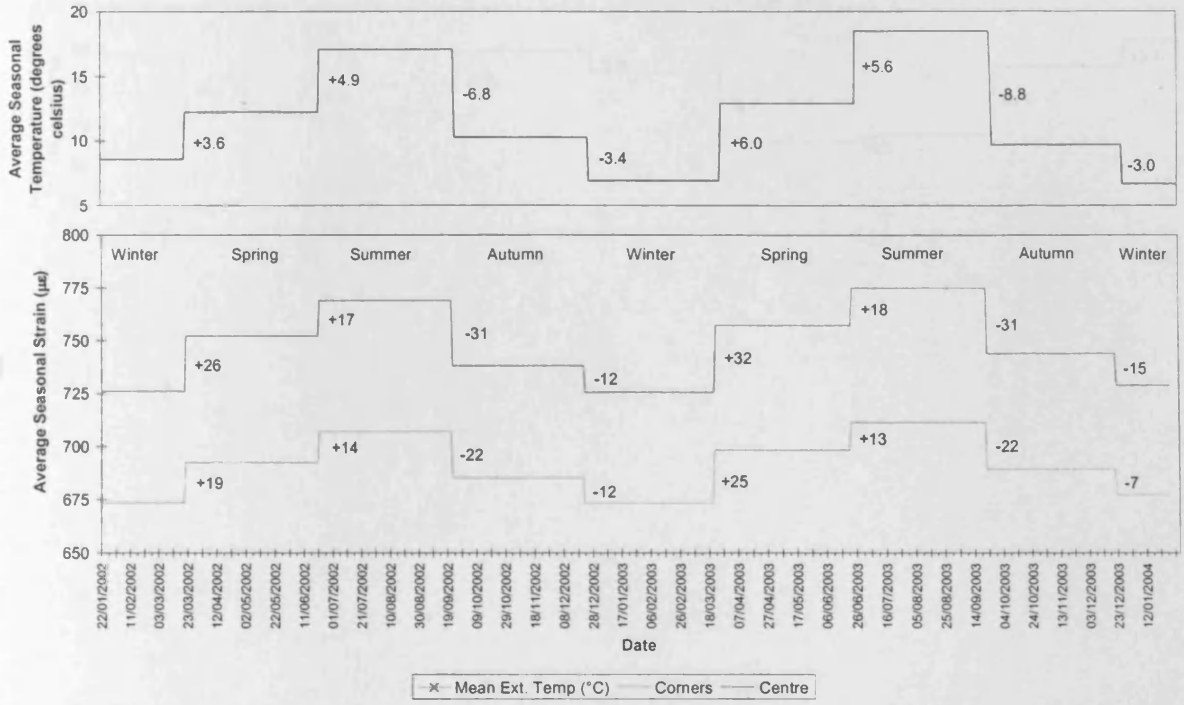

Figure 6.5. Comparison between the change in average seasonal strain with the change in average seasonal temperature in the top flange of segment 1, Cogan Viaduct.

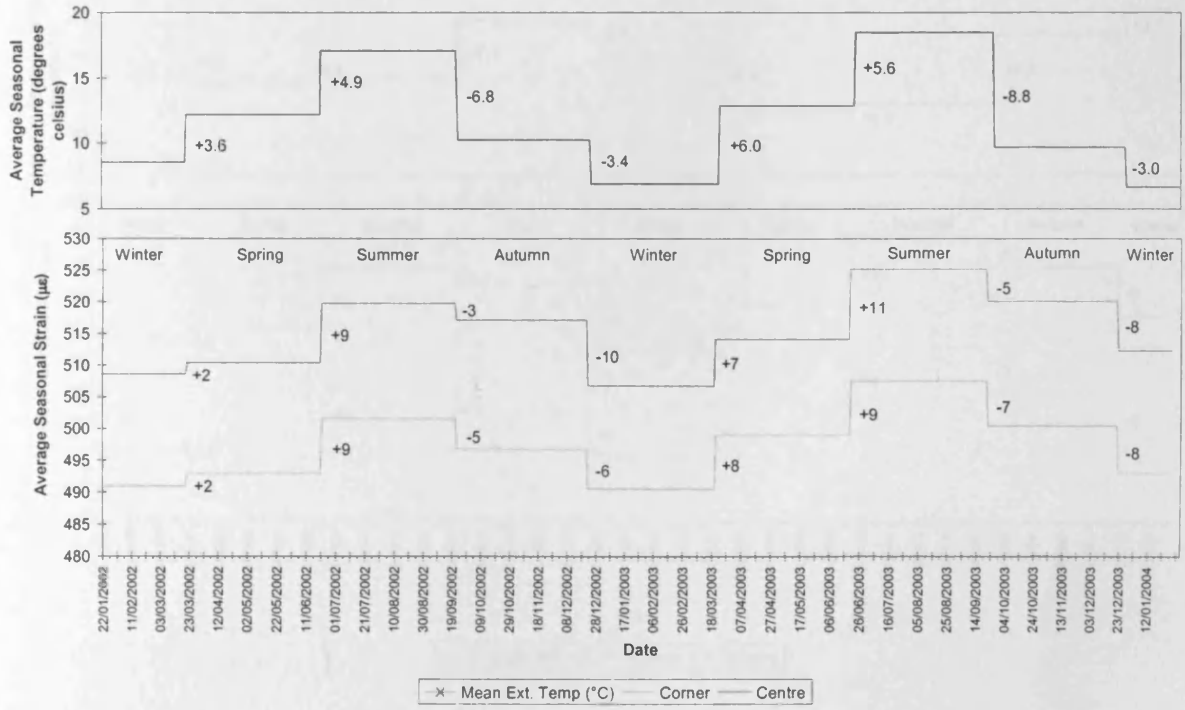

Figure 6.6. Comparison between the change in average seasonal strain with the change in average seasonal temperature in the bottom flange of segment 1, Cogan Viaduct.

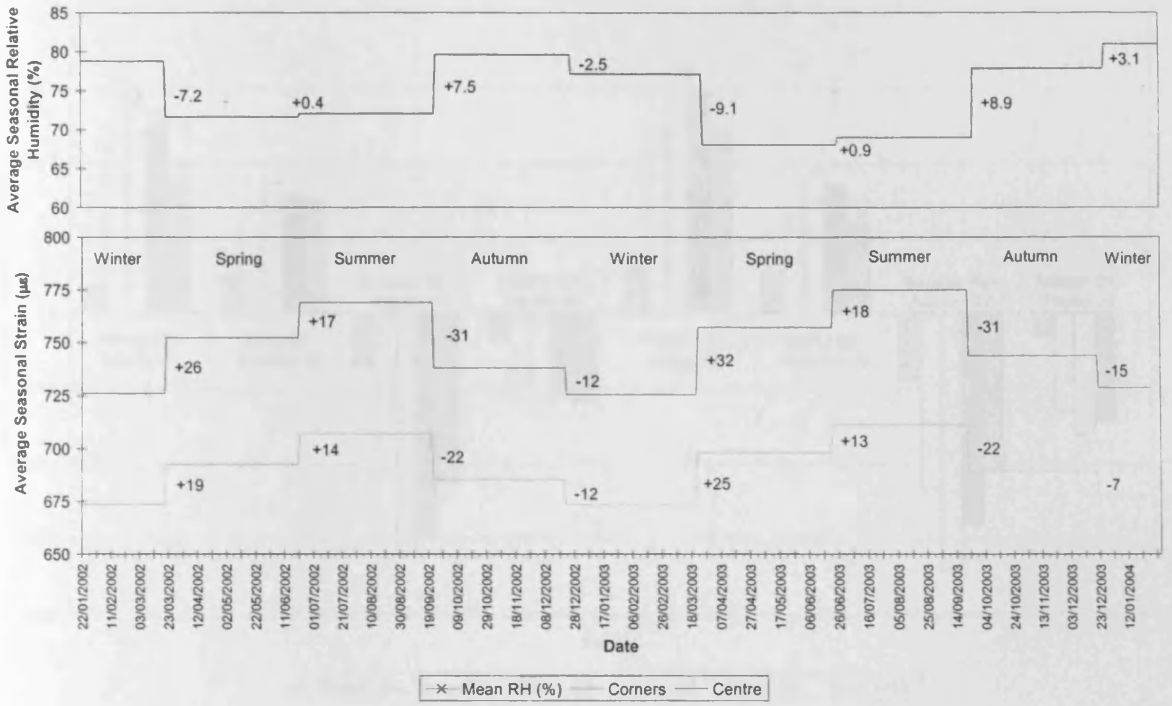

Figure 6.7. Comparison between the change in average seasonal strain with the change in average seasonal relative humidity in the top flange of segment 1, Cogan Viaduct.

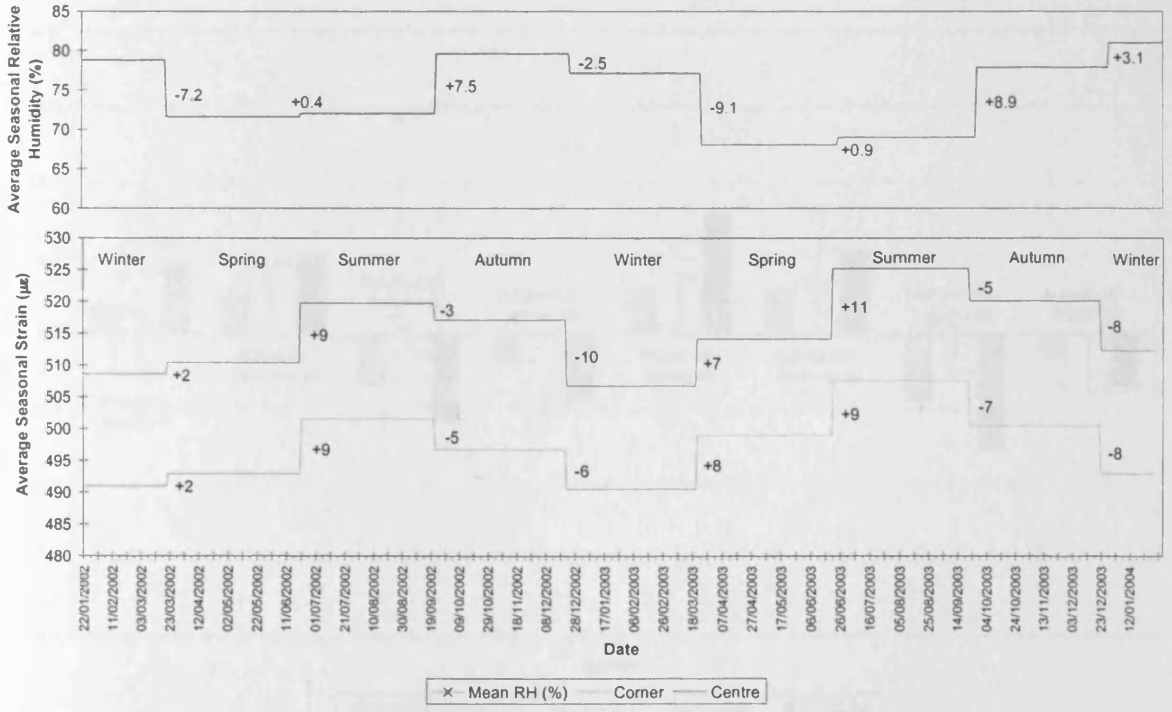

Figure 6.8. Comparison between the change in average seasonal strain with the change in average seasonal relative humidity in the bottom flange of segment 1, Cogan Viaduct.

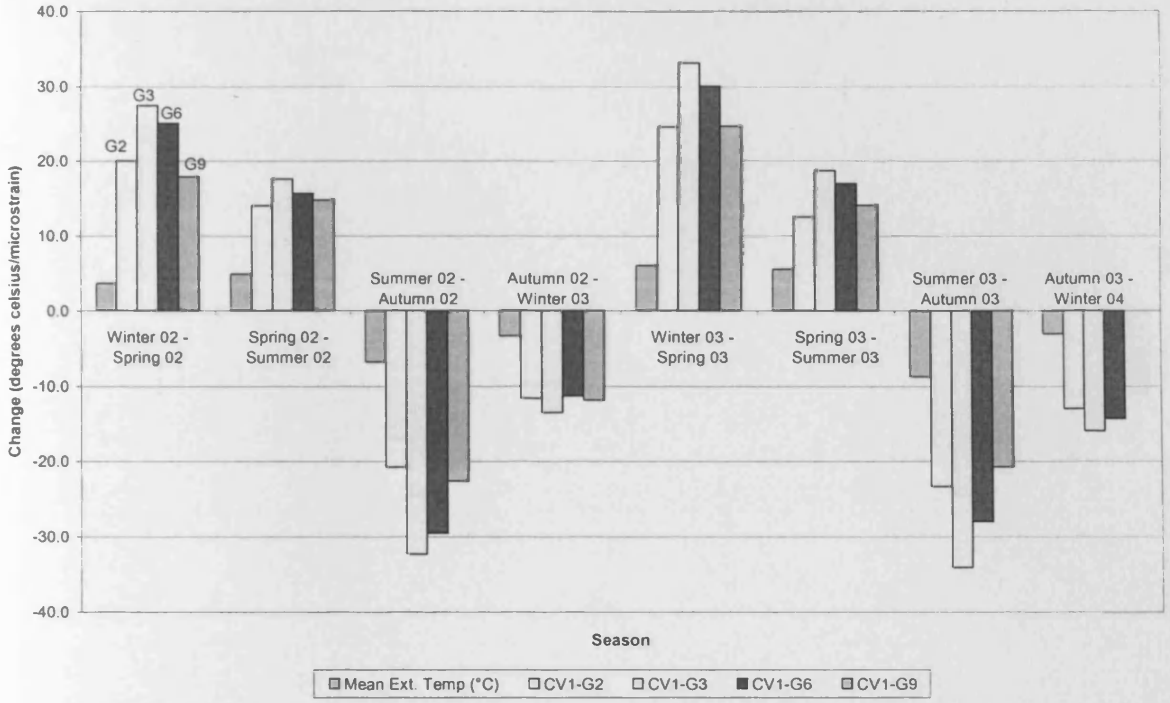

Figure 6.9. Comparison between the change in average seasonal temperature and the change in average seasonal strain for gauges in the top flange of segment 1, Cogan Viaduct.

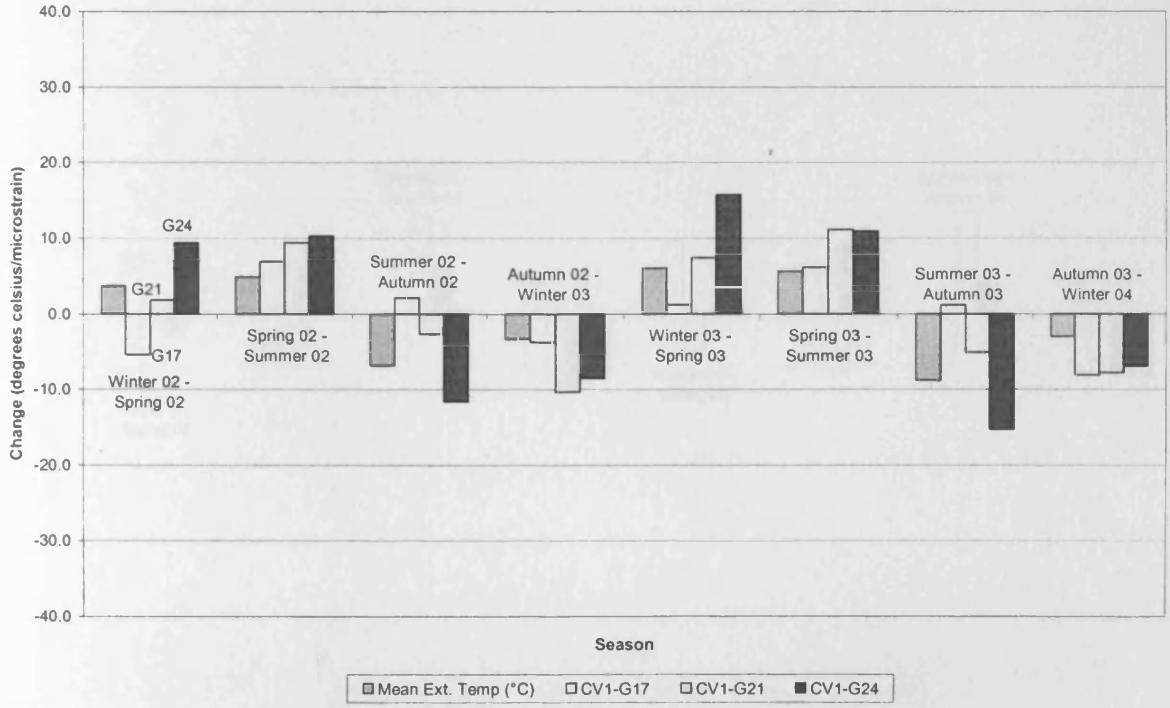

Figure 6.10. Comparison between the change in average seasonal temperature and the change in average seasonal strain for gauges in the bottom flange of segment 1, Cogan Viaduct.

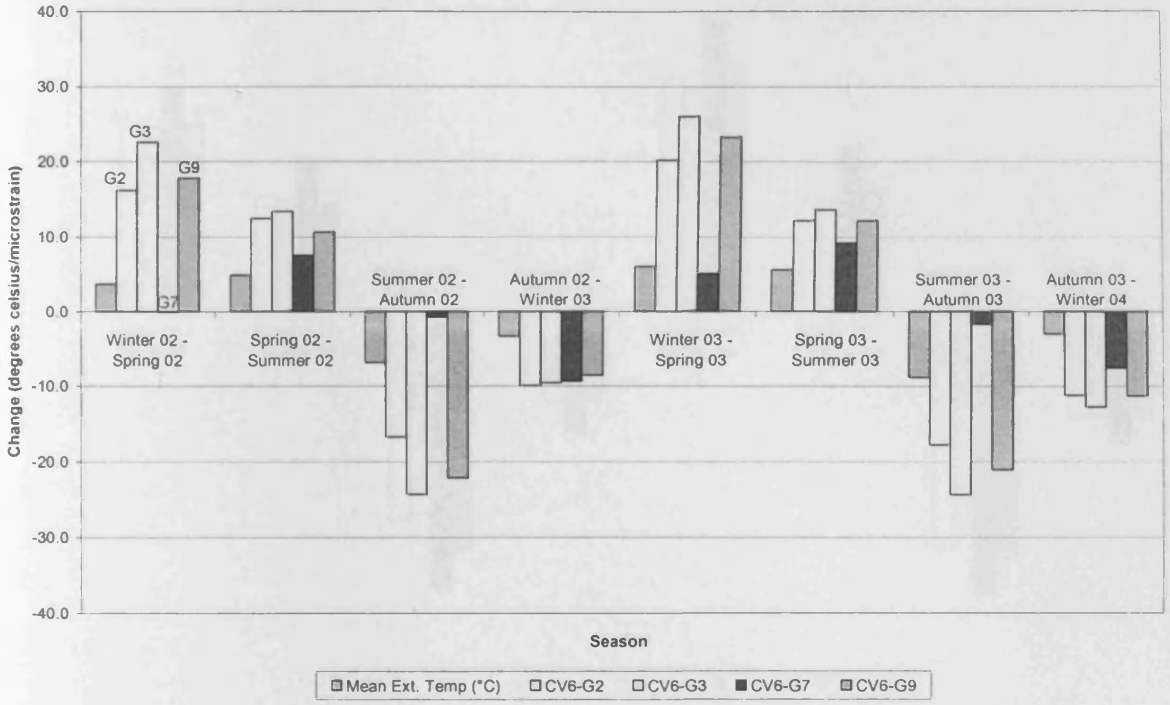

Figure 6.11. Comparison between the change in average seasonal temperature and the change in average seasonal strain for gauges in the top flange of segment 6, Cogan Viaduct.

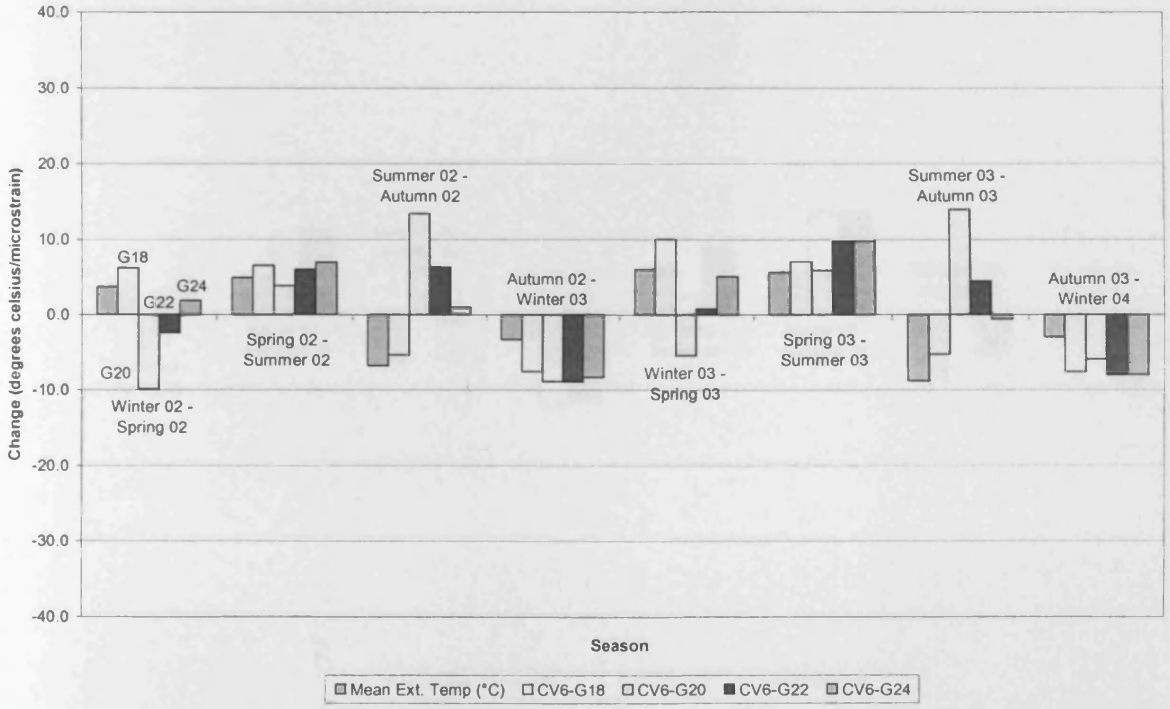

Figure 6.12. Comparison between the change in average seasonal temperature and the change in average seasonal strain for gauges in the bottom flange of segment 6, Cogan Viaduct.

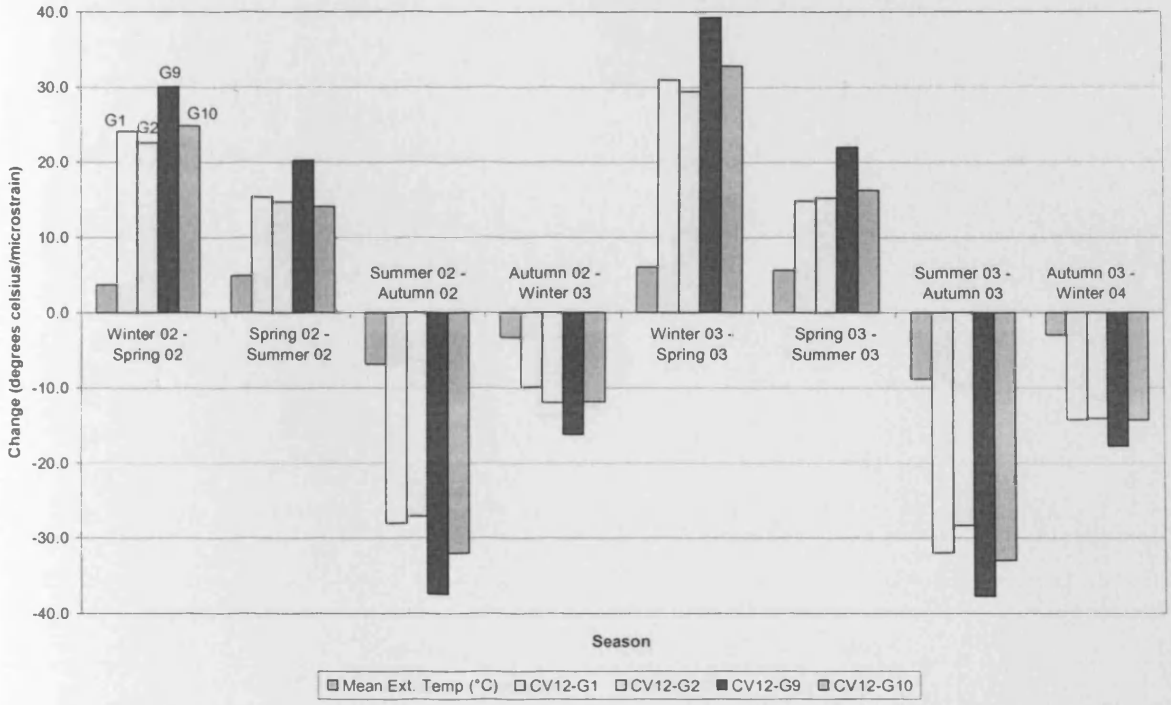

Figure 6.13. Comparison between the change in average seasonal temperature and the change in average seasonal strain for gauges in the top flange of segment 12, Cogan Viaduct.

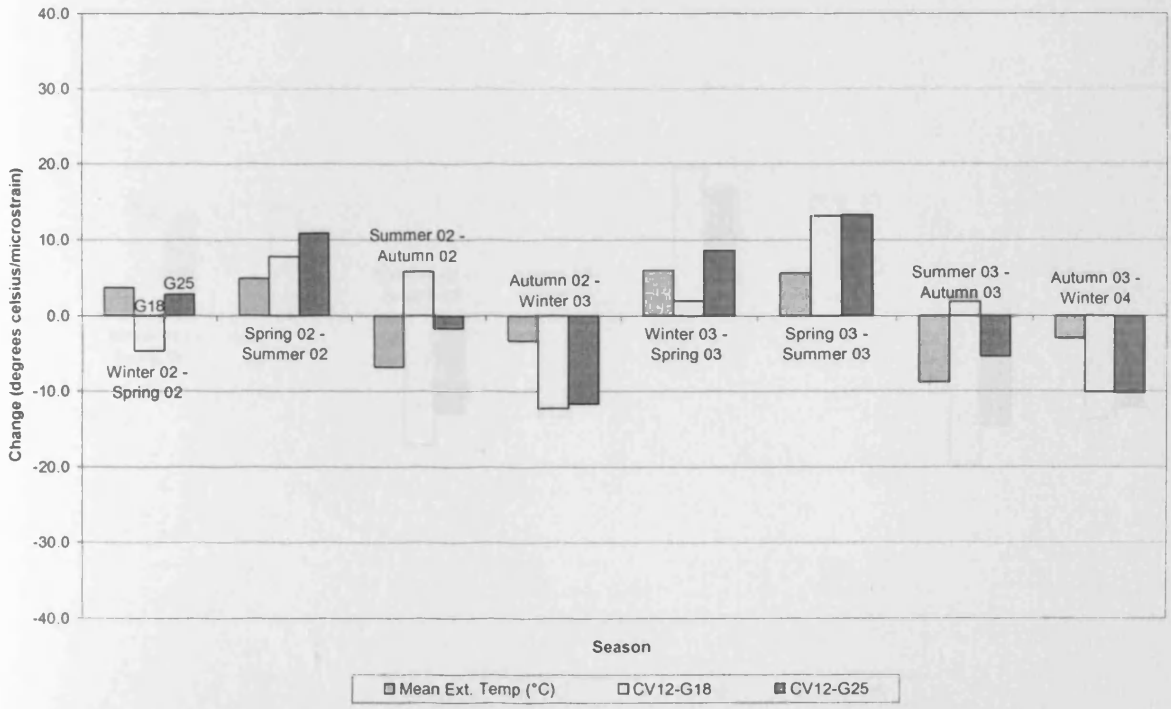

Figure 6.14. Comparison between the change in average seasonal temperature and the change in average seasonal strain for gauges in the bottom flange of segment 12, Cogan Viaduct.

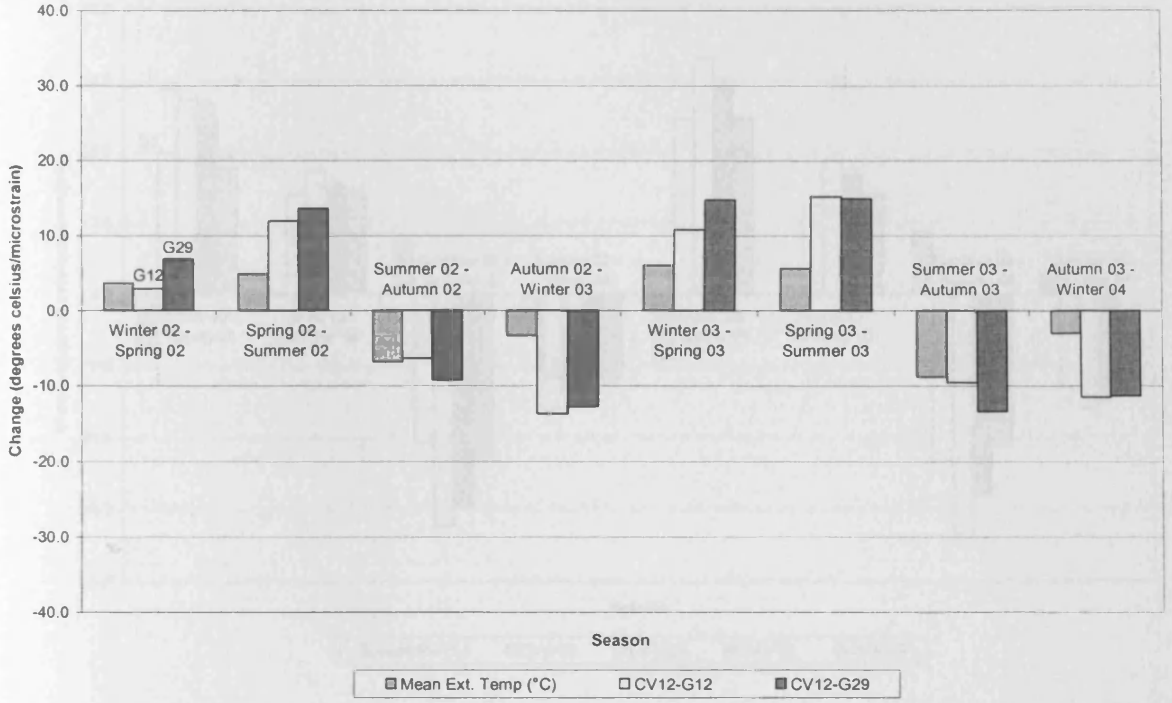

Figure 6.15. Comparison between the change in average seasonal temperature and the change in average seasonal strain for gauges in the webs of segment 12, Cogan Viaduct.

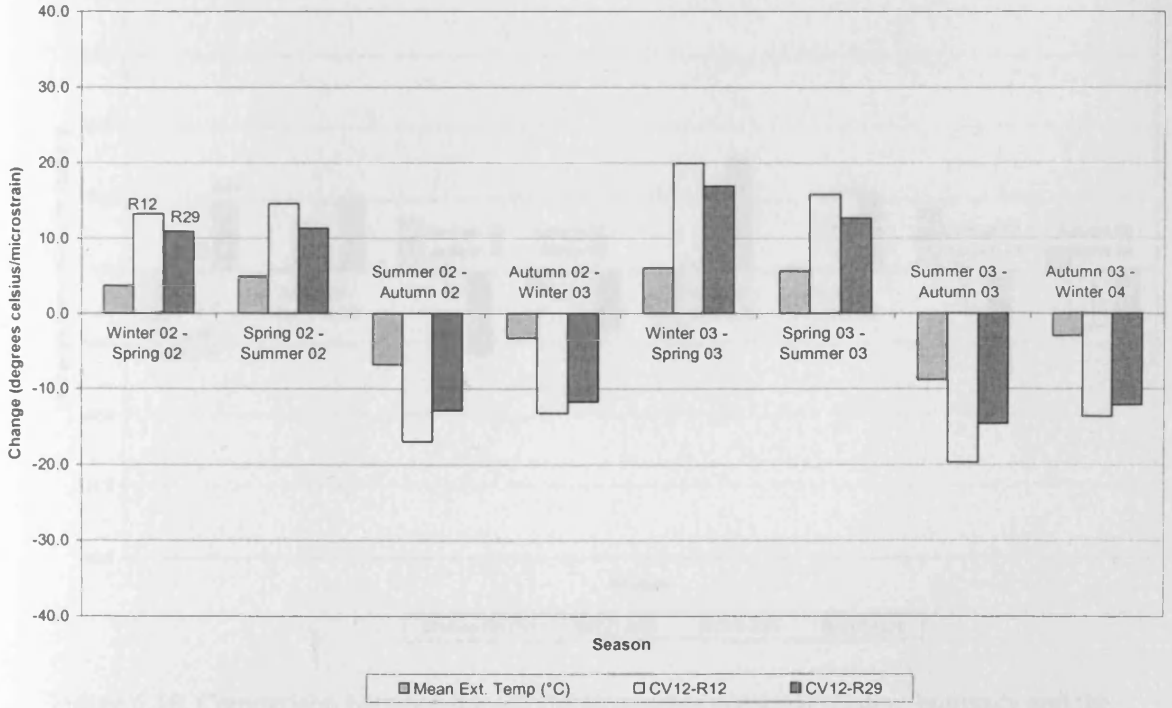

Figure 6.16. Comparison between the change in average seasonal temperature and the change in average seasonal *transverse* strain for gauges in the webs of segment 12, Cogan Viaduct.

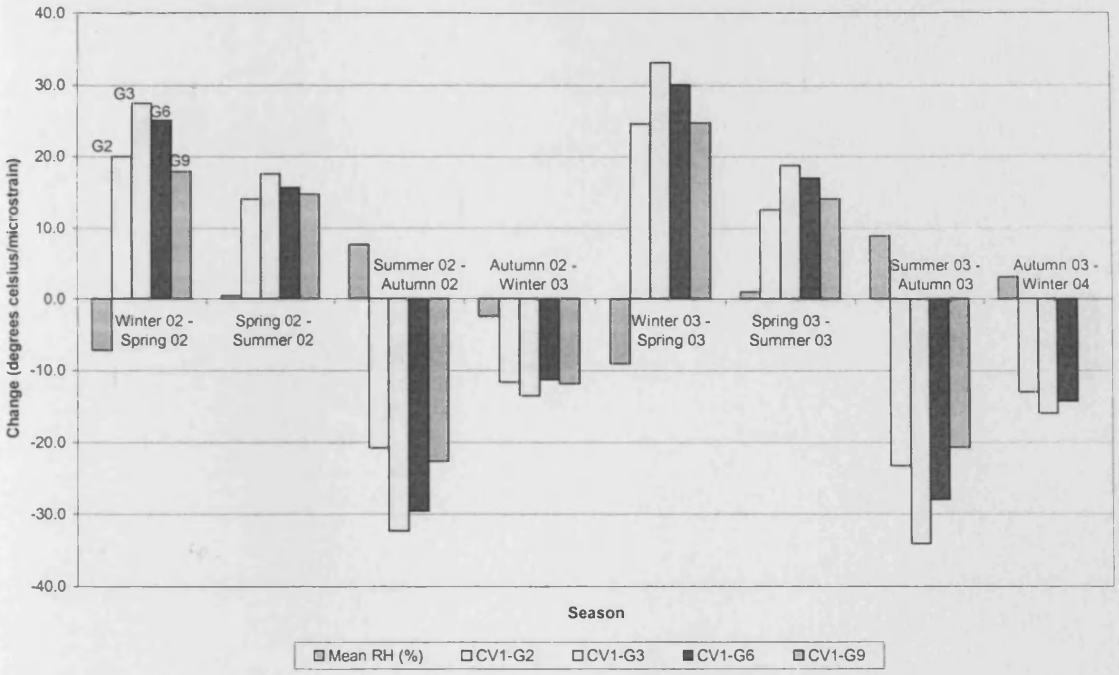

Figure 6.17. Comparison between the change in average seasonal relative humidity and the change in average seasonal strain for gauges in the top flange of segment 1, Cogan Viaduct.

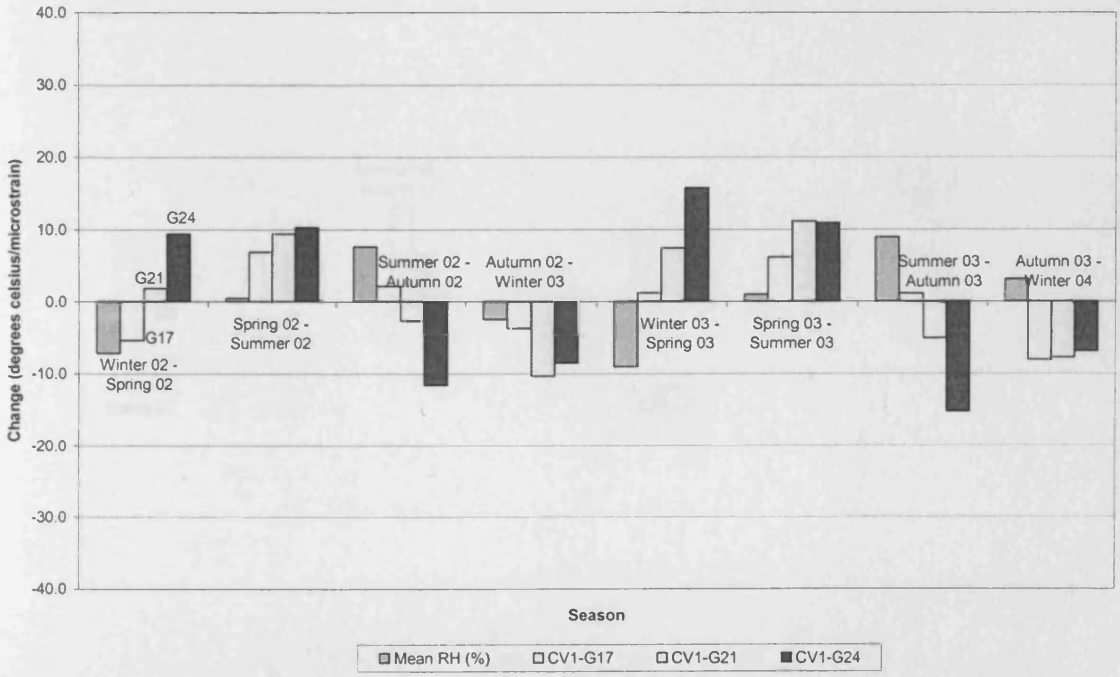

Figure 6.18. Comparison between the change in average seasonal relative humidity and the change in average seasonal strain for gauges in the bottom flange of segment 1, Cogan Viaduct.

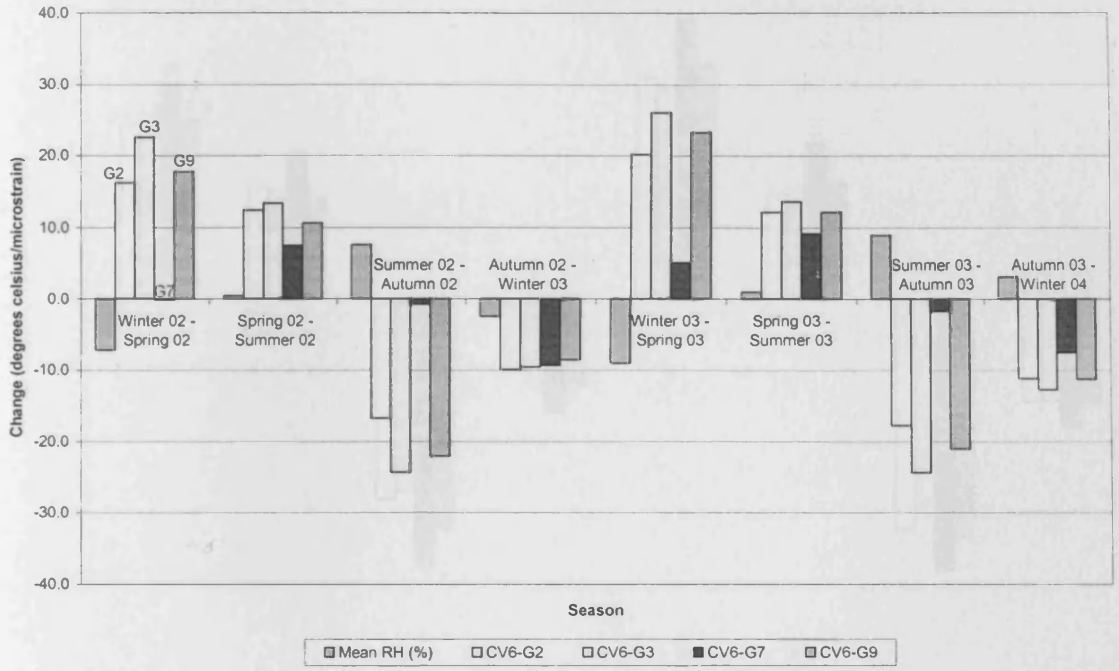

Figure 6.19. Comparison between the change in average seasonal relative humidity and the change in average seasonal strain for gauges in the top flange of segment 6, Cogan Viaduct.

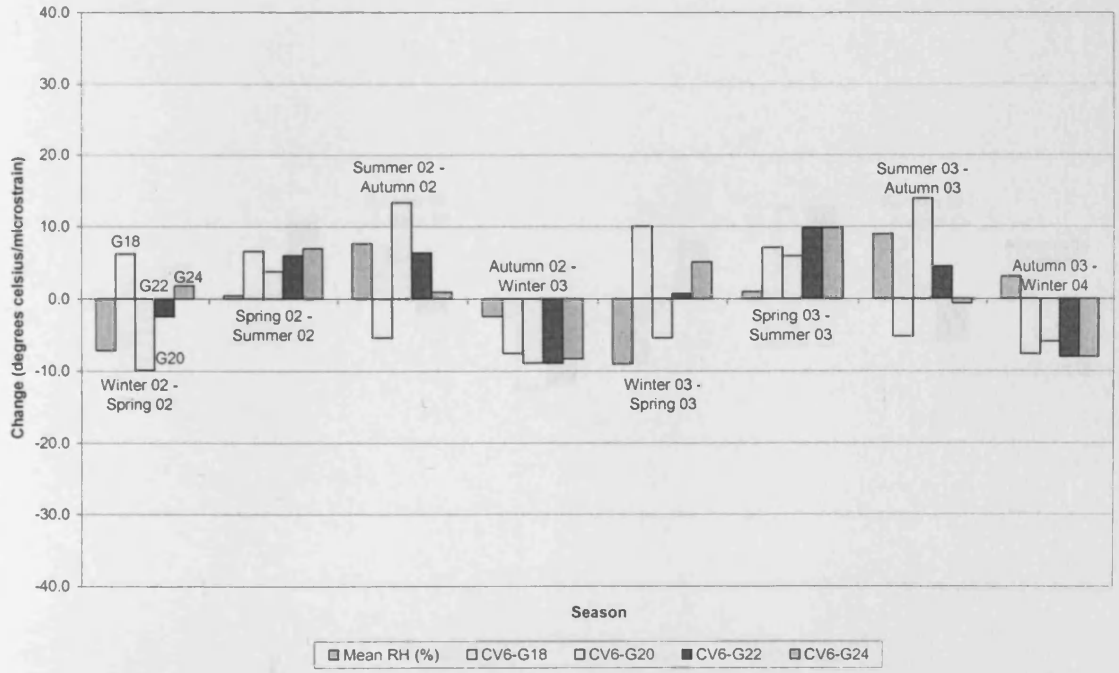

Figure 6.20. Comparison between the change in average seasonal relative humidity and the change in average seasonal strain for gauges in the bottom flange of segment 6, Cogan Viaduct.

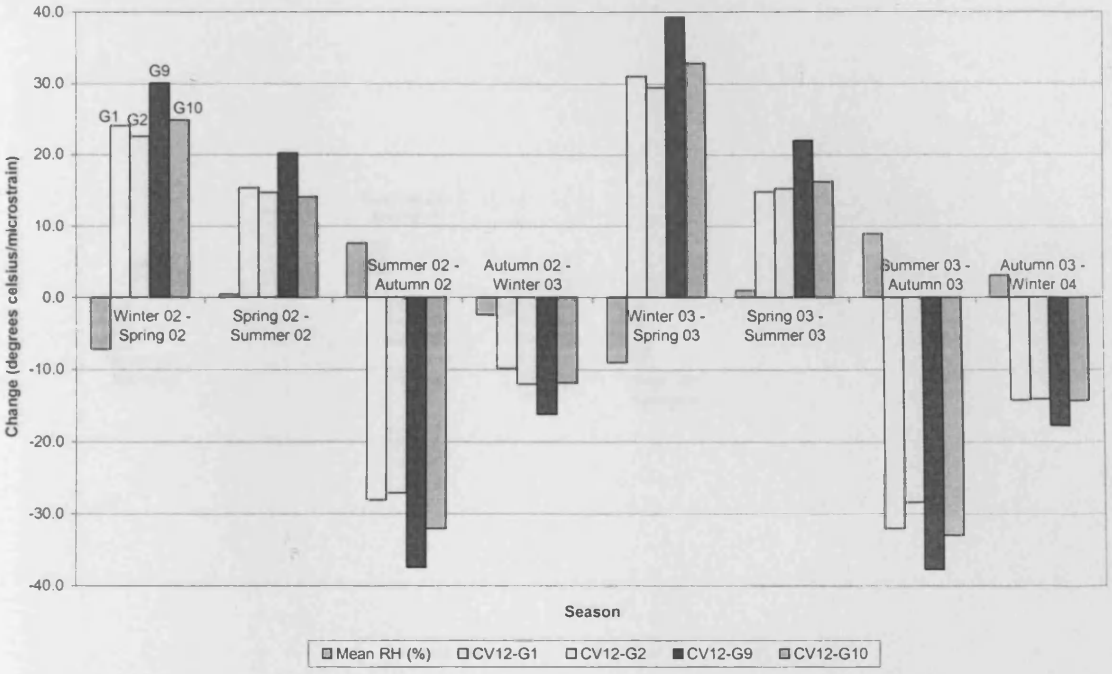

Figure 6.21. Comparison between the change in average seasonal relative humidity and the change in average seasonal strain for gauges in the top flange of segment 12, Cogan Viaduct.

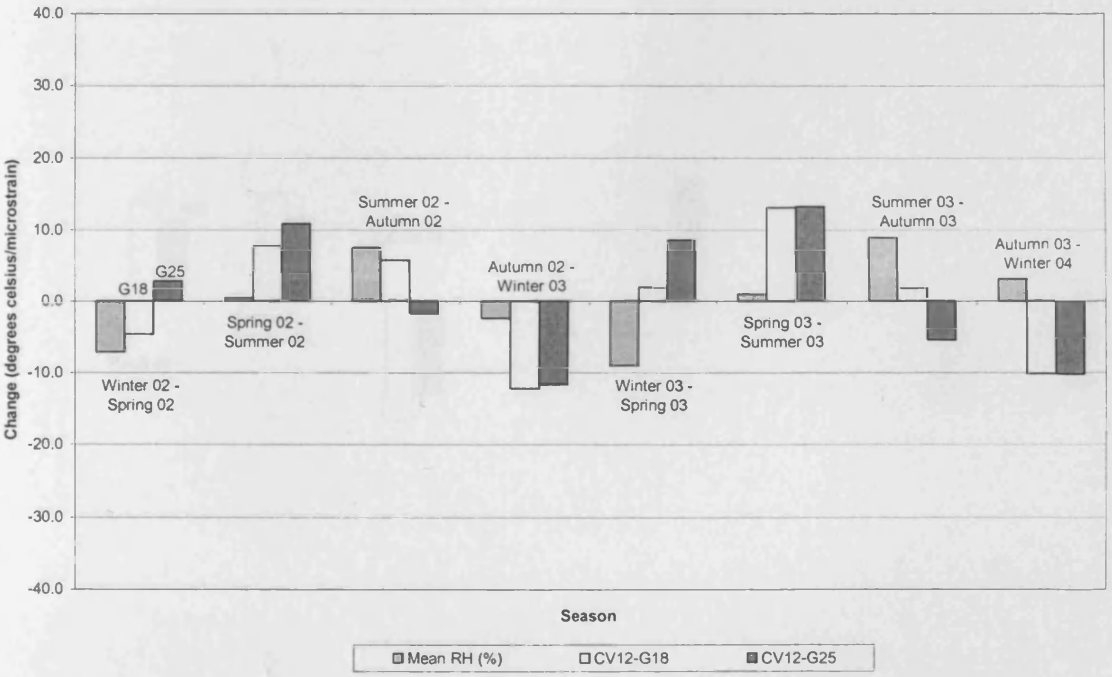

Figure 6.22. Comparison between the change in average seasonal relative humidity and the change in average seasonal strain for gauges in the bottom flange of segment 12, Cogan Viaduct.

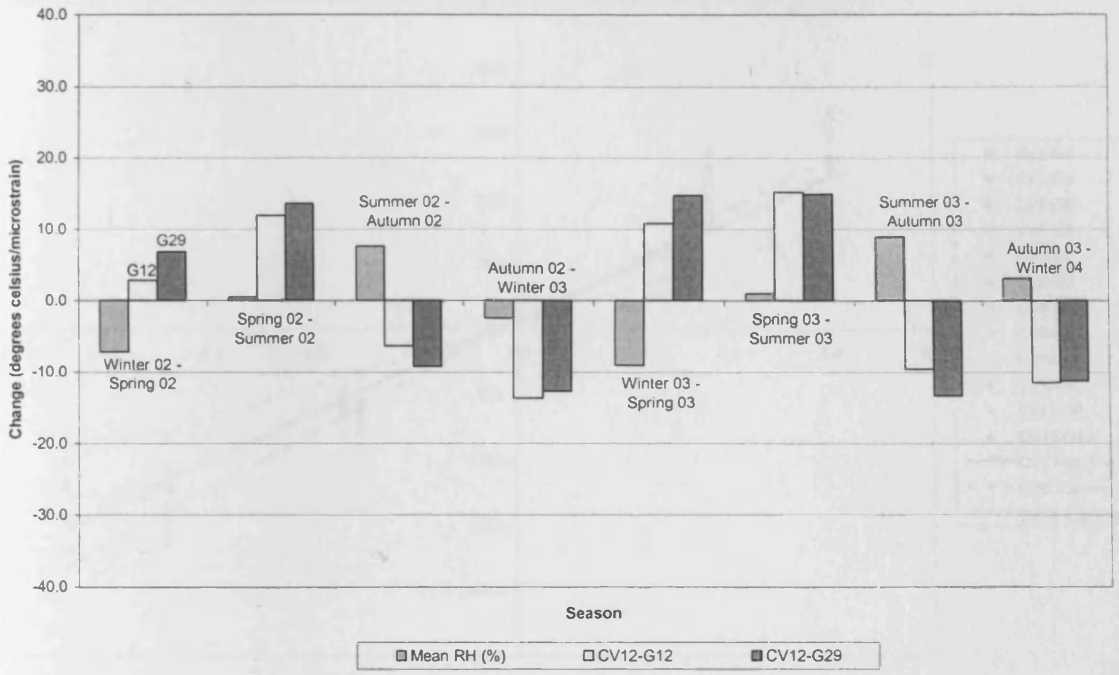

Figure 6.23. Comparison between the change in average seasonal relative humidity and the change in average seasonal strain for gauges in the webs of segment 12, Cogan Viaduct.

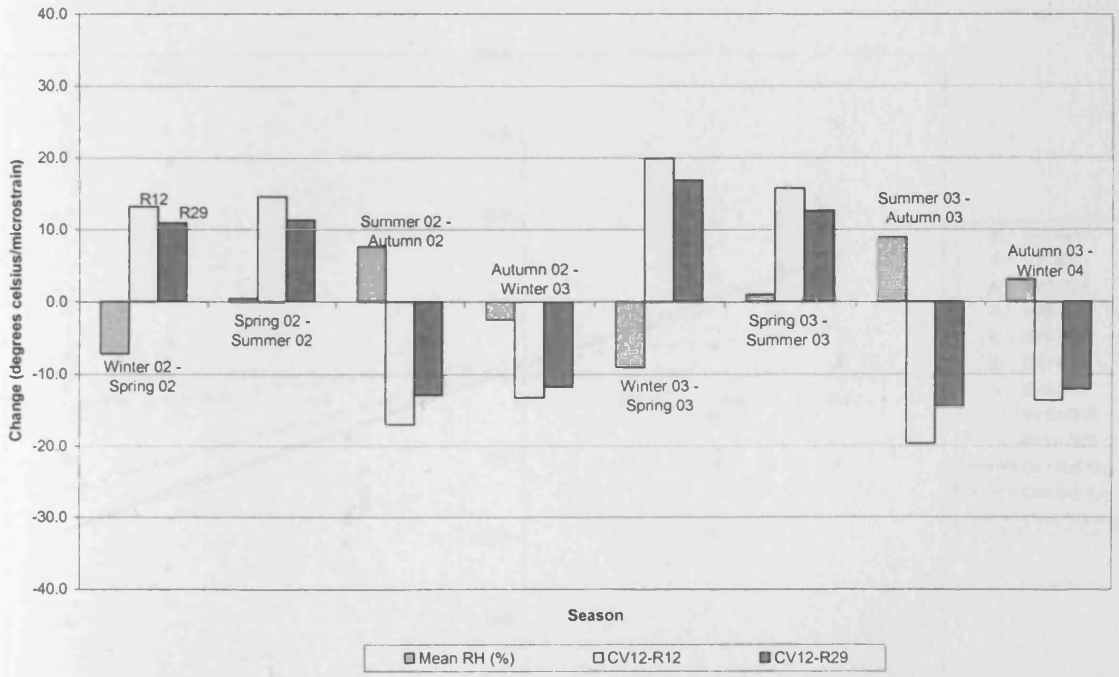

Figure 6.24. Comparison between the change in average seasonal relative humidity and the change in average seasonal *transverse* strain for gauges in the webs of segment 12, Cogan Viaduct.

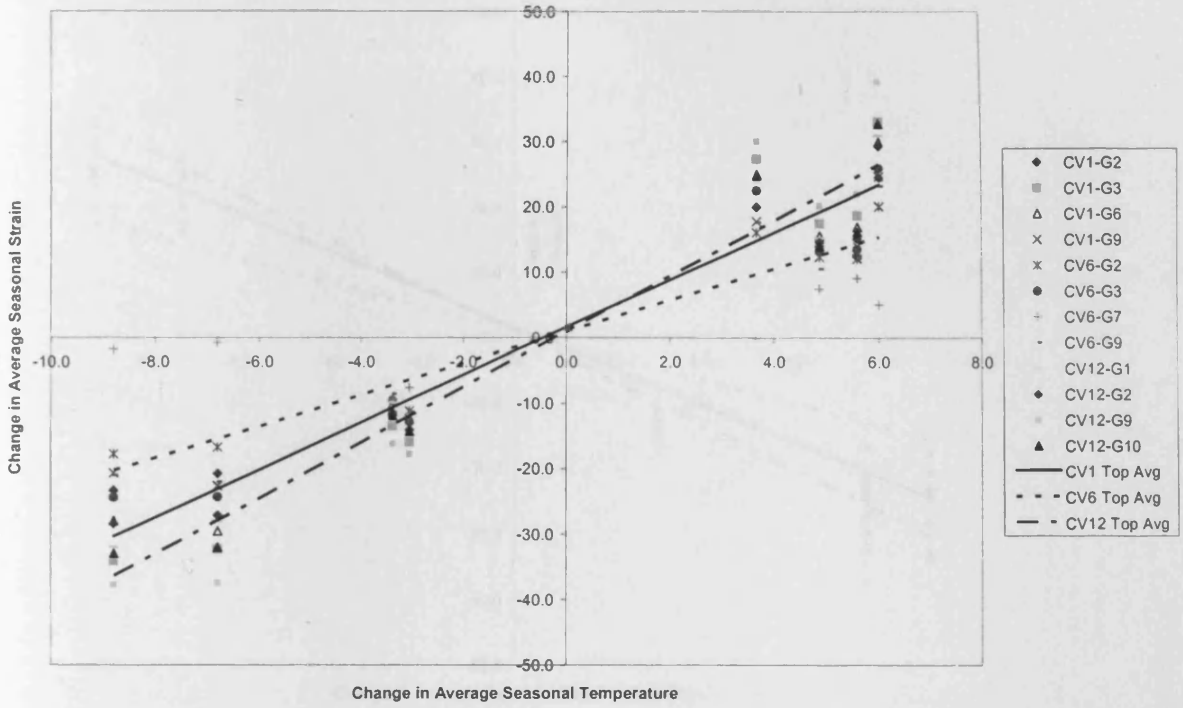

Figure 6.25. Relationship between the change in average seasonal temperature and the change in average seasonal strain for all gauges in the top flange of Cogan Viaduct.

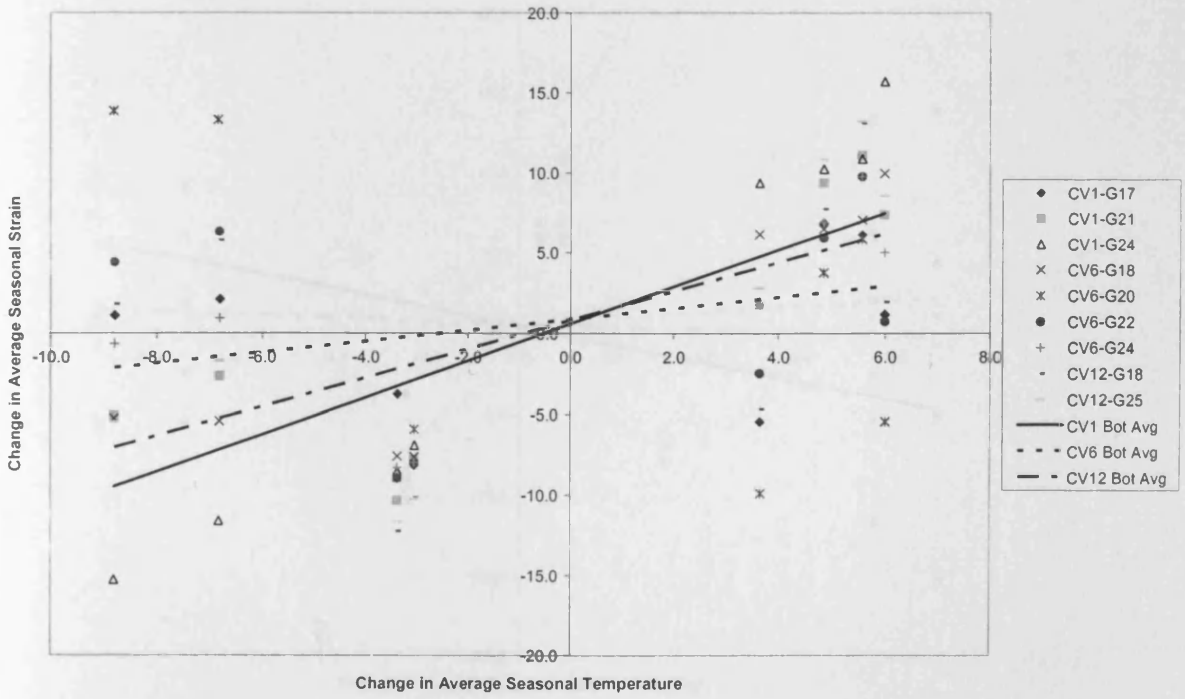

Figure 6.26. Relationship between the change in average seasonal temperature and the change in average seasonal strain for all gauges in the bottom flange of Cogan Viaduct.

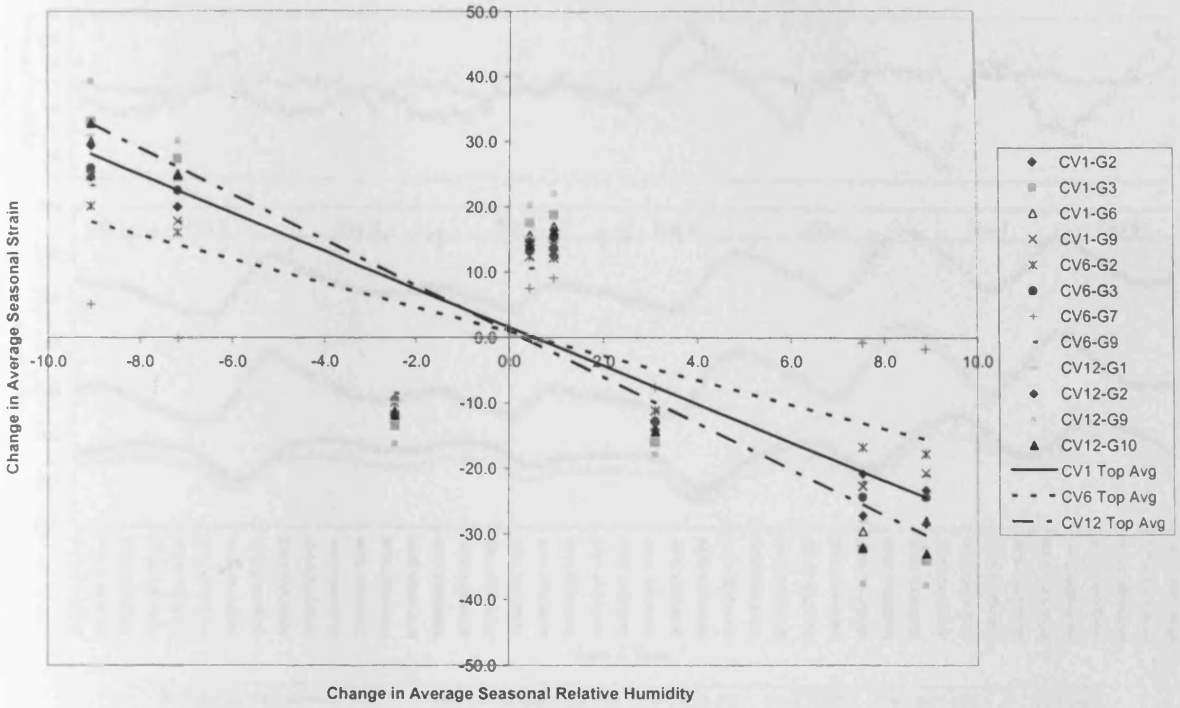

Figure 6.27. Relationship between the change in average seasonal relative humidity and the change in average seasonal strain for all gauges in the top flange of Cogan Viaduct.

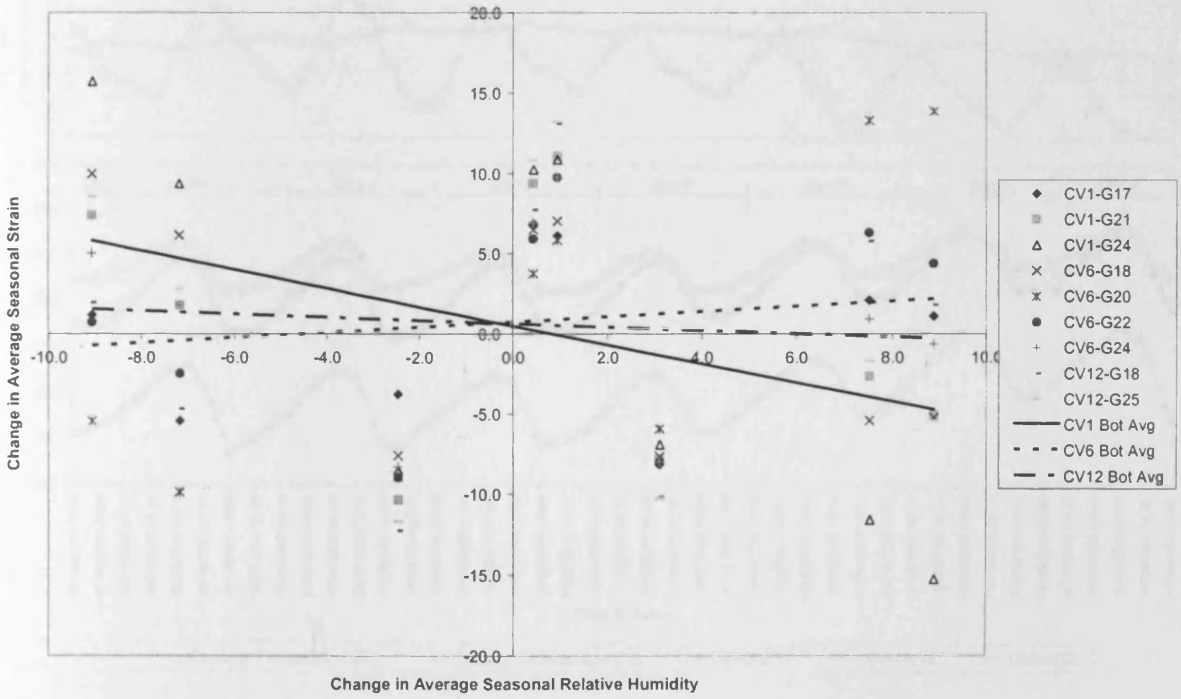

Figure 6.28. Relationship between the change in average seasonal relative humidity and the change in average seasonal strain for all gauges in the bottom flange of Cogan Viaduct.

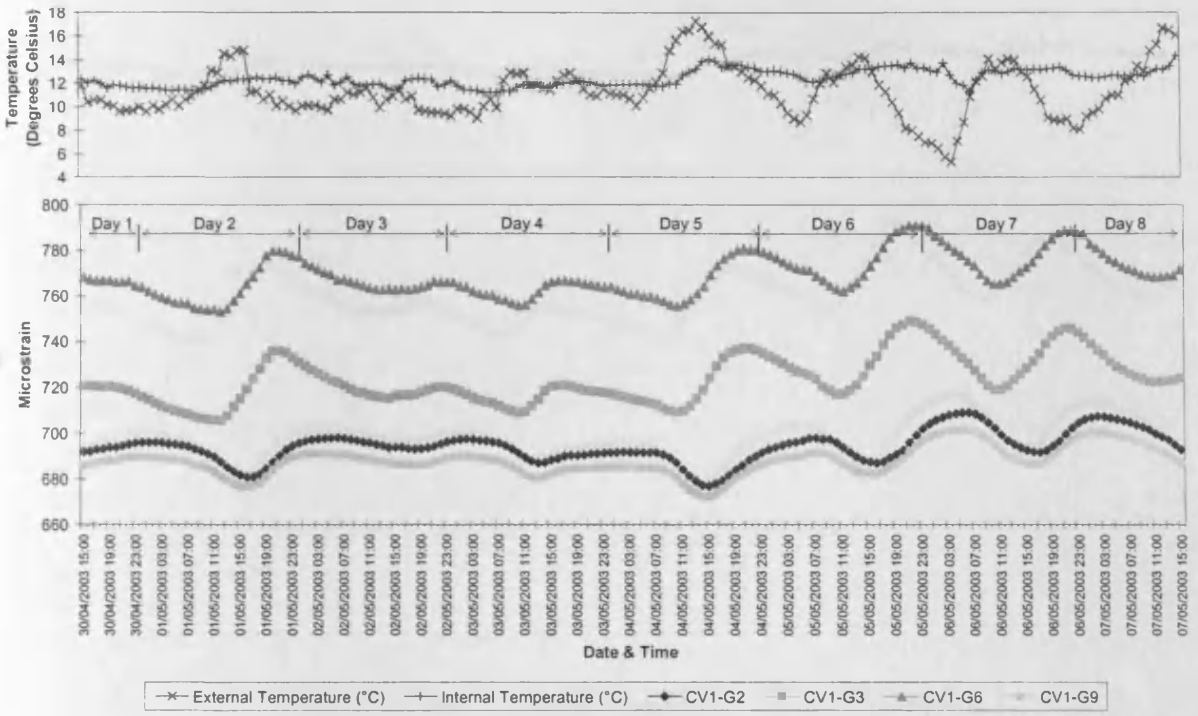

Figure 6.29. Comparison between hourly measured strains and hourly external and internal air temperature in the top flange of segment 1, Cogan Viaduct, spring 2003.

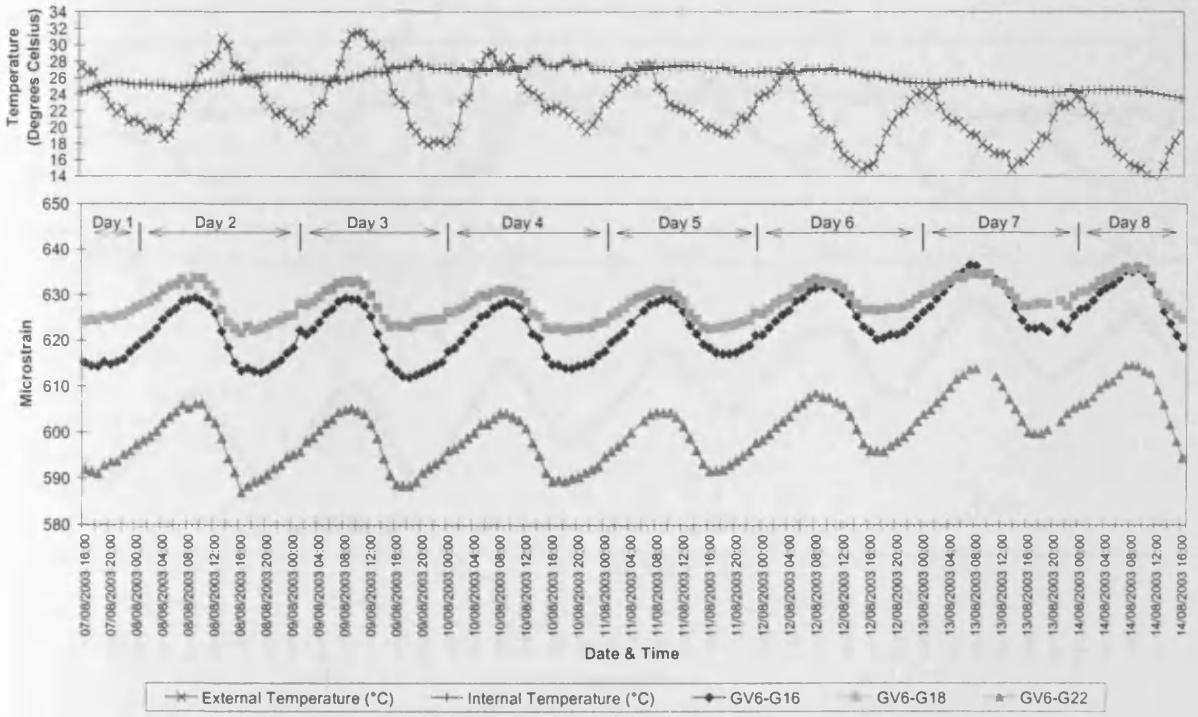

Figure 6.30. Comparison between hourly measured strains and hourly external and internal air temperature in the bottom flange of segment 6, Grangetown Viaduct, summer 2003.

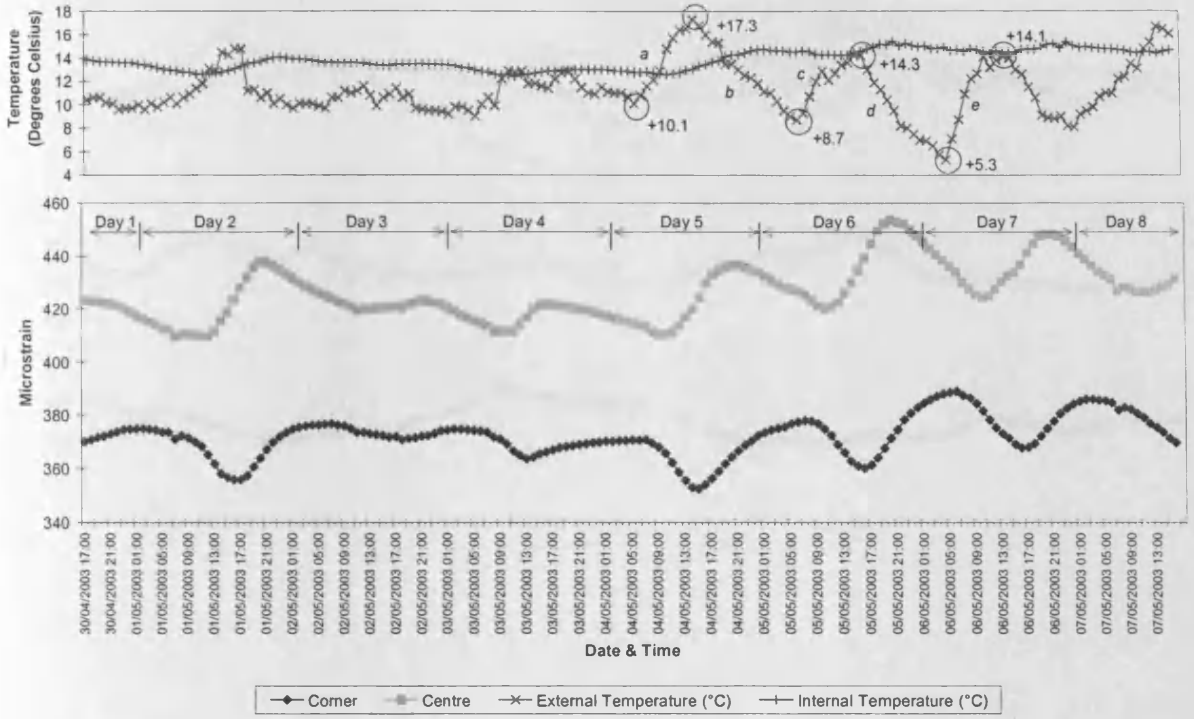

Figure 6.31. Comparison between hourly measured strains and hourly external and internal air temperature for locations in the top flange of segment 1, Grangetown Viaduct, spring 2003.

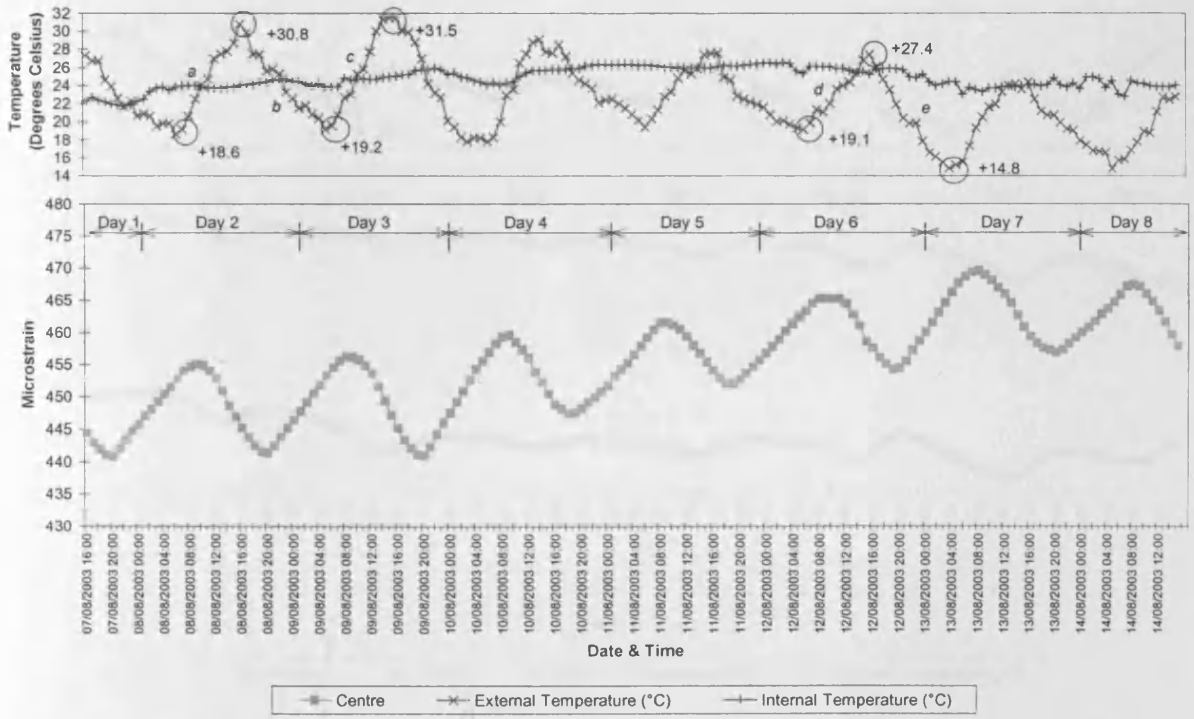

Figure 6.32. Comparison between hourly measured strains and hourly external and internal air temperature for locations in the webs of segment 12, Cogan Viaduct, summer 2003.

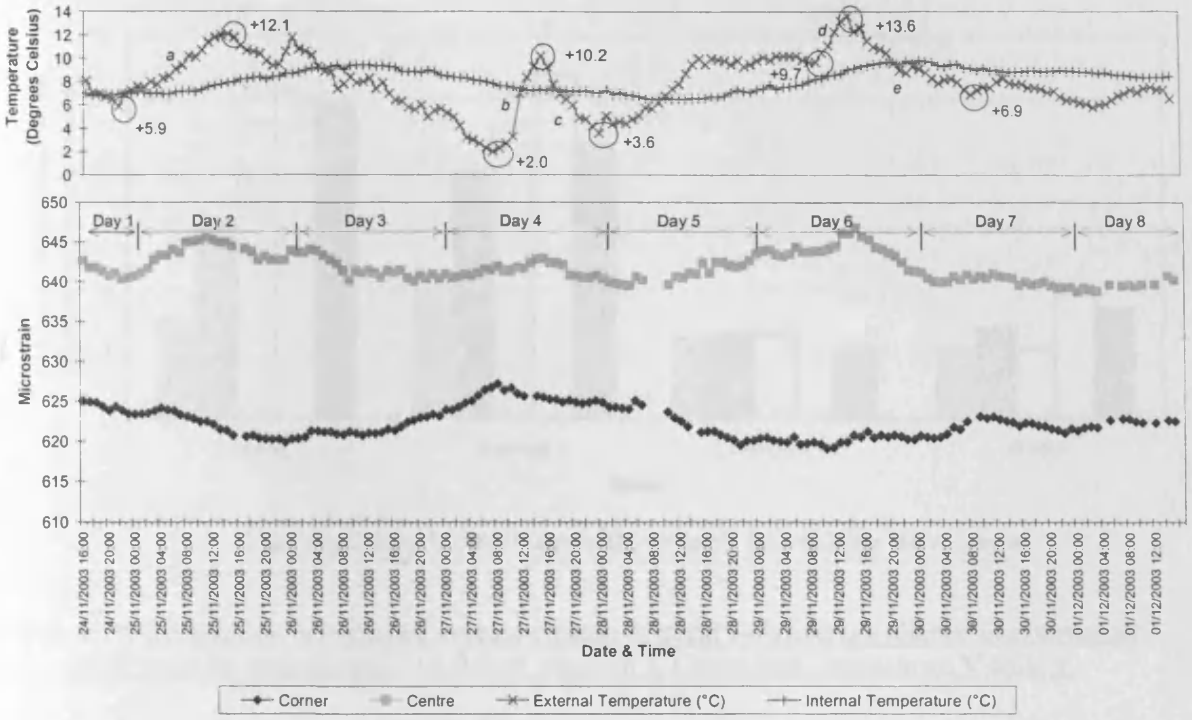

Figure 6.33. Comparison between hourly measured strains and hourly external and internal air temperature for locations in the bottom flange of segment 6, Grangetown Viaduct, autumn 2003.

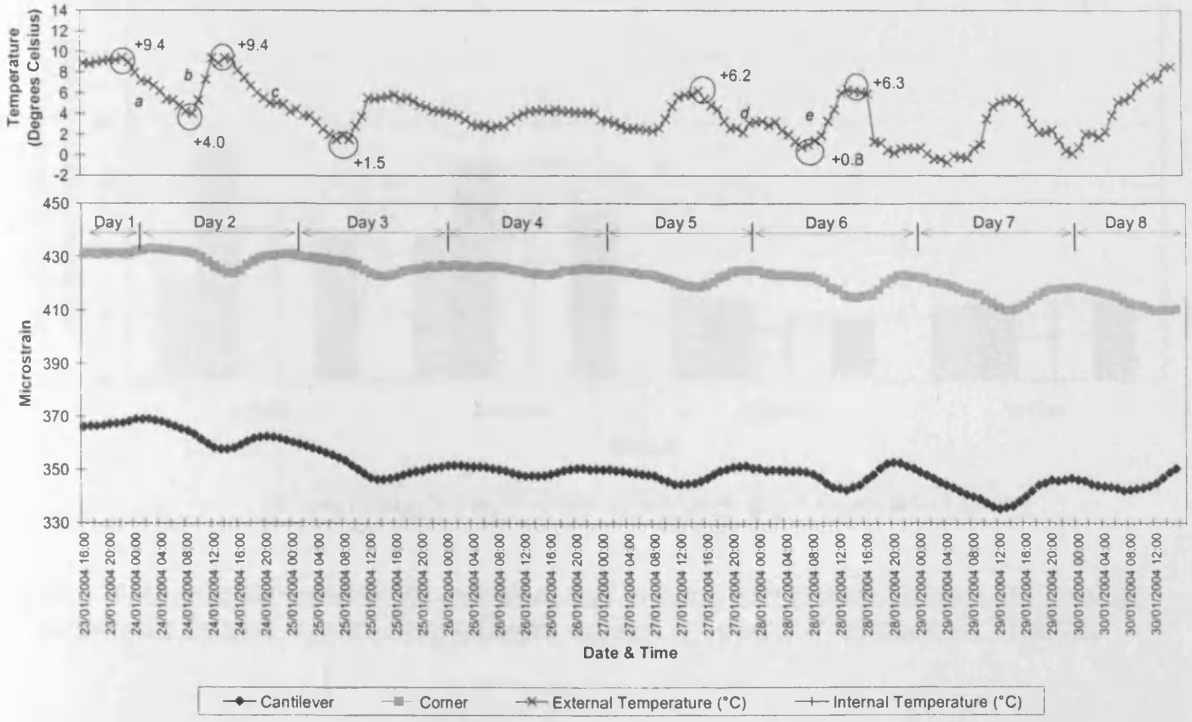

Figure 6.34. Comparison between hourly measured strains and hourly external and internal air temperature for locations in the top flange of segment 12, Cogan Viaduct, winter 2004.

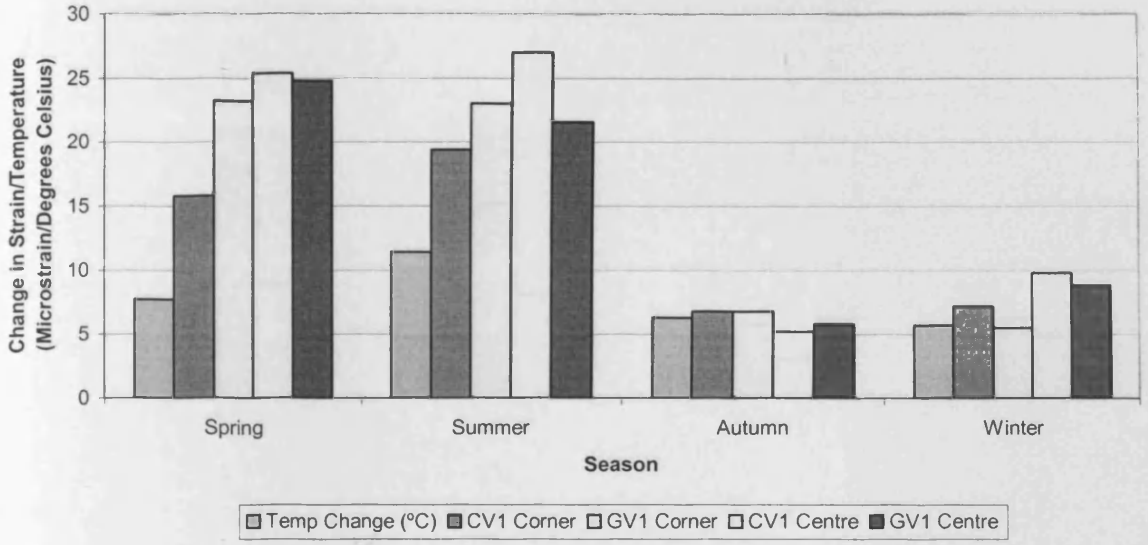

Figure 6.35. Comparison between the average change in strain with average change in external air temperature for each season - top flange, segment 1, Cogan and Grangetown Viaducts.

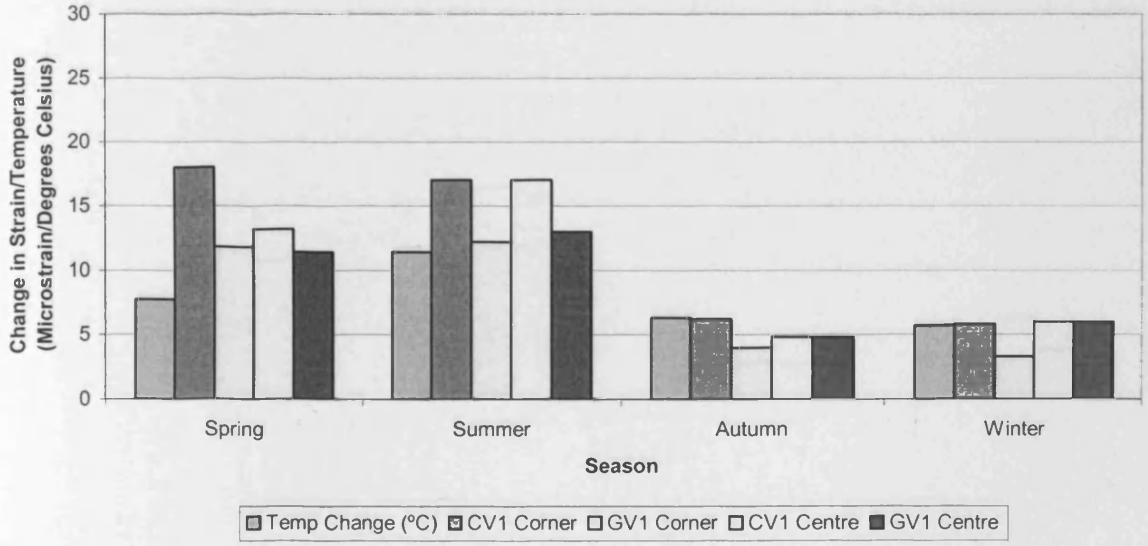

Figure 6.36. Comparison between the average change in strain with average change in external air temperature for each season - bottom flange, segment 1, Cogan and Grangetown Viaducts.

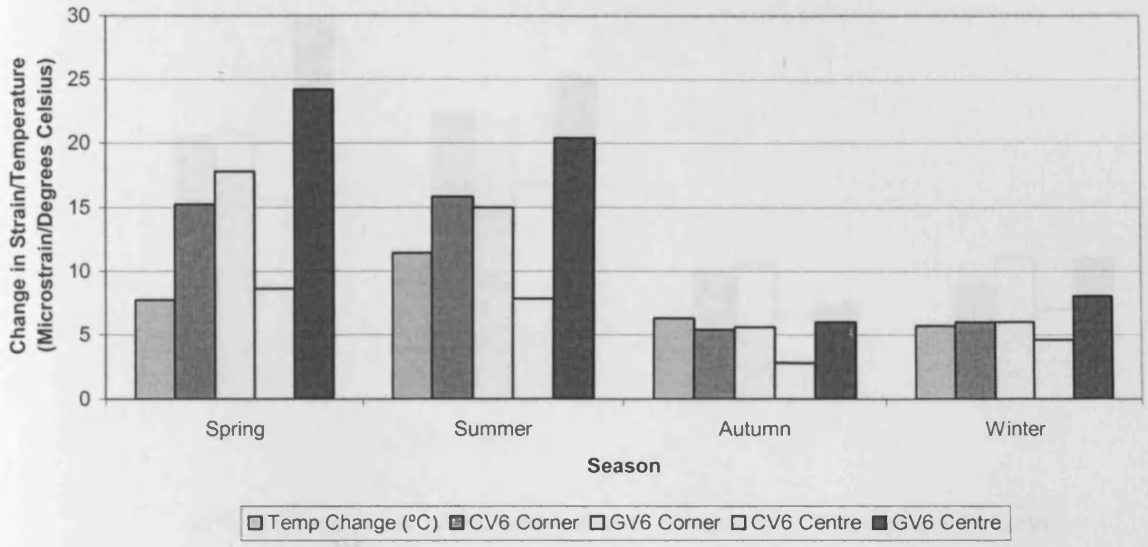

Figure 6.37. Comparison between the average change in strain with average change in external air temperature for each season - top flange, segment 6, Cogan and Grangetown Viaducts.

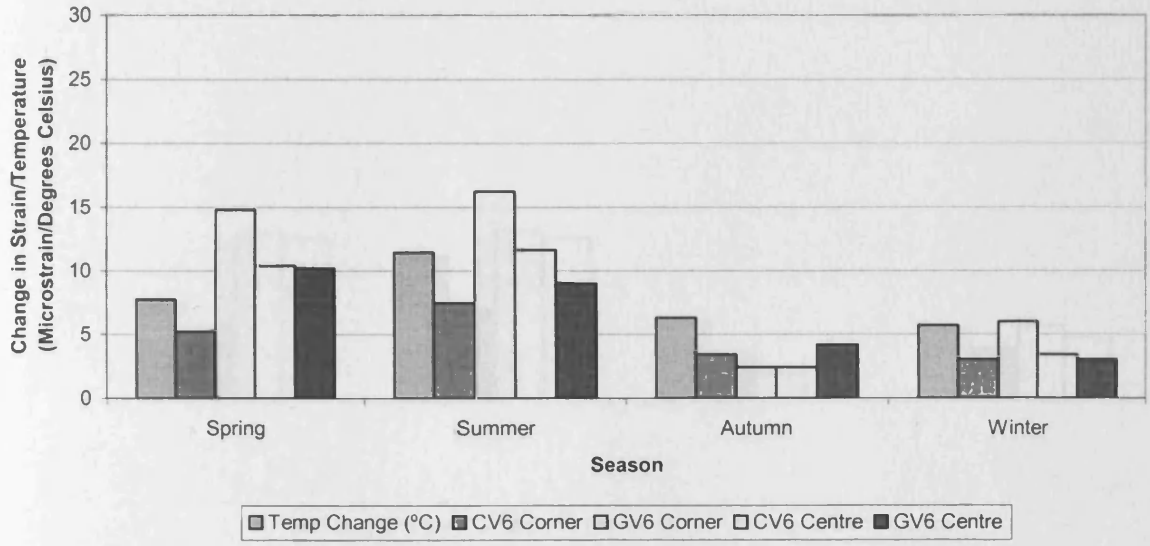

Figure 6.38. Comparison between the average change in strain with average change in external air temperature for each season - bottom flange, segment 6, Cogan and Grangetown Viaducts.

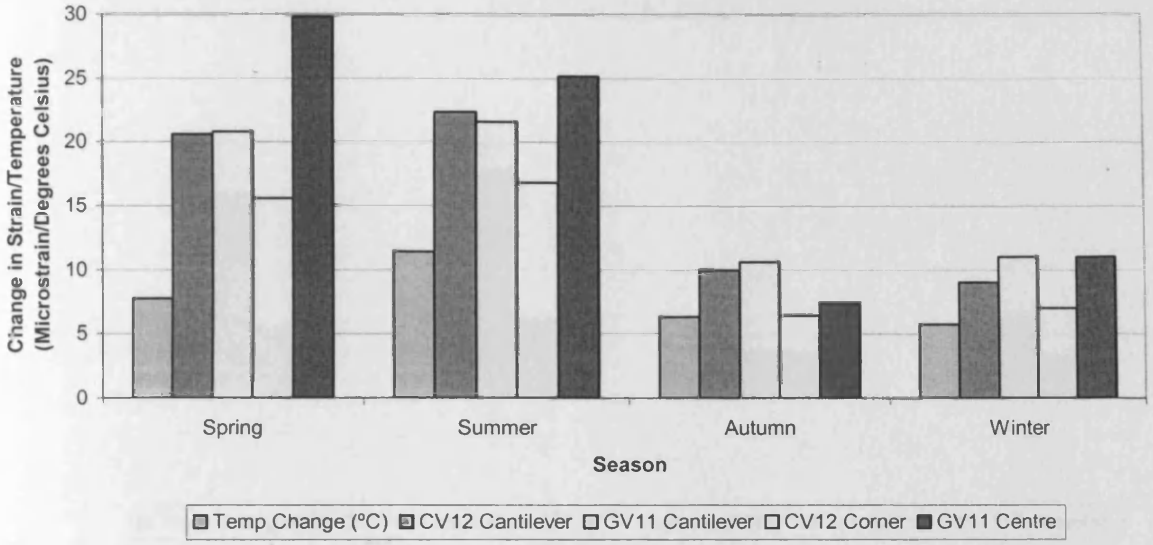

Figure 6.39. Comparison between the average change in strain with average change in external air temperature for each season - top flange, segment 12/11, Cogan and Grangetown Viaducts.

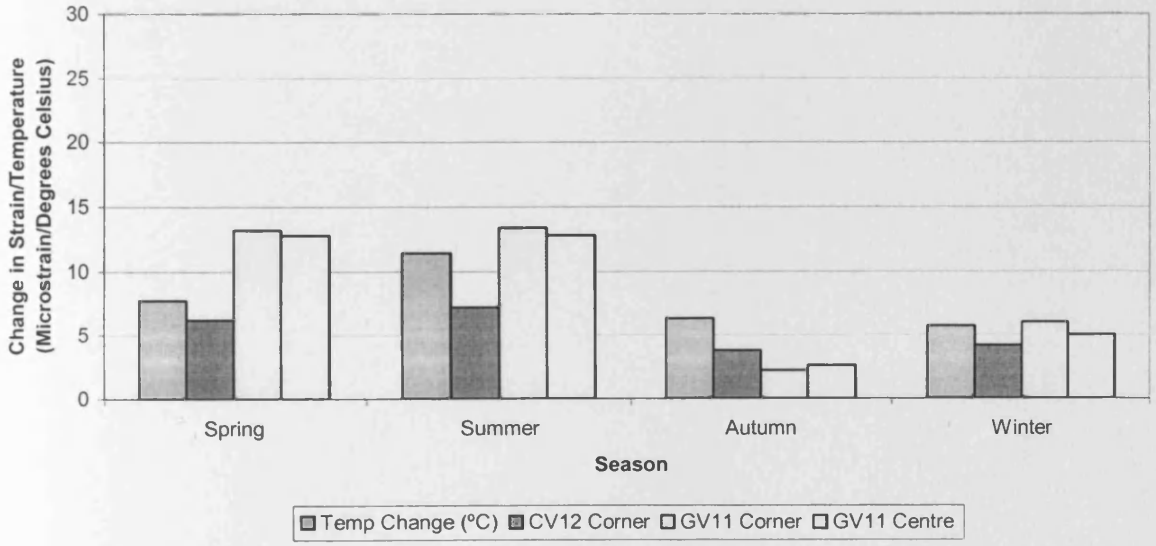

Figure 6.40. Comparison between the average change in strain with average change in external air temperature for each season - bottom flange, segment 12/11, Cogan and Grangetown Viaducts.

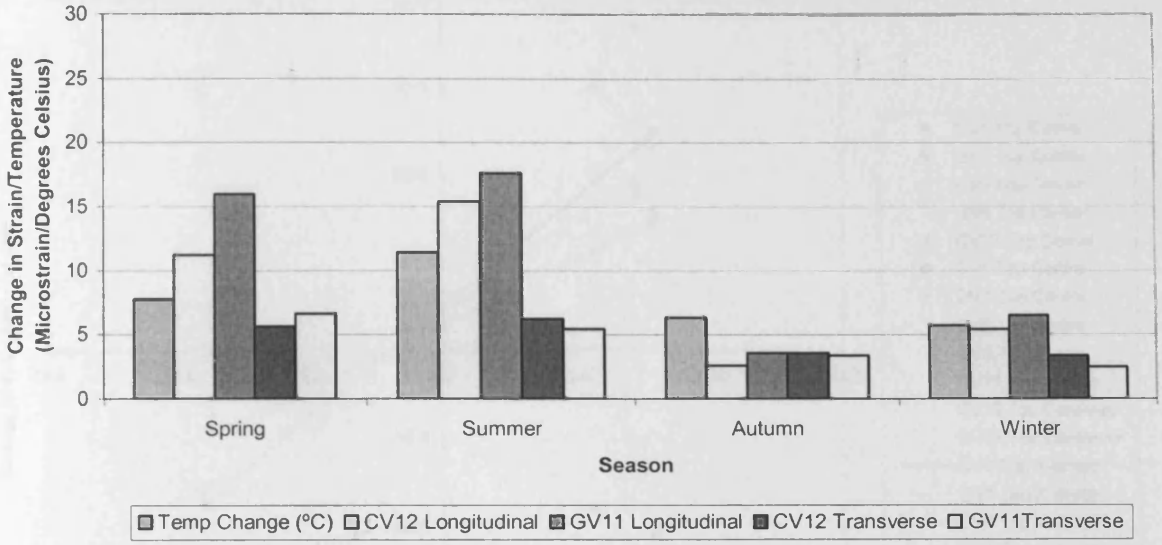

Figure 6.41. Comparison between the average change in strain with average change in external air temperature for each season - webs, segment 12/6, Cogan and Grangetown Viaducts.

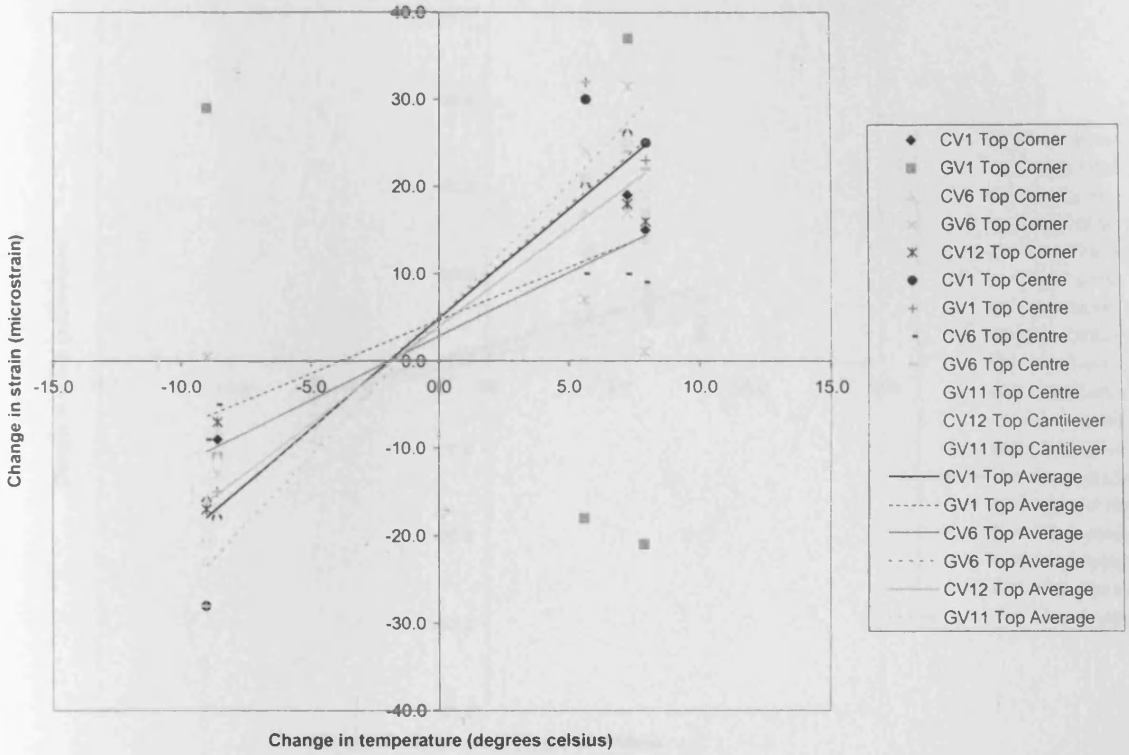

Figure 6.42. Relationship between the change in external air temperature and corresponding change in strain for all gauges in the top flange of all segments - Cogan and Grangetown Viaducts – Spring 2003.

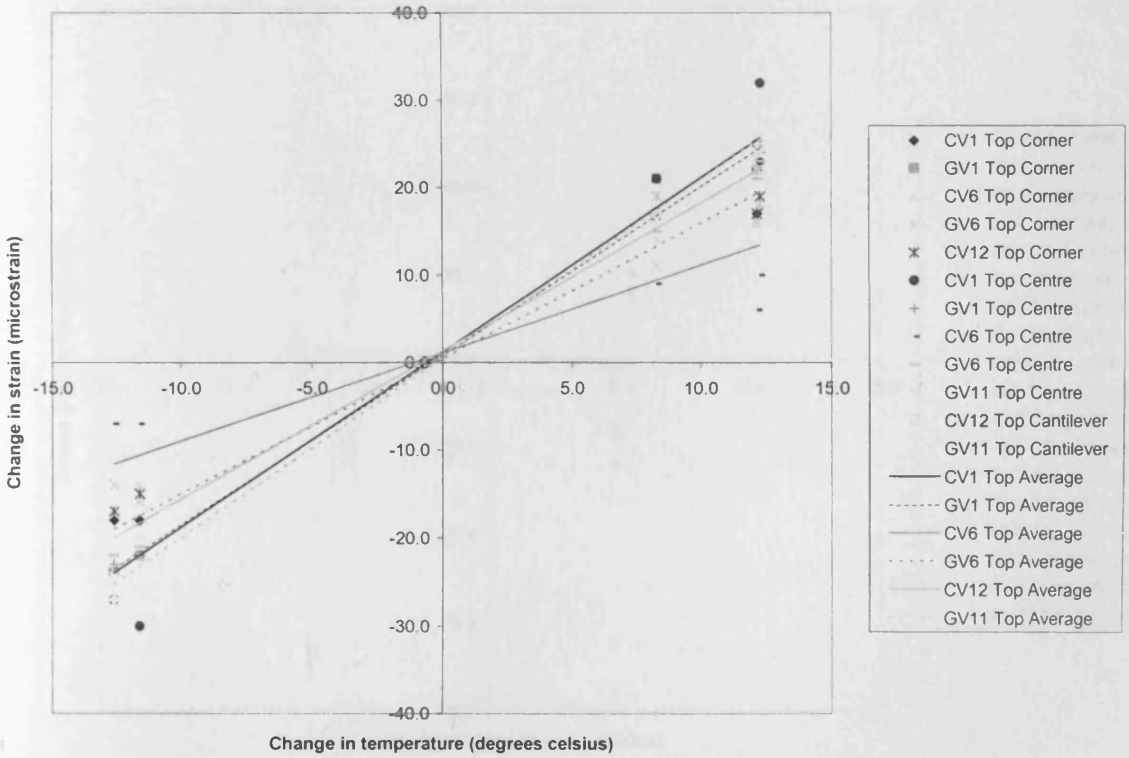

Figure 6.43. Relationship between the change in external air temperature and corresponding change in strain for all gauges in the top flange of all segments - Cogan and Grangetown Viaducts – Summer 2003.

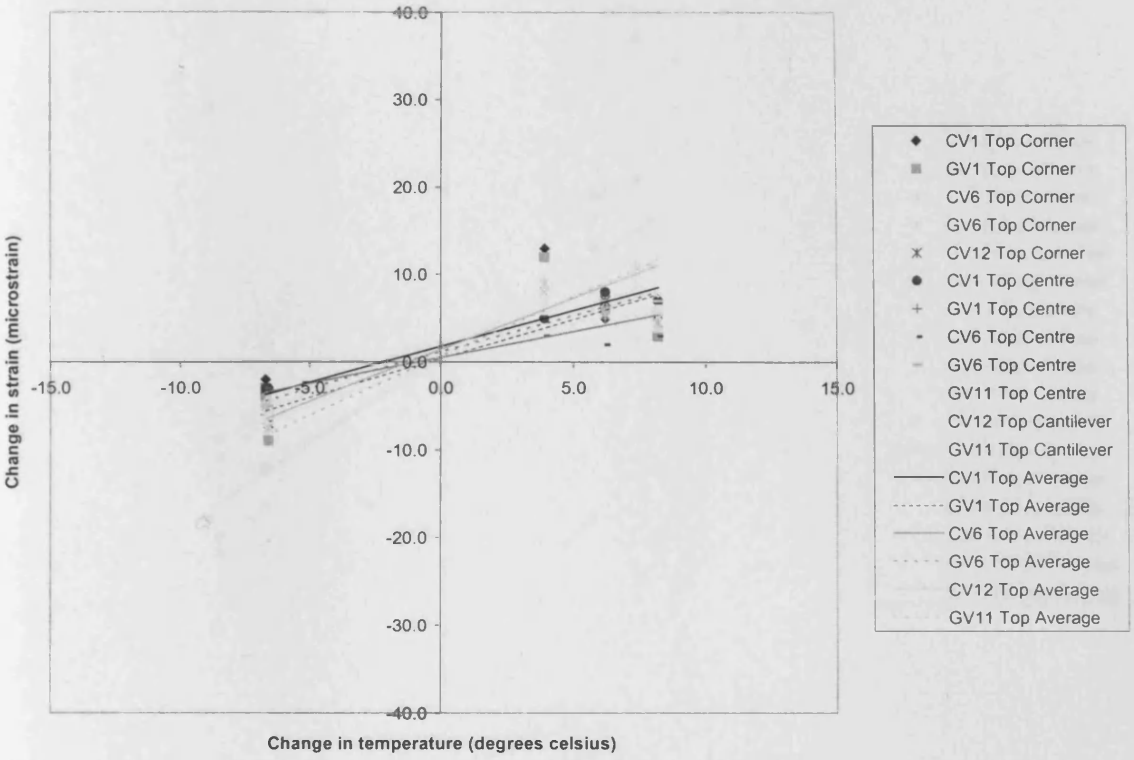

Figure 6.44. Relationship between the change in external air temperature and corresponding change in strain for all gauges in the top flange of all segments - Cogan and Grangetown Viaducts – Autumn 2003.

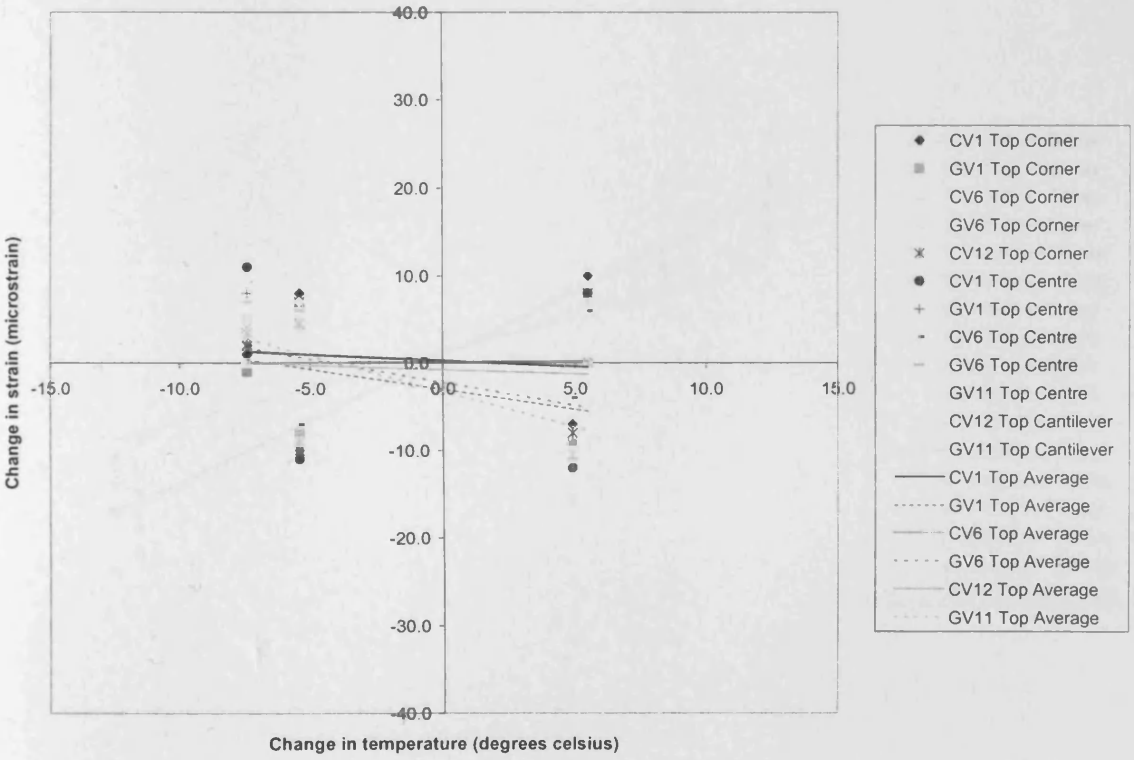

Figure 6.45. Relationship between the change in external air temperature and corresponding change in strain for all gauges in the top flange of all segments - Cogan and Grangetown Viaducts – Winter 2003.

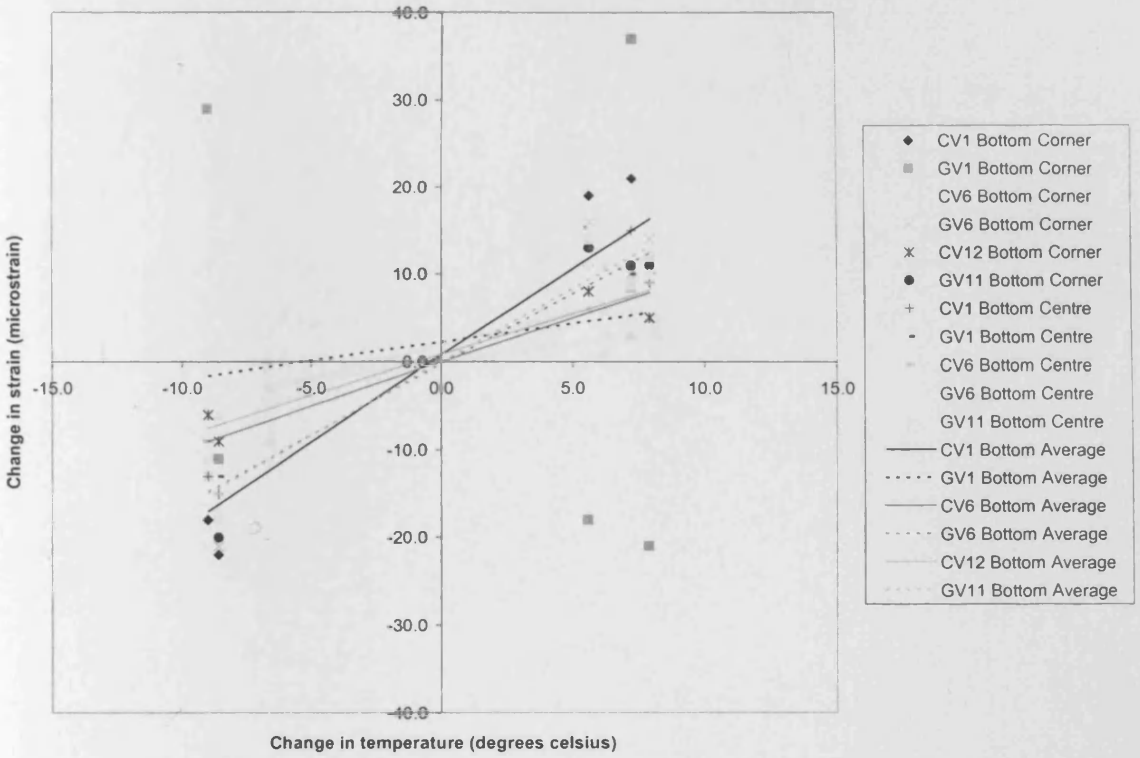

Figure 6.46. Relationship between the change in external air temperature and corresponding change in strain for all gauges in the bottom flange of all segments - Cogan and Grangetown Viaducts – Spring 2003.

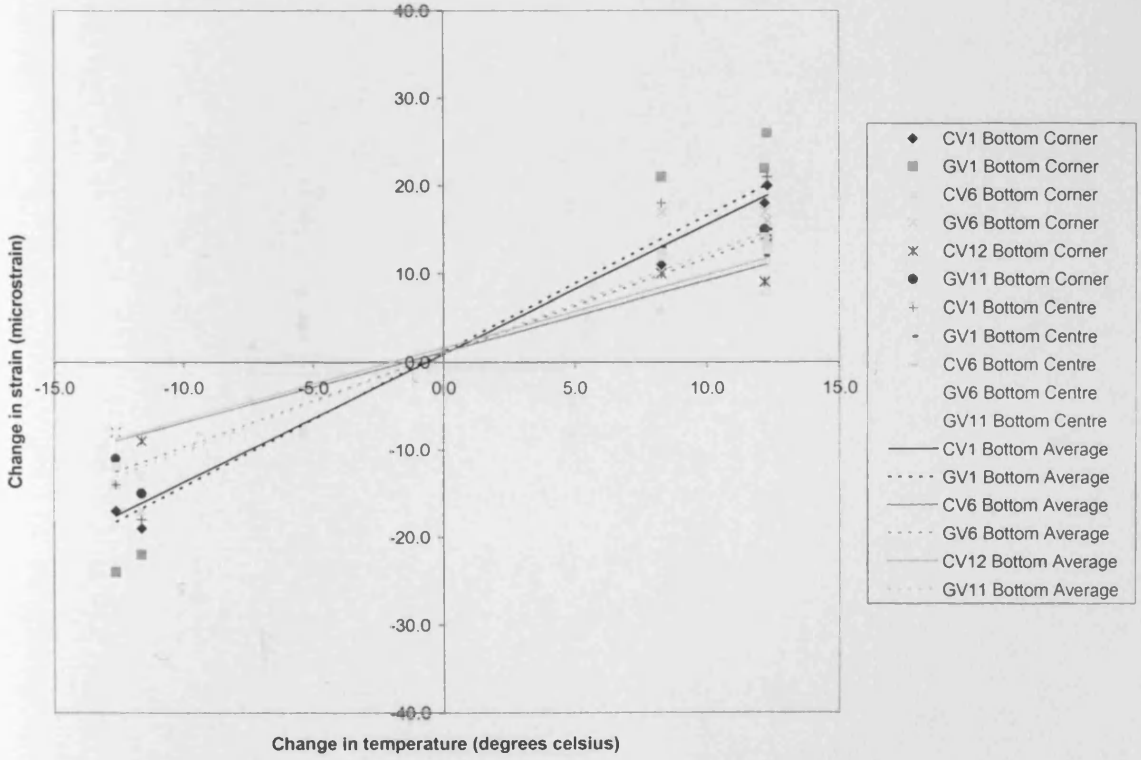

Figure 6.47. Relationship between the change in external air temperature and correpsonding change in strain for all gauges in the bottom flange of all segments - Cogan and Grangetown Viaducts – Summer 2003.

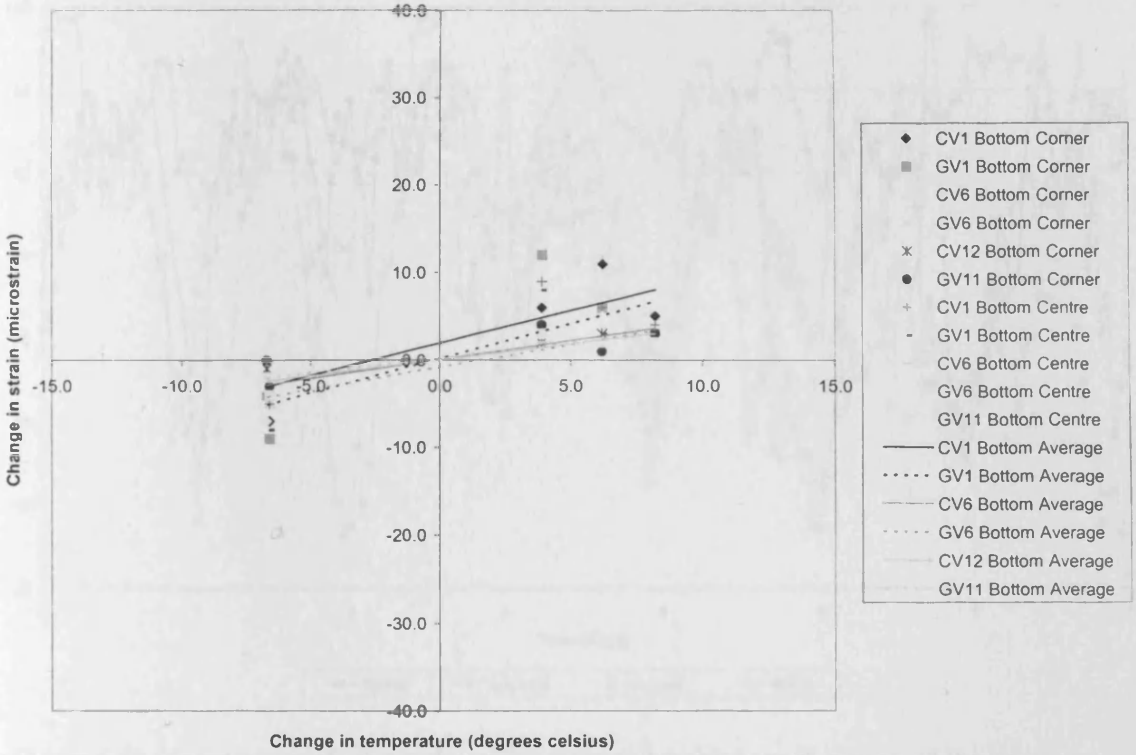

Figure 6.48. Relationship between the change in external air temperature and corresponding change in strain for all gauges in the bottom flange of all segments - Cogan and Grangetown Viaducts – Autumn 2003.

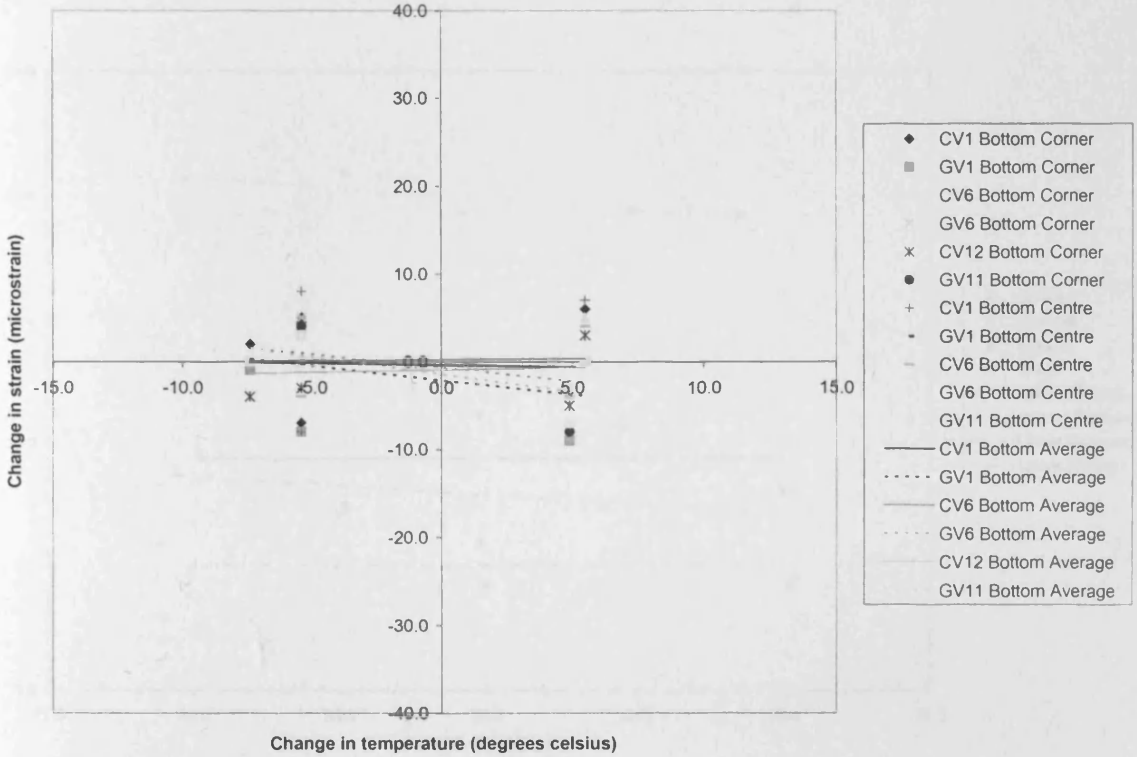

Figure 6.49. Relationship between the change in external air temperature and corresponding change in strain for all gauges in the bottom flange of all segments - Cogan and Grangetown Viaducts – Winter 2003.

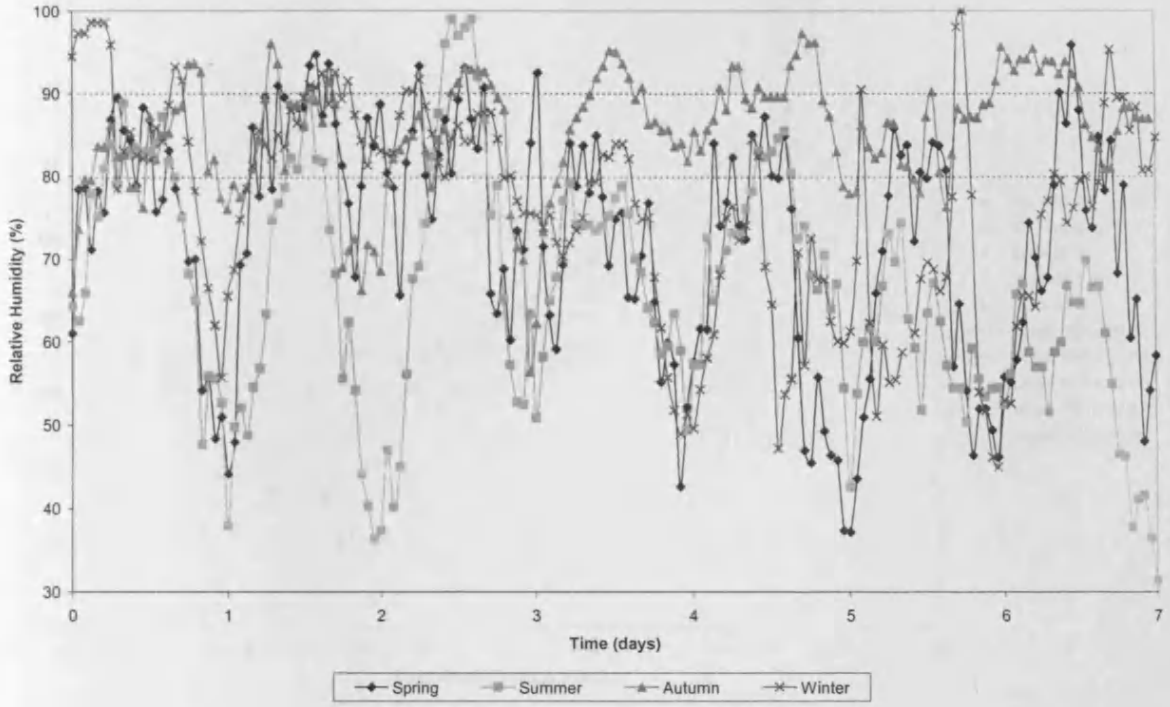

Figure 6.50. Comparison of relative humidity (%) for 1 week in each season of the year.

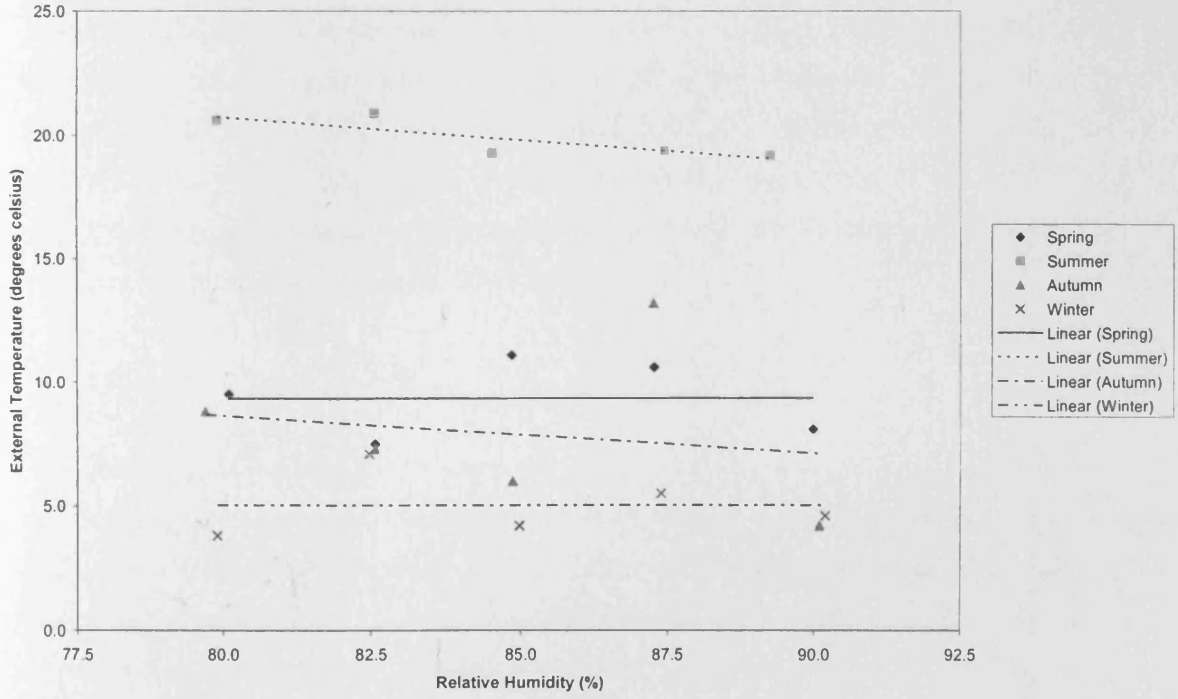

Figure 6.51. Relationship between temperature (°C) with relative humidity (%) for a confined range of similar relative humidities in each season.

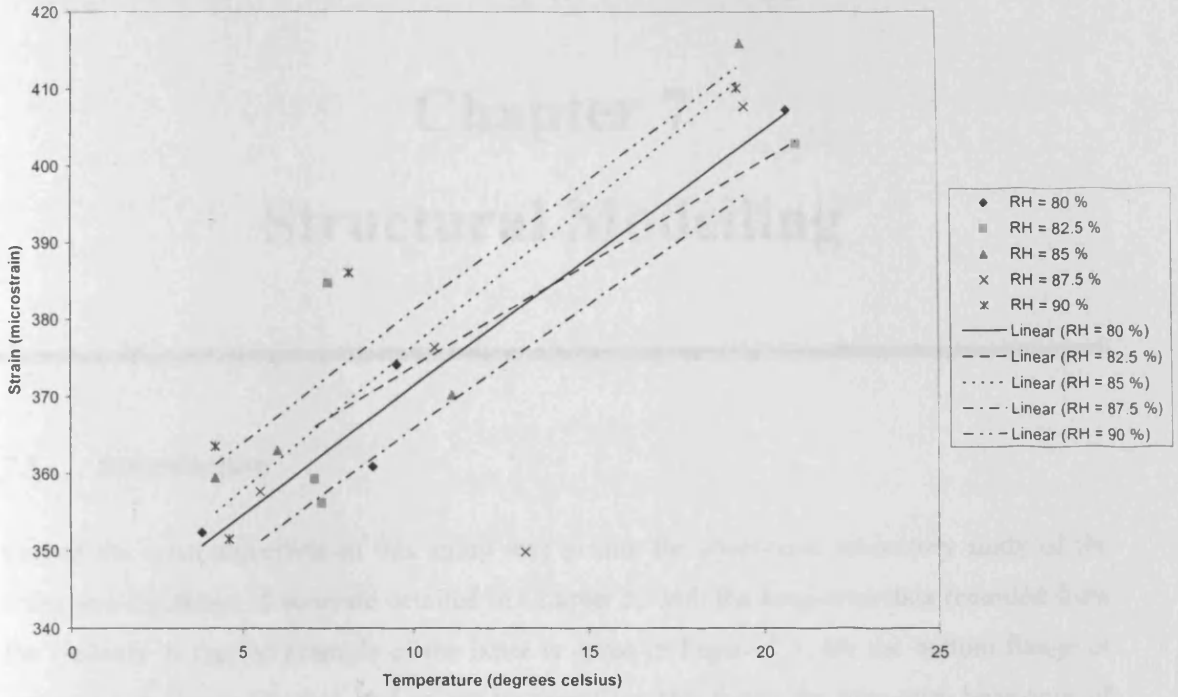

Figure 6.52. Relationship between strain ($\mu\varepsilon$) and temperature (°C) for a confined range of similar relative humidities in each season – Top flange, Segment 1, Grangetown Viaduct.

Chapter 7
Structural Modelling

7.1 Introduction

One of the main objectives of this study was to link the short-term laboratory study of the creep and shrinkage of concrete detailed in Chapter 5, with the long-term data recorded from the viaducts. A typical example of the latter is given in Figure 7.1, for the bottom flange of segment 1 in Cogan Viaduct, and as can be seen from this figure the long-term behaviour of the viaduct is influenced by the construction procedure and short-term behaviour of the structure. Modern construction techniques actually enable concrete structures to be assembled much faster than in the case of the Grangetown and Cogan Viaducts, and the loads occurring due to the construction process can be as large as the design service load. These construction loads can therefore cause significant immediate deflections due to concrete cracking and its low early-age modulus and the time dependant behaviour may be influenced even further. Some method of gaining an idea of the magnitude of the strains that develop in such structures should be invaluable to engineers at the design stage. Therefore, the aim of the this study was to determine whether it is possible to accurately predict the behaviour in such structures over time by comparing predicted strain data from some of the more recent models with the actual strains recorded in the viaducts.

7.2 Reference Data

It has already been reported in Chapter 6 that a vast quantity of strain data is available for individual bridge segments (at the support, quarterspan and midspan) in span 2 of Cogan Viaduct. Strains have been recorded at regular intervals from the casting of each segment through to the present day, some 16 years later. The instrumentation of Cogan Viaduct is detailed in Sections 3.8 and 6.1. Segment 1 of Cogan Viaduct was cast on 05/03/1987, while segment 6 was cast on 14/03/1987 and segment 12 was cast on 25/03/1987. These dates mark the beginning of the global timescale for each segment, to which all subsequent data is referred. The critical dates for Cogan Viaduct are summarised in Table 7.1. Initially, strain

readings were taken at either weekly, fortnightly or monthly intervals for the first year and a half. However, at the time of erection of the instrumented span, the interval was reduced in order to pick up all major events. These included segment placing, temporary prestressing and final prestressing. Eventually, readings were taken at yearly intervals until the installation of dataloggers by Cardiff University in 2000 since when readings have been recorded on a daily basis.

7.3 Current Study

The models that were used were the CEB-FIP Model Code 1990[121]/Eurocode 2 1992[131], the ACI Model 1992[117], the GZ Model 1993[128], the BP-KX Model 1991[125] the BP-KX+ Model 1993[126], the B3 Model 1995[114], the B3+ Model 1996[127] and the GL Model 2001[129]. The British Standard BS 5400: Part 4: 1990[130], detailed in Section 2.8.3, was also applied to assess the validity of the design model. In using these models, all material and environmental data was the same as that used/recorded during the construction of Cogan Viaduct. Since these prediction models do not take into account the inclusion of admixtures, the cement and fine aggregate contents were increased in order to take into account the inclusion of pfa in the mix as detailed in Section 5.9.2 and Table 5.20. The applied constant stresses were those calculated at the design stage and reported in site correspondence, and are the summation of the stresses due to the two stages of continuity prestressing, the superimposed dead loads (SDL) and the dead loads (DL) in each flange of each segment. These details are summarised in Table 7.2. Since such information was not available at the location of the gauges in the webs, this study will focus on the top and bottom flanges.

Figures 7.2 and 7.3 show comparisons of predicted total strains made using the aforementioned prediction models, with the recorded strains in the top flange of segment 1 and the bottom flange of segment 12 respectively, from erection of the segment through to the present day. It should be noted that shrinkage strains prior to erection have not been included in the predicted data as is the case with the recorded data since it is the strain in the segments after they become part of the structure that is required. The age of the segment after casting is represented on the x-axis while the total strain observed is shown on the y-axis. The model and recorded strains are represented by a different line as denoted by the legend. Similar comparisons at all other locations can be found in Appendix F. As can be observed, in all cases the prediction models significantly over-predict the strain behaviour of the viaduct by increasing orders of magnitude. BS5400 gives the closest agreement with the recorded data, predicting very similar long-term behaviour in the top flange of segment 1 and strains which are approximately double the recorded values in all other cases. It is also worth noting that all

other predicted strains are much greater in the bottom flange (almost 2900 $\mu\epsilon$ larger in the most extreme case) than the top flange (1300 $\mu\epsilon$ larger in the most extreme case).

The application of these prediction models is generally limited to simple structures such as beams or slabs, which have a uniform cross-section over their length and are made from one type of concrete. All loads and stresses have to be applied at one point in time and it is only after their application that the time-dependent strains are predicted. Also, with the exception of the CEB-FIP Model Code 1990, there is no allowance for prestressing. Hence, these prediction models can only truly be applied to individual elements within a structure, rather than the structure as a whole, and subsequently do not take into account the effect imposed upon them by the other elements and the overall response of the structure itself. The fact that the stresses imposed on the structure can only be applied at one time raises further problems when modelling the strain behaviour developed in the structure during construction. During the construction of a post-tensioned, glued segmental viaduct, the structure is constantly changing with new elements being assembled, temporary and/or initial prestressing being added and eventually continuity stressing being applied. It is therefore extremely difficult to take all these changes in loading and stressing into account at the times when they occur using these simple prediction models, and thus, if an accurate representation of the strains developed during construction is desired, a more sophisticated approach is required.

It has already been shown by Vitek and Barr[1-3] that it is possible to accurately predict the creep and shrinkage behaviour of the Cogan Viaduct during its construction and early service life using the DOMO computer code 1986[4], while Barr *et al*[5] have further shown that a prediction based on the actual properties of the viaduct as constructed is also accurate in the longer term using an updated version of the DOMO computer code, DOMO98[6]. The results of this analysis on the time-dependant behaviour in the top flange of segment 1 and the bottom flange of segment 12 are compared with the recorded strains at the same locations in Figures 7.4 and 7.5 respectively. The accuracy of the predicted strains relative to the measured strains during construction, in the short-term and in the long-term, is clear to see. Details of the theory behind the DOMO98 Computer Code taken from the instruction manual provided by Vitek[6] are given in Appendix G. Essentially, DOMO98 is a tool for analysing creep and shrinkage in concrete structures using a far more sophisticated technique than standard prediction models since it enables the effects of creep and shrinkage to be predicted in structures which are statically indeterminate, which have a number of different structural forms during their assembly or casting and which are made from different kinds of concrete or with concrete of different ages. Furthermore, the analysed structure may also be prestressed. Tendons can be allocated to individual sections or elements within the structure

and prestressing forces can be applied at times specified by the designer. The information obtained during the construction of the Cogan Viaduct extends to detailed dimensional data, actual material properties, casting and erection times, dead and superimposed dead loads, and detailed prestressing records. However, it is uncommon to have this amount of information about a structure.

Initially, a study was undertaken to address how sensitive this prediction is to the level of detail available. In order to achieve this it was necessary to identify the effects that the three main input parameters (material data, construction sequence and prestressing data) have on the predicted strains. DOMO98 was used to assess the influence of both the construction procedure and the amount of prestressing data required. This study is reported in detail here.

The influence that material data has on the predicted strains is dependent upon the identification of the most efficient of the aforementioned creep and shrinkage prediction models. It is then possible to identify the influencing material parameters that constitute the input data. A sensitivity study of parameters used in these prediction models was reported in Chapter 4. One of the main findings of the study was that no one model can be considered to be more accurate in every situation and circumstances should dictate which model to use. This was confirmed in the comparison of predicted strains made using the same models with the laboratory test data reported in Chapter 5, and the recorded strains from the Cogan Viaduct reported earlier in this chapter (Figures 7.2 and 7.3). The models that gave the closest agreement in the laboratory study were not the same as those which gave the closest agreement to the measured strains in Cogan Viaduct.

The DOMO98 computer code also uses creep and shrinkage prediction formulae in strain calculation. The program was written in such a way that the values of shrinkage and the creep function are calculated in advance and then transferred into Dirichlet series. In the analysis only the Dirichlet series are used, which means that the analysis is independent of the original shrinkage and creep function formulae. Therefore, a comparison of the strains predicted using the different creep and shrinkage models within the DOMO98 program was necessary to determine which model predicts strains that gave the best agreement with the recorded data in this case. The DOMO98 computer code utilises a number of creep and shrinkage prediction models that include the rate of creep theory (classical function Dischinger or Morsch), the triple power law (double power law) for basic creep coupled with the BP model for drying creep, the log-double power law for basic creep coupled with the BP model for drying creep, the EC2, and a variation on the BP-KX model. In the analysis made by Vitek and Barr[1-3], the EC2 model was used. Advances in the development of prediction models has resulted in a number of the models employed by the DOMO98 code becoming superseded, and if used

would not allow a fair comparison to be made with the prediction models used throughout this study. Therefore, in collaboration with the author of the DOMO98 computer code (Professor Jan Vitek), the program code was updated to include additional creep and shrinkage prediction models for the expressed sole use in this research project. The program source code, written in the Fortran 77 computer language, was made available and additional lines of code were added to enable the time-dependant analysis of structures using the original BP-KX model, the short-form BP-KX model, the B3 model, the short-form B3 model, the ACI model, the GZ model and the GL model to be made. The updated program was compiled and tested using a simplified structure in order to ensure the program modifications were successful. This process required significant effort much of which is not reported in detail here.

7.4 Data Preparation

The original prediction of the strains for Cogan Viaduct made by Vitek and Barr[1-3] using the original DOMO computer code made use of a wealth of material, geometry, prestressing and construction data accumulated by Vitek from information recorded during the construction period. Collecting and assembling this information into a form suitable for use with the DOMO and DOMO98 computer code is a time consuming process which is particularly labour intensive. One of the main objectives of this study was to try and make realistic strain prediction more efficient at the design stage. Therefore, it was decided to simplify the model, making it as basic as possible, with subsequent models becoming more and more complex so that the agreement with the original DOMO model could be investigated. It was anticipated that as the models became more complex, then the strain behaviour would become closer to that of the original DOMO model i.e. a convergence would occur. The first 'new' modelling of the viaduct was denoted Cogan01 with the number increasing as subsequent, more sophisticated, models were developed. In order to gain an appreciation of the differences between each of the DOMO98 Cogan models used in this study (Cogan01 – 05), the construction sequence and structural layout of the Viaduct used in each case is shown in Appendix F. The original analysis was very successful, although the fit of the predicted strains to the recorded data was not always perfect, with variations of up to 100 με being encountered. Therefore, the strain behaviour predicted by the original analysis was assumed to give a good representation of the actual behaviour and in order to ensure a more realistic model comparison, predicted strains were compared with the original predictions rather than the recorded data. Using the original data used by Barr *et al*[5] as a guide, the main variables necessary for input into the DOMO98 computer code were identified and simplified, as reported later.

7.4.1 Segment Data

Cogan Viaduct is made up of 96 individual segments or elements. In the original DOMO computer code, the same number of elements were used and connected by 101 nodes the difference is due to the connection of mid-span joints. This is a feature of the earlier version of the code used in the analysis by Vitek and Barr[1-3], but not in the latest revision which is being used in this study. Each element is 1.25m long (at piers), 2.5m or 5m long in the spans. This level of detail is comprehensive, and so in order to simplify the analysis, elements were grouped together to give just two large elements for each cantilever. This would be very unlikely in practice, but provides the simplest and quickest analysis. In order for the computer code to work, the mid-span closure joints have to remain as one single element. Therefore the number of elements used in the analysis was reduced from 96 to 17 and the number of connecting nodes was adjusted accordingly and reduced from 101 to 18.

Another important feature of the segment geometry is the segment depth. In the original analysis, each segment had its own specific depth relating to its position in the structure i.e. segments at mid-span were not as deep as segments at supports. The segment depth to be used in the analysis had to be addressed when grouping a large number of elements of varying depth together. In the structure itself, two of the three instrumented segments are located in span 2 and are of the same depth, while the other segment is at support 3 and consequently has a greater depth. Other elements in the original analysis had deeper segment depths depending on their location (i.e. over the main span). Since the strains predicted are compared with the strains recorded in the three instrumented segments, it was considered acceptable to use the geometry of either of these. Furthermore, since there are more segments in the entire bridge located within the spans as opposed to at supports and as a result are of a similar depth, it was decided to use the segment depth of the two instrumented span segments for the entire bridge. Again, this is unlikely in practice but provides the simplest and quickest method of analysis.

A further complication arose with regard to the times at which the segments were cast, erected and became part of the structure. The times factor for each element is represented in the DOMO98 code by means of the time difference between when the element was cast and the time when it was erected. Since the new elements are a composite of the original elements, the average of the times when the original elements were cast and the times when the original elements were erected was taken, and these new times were used to work out an average time difference for the new elements. The DOMO98 input data for the new element, as well as the segment data used in all other Cogan models can be found in Appendix F.

7.4.2 Prestressing Data

In the construction of the Cogan Viaduct, 200 prestressing cables were used. In the original DOMO analysis, this number was reduced to 100 due to program constraints by doubling cables at equivalent locations either side of the vertical centreline of the viaduct such that one cable in the DOMO analysis represented two cables in the bridge. In the DOMO98 computer code, each cable starts at the edge of a particular element and runs through other elements to the edge of another particular element, having cable eccentricities at either end in relation to the neutral axis of the element. Each cable had a specific prestressing force. In line with reducing the number of elements, it followed that the prestressing data should be reduced accordingly. Therefore the number of cables was reduced from 100 in the original model to 17. Based on the new segment lengths, all cables whose start or end points fell within the length of the new segment were grouped together into one larger cable carrying a greater force. The anomaly that this created was that the start and end points of each cable were now spread out over the length of the new longer elements and hence did not start and end at the beginning of the new element, as was necessary for modelling cables within the code. Therefore before grouping these cables together, the length of each cable was either extended or reduced such that the start and end points lay at the edge of the new elements, and the prestressing force in each cable was redistributed accordingly. Once this had occurred, cables were grouped with the new prestressing force calculated from the sum of the redistributed forces in the original cables. The new eccentricities were calculated by averaging the original eccentricities at the start and end of each cable. The DOMO98 input data for the revised prestressing cables, as well as the prestressing data used in all other Cogan models can be found in Appendix F.

7.4.3 Construction Time Intervals

A number of time intervals were allocated to the structure representing the time at which the strains were to be predicted. Each time interval can be a different duration depending on how detailed the analysis needed to be at a particular point in the life of the structure i.e. during the period when the viaduct is under construction, time intervals can be short depending on the erection of individual elements or the application of prestressing force, whereas after the construction process when the main contributing factors to the observed strains are the time-dependent deformation, time intervals can be much greater. The time intervals in the original DOMO model took into account the erection of every pair of segments in a cantilever set and the introduction of prestressing cables as soon as all the elements the cable would pass through, and hence affect, were erected. Furthermore, the time intervals took into account the

application of continuity stress to a particular span and also the application of additional dead load upon completion of the construction process. Therefore, a total of 51 time intervals were applied in the original model. Since the number of elements and prestressing cables has been drastically reduced, the next logical step was to reduce the number of time intervals based on the erection of the new elements in cantilever sets, and the continuity stressing of spans. Hence the number of construction time intervals was reduced to 8, with 7 further intervals to account for the time dependent strains developing over time giving a total of 15 intervals. The final time interval ends at 6100 days, which is the equivalent to a time span of nearly 17 years from the casting of segment 1 i.e. the total time from the beginning of the global timescale to the present day. The DOMO98 input data for the revised time intervals, for all Cogan models, can be found in Appendix F.

7.5 Comparisons with Recorded Data

As specified in Section 7.2, the global timescale for each element was assumed to begin when the instrumented segment was cast, and all other times were referenced to this. This is certainly the case with the data recorded in the viaducts. However, in the DOMO98 analysis there is one global timescale beginning at the time when the very first bridge element is cast i.e. element 1. Therefore, in order to be able to compare the strains predicted using DOMO98 with the strains recorded in the viaducts, the time difference between the global timescale for the instrumented segments and the global timescale for the DOMO98 elements was required. Table 7.3 shows actual erection times of the three instrumented segments after casting, as well as the erection times used for the equivalent elements in the original DOMO analysis by Barr *et al*[5] which were related to the casting of the very first element in the bridge. The time differences noted were used to relate the predicted strain data with the recorded data such that the predicted strains were moved along the timescale, but the magnitude of the predicted strains is not changed.

It was decided to present in this thesis, only the comparisons between the original strain behaviour and the predicted strains in the bottom flange of segment 1 and top flange of segment12. During the life of the viaduct, these two flanges are in compression. The effect of dead and live loads results in a redistribution due to creep, which in turn transfers the load to these locations causing an increase in sag at the midspan and an increase in hogging at the support. The increased compression in the compression flanges coupled with the effect of creep alone should result in increasing strains over time in the compression flanges and decreasing strains over time in the tension flanges. This can be observed by considering the stresses in the flanges. Due to the complex relationship between stress and strain in the

presence of time-dependent deformations, it is unrealistic to gain a true estimate the concrete stress from the measured strain. However, the DOMO98 computer code can be extended to predict a stress/strain relationship for the structure which allows the stress at the location of the gauges for a given strain to be determined as demonstrated by Lark *et al*[151]. Table 7.4 presents the results of such an analysis for the top and bottom flanges of each instrumented segment after 766 days (≈2 years) and 3141 days (≈8½ years). Hence, it can be observed that the stress in the top (tension) flange of segment 1 decreases over time while the stress in the bottom (compression) flange increases. Similarly, the stress in the bottom (tension) flange of segment 12 decreases over time and while the stress in the top (compression) flange also decreases, the rate is less in the top than in the bottom.

Figures 7.6 and 7.7 show a comparison of the strains predicted using each simplified model (Cogan01 – Cogan05) with the original strain behaviour for the bottom flange of segment 1 (pier) and the top flange of segment 12 (midspan). Corresponding results for all other locations can be found in Appendix F. The x-axis shows the time in days from the casting of the segment, while the y-axis shows the total strain. Each new model (as well as the original) is represented by a different curve as denoted by the legend. Table 7.5 gives the predicted strains after 17 years at all locations for all models, with strain values in bold type indicating that the strain is larger than the original, while strain values in italics indicate that the strain is smaller than the original.

Table 7.6 shows the difference between the model strain and the original data at all locations, again after 17 years. Strain values in bold type indicate that the strains are diverging, while strain values in italics indicate that the strains are converging. Considering model Cogan01, it can be observed that overall the strains give adequate agreement with the original data, especially in the top flange of segment 1 (only 1$\mu\epsilon$ difference at 17 years). All strains are larger than the original data by up to 101 $\mu\epsilon$ (bottom flange, segment 12). However, due to the fact that only one element was used to represent the entire instrumented cantilever in this analysis, caution must be employed when considering the accuracy of these strains, and further models were undertaken in order to confirm the validity of this model as will now be discussed.

7.6 Model Development

It was decided that when making the model more complex, the primary concern was to increase the number of segments needed to construct the bridge since changing this variable effectively controlled the number of prestressing cables and time intervals needed to model the structure. Therefore, the number of prestressing cables was increased since adding more

elements increased the number of potential start and end locations for individual cables, and the number of time intervals also increased. In Cogan01, each cantilever set was made up of two long elements and each element had the same section properties. In Cogan02, it was decided to double the number of elements in each cantilever set from 2 to 4, with the innermost elements (i.e. the elements connected at the pier) having the section properties of the instrumented pier segment no. 1, while the section properties of the outermost elements (i.e. the elements closest to the centre of the span) were the same as the instrumented quarter and midspan segments. In doing this, the number of elements was increased from 18 to 27, the number of prestressing cables was increased from 17 to 22 and the number of construction time intervals from 8 to 13. The results can be seen in Figures 7.6 and 7.7 for the bottom flange of segment 1 and the top flange of segment 12 respectively, and in Appendix F for all other locations.

When comparing the strains from the Cogan01 and Cogan02 models, it was found that the predicted strains were closer to those of the original model at 3 locations – the bottom flange of segment 1, the top flange of segment 6 and the top flange of segment 12. It is interesting to note that the locations where the strains give closer agreement with the original model at the support and midspan are in the compression flanges but not the tension flanges. It is difficult to know whether the top or bottom flanges at the quarterspan segment should be in tension or compression since it is close to the point of contraflexure. However at all other locations the strains from Cogan02 are further from the original model than those of Cogan 01, suggesting that the complexity of both models is insufficient to adequately represent the strain behaviour of the viaduct.

It was considered that the fact that the strains at certain locations diverged from the original data after the second model meant that a greater degree of accuracy was required. However, since the instrumented segments were part of only one cantilever set it was decided to make this set more complex while leaving all other spans as simplistic as possible i.e. 2 elements either side of the pier as was the case in model Cogan01. Therefore, in Cogan03 it was decided to make each element in the cantilever set under scrutiny equivalent to 2 elements in the original analysis. In the original analysis, the length of each of the elements in the instrumented span was 2.5m. The equivalent elements in Cogan03 were therefore changed to 5m long, but since the other cantilever sets are modelled in their simplest form (i.e. 2 long elements as in Cogan01) the total number of elements within the analysis actually decreased from 27 to 26. In changing the number of elements, the number of prestressing cables increased to 23 and the number of construction time intervals remained the same at 13,

although the construction sequence obviously changed to incorporate the erection of the new elements.

It was unusual to find that in changing the model from Cogan02 to Cogan03, in all cases bar the top flange of segment 1 the strain behaviour actually diverged even more from the original data. This was unexpected since the instrumented span was much more complex and so it was thought that the simplification of the other spans similar to that used in Cogan01 may have had a greater influence on the strain behaviour in the instrumented span than was first anticipated. Incidentally, when comparing the strain behaviour from Cogan01 with Cogan03 where the majority of the elements and prestressing data is the same, it was found that Cogan03 predicted strains which also diverged further from the original data with the exception of the strains in the top flange of segment 12 which were only marginally closer than those predicted by Cogan01. Therefore, the next logical step was to factor in to the model the influence of all input data which could influence the strains in the instrumented span.

The initial model changes centred on the complexity of the construction sequence (i.e. the number of elements). It was now considered that the reason for the divergence in the strain behaviour was more related to the level of prestressing detail in the instrumented and adjacent spans. Because there have only been 1 or 2 elements in the cantilever at the other side of the midspan joint in the instrumented span, it was necessary to extend the length of the prestressing cables in the span such that they have a definite start and end location for use in the analysis. In doing this, the force in the cables was redistributed over the new increased length as described in Section 7.4.2 which meant that the prestressing force in the cables reduced which could have been responsible for the divergence in strain behaviour. In order to rectify this, the cantilever set in which the instrumented span was located was made as complex as the original model (i.e. as constructed in real life) and the other cantilever set which made up the instrumented span was also made more complex, although not to the same detailed as the original model but to the level of detail used in the instrumented span in Cogan03. All other elements remained the same as in Cogan 01 and 03. Therefore, Cogan04 had 46 elements, 44 prestressing cables and 23 construction time intervals.

When comparing the strains from the Cogan03 and Cogan04 models, it was found that the strains were closer to the original model at 3 locations – the bottom flange of segment 1, the top flange of segment 6 and the bottom flange of segment 12. The fact that the strains get closer to the original data in the bottom flange of segments 1 and 12 in model Cogan04 can obviously be attributed to the increased prestressing forces in the bottom flange due to the greater complexity of the model in the instrumented span. However at all other locations the

strains from Cogan04 are further from the original modal than those of Cogan 03, which is again unexpected due to the increased complexity of the model which is approaching that used in the original model at and around the instrumented span.

The amount of information used in the Cogan04 model is approximately half of that used in the original model which could be considered to defeat the purpose of this study of finding a more efficient method of predicting the strain behaviour of the structure over time. The fact that the comparisons between these models and the original model has yielded results which do not give good agreement (and are becoming even more divergent in some cases), has lead to the conclusion that the strain behaviour in the instrumented span maybe related to the complexity of the structure as a whole i.e. the prestressing force in a cable in the top flange of span 6 affects the strain behaviour in the bottom flange of span 2 to a small degree. It is possible that the summation of the effects of every prestressing cable in the viaduct (no matter how small) is responsible for the fact that the anticipated convergence of strains with the original model is not occurring despite the increased complexity at the instrumented span. In order to test this theory, whilst keeping the model relatively simplistic, models Cogan02 and 03 were combined such that in the final model, Cogan05, the instrumented span was relatively complex while the other spans in the model were also more complex than in models Cogan01, 03 and 04. It was anticipated that the strains from Coagn05 should be closer to the original data than those predicted by models Cogan02 and 03, since the influence from both models is in fact combined. Hence, Cogan05 had 34 elements, 29 prestressing cables and 15 construction time intervals.

Despite the complexity of this model, the strain behaviour predicted by Cogan05 gave the least reliable agreement with the original model than any of the previous models at all locations bar the top flange of segment 12, which was marginally better than Cogan04. This was completely unexpected and led to the conclusion that in order to gain an accurate representation of the strain behaviour in a structure such as this, the construction sequence, and prestressing data must be exactly the same as that used in real life, as demonstrated by the original DOMO model. The assumptions made such as grouping elements and cables, redistributing the prestressing forces over greater lengths, and using section properties which are different to that which would be used in longer spans, have contributed to an accumulation of errors which have resulted in inaccurate strain prediction. The fact that making simplistic models marginally more complex generally resulted in an increased divergence for the original strain behaviour reinforces this suggestion, and therefore a more efficient method of predicting short and long term strains in this structure at the design stage is not possible using the standard prediction models, nor the more complicated computer code. The DOMO98

computer code is a valuable tool for this purpose, but only if the construction process of such a structure is modelled to a level of detail which is similar to that which would be used to construct the structure in real life as demonstrated by the original analysis by Barr *et al*[5].

7.7 Influence of Material Properties

In order to ascertain the influence that material properties have on the predicted strains, it was necessary to model the viaduct with the different creep and shrinkage prediction models which were incorporated into the DOMO98 computer code as part of this study and detailed in Section 7.3. It was originally anticipated that the results of the study on the construction sequence and prestressing data would yield a simplified model which predicted strain behaviour which gave good agreement with the original DOMO model, and hence the recorded strains. Unfortunately this was not the case due to the sensitivity of the program to the aforementioned construction sequence and prestressing data. However, since the DOMO98 code models the strain behaviour of the structure independently of the creep and shrinkage model once the creep and shrinkage functions have been calculated, it can be concluded that the effects of the creep and shrinkage function will be the same in any model regardless of the accuracy of the construction sequence and prestressing data. Therefore, it was decided to select one of the Cogan models and use this model in conjunction with each of the different creep and shrinkage models to determine which has the largest impact on the predicted strains. It is then possible to determine to which material properties the strain behaviour is most sensitive.

It was decided to neglect the Cogan01 and 02 models since the instrumented span was only made up of one and two elements respectively i.e. in the first instance the instrumented cantilever was represented by one element in the model and so the strains in that element were taken to be the same for each of the three segments, and in the second instance the instrumented cantilever was represented by two elements in the model and so strains in the outermost element were taken to be the same for the quarterspan and midspan segments. Hence it was decided to use the simplest of the other three models i.e. Cogan03 where each instrumented segment was represented by one equivalent element in the model.

In order to determine which creep and shrinkage models are the most accurate, when used in conjunction with the DOMO98 computer code, it was necessary to identify some basis for comparison since it has already been established that the models created in this study do not give accurate results due to the need for significant detail in the model. Since the original analysis used the CEB-FIP/EC2 model with the code, it was decided to compare the data from the original analysis with the recorded strains to establish how much greater or smaller the

predicted strains will be. Once the difference and the direction of the difference was known (i.e. increasing or decreasing), it was possible to compare this with the differences in strain calculated for the different creep and shrinkage functions using the Cogan03 model. Table 7.7 shows the measured strains and predicted strains from the original DOMO analysis at 17 years. It can be seen that for all locations the original analysis using the CEB-FIP/EC2 model slightly overestimated the strains at every location by between 2 and 27%. This would suggest that in comparing the Cogan03 model strains for the different prediction models, any models which predict strains which are less than the CEB-FIP/EC2 model (to within twice the percentage change between the measured and original strains in Table 7.7), can be considered to give a closer agreement with the measured data, while any strains that are greater than the CEB-FIP/EC2 model can be considered to give strains which are less accurate. This is obviously an arbitrary and approximate method of determining the accuracy of the creep and shrinkage models, but it is sufficient since it is not possible to repeat the original analysis due to time constraints.

Figures 7.8 and 7.9 show the comparison of predicted strains made for model Cogan03 using the different creep and shrinkage functions within the DOMO98 code for the bottom flange of segment 1 and the top flange of segment 12 respectively. Comparisons at all other locations can be found in Appendix F. The x-axis represents the age of the concrete after casting in days, while the y-axis shows the total strain. The strains predicted using the various creep and shrinkage models are represented by the different curves as denoted by the legend. Since it is known that all measured strains will be lower than the strains predicted using the CEB-FIP/EC2 creep function, then this model will serve as the upper boundary for improved agreement with the measured data, while the lower boundary line is represented by the dashed line on the chart.

It can be observed from Figures 7.8 and 7.9 that even though the shapes of the curves are slightly different, the magnitudes of the predicted strains are very similar, and there are three distinct groups of results. At 17 years, the CEB-FIP/EC2, ACI and B3+ models give strains in the range of 500 – 600με at both locations, the BP-KX+, B3, GZ and GL models give strains in the range of 845 – 935 με in the bottom flange of segment 1 and 940 – 1100 με in the top flange of segment 12, while the BP-KX model predicts a strain of 1200 με in the bottom flange of segment 1 and 1257 με in the top flange of segment 12. The same groups of results can be observed in all other locations with the exception of the bottom flange of segment 12 where the magnitude of the predicted strains is much less and as such the same groups are not as readily distinguishable.

Examination of Figure 7.8 shows that in the bottom flange of segment 1, after 17 years, the B3+ model predicts a strain behaviour that is very similar to the CEB-FIP/EC2 model but approximately 100 $\mu\epsilon$ less i.e. within the upper and lower boundary lines, indicating that this creep and shrinkage model gives a different overall agreement with the recorded strains. The ACI model predicts strains that are marginally less than the CEB-FIP/EC2 model after 17 years although the strain behaviour differs in that the strains are greater over the first 4000 days and outside the upper boundary line since the strains predicted by the CEB-FIP/EC2 model are increasing at a slower rate suggesting that the agreement with the recorded data is poorer when used in conjunction with DOMO98. After 17 years, the group of strains predicted using the BP-KX+, GZ, B3 and GL models are much greater than the CEB-FIP/EC2 model (in the range of 240 – 330 $\mu\epsilon$ larger), while the BP-KX model is over 600 $\mu\epsilon$ greater indicating that the strain behaviour predicted by these models is much less accurate when used in conjunction with the DOMO98 computer code.

The same patterns can be observed in the top flange of segment 12 (Figure 7.9). After 17 years, the ACI model predicts strains that are 82 $\mu\epsilon$ less than the CEB-FIP/EC2 model although the strain behaviour over time is again different i.e. initially greater over the first 1500 days but since the behaviour shows that the majority of the strain has taken place after 700 days, there is very little increase after this time and hence the strains predicted using the CEB-FIP/EC2 model eventually are greater. Despite the fact that most of the strains predicted by the ACI model lie within the two boundaries, since the strain behaviour is different than the CEB-FIP/EC2 model it can be said that the ACI model gives adequate agreement with the measured data in this instance. The B3+ model again predicts strain behaviour that is very similar to the CEB-FIP model, with the B3+ strains lying within the two boundaries, although the rate at which strain develops is slightly greater and so the strains predicted by the B3+ model are only marginally smaller at 17 years. The group of strains predicted using the BP-KX+, GZ, B3 and GL models are again much larger than the CEB-FIP/EC2 model by between 350 and 510 $\mu\epsilon$, while the BP-KX model is over 670 $\mu\epsilon$ greater and so can be said to give poor agreement with the measured data when used in conjunction with DOMO98.

Comparisons of the strains predicted using DOMO98 with the different creep and shrinkage models, at all other locations can be observed in the Figures in Appendix F. Exactly the same conclusions can be reached for the top flange of segment 1, and the top and bottom flanges of segment 6. The B3+ model in all cases predicts strains which lie within the upper and lower boundaries, indicating that this model would give the best overall agreement with the measured data. The ACI model predicts slightly different strain behaviour which is initially outside the upper boundary, but ends up within the two boundaries due to the lower rate of

strain gain indicating that this model would give adequate agreement with the measured data. All other models considerably over-predict the strain behaviour when used in conjunction with the DOMO98 computer code. Due to the closeness of the original DOMO data and the measured data at 17 years in the bottom flange of segment 12 (1 $\mu\epsilon$ difference), no model gives closer agreement with the measured data than the original model which used the CEB-FIP/EC2 model.

Since it has been concluded that the CEB-FIP/EC2 and B3+ creep functions predict strains which give the best agreement with the measured data when used in conjunction with the DOMO98 computer code, the influence of the material properties can be addressed by comparing the input data that is needed by these two models before modelling can take place. Table 7.8 shows a comparison of the material parameters needed by both models before strains can be predicted using the DOMO98 computer code. The B3+ model calculates the 28-day elastic modulus using the average cylinder strength, and so the only other significant difference is the inclusion of the concrete mix properties. From the results of sensitivity study on the influence of the prediction model input data detailed in Chapter 4, it was found that the main material factors that influence the strain behaviour of concrete over time are the 28-day compressive strength of the concrete, the 28-day elastic modulus, the relative humidity of the environment, and the size and shape of the material, while all other material parameters have a negligible influence over time. Therefore, initially it would appear that the main influencing material factors are the same as those determined from the sensitivity study, since both models include them as part of the input data, although further analysis in the form of a sensitivity study on these parameters as part of the DOMO98 computer code would be required to confirm this.

7.8 Conclusions

The results presented here are confined to the strains obtained from modelling the strain behaviour in the bottom flange of segment 1 and the top flange of segment 12. A more complete set of results showing the full scope of the work carried out is presented in Appendix F. This includes comparisons between the strains predicted using each of the Cogan DOMO98 models and the strains predicted using the original version of DOMO for all other locations where recorded data was available. Furthermore, for each of these locations Appendix F contains comparisons between the DOMO98 Cogan03 model strains predicted using the creep and shrinkage functions added to the DOMO98 computer code by the author. The results summarised in Appendix F represent a significant effort in terms of time and decision making including detailed discussions with the author of the DOMO98 program in

Prague. However, the main conclusions arising from the complete study may be appreciated by concentrating attention on the results obtained for the bottom flange of segment 1, and the top flange of segment 12 which are reported in this chapter.

One of the main objectives of this study was to investigate methods of predicting the long-term behaviour of the Cogan Viaduct using current creep and shrinkage prediction models. It was found that:

- The strains predicted using the creep and shrinkage prediction models investigated in this research project (based on the residual stresses obtained after construction), were far greater than those measured, sometimes by a factor of eight.

- The closest agreement with the recorded strains was given by the BS5400 design code which predicted strains which were no more than twice that measured indicating that the structure was performing within the original design assumptions after a period of 17 years.

The DOMO98 computer code uses detailed information pertaining to the construction sequence, prestressing information and material properties and has previously been shown to accurately predict the strain behaviour of the viaduct over time. From the results of a study on the level of detail of the input necessary to replicate the success of the original analysis, it was found that:

- No matter how simple or complex the simplification of the construction sequence and prestressing data, if the structure is not modelled to a level of detail that is similar to that used in real life, the prediction of the strain behaviour of the structure is unreliable.

- The errors induced in the model by the assumptions made in simplifying the construction sequence and prestressing data, had an accumulative effect resulting in predicted strains which did not agree well with the measured strains.

- Increasing levels of detail of the construction sequence and prestressing data did not necessarily give predicted strains that were closer to the recorded strains. In fact the opposite was often the case.

In updating the DOMO98 computer code to include the creep and shrinkage prediction models used throughout this research project, it was found that:

- The CEB-FIP/EC2 and B3+ models predicted strains which gave the best agreement with the measured data when used in conjunction with the DOMO98 computer code. The ACI model gave adequate agreement while all other models predicted strains which did not agree well with the measured data when used in conjunction with the DOMO98 computer code.
- From inspection of the input data required by these two models, initial conclusions suggest that the material properties which are most influential in predicting the strain behaviour of the viaduct are the 28-day compressive strength and elastic modulus of the concrete, the relative humidity of the environment, and the specimen geometry.

Table 7.1. Critical Dates for Cogan Viaduct (Vitek and Barr[2]).

Segment No.	Date of Casting	Time Difference (days)	Date of Erection
1	05/03/1987	-	02/08/1987
6	14/03/1987	9	07/08/1987
12	25/03/1987	20	17/08/1987

Table 7.2. Constant stress applied at time t_0, in prediction models.

Segment	Flange	Continuity Stressing - Phase 1 (N/mm^2)	Continuity Stressing – Phase 2 (N/mm^2)	Superimposed Dead Load (N/mm^2)	Dead Load (N/mm^2)	Total (N/mm^2)
1	Top	-12.3	-11.9	+1.9	+8.8	-13.5
	Bottom	-5.1	-5.2	-2.3	-10.7	-23.3
6	Top	-7.5	-7.8	-0.7	+2.6	-13.4
	Bottom	-8.6	-7.7	+1.2	-4.3	-19.4
12	Top	-3.7	-6.4	-1.1	0	-11.2
	Bottom	-6.5	-9.6	+1.8	0	-14.3

Table 7.3. Differences in erection times between the actual global timescale and the DOMO98[6] model timescale.

Recorded Data		DOMO98 Model Data		
Designation	Time Erected (days)	Designation	Time Erected (days)	Time Difference (days)
Segment No. 1	139	Element No. 19	367	228
Segment No. 6	130	Element No. 27	372	242
Segment No. 12	119	Element No. 36	382	263

Table 7.4. Calculated compression stresses (N/mm^2) at the location of the strain gauges (Lark *et al*[151]).

	Age: 766 days		Age: 3141 days	
Location	**Top**	**Bottom**	**Top**	**Bottom**
Segment 1	10.50	7.07	9.98	7.27
Segment 6	8.42	6.54	8.17	6.58
Segment 12	8.45	7.56	8.38	7.36

Table 7.5. Predicted strains (microstrain) at all locations for all models at 17 years.

Segment	Flange	Original	Cogan01	Cogan02	Cogan03	Cogan04	Cogan05
1	Top	**594**	**593**	*377*	*515*	*397*	*361*
	Bottom	**425**	**489**	**466**	**604**	**484**	**812**
6	Top	**494**	**594**	*424*	*376*	*427*	*297*
	Bottom	**400**	**489**	**516**	**555**	**623**	**745**
12	Top	**420**	**594**	**424**	**586**	**778**	**763**
	Bottom	**388**	**489**	**516**	*217*	*288*	*166*

Table 7.6. Difference between new model strains and original model strains (microstrain) at 17 years.

Segment	Flange	Cogan01	Cogan02	Cogan03	Cogan04	Cogan05
1	Top	*1*	*217*	*79*	*197*	*233*
	Bottom	**64**	**41**	**179**	**59**	**387**
6	Top	**100**	*70*	*118*	*67*	*197*
	Bottom	**89**	**116**	**155**	**223**	**345**
12	Top	**174**	**4**	**166**	**358**	**343**
	Bottom	**101**	**128**	*171*	*100*	*222*

Table 7.7. Differences between average measured strain (microstrain) at each location and predicted strains made using the original DOMO[4] model at 17 years.

Segment	Flange	Measured Strain	Predicted Strain	% Decrease
1	Top	594	510	14
	Bottom	425	342	20
6	Top	494	383	22
	Bottom	414	303	27
12	Top	419	320	24
	Bottom	400	392	2

Table 7.8. Model parameters necessary for predicting strains using the CEB-FIP[121]/EC2[131] and B3+[127] models in conjunction with the DOMO98[6] computer code.

Model Parameter	CEB-FIP/EC2	B3+
28-day Compressive Strength (N/mm^2)	√	√
28-day Elastic Modulus (kN/mm^2)	√	
Water Content (kg/m^3)		√
Cement Type		√
Age of Concrete at Drying (days)	√	√
Relative Humidity (%)	√	√
Effective Thickness (mm)	√	√

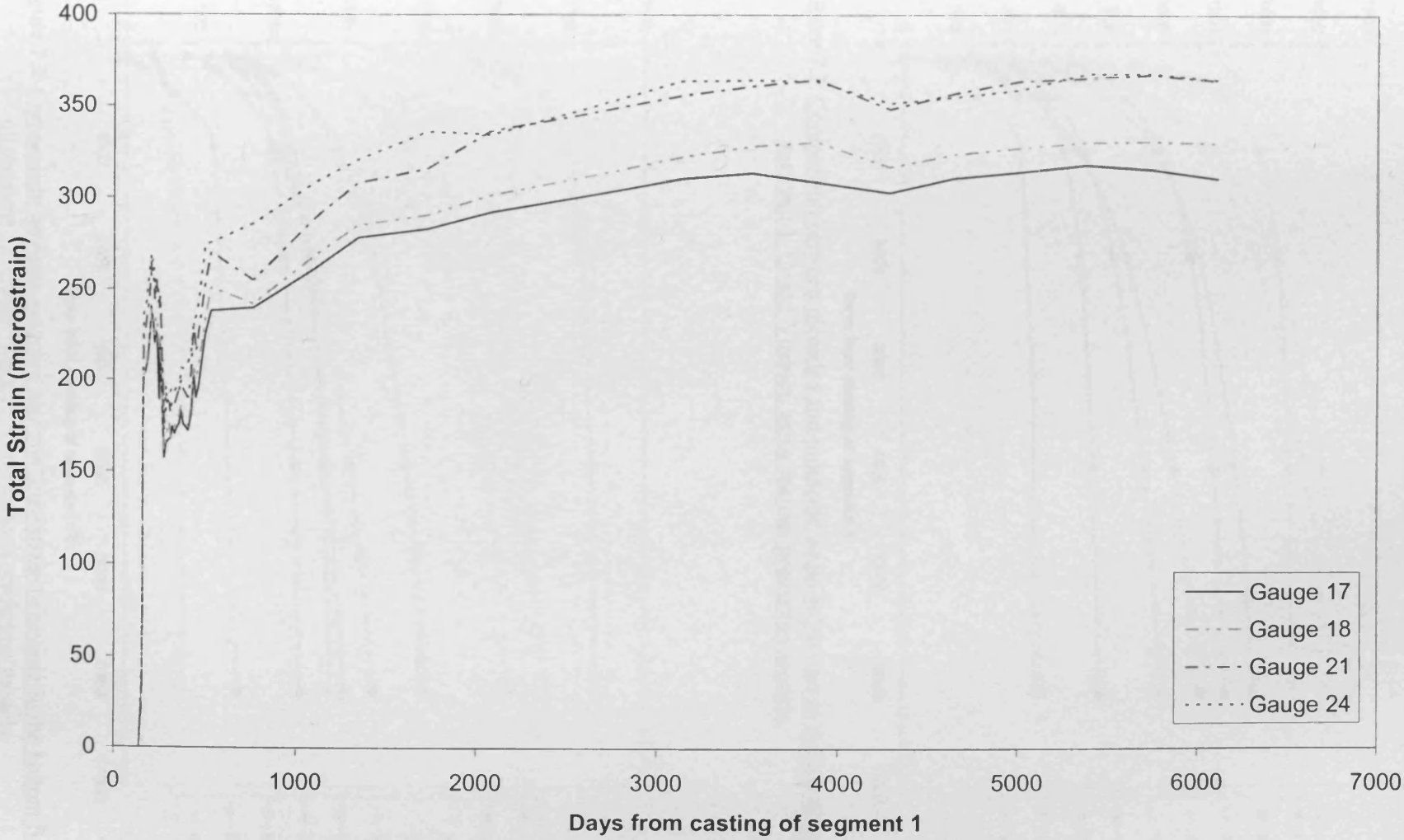

Figure 7.1. Typical long-term strain behaviour in the bottom flange of segment 1, Cogan Viaduct.

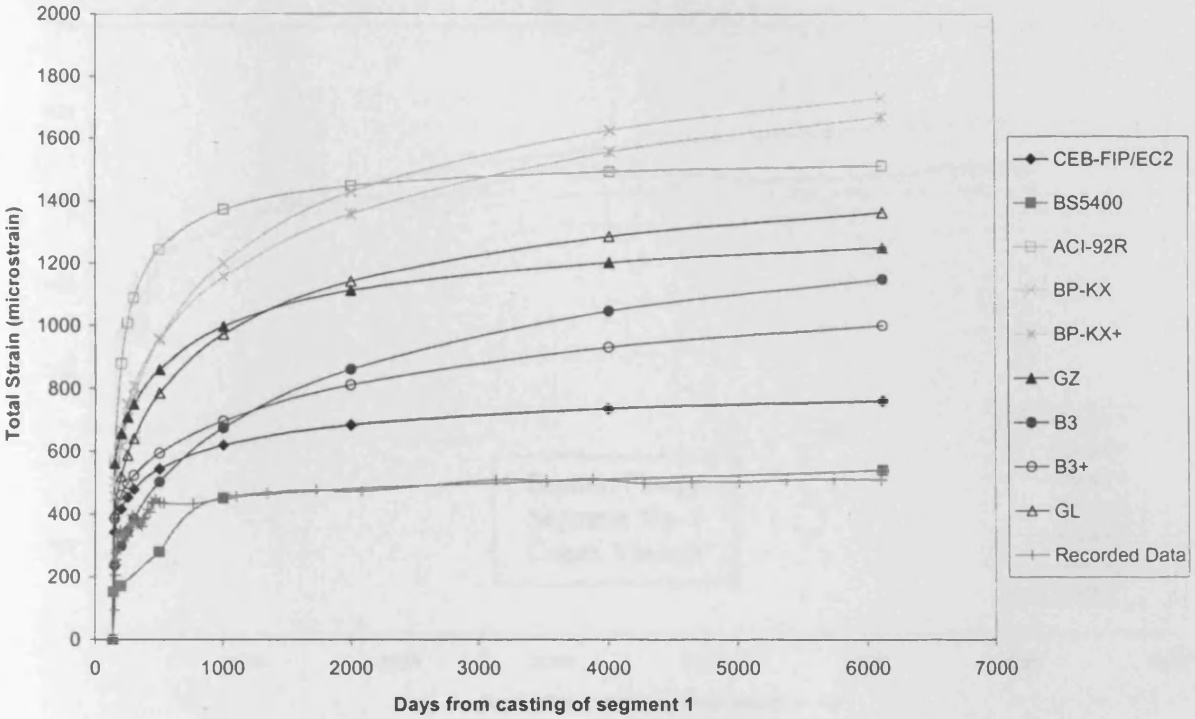

Figure 7.2. Comparison between recorded and predicted strain behaviour in the top flange of segment 1, Cogan Viaduct, using various prediction models.

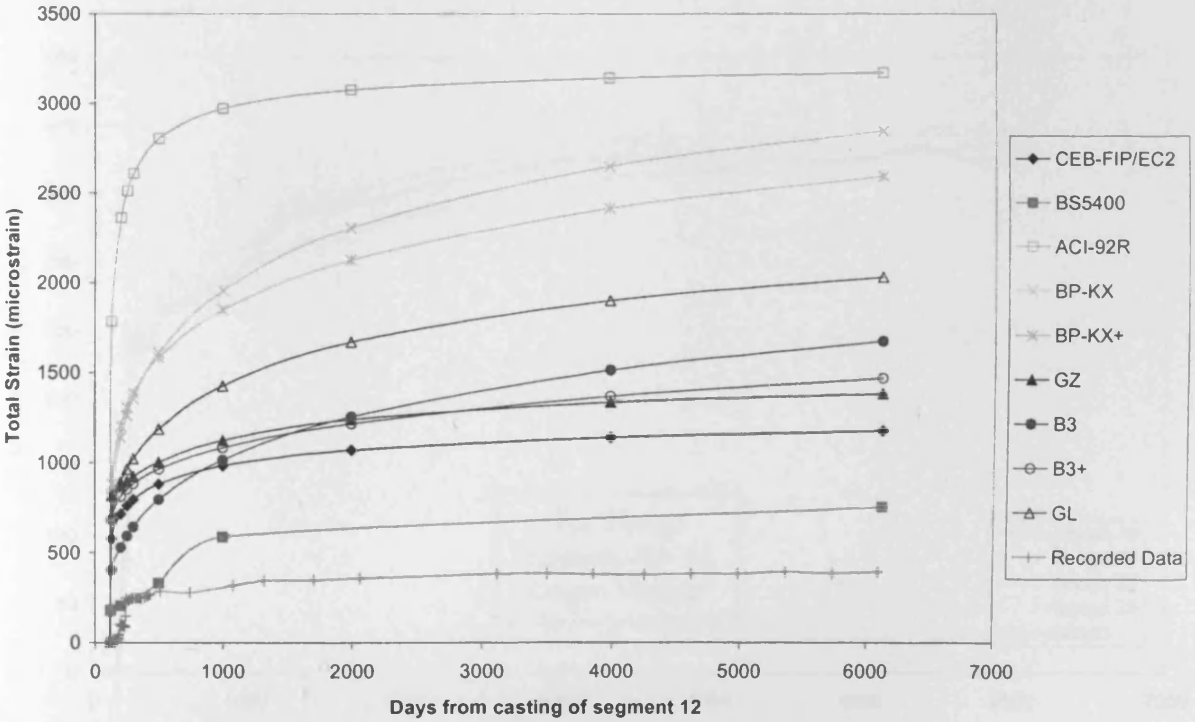

Figure 7.3. Comparison between recorded and predicted strain behaviour in the bottom flange of segment 12, Cogan Viaduct, using various prediction models.

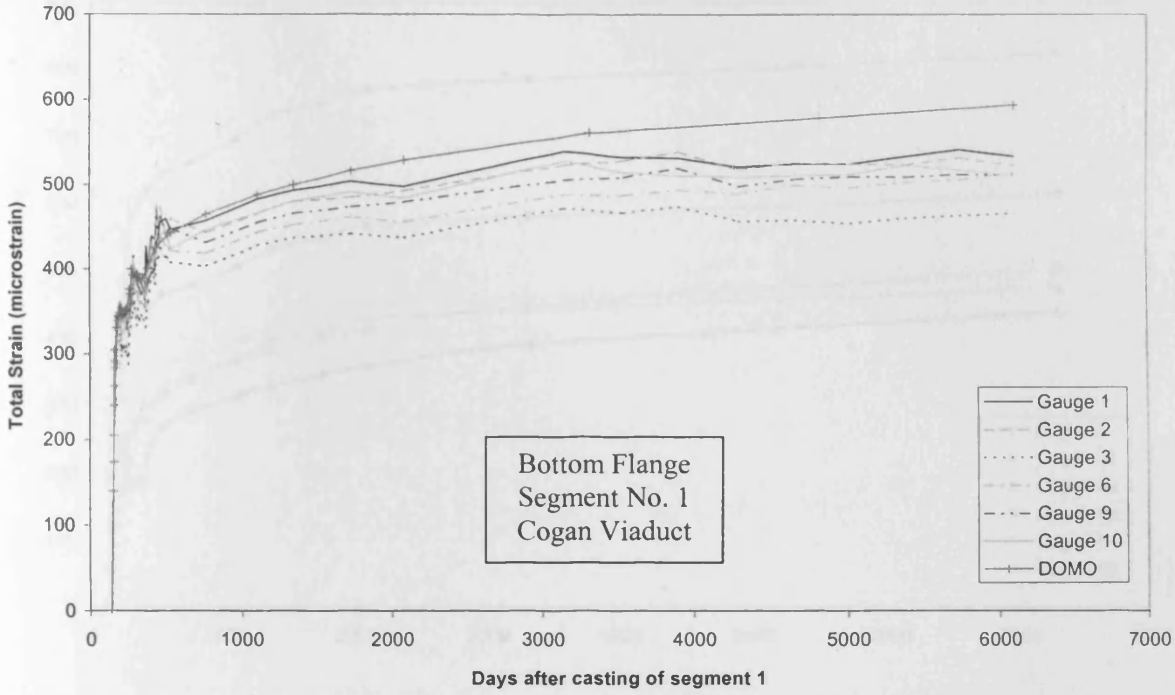

Figure 7.4. Comparison of the strain behaviour predicted using the original DOMO[4] computer code by Barr *et al*[5], with the recorded strain behaviour.

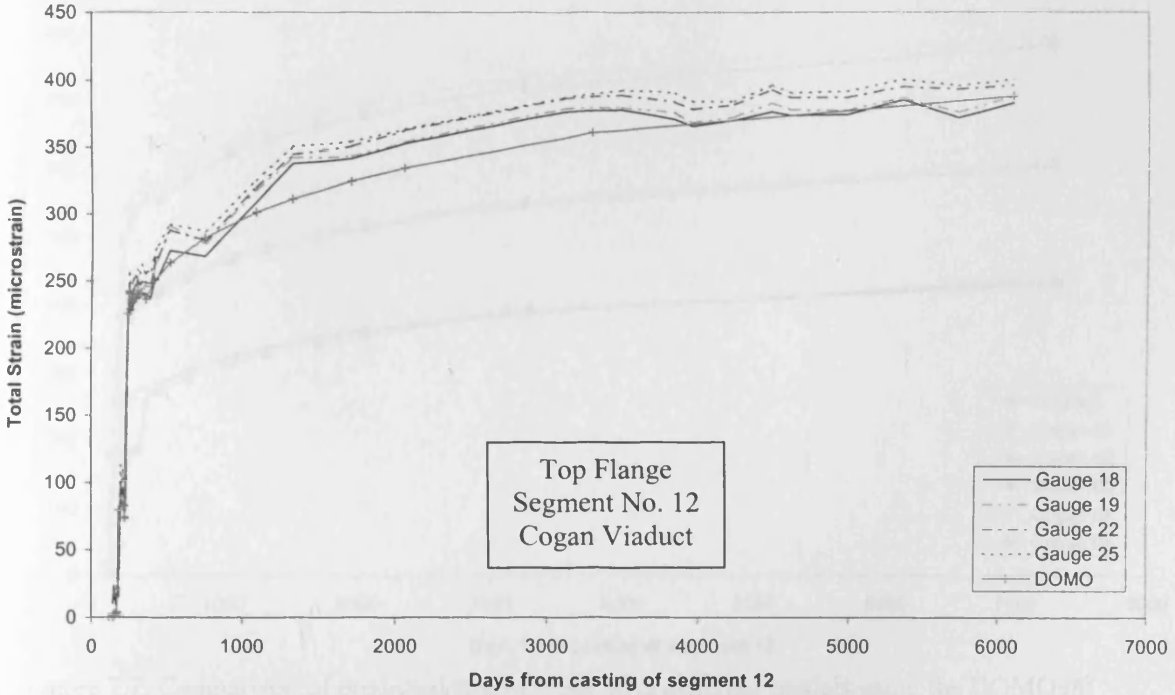

Figure 7.5. Comparison of the strain behaviour predicted using the original DOMO[4] computer code by Barr *et al*[5], with the recorded strain behaviour.

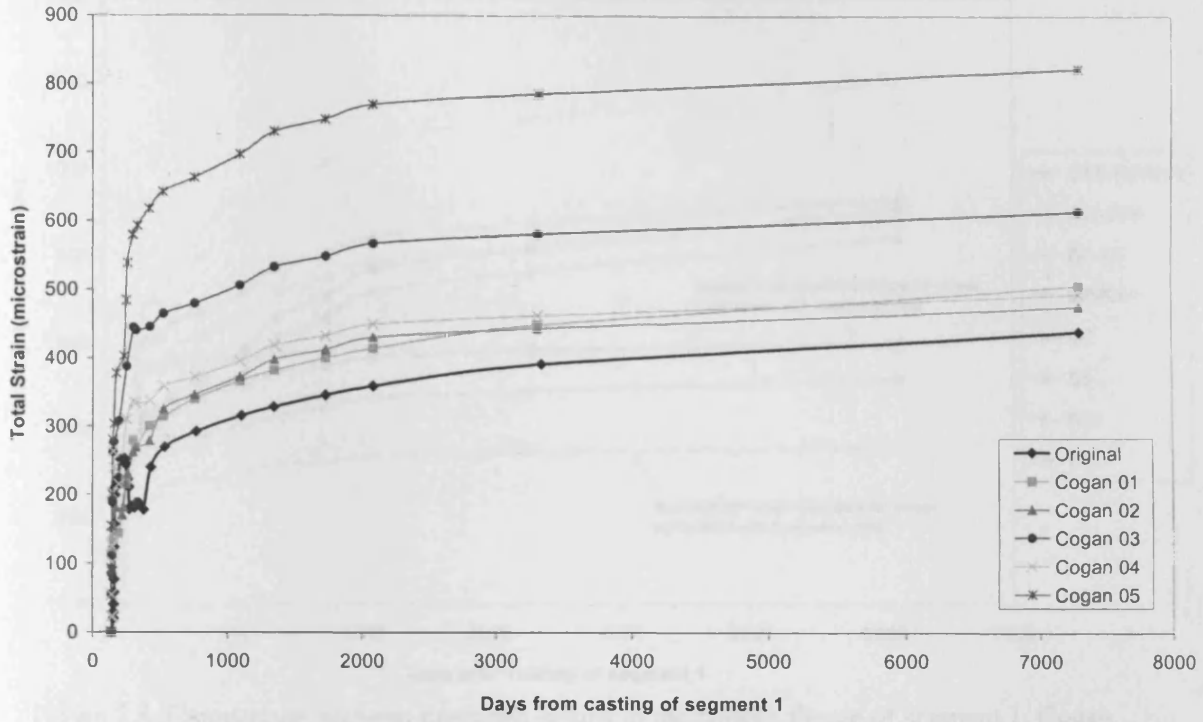

Figure 7.6. Comparison of predicted strains made with different models using the DOMO98[6] computer code in the bottom flange of segment 1, Cogan Viaduct.

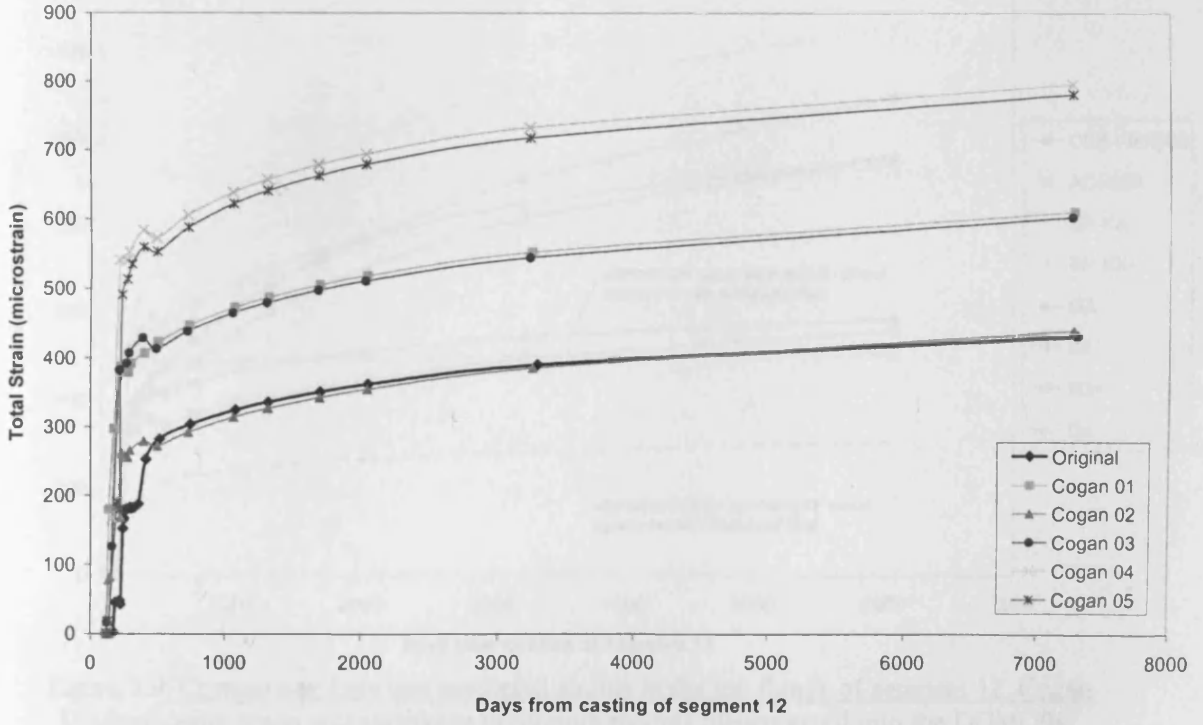

Figure 7.7. Comparison of predicted strains made with different models using the DOMO98[6] computer code in the top flange of segment 12, Cogan Viaduct.

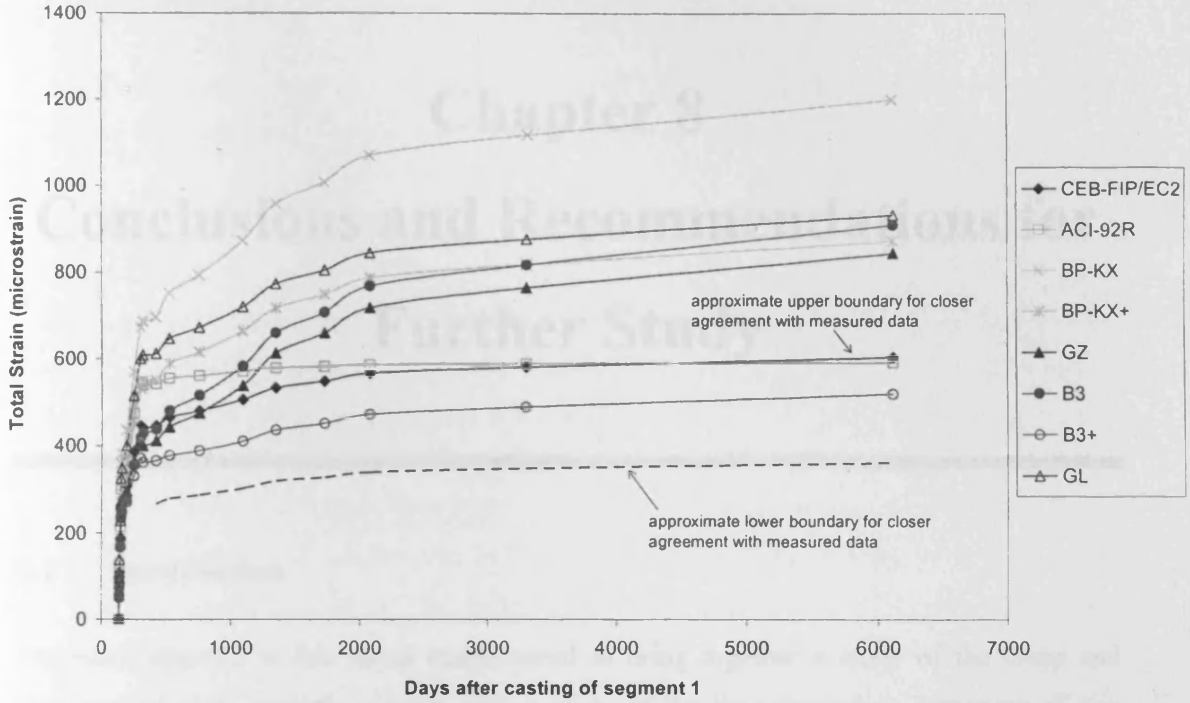

Figure 7.8. Comparison between predicted strains in the bottom flange of segment 1, Cogan Viaduct, using creep and shrinkage prediction models incorporated into the DOMO98[6] computer code.

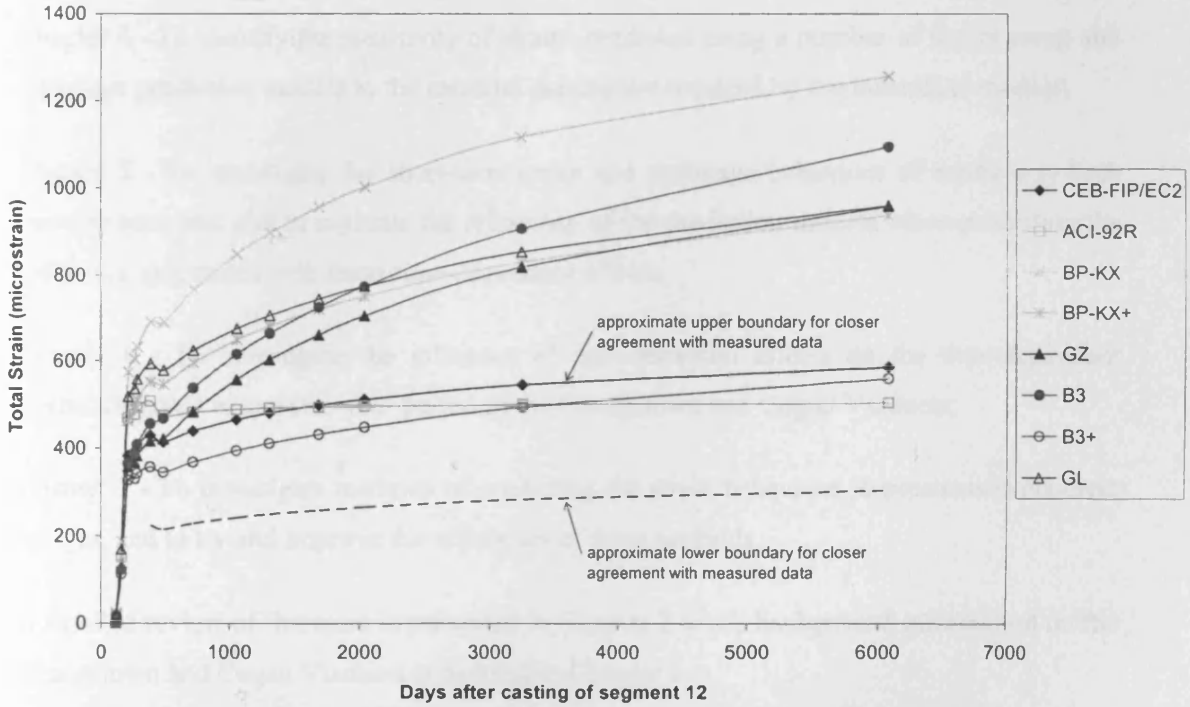

Figure 7.9. Comparison between predicted strains in the top flange of segment 12, Cogan Viaduct, using creep and shrinkage prediction models incorporated into the DOMO98[6] computer code.

Chapter 8
Conclusions and Recommendations for Further Study

8.1 Introduction

The work reported in this thesis endeavoured to bring together a study of the creep and shrinkage of high strength concrete with a study of the time-dependant behaviour of two concrete viaducts. The main objectives of this study were reported in detail in Chapter 1. Generally, these objectives covered four main areas (of interest) and were detailed in the following chapters:

Chapter 4 - To identify the sensitivity of strains predicted using a number of recent creep and shrinkage prediction models to the material parameters required by the individual models;

Chapter 5 - To investigate the short-term creep and shrinkage behaviour of medium to high strength concrete, and to evaluate the reliability of the prediction models when predicting the behaviour associated with these time-dependant effects;

Chapter 6 - To investigate the influence of environmental effects on the time-dependant strains observed over a two-year period in the Grangetown and Cogan Viaducts;

Chapter 7 - To investigate methods of predicting the strain behaviour in prestressed concrete bridges, and to try and improve the efficiency of these methods.

A detailed review of literature is presented in Chapter 2 while background information on the Grangetown and Cogan Viaducts is detailed in Chapter 3.

8.2 Conclusions

Conclusions for each aspect of the investigation have been drawn and are given at the end of their respective chapters. The main conclusions from each are summarised here

8.2.1 Prediction Model Sensitivity Study

A study of how sensitive predicted strains are to the material parameters used in the CEB-FIP Model Code 1990, Eurocode 2 1992, ACI Model 1992, BP-KX Model 1991, BP-KX+ Model 1993, GZ Model 1993, B3 Model 1995, B3+ Model 1996, and GL Model 2001, found that:

- The two most influential parameters on the shrinkage and creep of concrete are the relative humidity of the environment and the compressive strength of concrete. The Young's Modulus of concrete has an effect on the creep strain, although to a lesser extent.

- Individual models are more sensitive to certain parameters than others. Because of this difference in sensitivity between models, it was determined that no one model can be said to be more accurate. It is proposed that when deciding which model to use when predicting shrinkage and creep strains, it is prudent to look at the individual parameters on which each model is dependent and assess the sensitivity level of each of these parameters.

8.2.2 Laboratory Study

The main conclusions from the shrinkage and creep studies of laboratory specimens of a range of normal to high strength concretes were:

8.2.2.1 Shrinkage

- As concrete strength increased from 40 N/mm^2 to 80 N/mm^2 to 100 N/mm^2, the amount of total and drying shrinkage decreased. Furthermore, as concrete strength increased the percentage of total shrinkage that is autogenous shrinkage increased while drying shrinkage decreased, indicating that autogenous shrinkage is more prevalent in high strength concrete.

- pfa concrete has the lowest shrinkage of all despite having a nominal strength of 65 N/mm^2, indicating that the inclusion of pfa within the mix results in a reduction of the total shrinkage.

- A linear relationship between total shrinkage and percentage weight loss was observed for all concrete strengths, indicating that shrinkage is dependent upon water content.

8.2.2.2 Creep

- For concretes of strength 40 N/mm^2, 80 N/mm^2 and 100 N/mm^2 concretes, the rate at which creep strain developed increased with increasing concrete strength. pfa concrete strains developed quickest of all despite the fact that the pfa concrete is weaker than both the C80 and C100 concretes indicating that the inclusion of pfa reduces creep.

- A linear relationship exists between creep strain and stress/strength ratio. However, as the stress/strength ratio increased, the rate at which creep strain developed also increased indicating that creep effects are more pronounced for longer at higher stress/strength ratios.

8.2.2.3 Comparisons with Prediction Models

- Generally, all models predicted strains that gave good to adequate predictions of the recorded shrinkage, creep and total strains for concrete when the material parameters were within the ranges specified by the models. When the concrete properties exceeded the recommended values for the model under consideration, then the agreement given between the predicted and measured strains became unreliable and the user must be selective when choosing which model to use, basing the selection on the concrete properties.

8.2.3 Environmental Effects Resulting in Strain Variation

The influence of environmental effects on the strain behaviour of the Grangetown and Cogan Viaducts was investigated both throughout a year and on a daily basis over selected weeks typical of the four seasons within a year.

8.2.3.1 Annual Study

From strains recorded in the Cogan Viaduct, and it was found that:

- As the temperature increased and RH decreased, strain increased and vice versa.

- The largest changes in strain occurred when the seasons changed from Winter to Spring and Summer to Autumn (20 and 10 $\mu\epsilon$ in the top and bottom flanges respectively). These strains were inversely proportional to the change in temperature.

- A linear relationship existed between changes in average seasonal strain and average seasonal temperature/RH, for the top flange of Cogan Viaduct, but not for the bottom flange.

- Strain response depended on temperature which in turn was related to exposure to direct sunlight (including through cloud cover). Since sunlight was generally responsible for increased temperature, there was a temperature differential between the two flanges leading to a greater strain response in the top flange than in the bottom.

- The relationships between strain and temperature, and strain and RH were opposite since increasing temperature corresponded to a decrease in strain and increasing RH lead to an increase in strain. These linear relationships differed slightly depending on the location of the segment along the span.

8.2.3.2 Weekly Study

The influence of environmental effects on the strain behaviour of the Grangetown and Cogan Viaducts was investigated over selected weeks of the year typical of the four seasons for both viaducts. It was found that:

- A change in external temperature resulted in a delayed change in strain of up to 24 hours.

- The average daily change in strain was of similar magnitude in the Spring and Summer (up to 15 $\mu\epsilon$), and also in the Autumn and Winter, although in the latter seasons was much smaller (maximum of 5 $\mu\epsilon$).

- A linear relationship again existed between strain and temperature for each season of the year but this varied slightly according to the location at which the strain was measured. The gradient of the linear relationship was different for each season. This change can be attributed to the differential temperature effects since the differential temperature profile also changes from season to season indicated that response of the structure to overall temperature change is not solely due to the direct expansion and contraction of the concrete.

- A linear relationship between strain and temperature was observed when RH was within the range 80 – 90% indicating that temperature was the dominant influencing factor in strain variation in structures such as these.

- A change in temperature of around 15°C can cause an increase in strain of approximately 50 $\mu\epsilon$.

8.2.4 Structural Modelling

Methods of predicting the strain behaviour of the Cogan Viaduct were investigated. This was undertaken in three phases.

8.2.4.1 Comparisons with Standard Prediction Models

A comparison of the strains predicted using the creep and shrinkage prediction models used throughout this study with the strains recorded in the viaduct was undertaken. It was found that the strains predicted using the creep and shrinkage prediction models were far greater than those measured, sometimes by a factor of eight. The closest agreement with the recorded strains was given by the BS5400 design code which predicted strains which were no more than twice those measured.

8.2.4.2 DOMO98 Sensitivity Study

A study of the sensitivity of the DOMO98 Computer Code to the detail of the input data required was undertaken. This input data consisted of prestressing, segment and construction details. A previous study used DOMO to successfully model the strain behaviour of the Cogan Viaduct using input data similar in detail to that actually used during the design and construction of the viaduct. An attempt was made to reduce the amount of input data such that a more efficient analysis could be undertaken, which nevertheless predicted strains that gave satisfactory agreement with the strain behaviour observed in the viaduct. This involved various degrees of simplification of the input data and the results obtained were compared with those of the previous study. It was found that:

- No matter how great the simplification of the construction sequence and prestressing data, if the analysis did not model the actual construction sequence as closely as possible, the prediction of strain was unreliable.

- The errors induced in the model by the assumptions made in simplifying the construction sequence and prestressing data, had an accumulative effect resulting in predicted strains which did not agree well with the measured strains.

- Increasing levels of detail describing the construction sequence and prestressing data did not necessarily give predicted strains that were closer to the recorded strains. In fact the opposite was often the case.

8.2.4.3 Influence of Material Properties

The DOMO98 computer code uses the creep and shrinkage function from various prediction models when predicting strains. The code was updated to include the creep and shrinkage functions from the prediction models used throughout this study, so that the most reliable model could be identified when used in conjunction with DOMO98 and a closer agreement with the recorded data could be obtained. It was found that:

- The CEB-FIP/EC2 and B3+ models predicted strains which gave the best agreement with the measured data when used in conjunction with the DOMO98 computer code.

- From inspection of the input data required by these two models, the material properties which are most influential in predicting the strain behaviour of the viaduct are the 28-day compressive strength and elastic modulus of the concrete, the relative humidity of the environment, and the specimen geometry.

8.2.5 Final Conclusions

In summary it can be said that the aim of bringing together two areas of research on the time-dependant behaviour in concrete, and concrete structures, was achieved. The benefits and limitations of using current shrinkage and creep prediction models have been determined through a sensitivity study of their input parameters, through comparisons with shrinkage and creep strains measured in a range of medium to high strength concretes, and through comparisons with shrinkage and creep strains measured in two prestressed concrete viaducts. The prediction of the time-dependant behaviour in these two bridges has been extended further using a complex computer code in conjunction with these models, and while it was not possible to improve the efficiency of predicting reliable strain behaviour over time, an appreciation of the level of detail necessary to do this has been acquired. Finally, the influence of environmental conditions on the strain behaviour of these two structures has been shown to be more prominent than was anticipated. These studies, while valuable in their own

right, have also shown that there is still much to learned about time-dependant behaviour and its prediction in concrete and concrete structures.

8.3 Recommendations for Future Work

Based on the conclusions described above, the following research topics are recommended for future study.

8.3.1 Laboratory Studies

The inclusion of pfa in concrete has a noticeable effect on the material and time-dependant properties of concrete. In this study, pfa was only included in one concrete mix and so it was not possible to determine the effect of increasing or decreasing the amount of pfa in the mix on the material and time-dependant properties of the relevant concrete. Furthermore, due to problems with the environmental controls in the laboratory, it was not possible to fully investigate the effect of pfa on autogenous and drying shrinkage. An understanding of this influence is vital in order to make best use of the advantages associated with using this material as a partial replacement for cement.

As yet, the current prediction models used throughout this study do not take into account the inclusion of pfa in concrete when predicting strains, and the volume of pfa has to be divided between the cement and fine aggregate content parameters. The amount of pfa assumed to contribute to the cement and fine aggregate parameters should be investigated and the strains compared to measured values to determine the optimum proportions.

8.3.2 Field Studies

The linear relationship between strain and temperature observed in the top flanges of the two viaducts was attributed to the temperature differential between the top and bottom flanges in each structure. In order to confirm this, a study of the strain and temperature variation throughout the depth of the section should be undertaken. This would be possible in both structures since each has a number of thermocouples at the location of the strain gauges which were unused in this study due to the capacity of the dataloggers. Since it has been shown that the strain can vary by up to 50 $\mu\epsilon$ due to variations in external temperature, a better understanding of the effect of seasonal variations is necessary.

8.3.4 Structural Modelling Studies

Due to the complexity of the construction sequence, it was not possible to obtain a more efficient method of predicting reliable strain behaviour in the Cogan Viaduct using the DOMO98 Computer Code. It was anticipated that after simplifying the input data, subsequent models where the input data was refined would generate strains that were closer to those of the original analysis. Surprisingly, this was not the case. To further investigate this phenomenon, it is recommended that the Grangetown Viaduct is modelled using the five DOMO98 models to identify if the same behaviour is observed. If it is, then the process of refining the input data should be investigated further using the Cogan Viaduct, until a point is reached where convergence is identified and better agreement with the original analysis is obtained. When this has been done, it should then be possible to model the Grangetown Viaduct in such a way to obtain good agreement with the measured strains. Finally, a sensitivity study of the material parameters used by the creep and shrinkage functions within the various prediction models should be undertaken for a second time to confirm the findings of this study.

Chapter 9
Bibliography

[1] Vitek, J.L., and Barr, B.I.G., 'Cogan and Grangetown Viaducts - Shrinkage Study', Cardiff School of Engineering, University of Wales, Cardiff (1991).

[2] Vitek, J.L., and Barr, B.I.G., 'Cogan Viaduct - Creep Study (Construction and Early Service Life)', Cardiff School of Engineering, University of Wales, Cardiff (1991).

[3] Vitek, J.L., and Barr, B.I.G., 'Cogan Viaduct – Creep Study (Cantilever Construction)', Cardiff School of Engineering, University of Wales, Cardiff (1991).

[4] Vitek, J.L., 'Creep analysis of concrete structures', FIP Congress National Report 1986 (New Delhi), *Civil Engineering Special Issue* **11-12** (1986) 679-683.

[5] Barr, B.I.G., Lark, R.J. and Vitek, J.L., 'Long-term monitoring of prestressed concrete bridges', *Proceeding of the 4th International Bridge Symposium*, Brno, Czech Republic (April 1999) 124-139.

[6] Vitek, J.L., 'Creep and shrinkage analysis of concrete structures. Computer code DOMO98', *Unpublished.*

[7] Lark, R.J., Maguire, J.R., and Thomas, E., 'Condition Monitoring of Concrete Bridges', *Proceedings of the BCA Concrete Communications Conference*, Cardiff (1999).

[8] Beygi, M.H., 'Time dependent behaviour of segmentally erected prestressed concrete bridges', PhD. Thesis submitted to the division of Civil Engineering, School of Engineering, University of Wales, Cardiff (1994).

[9] Barr, B.I.G., Vitek, J. L. and Beygi, M. A., 'Seasonal shrinkage variation in bridge segments', *Materials and Structures* **30** (1997) 106-111.

[10] Hoseinian, S.B., 'Shrinkage of high strength concrete', PhD. Thesis submitted to the division of Civil Engineering, School of Engineering, University of Wales, Cardiff, (2000).

[11] El-Baden, A.S.A., 'Shrinkage of high strength concrete', PhD. Thesis submitted to the division of Civil Engineering, School of Engineering, University of Wales, Cardiff, (2000).

[12] Bush, R.J., 'Creep and shrinkage of high strength concrete', PhD. Thesis submitted to the division of Civil Engineering, School of Engineering, University of Wales, Cardiff, (2002).

[13] Howells R.W., 'Creep of high strength concrete', Undergraduate Final Year Project, submitted to the division of Civil Engineering, School of Engineering, University of Wales, Cardiff, (2001).

[14] Illston, J.M., 'Construction Materials', 2nd Edition, E & FN Spon, London (1994).

[15] Shirley, D.E., 'Introduction to Concrete', 3rd Edition, C & CA, Slough (1985).

[16] Jackson, N. and Dhir, R.K., 'Civil Engineering Materials', 4th Edition, MacMillan, London (1988).

[17] Ohring, M., 'Engineering Materials Science', 1st Edition, Academic Press, London (1995)

[18] British Standards: Structural use of concrete. Code of practice for design and construction. BS 8110: Part 1, British Standards Institution, (1997).

[19] Chamberlain, T., 'Concrete – A Materials Engineers Point of View', Vice-Chairman's Presentation, Concrete Society – Wales Region, (1999).

[20] British Standards: Specification for Portland cement. BS 12, British Standards Institution, (1996).

[21] British Standards: Cement – Part 1: Composition, specifications and conformity criteria for common cements. BS EN 197-1, British Standards Institution, (2000).

[22] British Cement Association, 'Changing from British to European Cement Standards', New Eurocements – Information Sheet 1, BCA (2000).

[23] Neville, A.M., and Brooks, J.J., 'Concrete Technology', 1st Edition Updated, Longman, Harlow (1994).

[24] Neville, A.M., 'Properties of Concrete', 4th Edition, Longman, Harlow (1996).

[25] Soroka, I., 'Portland cement paste and concrete', Macmillan, London (1979).

[26] Bogue, R.H., 'Chemistry of Portland Cement', Van Nostrand Reinhold, New York (1955).

[27] Weidmann,G., Lewis, P., and Reid, N., 'Structural Materials', Butterworths, London (1990).

[28] British Standards: Specification for aggregates from natural sources for concrete. BS 882, British Standards Institution, (1992).

[29] Brown, B., 'Aggregates for Concrete', *Concrete* **32** (1998) 12-14.

[30] Dhir, R.K., McCarthy, M.J., and Tittle, P.A.J., 'Use of conditioned PFA as a fine aggregate component in concrete', *Materials and Structures* **33** (2000) 38-42.

[31] Siddique, R., 'Performance characteristics of high-volume Class F fly ash concrete', *Cement and Concrete Research* **34** (2004) 487-493.

[32] Russell, H.G., 'ACI Defines High-Performance Concrete', *Concrete International* **21** (1999) 56-57.

[33] Neville, A.M., and Aïtcin, P.-C., 'High performance concrete – An overview', *Materials and Structures* **31** (1998) 111-117.

[34] ACI Committee 363, 'State-of-the-Art Report on High Strength Concrete', ACI 363 R-92, American Concrete Institute, (1992).

[35] Breitenbücher, R., 'Developments and applications of high-performance concrete', *Materials and Structures* **31** (1998) 209-215.

[36] Mazloom, M., Ramezanianpour, A.A., and Brooks, J.J., 'Effect of silica fume on mechanical properties of high-strength concrete', *Cement and Concrete Composites* **26** (2004) 347-357.

[37] Bhanja, S., and Sengupta, B., 'Optimum silica fume content and its mode of action on concrete', *ACI Materials Journal* **100** (2003) 407-412.

[38] Kjellsen, K.O., Wallevik, O.H., and Fjällberg, L., 'Microstructure and microchemistry of the paste-aggregate interfacial transition zone of high-performance concrete', *Advances in Cement Research* **10** (1998) 33-40.

[39] Phelan, W.S., 'Admixtures and HPC: A Happy Marriage', *Concrete International* **20** (1998) 27-30.

[40] Agarwal, S.K., Masood, I., and Malhotra, S.K., 'Compatibility of superplasticizers with different cements', *Construction and Building Materials* **14** (2000) 253-259.

[41] Taylor, M.R., Lydon, F.D., and Barr, B.I.G., 'Mix proportions for high strength concrete', *Construction and Building Materials* **10** (1996) 445-450.

[42] Teychenné, D.C., 'Design of normal concrete mixes', Building Research Establishment: Department of the Environment, Watford (1988).

[43] Singh, B.G., 'Specific surface of aggregates related to compressive and flexural strength of concrete', *Journal of American Concrete Institution* **54** (1958) 897-907.

[44] Faroug, F., Szwabowski, J., and Wild, S., 'Influence of Superplasticizers on Workability of Concrete', *ASCE Journal of Materials in Civil Engineering* **11** (1999) 151-157.

[45] Zain, M.F.M., Safiuddin, M., and Yusof, K.M., 'A study on the properties of freshly mixed high performance concrete', *Cement and Concrete Research* **29** (1999) 1427-1432.

[46] Portland Cement Association, 'Design and Control of Concrete Mixes', 11th Edition, Stokie, Illinois (1968).

[47] British Standards: Method for determination of compressive strength of concrete cubes. BS 1881: Part 116, British Standards Institution, (1983).

[48] Bentur, A., and Goldman, A., 'Curing Effects, Strength and Physical Properties of High Strength Silica Fume Concretes', *ASCE Journal of Materials in Civil Engineering* **1** (1989) 46-58.

[49] Kjellsen, K.O., Wallevik, O.H., and Hallgren, M., 'On the compressive strength development of high-performance concrete and paste – effect of silica fume', *Materials and Structures* **32** (1999) 63-69.

[50] Wiegrink, K., Marikunte, S., and Shah, S.P., 'Shrinkage Cracking of High-Strength Concrete', *ACI Materials Journal* **93** (1996) 409-415.

[51] Sabir, B.B., 'High-strength condensed silica fume concrete', *Magazine of Concrete Research* **47** (1995) 219-226.

[52] British Standards: Method for determination of tensile splitting strength. BS 1881: Part 117, British Standards Institution, (1983).

[53] British Standards: Method for determination of flexural strength. BS 1881: Part 118, British Standards Institution, (1983).

[54] Carrasquillo, R.L., Nilson, A.H., and Slate, F.O., 'Properties of high strength concrete subjected to short-term loads', *Journal of The American Concrete Institute* **78** (1981) 171-178.

[55] Persson, B., 'Influence of maturity on creep of high performance concrete with sealed curing', *Materials and Structures* **32** (1999) 506-519.

[56] Gutierrez, P.A., and Canovas, M.F., 'The modulus of elasticity of high performance concrete', *Materials and Structures* **28** (1995) 559-568.

[57] Aïtcin, P.-C., 'Does Concrete Shrink or Swell?' *Concrete International* **21** (1999) 77-80.

[58] Aïtcin, P.-C., Neville, A.M., and Acker, P., 'Integrated View of Shrinkage Deformation', *Concrete International* **19** (1997) 35-41.

[59] Samman, T.A., Mirza, W.H., and Wafa, F.F., 'Plastic Shrinkage Cracking of Normal and High-Strength Concrete: A Comparative Study', *ACI Materials Journal* **93** (1996) 36-40.

[60] Branch, J., Hannant, D.J., and Mulheron, M., 'Factors affecting the plastic shrinkage of high-strength concrete', *Magazine of Concrete Research* **54** (2002) 347-354.

[61] Hammer, T.A., 'Effect of silica fume on the plastic shrinkage and pore water pressure of high strength concrete', , *Materials and Structures* **34** (2001) 273-278.

[62] Aïtcin, P.-C., 'Demystifying Autogenous Shrinkage', *Concrete International* **21** (1999) 54-56.

[63] Tazawa, E., and Miyazawa, S., 'Influence of cement and admixture on autogenous shrinkage of cement paste', *Cement and Concrete Research* **25** (1995) 281-287.

[64] Tazawa, E., and Miyazawa, S., 'Experimental study on mechanism of autogenous shrinkage of concrete', *Cement and Concrete Research* **25** (1995) 1633-1638.

[65] Lee, H.K., Lee, K.M., and Kim, B.G., 'Autogenous shrinkage of high-performance concrete containing fly ash', *Magazine of Concrete Research* **55** (2003) 507-515.

[66] Igarashi, S., Bentur, A., and Kovler, K., 'Autogenous shrinkage and induced restraining stresses in high-strength concretes', *Cement and Concrete Research* **30** (2000) 1701-1707.

[67] Igarashi, S., Bentur, A., and Kovler, K., 'Stresses and creep relaxation induced in restrained autogenous shrinkage of high-strength pastes and concretes', *Advances in Cement Research* **11** (1999) 169-177.

[68] Miyazawa, S., and Monteiro, P.J.M., 'Volume change of high-strength concrete in moist conditions', *Cement and Concrete Research* **26** (1996) 567-572.

[69] Persson, B., 'Eight-year exploration of shrinkage in high-performance concrete', *Cement and Concrete Research* **32** (2002) 1229-1237.

[70] Shah, S.P., Weiss, W.J., and Yang, W., 'Shrinkage Cracking – Can It Be Prevented?', *Concrete International* **20** (1998) 51-55.

[71] Hindy, E.E., Miao, B., Chaallal, O., and Aïtcin, P.-C., 'Drying Shrinkage of Ready-Mixed High-Performance Concrete', *ACI Structural Journal* **91** (1994) 300-305.

[72] Persson, B., 'Experimental studies on shrinkage of high-performance concrete', *Cement and Concrete Research* **28** (1998) 1023-1036.

[73] Nagataki, S., and Yonekura, A., 'Drying Shrinkage and Creep of High-Strength Concrete with Superplasticizer" *Designing for Creep and Shrinkage in Concrete Structures: A Tribute to Adrian Pauw*, American Concrete Institute Publication SP-76, Detroit, Michigan (1982) 403-420.

[74] Verbeck, G.J., 'Carbonation of hydrated Portland cement', *ASTM Special Technical Publication No.* 205 (1958) 17-36.

[75] Kovler, K., 'Why Sealed Concrete Swells', *ACI Materials Journal* **93** (1996) 334-340.

[76] Bažant, Z. P., 'Thermodynamics of hindered absorption and its implications for hardened cement paste and concrete', *Cement and Concrete Research* **2** (1972) 1-16.

[77] Verbeck, G.J., and Helmuth, R.A., 'Structure and Physical Properties of Cement Paste', *Proceedings of the Symposium on the Chemistry of Cement, Tokyo* **3** (1968) 1-37.

[78] Feldman, R.F., and Sereda, P.J., 'A New Model for Hydrated Portland Cement and its Practical Implications', *The Engineering Journal* **53** (1970) 53-59.

[79] Haller, P., 'Shrinkage and Creep of Mortar and Concrete', *Diskussionbericht No.* 124, EMPA, Zurich (1940).

[80] Tazawa, E., and Miyazawa, S., 'Influence of constituents and composition on autogenous shrinkage of cementitious materials', *Magazine of Concrete Research* **49** (1997) 15-22.

[81] Pickett, G., 'Effect of Aggregate on Shrinkage of Concrete and a Hypothesis Concerning Shrinkage', *Journal of the American Concrete Institute* **52** (1956) 581-590.

[82] Ödman, S.T.A., 'Effects of variations in volume, surface area exposed to drying and composition of concrete on shrinkage', *RILEM/CEMBUREAU International Colloqium on the Shrinkage of Hydraulic Concretes* **1** (1968) 20.

[83] Shoya, M., 'Drying shrinkage and moisture loss of super plasticizer admixed concrete of low water cement ratio', *Transactions of the Japan Concrete Institute II* **5** (1979) 103-110.

[84] Mindess, S. and Young, J.F., 'Concrete', Prentice-Hall, New Jersey (1981).

[85] Troxell, G.E., Raphael, J.M., and Davis, R.E., ' Long-time creep and shrinkage tests of plain and reinforced concrete', *Proceedings of the ASTM* **58** (1958) 1101-1120.

[86] Pihlajavaara, S.E., 'A review of some of the main results of a research on the main ageing phenomena of concrete: Effect of moisture conditions on strength, shrinkage and creep of mature concrete', *Cement and Concrete Research* **4** (1974) 761-771.

[87] Parrott, L.J., 'Factors influencing relative humidity in concrete', *Magazine of Concrete Research* **43** (1991) 45-52

[88] British Standards: Structural use of concrete. BS 8110: Part 2, British Standards Institution, (1985).

[89] Almudaiheem, J.A., and Hansen, W., 'Effect of Specimen Size and Shape on Drying Shrinkage of Concrete', *ACI Materials Journal* **84** (1987) 130-135.

[90] Jianyong, L., and Yan, Y., 'A study on creep and drying shrinkage of high performance concrete', *Cement and Concrete Research* **31** (2001) 1203-1206.

[91] Brooks, J.J., 'How Admixtures Affect Shrinkage and Creep', *Concrete International* **21** (1999) 35-38.

[92] Nmai, C.K., Tomita, R., Honda, F., and Buffenbarger, J., 'Shrinkage-Reducing Admixtures', *Concrete International* **20** (1998) 31-37.

[93] Bentz, D.P., Geiker, M.R., and Hansen, K.K., 'Shrinkage-reducing admixtures and early-age desiccation in cement pastes and mortars', *Cement and Concrete Research* **31** (2001) 1075-1085.

[94] Neville, A.M., Dilger, W.H., and Brooks, J.J., 'Creep of plain and structural concrete', Construction Press, London and New York (1983).

[95] Ali, I., and Kesler, C.E., 'Mechanisms of Creep in Concrete', *Symposium on Creep of Concrete*, American Concrete Institute Publication SP-9, Detroit, Michigan (1964) 35-57.

[96] Kovler, K., 'Interdependance of Creep and Shrinkage for Concrete under Tension', *ASCE Journal of Materials in Civil Engineering* **7** (1995) 96-101.

[97] Kovler, K., 'A New Look at the Problem of Drying Creep of Concrete under Tension', *ASCE Journal of Materials in Civil Engineering* **11** (1999) 84-87.

[98] Neville, A.M., and Meyers, B.L., 'Creep of Concrete: Influencing Factors and Prediction', *Symposium on Creep of Concrete*, American Concrete Institute Publication SP-9, Detroit, Michigan (1964) 1-31.

[99] Evans, R.H., and Kong, F.K., 'Creep of Prestressed Concrete', *Developments in Prestressed Concrete – 1*, Applied Science Publishers, London (1978) 95-123.

[100] Kovler, K., Igarashi, S., and Bentur, A., 'Tensile creep behaviour of high strength concretes at early ages', *Materials and Structures* **32** (1999) 383-387.

[101] Sicard, V., Francois, R., Ringot, E., and Pons, G., 'Influence of creep and shrinkage on cracking in high strength concrete', *Cement and Concrete Research* **22** (1992) 159-168.

[102] Ghosh, S., and Hasser, K.W., 'Effects of High Temperature and Pressure on Strength and Elasticity of Lignite Fly Ash and Silica Fume Concrete', *ACI Materials Journal* **93** (1996) 51-60.

[103] Alsayed, S.H., and Amjad, M.A., 'Effect of curing conditions on strength, porosity, absorptivity, and shrinkage of concrete in hot and dry climate', *Cement and Concrete Research* **24** (1994) 1390-1398.

[104] Almusallam, A.A., 'Effect of environmental conditions on the properties of fresh and hardened concrete', *Cement and Concrete Composites* **23** (2001) 353-361.

[105] Chan, S.Y.N., Luo, X., and Sun, W., 'Effect of high temperature and cooling regimes on the compressive strength and pore properties of high strength concrete', *Construction and Building materials* **14** (2000) 261-266.

[106] Bairagi, N.K., and Dubal, N.S., 'Effect of thermal cycles on the compressive strength, modulus of elasticity, modulus of rupture and dynamic modulus of concrete', *Indian Concrete Journal* **70** (1996) 423-426.

[107] Luo, X., Sun, W., and Chan, Y.N., 'Residual compressive strength and microstructure of high performance concrete after exposure to high temperature', *Materials and Structures* **33** (2000) 294-298.

[108] Chakrabarti, S.C., and Jain, A.K., 'Strength properties of concrete at elevated temperature', *Indian Concrete Journal* **73** (1999) 495-501.

[109] Chan, Y.N., Luo, X., and Sun, W., 'Compressive strength and pore structure of high-performance concrete after exposure to high temperature up to 800°C', *Cement and Concrete Research* **30** (2000) 247-251.

[110] Saad, M., Abo-El-Enein, S.A., Hanna, G.B., and Kotkata, M.F., 'Effect of temperature on physical and mechanical properties of concrete containing silica fume', *Cement and Concrete Research* **26** (1996) 669-675.

[111] Mohd Zain, M.F., and Radin, S.S., 'Physical properties of high-performance concrete with admixtures exposed to a medium temperature range 20°C to 50°C', *Cement and Concrete Research* **30** (2000) 1283-1287.

[112] Xu, Y., Wong, Y.L., Poon, C.S., and Anson, M., 'Impact of high temperature on PFA concrete', *Cement and Concrete Research* **31** (2001).

[113] Balendran, R.V., and Martin-Buades, W.H., 'The influence of high temperature curing on the compressive tensile and flexural strength of pulverised fuel ash concrete', *Building and Environment* **35** (2000) 415-423.

[114] Bažant, Z. P. and Baweja, S., 'Creep and shrinkage prediction model for analysis and design of concrete structures – Model B3', Published as a draft RILEM recommendation in *Materials and Structures* **28** (1995) 357-365, 415-430, 488-495, with Errata in **29** (1996) 126.

[115] Ross, A.D., 'Concrete creep data', *The Structural Engineer* **15** (1937) 314-326.

[116] ACI Committee 209, 'Prediction of creep, shrinkage and temperature effects in concrete structures, (ACI 209-82)', American Concrete Institute, Detroit (1982).

[117] ACI Committee 209, 'Prediction of creep, shrinkage and temperature effects in concrete structures, (ACI 209R-92)', American Concrete Institute, Detroit (1992).

[118] CEB-FIP, 'International Recommendations for the Design and Construction of Concrete Structures – a tentative draft for a complete set of provisional practical recommendations relating to all aspects of design and construction', Comité Euro-International du Béton - Fédération Internationale de la Précontraine, (1964).

[119] CEB-FIP, 'International Recommendations for the Design and Construction of Concrete Structures – Principles and Recommendations', Comité Euro-International du Béton - Fédération Internationale de la Précontraine, FIP Sixth Congress, Prague, (1970).

[120] CEB-FIP, 'Model code for concrete structures', Comité Euro-International du Béton - Fédération Internationale de la Précontraine, Paris, April (1978).

[121] CEB-FIP, 'CEB-FIP Model Code (1990), Design Code', Comité Euro-International du Béton - Fédération Internationale de la Précontraine, (Thomas Telford, London).

[122] Guénot, I., Torrenti, J.-M., and Laplante, P., 'Stresses in Early-Age Concrete: Comparison of Different Creep Models', *ACI Materials Journal* **93** (1996) 254-259.

[123] Bažant, Z. P. and Panula, L., 'Practical prediction of time dependent deformations of concrete', Parts I-VI, *Materials and Structures* **11** (1978) 307-316, 317-328, 425-434, **12** (1979) 169-183.

[124] Bažant, Z. P. and Panula, L., 'Creep and shrinkage characterisation for analyzing prestressed concrete structures', *Journal of the Prestressed Concrete Institute* **25** (1980) 86-122.

[125] Bažant, Z. P., Kim, J. K. and Panula, L., 'Improved prediction model for time dependent deformations of concrete', Part 1 – Shrinkage, *Materials and Structures* **24** (1991) 327-345, Part 2 – Basic creep, *ibid.* **24** (1991) 409-420, Part 3 – Creep at drying, *ibid.* **25** (1992) 21-28, Part 4 – Temperature effects, *ibid.* **25** (1992) 84-94, Part 5 – Cyclic load and cyclic humidity, *ibid.* **25** (1992) 163-169.

[126] Bažant, Z. P., Xi, Y. and Baweja, S., 'Improved prediction model for time dependent deformations of concrete', Part 7 – Short form of BP-KX model, statistics and extrapolation of short-time data, *Materials and Structures* **26** (1993) 567-574.

[127] Bažant, Z. P. and Baweja, S., 'Short form of creep and shrinkage prediction model B3 for structures of medium sensitivity', *Materials and Structures* **29** (1996) 587-593.

[128] Gardner, N.J. and Zhao, J.W., 'Creep and shrinkage revisited', *ACI Materials Journal* **90** (1993) 236-246.

[129] Gardner, N.J. and Lockman, M.J., 'Design provisions for drying shrinkage and creep of normal-strength concrete', *ACI Materials Journal* **98** (2001) 159-167.

[130] British Standards: Steel, concrete and composite bridges. BS 5400: Part 4, British Standards Institution, (1990).

[131] British Standards: Eurocode 2: Design of concrete structures – Part 1: General rules and rules for buildings. DD ENV 1992-1-1: 1993, British Standards Institution, (1992).

[132] Parrott, L.J., 'Simplified methods of predicting the deformation of structural concrete', Development Report, Cement and Concrete Association, (1979).

[133] Miller, M.D., 'State-of-the-Art-Report: Durability Survey of Segmental Concrete Bridges', *PCI Journal* **40** (1995) 110-114.

[134] Woodward, R.J., 'Collapse of a Segmental Post-Tensioned Concrete Bridge', *Transportation Research Record* **1211** (1989) 38-59.

[135] Ziadat, G.S., and Waldron, P., 'Segmental Construction of concrete bridges: A state-of-the-art report', Department of Civil Engineering, University of Bristol, UK, Report No. UBCE/C/86/1 (1986).

[136] County of South Glamorgan, 'Peripheral distributor road, Grangetown link', South Wales (1987).

[137] Mayne, K., A family of glued segmental bridges', *Bridge Assessment Management and Design, Proceedings of the Centenary Year Bridge Conference,* Cardiff (1994) 11-18.

[138] Barr, B.I.G., Waldron, P., and Evans, H.R., 'Instrumentation of glued segmental box girder bridges', *Proceedings of the IABSE Colloqium on Monitoring Large Structures and Assessment of their Safety*, Bergamo (1987) 175-189.

[139] Ramezankhani, M., Waldron, P., and Ziadat, G.S., 'Measurement of time-dependent behaviour in the Cogan Spur Viaduct: Vol 1. – Instrumentation and early results', Department of Civil Engineering, University of Bristol, UK, Report No. UBCE/C/91/20 (1991).

[140] Nicolaides, D., 'Performance monitoring of Cogan Viaduct', Dissertation submitted in partial fulfillment of the requirements for the degree of MSc in Structural Engineering, School of Engineering, University of Wales, Cardiff (2001).

[141] ASTM Standard Test Method, 'Test for creep of concrete in compression', designation: C 512-87, reapproved 1992.

[142] Khandri, F., *MPhil. Thesis in preparation.*

[143] British Standards: Pulverized-fuel ash. Specification for pulverized-fuel ash for use with Portland cement. BS 3892: Part 1, British Standards Institution, (1997).

[144] British Standards: Concrete admixtures. Specification for superplasticizing admixtures. BS 5075: Part 3, British Standards Institution, (1985).

[145] Hsu, K.C., Chiu, J.J., Chen, S.D., and Tseng, Y.C., 'Effect of addition time of a superplasticizer on cement absorption and on concrete workability', Cement and Concrete Composites **21** (1999) 425-430.

[146] British Standards: Testing concrete. Method for determination of slump. BS 1881: Part 102, British Standards Institution, (1983).

[147] British Standards: Testing concrete. Method for determination of Vebe time. BS 1881: Part 104, British Standards Institution, (1983).

[148] Gage Technique Ltd: Vibrating wire strain gauge technical data sheet no. TSR_55, Gage Technique Ltd, (1992).

[149] Harvey, R.J., 'Creep of concrete masonry', Phd. Thesis submitted to the division of Civil Engineering, School of Engineering, University of Wales, Cardiff, (1996).

[150] Norris, P., Wood, J. G. M. and Barr, B. I. G., 'A torsion test to evaluate the deterioration of concrete due to alkali-aggregate reaction', *Magazine of Concrete Research* **42** (1990) 239-244.

[151] Lark, R.J., Howells, R.W., and Barr, B.I.G., 'Behaviour of post-tensioned concrete box girders', *Proceedings of the Institution of Civil Engineers, Bridge Engineering* **157** (2004) 71 – 81.

Appendix A

Prediction Models

Contents

A1.0 CEB-FIP Model Code 1990/Eurocode 2 1992

The prediction of the material parameters of this model is restricted the following parameter ranges:

$12 \leq f_{ck} \leq 80$ f_{ck} in MPa,

$40 \leq RH \leq 100$ RH in %,

$\sigma_c(t_0)/f_{cm}(t_0) \leq 0.4$ at age of loading t_0.

The following equations are used in the calculation of shrinkage and creep strains in the CEB-FIP Model Code 1990 and Eurocode 2 1992.

A1.1 Notation

Parameter	Description
t	time, representing the age of the concrete (days)
t_s	age when drying begins (days) ($t_s \leq t_0$)
t_0	age at loading (days)
$\epsilon_{cs}(t, t_s)$	Total shrinkage strain at time, t (microstrain)
$\epsilon_{ci}(t_0)$	Instantaneous strain at loading time, t_0 (microstrain)
$\epsilon_{cc}(t, t_0)$	Total creep strain at time, t (microstrain)
$\sigma(t, t_0)$	Applied uniaxial stress at loading time, t_0 (N/mm^2)
f_{ck}	28-day standard cylinder strength (N/mm^2)
f_{cm}	28-day mean compressive strength (N/mm^2)
$f_{cm}(t_0)$	Compressive strength at loading time t_0 (N/mm^2)
E_{ci}	28-day Elastic Modulus (N/mm^2)
$E_c(t_0)$	Elastic Modulus at loading time t_0 (N/mm^2)
RH	Relative humidity of the environment (%)
A_c	Cross-sectional area of specimen (mm^2)
u	Perimeter of specimen in contact with the atmosphere (mm)

A1.2 Shrinkage strain

$$\varepsilon_{cs}(t, t_s) = \varepsilon_{cso}\beta_s(t - t_s) \qquad \text{(microstrain)} \qquad \text{(A1.01)}$$

reference equations: A1.02 and A1.07.

Notional shrinkage coefficient:

$$\varepsilon_{cso} = \varepsilon_s(f_{cm})\beta_{RH} \qquad \text{(microstrain)} \qquad \text{(A1.02)}$$

reference equations: A1.03 and A1.05.

Humidity dependence:

$$\beta_{RH} = \begin{cases} -1.55\beta_{sRH} & \text{for } 40 \le RH \le 99 \text{ (stored in air)} \\ +0.25 & \text{for } RH \ge 99 \text{ (immersed in water)} \end{cases} \quad \text{(A1.03)}$$

reference equation: A1.04.

Humidity coefficient:

$$\beta_{sRH} = 1 - [RH/100]^3 \quad \text{(A1.04)}$$

Parameter based on concrete strength:

$$\varepsilon_s(f_{cm}) = \{160 + 10\beta_{sc}[9 - (f_{cm}/10)]\} \times 10^{-6} \quad \text{(microstrain)} \quad \text{(A1.05)}$$

reference equation: A1.06.

Cement type:

$$\beta_{sc} = \begin{cases} 4 \text{ for slowly hardening cements, S} \\ 5 \text{ for normal or rapid hardening cements, N,R} \\ 8 \text{ for rapid hardening high strength cements, RS} \end{cases} \quad \text{(A1.06)}$$

Coefficient for shrinkage development with time:

$$\beta_s(t - t_s) = \left[\frac{t - t_s}{350(h/100)^2 + t - t_s} \right]^{0.5} \quad \text{(A1.07)}$$

reference equation: A1.08.

Notional member size:

$$h = 2A_c/u \quad \text{(mm)} \quad \text{(A1.08)}$$

A1.3 Instantaneous strain

$$\varepsilon_{ci}(t_0) = \sigma(t_0)/E_c(t_0) \quad \text{(A1.09)}$$

reference equation: A1.10.

Elastic Modulus at time of loading:

$$E_c(t_0) = \beta_E(t_0)E_{ci} \quad \text{(A1.10)}$$

reference equation: A1.11.

Coefficient depending on concrete age:

$$\beta_E(t_0) = [\beta_{cc}(t_0)]^{0.5} \tag{A1.11}$$

reference equation: A1.12.

Coefficient depending on concrete age:

$$\beta_{cc}(t_0) = \exp\left\{ s\left[\frac{28}{t_0}\right]^{1/2} \right\} \tag{A1.12}$$

reference equation: A1.13.

Coefficient depending on concrete age:

$$s = \begin{cases} 0.38 \text{ for slowly hardening cements, S} \\ 0.20 \text{ for normal or rapid hardening cements, N,R} \\ 0.25 \text{ for rapid hardening high strength cements, RS} \end{cases} \tag{A1.13}$$

A1.4 Creep strain

$$\varepsilon_{cc}(t,t_0) = \frac{\sigma(t_0)}{E_{ci}}\phi(t,t_0) \qquad \text{(microstrain)} \tag{A1.14}$$

reference equation: A1.15.

Creep coefficient:

$$\phi(t,t_0) = \phi_0 \beta_c(t-t_0) \tag{A1.15}$$

reference equations: A1.16 and A1.20.

Notional creep coefficient:

$$\phi_0 = \phi_{RH}\beta(f_{cm})\beta(t_0) \tag{A1.16}$$

reference equations: A1.17, A1.18 and A1.19.

Relative humidity factor:

$$\phi_{RH} = 1 + \frac{1 - RH/100}{0.46(h/100)^{1/3}} \tag{A1.17}$$

reference equation: A1.08.

Concrete strength factor:

$$\beta(f_{cm}) = 5.3/\sqrt{f_{cm}} \tag{A1.18}$$

Age at loading factor:

$$\beta(t_0) = 1/[0.1 + (t_0)^{0.2}] \tag{A1.19}$$

Development of creep with time coefficient:

$$\beta_c(t-t_0)=\left[\frac{(t-t_0)}{(\beta_H+t-t_0)}\right]^{0.3} \qquad \text{(A1.20)}$$

reference equation: A1.21.

Relative humidity coefficient:

$$\beta_H=150\left\{1+\left(1.2\frac{RH}{100}\right)^{18}\right\}\frac{h}{100}+250 \qquad \leq 1500 \qquad \text{(A1.21)}$$

reference equation: A1.08.

A2.0 ACI Model 1992

This material parameters considered by this model are subject to the following standard conditions for each variable:

Cement types I and III,
279 $\leq c \leq$446 kg/m^3,
Slump = 70 mm,
Air content $\leq$6%,
Fine aggregate percentage = 50%,
Moist and steam curing regimes,
Curing period = 7 days for moist cured, 1-3 days for steam cured,
Ambient relative humidity $\geq$40%,
Volume/surface ratio = 38 mm,
Stress/strength ratio $\leq$0.5.

If conditions are other than standard, correction factors are used for the variable in question. These correction factors along with the equations used in the calculation of shrinkage and creep strains in the ACI Model will now be detailed.

A2.1 Notation

Parameter	Description
t	time, representing the age of the concrete (days)
t_{la}	age at loading (days)
$(\epsilon_{sh})_t$	Total shrinkage strain at time t (microstrain)
ϵ_i	Instantaneous strain at loading (microstrain)
$(\epsilon_c)_t$	Total creep strain at time t (microstrain)
σ	Applied uniaxial stress at loading (N/mm^2)
E_{ci}	Elastic Modulus at loading (N/mm^2)
λ	Relative humidity of the environment (%)
v/s	Specimen volume/ surface area ratio (mm)
s	Observed concrete slump (mm)
ψ	Fine/total aggregate ratio (%)
c	Cement content (kg/m^3)
α	Air content (%)

A2.2 Shrinkage strain

$$(\varepsilon_{sh})_t = \frac{t}{55+t}(\varepsilon_{sh})_u \qquad \text{(microstrain)} \qquad \text{(A2.01)}$$

reference equation: A2.02.

Ultimate shrinkage:

$$(\varepsilon_{sh})_u = 780\gamma_{sh} \qquad \text{(microstrain)} \qquad \text{(A2.02)}$$

reference equation: A2.03.

Product of shrinkage correction factors:

$$\gamma_{sh} = \gamma_{cp} \times \gamma_{\lambda} \times \gamma_{vs} \times \gamma_{s} \times \gamma_{\psi} \times \gamma_{c} \times \gamma_{\alpha} \qquad \text{(A2.03)}$$

reference equations: A2.04, A2.05, A2.06, A2.07, A2.08, A2.09 and A2.10.

Shrinkage initial moist curing correction factor: (A2.04)

Moist curing duration, (days)	Correction factor, γ_{cp}
1	1.20
3	1.10
7	1.00
14	0.93
28	0.86
90	0.75

Linear interpolation may be used between values.

Shrinkage relative humidity correction factor:

$$\gamma_{\lambda} = \begin{cases} 1.40 - 0.010\lambda & \text{for } 40 \leq \lambda \leq 80 \\ 3.00 - 0.030\lambda & \text{for } 80 > \lambda \leq 100 \end{cases} \qquad \text{(A2.05)}$$

Shrinkage volume/surface ratio correction factor:

$$\gamma_{vs} = 1.2 \exp(-0.00472\ v/s) \qquad \text{(A2.06)}$$

Shrinkage slump correction factor:

$$\gamma_{s} = 0.89 + 0.00161\ s \qquad \text{(A2.07)}$$

Shrinkage fine aggregate percentage correction factor:

$$\gamma_{\psi} = \begin{cases} 0.30 + 0.014\psi & \text{for } \psi \leq 50 \\ 0.90 + 0.002\psi & \text{for } \psi > 50 \end{cases} \qquad \text{(A2.08)}$$

Shrinkage cement content correction factor:

$$\gamma_{c} = 0.75 + 0.00061\ c \qquad \text{(A2.09)}$$

Shrinkage air content correction factor:

$$\gamma_\alpha = 0.95 + 0.008\ \alpha \tag{A2.09}$$

A2.3 Instantaneous strain

$$\varepsilon_i = \frac{\sigma}{E_{ci}} \tag{A2.10}$$

A2.4 Creep strain

$$(\varepsilon_c)_t = v_t \sigma \qquad \text{(microstrain)} \tag{A2.11}$$

reference equation: A2.12.

Creep compliance function:

$$v_t = \frac{t^{0.6}}{10 + t^{0.6}} v_u \tag{A2.12}$$

reference equation: A2.13.

Ultimate creep coefficient:

$$v_u = 2.35\gamma_c \tag{A2.13}$$

reference equation: A2.14.

Product of creep correction factors:

$$\gamma_c = \gamma_{la} \times \gamma_\lambda \times \gamma_{vs} \times \gamma_s \times \gamma_\psi \times \gamma_\alpha \tag{A2.14}$$

reference equations: A2.15, A2.16, A2.17, A2.18, A2.19 and A2.20.

Creep loading age correction factor:

$$\gamma_{la} = \begin{cases} 1.25(t_{la})^{-0.118} & \text{for moist cured concrete} \\ 1.13(t_{la})^{-0.094} & \text{for steam cured concrete} \end{cases} \tag{A2.15}$$

Creep relative humidity correction factor:

$$\gamma_\lambda = 1.27 - 0.0067\ \lambda \qquad \text{for } \lambda > 40 \tag{A2.16}$$

Creep volume/surface ratio correction factor:

$$\gamma_{vs} = \tfrac{2}{3}\ [1 + 1.13 \exp(-0.0213\ v/s)] \tag{A2.17}$$

Creep slump correction factor:

$$\gamma_s = 0.82 + 0.00264\, s \qquad \text{(A2.18)}$$

Creep fine aggregate percentage correction factor:

$$\gamma_\psi = 0.88 + 0.0024\,\psi \qquad \text{(A2.19)}$$

Creep air content correction factor:

$$\gamma_\alpha = 0.46 + 0.09\ \alpha \qquad \text{for } \alpha \geq 1 \qquad \text{(A2.20)}$$

A3.0 BP-KX Model 1991-1992

The prediction of the material parameters of this model is restricted to Portland cement concretes with the following parameter ranges:

$21 \leq f_c' \leq 62$ f_c' in N/mm^2,

$3 \leq t_0 \leq 40$ days,

$3 \leq t' \leq 365$ days,

$1.0 \leq g/s \leq 3.5$,

$\sigma / f_c' \leq 0.3$ at age of loading t'.

where $t' \geq t_0$.

The following equations are used in the calculation of shrinkage and creep strains in the BP-KX Model.

A3.1 Notation

Parameter	Description
t	time, representing the age of the concrete (days)
t'	age at loading (days)
t_0	age when drying begins (days) ($t_0 \leq t'$)
$\epsilon_{sh}(t, t_0)$	Total shrinkage strain at time t (microstrain)
q_1	Instantaneous strain at loading, time t' (microstrain)
$\epsilon_c(t)$	Total creep strain at time t (microstrain)
$J(t, t')$	Creep compliance function
$C_0(t, t')$	Basic creep compliance function
$C_d(t, t', t_0)$	Drying creep compliance function
σ	Applied uniaxial stress at loading, time t' (N/mm^2)
f_c'	28-day standard cylinder strength (N/mm^2)
E_{28}	28-day Elastic Modulus (N/mm^2)
h	Relative humidity of the environment (expressed as a decimal)
v/s	Specimen volume/ surface area ratio (mm)
c	Cement content (kg/m^3)
w	Water content (kg/m^3)
a	Total aggregate content (kg/m^3)
s	Fine aggregate content (kg/m^3)
g	Coarse aggregate content (kg/m^3)
ρ_c	Concrete density (kg/m^3)

A3.2 Shrinkage strain

$$\varepsilon_{sh}(t,t_0) = \varepsilon_{sh\infty} k_h S(t) \qquad \text{(microstrain)} \qquad \text{(A3.01)}$$

reference equations: A3.02, A3.03 and A3.09.

Time curve:

$$S(t) = \tanh\left(\frac{t-t_0}{\tau_{sh}}\right)^{1/2} \qquad \text{(A3.02)}$$

reference equation: A3.04.

Humidity dependence:

$$k_h = \begin{cases} 1-h^3 & \text{for } h \le 0.98 \\ -0.2 & \text{for } h = 1 \text{ (swelling in water)} \\ \text{linear interpolation} & \text{for } 0.98 \le h \le 1 \end{cases} \qquad \text{(A3.03)}$$

Shrinkage half-time:

$$\tau_{sh} = \frac{0.32(k_s D)^2}{C_1(t_{0e})} \qquad \text{(days)} \qquad \text{(A3.04)}$$

reference equations: A3.05, A3.06 and A3.07.

Effective cross-section thickness:

$$D = 2v/s \qquad \text{(mm)} \qquad \text{(A3.05)}$$

Cross-section shape factor:

$$k_h = \begin{cases} 1.00 \text{ for an infinite slab} \\ 1.15 \text{ for an infinite cylinder} \\ 1.25 \text{ for an infinite square prism} \\ 1.30 \text{ for a sphere} \\ 1.55 \text{ for a cube} \end{cases} \qquad \text{(A3.06)}$$

Age dependence:

$$C_1(t_0) = 10\left[0.6 + \left(\frac{4.5}{t_{0e}}\right)^{1/2}\right] \qquad C_1(t_0) \le 18 \qquad \text{(A3.07)}$$

reference equation: A3.08.

Maturity dependence:

$$t_{0e} = \begin{cases} 25 + t_0 & \text{for a steam-cured specimen} \\ t_0 & \text{otherwise} \end{cases} \qquad \text{(A3.08)}$$

Time dependence of ultimate shrinkage:

$$\varepsilon_{sh\infty} = \varepsilon_{s\infty}\left[G\left(17+\frac{\tau_{sh}}{40}\right)G(12+t_{0e})\right]^{-1} \quad \text{(microstrain)} \qquad \text{(A3.09)}$$

reference equations: A3.04, A3.08, A3.10 and A3.11.

Shrinkage Parameter:

$$G(x) = \left(\frac{x}{4+0.9x}\right)^{1/2} \qquad \text{(A3.10)}$$

Ultimate shrinkage:

$$\varepsilon_{s\infty} = (1.15\alpha_1 + 0.16)\alpha_2\alpha_3 \quad \text{(microstrain)} \qquad \text{(A3.11)}$$

reference equations: A3.12, A3.13 and A3.14.

Material composition parameter:

$$\alpha_1 = (w/c)^{1.5} c^{1.1} f_c{}'^{-0.2}\left(1-\frac{a}{\rho_c}\right)\alpha_4 \qquad \text{(A3.12)}$$

reference equation: A3.15.

Cement type:

$$\alpha_2 = \begin{cases} 1.00 \text{ for type I cement} \\ 0.85 \text{ for type II cement} \\ 1.10 \text{ for type III cement} \end{cases} \qquad \text{(A3.13)}$$

Curing regime:

$$\alpha_3 = \begin{cases} 0.74 \text{ for steam cured specimens} \\ 1.00 \text{ for specimens cured in water or at 100\% relative humidity} \\ 1.40 \text{ for specimens sealed during curing} \end{cases} \qquad \text{(A3.14)}$$

Material strength parameter:

$$\alpha_4 = \begin{cases} 0.7 + 0.3(a/s - 1.6)^{-3} & \text{for } a/s > 2.6 \\ 1 & \text{otherwise} \end{cases} \qquad \text{(A3.15)}$$

A3.3 Instantaneous strain

$$q_1 = \frac{10^6}{1.5E_{28}} \tag{A3.16}$$

A3.4 Basic Creep

Basic creep compliance:

$$C_0(t,t') = q_2 Q(t,t') + q_3 \ln[1+(t-t')^{0.1}] + q_4\left(\frac{t}{t'}\right) \tag{A3.17}$$

reference equations: A3.18, A3.19, A3.21 and A3.22.

Ageing viscoelastic compliance:

$$q_2 = 0.011(w/c)^{0.8} c^{1.5} (1-a/\rho_c)^{-0.9} (0.001 f_c')^{-0.5} (s/g)^{0.02} - 0.39 \tag{A3.18}$$

Non-ageing viscoelastic compliance:

$$q_3 = \alpha q_2 \tag{A3.19}$$

reference equations: A3.18 and A3.20.

Non-ageing viscoelastic compliance parameter:

$$\alpha = \begin{cases} 0.0003c + 0.0125 & \text{for } c \geq 416 \text{ kg/m}^3 \\ 0.001c - 0.005 & \text{for } 240 \leq c \leq 416 \text{ kg/m}^3 \\ 0.01 & \text{for } c \leq 240 \text{ kg/m}^3 \end{cases} \tag{A3.20}$$

Ageing viscous strain compliance:

$$q_4 = 0.072(w/c)^{2.3} c^{0.2} (1-a/\rho_c)^{0.39} (0.001 f_c')^{0.46} (s/g)^{-0.73} \tag{A3.21}$$

Binomial integral function:

$$Q(t,t') = Q_f(t')\left[1+\left(\frac{Q_f(t')}{Z(t,t')}\right)^{r(t')}\right]^{-1/r(t')} \tag{A3.22}$$

reference equation: A3.23, A3.24 and A3.25.

Binomial integral function:

$$Q_f(t') = [0.086(t')^{2/9} + 1.21(t')^{4/9}]^{-1} \tag{A3.23}$$

Binomial integral function:

$$Z(t,t') = (t')^{-0.5} \ln[1+(t-t')^{0.1}] \tag{A3.24}$$

Binomial integral function:

$$r(t') = 1.7(t')^{0.12} + 8 \qquad \text{(A3.25)}$$

A3.5 Drying creep

Drying creep compliance:

$$C_d(t,t',t_0) = q_5 k_h \varepsilon_{sh\infty}\left[S\left(\frac{t-t_0}{\tau_m}\right) - S\left(\frac{t'-t_0}{\tau_m}\right)\right]^{1/2} \qquad \text{(A3.26)}$$

reference equation: A3.03, A3.09, A3.27 and A3.28.

Drying creep function:

$$q_5 = \frac{40}{(f_c')^{1/2}} \qquad \text{(A3.27)}$$

Drying creep half-time

$$\tau_m = 2\left(1+\frac{3.5}{t_0^{1/2}}\right)\left(1+\frac{5}{(t'+t_0)^{1/2}}\right)^{-1}\tau_{sh} \qquad \text{(A3.28)}$$

reference equation: A3.04.

A3.6 Creep strain

$$\varepsilon_c(t) = J(t,t')\sigma(t') \qquad \text{(microstrain)} \qquad \text{(A3.29)}$$

reference equation: A3.30.

Creep compliance function:

$$J(t,t') = q_1 + C_0(t,t') + C_d(t,t',t_0) \qquad \text{(A3.30)}$$

reference equation: A3.16, A3.17 and A3.26.

A4.0 Short-form BP-KX Model 1993

The prediction of the material parameters of this model is restricted to Portland cement concretes with the following parameter ranges:

$21 \leq f_c' \leq 62$ in N/mm^2,

$3 \leq t_0 \leq 40$ days,

$3 \leq t' \leq 365$ days,

$1.0 \leq g/s \leq 3.5$,

where $t' \geq t_0$.

The following equations are used in the calculation of shrinkage and creep strains in the short-form BP-KX Model.

A4.1 Notation

Parameter	Description
t	time, representing the age of the concrete (days)
t'	age at loading (days)
t_0	age when drying begins (days) ($t_0 \leq t'$)
$\epsilon_{sh}(t, t_0)$	Total shrinkage strain at time t (microstrain)
q_1	Instantaneous strain at loading, time t' (microstrain)
$\epsilon_c(t)$	Total creep strain at time t (microstrain)
$J(t, t')$	Creep compliance function
$C_0(t, t')$	Basic creep compliance function
$C_d(t, t', t_0)$	Drying creep compliance function
σ	Applied uniaxial stress at loading, time t' (N/mm^2)
f_c'	28-day standard cylinder strength (N/mm^2)
E_{28}	28-day Elastic Modulus (N/mm^2)
h	Relative humidity of the environment (expressed as a decimal)
v/s	Specimen volume/ surface area ratio (mm)
c	Cement content (kg/m^3)
w	Water content (kg/m^3)
a	Total aggregate content (kg/m^3)
ρ_c	Concrete density (kg/m^3)

A4.2 Shrinkage strain

$$\varepsilon_{sh}(t, t_0) = \varepsilon_{sh\infty} k_h S(t) \qquad \text{(microstrain)} \qquad \text{(A4.01)}$$

reference equations: A4.02, A4.03 and A4.06.

Time curve:

$$S(t) = \tanh\left(\frac{t - t_0}{\tau_{sh}}\right)^{1/2} \qquad \text{(A4.02)}$$

reference equation: A4.04.

Humidity dependence:

$$k_h = \begin{cases} 1 - h^3 & \text{for } h \le 0.98 \\ -0.2 & \text{for } h = 1 \text{ (swelling in water)} \\ \text{linear interpolation} & \text{for } 0.98 \le h \le 1 \end{cases} \qquad \text{(A4.03)}$$

Shrinkage half-time:

$$\tau_{sh} = 0.033D^2 \qquad \text{(days)} \qquad \text{(A4.04)}$$

reference equation: A4.05.

Effective cross-section thickness:

$$D = 2v/s \qquad \text{(mm)} \qquad \text{(A4.05)}$$

Ultimate shrinkage:

$$\varepsilon_{sh\infty} = \alpha_1 \alpha_2 \{1.12(w/c)^{1.5} c^{1.1} (f_c')^{-0.2} [1 - (a/c)/(\rho_c/c)] + 0.16\} \quad \text{(in } 10^{-3}\text{)} \qquad \text{(A4.06)}$$

reference equations: A4.07 and A4.08.

Cement type:

$$\alpha_1 = \begin{cases} 1.00 \text{ for type I cement} \\ 0.85 \text{ for type II cement} \\ 1.10 \text{ for type III cement} \end{cases} \qquad \text{(A4.07)}$$

Curing regime:

$$\alpha_2 = \begin{cases} 0.75 \text{ for steam cured specimens} \\ 1.00 \text{ for specimens cured in water or at 100\% relative humidity} \\ 1.40 \text{ for specimens sealed during curing} \end{cases} \qquad \text{(A4.08)}$$

A4.3 Instantaneous strain

$$q_1 = \frac{0.68 \times 10^6}{E_{28}} \qquad \text{(A4.09)}$$

A4.4 Basic Creep

Basic creep compliance:

$$C_0(t,t') = q_0 \ln\{1 + 9.32[(t')^{-0.75} + 0.016](t-t')^{0.32}\} \qquad \text{(A4.10)}$$

reference equation: A4.11.

Empirical parameter:

$$q_0 = 0.88w^{1.58}(\log_{10} f_c')^{-4.18} \qquad \text{(A4.11)}$$

A4.5 Drying creep

Drying creep compliance:

$$C_d(t,t',t_0) = q_5 k_h \varepsilon_{sh\infty}\left[\tanh\left(\frac{t-t_0}{2\tau_{sh}}\right)^{1/2} - \tanh\left(\frac{t'-t_0}{2\tau_{sh}}\right)^{1/2}\right]^{1/2} \qquad \text{(A4.12)}$$

reference equation: A4.03, A4.04, A4.06 and A4.13.

Drying creep function:

$$q_5 = \frac{40}{(f_c')^{1/2}} \qquad \text{(A4.13)}$$

A4.6 Creep strain

$$\varepsilon_c(t) = J(t,t')\sigma(t') \qquad \text{(microstrain)} \qquad \text{(A4.14)}$$

reference equation: A4.15.

Creep compliance function:

$$J(t,t') = q_1 + C_0(t,t') + C_d(t,t',t_0) \qquad \text{(A4.30)}$$

reference equation: A4.09, A4.10 and A4.12.

A5.0 GZ Model 1993

The following equations are used in the calculation of shrinkage and creep strains in the GZ Model 1993.

A5.1 Notation

Parameter	Description
t	time, representing the age of the concrete (days)
t_c	age when drying begins (days) ($t_c \leq t_0$)
t_0	age at loading (days)
ϵ_{sh}	Total shrinkage strain at time, t (microstrain)
ϵ_i	Instantaneous strain at loading, time t_0 (microstrain)
ϵ_c	Total creep strain at time t (microstrain)
σ	Applied uniaxial stress at loading, time t_0 (N/mm^2)
f_{cm28}	28-day mean compressive strength (N/mm^2)
f_{cmt0}	Compressive strength at loading, time t_0 (N/mm^2)
f_{cmtc}	Compressive strength when drying begins, time t_0 (N/mm^2)
f_{cmt}	Compressive strength at time t (N/mm^2)
E_{cm28}	28-day Elastic Modulus (N/mm^2)
E_{cmt0}	Elastic Modulus at loading, time t_0 (N/mm^2)
E_{cmt}	Elastic Modulus at time t (N/mm^2)
h	Relative humidity of the environment (expressed as a decimal)
V/S	Specimen volume/ surface area ratio (mm)

A5.2 Shrinkage strain

$$\varepsilon_{sh} = \varepsilon_{shu}\beta(h)\beta(t) \qquad \text{(microstrain)} \qquad \text{(A5.01)}$$

reference equations: A5.02 A5.07 and A5.08.

Notional shrinkage coefficient:

$$\varepsilon_{shu} = 900K\left(\frac{f_{cm28}}{f_{cmtc}}\right)^{1/2}\left(\frac{25}{f_{cm28}}\right)^{1/2} \times 10^{-6} \qquad \text{(microstrain)} \qquad \text{(A5.02)}$$

reference equations: A5.03 and A5.06.

Strength development with time:

$$f_{cmt} = f_{cm28}\frac{t^{3/4}}{a + bt^{3/4}} \qquad \text{N/mm}^2 \qquad \text{(A5.03)}$$

reference equations: A5.04 and A5.05.

Cement type factor:

$$a = \begin{cases} 2.8 \text{ for Type I cement} \\ 3.4 \text{ for Type II cement} \\ 1.0 \text{ for Type III cement} \end{cases} \quad \text{(A5.04)}$$

Cement type factor:

$$b = \begin{cases} 0.77 \text{ for Type I cement} \\ 0.72 \text{ for Type II cement} \\ 0.92 \text{ for Type III cement} \end{cases} \quad \text{(A5.05)}$$

Cement type factor:

$$K = \begin{cases} 1.00 \text{ for Type I cement} \\ 0.70 \text{ for Type II cement} \\ 1.33 \text{ for Type III cement} \end{cases} \quad \text{(A5.06)}$$

Relative humidity correction factor:

$$\beta(h) = \begin{cases} (1 - h^4) & \text{for } h < 0.99 \\ & \\ -0.20 & \text{for } h = 1.00 \text{ (swelling only)} \end{cases} \quad \text{(A5.07)}$$

Coefficient for shrinkage development with time:

$$\beta(t) = \left[\frac{7.27 + \ln(t - t_c)}{17.18}\right]\left[\frac{t - t_c}{t - t_c + 0.0125(V/S)^2}\right] \quad \text{(A5.08)}$$

A5.3 Instantaneous strain

$$\varepsilon_i = \sigma / E_{cmt0} \qquad \text{(microstrain)} \qquad \text{(A5.09)}$$

reference equation: A5.10.

Elastic Modulus development with time:

$$E_c = 3500 + 4300(f_{cmt})^{1/2} \qquad \text{N/mm}^2 \qquad \text{(A5.10)}$$

reference equation: A5.03.

A5.4 Creep strain

$$\varepsilon_c = \frac{\sigma}{E_{cm28}}\phi \qquad \text{(microstrain)} \qquad \text{(A5.07)}$$

reference equation: A508.

Creep coefficient:

$$\phi = \left[\frac{7.27 + \ln(t - t_0)}{17.18}\right]\left[1.57 + 2.98\left(\frac{f_{cm28}}{f_{cmt0}}\right)\left(\frac{25}{f_{cm28}}\right)(1 - h^2)\left(\frac{t - t_0}{0.1(t - t_0)(V/S)^2}\right)\right] \quad \text{(A5.08)}$$

A6.0 B3 Model 1995

The prediction of the material parameters of this model is restricted to Portland cement concretes with the following parameter ranges:

$17 \leq f_c' \leq 69$ f_c' in N/mm^2,

$160 \leq c \leq 721$ c in kg/m^3,

$0.3 \leq w/c \leq 0.85$,

$2.5 \leq a/c \leq 13.5$,

$\sigma / f_c' \leq 0.4$ at age of loading t'.

The following equations are used in the calculation of shrinkage and creep strains in the B3 Model.

A6.1 Notation

Parameter	Description
t	time, representing the age of the concrete (days)
t'	age at loading (days)
t_0	age when drying begins (days) ($t_0 \leq t'$)
$\epsilon_{sh}(t, t_0)$	Total shrinkage strain at time t (microstrain)
q_1	Instantaneous strain at loading, time t' (microstrain)
$\epsilon_c(t)$	Total creep strain at time t (microstrain)
$J(t, t')$	Creep compliance function
$C_0(t, t')$	Basic creep compliance function
$C_d(t, t', t_0)$	Drying creep compliance function
σ	Applied uniaxial stress at loading, time t' (N/mm^2)
f_c'	28-day standard cylinder strength (N/mm^2)
E_{28}	28-day Elastic Modulus (N/mm^2)
$E(t)$	Elastic Modulus at time t (N/mm^2)
h	Relative humidity of the environment (expressed as a decimal)
v/s	Specimen volume/ surface area ratio (mm)
c	Cement content (kg/m^3)
w	Water content (kg/m^3)
a	Total aggregate content (kg/m^3)

A6.2 Shrinkage strain

$$\varepsilon_{sh}(t, t_0) = -\varepsilon_{sh\infty} k_h S(t) \qquad \text{(microstrain)} \qquad \text{(A6.01)}$$

reference equations: A6.02, A6.03 and A6.08.

Time curve:

$$S(t) = \tanh\left(\frac{t - t_0}{\tau_{sh}}\right)^{1/2} \qquad \text{(A6.02)}$$

reference equation: A6.04.

Humidity dependence:

$$k_h = \begin{cases} 1 - h^3 & \text{for } h \le 0.98 \\ -0.2 & \text{for } h = 1 \text{ (swelling in water)} \\ \text{linear interpolation} & \text{for } 0.98 \le h \le 1 \end{cases} \qquad \text{(A6.03)}$$

Shrinkage half-time:

$$\tau_{sh} = k_t (k_s D)^2 \qquad \text{(days)} \qquad \text{(A6.04)}$$

reference equations: A6.05, A6.06 and A6.07.

Effective cross-section thickness:

$$D = 2v/s \qquad \text{(inches)} \qquad \text{(A6.05)}$$

Cross-section shape factor:

$$k_s = \begin{cases} 1.00 \text{ for an infinite slab} \\ 1.15 \text{ for an infinite cylinder} \\ 1.25 \text{ for an infinite square prism} \\ 1.30 \text{ for a sphere} \\ 1.55 \text{ for a cube} \end{cases} \qquad \text{(A6.06)}$$

Parameter based on concrete strength and loading age:

$$k_t = 190.8\, t_0^{-0.08} f_c'^{-1/4} \qquad \text{(days in}^{-2}\text{)} \qquad \text{(A6.07)}$$

Time dependence of ultimate shrinkage:

$$\varepsilon_{sh\infty} = \varepsilon_{s\infty} \frac{E(7+600)}{E(t_0 + \tau_{sh})} \qquad \text{(microstrain)} \qquad \text{(A6.08)}$$

reference equations: A6.04, A6.09 and A6.10.

Elastic Modulus at time t:

$$E(t) = E_{28}\left[\frac{t}{(4+0.85t)}\right]^{1/2} \qquad \text{(psi)} \qquad \text{(A6.09)}$$

Ultimate shrinkage:

$$\varepsilon_{s\infty} = \alpha_1 \alpha_2 [26 w^{2.1} (f_c')^{-0.28} + 270] \qquad \text{(microstrain)} \qquad \text{(A6.10)}$$

reference equations: A6.11 and A6.12.

Cement type:

$$\alpha_1 = \begin{cases} 1.00 \text{ for type I cement} \\ 0.85 \text{ for type II cement} \\ 1.10 \text{ for type III cement} \end{cases} \quad \text{(A6.11)}$$

Curing regime:

$$\alpha_2 = \begin{cases} 0.75 \text{ for steam cured specimens} \\ 1.00 \text{ for specimens cured in water or at 100\% relative humidity} \\ 1.20 \text{ for specimens sealed during curing} \end{cases} \quad \text{(A6.12)}$$

A6.3 Instantaneous strain

$$q_1 = \frac{0.6 \times 10^6}{E_{28}} \quad \text{(A6.13)}$$

A6.4 Basic Creep

Basic creep compliance:

$$C_0(t,t') = q_2 Q(t,t') + q_3 \ln[1 + (t-t')^{0.1}] + q_4 \left(\frac{t}{t'}\right) \quad \text{(A6.14)}$$

reference equations: A6.15, A6.16, A6.17 and A6.18.

Ageing viscoelastic compliance:

$$q_2 = 451.1c^{0.5} (f_c')^{-0.9} \quad \text{(A6.15)}$$

Non-ageing viscoelastic compliance:

$$q_3 = 0.29(w/c)^4 q_2 \quad \text{(A6.16)}$$

reference equation: A6.15.

Flow compliance:

$$q_4 = 0.14(a/c)^{-0.7} \quad \text{(A6.17)}$$

Binomial integral function:

$$Q(t,t') = Q_f(t') \left[1 + \left(\frac{Q_f(t')}{Z(t,t')} \right)^{r(t')} \right]^{-1/r(t')} \quad \text{(A6.18)}$$

reference equation: A6.19, A6.20 and A6.21.

Binomial integral function:

$$Q_f(t') = [0.086(t')^{2/9} + 1.21(t')^{4/9}]^{-1} \quad \text{(A6.19)}$$

Binomial integral function:

$$Z(t,t') = (t')^{-0.5} \ln[1 + (t - t')^{0.1}] \qquad \text{(A6.20)}$$

Binomial integral function:

$$r(t') = 1.7(t')^{0.12} + 8 \qquad \text{(A6.21)}$$

A6.5 Drying creep

Drying creep compliance:

$$C_d(t,t',t_0) = q_5[\exp\{-8H(t)\} - \exp\{-8H(t')\}]^{1/2} \qquad \text{(A6.22)}$$

reference equation: A6.23 and A6.24.

Drying creep function:

$$q_5 = 7.57 \times 10^5 (f_c')^{-1} (\varepsilon_{sh\infty})^{-0.6} \qquad \text{(A6.23)}$$

Humidity curve:

$$H(t) = 1 - (1 - h)S(t) \qquad \text{(A6.24)}$$

reference equation: A6.02.

A6.6 Creep strain

$$\varepsilon_c(t) = J(t,t')\sigma(t') \qquad \text{(microstrain)} \qquad \text{(A6.25)}$$

reference equation: A6.26.

Creep compliance function:

$$J(t,t') = q_1 + C_0(t,t') + C_d(t,t',t_0) \qquad \text{(A6.26)}$$

reference equation: A6.13, A6.14 and A6.22.

A7.0 Short-form B3 Model 1996

The prediction of the material parameters of this model is restricted to Portland cement concretes with the following parameter ranges:

$17 \leq f_c' \leq 70$ f_c' in MPa,

$160 \leq c \leq 720$ c in kg m^{-3},

$0.3 \leq w/c \leq 0.85$,

$2.5 \leq a/c \leq 13.5$.

The following equations are used in the calculation of shrinkage and creep strains in the B3+ Model.

A7.1 Notation

Parameter	Description
t	time, representing the age of the concrete (days)
t'	age at loading (days)
t_0	age when drying begins (days) ($t_0 \leq t'$)
$\epsilon_{sh}(t, t_0)$	Total shrinkage strain at time t (microstrain)
q_1	Instantaneous strain at loading, time t' (microstrain)
$\epsilon_c(t)$	Total creep strain at time t (microstrain)
$J(t, t')$	Creep compliance function
$C_0(t, t')$	Basic creep compliance function
$C_d(t, t', t_0)$	Drying creep compliance function
σ	Applied uniaxial stress at loading, time t' (N/mm^2)
f_c'	28-day standard cylinder strength (N/mm^2)
E_{28}	28-day Elastic Modulus (N/mm^2)
h	Relative humidity of the environment (expressed as a decimal)
v/s	Specimen volume/ surface area ratio (cm)
w	Water content (kg/m^3)

A7.2 Shrinkage strain

$$\varepsilon_{sh}(t, t_0) = -\varepsilon_{sh\infty} k_h S(t) \qquad \text{(microstrain)} \qquad \text{(A7.01)}$$

reference equations: A7.02, A7.03 and A7.06.

Time curve:

$$S(t) = \tanh\left(\frac{t - t_0}{\tau_{sh}}\right)^{1/2} \qquad \text{(A7.02)}$$

reference equation: A7.04.

Humidity dependence:

$$k_h = \begin{cases} 1 - h^3 & \text{for } h \le 0.98 \\ -0.2 & \text{for } h = 1 \text{ (swelling in water)} \\ \text{linear interpolation} & \text{for } 0.98 \le h \le 1 \end{cases} \qquad \text{(A7.03)}$$

Shrinkage half-time:

$$\tau_{sh} = 4.9D^2 \qquad \text{(days)} \qquad \text{(A7.04)}$$

reference equation: A7.05.

Effective cross-section thickness:

$$D = 2v/s \qquad \text{(cm)} \qquad \text{(A7.05)}$$

Ultimate shrinkage:

$$\varepsilon_{sh\infty} = \alpha_1 \alpha_2 [0.019 w^{2.1} (f_c')^{-0.28} + 270] \qquad \text{(microstrain)} \qquad \text{(A7.06)}$$

reference equations: A7.08 and A7.09.

Cement type:

$$\alpha_1 = \begin{cases} 1.00 \text{ for type I cement} \\ 0.85 \text{ for type II cement} \\ 1.10 \text{ for type III cement} \end{cases} \qquad \text{(A7.07)}$$

Curing regime:

$$\alpha_2 = \begin{cases} 0.75 \text{ for steam cured specimens} \\ 1.00 \text{ for specimens cured in water or at 100\% relative humidity} \\ 1.20 \text{ for specimens sealed during curing} \end{cases} \qquad \text{(A7.08)}$$

A7.3 Instantaneous strain

$$q_1 = \frac{0.6 \times 10^6}{E_{28}} \qquad \text{(A7.09)}$$

A7.4 Basic Creep

Basic creep compliance:

$$C_0(t,t') = q_0 \ln\{1 + 0.3[(t')^{-0.5} + 0.001](t - t')^{0.1}\} \qquad \text{(A7.10)}$$

reference equations: A7.11.

Empirical parameter:

$$q_0 = 2408(f_c')^{-0.5} \qquad \text{(A7.11)}$$

A7.5 Drying creep

Drying creep compliance:

$$C_d(t,t',t_0) = q_5[\exp\{-8H(t)\} - \exp\{-8H(t')\}]^{1/2} \qquad \text{(A7.12)}$$

reference equation: A7.13 and A7.14.

Drying creep function:

$$q_5 = 6000(f_c')^{-1} \qquad \text{(A7.13)}$$

Humidity curve:

$$H(t) = 1-(1-h)S(t) \qquad \text{(A7.14)}$$

reference equation: A7.02.

A7.6 Creep strain

$$\varepsilon_c(t) = J(t,t')\sigma \qquad \text{(microstrain)} \qquad \text{(A7.15)}$$

reference equation: A7.26.

Creep compliance function:

$$J(t,t') = q_1 + C_0(t,t') + C_d(t,t',t_0) \qquad \text{(A7.16)}$$

reference equation: A7.09, A7.10 and A7.12.

A8.0 GL Model 2001

The following equations are used in the calculation of shrinkage and creep strains in the GL Model 2001.

A8.1 Notation

Parameter	Description
t	time, representing the age of the concrete (days)
t_c	age when drying begins (days) ($t_c \leq t_0$)
t_0	age at loading (days)
ϵ_{sh}	Total shrinkage strain at time, t (microstrain)
ϵ_i	Instantaneous strain at loading, time t_0 (microstrain)
ϵ_c	Total creep strain at time t (microstrain)
σ	Applied uniaxial stress at loading, time t_0 (N/mm^2)
f_{cm28}	28-day mean compressive strength (N/mm^2)
f_{cmt0}	Compressive strength at loading, time t_0 (N/mm^2)
f_{cmtc}	Compressive strength when drying begins, time t_0 (N/mm^2)
f_{cmt}	Compressive strength at time t (N/mm^2)
E_{cm28}	28-day Elastic Modulus (N/mm^2)
E_{cmt0}	Elastic Modulus at loading, time t_0 (N/mm^2)
E_{cmt}	Elastic Modulus at time t (N/mm^2)
h	Relative humidity of the environment (expressed as a decimal)
V/S	Specimen volume/ surface area ratio (mm)

A8.2 Shrinkage strain

$$\varepsilon_{sh} = \varepsilon_{shu}\beta(h)\beta(t) \qquad \text{(microstrain)} \qquad \text{(A8.01)}$$

reference equations: A8.02, A8.04 and A8.05.

Notional shrinkage coefficient:

$$\varepsilon_{shu} = 1000K\left(\frac{30}{f_{cm28}}\right)^{1/2} \times 10^{-6} \qquad \text{(microstrain)} \qquad \text{(A8.02)}$$

reference equation: A8.03.

Cement type:

$$K = \begin{cases} 1.00 \text{ for Type I cement} \\ 0.70 \text{ for Type II cement} \\ 1.15 \text{ for Type III cement} \end{cases} \qquad \text{(A8.03)}$$

Relative humidity correction factor:

$$\beta(h) = (1 - 1.18h^4) \qquad \text{(A8.04)}$$

Coefficient for shrinkage development with time:

$$\beta(t) = \left(\frac{t - t_c}{t - t_c + 0.15(V/S)^2} \right)^{0.5} \qquad \text{(A8.05)}$$

A8.3 Instantaneous strain

$$\varepsilon_i = \sigma / E_{cmt0} \qquad \text{(microstrain)} \qquad \text{(A8.06)}$$

reference equation: A8.07.

Elastic Modulus development with time:

$$E_c = 3500 + 4300(f_{cmt})^{1/2} \qquad \text{N/mm}^2 \qquad \text{(A8.07)}$$

reference equation: A8.08.

Strength development with time:

$$f_{cmt} = f_{cm28} \frac{t^{3/4}}{a + bt^{3/4}} \qquad \text{N/mm}^2 \qquad \text{(A8.08)}$$

reference equations: A8.09 and A8.10.

Cement type factor:

$$a = \begin{cases} 2.8 \text{ for Type I cement} \\ 3.4 \text{ for Type II cement} \\ 1.0 \text{ for Type III cement} \end{cases} \qquad \text{(A8.09)}$$

Cement type factor:

$$b = \begin{cases} 0.77 \text{ for Type I cement} \\ 0.72 \text{ for Type II cement} \\ 0.92 \text{ for Type III cement} \end{cases} \qquad \text{(A8.10)}$$

A8.4 Creep strain

$$\varepsilon_c(t) = J(t, t_0)\sigma(t_0) \qquad \text{(microstrain)} \qquad \text{(A8.11)}$$

reference equation: A8.12.

Creep compliance:

$$J(t, t_0) = \frac{1}{E_{cmt0}} + \frac{\phi_{28}}{E_{cm28}} \qquad \text{(A8.12)}$$

reference equation: A8.13.

Creep coefficient:

$$\phi_{28} = \Phi(t_c)\left[2\left(\frac{(t-t_0)^{0.3}}{(t-t_0)^{0.3}+14}\right)+\left(\frac{7}{t_0}\right)^{0.5}\left(\frac{t-t_0}{t-t_0+7}\right)^{0.5}+2.5(1-1.086h^2)\left(\frac{t-t_0}{t-t_0+0.15(V/S)^2}\right)^{0.5}\right] \quad \text{(A8.13)}$$

reference equation: A8.14.

Drying creep coefficient:

If $t_0 = t_c$, $\Phi(t_c) = 1$, else when $t_0 > t_c$:

$$\Phi(t_c) = \left[1-\left(\frac{t_0-t_c}{t_0-t_c+0.15(V/S)^2}\right)^{0.5}\right]^{0.5} \quad \text{(A8.14)}$$

Appendix B

Proving Ring Calibration Curves

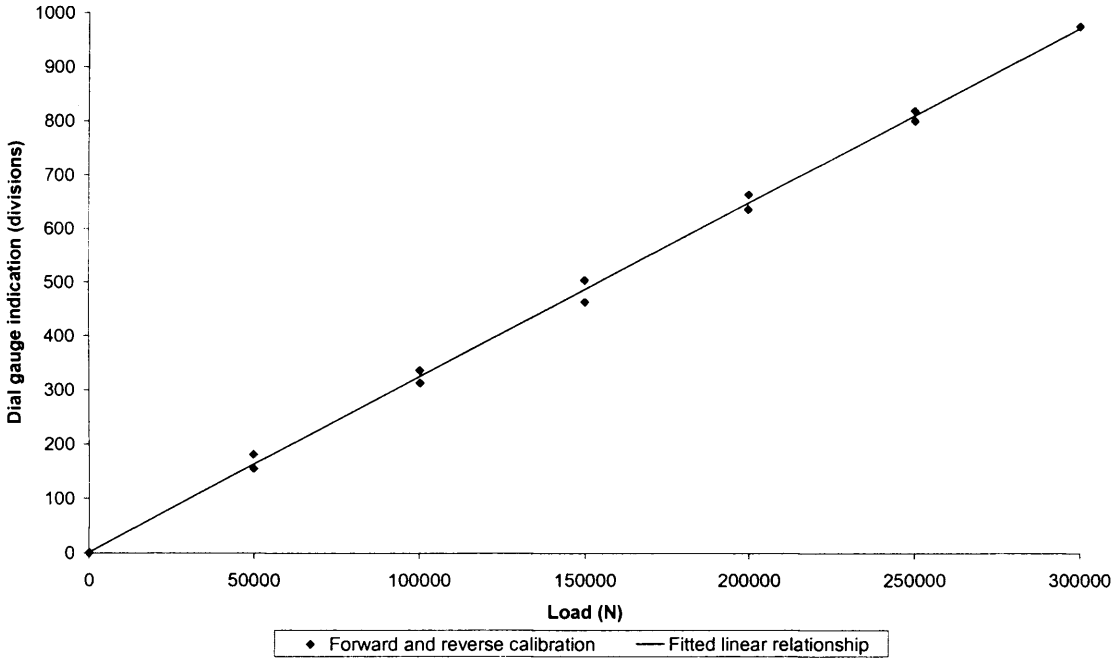

Figure B1.0. Calibration curve for 400kN (column) proving ring, Machine 1, Ring 1. Output 309.27 N/division, $r^2 = 0.9985$.

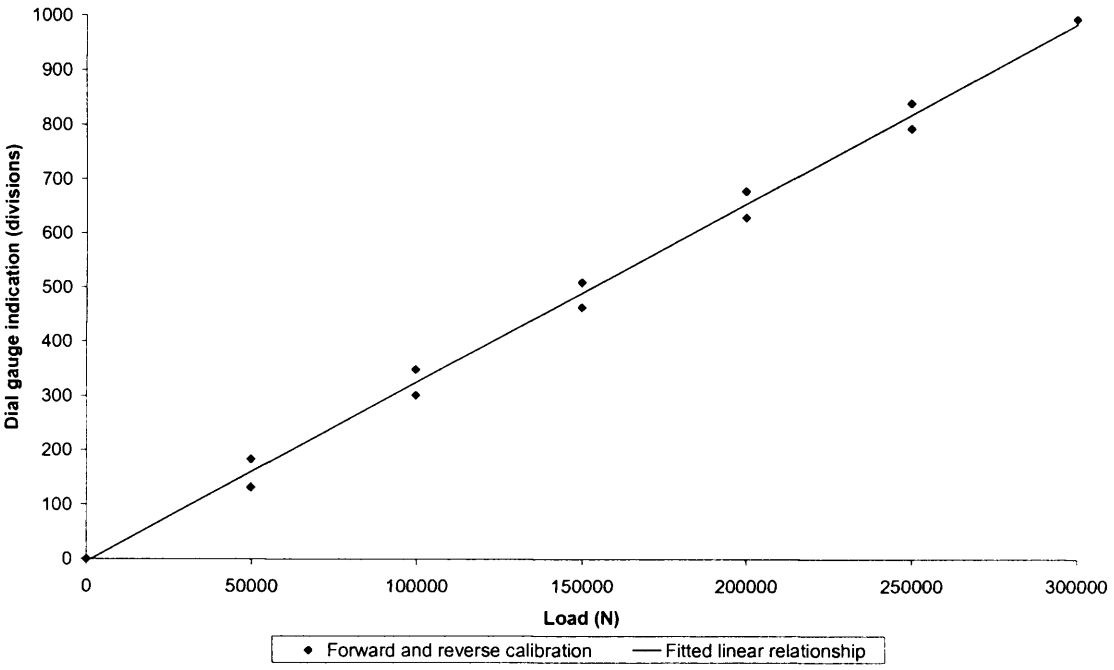

Figure B2.0. Calibration curve for 400kN (column) proving ring, Machine 1, Ring 2. Output 306.45 N/division, $r^2 = 0.9951$.

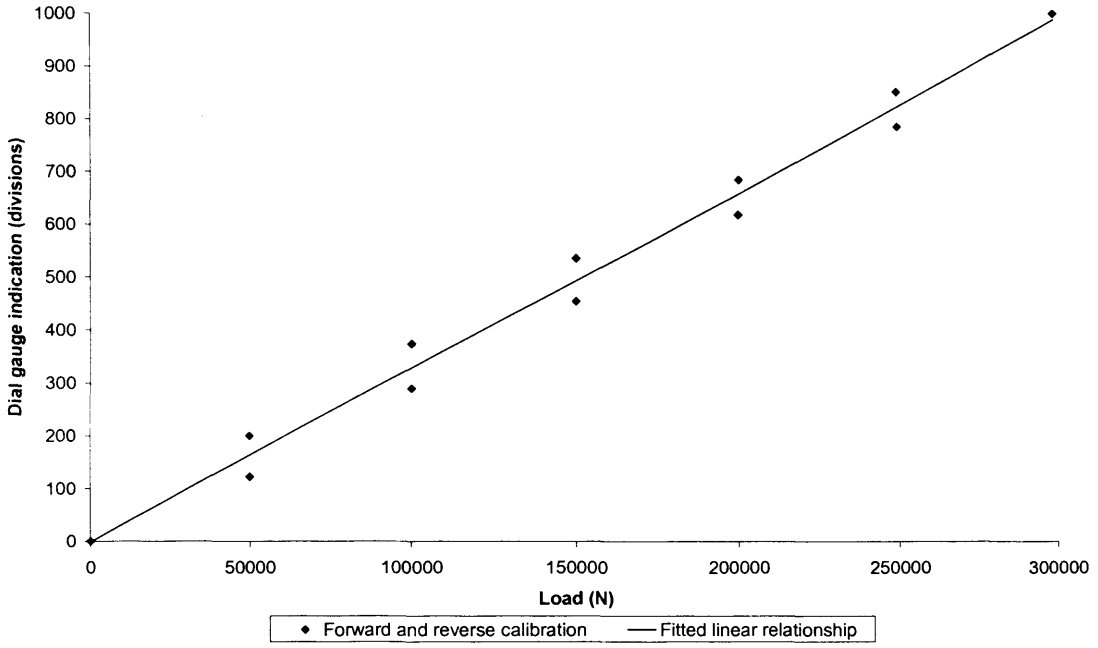

Figure B3.0. Calibration curve for 400kN (column) proving ring, Machine 1, Ring 3. Output 305.09 N/division, $r^2 = 0.9885$.

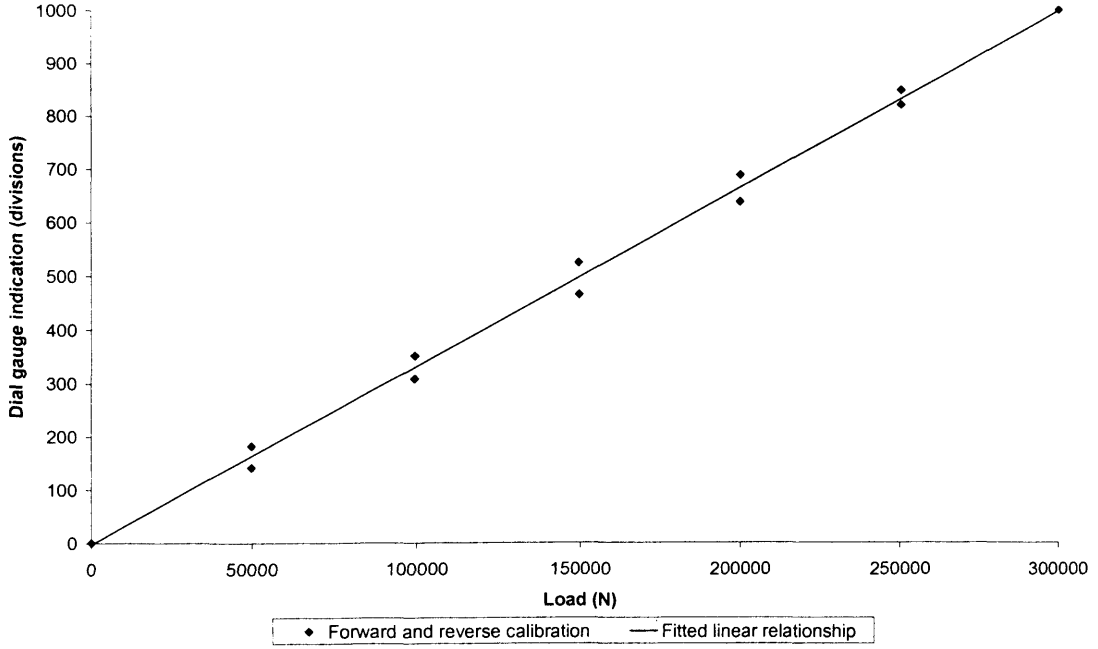

Figure B4.0. Calibration curve for 400kN (column) proving ring, Machine 1, Ring 4. Output 301.66 N/division, $r^2 = 0.9959$.

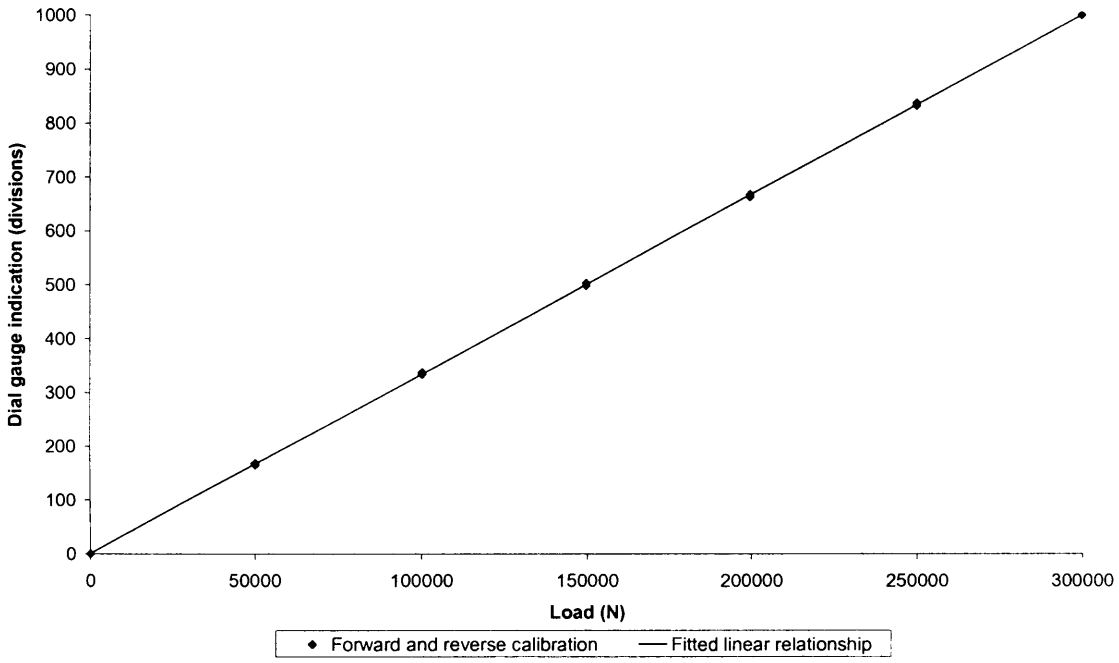

Figure B5.0. Calibration curve for 400kN (column) proving ring, Machine 2, Ring 1. Output 300.93 N/division, $r^2 = 0.9999$.

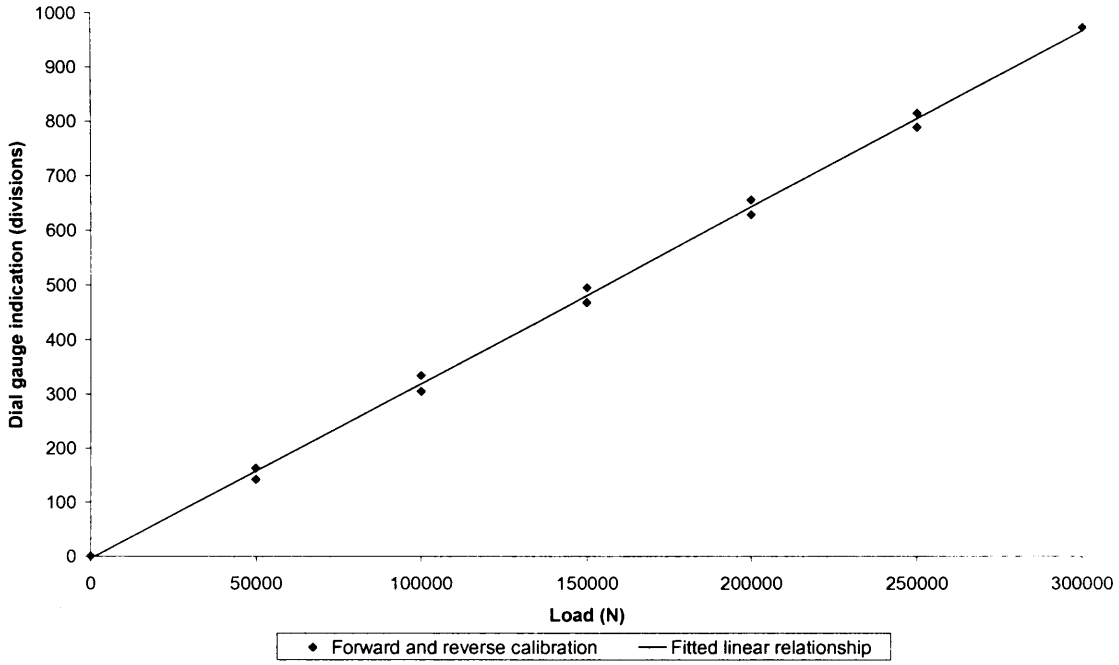

Figure B6.0. Calibration curve for 400kN (column) proving ring, Machine 2, Ring 2. Output 312.30 N/division, $r^2 = 0.9985$.

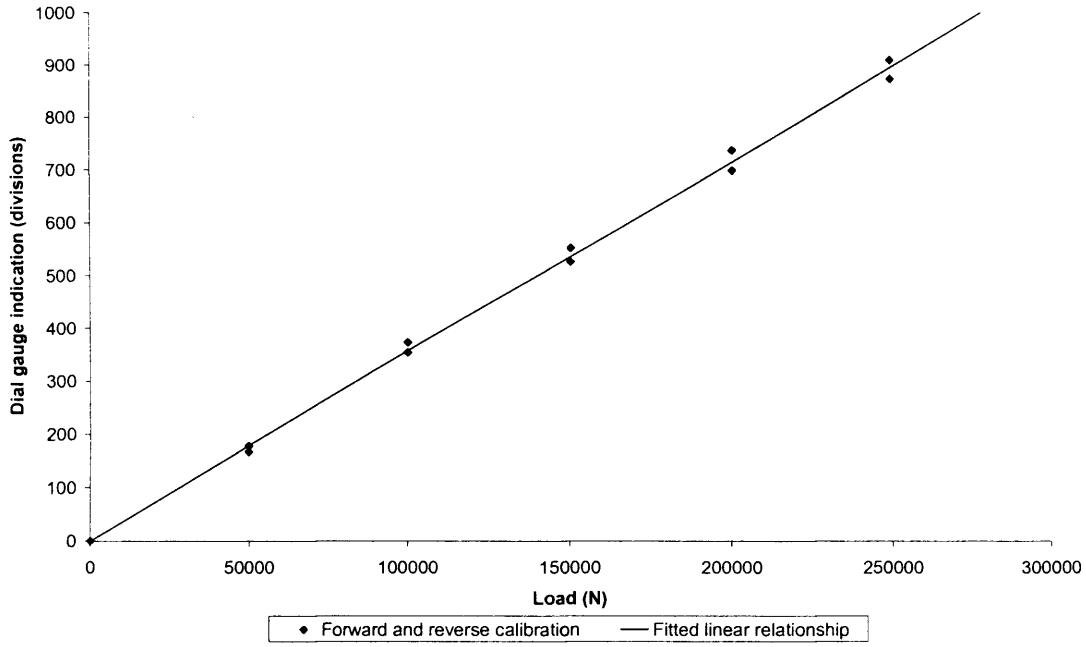

Figure B7.0. Calibration curve for 400kN (column) proving ring, Machine 2, Ring 3. Output 280.66 N/division, $r^2 = 0.9984$.

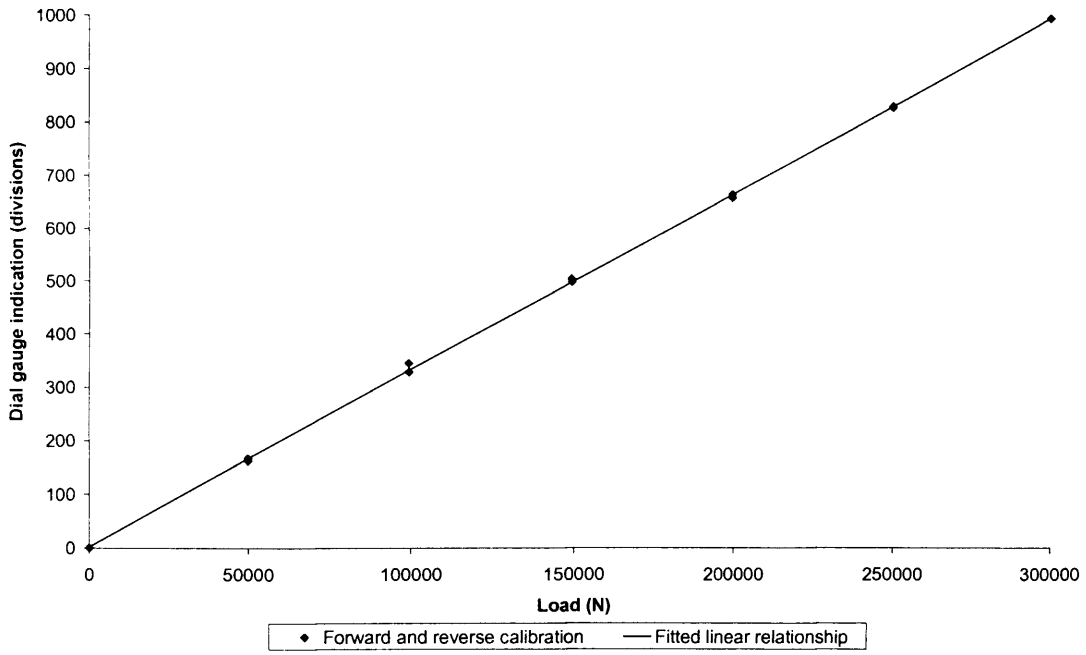

Figure B8.0. Calibration curve for 400kN (column) proving ring, Machine 2, Ring 4. Output 303.40 N/division, $r^2 = 0.9999$.

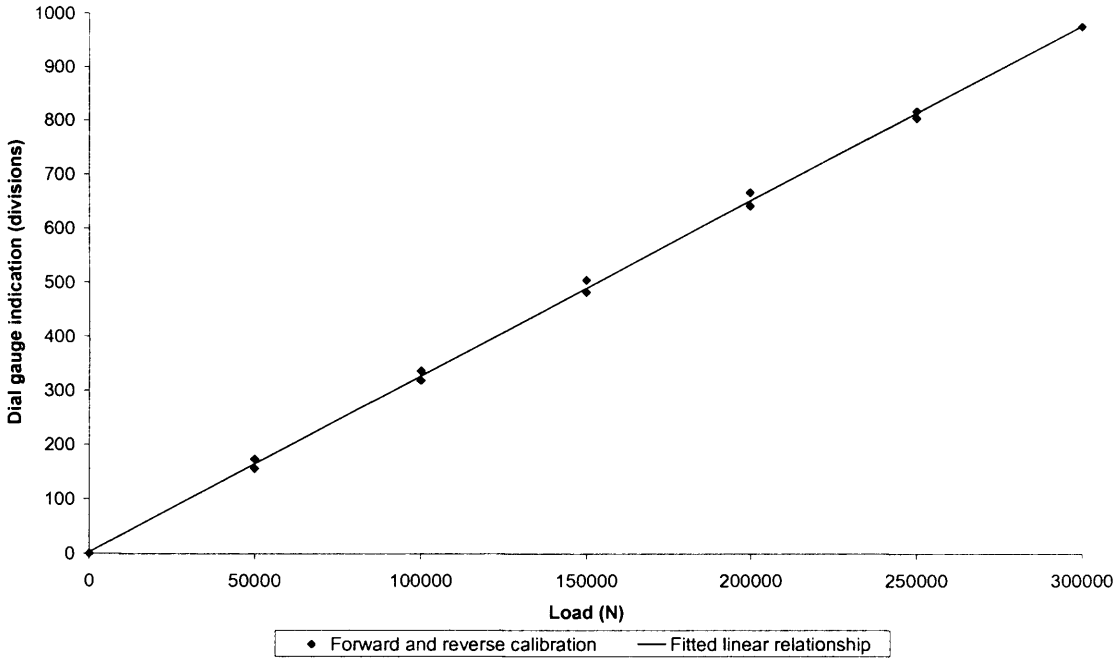

Figure B9.0. Calibration curve for 400kN (column) proving ring, Machine 3, Ring 1. Output 307.79 N/division, $r^2 = 0.9992$.

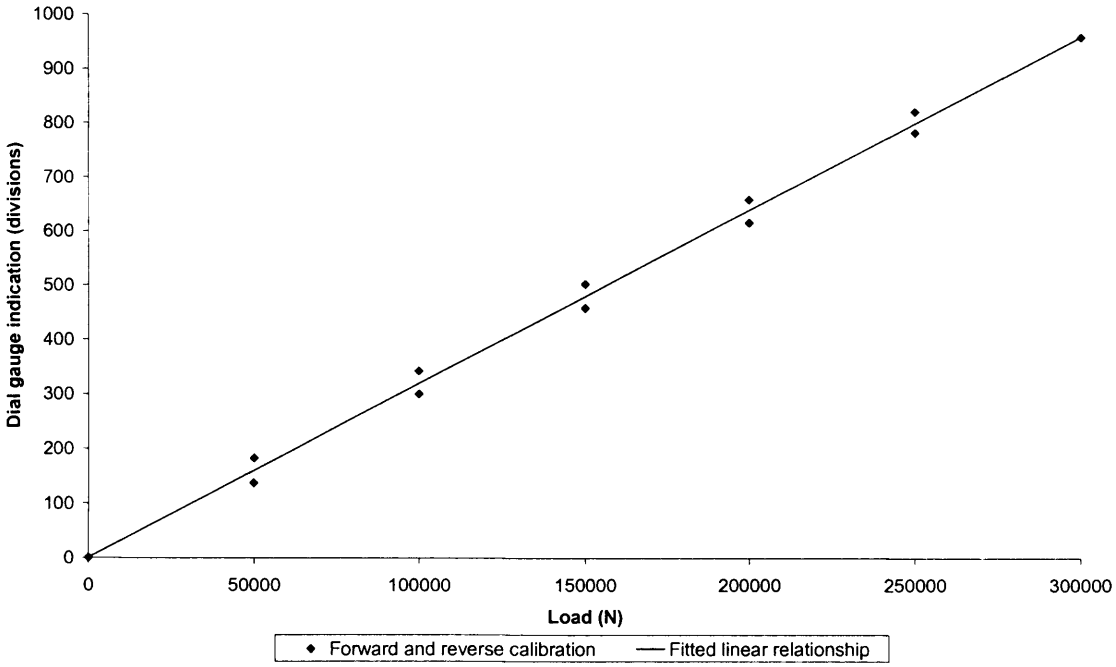

Figure B10.0. Calibration curve for 400kN (column) proving ring, Machine 3, Ring 2. Output 314.17 N/division, $r^2 = 0.9963$.

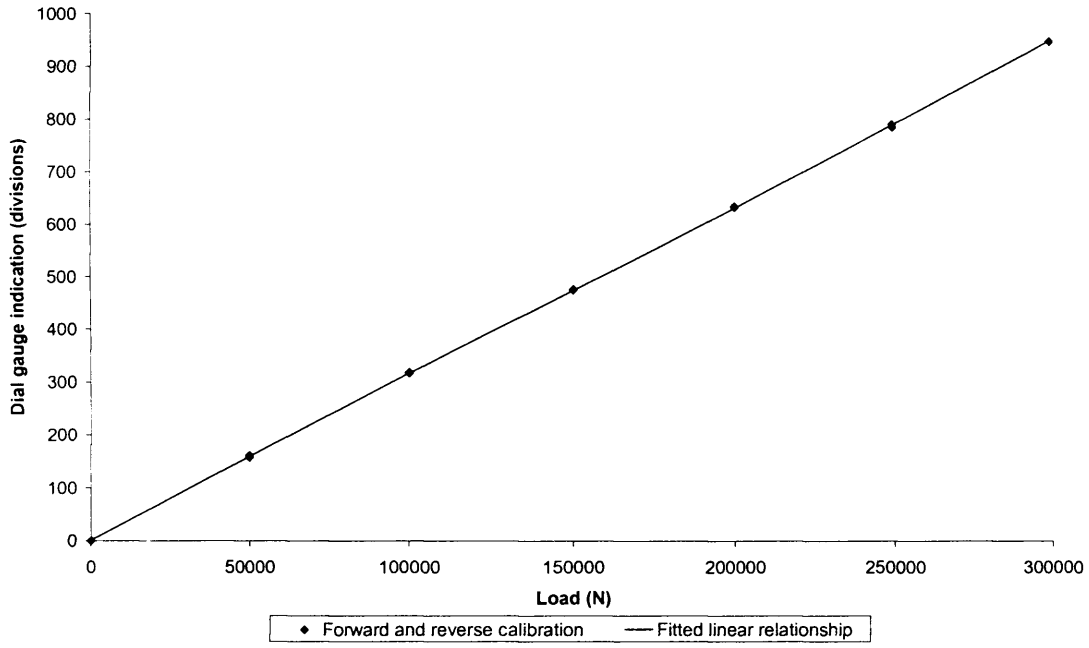

Figure B11.0. Calibration curve for 400kN (column) proving ring, Machine 3, Ring 3. Output 317.76 N/division, $r^2 = 0.9999$.

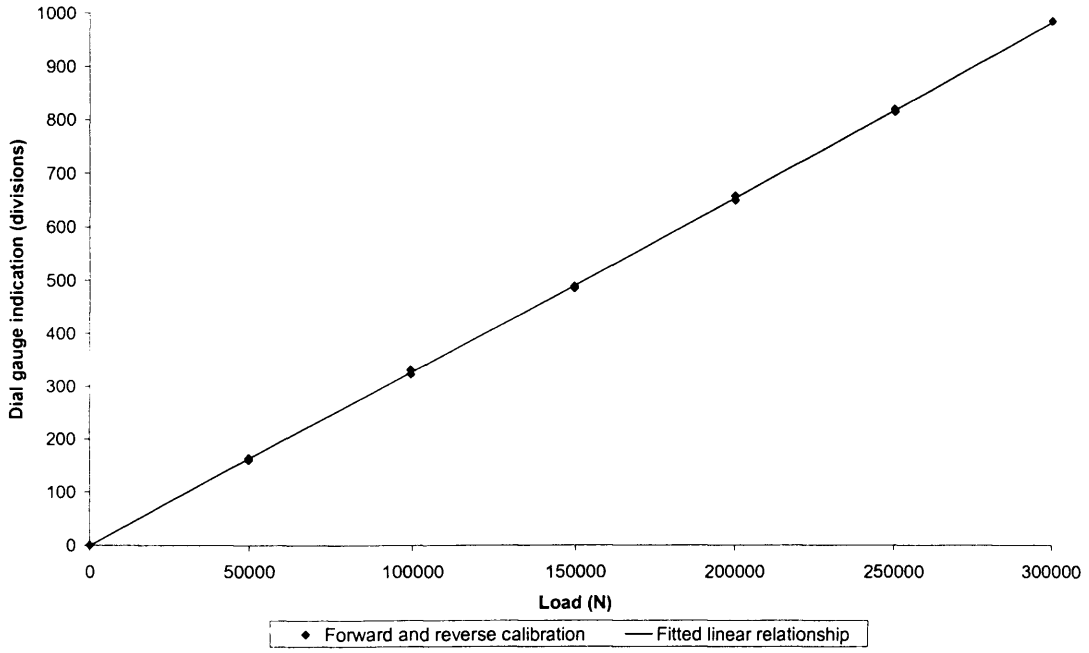

Figure B12.0. Calibration curve for 400kN (column) proving ring, Machine 3, Ring 4. Output 306.56 N/division, $r^2 = 0.9998$.

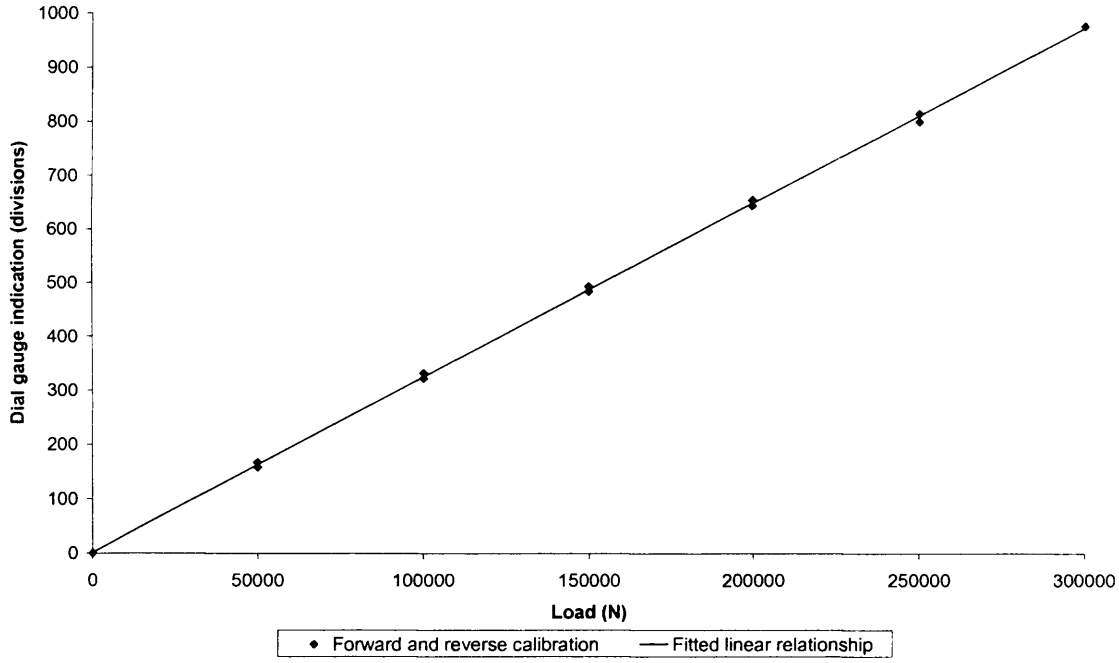

Figure B13.0. Calibration curve for 400kN (column) proving ring, Machine 4, Ring 1. Output 309.41 N/division, $r^2 = 0.9998$.

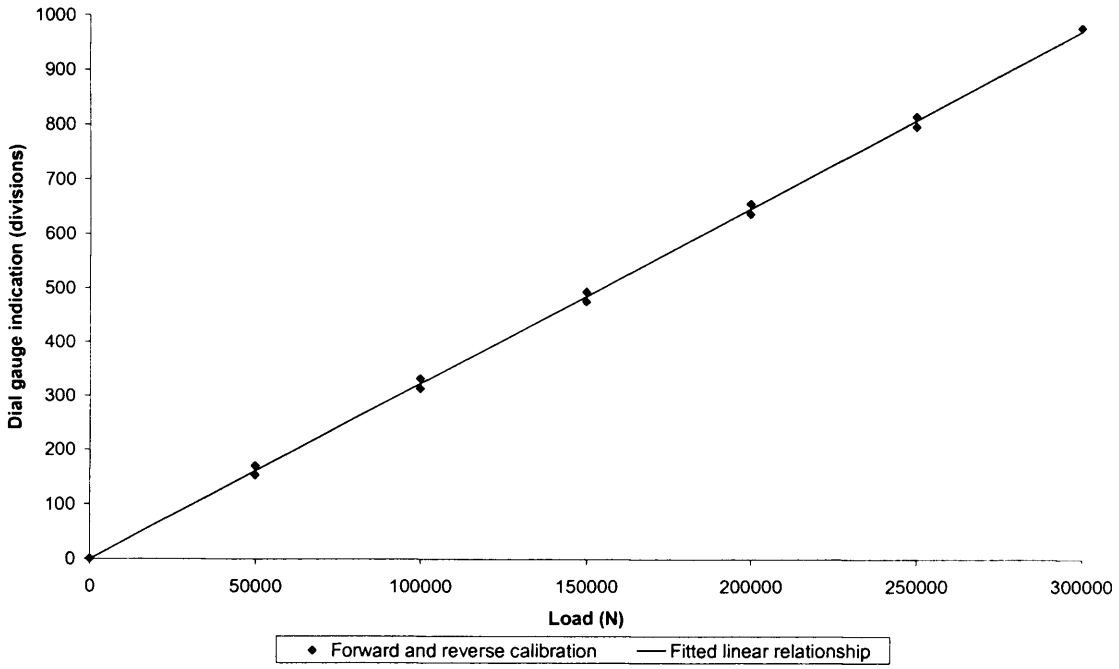

Figure B14.0. Calibration curve for 400kN (column) proving ring, Machine 4, Ring 2. Output 310.17 N/division, $r^2 = 0.9992$.

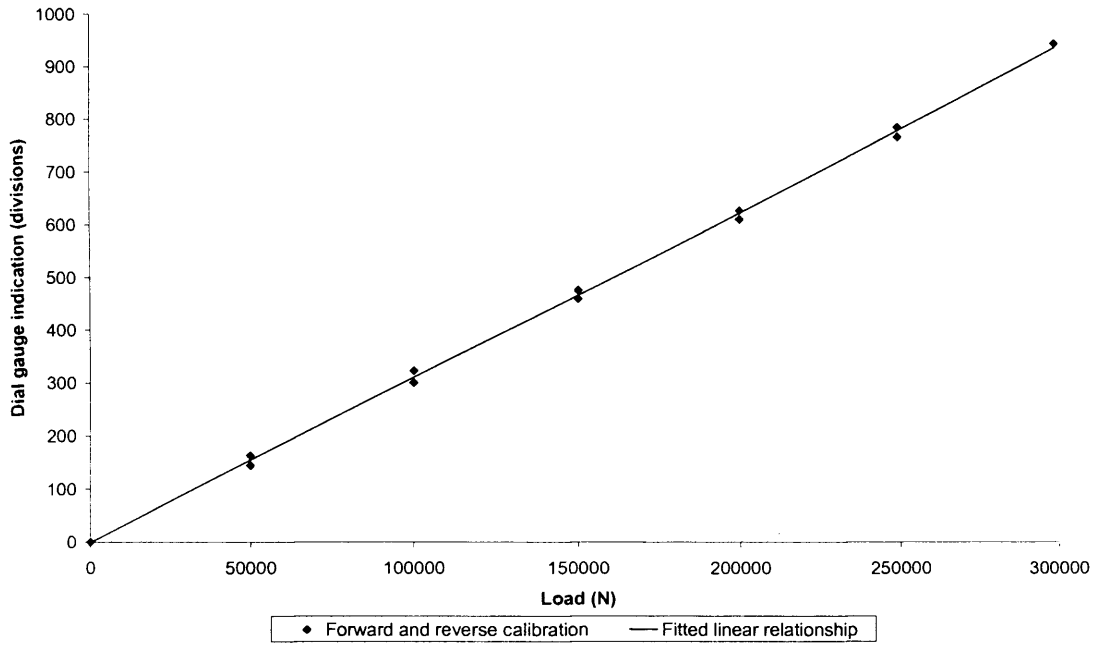

Figure B15.0. Calibration curve for 400kN (column) proving ring, Machine 4, Ring 3. Output 321.44 N/division, $r^2 = 0.9992$.

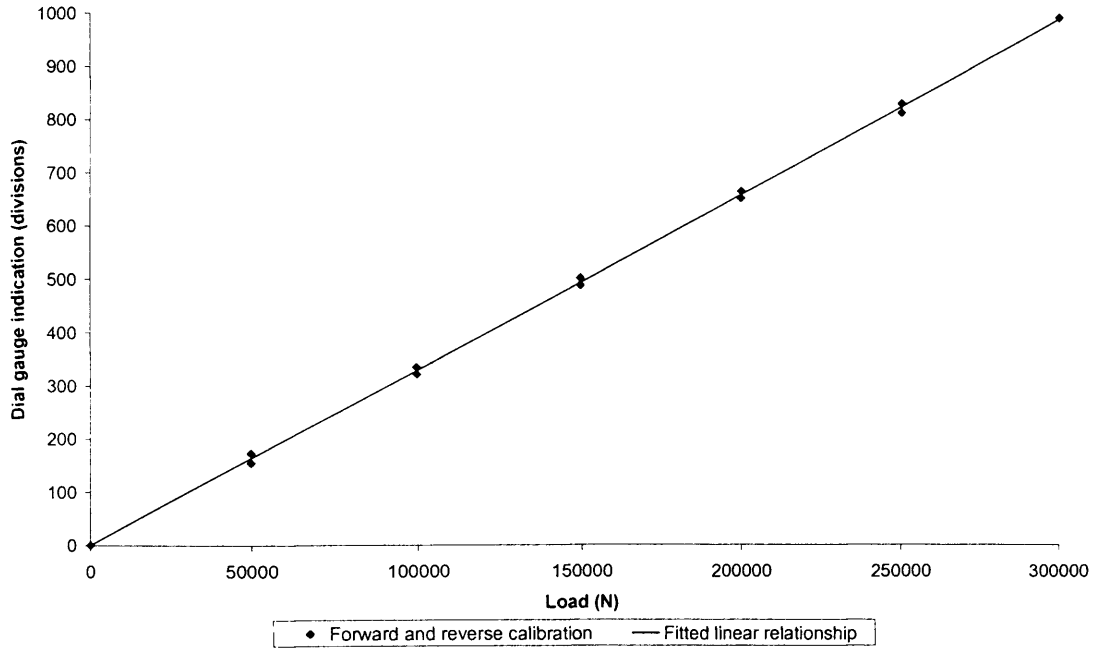

Figure B16.0. Calibration curve for 400kN (column) proving ring, Machine 4, Ring 4. Output 305.44 N/division, $r^2 = 0.9995$.

Appendix C

Torsion Test Theory

Contents

C1.0 Theory

The application of torsion to a solid concrete cylinder will produce shearing stresses on certain planes equal in magnitude to the principal stresses (i.e. diagonal tension and compression stresses). In order to determine the magnitude of these stresses, the following assumptions are made:

1. the twisting is uniform along the shaft
2. cross-sections remain planar and radii remain straight during twisting
3. the material is elastic
4. a linear variation in shearing stress exists over the cross-section, from zero at the centre to a maximum value at the circumference.

These assumptions allow the use of the following standard textbook solution for the torque-twist relationship in a linear elastic material:

$$\frac{T}{J} = \frac{\tau}{r} = \frac{G\gamma}{L} \qquad \text{(C1)}$$

where:

T = torque,

J = polar second moment of area,

τ = shear stress at radius r,

r = average radius of the specimen,

G = shearing modulus,

γ = rotation,

L = length over which rotation is measured.

Figure C1 shows the deformation at the surface of a concrete cylinder in torsion, while Figure C2 shows the cylinder in cross-section, where:

P = applied load

θ = angle rotated through,

S = distance over which concrete surface rotates,

Δ = distance over which applied load rotates,

r = specimen radius,

D = lever arm.

From Figure C1 it can be seen that:

The applied torque: $$T = 2 \times D \times P \quad \text{(C2)}$$

The longitudinal angle rotated through, γ:

$$\gamma = \frac{S}{L} \quad \text{(C3)}$$

The transverse angle rotated through, θ:

$$\theta = \frac{\Delta}{D} = \frac{S}{r} \quad \text{(C4)}$$

Rearranging:

$$S = \frac{r\Delta}{D} \quad \text{(C5)}$$

From Figure C2 it can be seen that: $$\theta = \gamma \quad \text{(C6)}$$

Substituting for Equations C3 in C5:

$$\gamma = \frac{r\Delta}{LD} \quad \text{(C7)}$$

Substituting for Equations C2 in C1:

$$\tau = \frac{2DPr}{J} \quad \text{(C8)}$$

For a cylinder: $$J = \frac{\pi(2r)^4}{32} \quad \text{(C9)}$$

The elastic modulus E, can be calculated using the formula:

$$E = 2G(1+\upsilon) \tag{C10}$$

where G is the shearing modulus and υ is the Poisson ratio.

The shearing modulus G, can be calculated from the formula:

$$G = \frac{\tau}{\gamma} \tag{C11}$$

Dividing Equation C8 by C7 and substituting in C11:

$$G = \frac{2D^2L}{J}\frac{P}{\Delta} \tag{C12}$$

Since D, L and J are constants, then the shear modulus can be calculated from the gradient of a graph of load and displacement.

C2.0 Example

Figure C3 shows the relationship between load P and displacement Δ for a concrete test specimen of nominal strength 40 N/mm^2 and dimensions 200mm × 100mm diameter. The lever arm D in all tests in 125mm, and the distance over which rotation is measured L is 100mm. It can be observed that the relationship is almost linear up to the yield point. In order to ensure that this is the case in the calculations, the gradient is calculated over the lower portion of the curve where the relationship will be most linear i.e. between 10 and 25% of the maximum load.

In this case, the maximum load is 2.46kN.

10% of the maximum load is 0.120kN, which corresponds to a displacement of 0.002mm.
25% of the maximum load is 0.615kN, which corresponds to a displacement of 0.014mm.

Therefore, the gradient: $$\frac{P}{\Delta} = \frac{0.615-0.120}{0.014-0.002} = 41.25$$

From C9, the polar second moment of area $J = \frac{\pi \times (2\times 50)^4}{32} = 9817477$ mm^4.

Substituting for $\frac{P}{\Delta}$, J, L and D in Equation C12:

$$G = \frac{2\times 125^2 \times 100}{9817477} \times 41.25 = 13.13 \text{ kN/mm}^2.$$

Assuming a Poisson ratio of 0.2 and substituting for G in Equation C10:

Elastic Modulus, $E = 2 \times 13.12 \times (1 + 0.2) =$ 31.49 kN/mm^2.

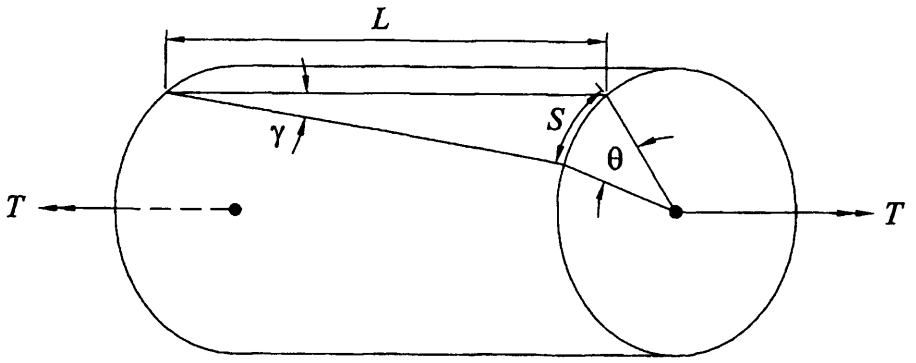

Figure C1. Cylindrical specimen subjected to torsion.

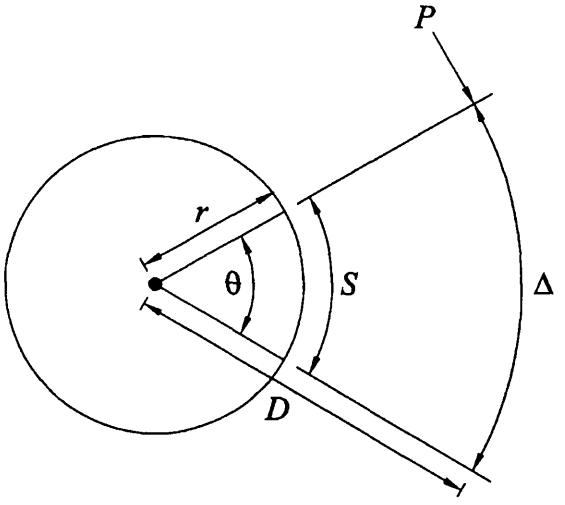

Figure C2. Cross-section of a cylindrical specimen in torsion.

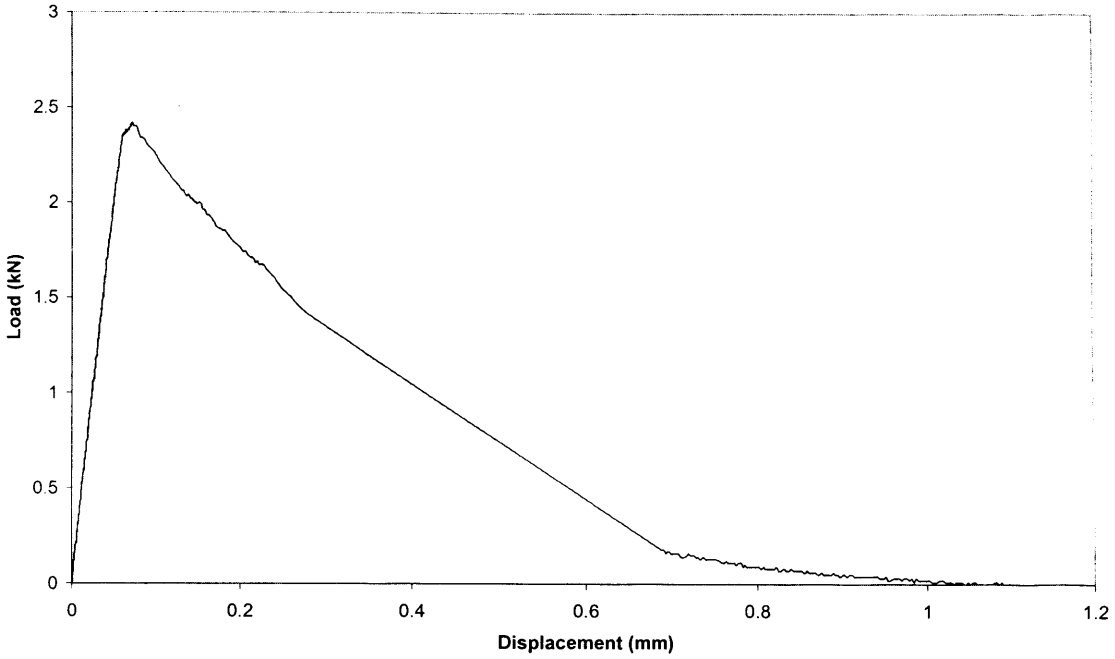

Figure C3. Relationship between applied load P, and displacement Δ, for a concrete test specimen of nominal strength 40 N/mm^2.

Appendix D

Additional Information For Chapter 5

Contents

D1.0 Measured Shrinkage Strains

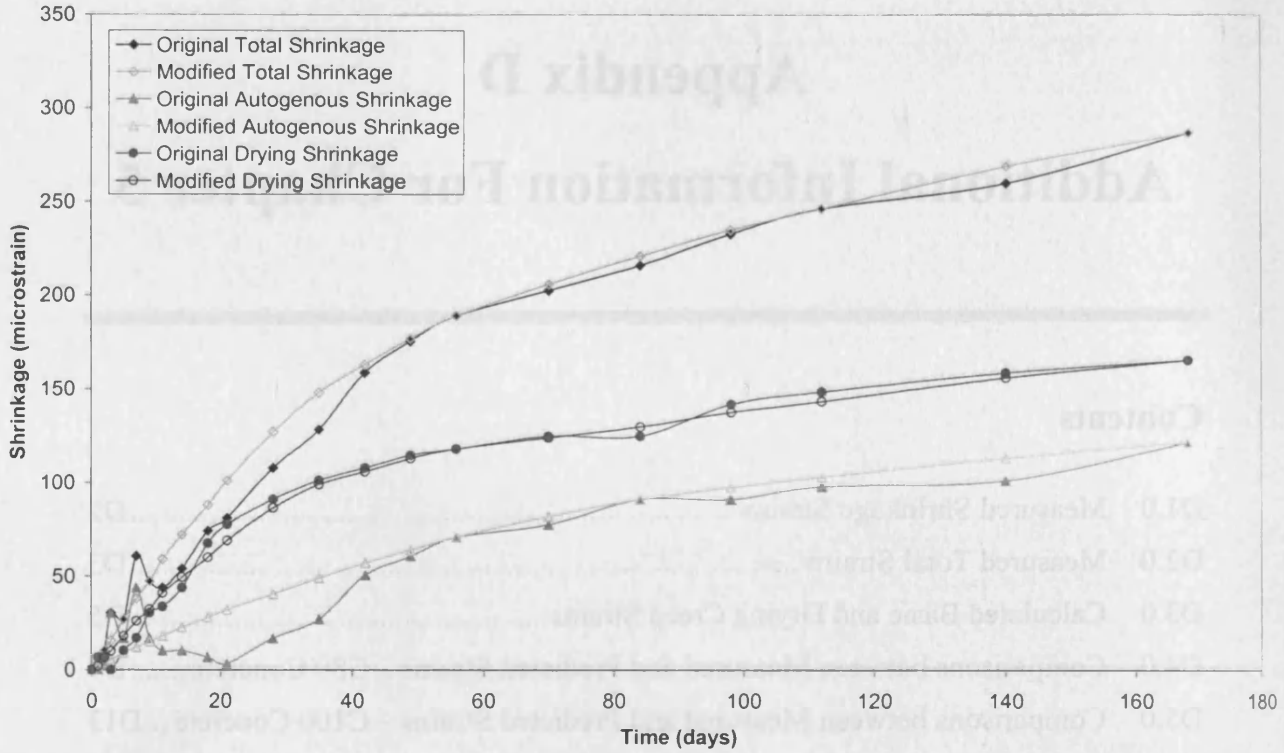

Figure D1.1. Measured and modified total, drying and autogenous shrinkage (με) for concrete of nominal strength 80 N/mm^2.

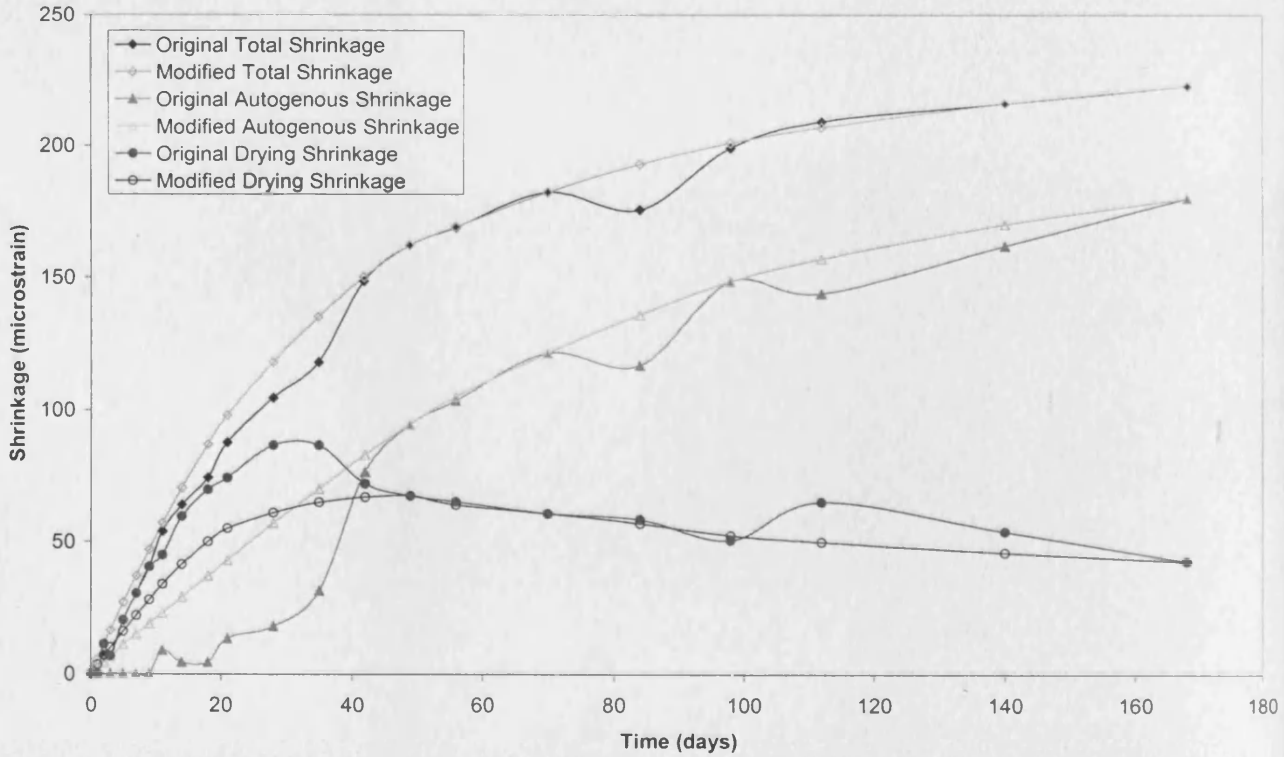

Figure D1.2. Measured and modified total, drying and autogenous shrinkage (με) for concrete of nominal strength 100 N/mm^2.

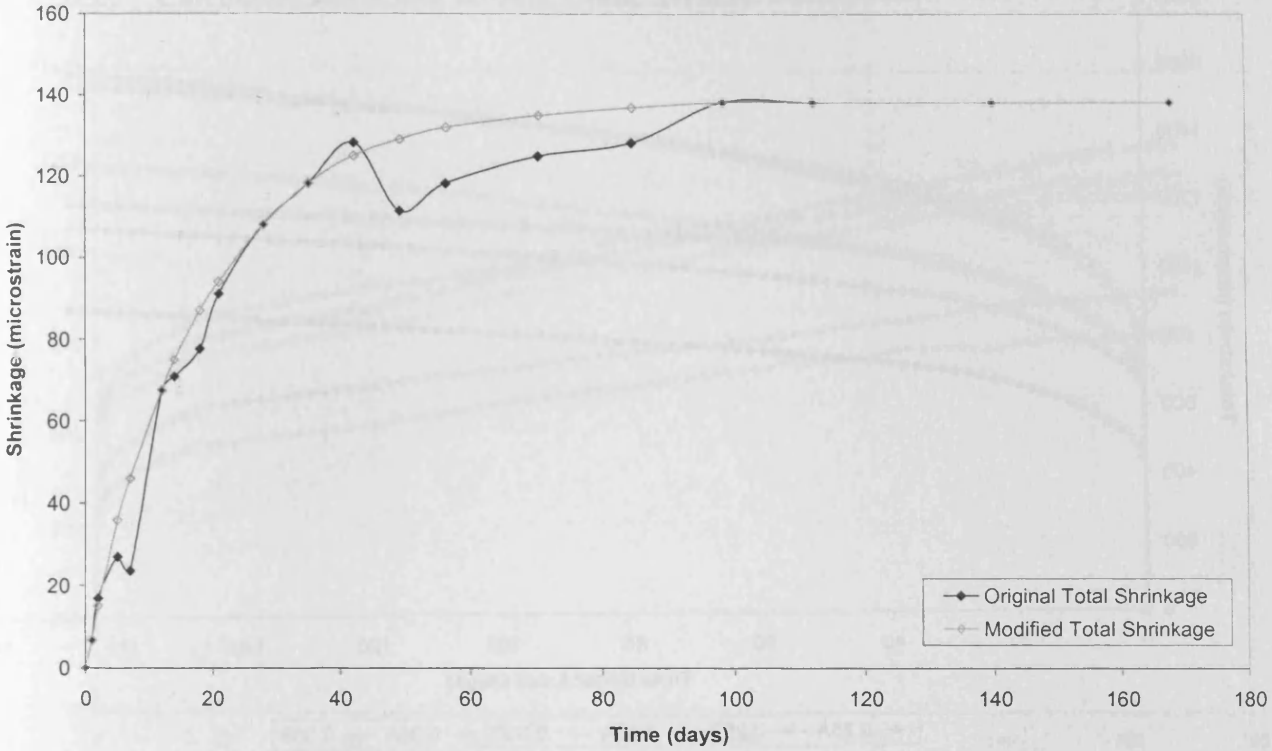

Figure D1.3. Measured and modified total, drying and autogenous shrinkage (με) for PFA concrete of nominal strength 65 N/mm^2.

D2.0 Measured Total Strains

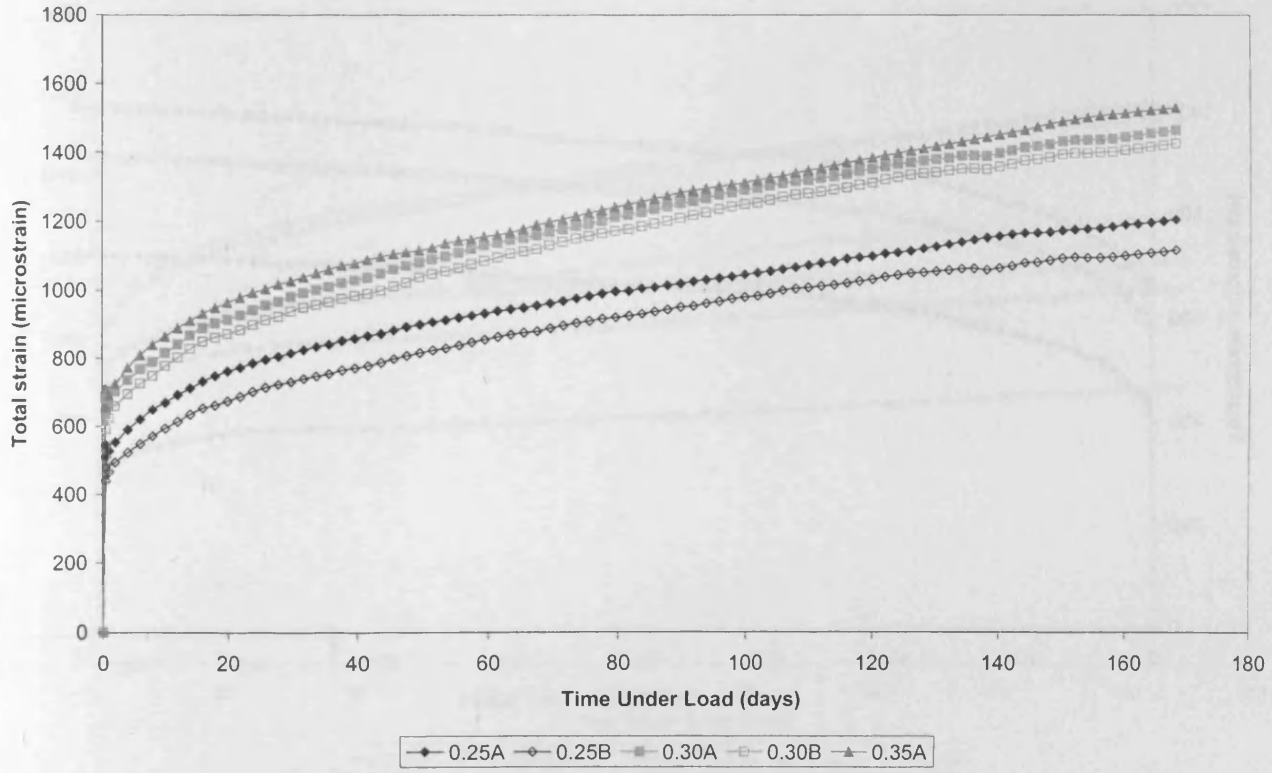

Figure D2.1. Measured total strain (με) under load for concrete of nominal strength 80 N/mm^2.

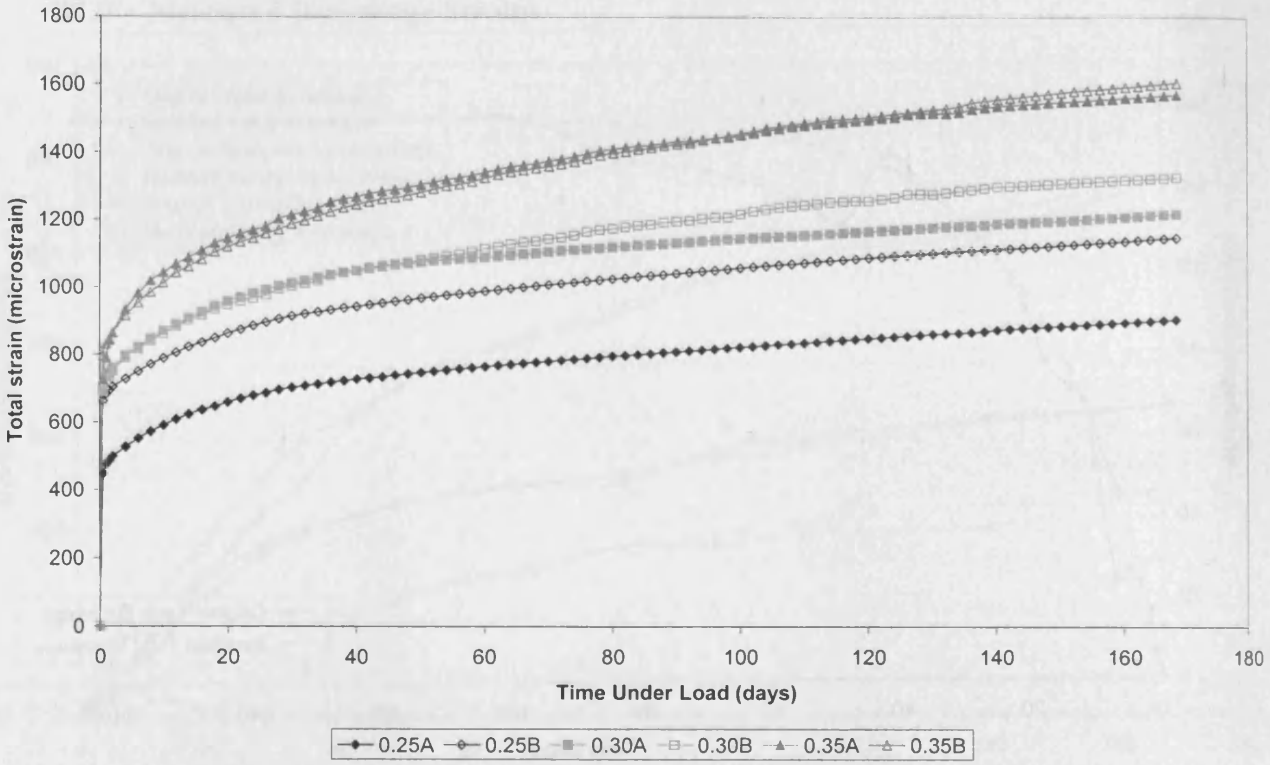

Figure D2.2. Measured total strain (με) under load for concrete of nominal strength 100 N/mm^2.

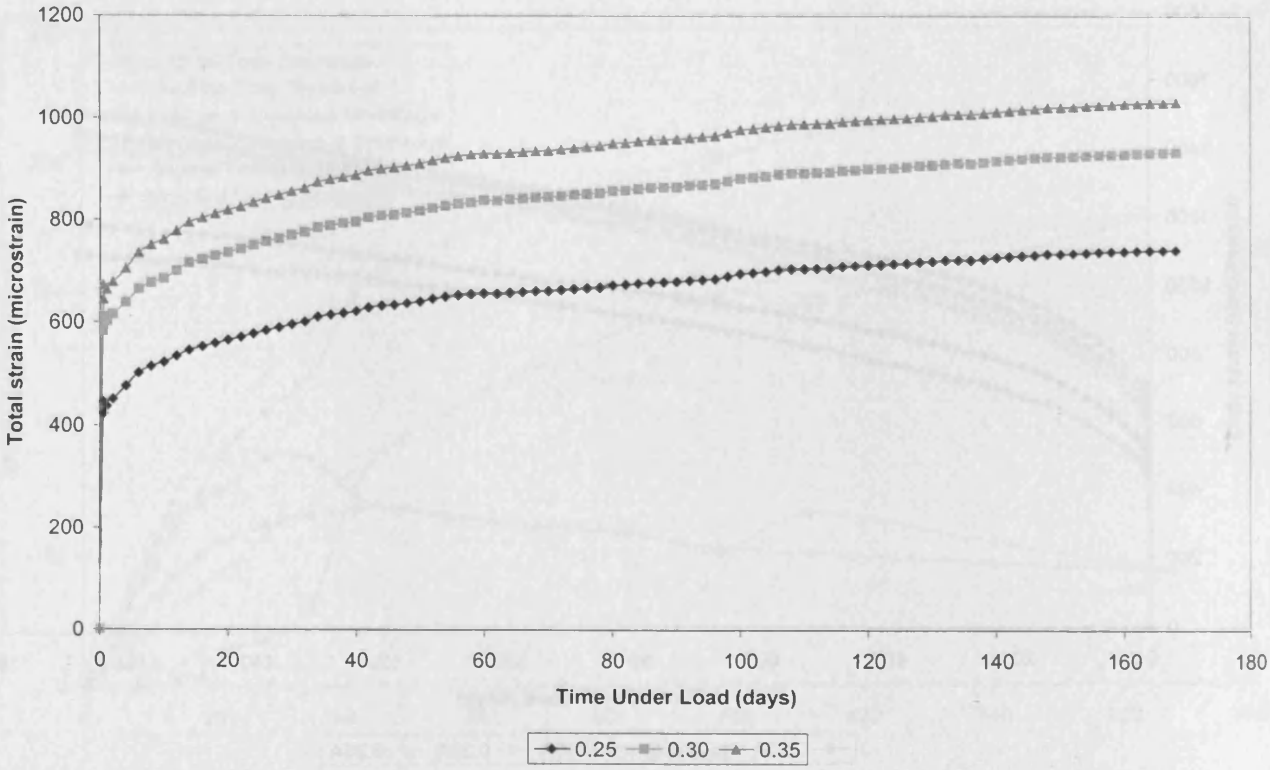

Figure D2.3. Measured total strain (με) under load for PFA concrete of nominal strength 65 N/mm^2.

D3.0 Calculated Basic and Drying Creep Strains

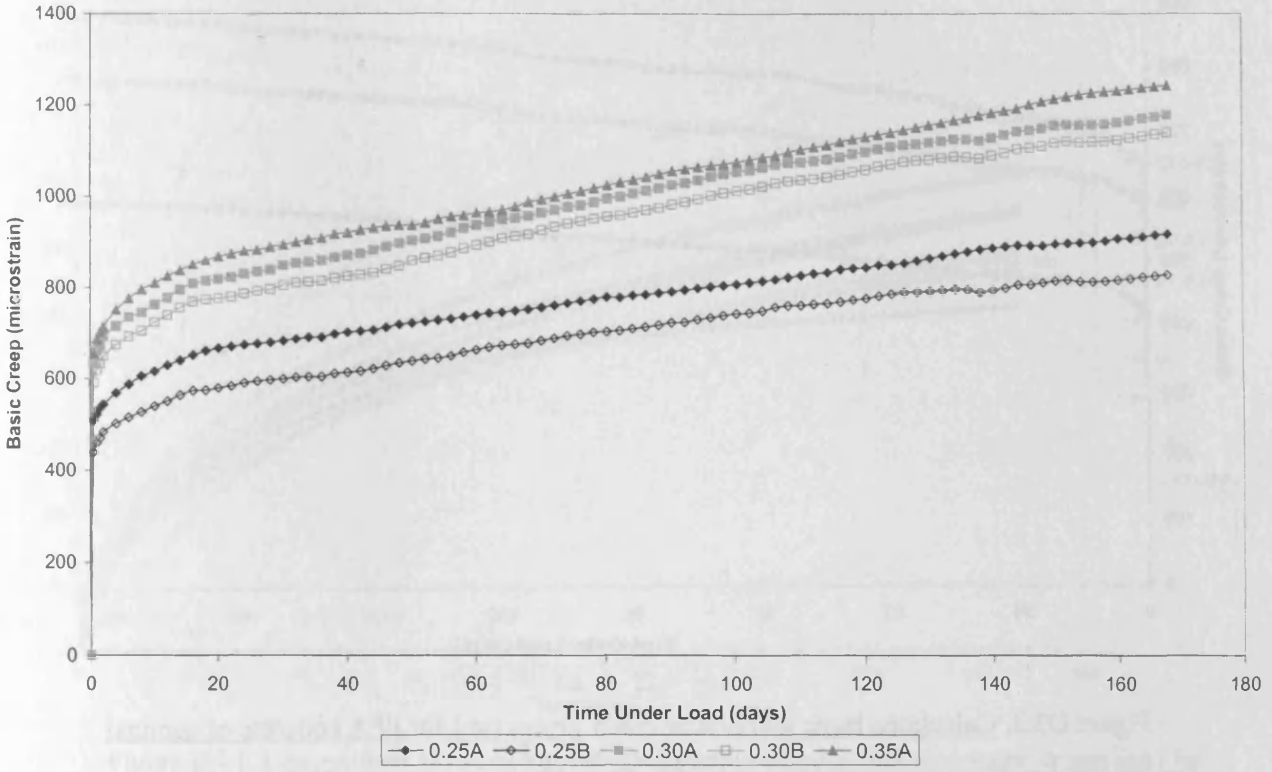

Figure D3.1. Calculated basic and drying creep strains (με) for concrete of nominal strength 80 N/mm^2.

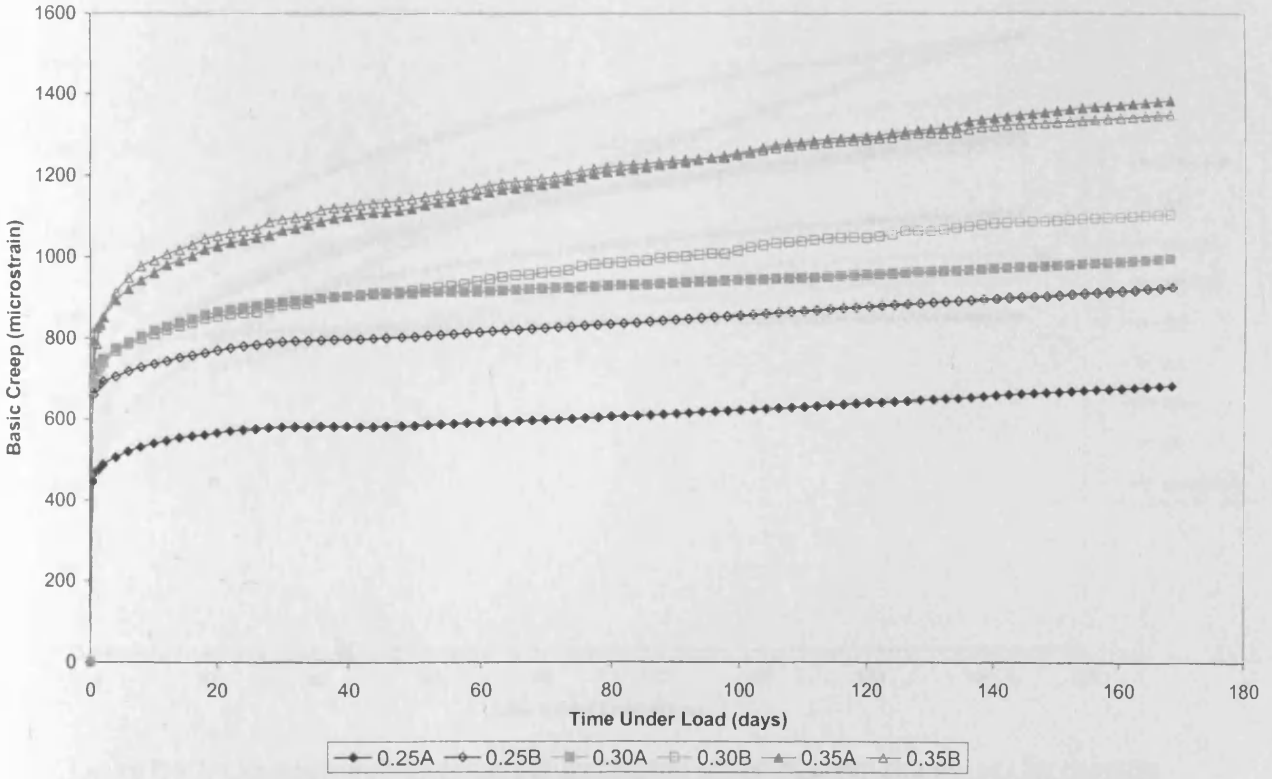

Figure D3.2. Calculated basic and drying creep strains (με) for concrete of nominal strength 100 N/mm^2.

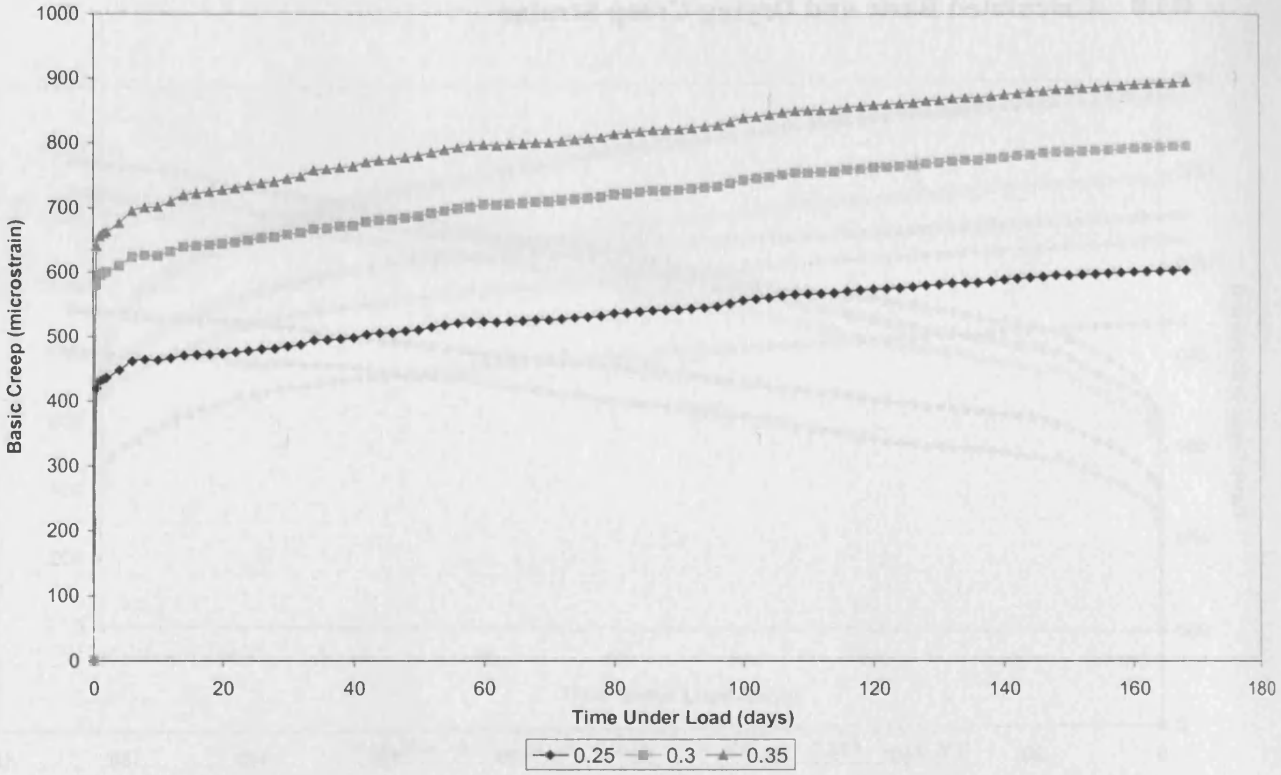

Figure D3.3. Calculated basic and drying creep strains (με) for PFA concrete of nominal strength 65 N/mm^2.

D4.0 Comparisons between Measured and Predicted Strains – C80 Concrete

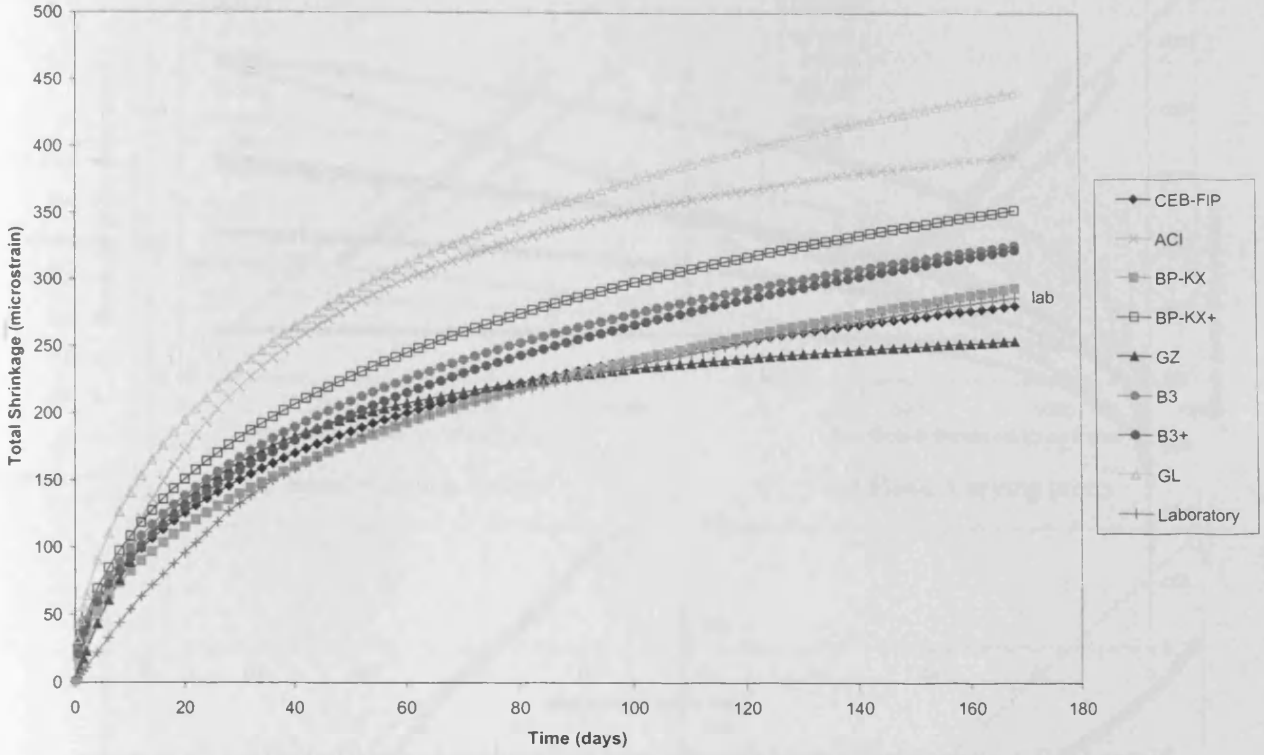

Figure D4.1. Comparison between experimental and predicted total shrinkage strains (με) for concrete of design strength 80 N/mm^2, using selected prediction models.

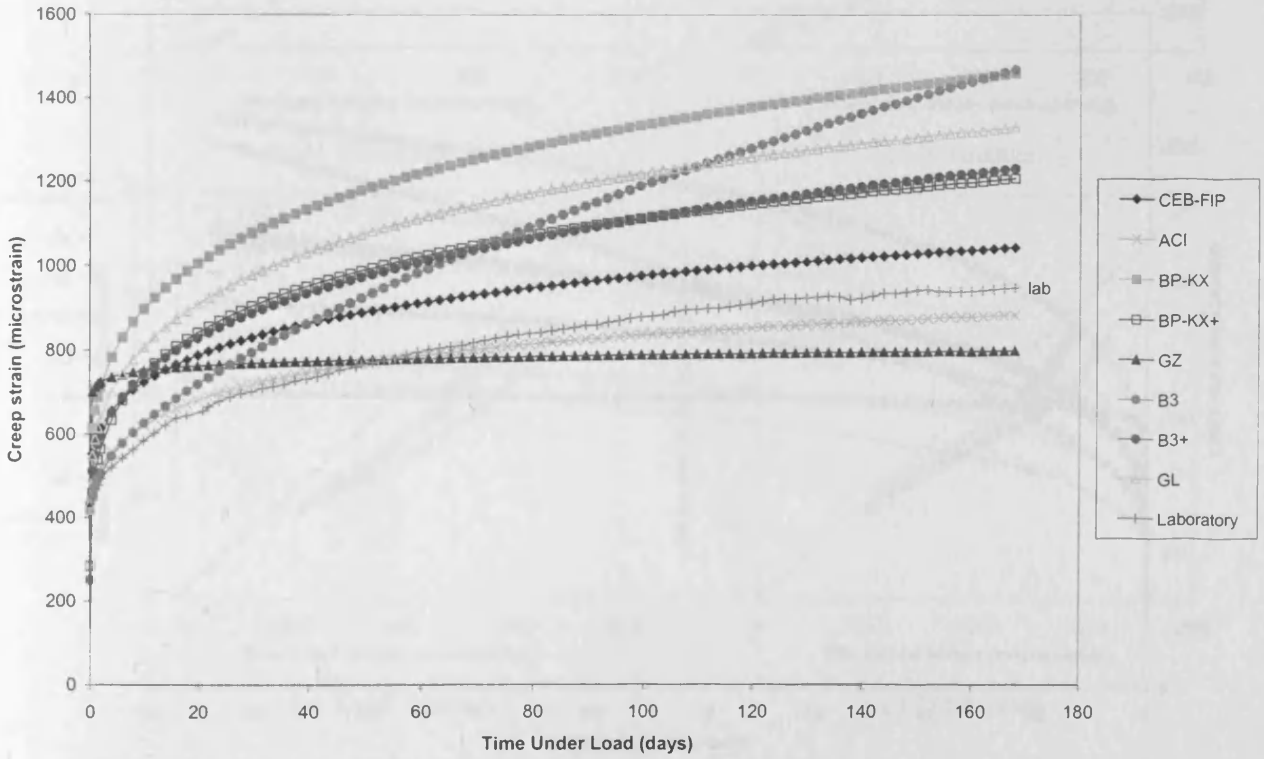

Figure D4.2. Comparison between experimental and predicted creep strains (με) for concrete of design strength 80 N/mm^2, loaded to a stress/strength ratio of 0.23 of the compressive strength at loading, using selected prediction models.

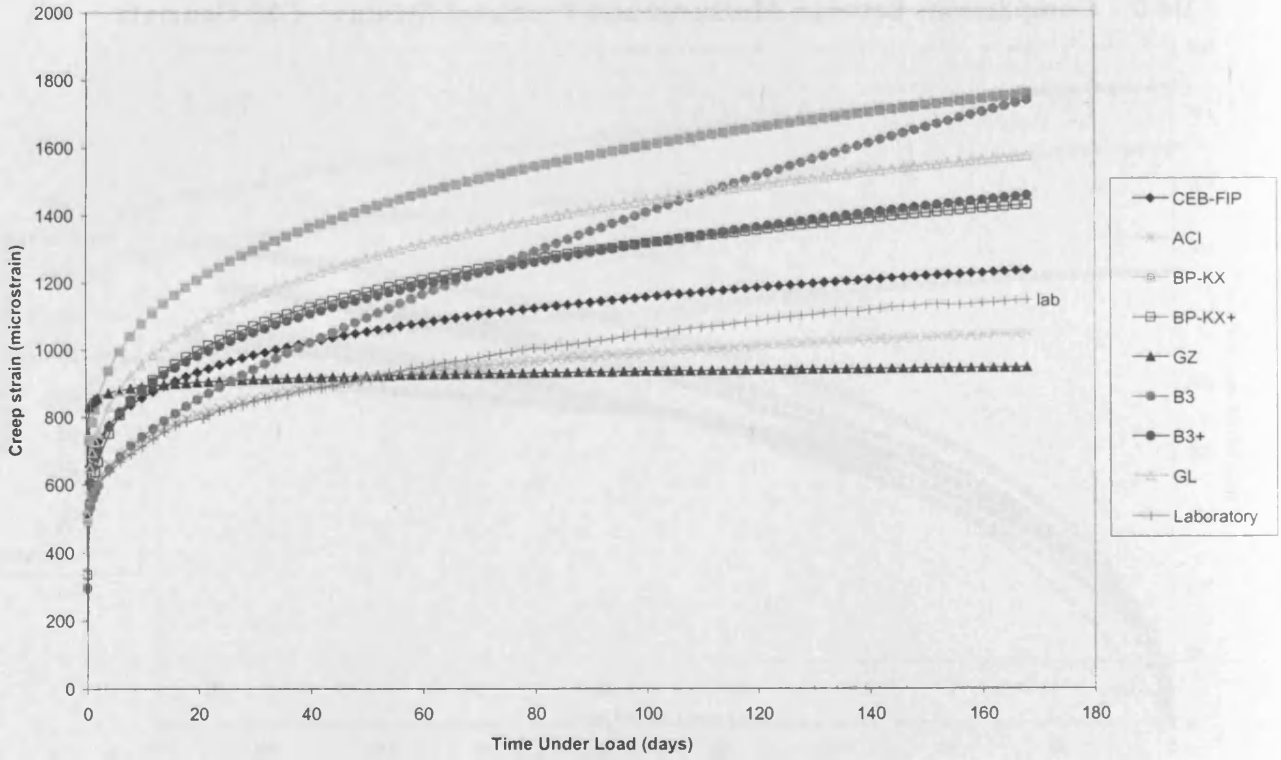

Figure D4.3. Comparison between experimental and predicted creep strains (με) for concrete of design strength 80 N/mm^2, loaded to a stress/strength ratio of 0.32 of the compressive strength at loading, using selected prediction models.

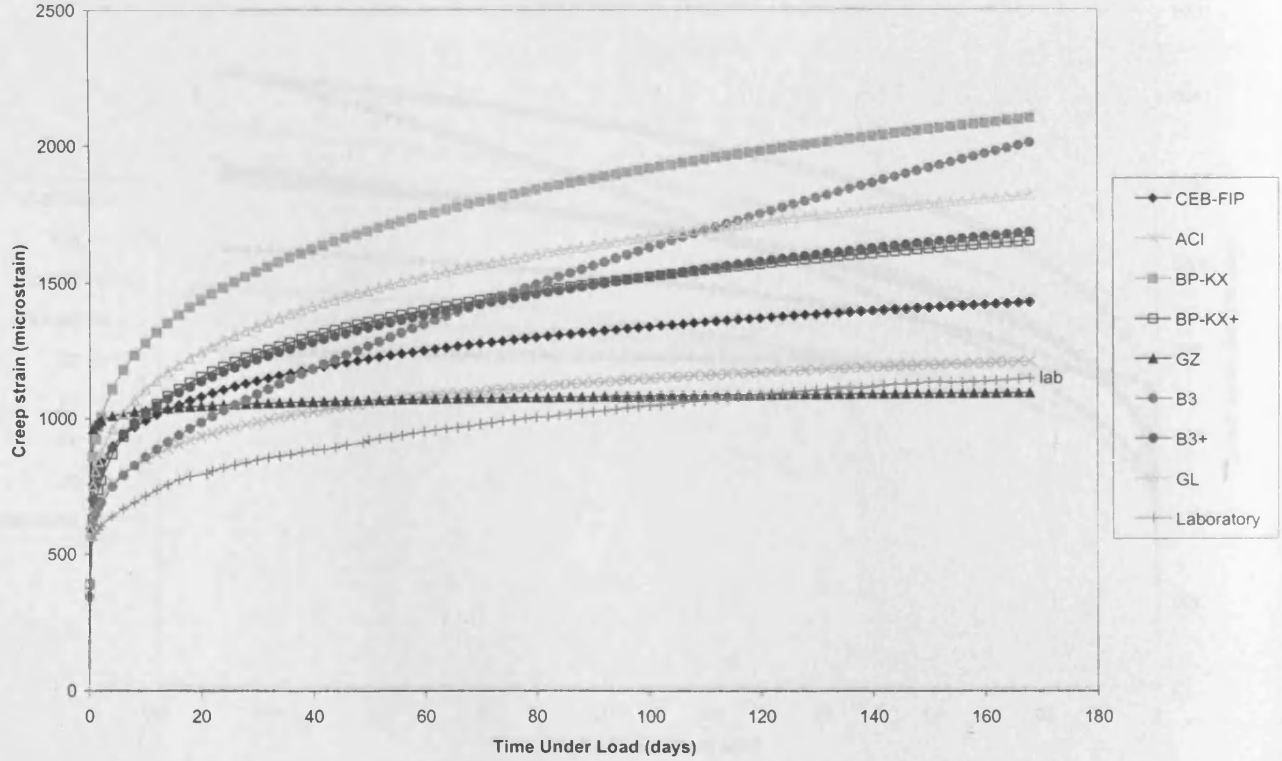

Figure D4.4. Comparison between experimental and predicted creep strains (με) for concrete of design strength 80 N/mm^2, loaded to a stress/strength ratio of 0.37 of the compressive strength at loading, using selected prediction models.

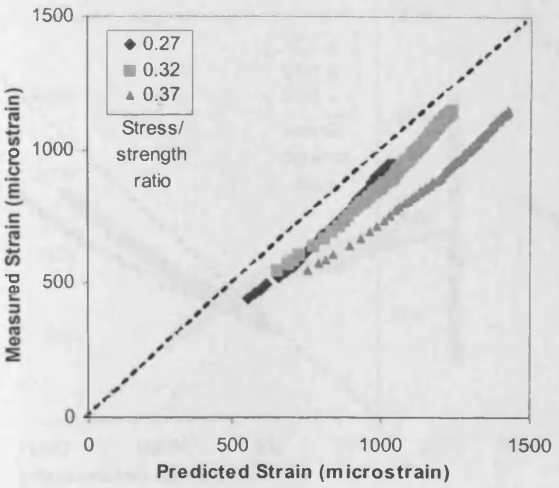

(a) Basic + drying creep

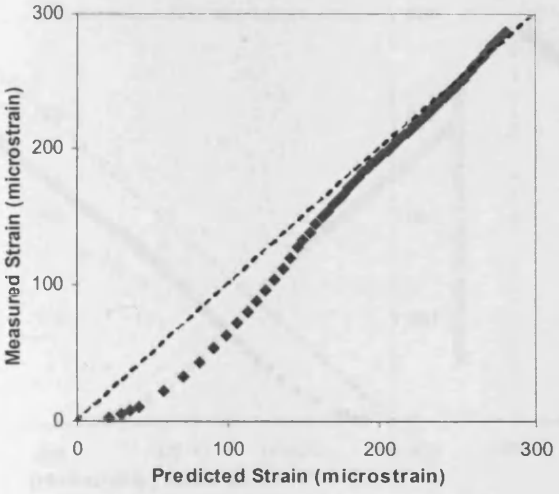

(b) Shrinkage

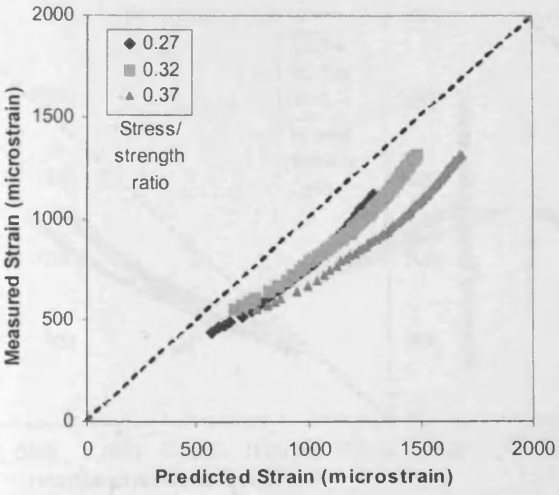

(c) Total strain

Figure D4.5. Comparison of measured and predicted strains for concrete of nominal strength 80 N/mm^2, using the CEB-FIP Model Code 1990.

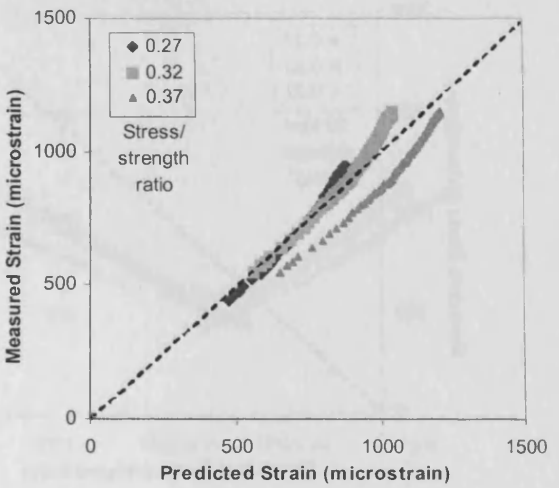

(a) Basic + drying creep

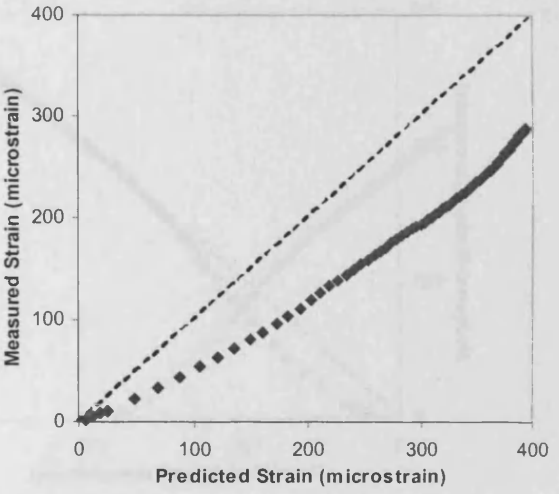

(b) Shrinkage

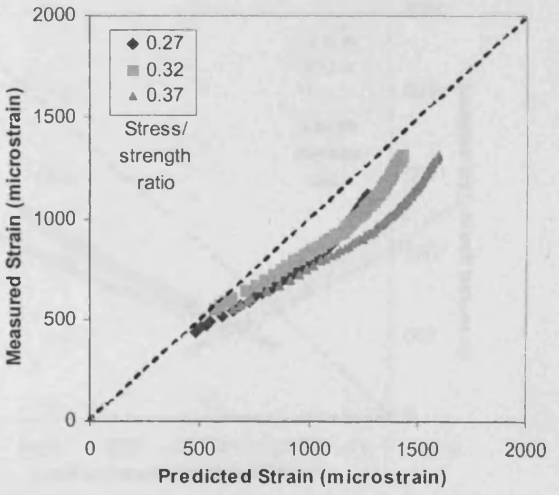

(c) Total strain

Figure D4.6. Comparison of measured and predicted strains for concrete of nominal strength 80 N/mm^2, using the ACI Model 1992.

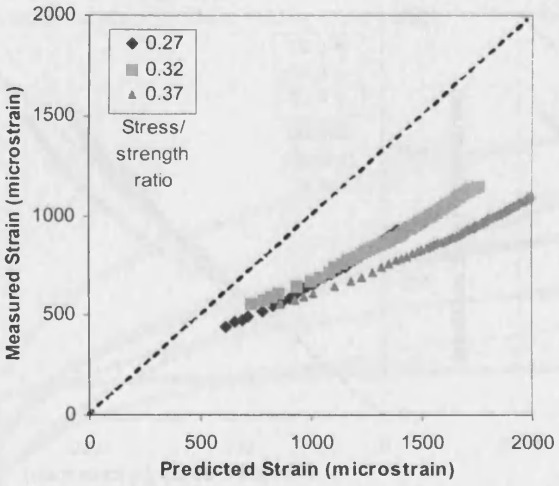

(a) Basic + drying creep

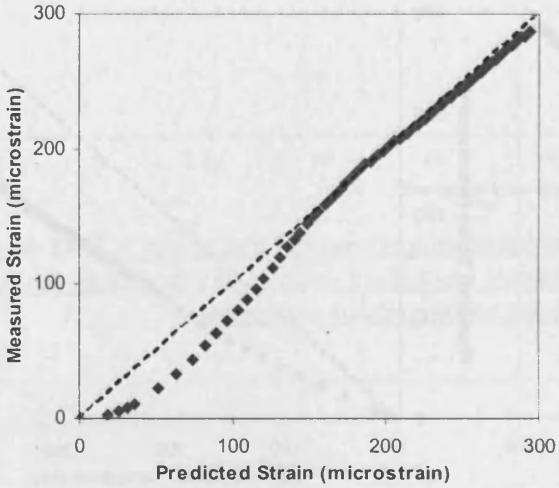

(b) Shrinkage

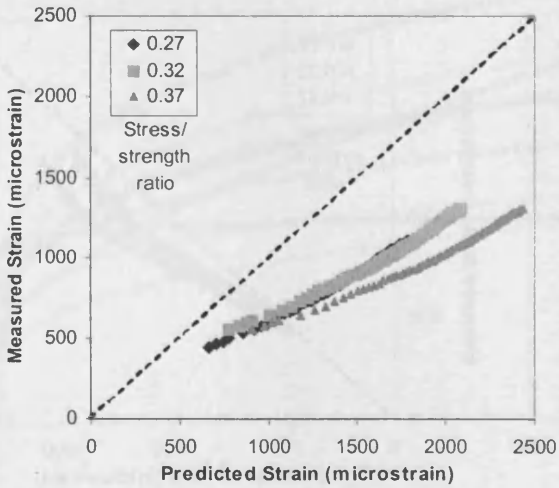

(c) Total strain

Figure D4.7. Comparison of measured and predicted strains for concrete of nominal strength 80 N/mm^2, using the BP-KX Model 1991.

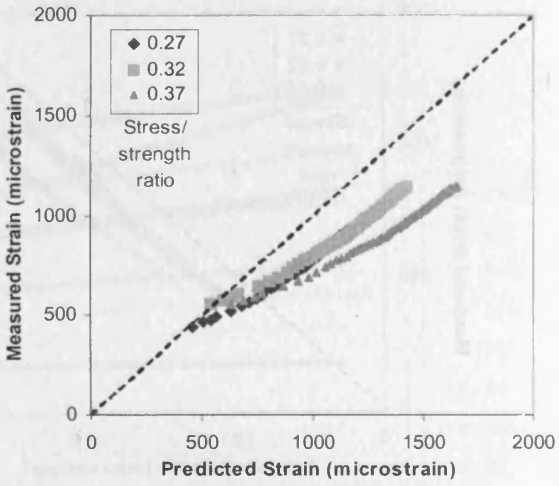

(a) Basic + drying creep

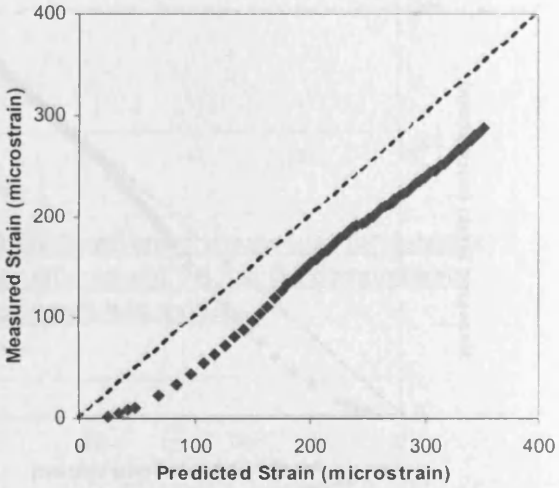

(b) Shrinkage

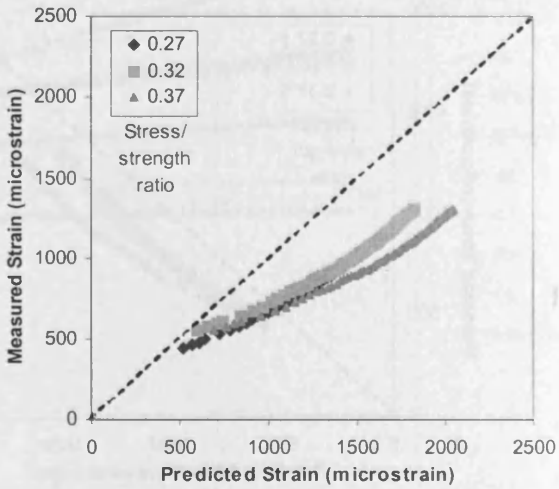

(c) Total strain

Figure D4.8. Comparison of measured and predicted strains for concrete of nominal strength 80 N/mm^2, using the short-form BP-KX Model 1993.

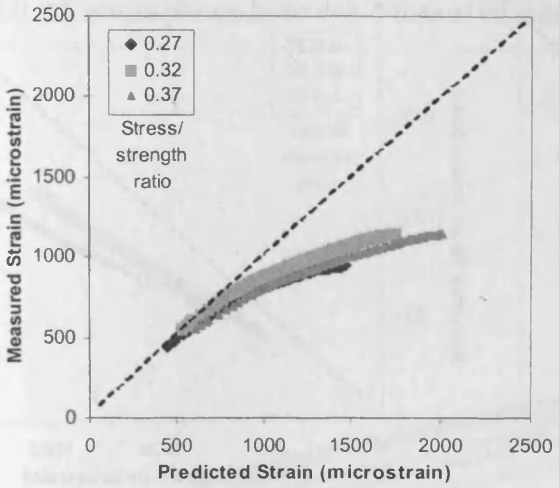

(a) Basic + drying creep

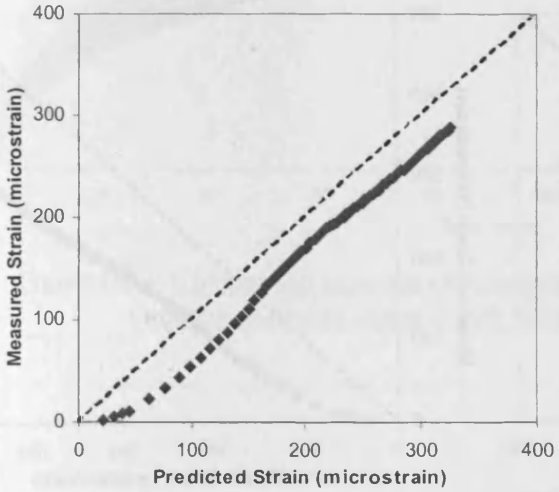

(b) Shrinkage

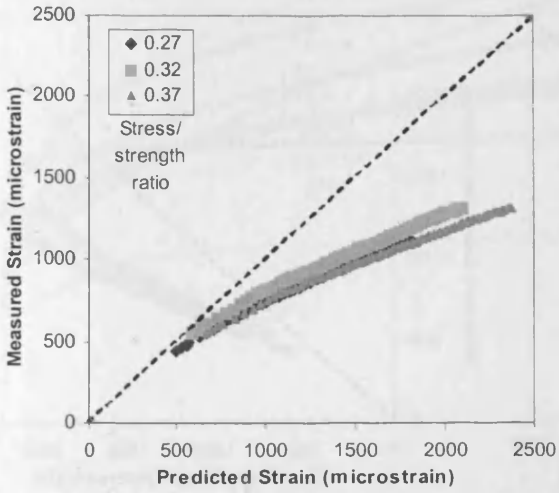

(c) Total strain

Figure D4.9. Comparison of measured and predicted strains for concrete of nominal strength 80 N/mm^2, using the B3 Model 1995.

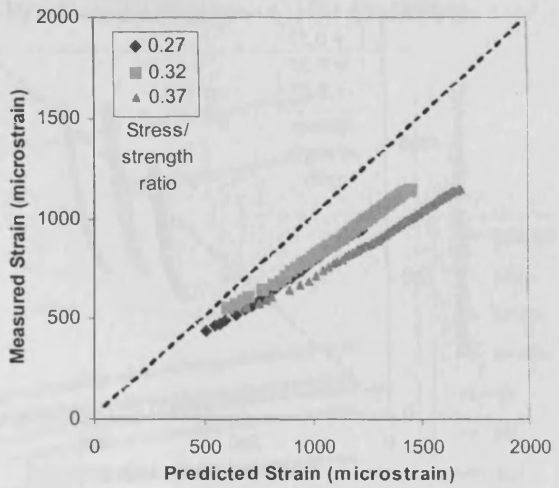

(a) Basic + drying creep

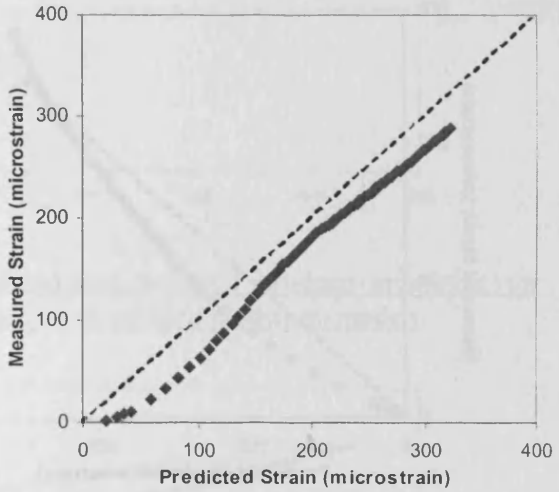

(b) Shrinkage

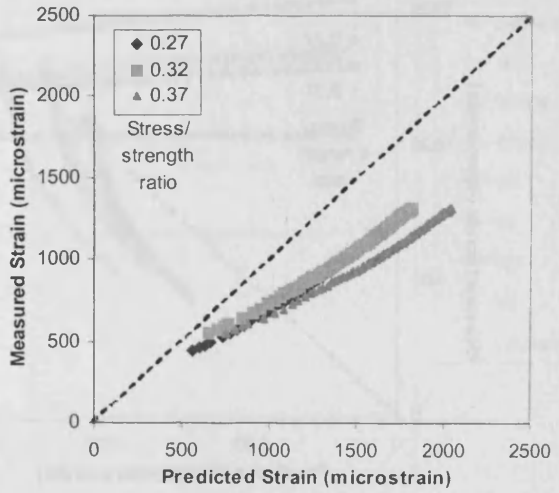

(c) Total strain

Figure D4.10. Comparison of measured and predicted strains for concrete of nominal strength 80 N/mm^2, using the short-form B3 Model 1996.

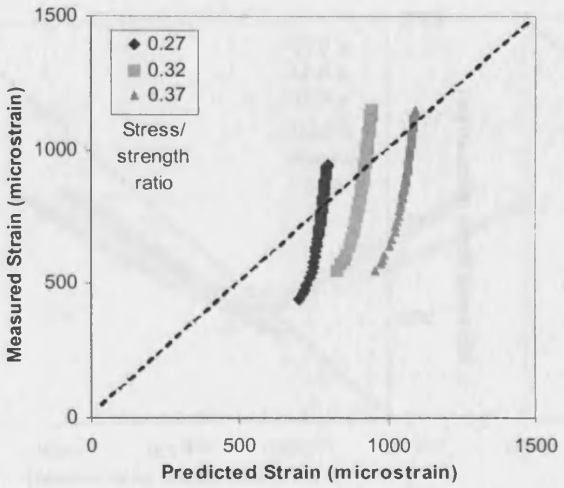

(a) Basic + drying creep

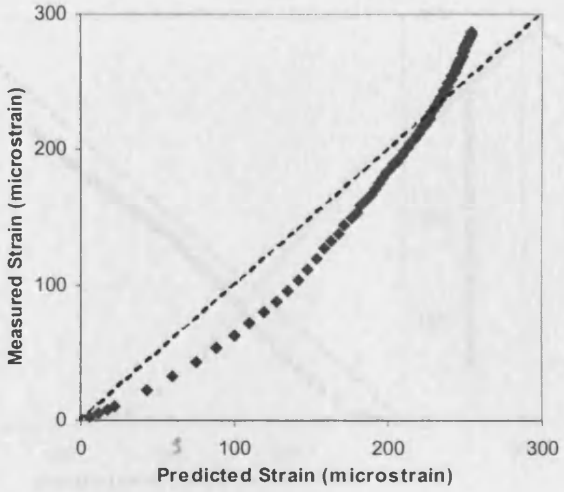

(b) Shrinkage

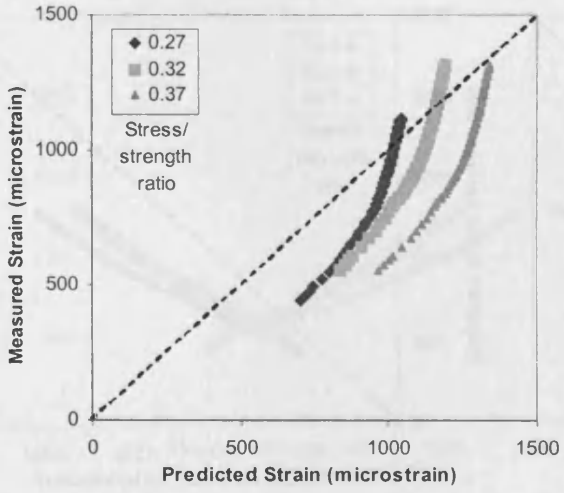

(c) Total strain

Figure D4.11. Comparison of measured and predicted strains for concrete of nominal strength 80 N/mm^2, using the GZ Model 1993.

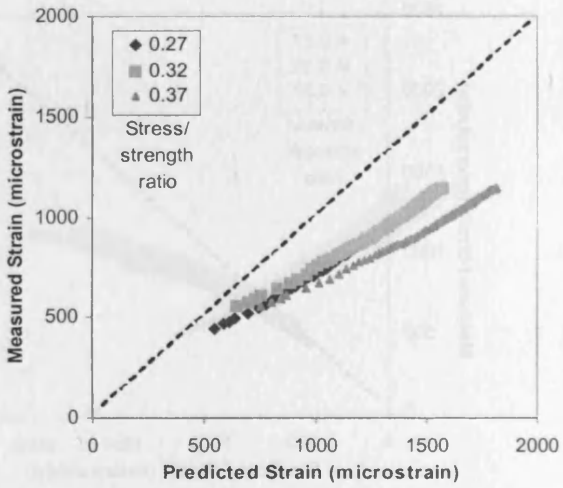

(a) Basic + drying creep

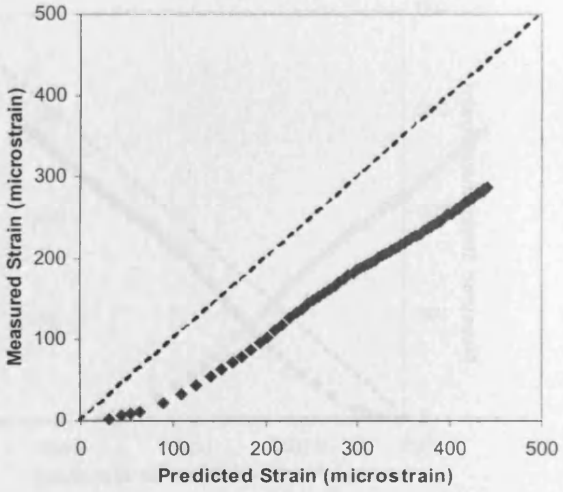

(b) Shrinkage

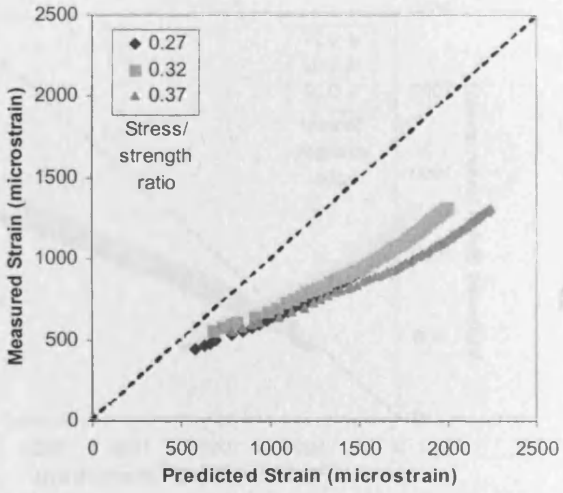

(c) Total strain

Figure D4.12. Comparison of measured and predicted strains for concrete of nominal strength 80 N/mm^2, using the GL Model 2001.

D5.0 Comparisons between Measured and Predicted Strains – C100 Concrete

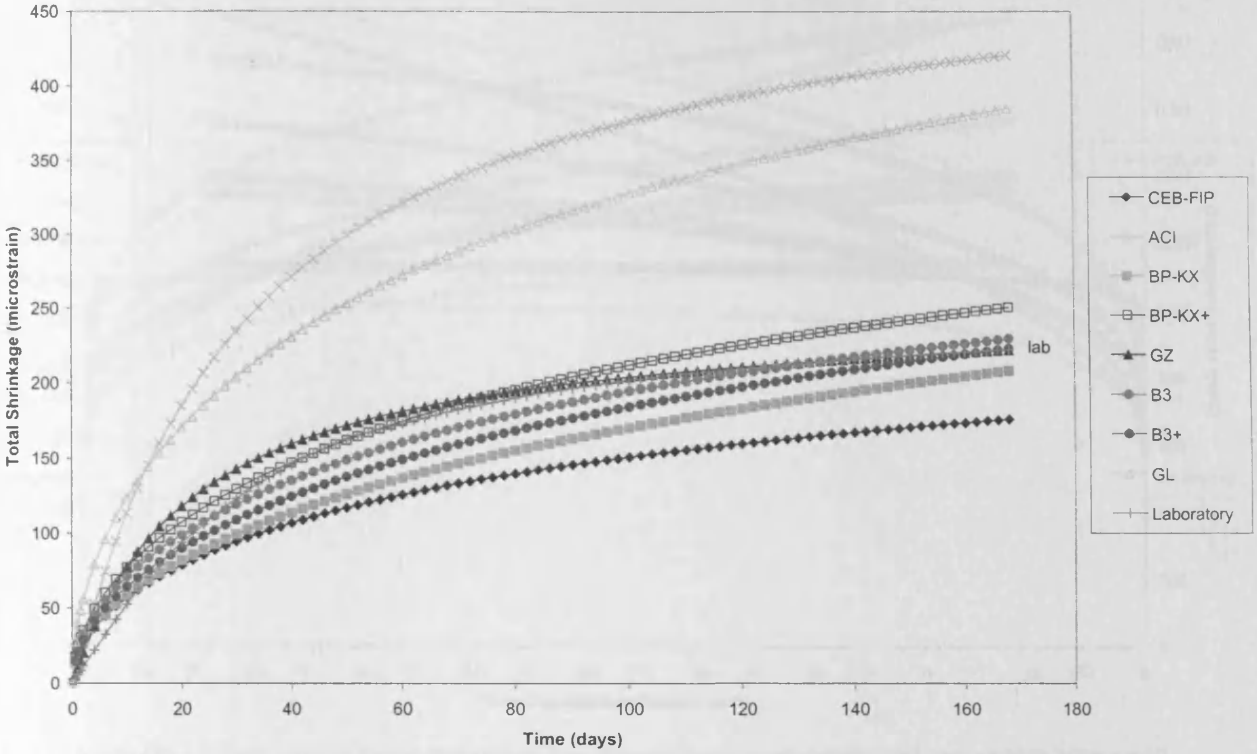

Figure D5.1. Comparison between experimental and predicted total shrinkage strains (με) for concrete of design strength 100 N/mm^2, using selected prediction models.

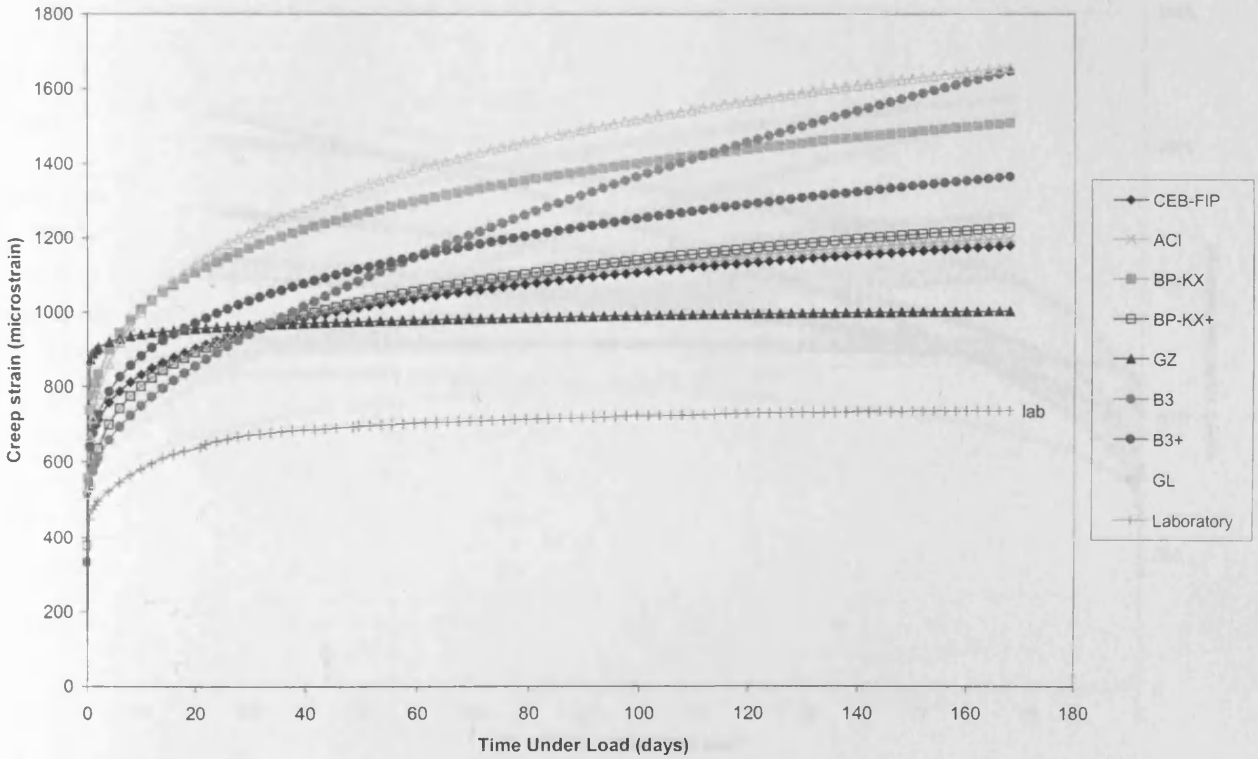

Figure D5.2. Comparison between experimental and predicted creep strains (με) for concrete of design strength 100 N/mm^2, loaded to a stress/strength ratio of 0.22 of the compressive strength at loading, using selected prediction models.

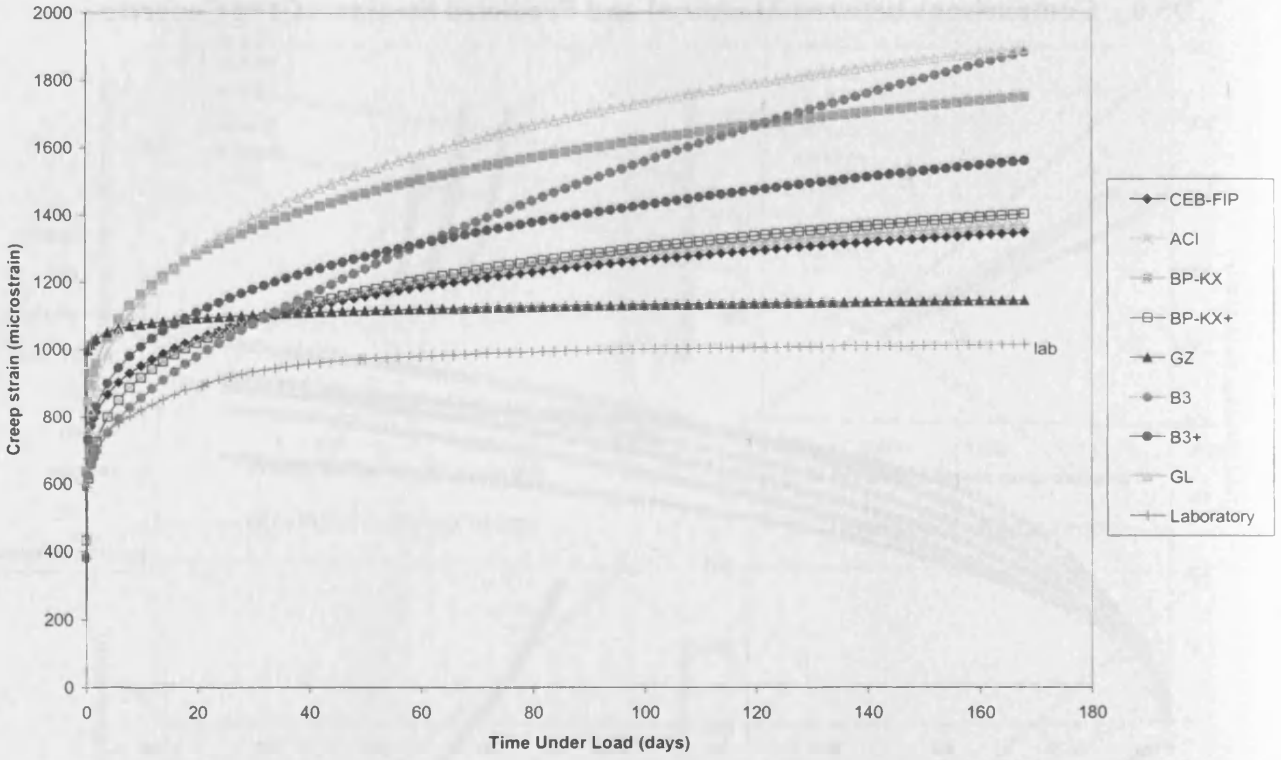

Figure D5.3. Comparison between experimental and predicted creep strains (με) for concrete of design strength 100 N/mm^2, loaded to a stress/strength ratio of 0.32 of the compressive strength at loading, using selected prediction models.

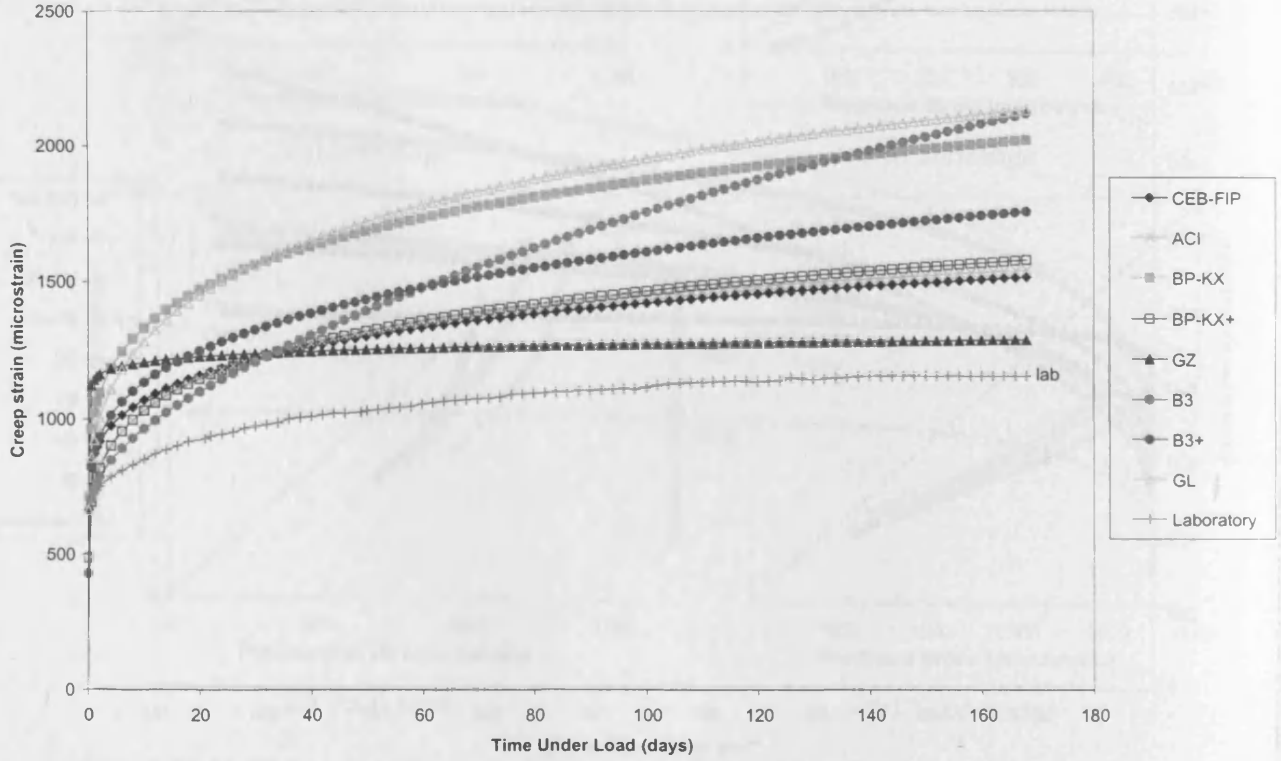

Figure D5.4. Comparison between experimental and predicted creep strains (με) for concrete of design strength 100 N/mm^2, loaded to a stress/strength ratio of 0.36 of the compressive strength at loading, using selected prediction models.

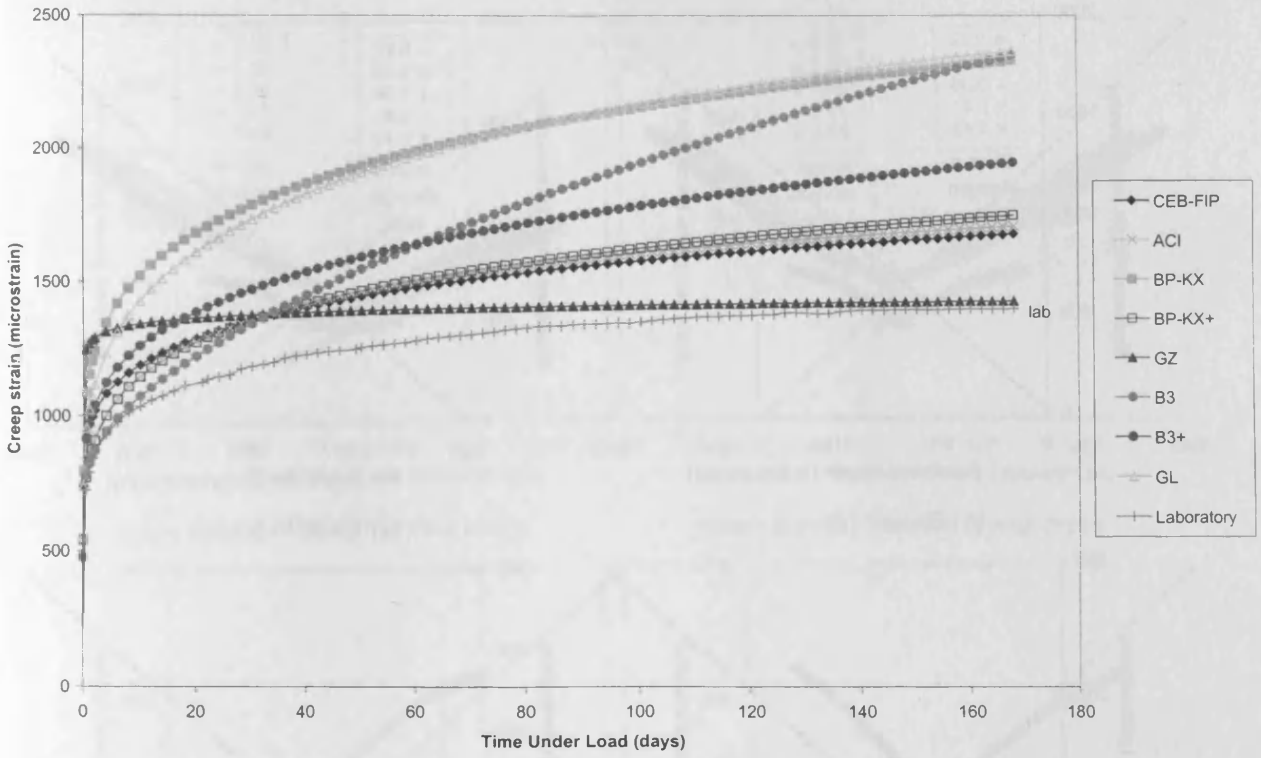

Figure D5.5. Comparison between experimental and predicted creep strains (με) for concrete of design strength 100 N/mm^2, loaded to a stress/strength ratio of 0.41 of the compressive strength at loading, using selected prediction models.

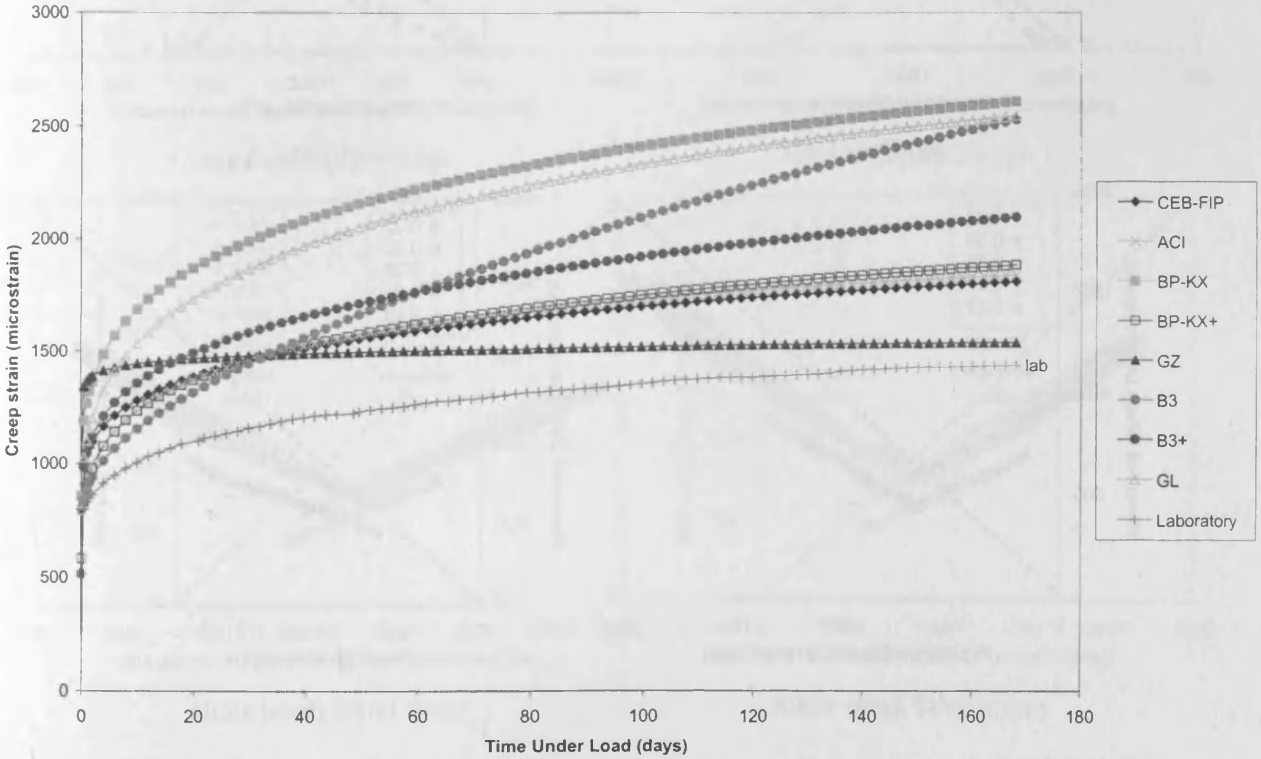

Figure D5.6. Comparison between experimental and predicted creep strains (με) for concrete of design strength 100 N/mm^2, loaded to a stress/strength ratio of 0.43 of the compressive strength at loading, using selected prediction models.

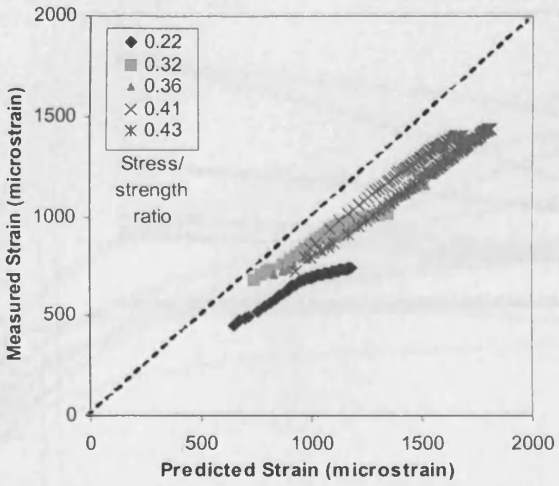

(a) Basic + drying creep

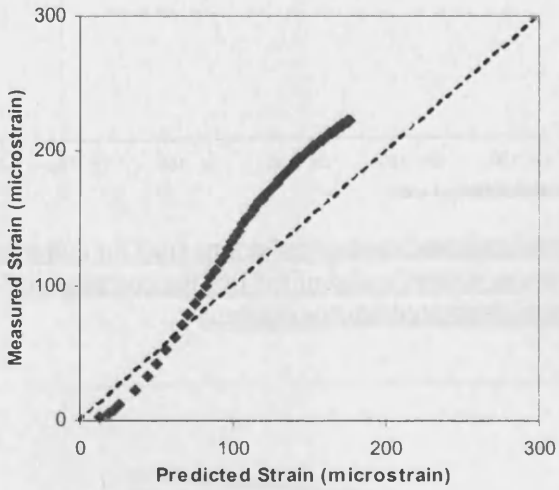

(b) Shrinkage

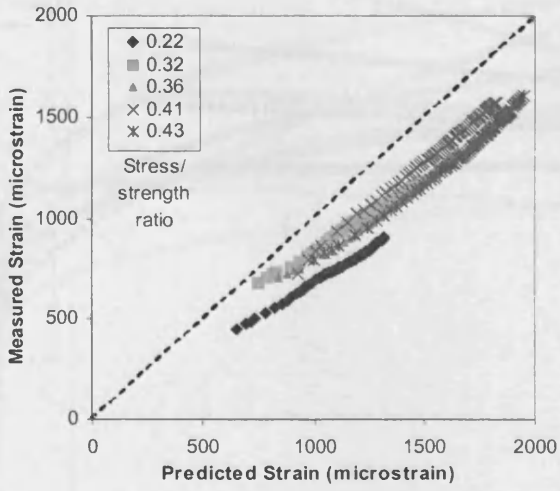

(c) Total strain

Figure D5.7. Comparison of measured and predicted strains for concrete of nominal strength 100 N/mm^2, using the CEB-FIP Model Code 1990.

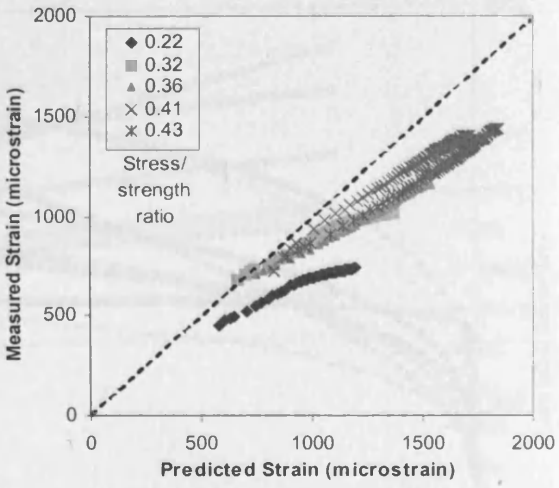

(a) Basic + drying creep

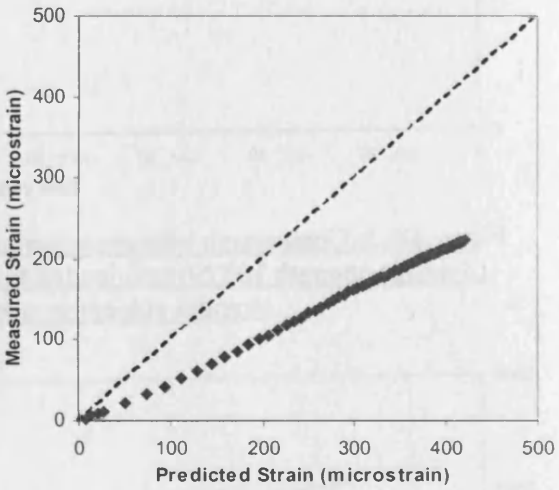

(b) Shrinkage

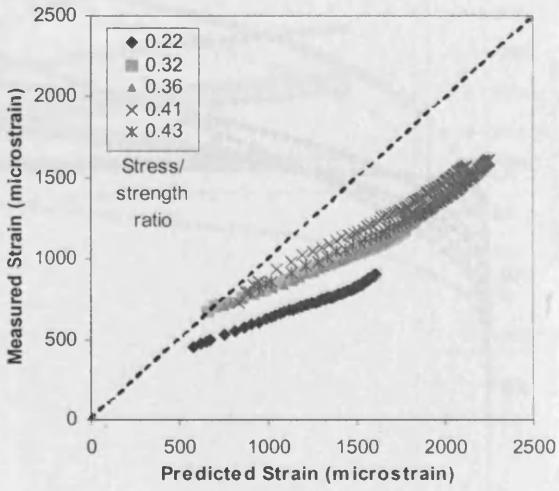

(c) Total strain

Figure D5.8. Comparison of measured and predicted strains for concrete of nominal strength 100 N/mm^2, using the ACI Model 1992.

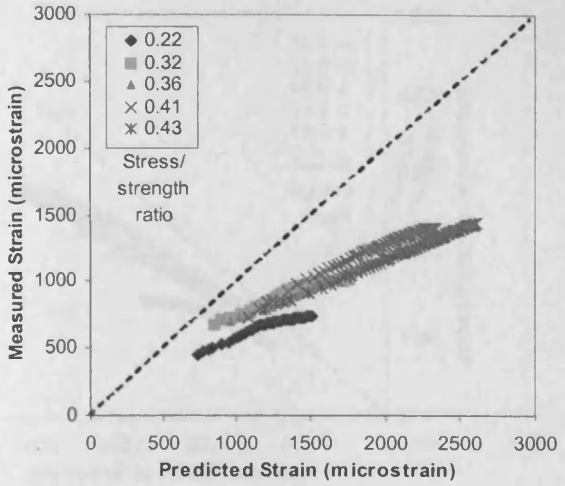

(a) Basic + drying creep

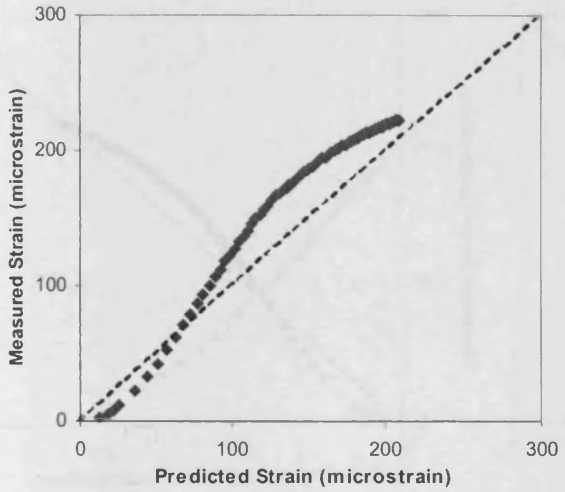

(b) Shrinkage

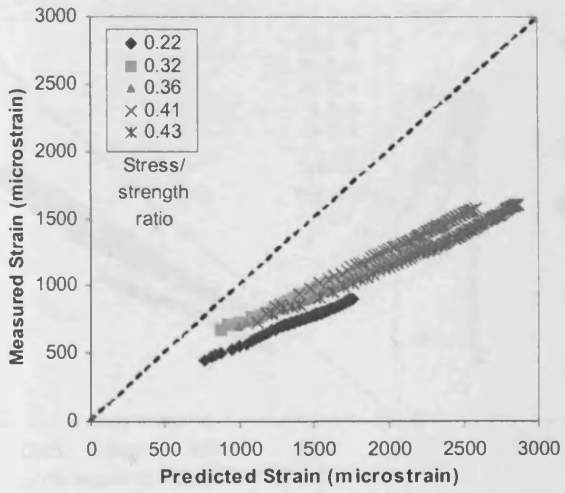

(c) Total strain

Figure D5.9. Comparison of measured and predicted strains for concrete of nominal strength 100 N/mm^2, using the BP-KX Model 1991.

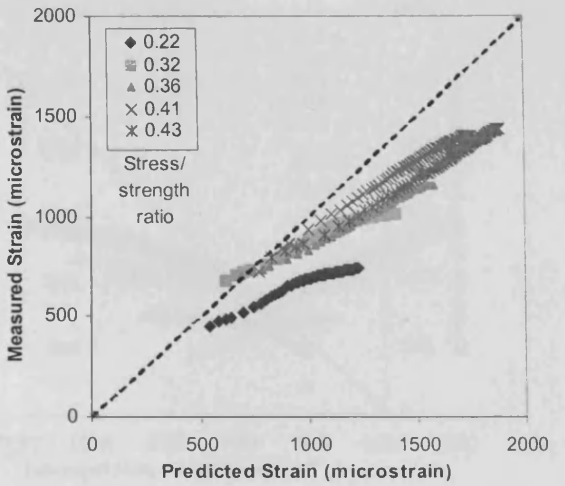

(a) Basic + drying creep

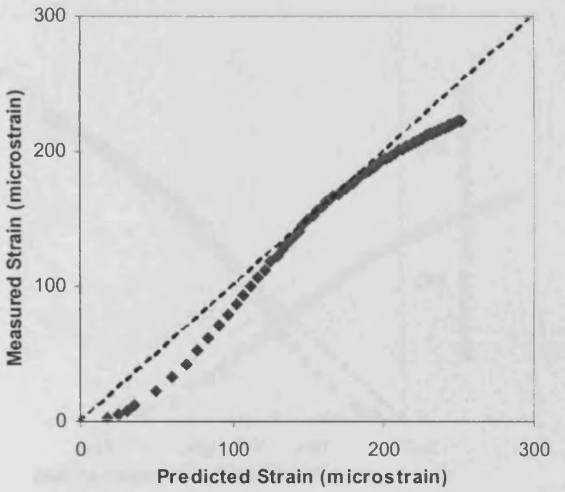

(b) Shrinkage

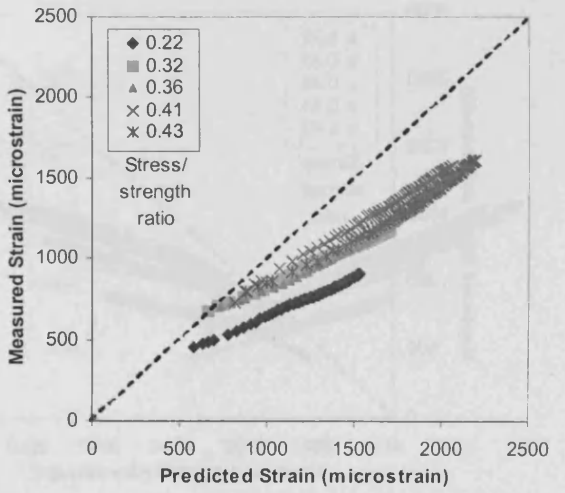

(c) Total strain

Figure D5.10. Comparison of measured and predicted strains for concrete of nominal strength 100 N/mm^2, using the short-form BP-KX Model 1993.

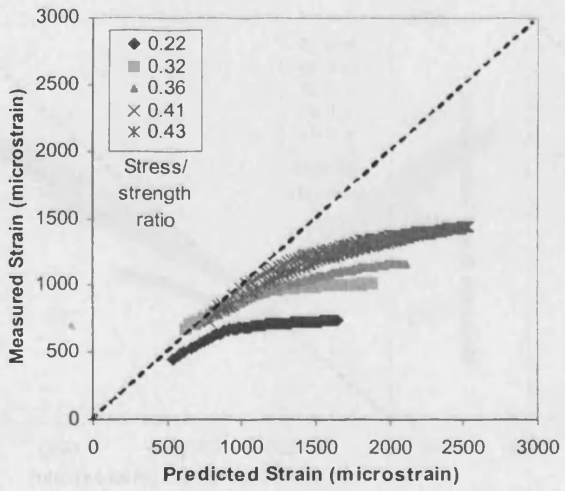

(a) Basic + drying creep

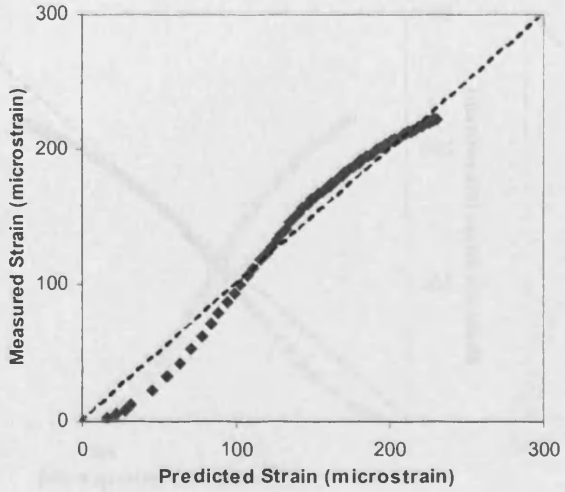

(b) Shrinkage

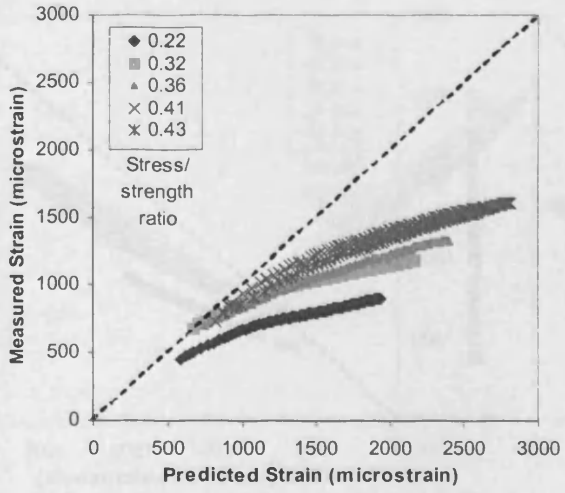

(c) Total strain

Figure D5.11. Comparison of measured and predicted strains for concrete of nominal strength 100 N/mm^2, using the B3 Model 1995.

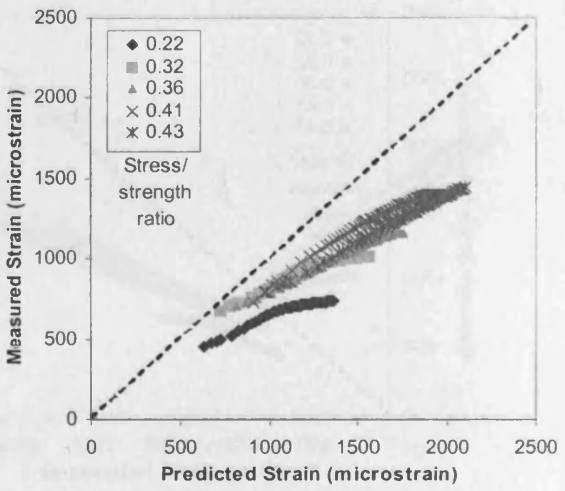

(a) Basic + drying creep

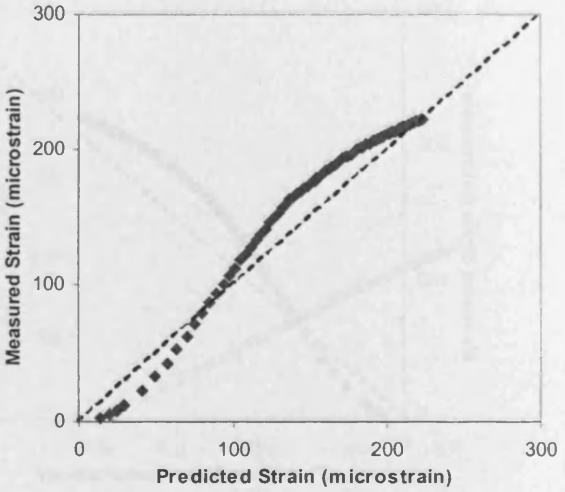

(b) Shrinkage

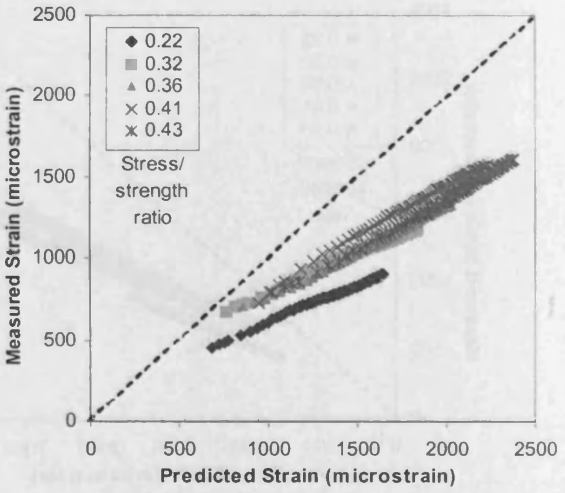

(c) Total strain

Figure D5.12. Comparison of measured and predicted strains for concrete of nominal strength 100 N/mm^2, using the short-form B3 Model 1996.

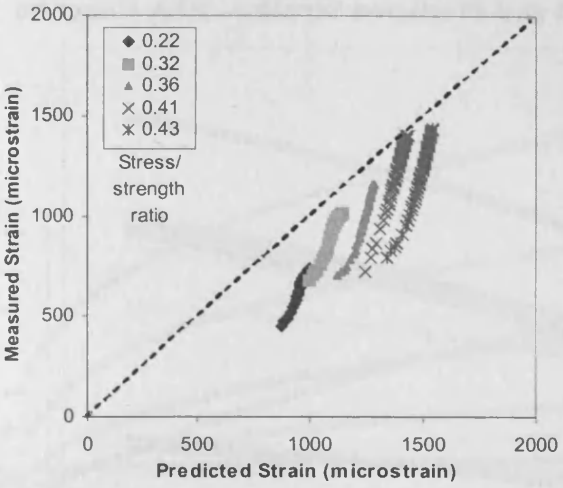

(a) Basic + drying creep

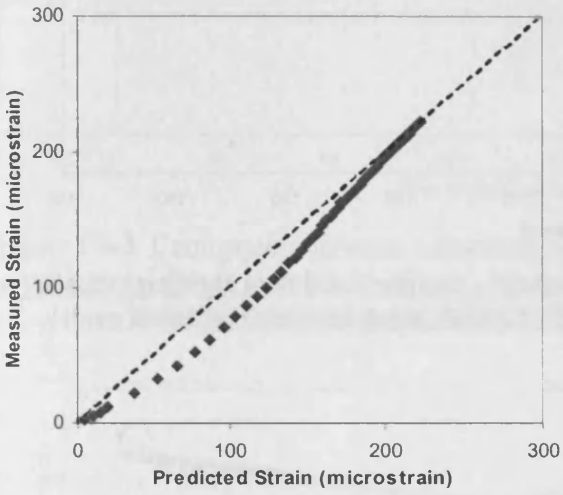

(b) Shrinkage

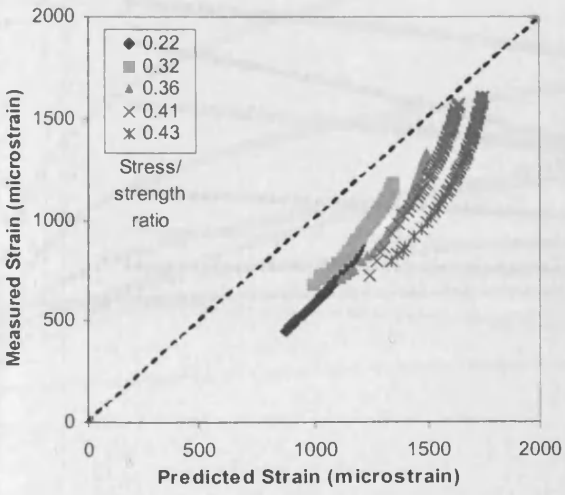

(c) Total strain

Figure D5.13. Comparison of measured and predicted strains for concrete of nominal strength 100 N/mm^2, using the GZ Model 1993.

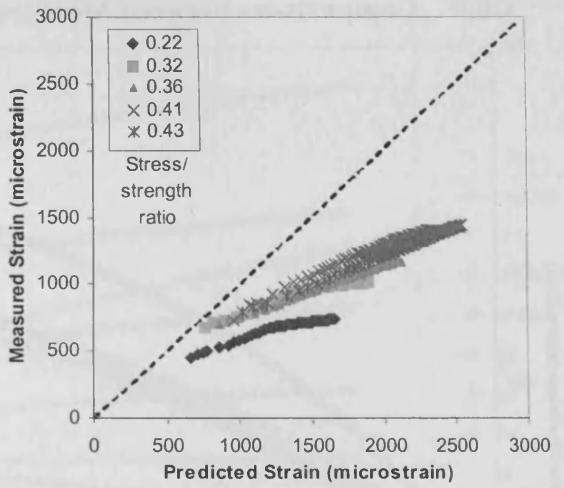

(a) Basic + drying creep

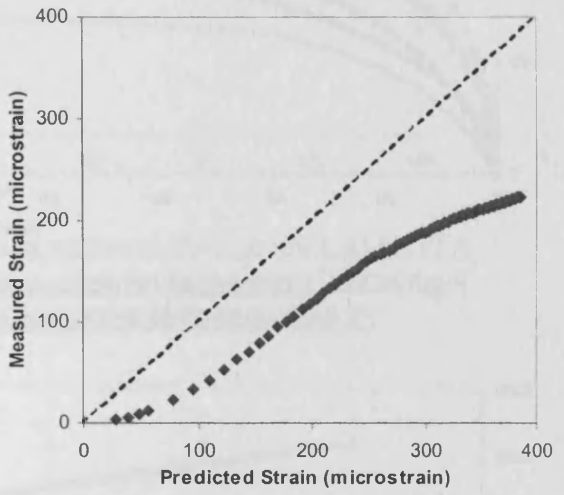

(b) Shrinkage

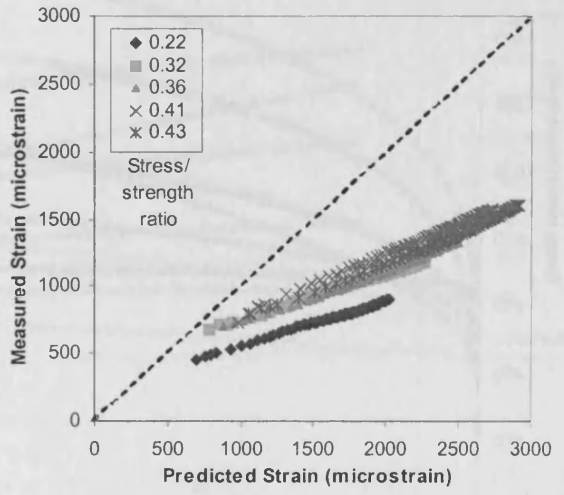

(c) Total strain

Figure D5.14. Comparison of measured and predicted strains for concrete of nominal strength 100 N/mm^2, using the GL Model 2001.

D6.0 Comparisons between Measured and Predicted Strains – PFA Concrete

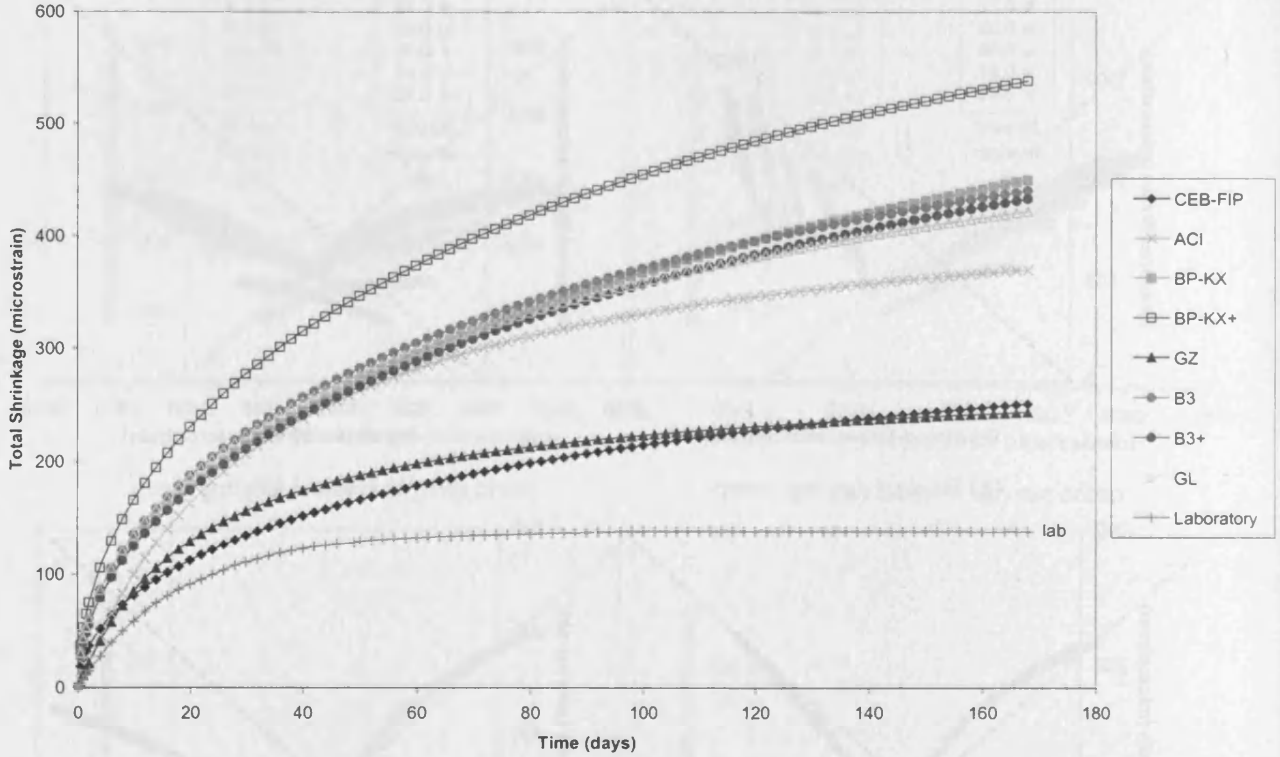

Figure D6.1. Comparison between experimental and predicted total shrinkage strains (με) for PFA concrete of design strength 65 N/mm^2, using selected prediction models.

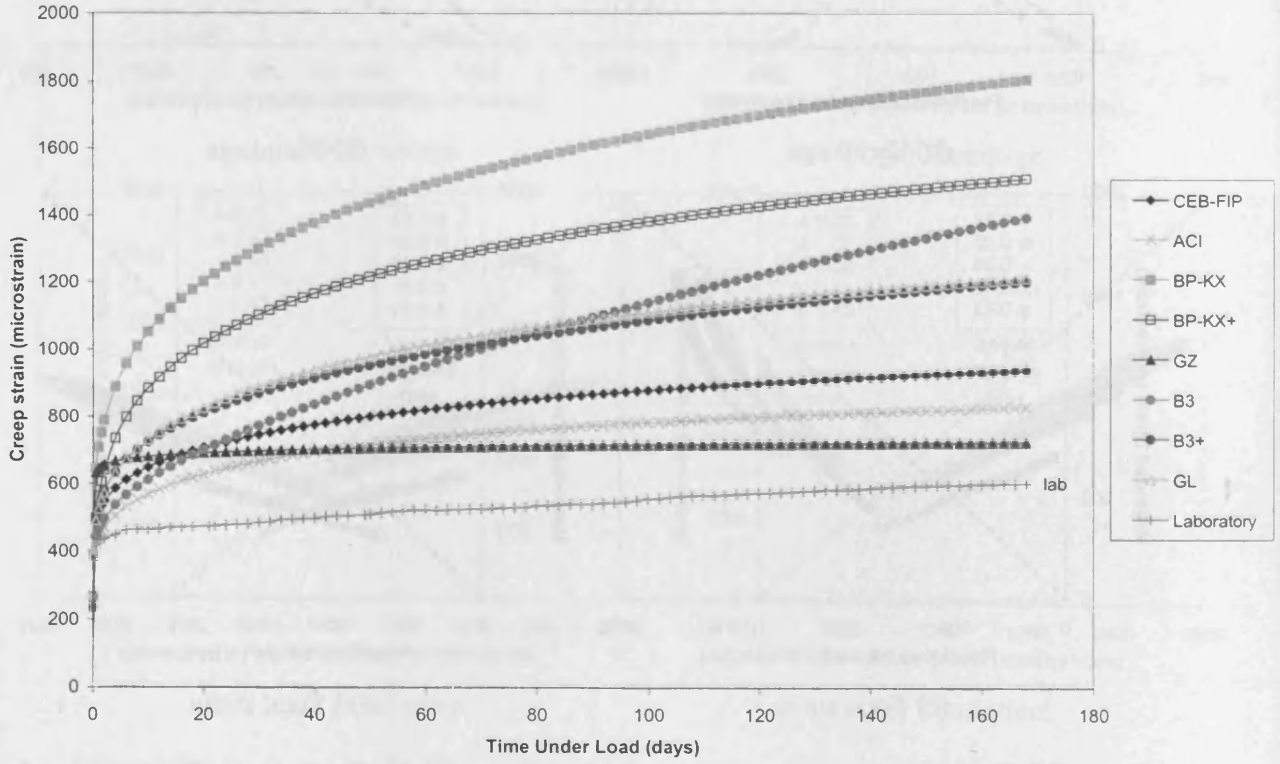

Figure D6.2. Comparison between experimental and predicted creep strains (με) for PFA concrete of design strength 65 N/mm^2, loaded to a stress/strength ratio of 0.23 of the compressive strength at loading, using selected prediction models.

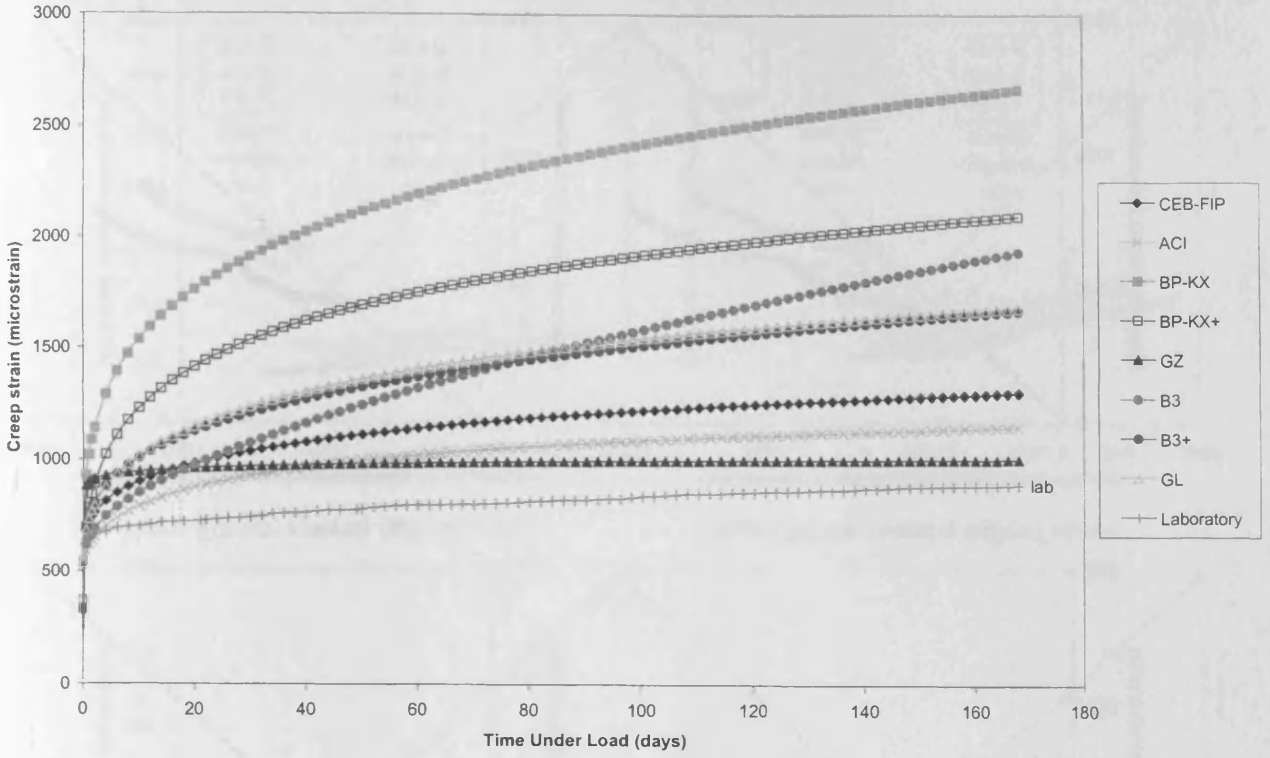

Figure D6.3. Comparison between experimental and predicted creep strains (με) for PFA concrete of design strength 65 N/mm^2, loaded to a stress/strength ratio of 0.32 of the compressive strength at loading, using selected prediction models.

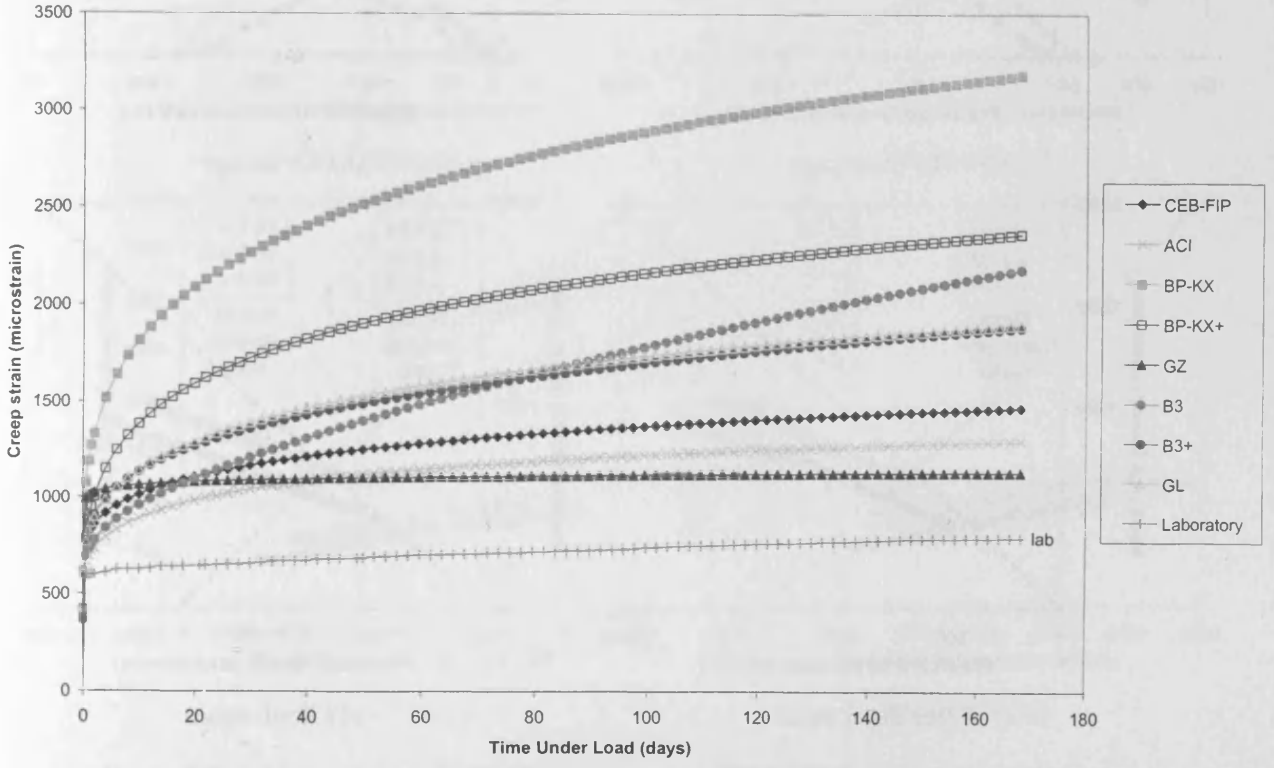

Figure D6.4. Comparison between experimental and predicted creep strains (με) for PFA concrete of design strength 65 N/mm^2, loaded to a stress/strength ratio of 0.36 of the compressive strength at loading, using selected prediction models.

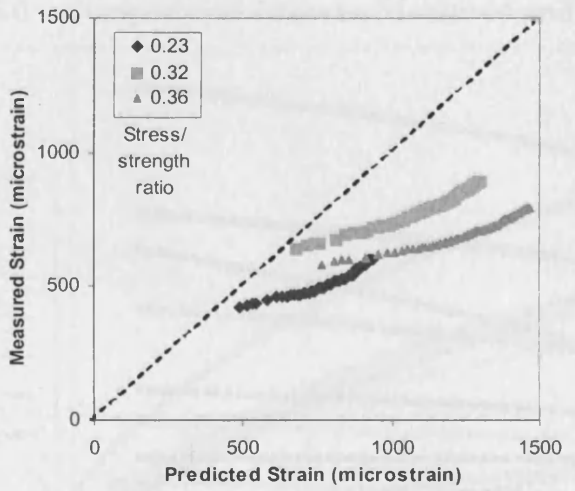

(a) Basic + drying creep

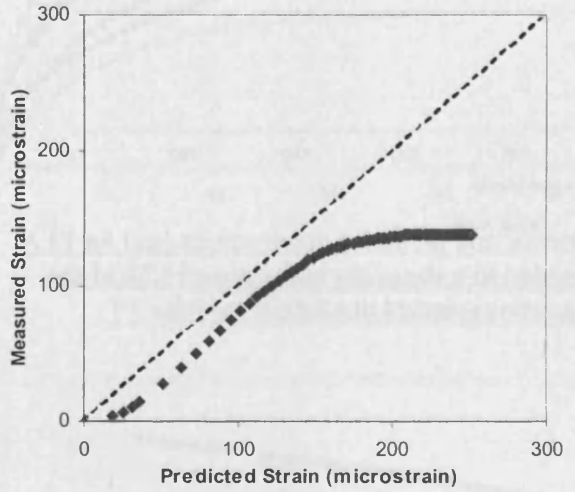

(b) Shrinkage

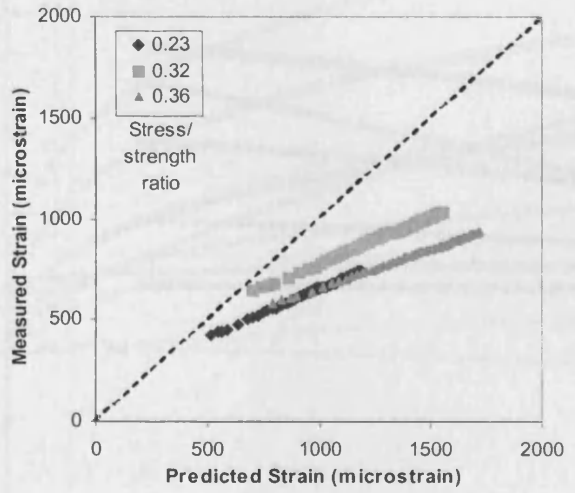

(c) Total strain

Figure D6.5. Comparison of measured and predicted strains for PFA concrete of nominal strength 65 N/mm^2, using the CEB-FIP Model Code 1990.

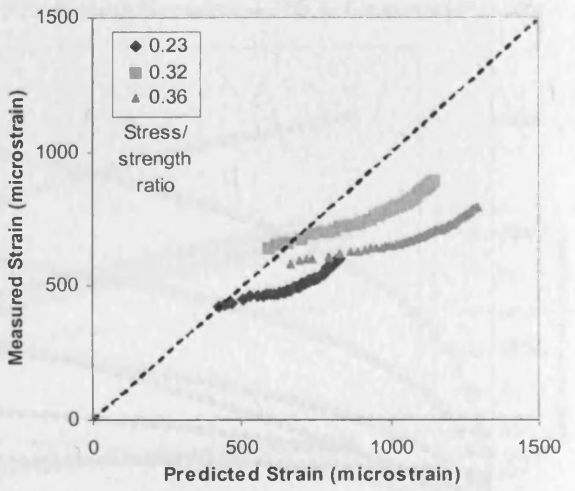

(a) Basic + drying creep

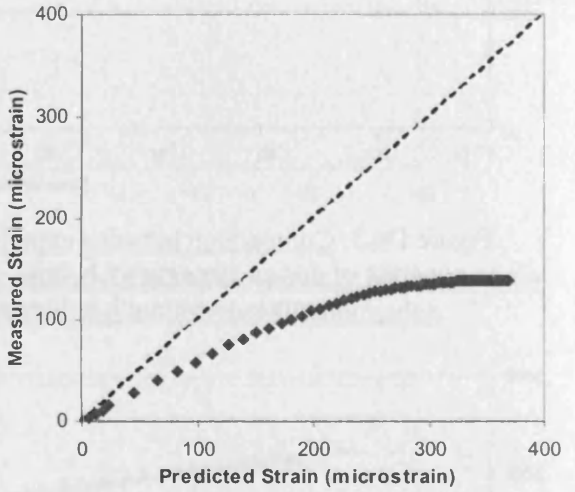

(b) Shrinkage

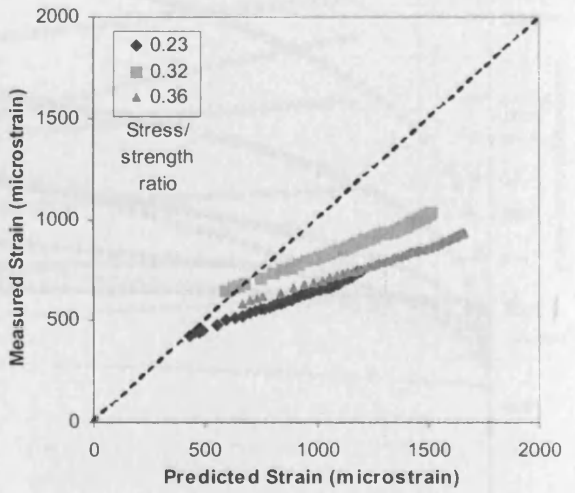

(c) Total strain

Figure D6.6. Comparison of measured and predicted strains for PFA concrete of nominal strength 65 N/mm^2, using the ACI Model 1992.

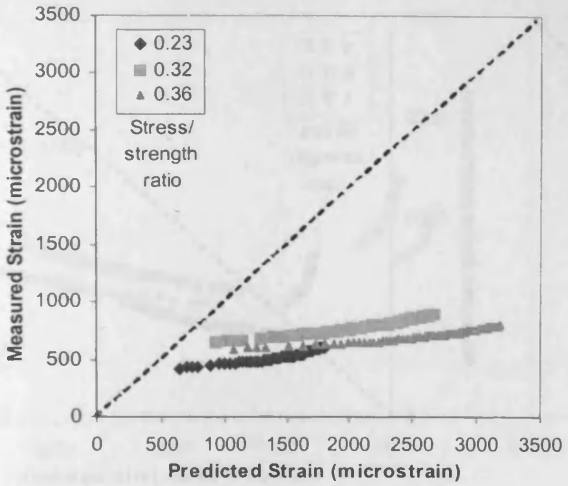

(a) Basic + drying creep

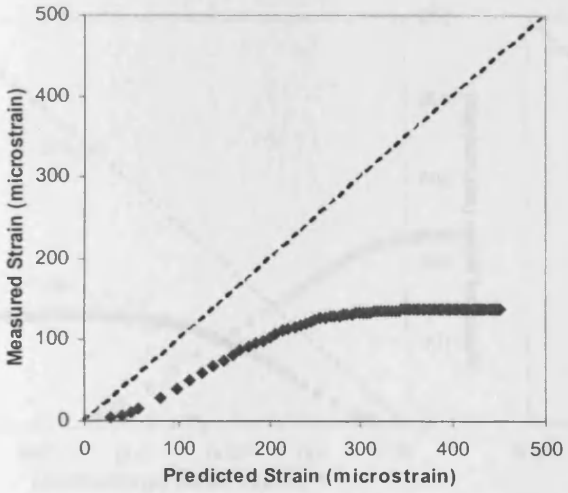

(b) Shrinkage

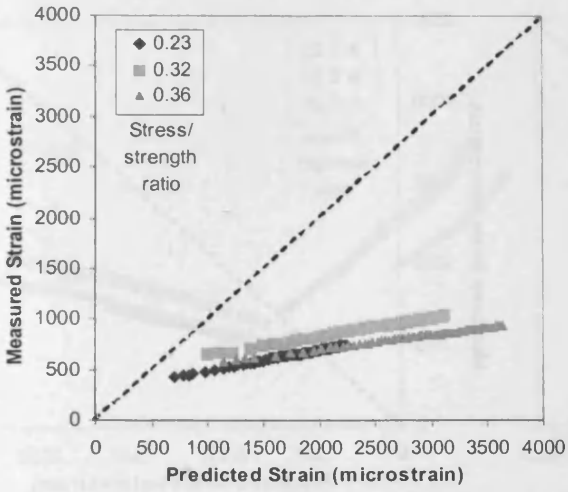

(c) Total strain

Figure D6.7. Comparison of measured and predicted strains for PFA concrete of nominal strength 65 N/mm^2, using the BP-KX Model 1991.

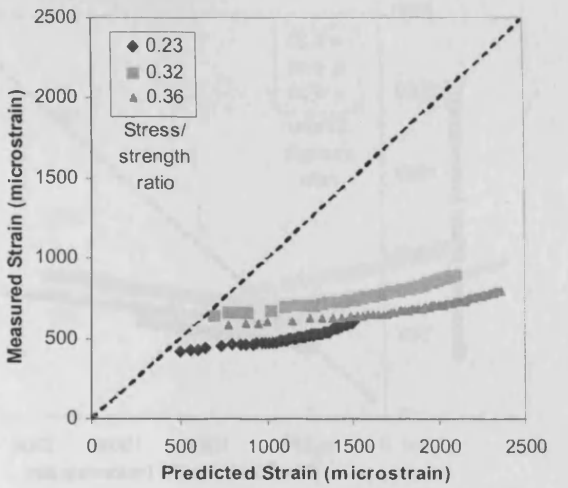

(a) Basic + drying creep

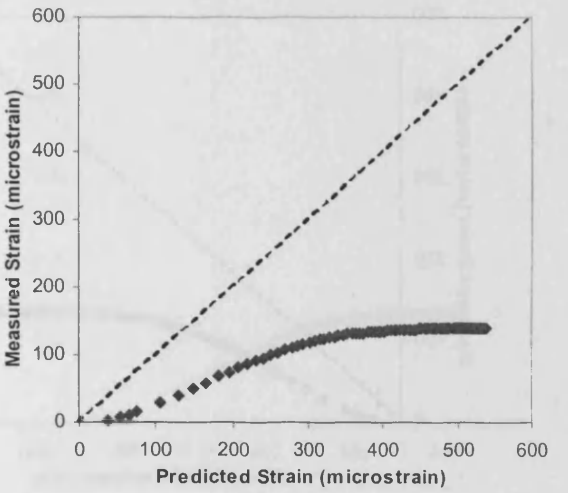

(b) Shrinkage

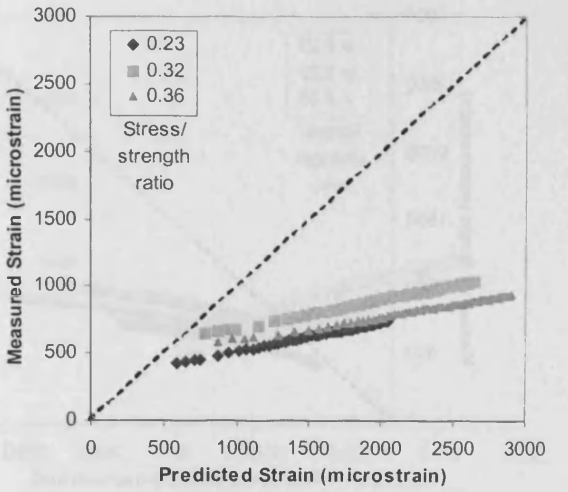

(c) Total strain

Figure D6.8. Comparison of measured and predicted strains for PFA concrete of nominal strength 65 N/mm^2, using the short-form BP-KX Model 1993.

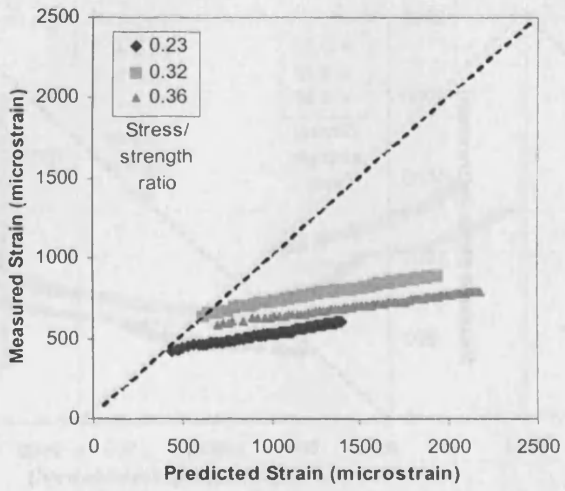

(a) Basic + drying creep

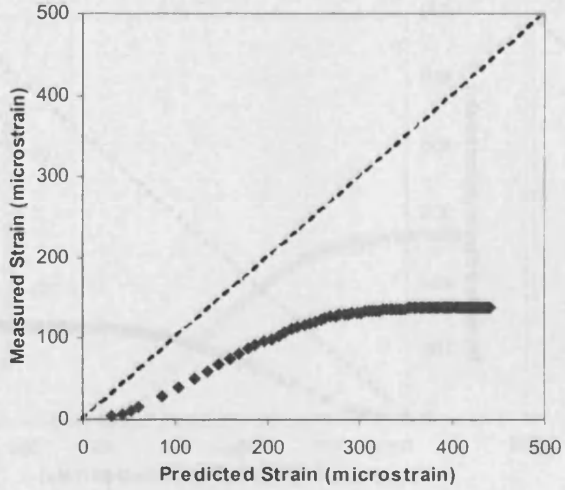

(b) Shrinkage

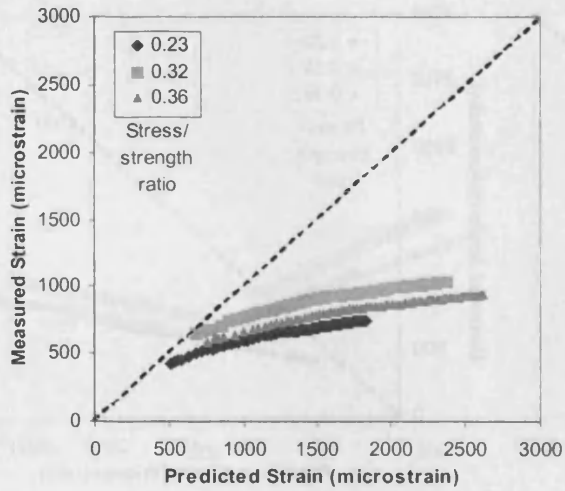

(c) Total strain

Figure D6.9. Comparison of measured and predicted strains for PFA concrete of nominal strength 65 N/mm^2, using the B3 Model 1995.

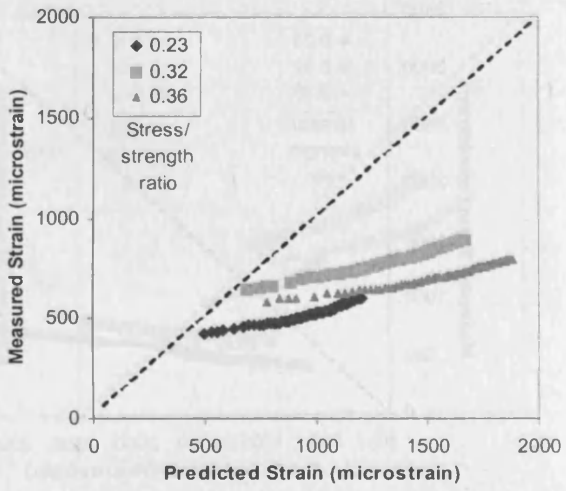

(a) Basic + drying creep

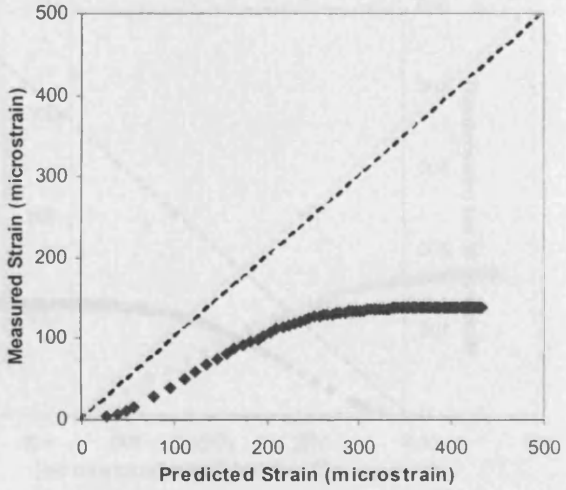

(b) Shrinkage

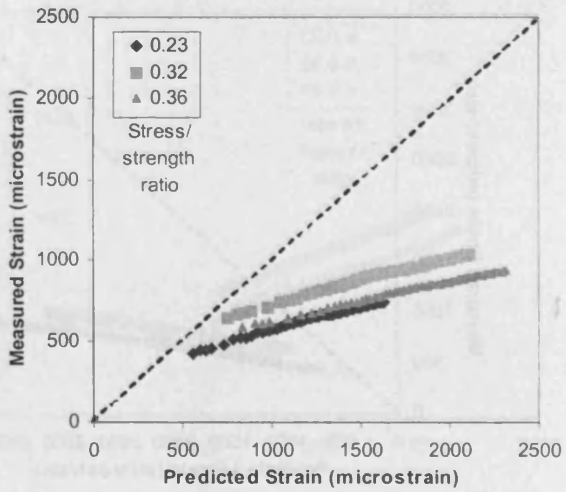

(c) Total strain

Figure D6.10. Comparison of measured and predicted strains for PFA concrete of nominal strength 65 N/mm^2, using the short-form B3 Model 1996.

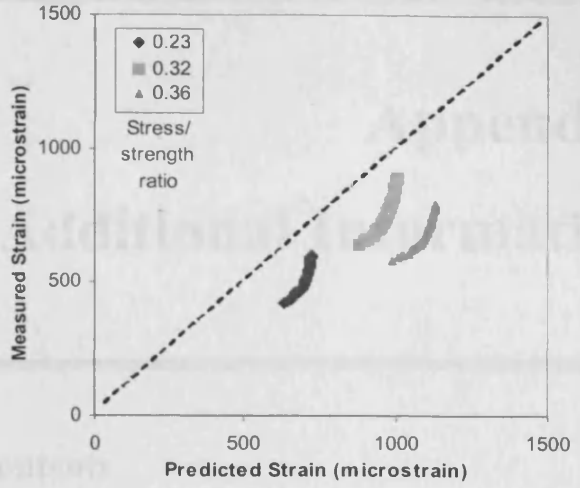

(a) Basic + drying creep

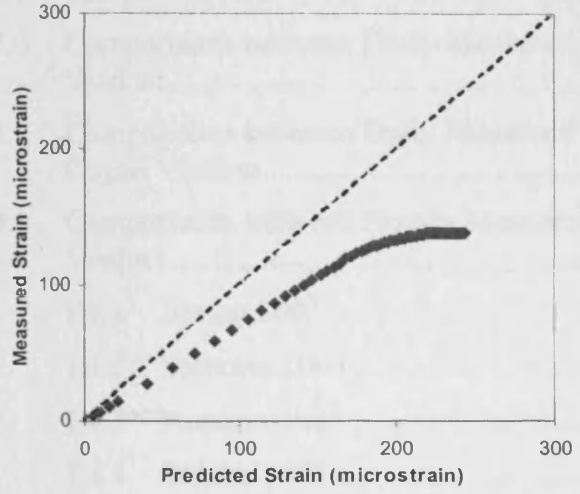

(b) Shrinkage

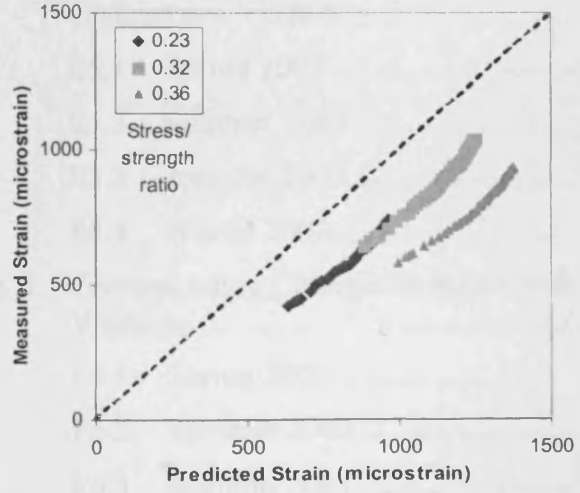

(c) Total strain

Figure D6.11. Comparison of measured and predicted strains for PFA concrete of nominal strength 65 N/mm^2, using the GZ Model 1993.

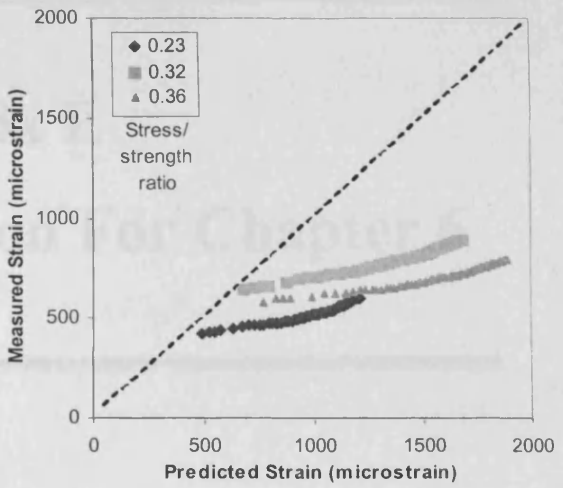

(a) Basic + drying creep

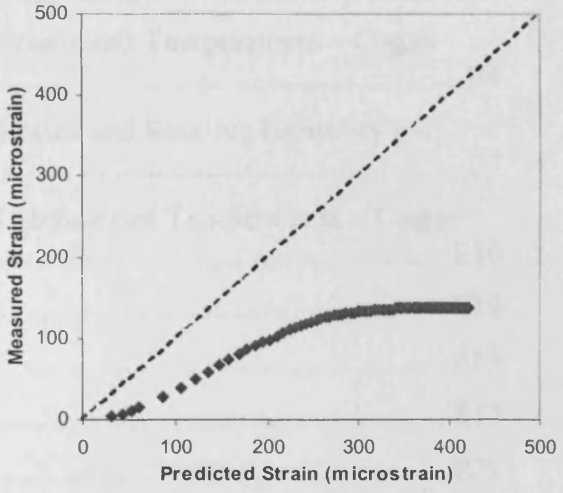

(b) Shrinkage

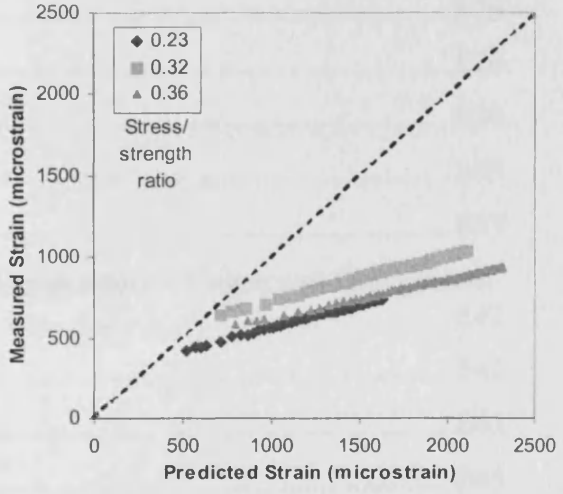

(c) Total strain

Figure D6.12. Comparison of measured and predicted strains for PFA concrete of nominal strength 65 N/mm^2, using the GL Model 2001.

Appendix E

Additional Information For Chapter 6

Contents

E1.0 Temperature Study for Vibrating Wire Strain Gauges

Type used – Type T/E/S – length of vibrating wire = 140 mm.

Assumptions:

1. Coefficient of temperature sensitivity is roughly the same for the wire and for the material making up the body of the gauge.

2. By heating or cooling of the gauge the stress in the wire doesn't change.

3. The length of the wire is different after temperature change due to the temperature extension/contraction of the gauge.

Example showing the temperature sensitivity on measured values of strains.

Gauge parameters[1]:

Basic temperature = 20 °C

Initial length of wire = 140 mm

Initial frequency = 800 Hz

The frequency f, of the wire can be calculated from the following formula[2]:

$$f = \frac{1}{2l}\frac{\sigma g}{\rho}^{0.5} \qquad [1]$$

where:

l = vibrating wire length,
σ = tension in the wire,
g = acceleration due to gravity,
ρ = density of the wire.

From the above assumptions, it can be noted that σ, g and ρ are constant values. Thus the frequency is dependent only upon l.

Assuming a drop in temperature of 10 °C:

Original length, l_0 = 140 mm (T = 20 °C)

Temperature coefficient[1], $\alpha = 11 \times 10^{-6}$ per °C.

Actual temperature, $\Delta T = 20 - 10 = 10$ °C.

Actual length of the wire, $l = l_0 \alpha \Delta T + l_0$
$= [140 \times 11 \times 10^{-6} \times (10)] + 140$
$= 140.0154$ mm

Ratio of frequencies due to temperature change (from [1]):

$$f_2 / f_1 = 140 / 140.0154 = 0.99989$$

Originally the frequency was 800 Hz[1].

Actual frequency = 800 × 0.99989 = 799.912 Hz.

Gauge equation[2] is given by:

$$\delta_s = k(f_1^2 - f_2^2)$$

where:

δ_s = change in strain,
k = the gauge factor[1] = 3.025×10^{-3},
f_i = frequency in Hz.

In this case:

$$\delta_s = 3.025 \times 10^{-3} (800^2 - 799.912^2) = 0.426\ \mu\epsilon$$

Assuming a larger basic frequency of 1200 Hz:

$$f_2 = 0.99989 \times 1200 = 1199.868\ \text{Hz}$$

$$\delta_s = 3.025 \times 10^{-3} (1200^2 - 1199.868^2) = 0.958\ \mu\epsilon$$

References:

[1] Gage Technique Ltd., Technical specifications for T/E/S gauges. Structural Instrumentation Engineers, Trowbridge, England.

[2] Gage Technique Ltd., Acoustic vibrating wire gauge – Data conversion tables. Structural Instrumentation Engineers, Trowbridge, England.

E2.0 Comparisons between Daily Measured Strains and Temperatures – Cogan Viaduct

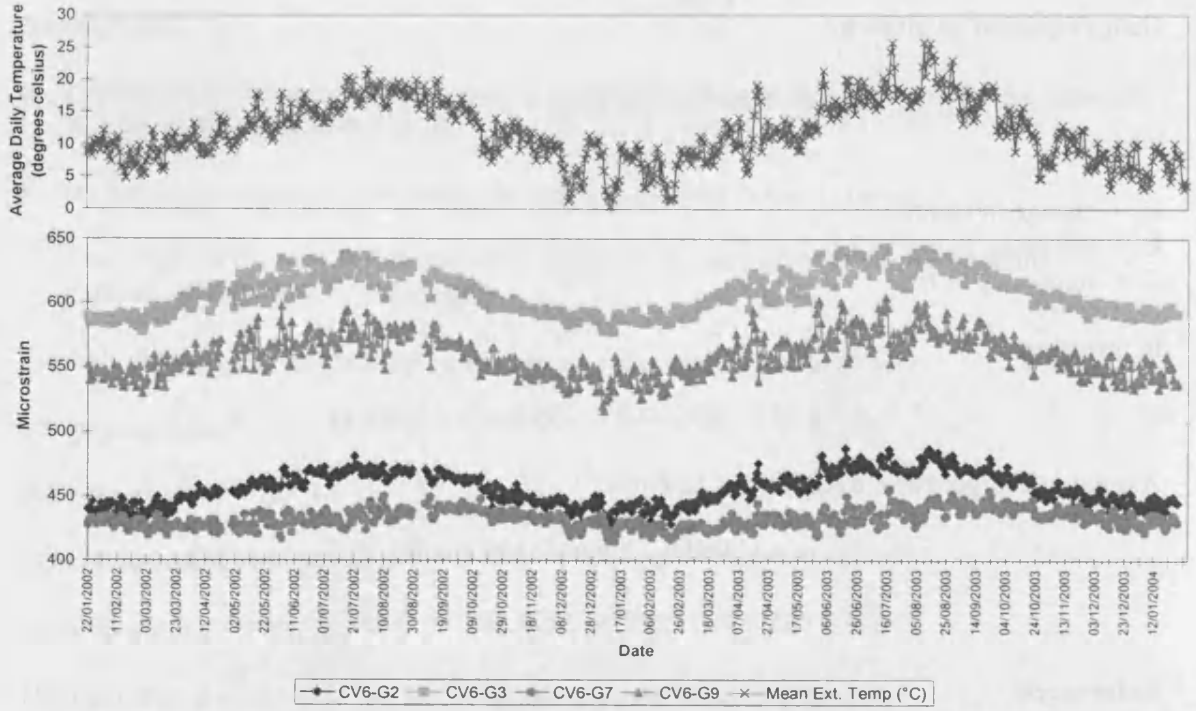

Figure E2.1. Comparison between daily measured strains (με) and daily average temperature (°C) in the top flange of segment 6, Cogan Viaduct.

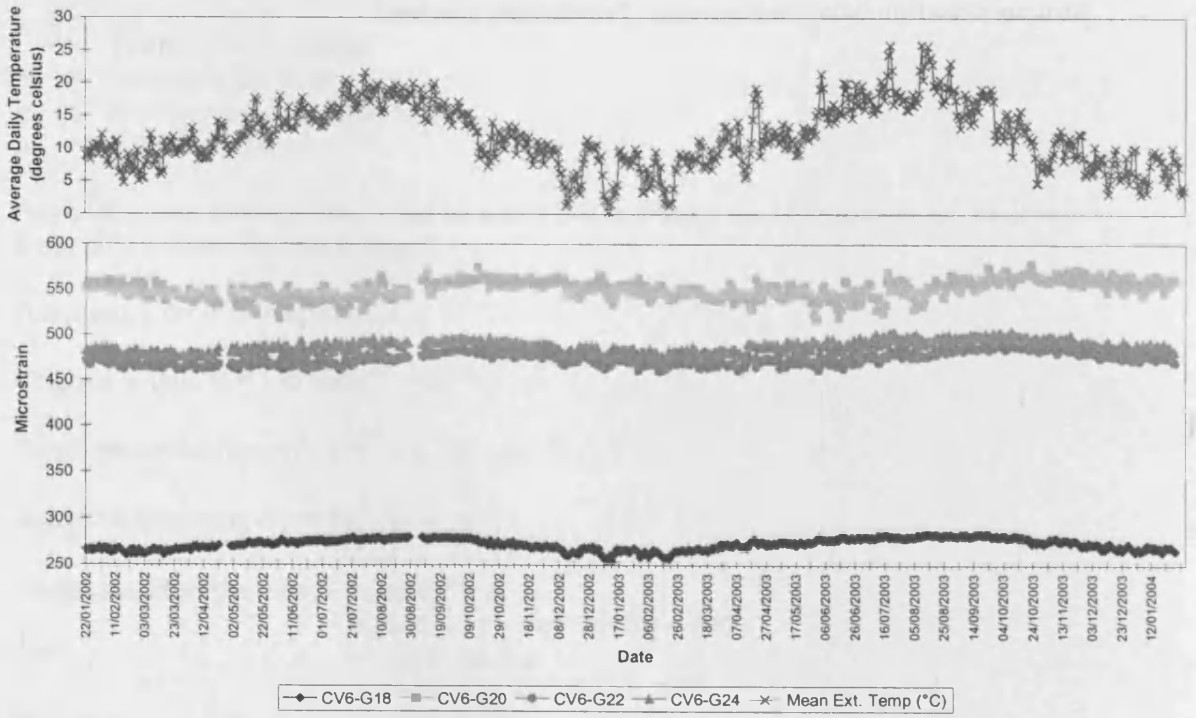

Figure E2.2. Comparison between daily measured strains (με) and daily average temperature (°C) in the bottom flange of segment 6, Cogan Viaduct.

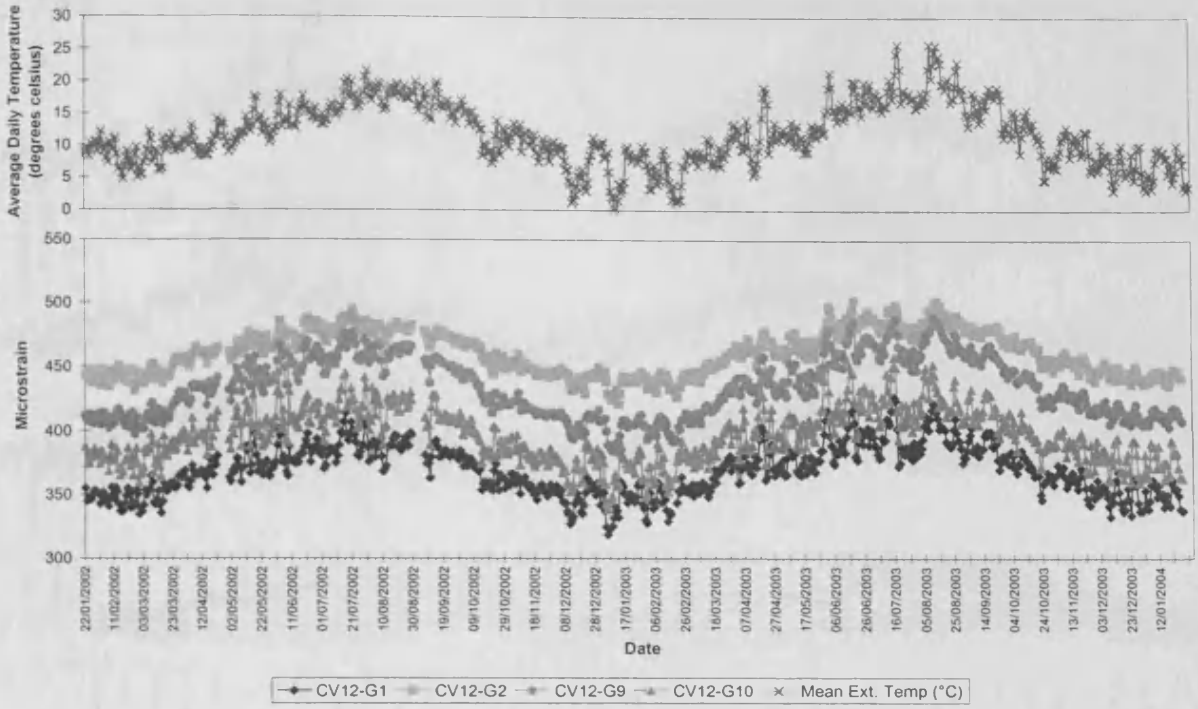

Figure E2.3. Comparison between daily measured strains (με) and daily average temperature (°C) in the top flange of segment 12, Cogan Viaduct.

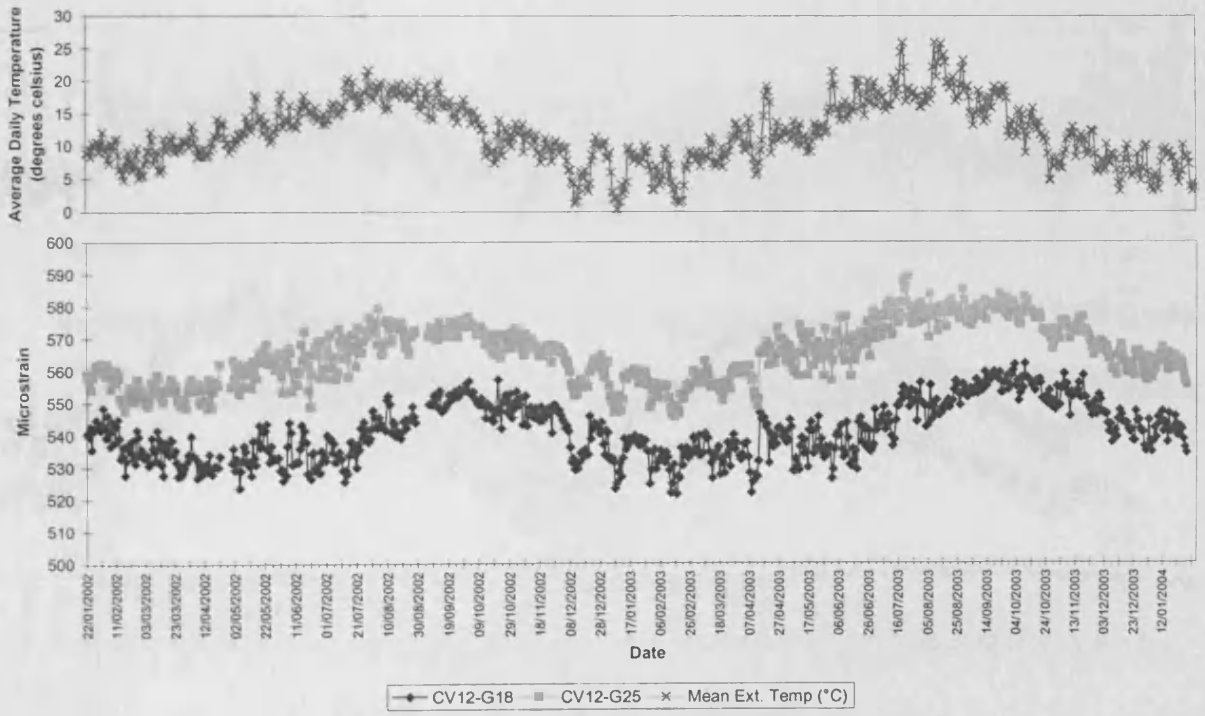

Figure E2.4. Comparison between daily measured strains (με) and daily average temperature (°C) in the bottom flange of segment 12, Cogan Viaduct.

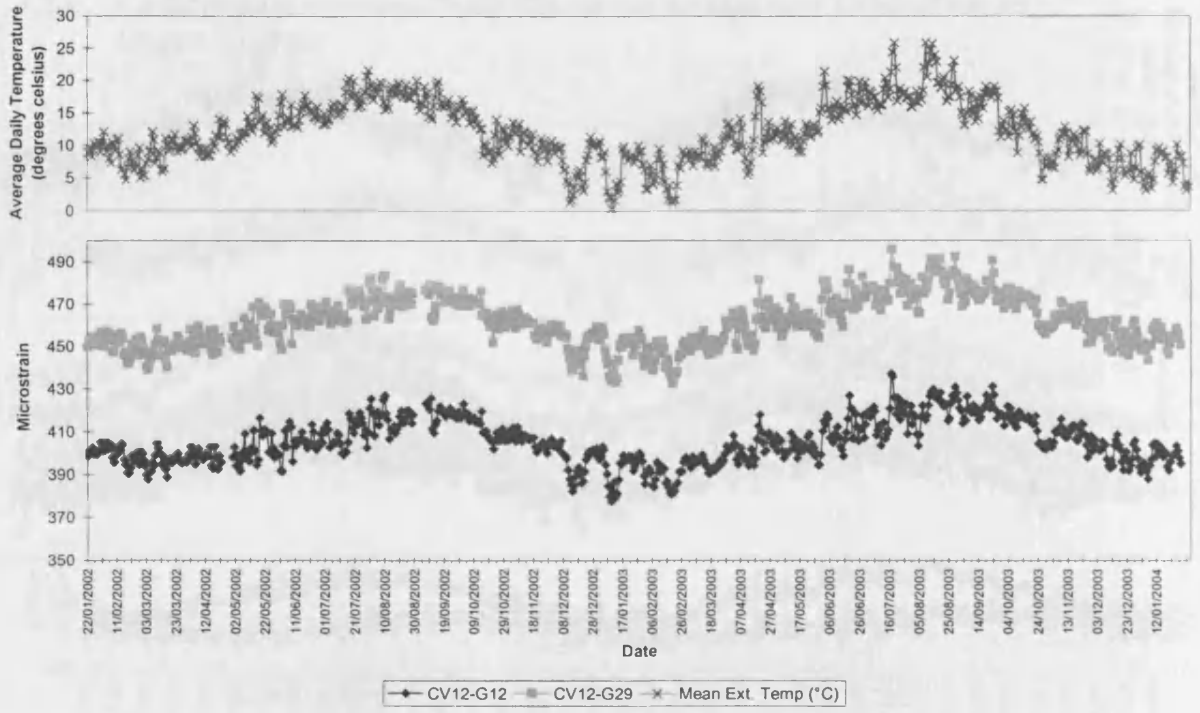

Figure E2.5. Comparison between daily measured longitudinal strains (με) and daily average temperature (°C) in the webs of segment 12, Cogan Viaduct.

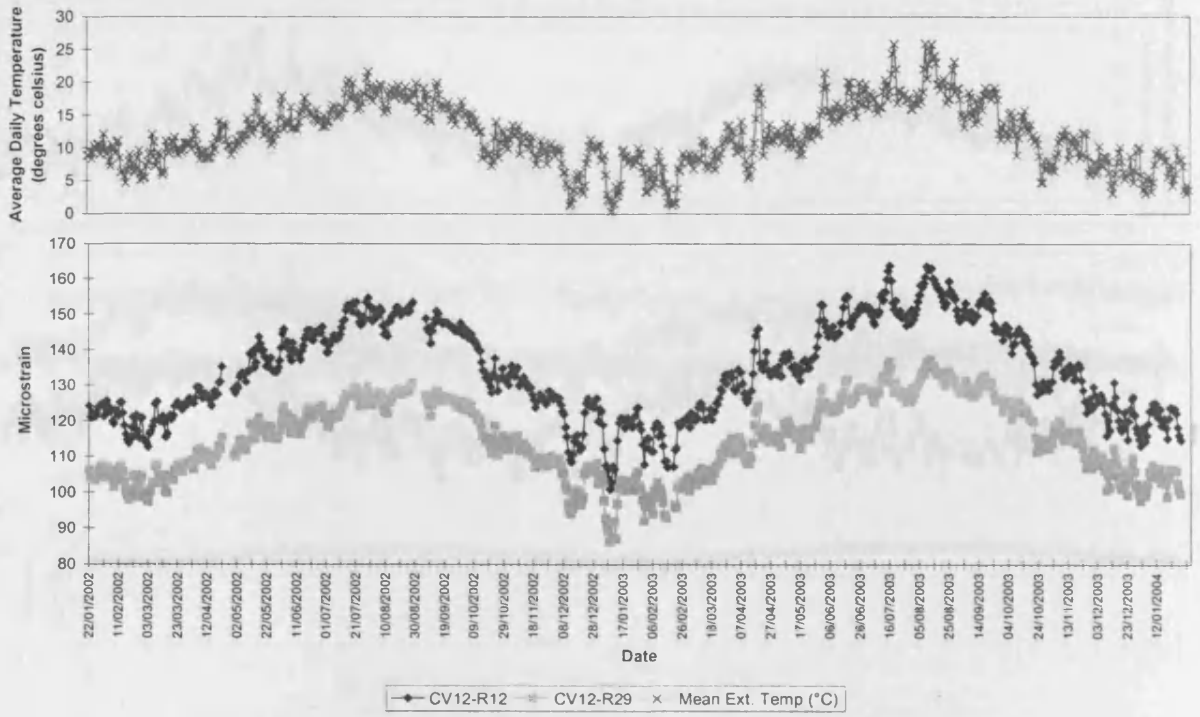

Figure E2.6. Comparison between daily measured transverse strains (με) and daily average temperature (°C) in the webs of segment 12, Cogan Viaduct.

E3.0 Comparisons between Daily Measured Strains and Relative Humidity's – Cogan Viaduct

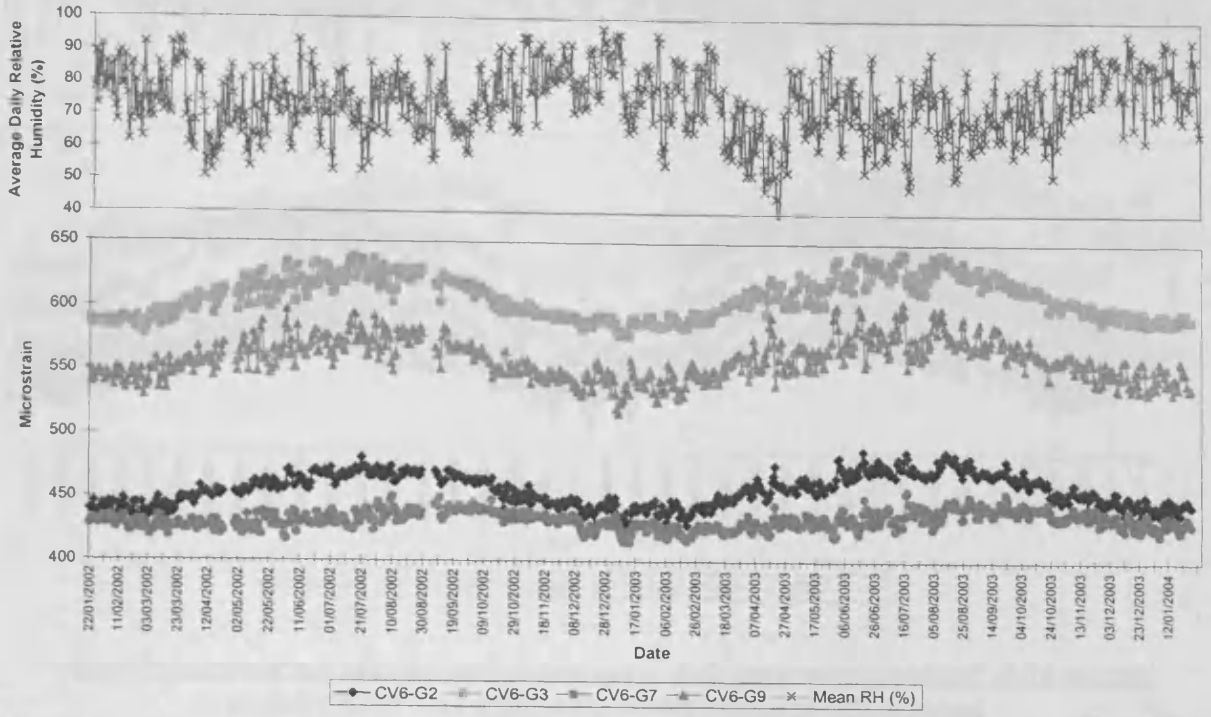

Figure E3.1. Comparison between daily measured strains (με) and daily average relative humidity (%) in the top flange of segment 6, Cogan Viaduct.

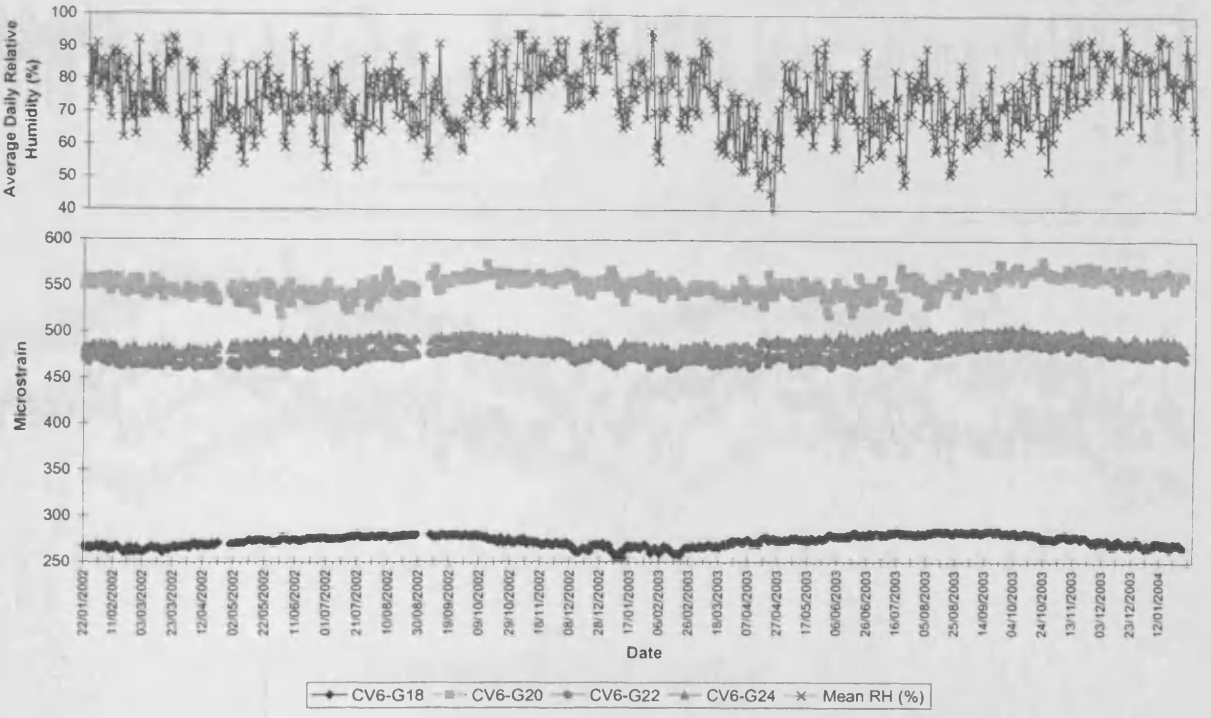

Figure E3.2. Comparison between daily measured strains (με) and daily average relative humidity (%) in the bottom flange of segment 6, Cogan Viaduct.

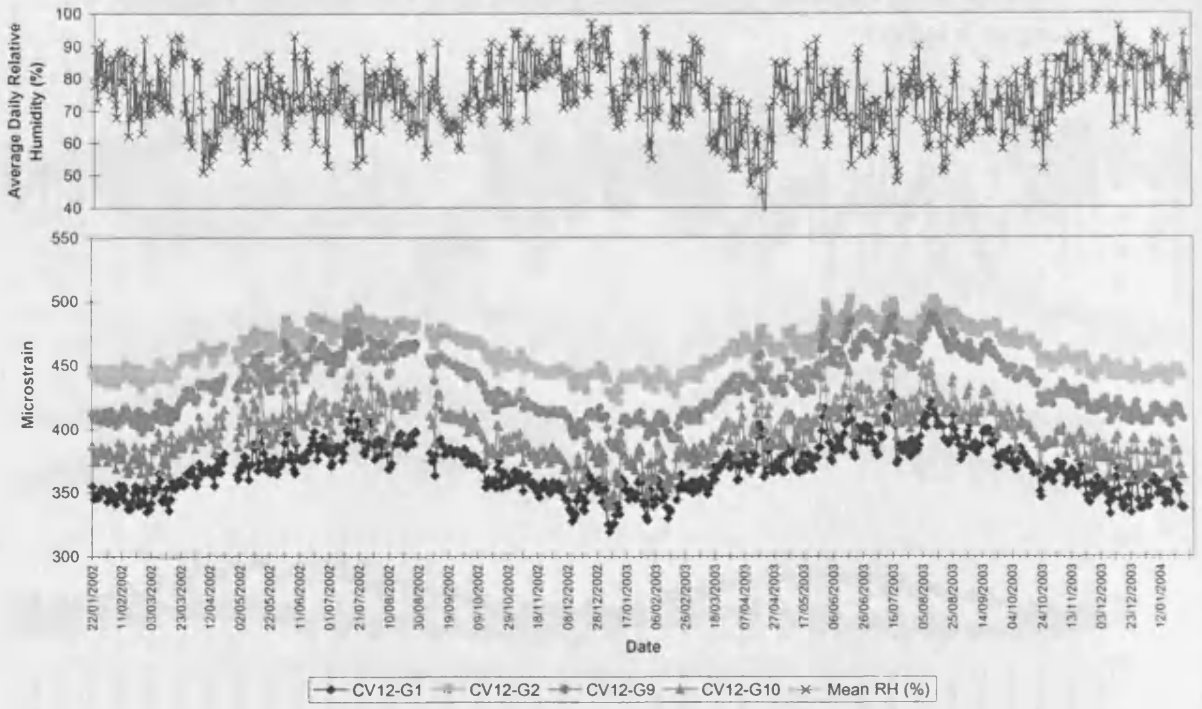

Figure E3.3. Comparison between daily measured strains (με) and daily average relative humidity (%) in the top flange of segment 12, Cogan Viaduct.

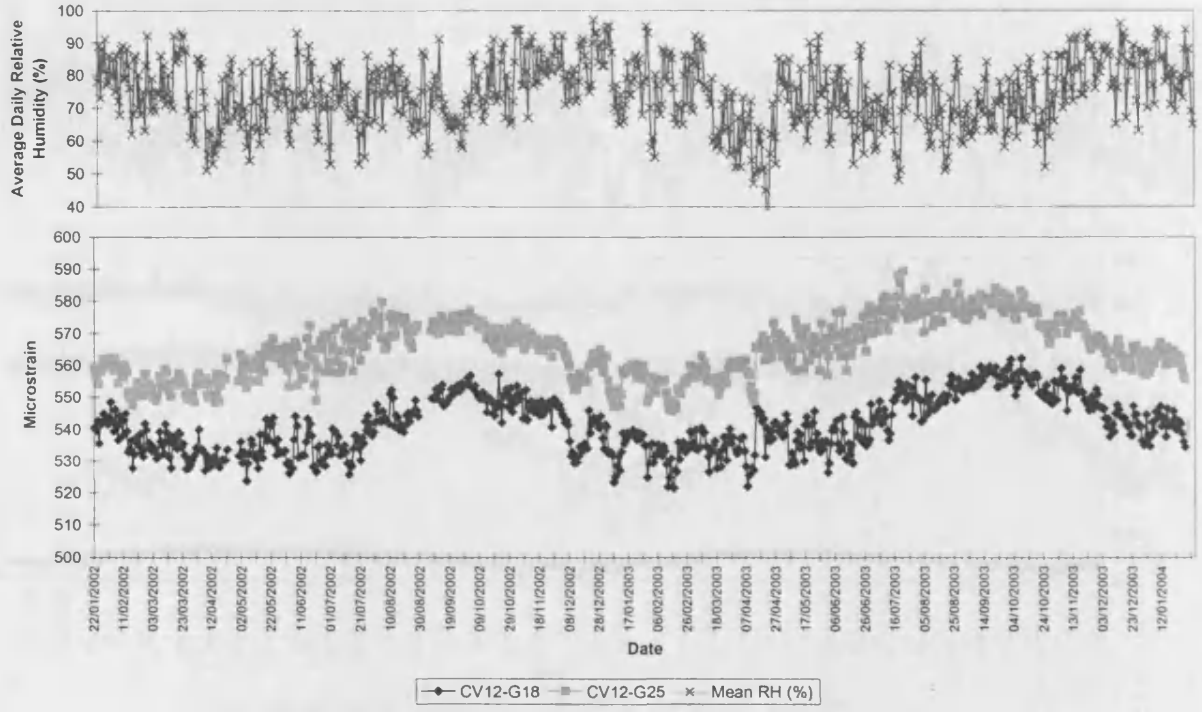

Figure E3.4. Comparison between daily measured strains (με) and daily average relative humidity (%) in the bottom flange of segment 12, Cogan Viaduct.

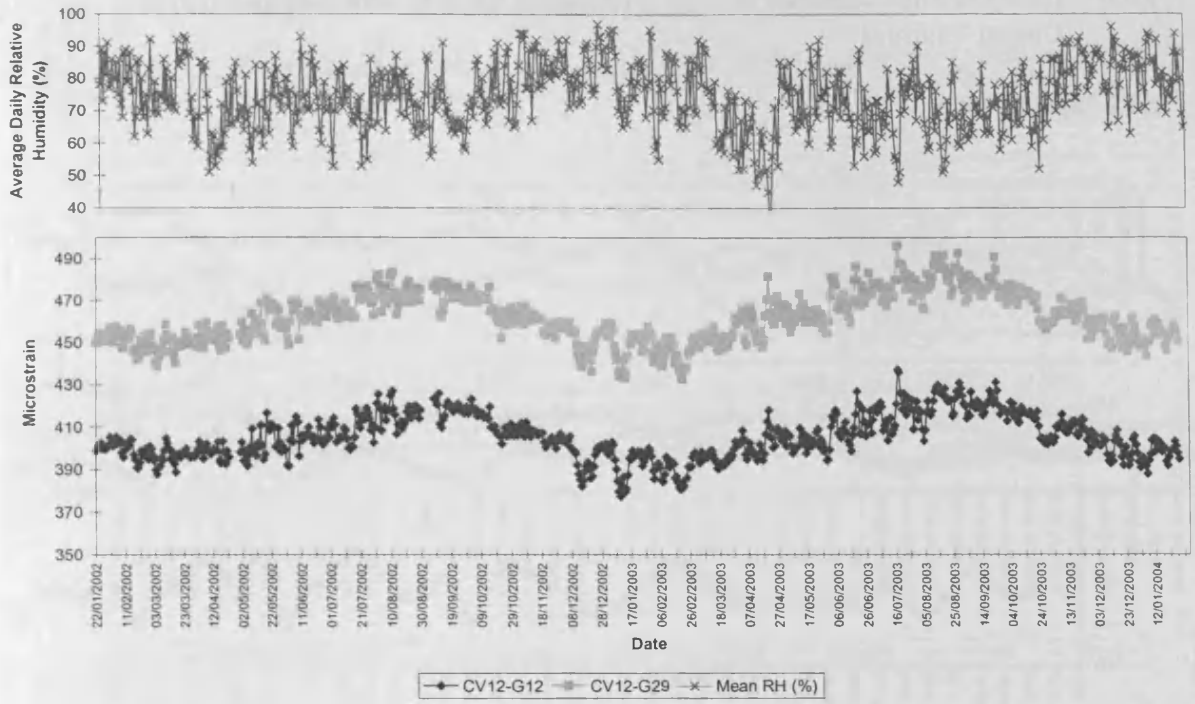

Figure E3.5. Comparison between daily measured longitudinal strains (με) and daily average relative humidity (%) in the webs of segment 12, Cogan Viaduct.

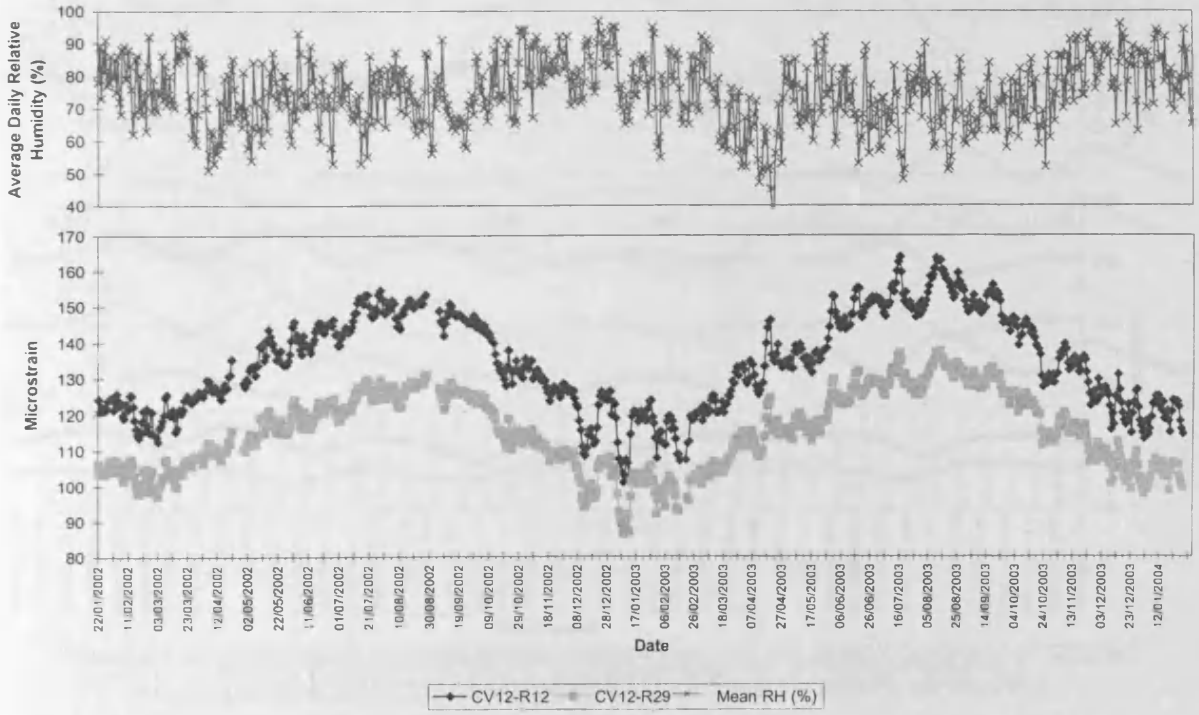

Figure E3.6. Comparison between daily measured transverse strains (με) and daily average relative humidity (%) in the webs of segment 12, Cogan Viaduct.

E4.0 Comparisons between Hourly Measured Strains and Temperatures – Cogan Viaduct

E4.1 Spring 2003

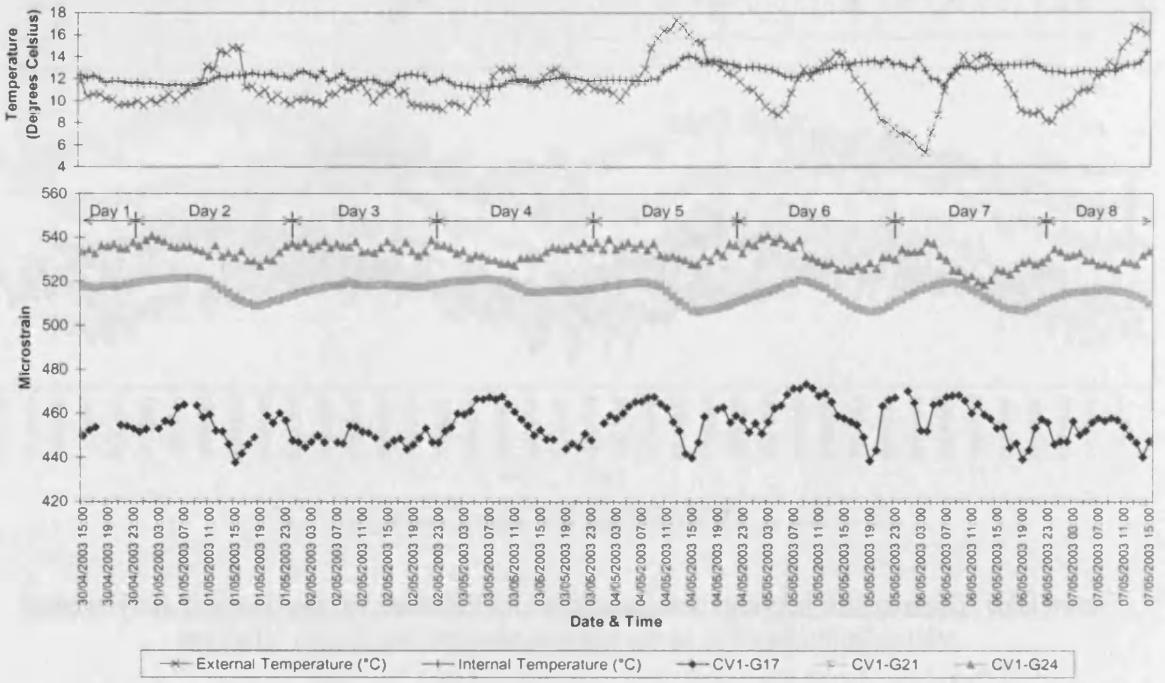

Figure E4.1. Comparison between hourly measured strains and hourly external and internal air temperature in the bottom flange of segment 1, Cogan Viaduct, Spring 2003.

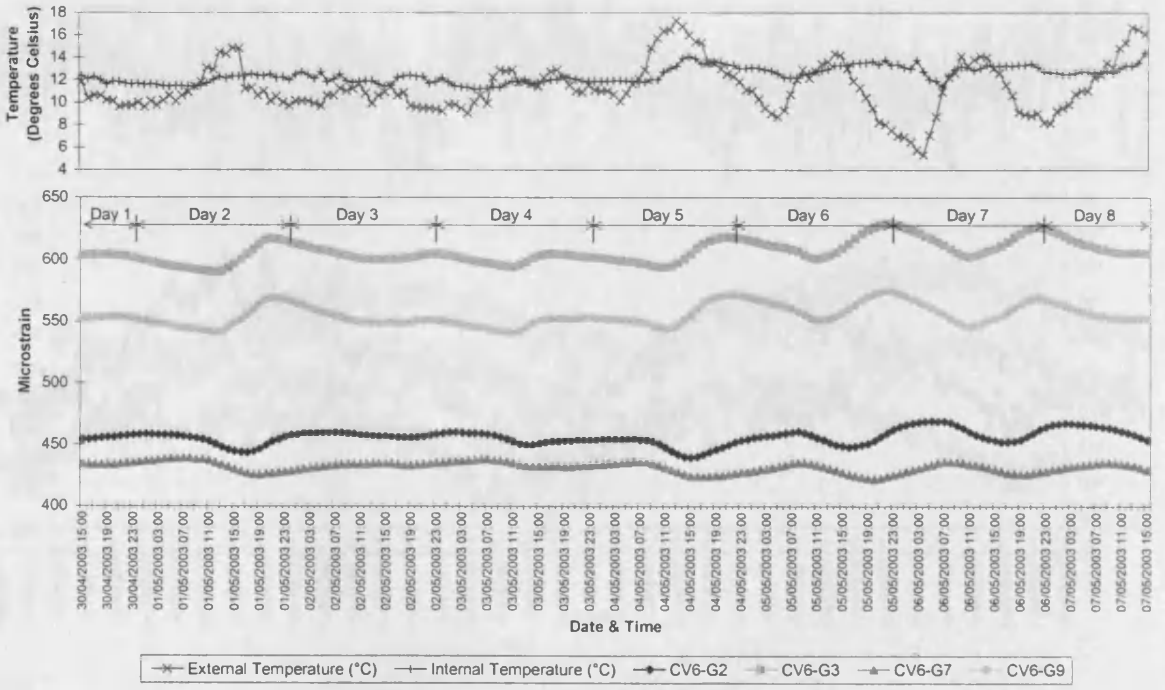

Figure E4.2. Comparison between hourly measured strains and hourly external and internal air temperature in the top flange of segment 6, Cogan Viaduct, Spring 2003.

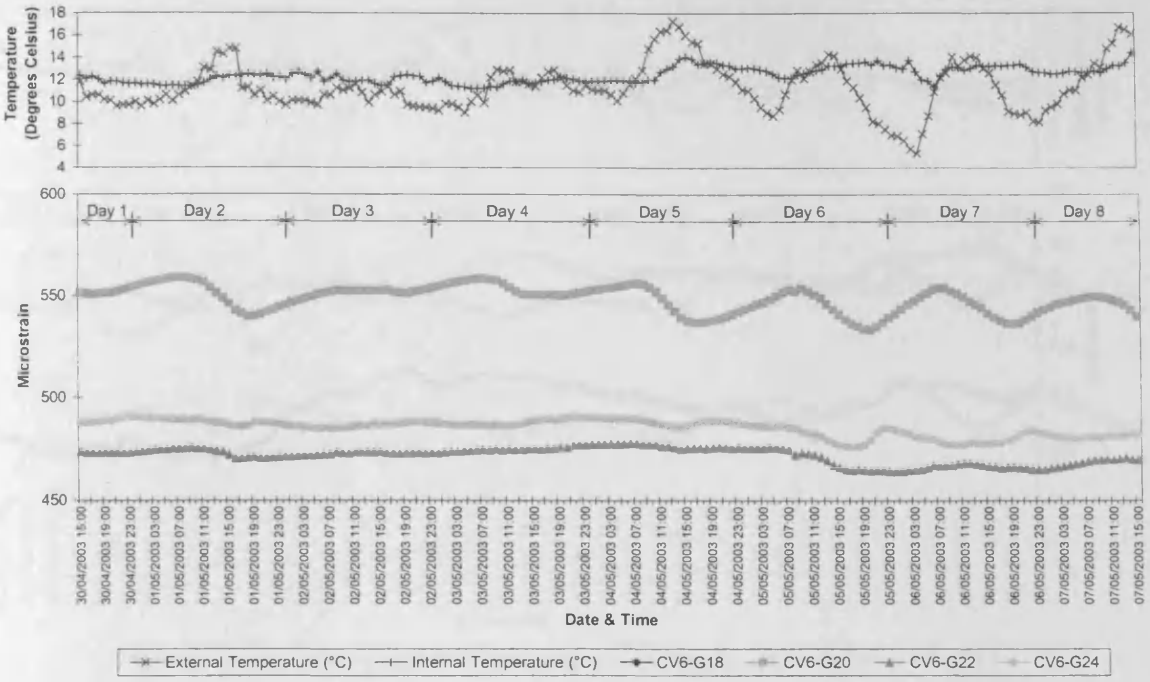

Figure E4.3. Comparison between hourly measured strains and hourly external and internal air temperature in the bottom flange of segment 6, Cogan Viaduct, Spring 2003.

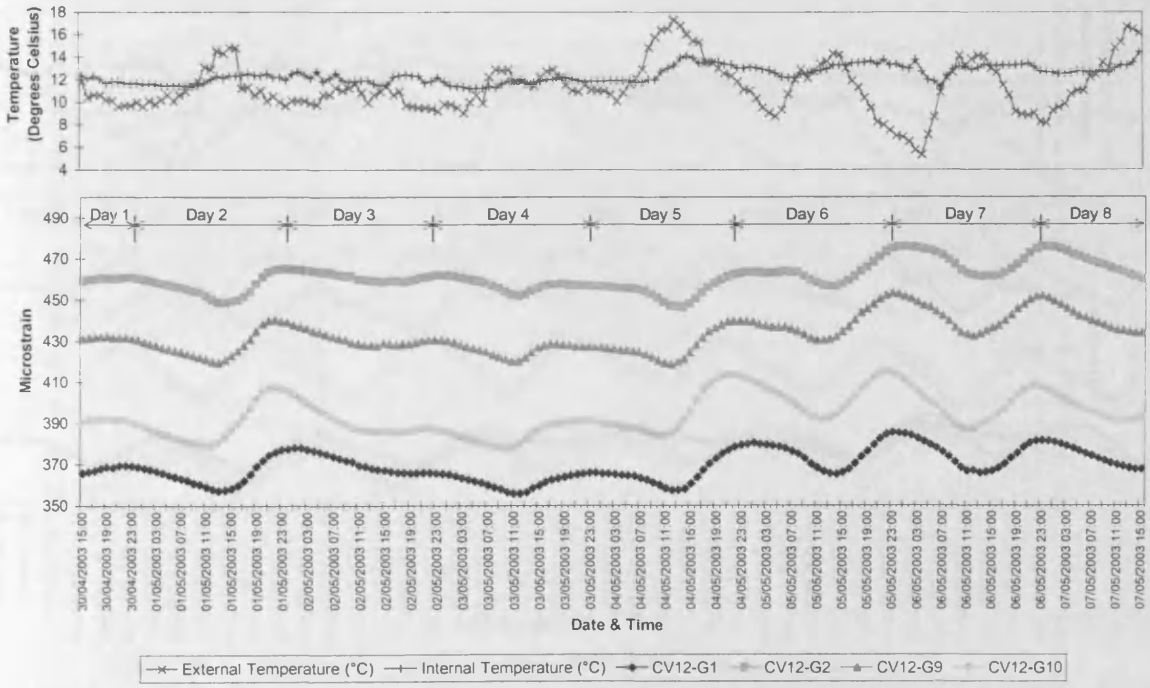

Figure E4.4. Comparison between hourly measured strains and hourly external and internal air temperature in the top flange of segment 12, Cogan Viaduct, Spring 2003.

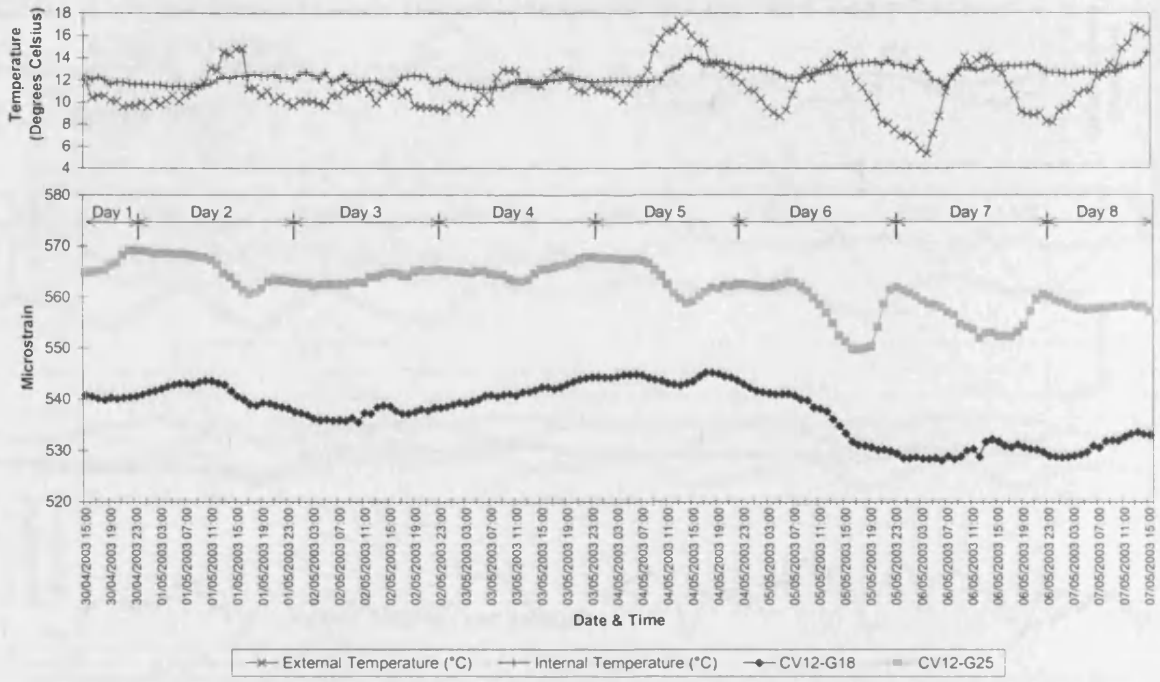

Figure E4.5. Comparison between hourly measured strains and hourly external and internal air temperature in the bottom flange of segment 12, Cogan Viaduct, Spring 2003.

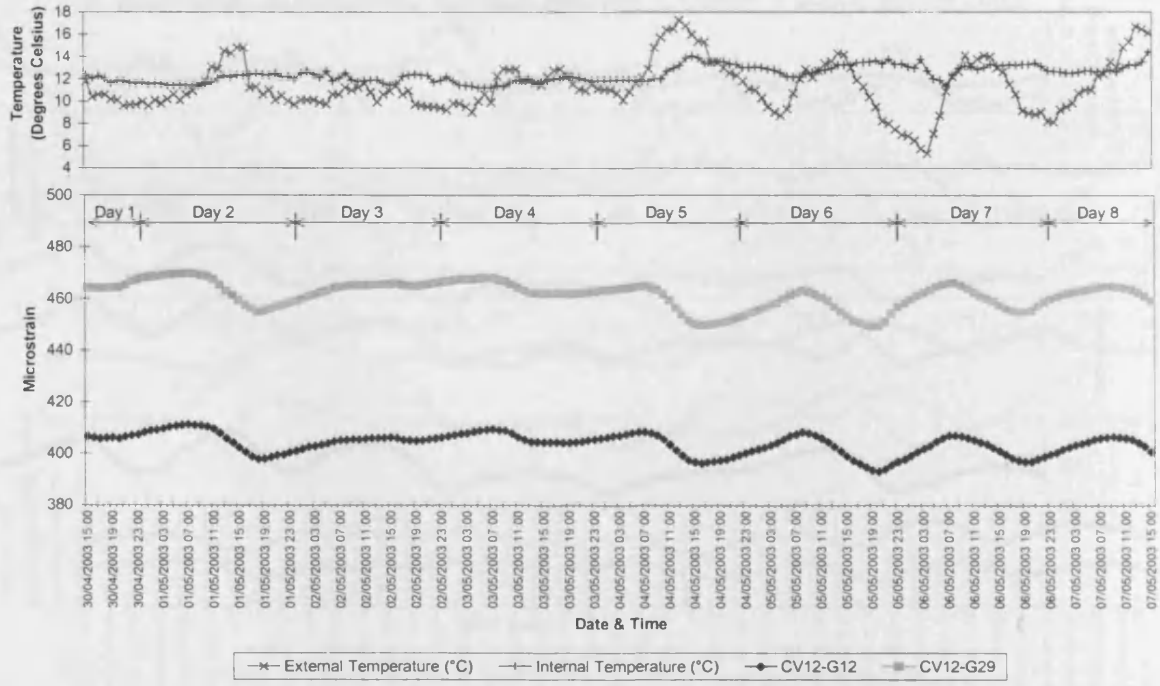

Figure E4.6. Comparison between hourly measured strains and hourly external and internal air temperature in the webs of segment 12, Cogan Viaduct, Spring 2003.

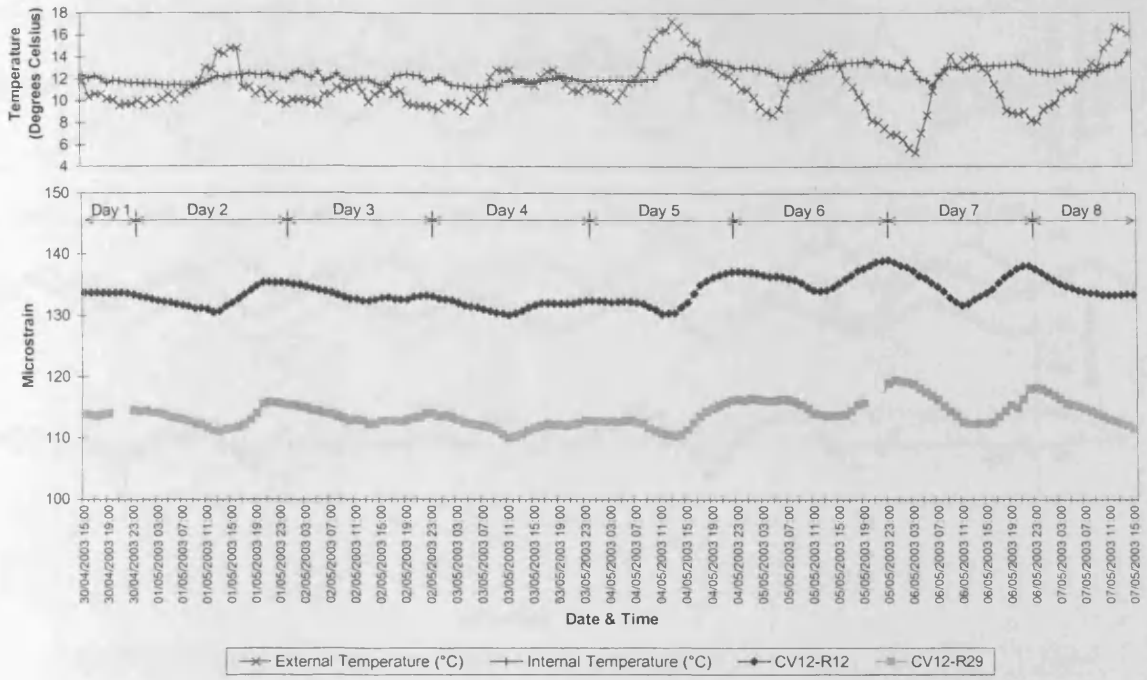

Figure E4.7. Comparison between hourly measured *transverse* strains and hourly external and internal air temperature in the webs of segment 12, Cogan Viaduct, Spring 2003.

E4.2 Summer 2003

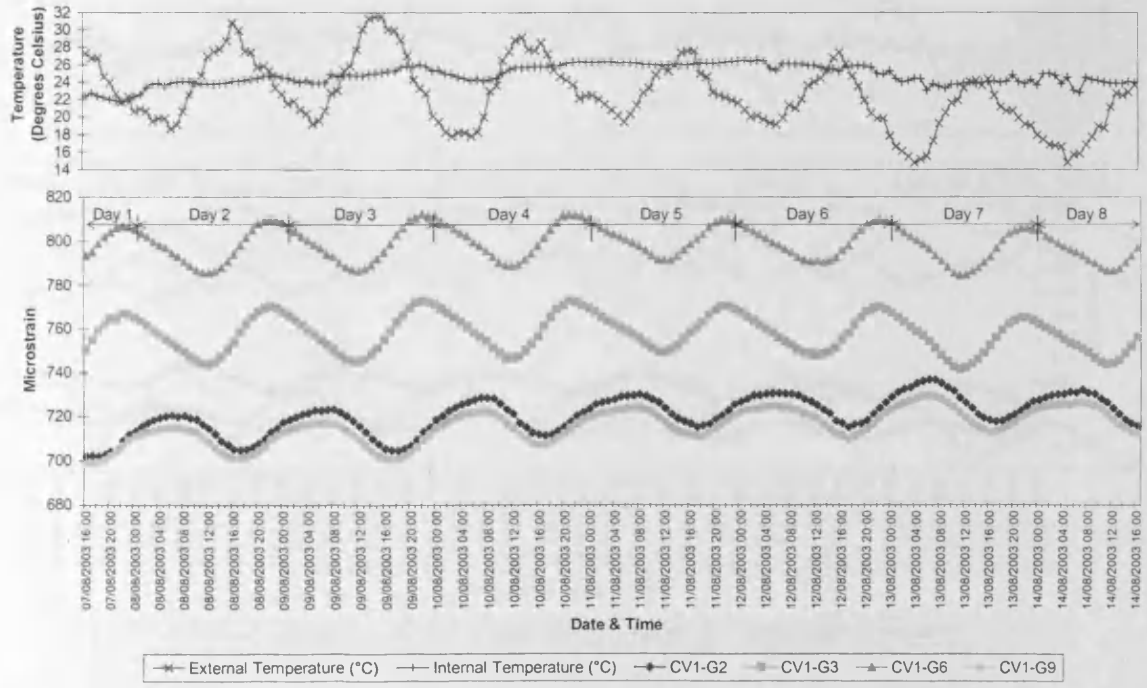

Figure E4.8. Comparison between hourly measured strains and hourly external and internal air temperature in the top flange of segment 1, Cogan Viaduct, Summer 2003.

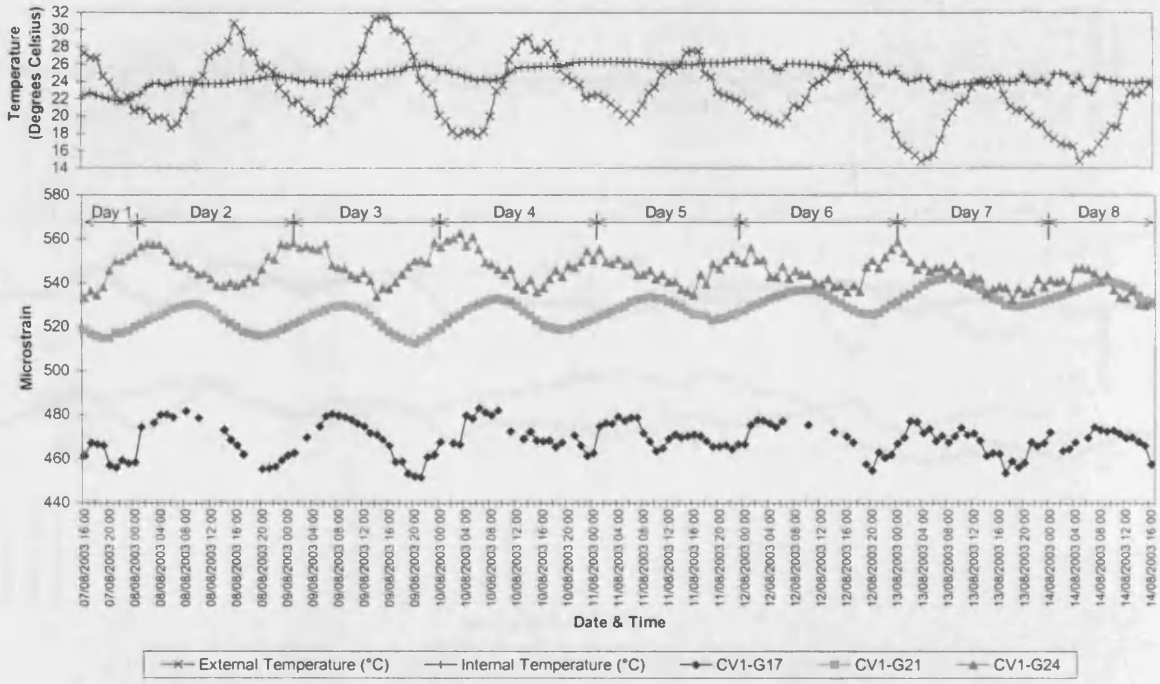

Figure E4.9. Comparison between hourly measured strains and hourly external and internal air temperature in the bottom flange of segment 1, Cogan Viaduct, Summer 2003.

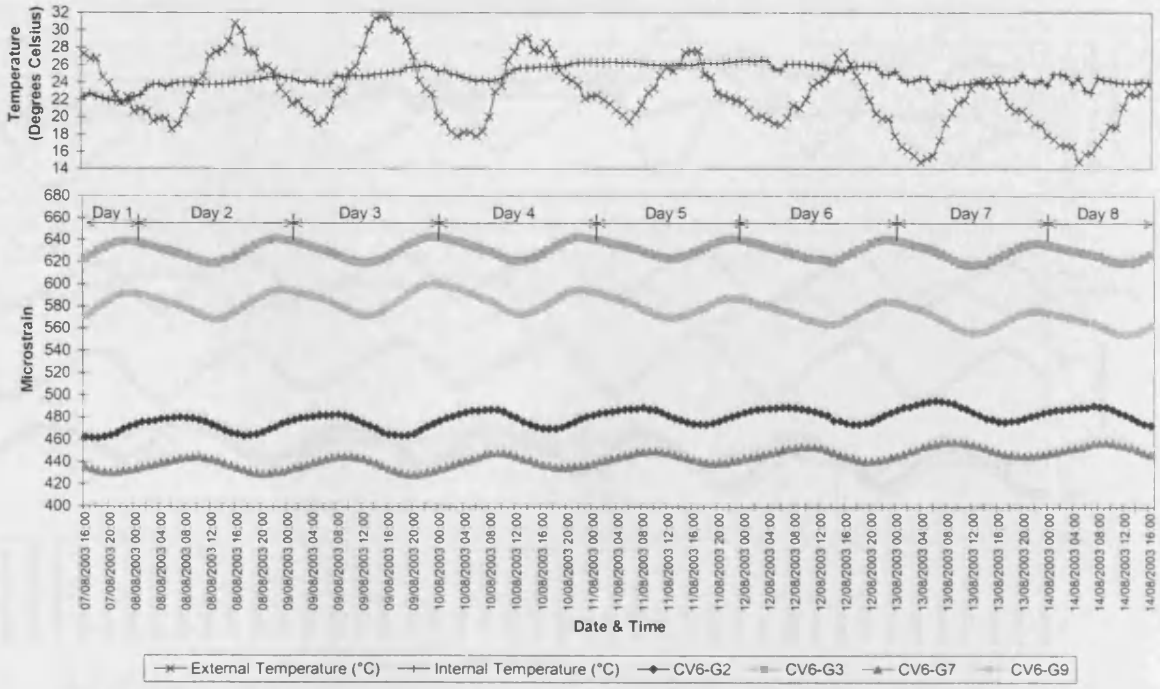

Figure E4.10. Comparison between hourly measured strains and hourly external and internal air temperature in the top flange of segment 6, Cogan Viaduct, Summer 2003.

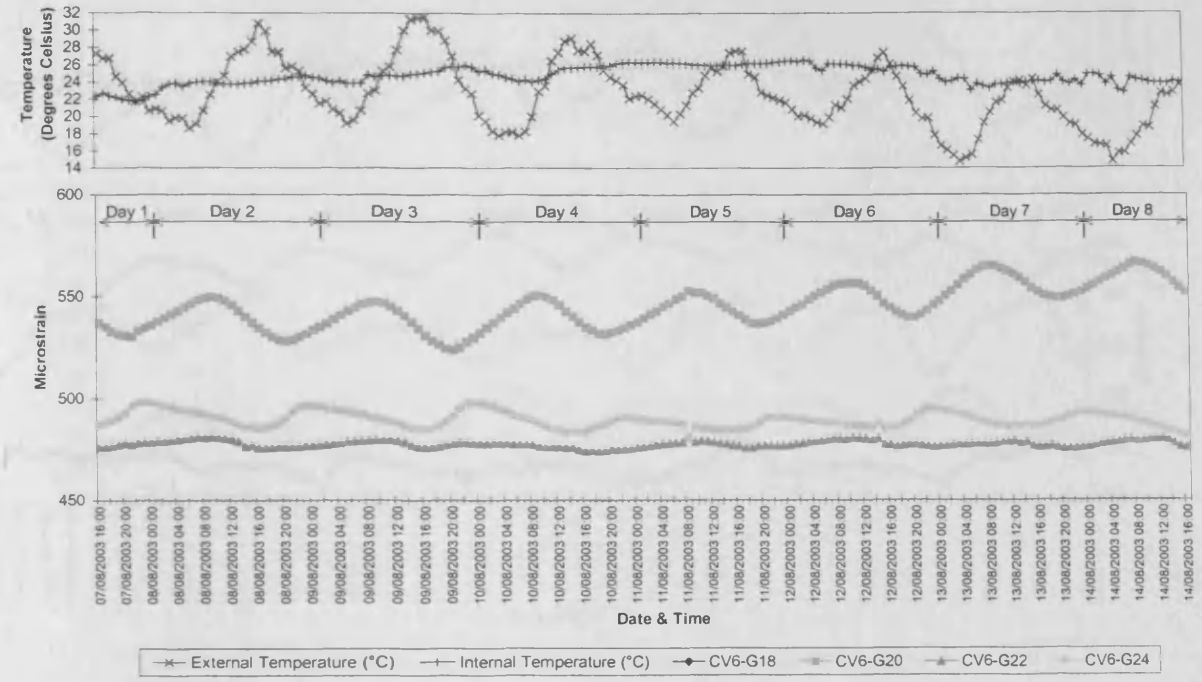

Figure E4.11. Comparison between hourly measured strains and hourly external and internal air temperature in the bottom flange of segment 6, Cogan Viaduct, Summer 2003.

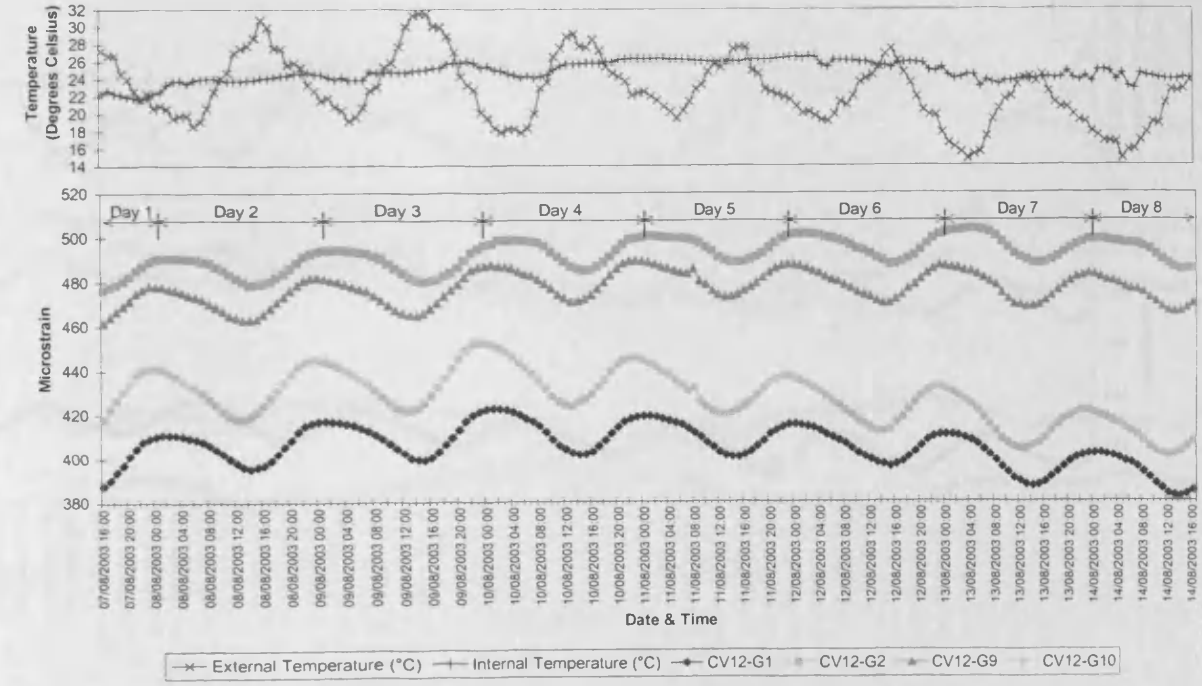

Figure E4.12. Comparison between hourly measured strains and hourly external and internal air temperature in the top flange of segment 12, Cogan Viaduct, Summer 2003.

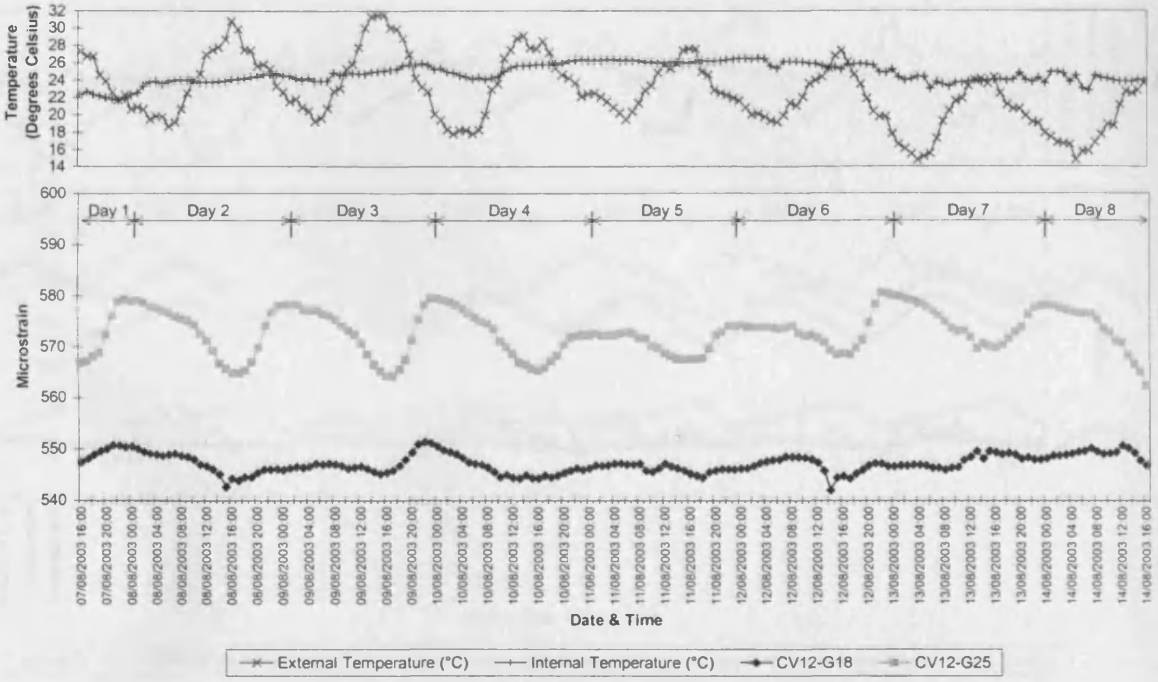

Figure E4.13. Comparison between hourly measured strains and hourly external and internal air temperature in the bottom flange of segment 12, Cogan Viaduct, Summer 2003.

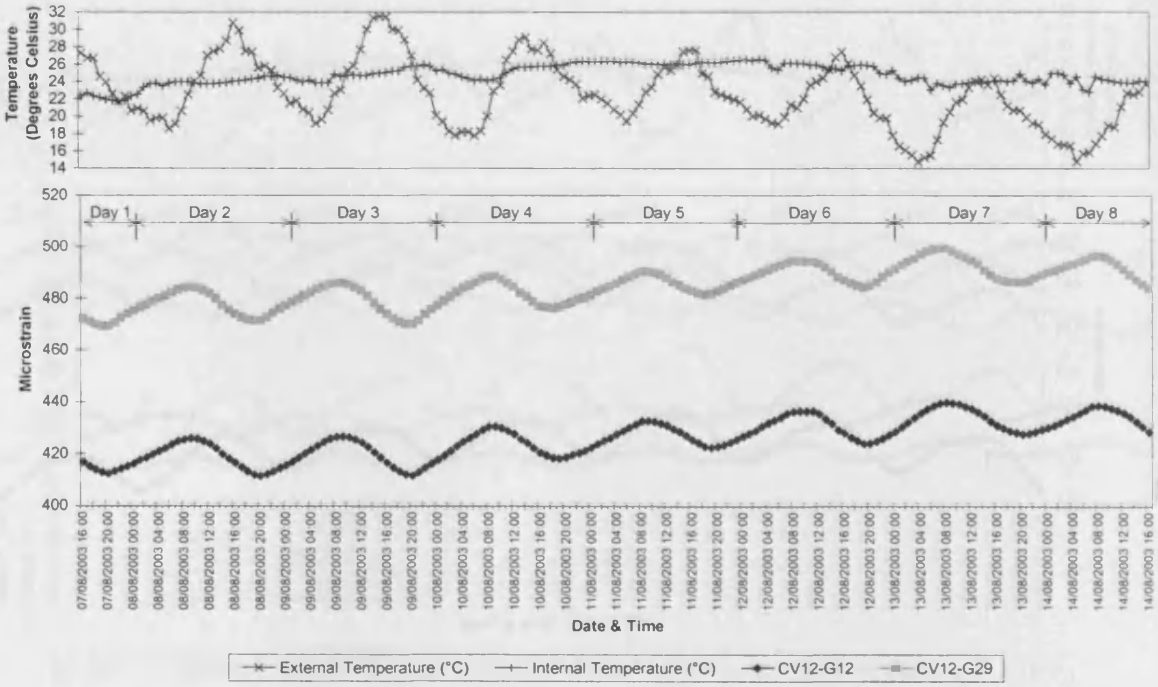

Figure E4.14. Comparison between hourly measured *transverse* strains and hourly external and internal air temperature in the webs of segment 12, Cogan Viaduct, Summer 2003.

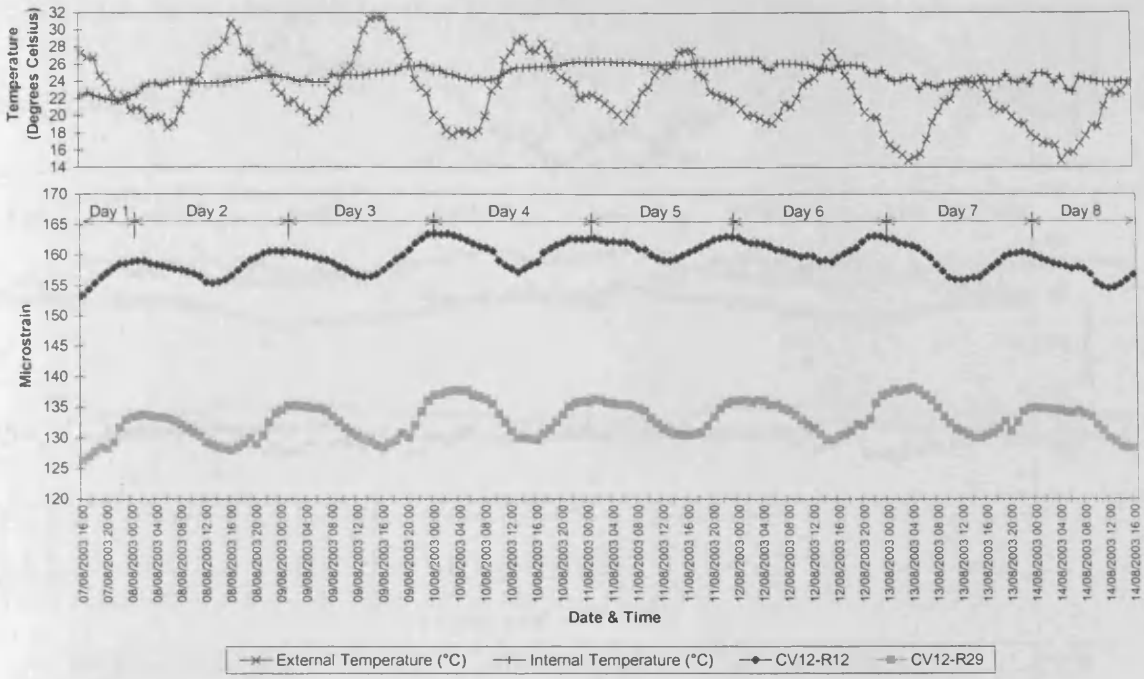

Figure E4.15. Comparison between hourly measured *transverse* strains and hourly external and internal air temperature in the webs of segment 12, Cogan Viaduct, Summer 2003.

E4.3 Autumn 2003

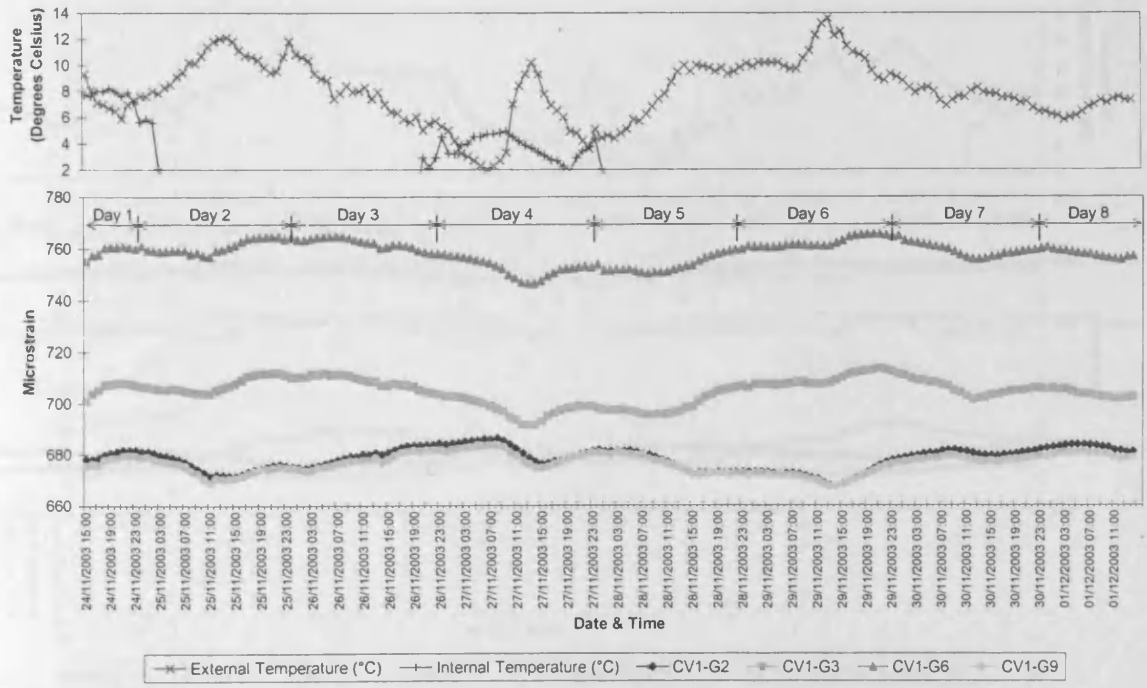

Figure E4.16. Comparison between hourly measured strains and hourly external and internal air temperature in the top flange of segment 1, Cogan Viaduct, Autumn 2003.

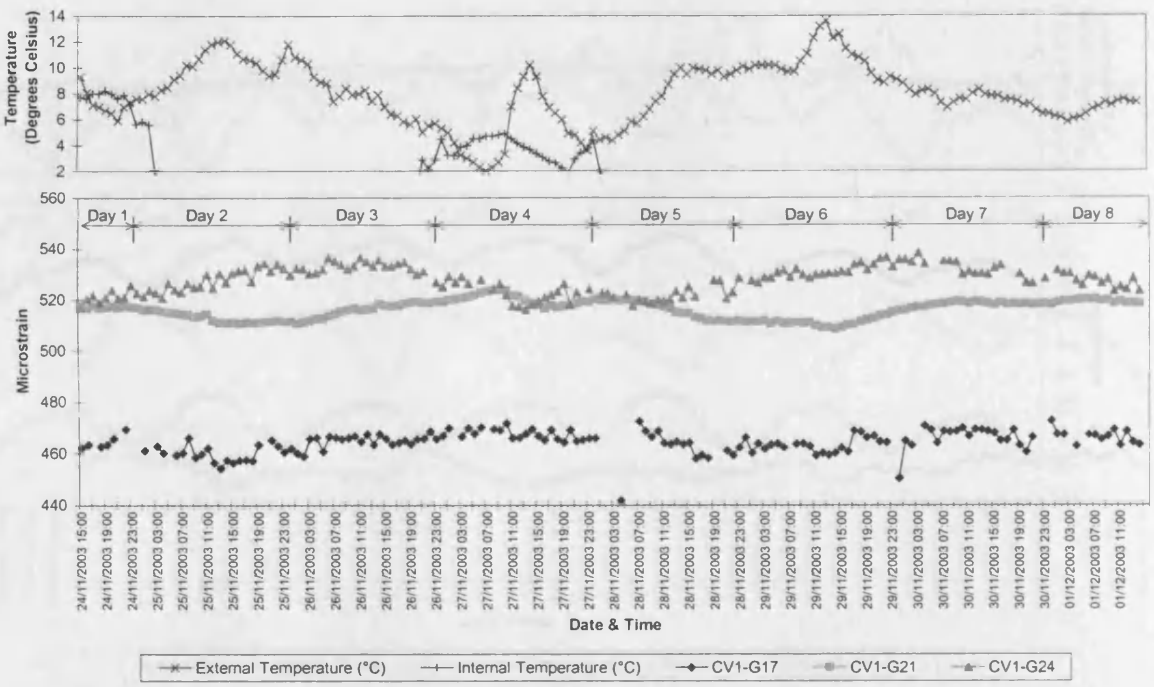

Figure E4.17. Comparison between hourly measured strains and hourly external and internal air temperature in the bottom flange of segment 1, Cogan Viaduct, Autumn 2003.

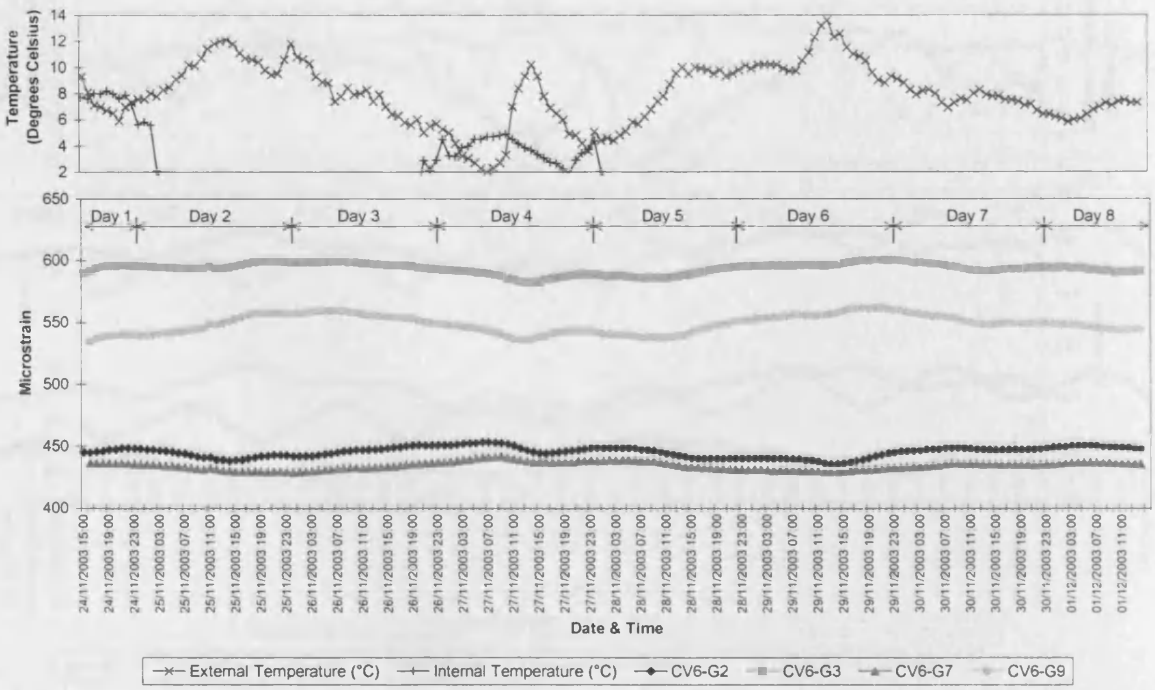

Figure E4.18. Comparison between hourly measured strains and hourly external and internal air temperature in the top flange of segment 6, Cogan Viaduct, Autumn 2003.

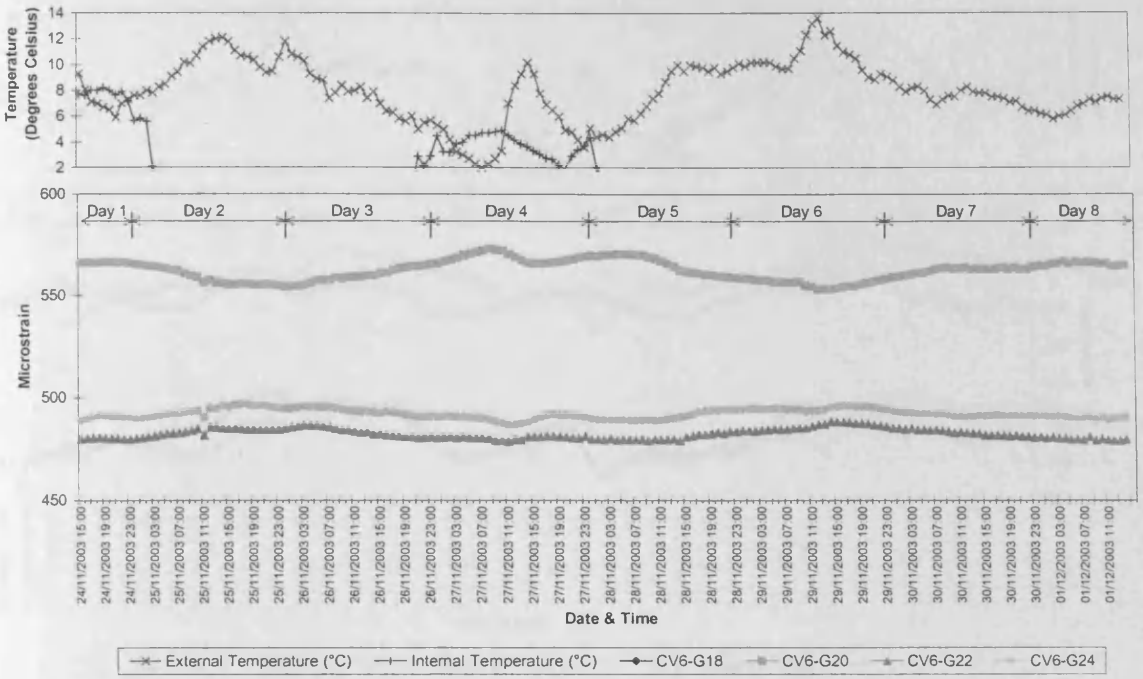

Figure E4.19. Comparison between hourly measured strains and hourly external and internal air temperature in the bottom flange of segment 6, Cogan Viaduct, Autumn 2003.

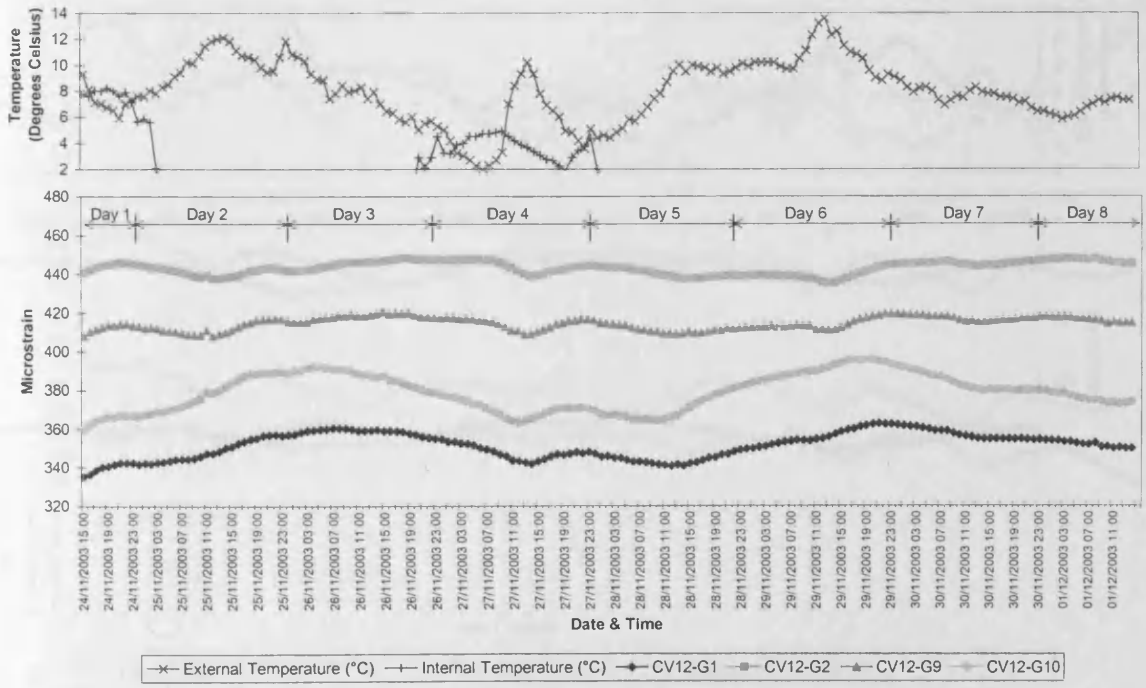

Figure E4.20. Comparison between hourly measured strains and hourly external and internal air temperature in the top flange of segment 12, Cogan Viaduct, Autumn 2003.

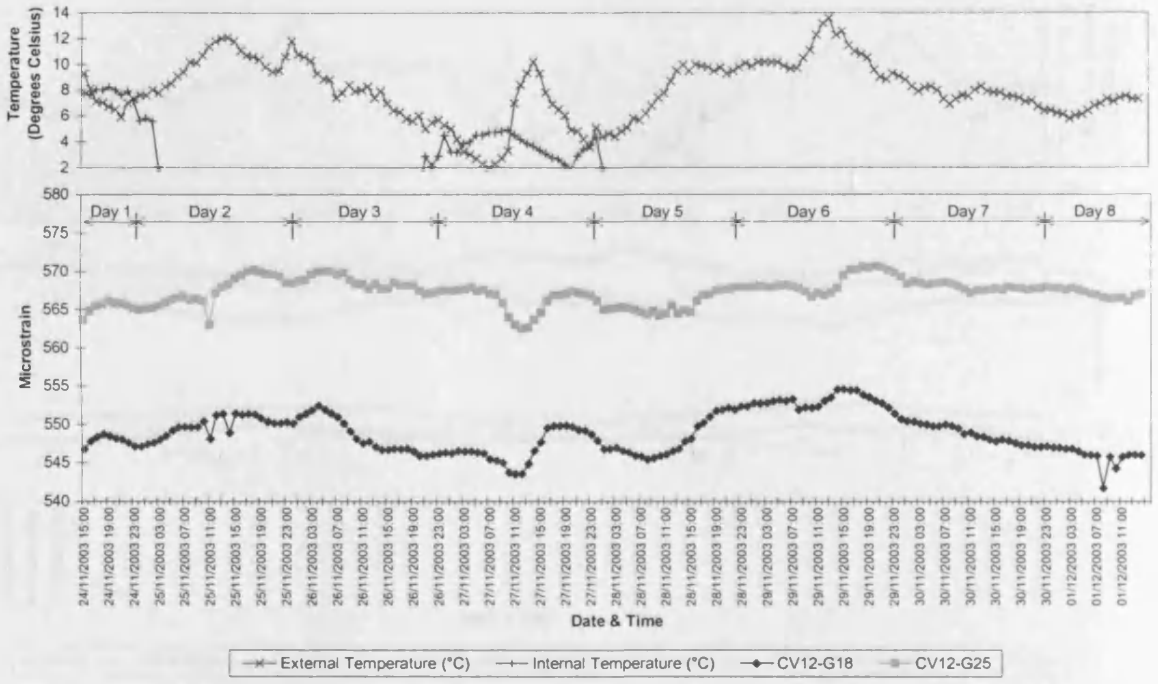

Figure E4.21. Comparison between hourly measured strains and hourly external and internal air temperature in the bottom flange of segment 12, Cogan Viaduct, Autumn 2003.

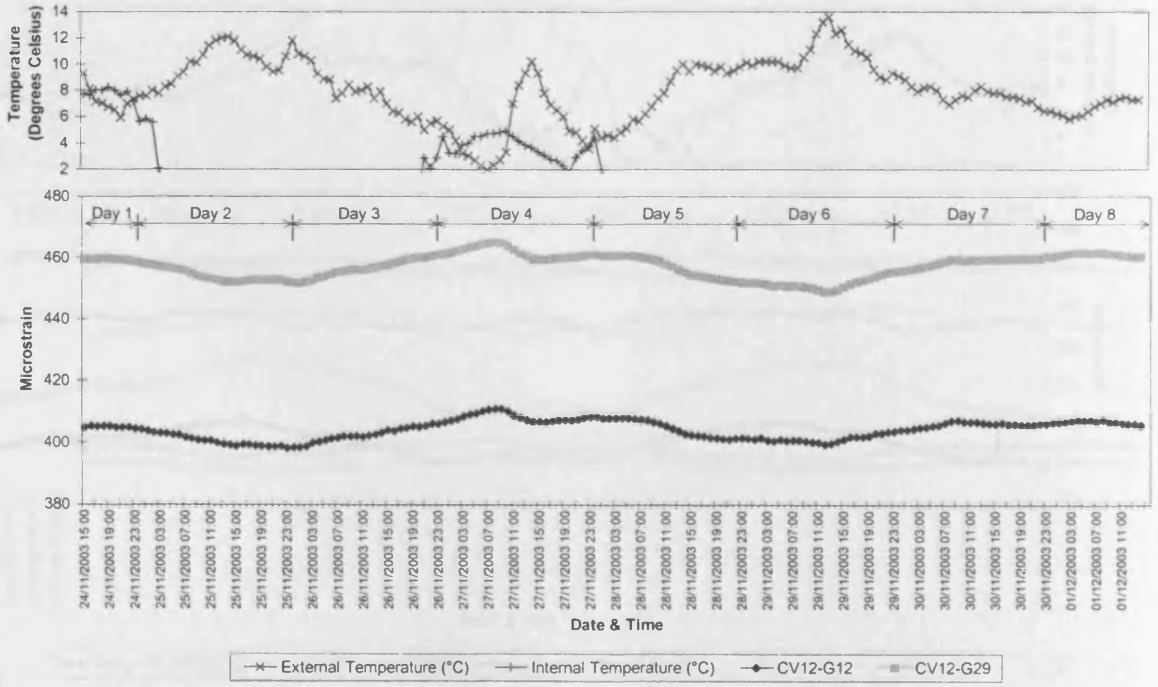

Figure E4.22. Comparison between hourly measured strains and hourly external and internal air temperature in the webs of segment 12, Cogan Viaduct, Autumn 2003.

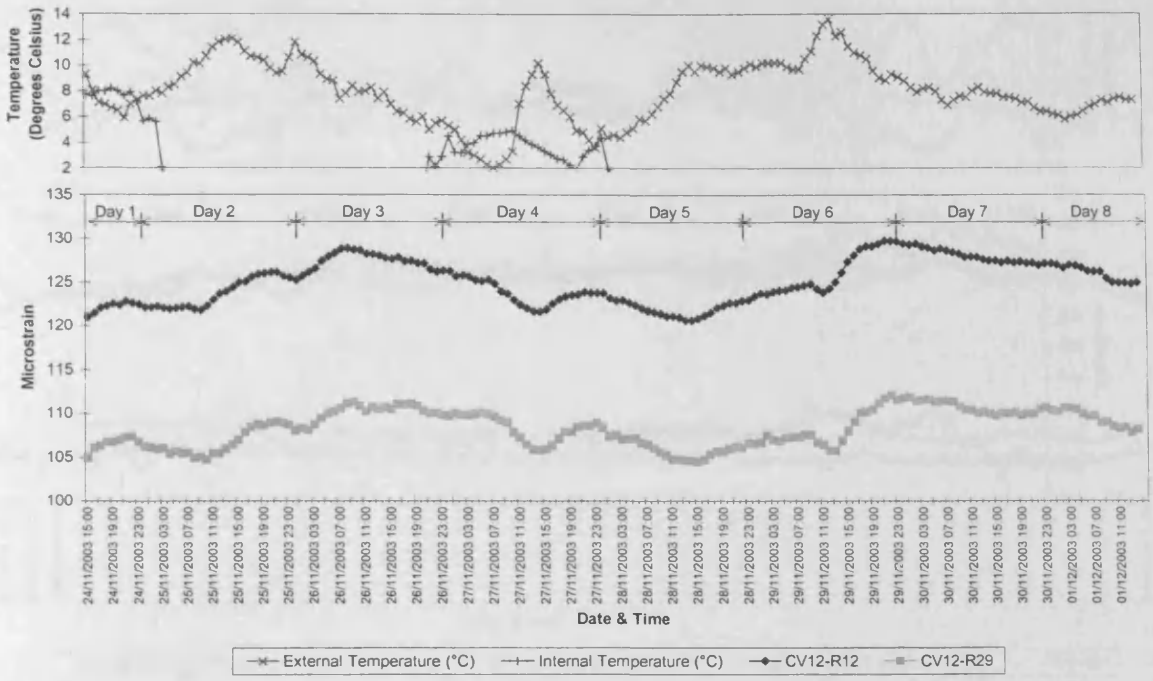

Figure E4.23. Comparison between hourly measured *transverse* strains and hourly external and internal air temperature in the webs of segment 12, Cogan Viaduct, Autumn 2003.

E4.4 Winter 2003

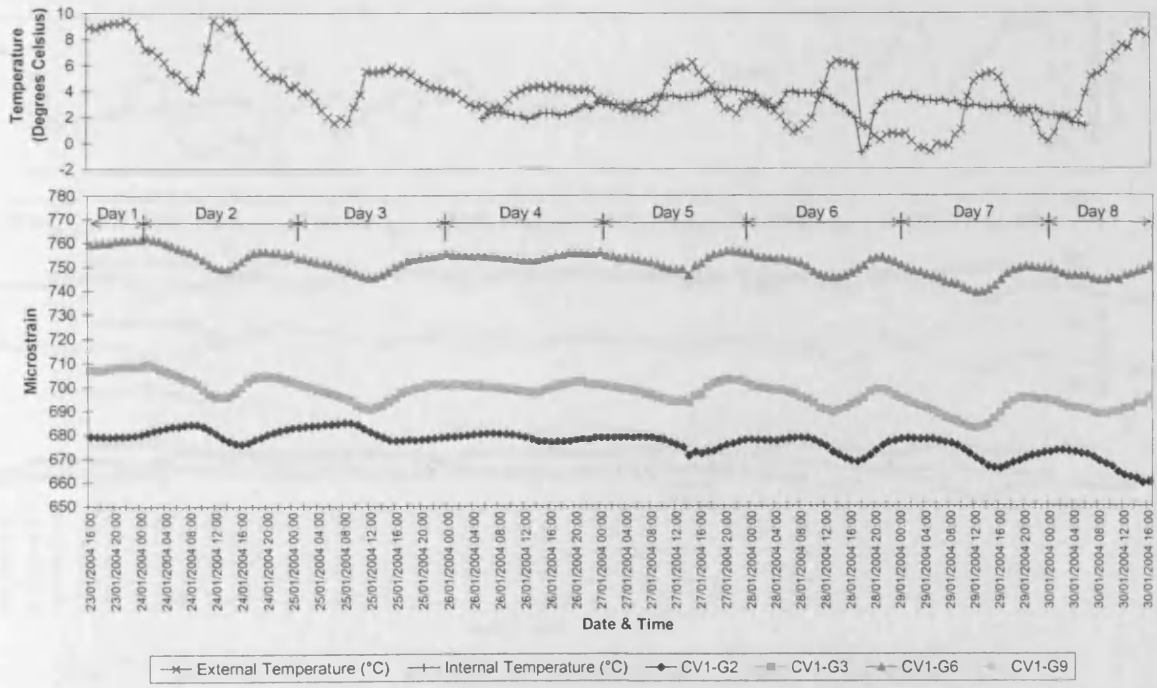

Figure E4.24. Comparison between hourly measured strains and hourly external and internal air temperature in the top flange of segment 1, Cogan Viaduct, Winter 2003.

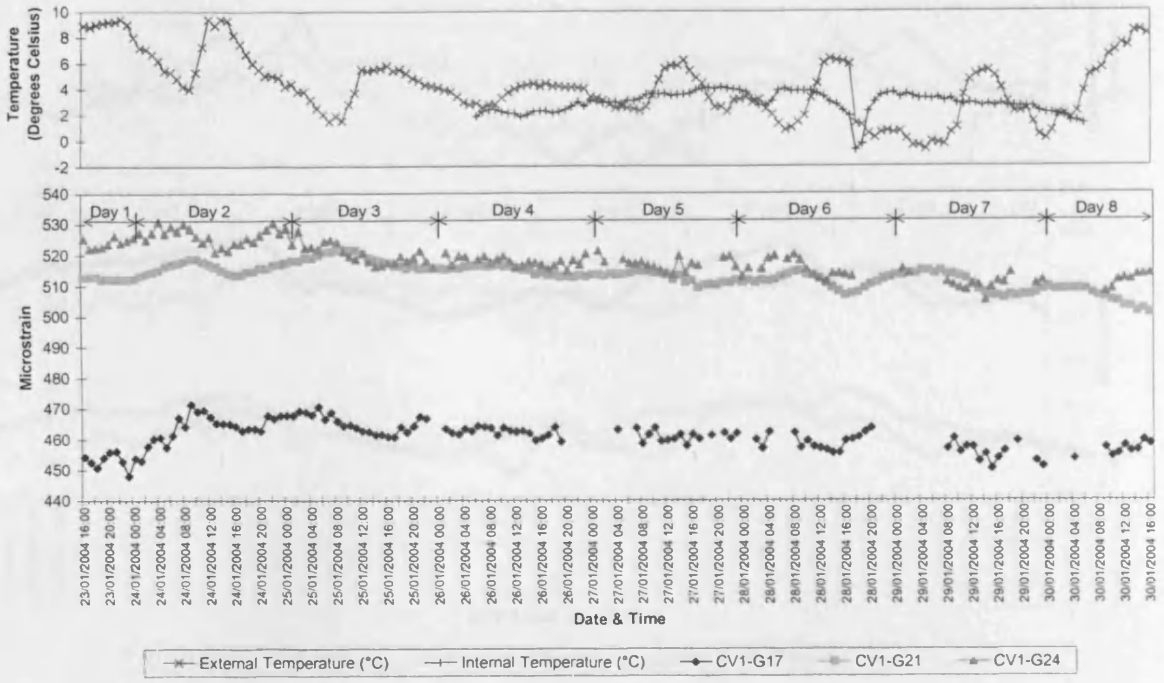

Figure E4.25. Comparison between hourly measured strains and hourly external and internal air temperature in the bottom flange of segment 1, Cogan Viaduct, Winter 2003.

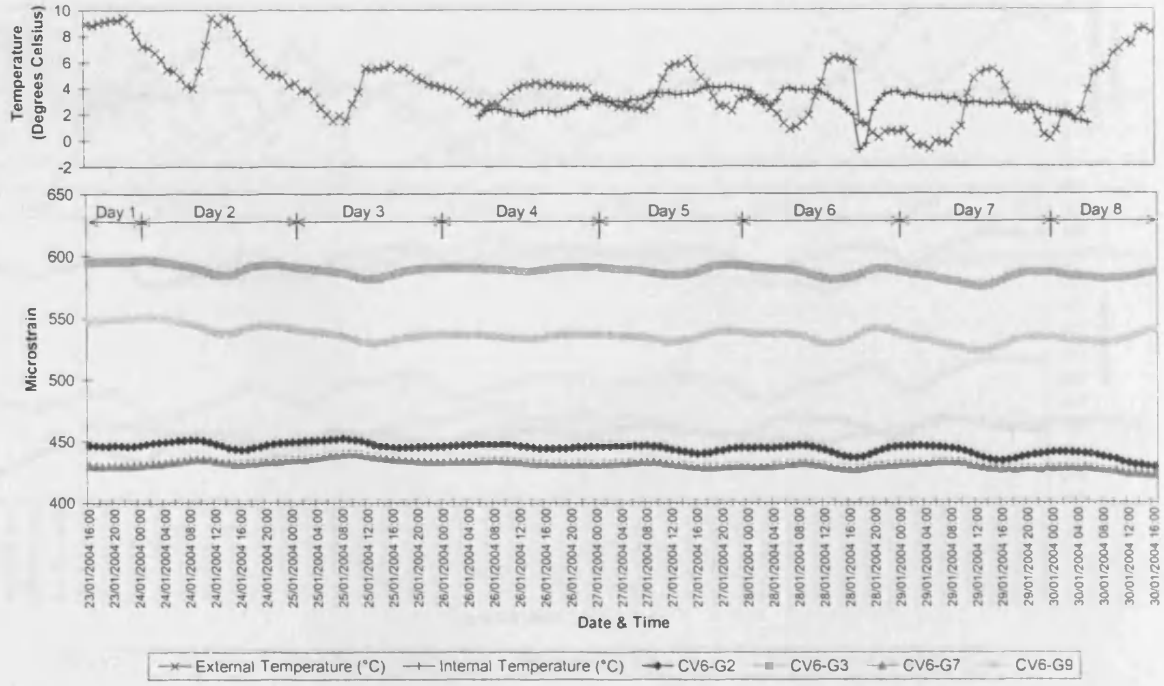

Figure E4.26. Comparison between hourly measured strains and hourly external and internal air temperature in the top flange of segment 6, Cogan Viaduct, Winter 2003.

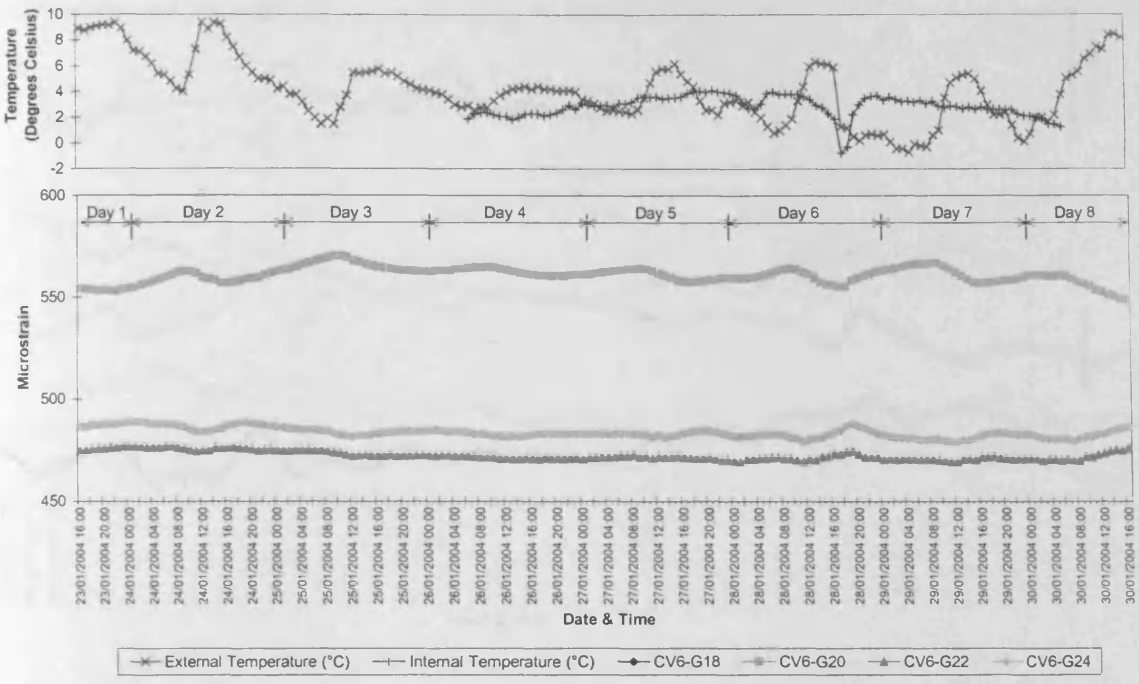

Figure E4.27. Comparison between hourly measured strains and hourly external and internal air temperature in the bottom flange of segment 6, Cogan Viaduct, Winter 2003.

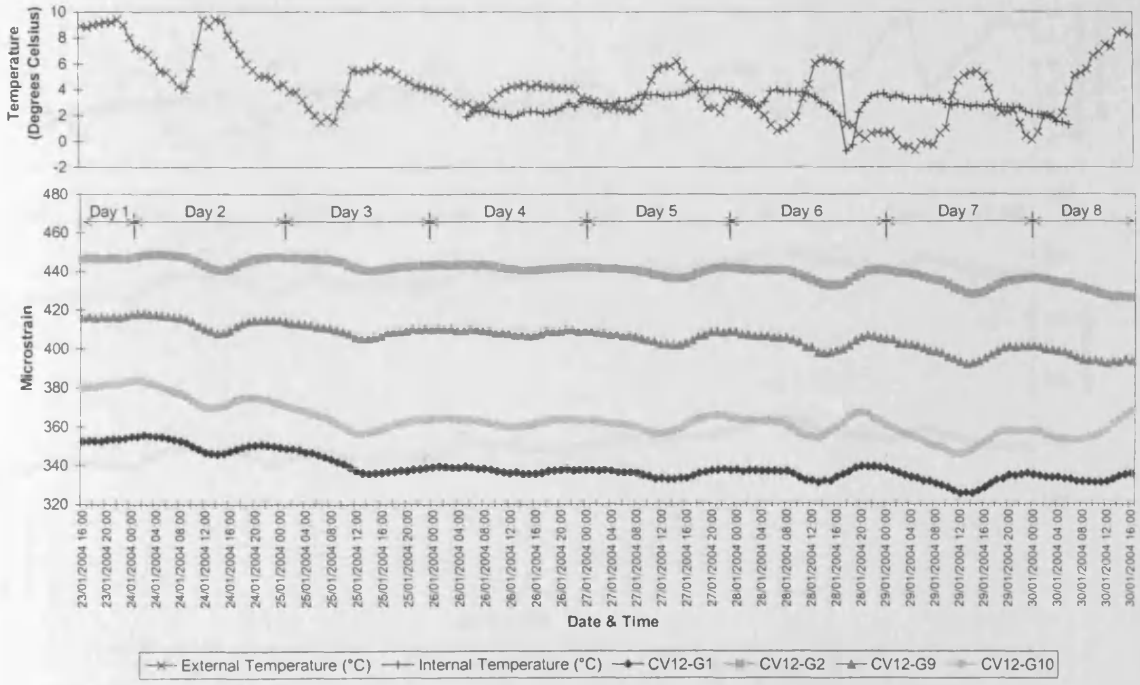

Figure E4.28. Comparison between hourly measured strains and hourly external and internal air temperature in the top flange of segment 12, Cogan Viaduct, Winter 2003.

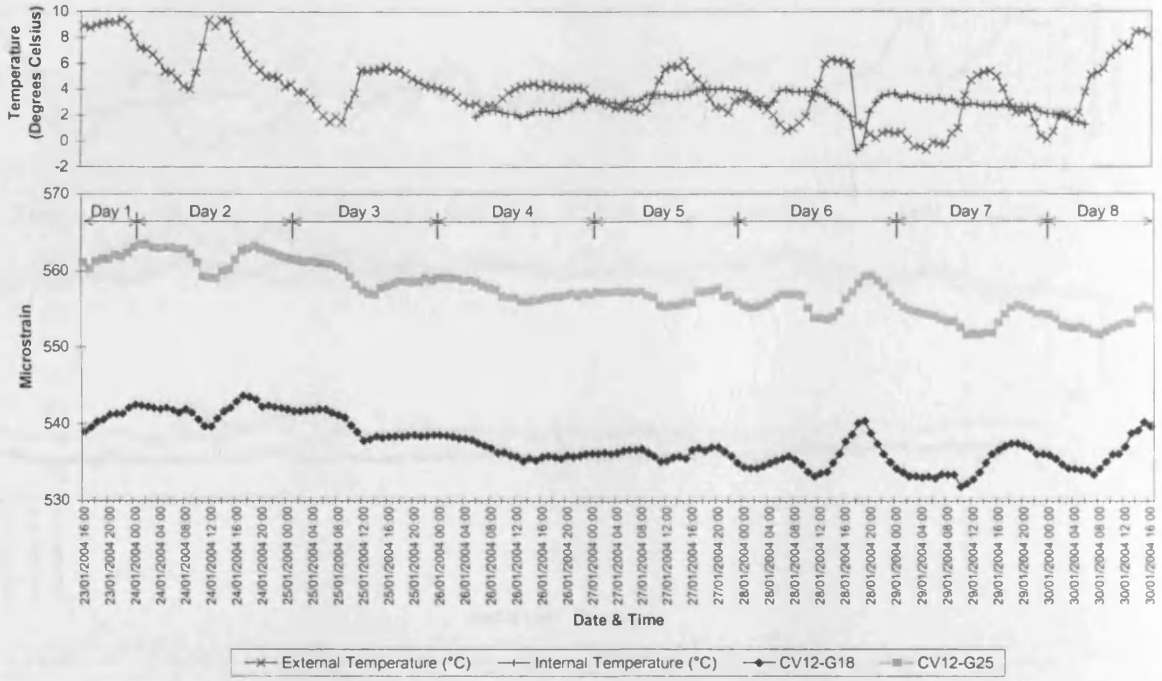

Figure E4.29. Comparison between hourly measured strains and hourly external and internal air temperature in the bottom flange of segment 12, Cogan Viaduct, Winter 2003.

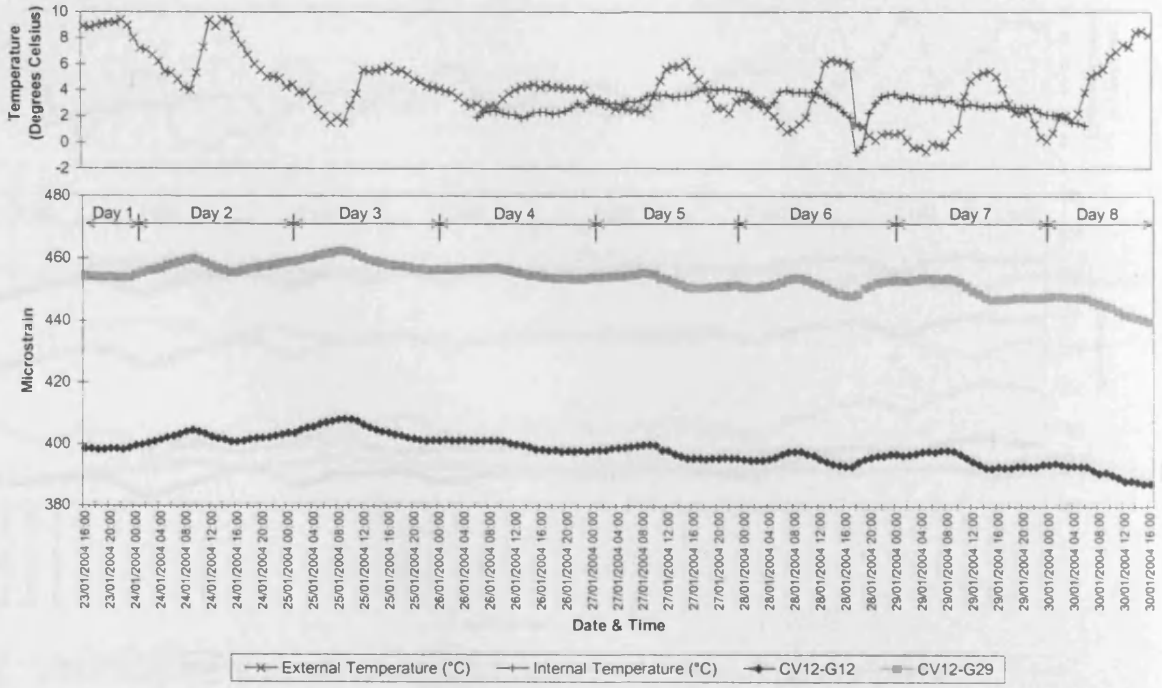

Figure E4.30. Comparison between hourly measured strains and hourly external and internal air temperature in the webs of segment 12, Cogan Viaduct, Winter 2003.

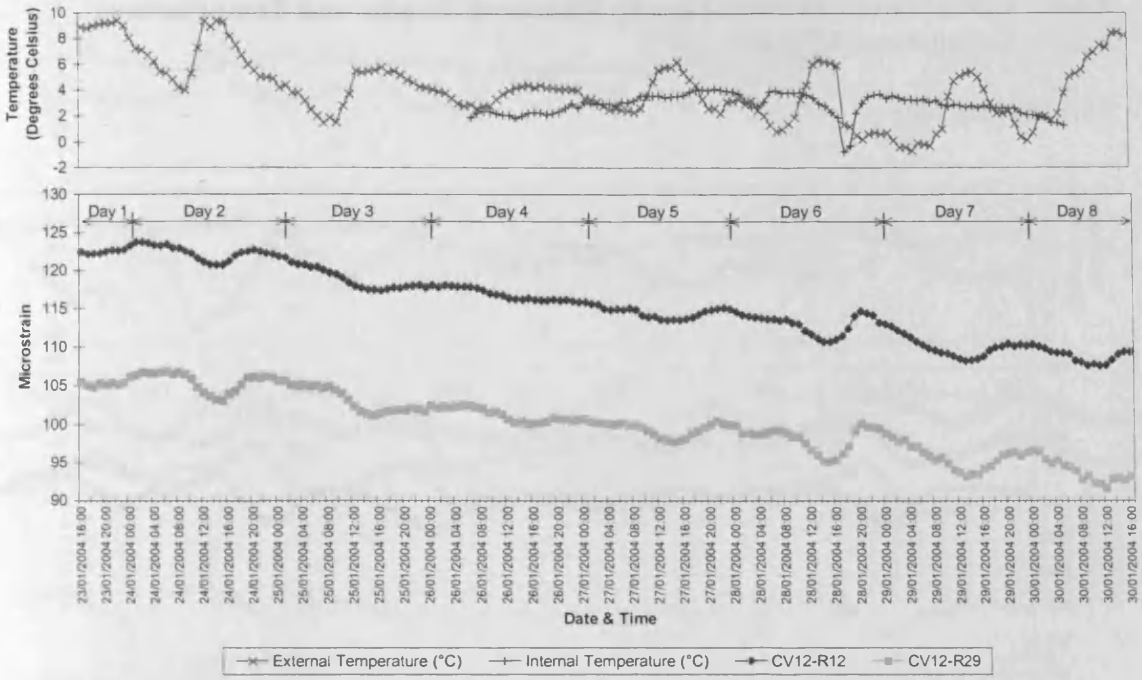

Figure E4.31. Comparison between hourly measured *transverse* strains and hourly external and internal air temperature in the webs of segment 12, Cogan Viaduct, Winter 2003.

E5.0 Comparisons between Hourly Measured Strains and Temperatures – Grangetown Viaduct

E5.1 Spring 2003

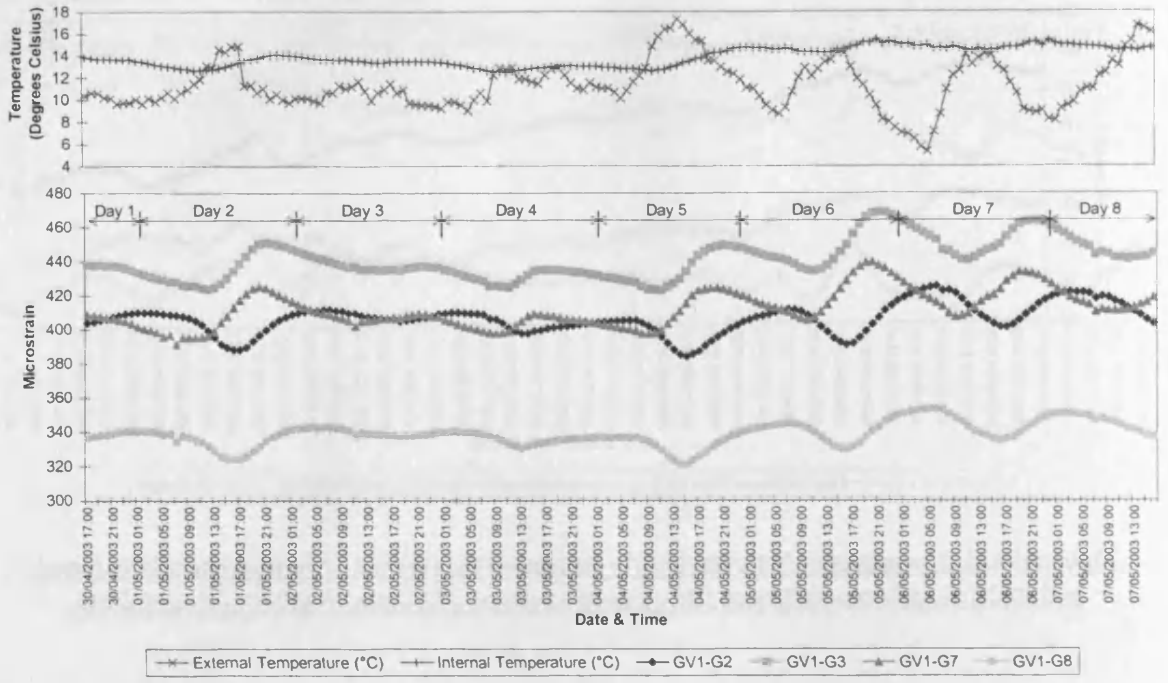

Figure E5.1. Comparison between hourly measured strains and hourly external and internal air temperature in the top flange of segment 1, Grangetown Viaduct, Spring 2003.

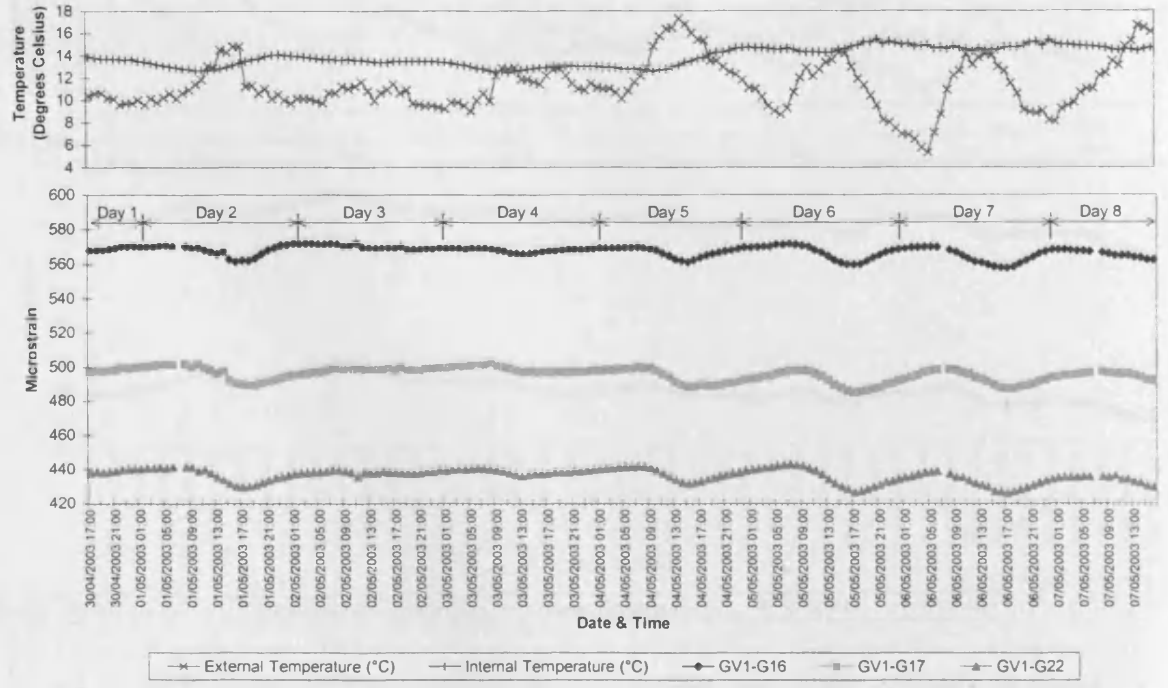

Figure E5.2. Comparison between hourly measured strains and hourly external and internal air temperature in the bottom flange of segment 1, Grangetown Viaduct, Spring 2003.

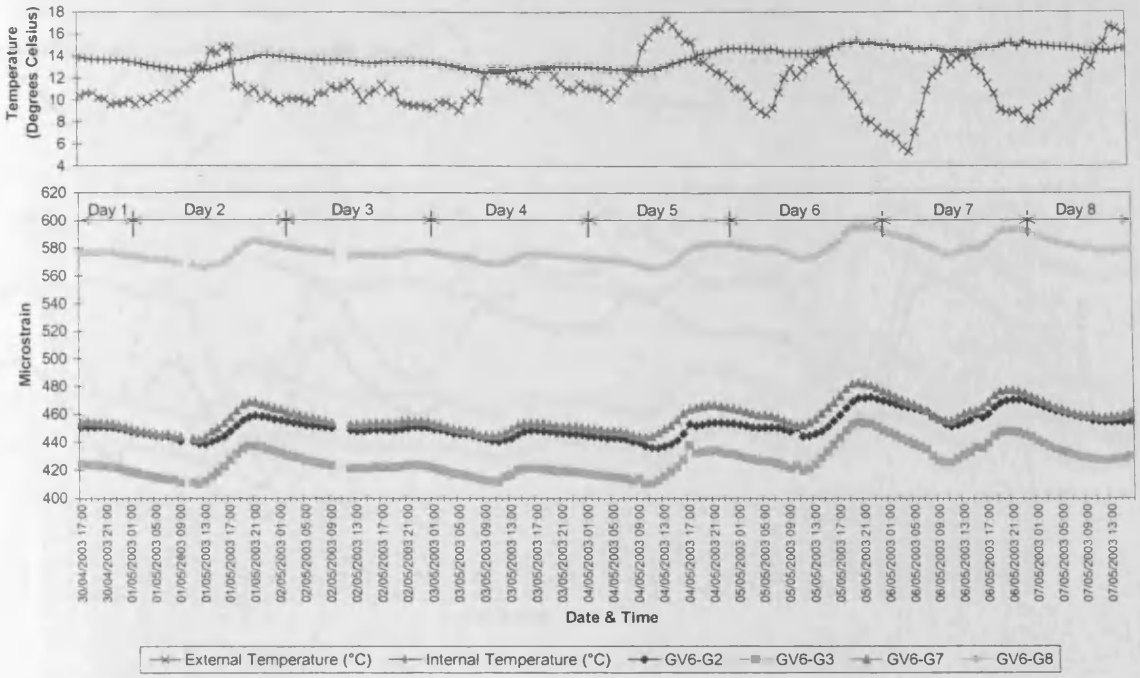

Figure E5.3. Comparison between hourly measured strains and hourly external and internal air temperature in the top flange of segment 6, Grangetown Viaduct, Spring 2003.

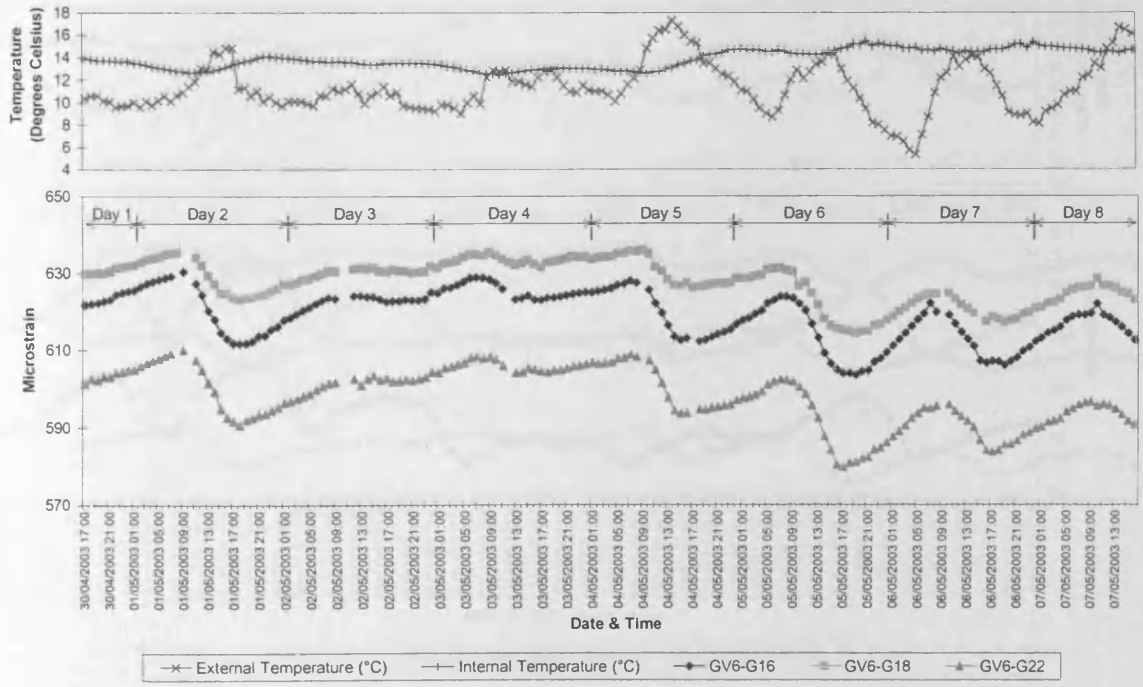

Figure E5.4. Comparison between hourly measured strains and hourly external and internal air temperature in the bottom flange of segment 6, Grangetown Viaduct, Spring 2003.

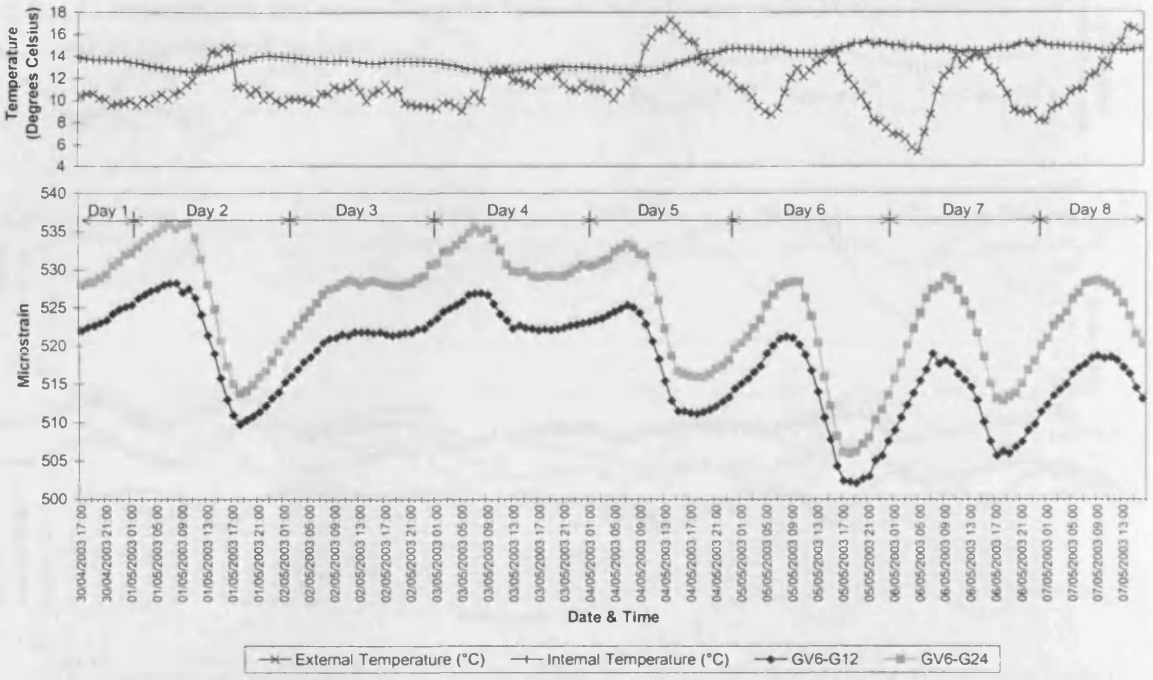

Figure E5.5. Comparison between hourly measured strains and hourly external and internal air temperature in the webs of segment 6, Grangetown Viaduct, Spring 2003.

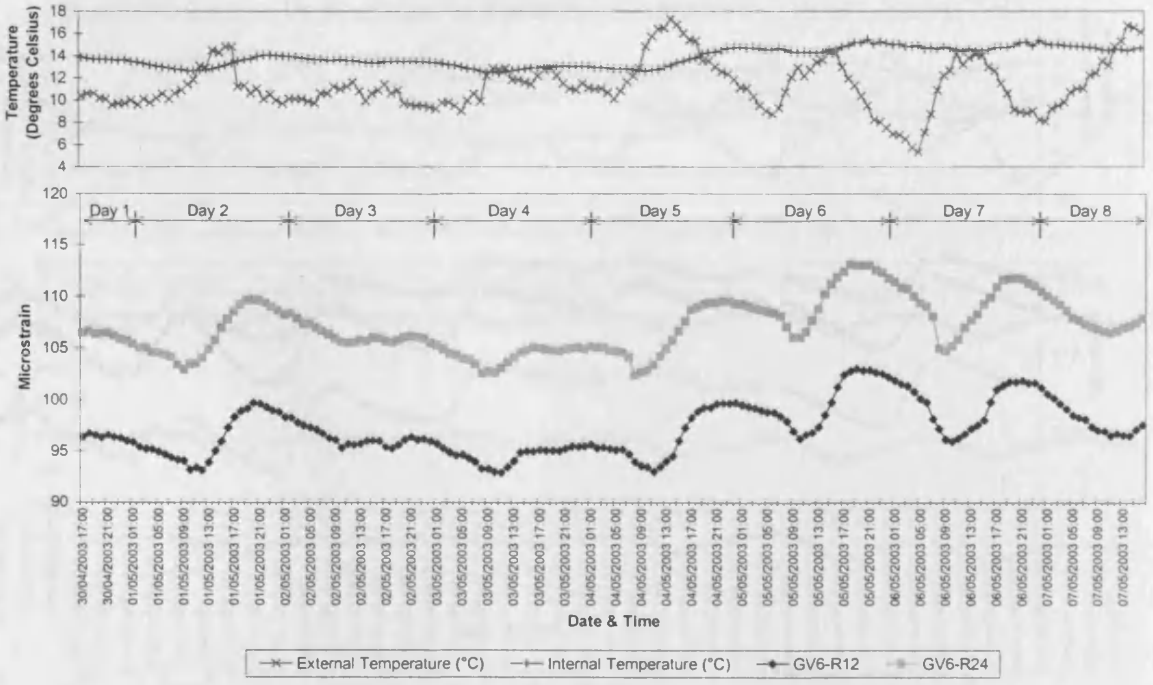

Figure E5.6. Comparison between hourly measured *transverse* strains and hourly external and internal air temperature in the webs of segment 6, Grangetown Viaduct, Spring 2003.

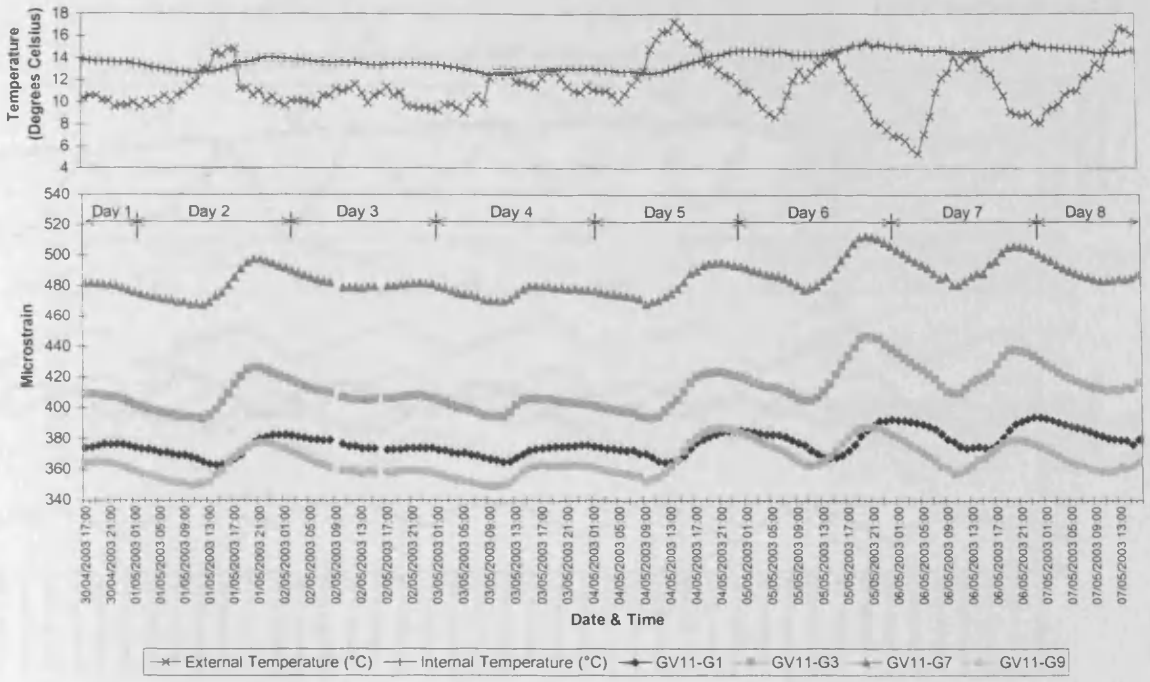

Figure E5.7. Comparison between hourly measured strains and hourly external and internal air temperature in the top flange of segment 12, Grangetown Viaduct, Spring 2003.

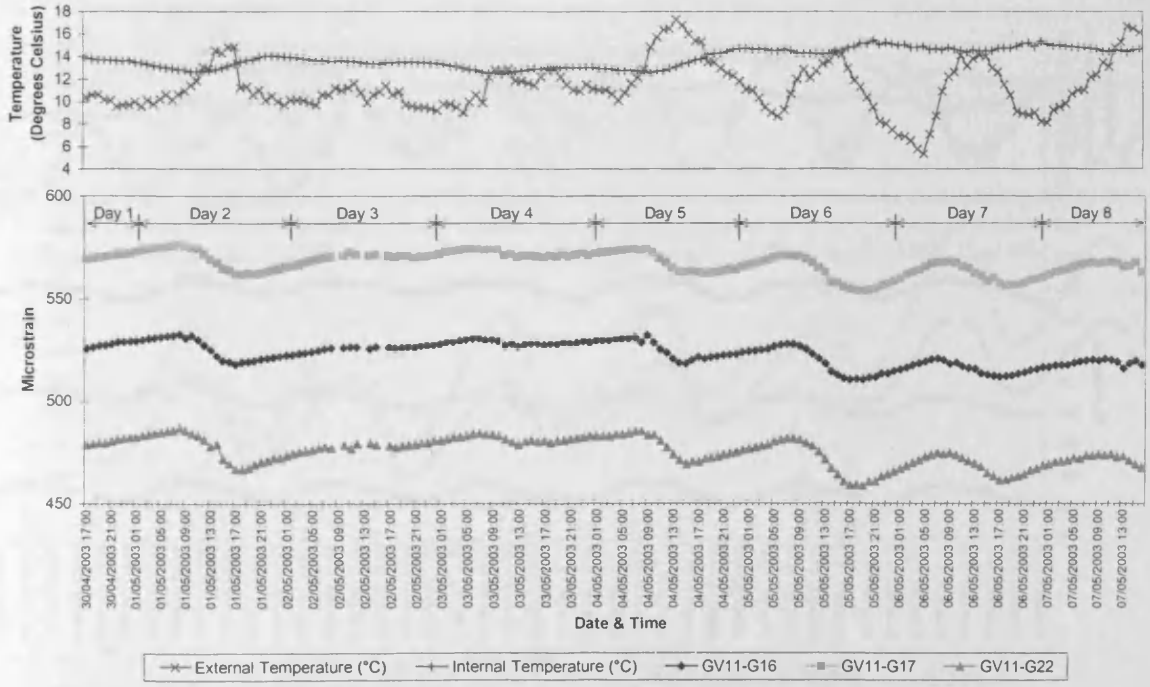

Figure E5.8. Comparison between hourly measured strains and hourly external and internal air temperature in the bottom flange of segment 12, Grangetown Viaduct, Spring 2003.

E5.2 Summer 2003

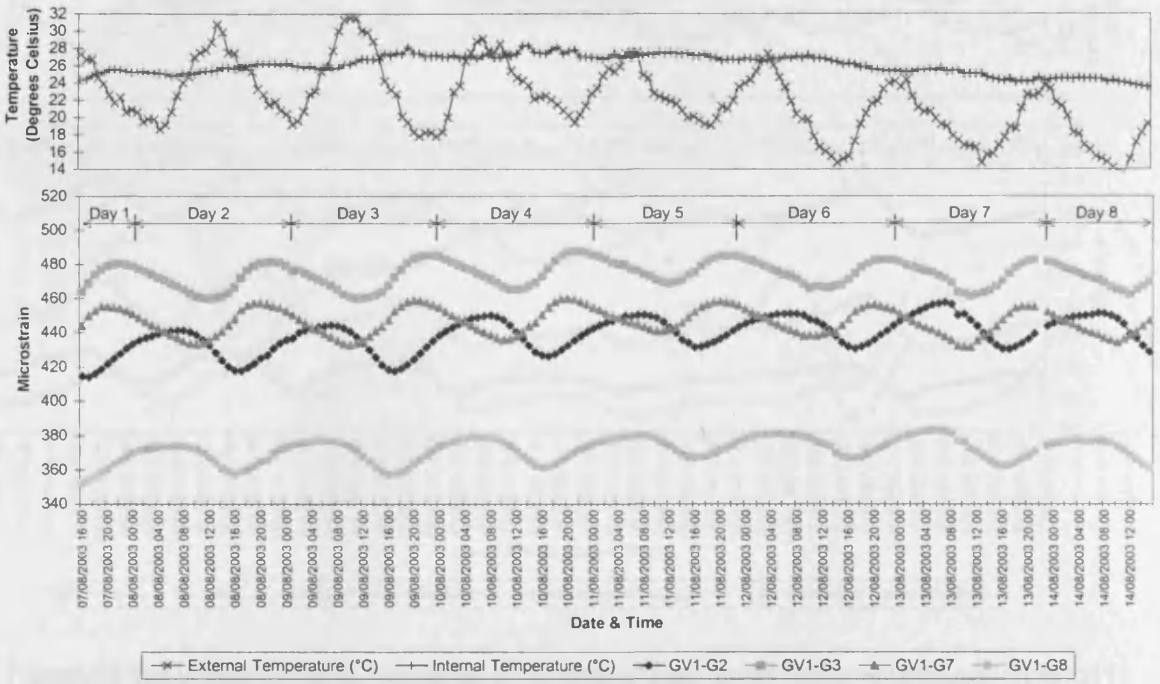

Figure E5.9. Comparison between hourly measured strains and hourly external and internal air temperature in the top flange of segment 1, Grangetown Viaduct, Summer 2003.

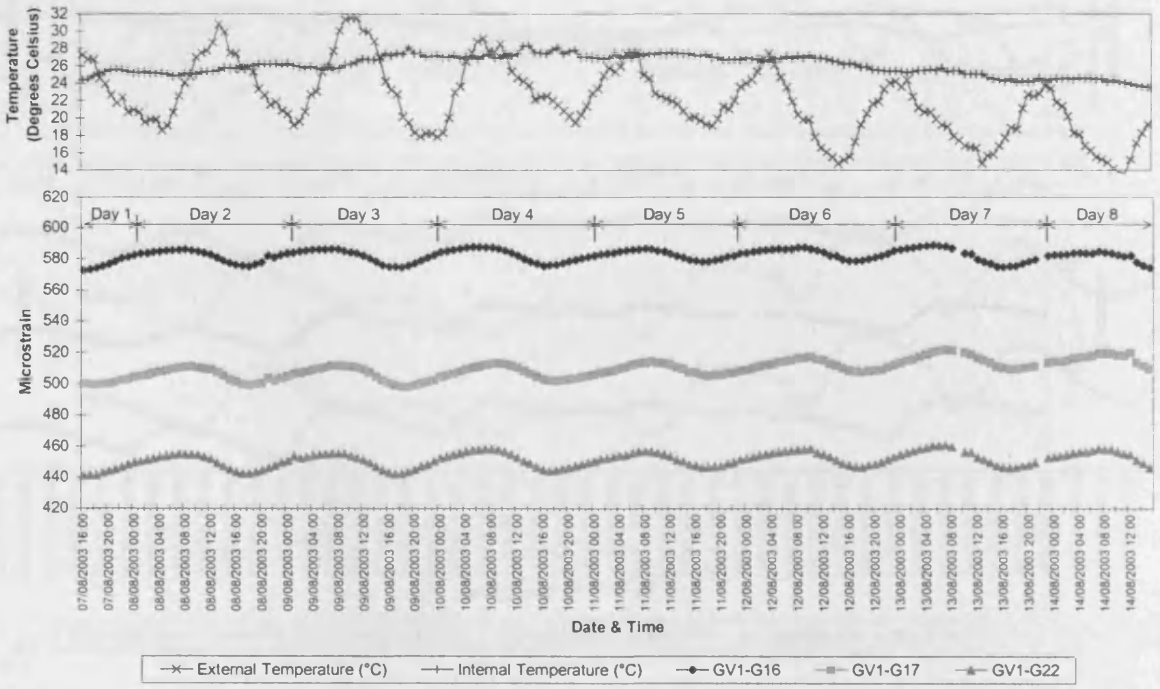

Figure E5.10. Comparison between hourly measured strains and hourly external and internal air temperature in the bottom flange of segment 1, Grangetown Viaduct, Summer 2003.

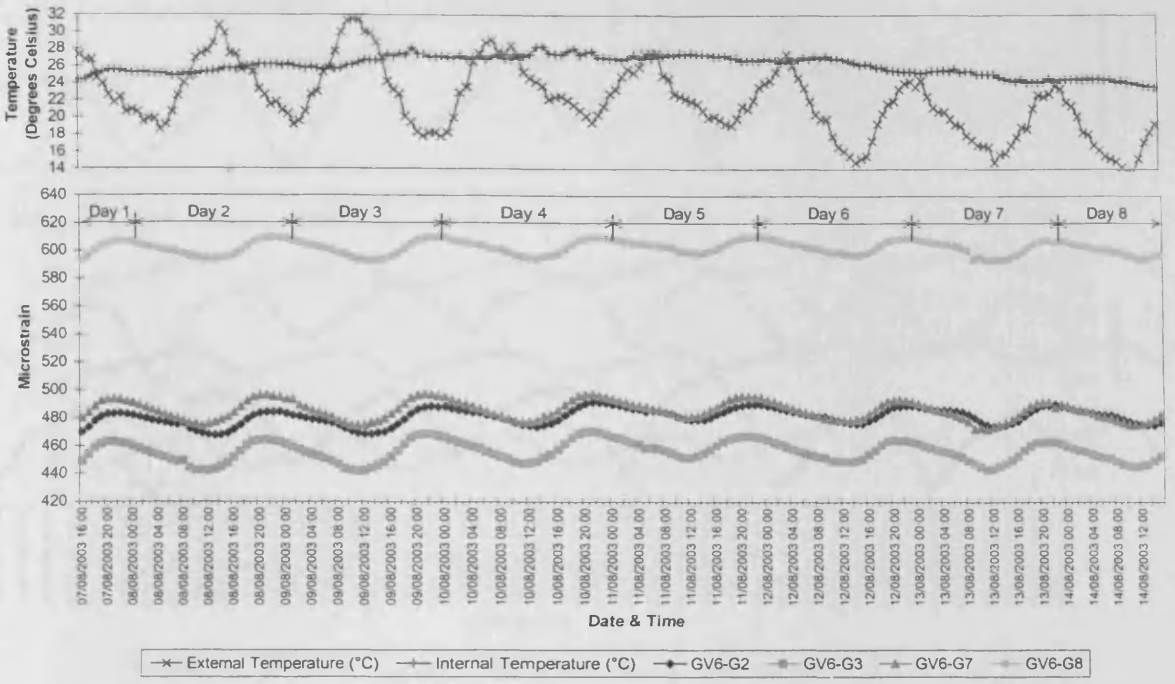

Figure E5.11. Comparison between hourly measured strains and hourly external and internal air temperature in the top flange of segment 6, Grangetown Viaduct, Summer 2003.

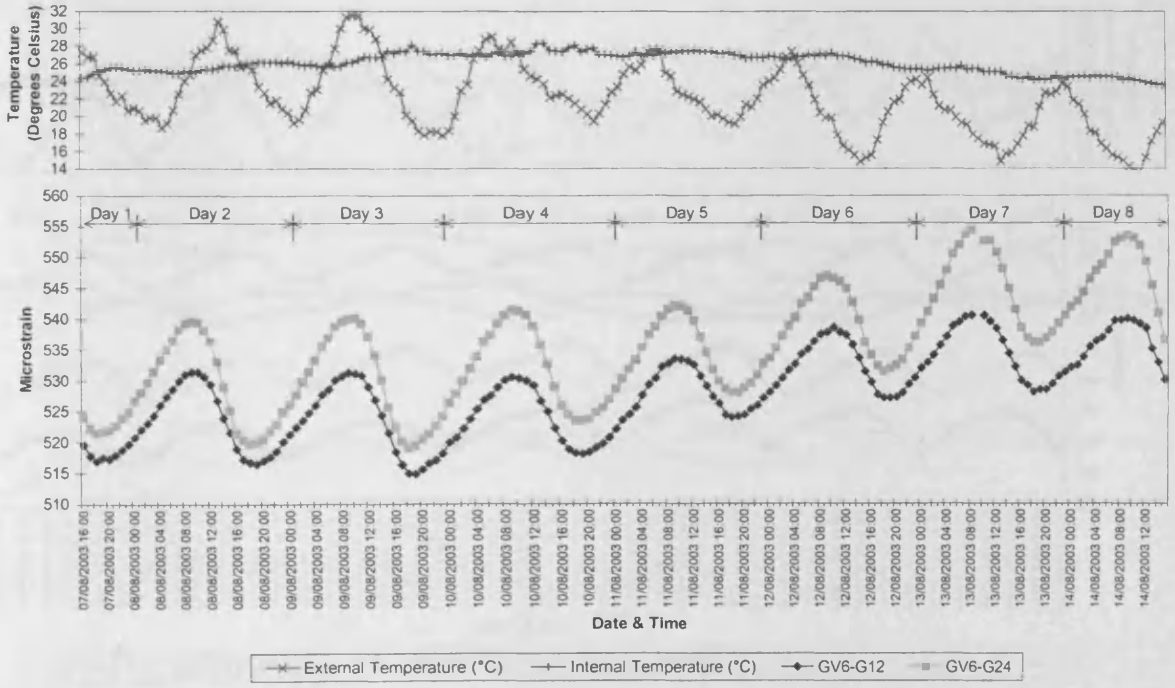

Figure E5.12. Comparison between hourly measured *transverse* strains and hourly external and internal air temperature in the webs of segment 6, Grangetown Viaduct, Summer 2003.

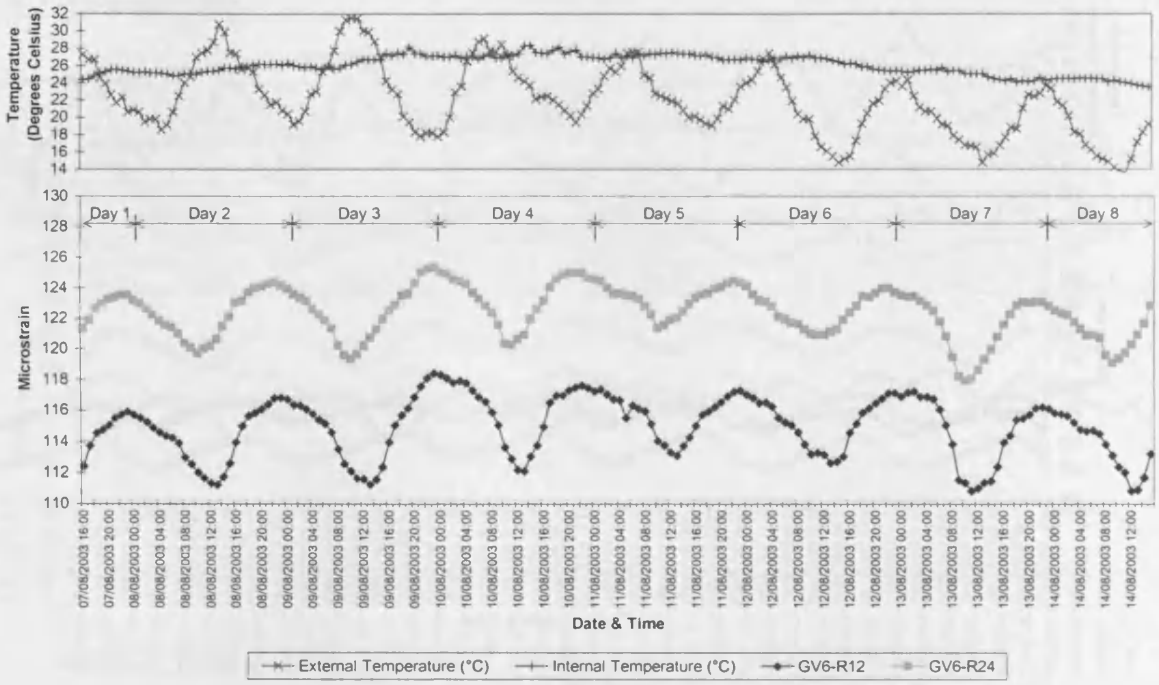

Figure E5.13. Comparison between hourly measured *transverse* strains and hourly external and internal air temperature in the webs of segment 6, Grangetown Viaduct, Summer 2003.

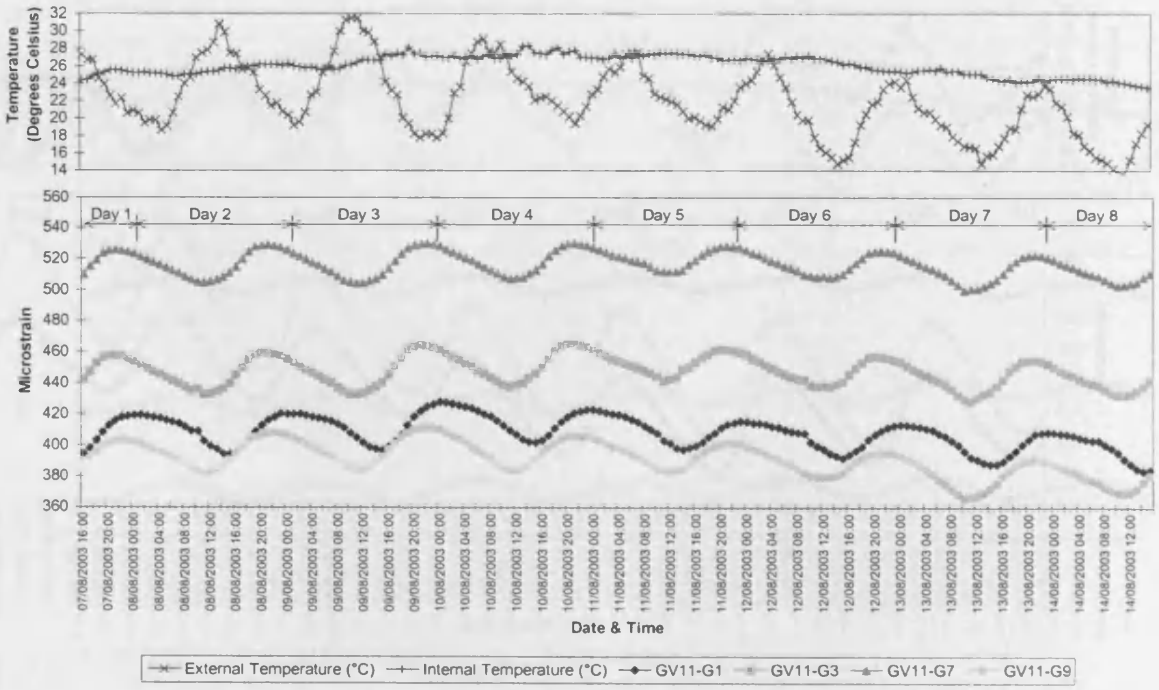

Figure E5.14. Comparison between hourly measured strains and hourly external and internal air temperature in the top flange of segment 12, Grangetown Viaduct, Summer 2003.

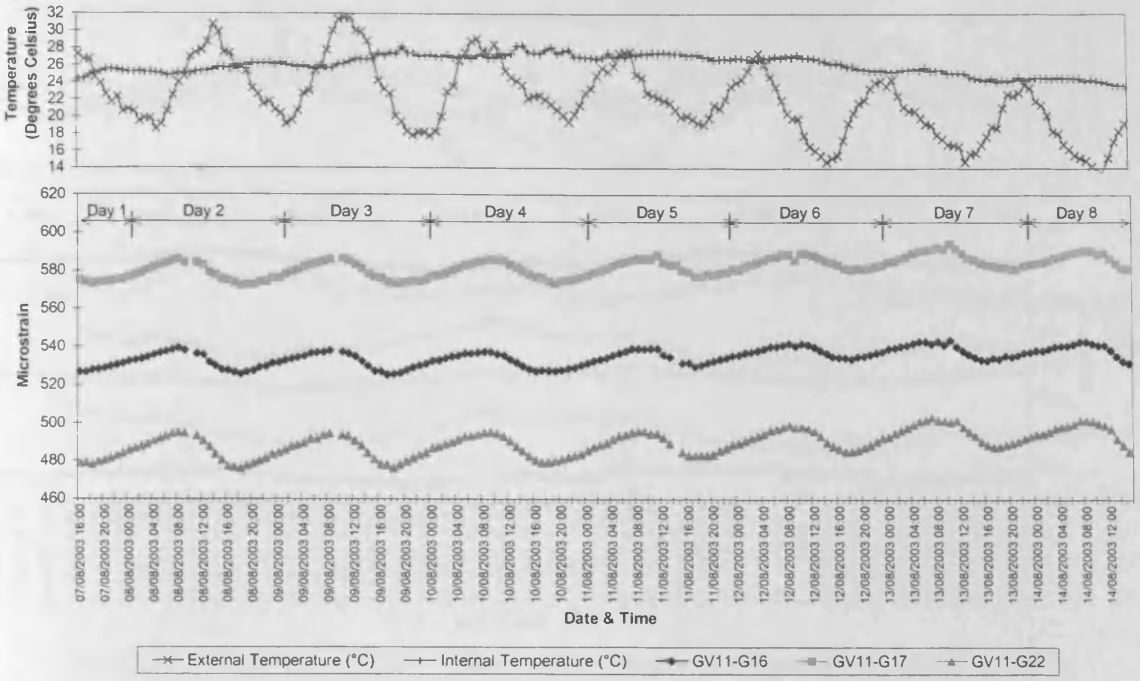

Figure E5.15. Comparison between hourly measured strains and hourly external and internal air temperature in the bottom flange of segment 12, Grangetown Viaduct, Summer 2003.

E5.3 Autumn 2003

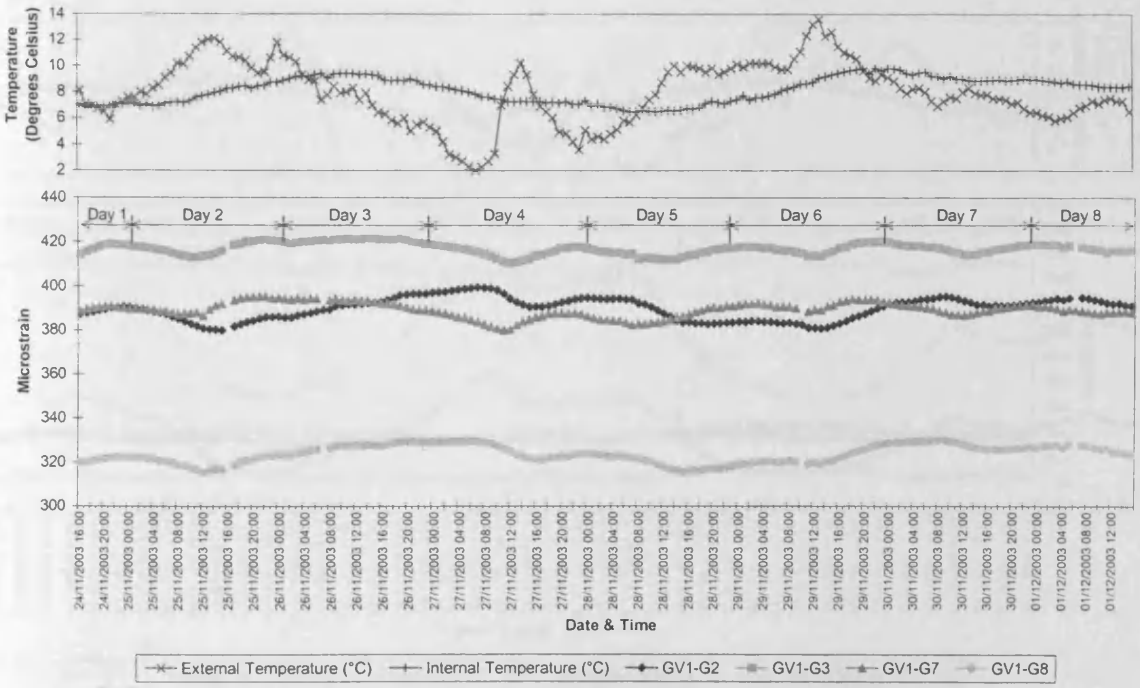

Figure E5.16. Comparison between hourly measured strains and hourly external and internal air temperature in the top flange of segment 1, Grangetown Viaduct, Autumn 2003.

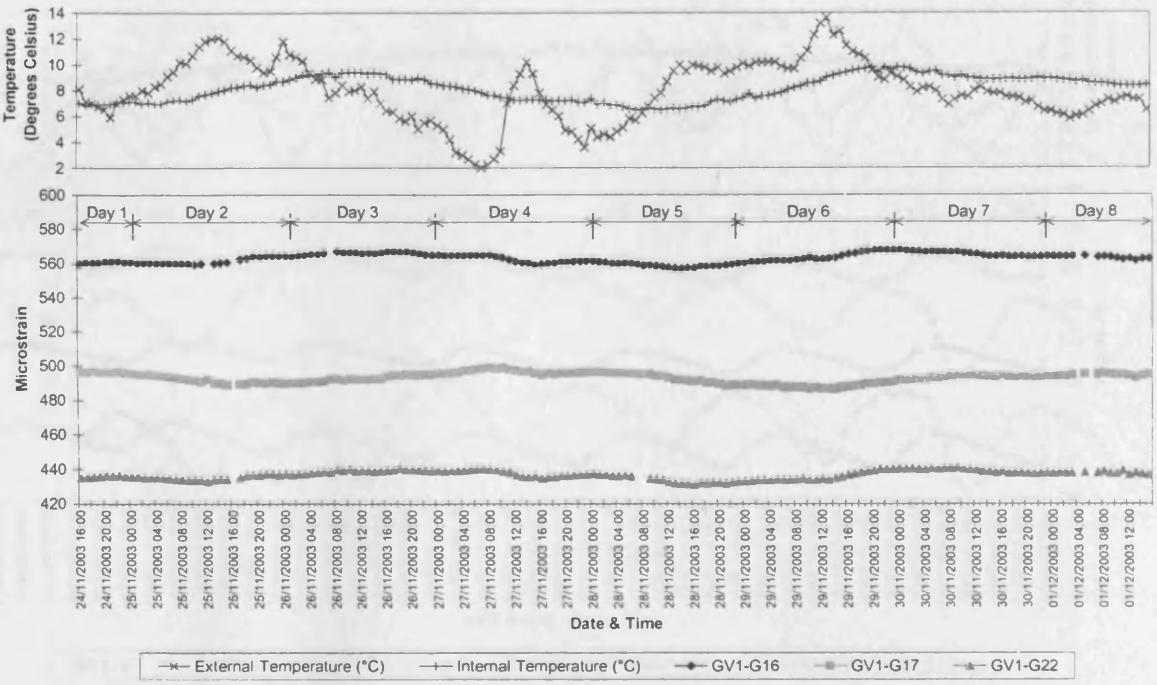

Figure E5.17. Comparison between hourly measured strains and hourly external and internal air temperature in the bottom flange of segment 1, Grangetown Viaduct, Autumn 2003.

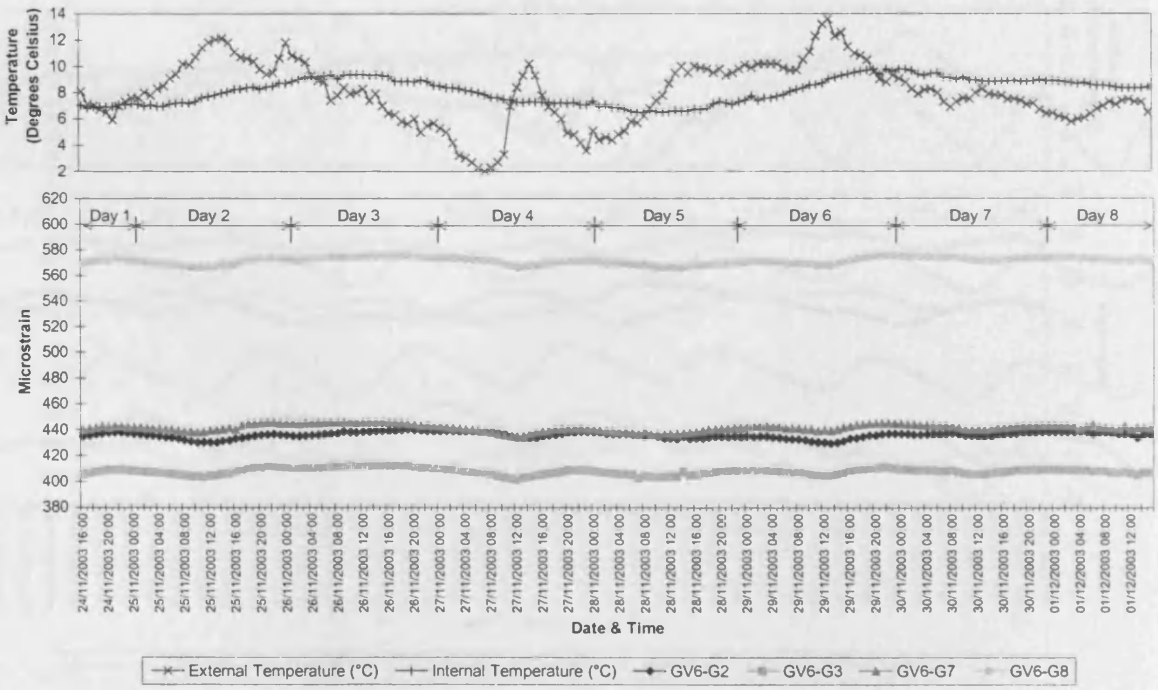

Figure E5.18. Comparison between hourly measured strains and hourly external and internal air temperature in the top flange of segment 6, Grangetown Viaduct, Autumn 2003.

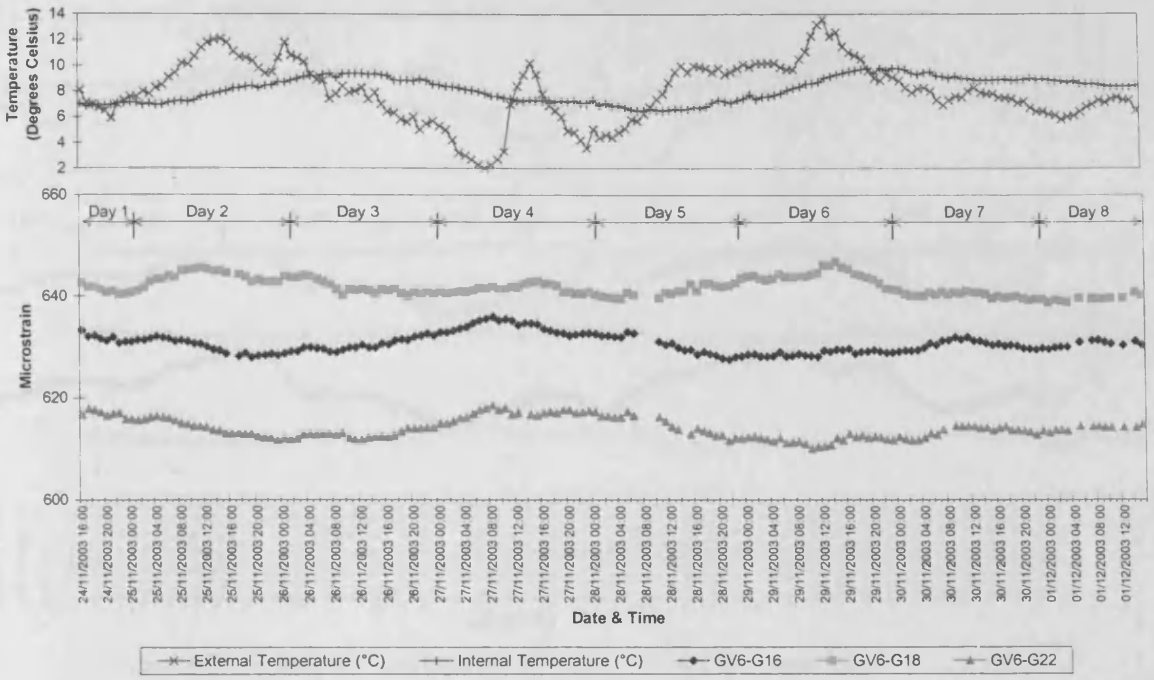

Figure E5.19. Comparison between hourly measured strains and hourly external and internal air temperature in the bottom flange of segment 6, Grangetown Viaduct, Autumn 2003.

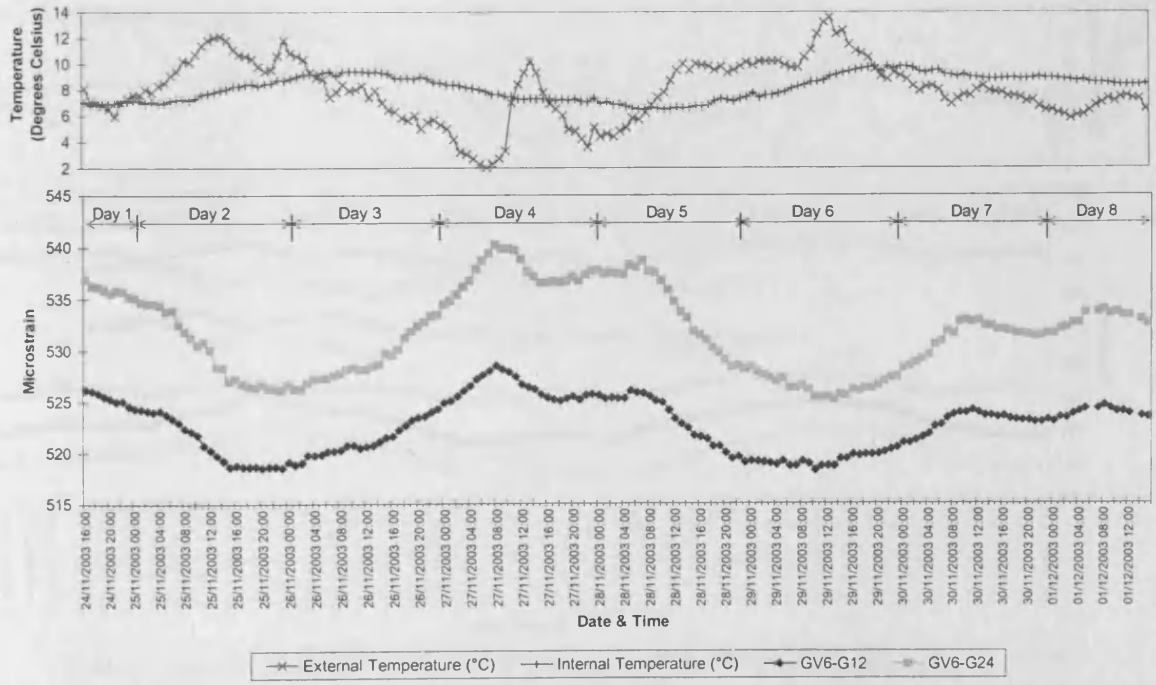

Figure E5.20. Comparison between hourly measured strains and hourly external and internal air temperature in the webs of segment 6, Grangetown Viaduct, Autumn 2003.

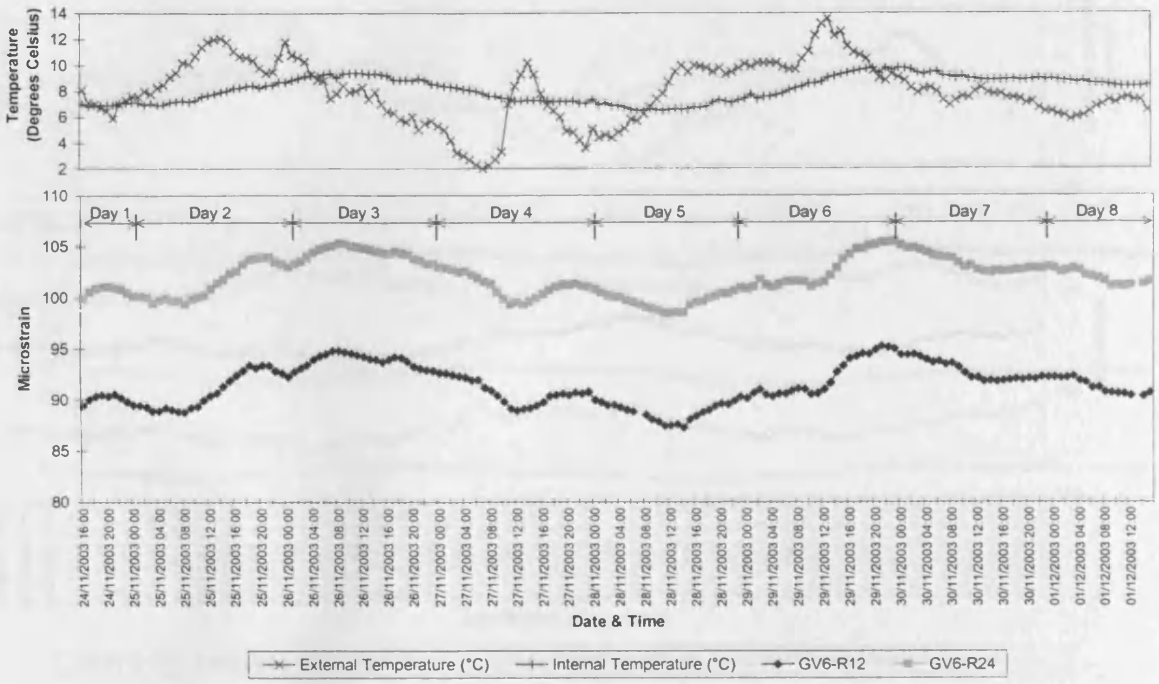

Figure E5.21. Comparison between hourly measured *transverse* strains and hourly external and internal air temperature in the webs of segment 6, Grangetown Viaduct, Autumn 2003.

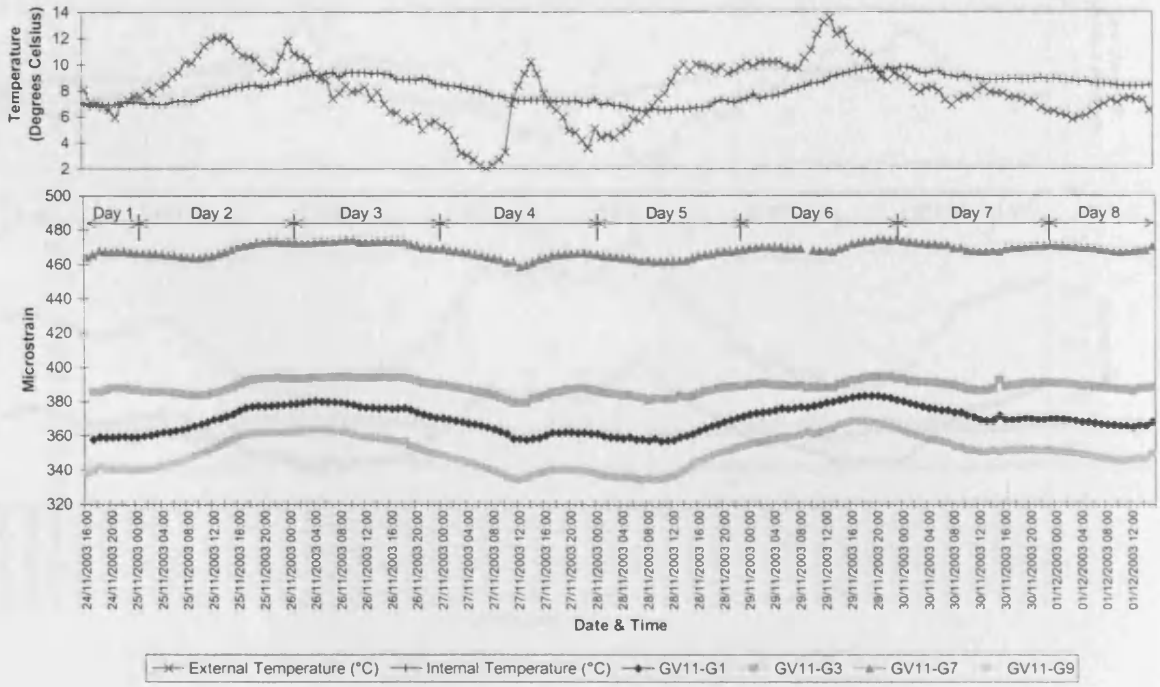

Figure E5.22. Comparison between hourly measured strains and hourly external and internal air temperature in the top flange of segment 12, Grangetown Viaduct, Autumn 2003.

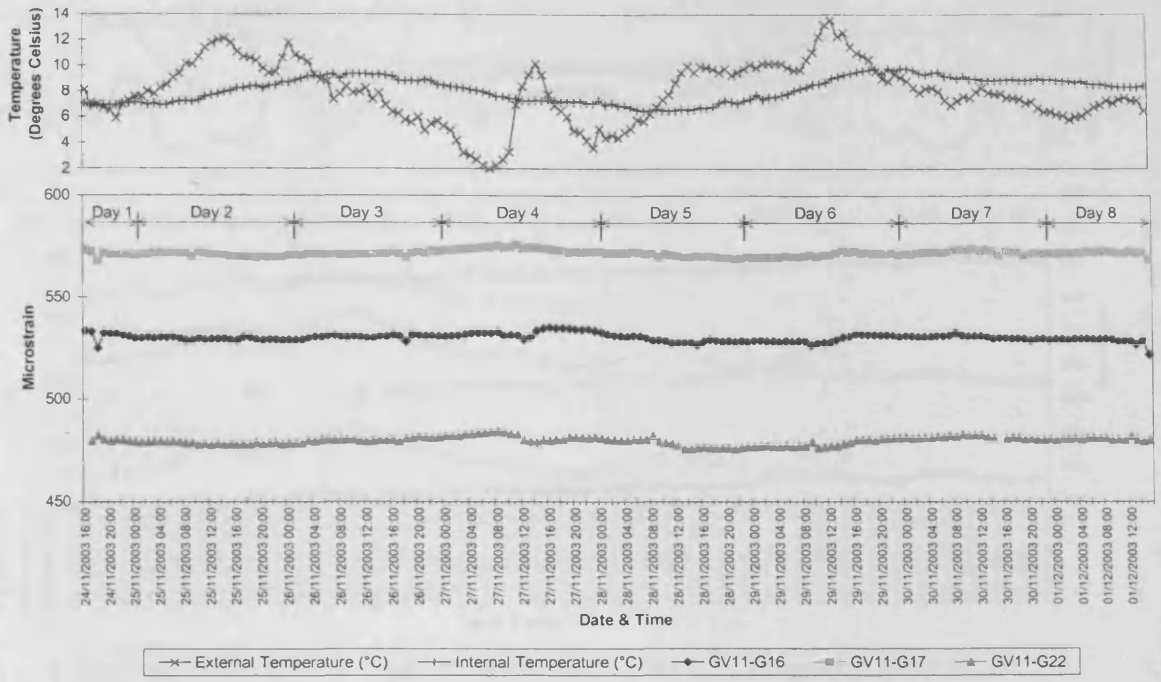

Figure E5.23. Comparison between hourly measured strains and hourly external and internal air temperature in the bottom flange of segment 12, Grangetown Viaduct, Autumn 2003.

E5.4 Winter 2003

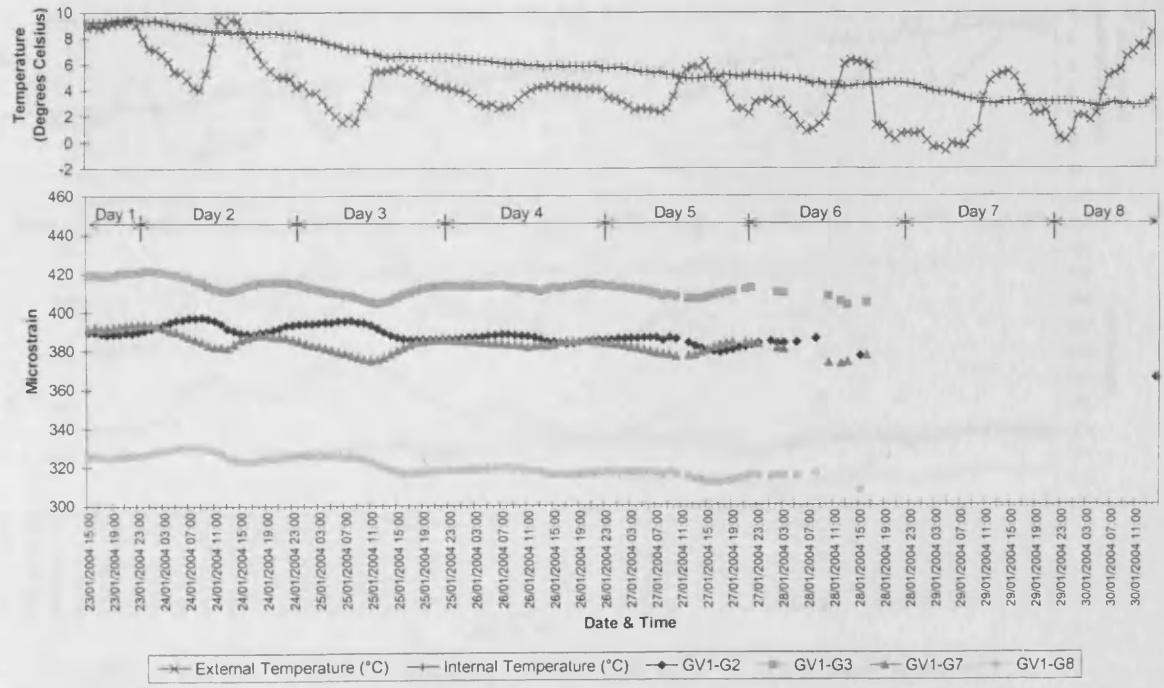

Figure E5.24. Comparison between hourly measured strains and hourly external and internal air temperature in the top flange of segment 1, Grangetown Viaduct, Winter 2003.

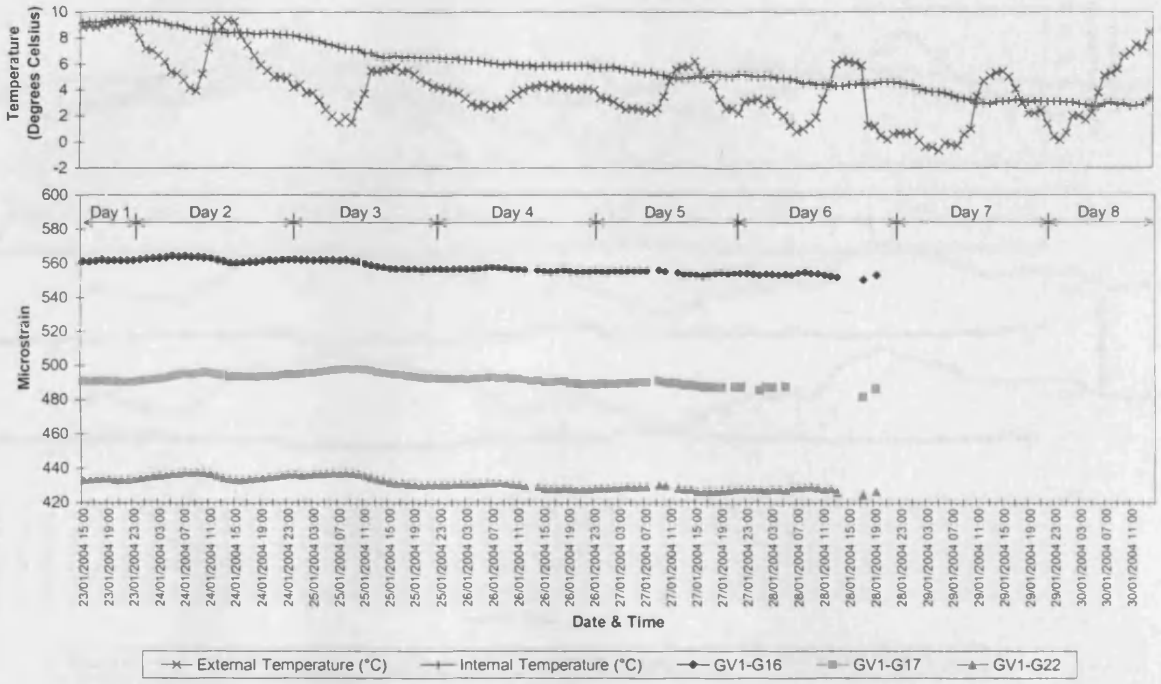

Figure E5.25. Comparison between hourly measured strains and hourly external and internal air temperature in the bottom flange of segment 1, Grangetown Viaduct, Winter 2003.

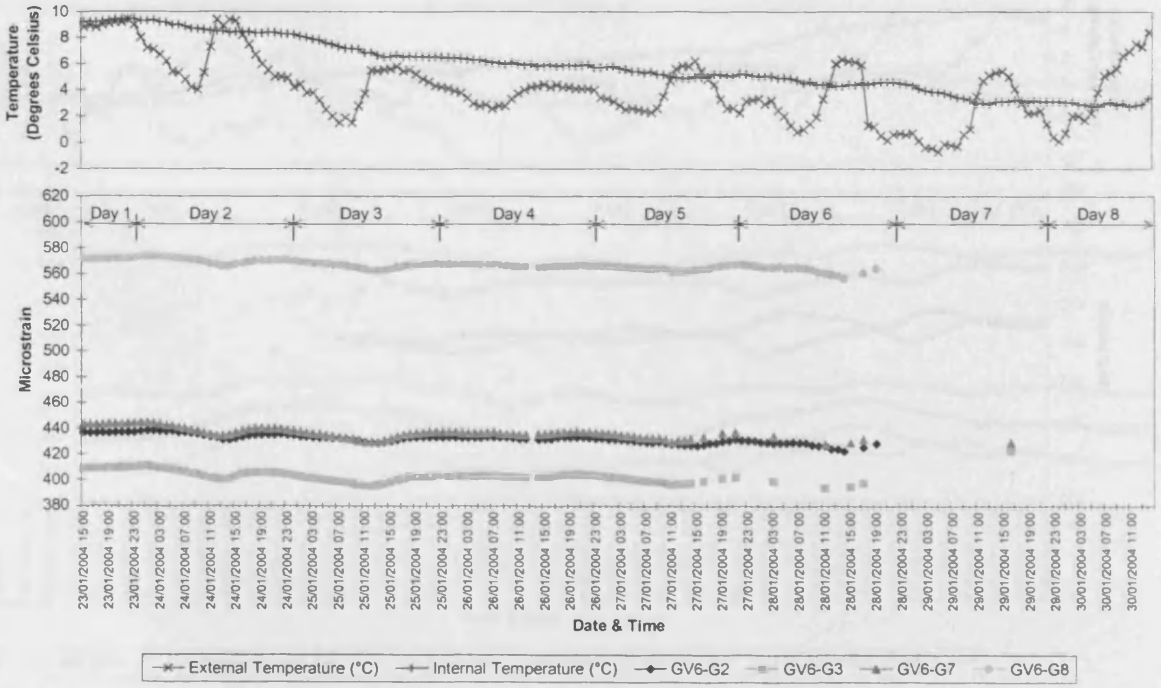

Figure E5.26. Comparison between hourly measured strains and hourly external and internal air temperature in the top flange of segment 6, Grangetown Viaduct, Winter 2003.

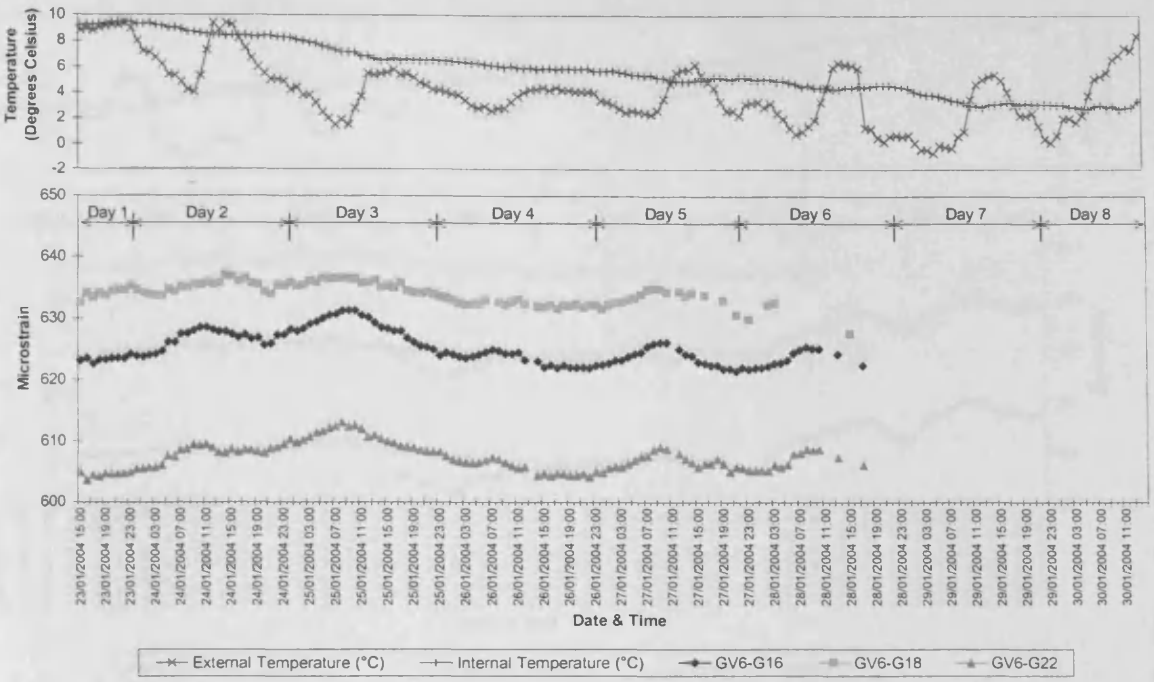

Figure E5.27. Comparison between hourly measured strains and hourly external and internal air temperature in the bottom flange of segment 6, Grangetown Viaduct, Winter 2003.

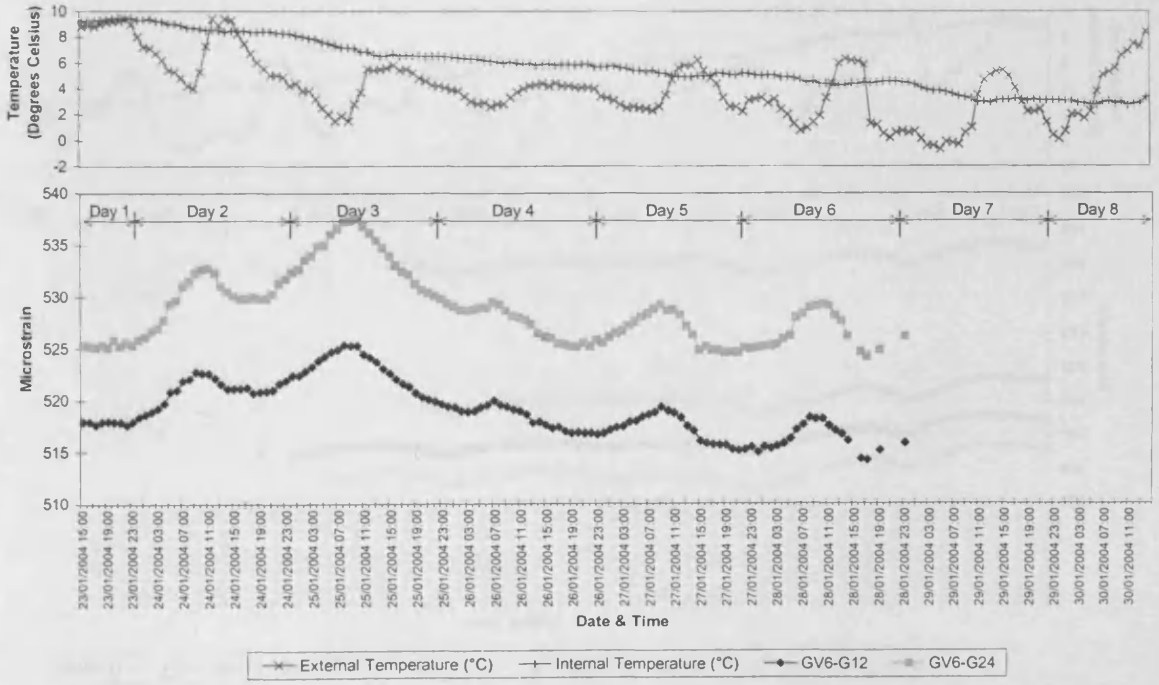

Figure E5.28. Comparison between hourly measured strains and hourly external and internal air temperature in the webs of segment 12, Grangetown Viaduct, Winter 2003.

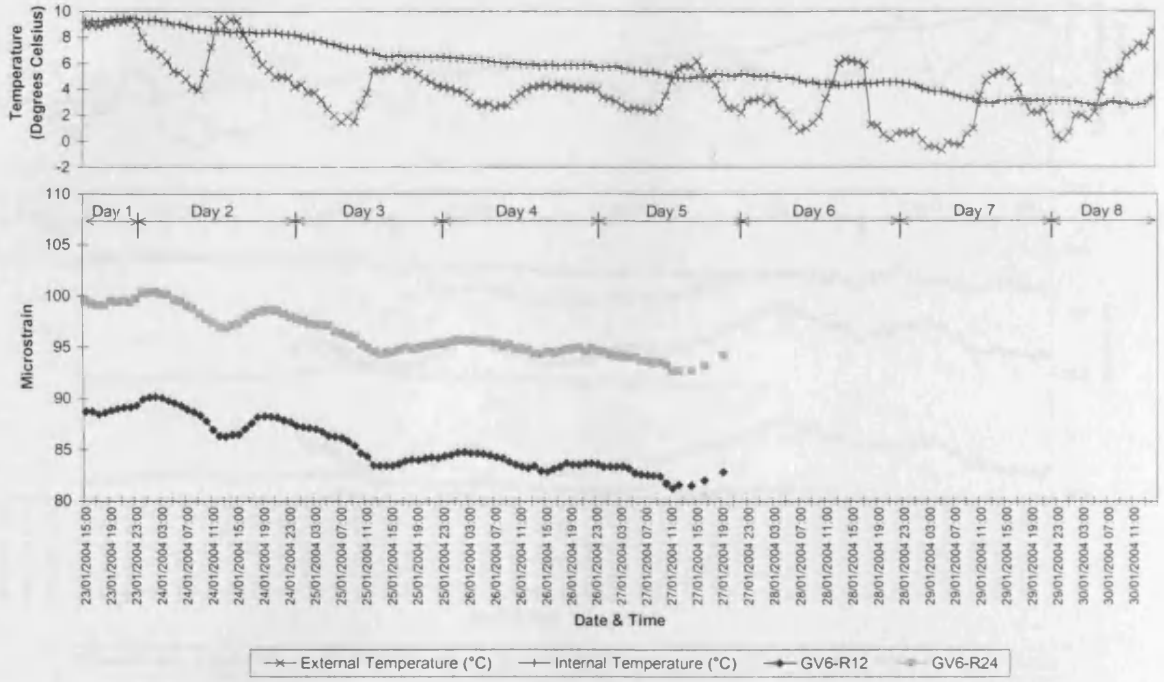

Figure E5.29. Comparison between hourly measured *transverse* strains and hourly external and internal air temperature in the webs of segment 12, Grangetown Viaduct, Winter 2003.

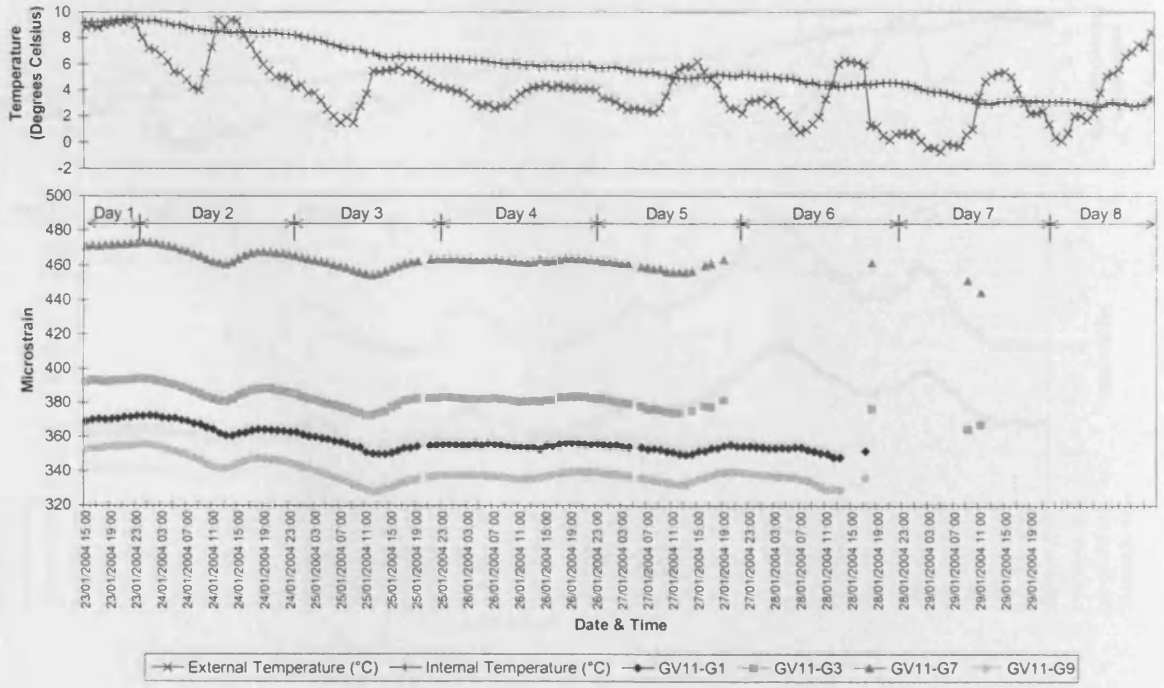

Figure E5.30. Comparison between hourly measured strains and hourly external and internal air temperature in the top flange of segment 12, Grangetown Viaduct, Winter 2003.

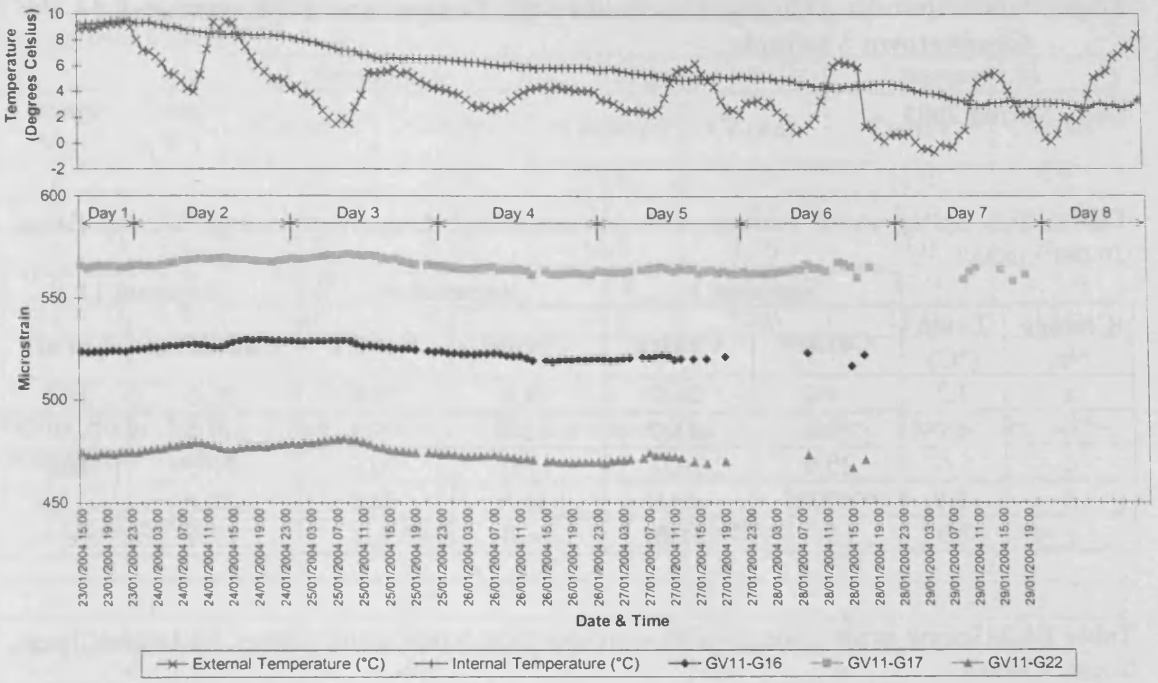

Figure E5.31. Comparison between hourly measured strains and hourly external and internal air temperature in the bottom flange of segment 12, Grangetown Viaduct, Winter 2003.

E6.0 Corresponding Changes in Strain with Temperature – Cogan and Grangetown Viaducts

E6.1. Spring 2003

Table E6.1. Spring strain changes with corresponding temperature change for top flange, Cogan Viaduct

		Segment 1		Segment 6		Segment 12	
Change No.	Temp (°C)	Corner	Centre	Corner	Centre	Cantilever	Corner
a	7.2	19.0	26.0	18.0	10.0	25.0	18.0
b	-8.6	-9.0	-18.0	-11.0	-5.0	-17.0	-7.0
c	5.6	20.0	30.0	17.0	10.0	21.0	20.0
d	-9.0	-16.0	-28.0	-16.0	-9.0	-23.0	-17.0
e	7.9	15.0	25.0	14.0	9.0	17.0	16.0

Table E6.2. Spring strain changes with corresponding temperature change for bottom flange, Cogan Viaduct

		Segment 1		Segment 6		Segment 12	
Change No.	Temp (°C)	Corner	Centre	Corner	Centre	Corner	Centre
a	7.2	21.0	15.0	3.0	8.0	3.0	-
b	-8.6	-22.0	-15.0	-6.0	-15.0	-13.0	-
c	5.6	19.0	14.0	6.0	11.0	6.0	-
d	-9.0	-18.0	-13.0	-6.0	-9.0	-5.0	-
e	7.9	10.0	9.0	5.0	9.0	4.0	-

Table E6.3. Spring strain changes with corresponding temperature change for webs, Cogan Viaduct

		Segment 12	
Change No.	Temp	Longitudinal	Transverse
a	7.2	-7.0	7.0
b	-8.6	-15.0	-3.0
c	5.6	15.0	5.0
d	-9.0	-10.0	-7.0
e	7.9	9.0	6.0

Table E6.4. Spring strain changes with corresponding temperature change for top flange, Grangetown Viaduct

		Segment 1		Segment 6		Segment 11	
Change No.	Temp (°C)	Corner	Centre	Corner	Centre	Cantilever	Centre
a	7.2	37.0	26.0	17.0	24.0	26.0	29.0
b	-8.6	-11.0	-15.0	-8.0	-15.0	-18.0	-19.0
c	5.6	-18.0	32.0	24.0	32.0	20.0	39.0
d	-9.0	29.0	-28.0	-21.0	-28.0	-21.0	-35.0
e	7.9	-21.0	23.0	19.0	22.0	19.0	27.0

Table E6.5. Spring strain changes with corresponding temperature change for bottom flange, Grangetown Viaduct

		Segment 1		Segment 6		Segment 11	
Change No.	Temp (°C)	Corner	Centre	Corner	Corner	Centre	Corner
a	7.2	11.0	10.0	10.0	5.0	11.0	9.0
b	-8.6	-15.0	-13.0	-21.0	-17.0	-20.0	-18.0
c	5.6	12.0	13.0	16.0	11.0	13.0	14.0
d	-9.0	-12.0	-11.0	-13.0	-8.0	-11.0	-11.0
e	7.9	9.0	10.0	14.0	10.0	11.0	12.0

Table E6.6. Spring strain changes with corresponding temperature change for webs, Grangetown Viaduct

		Segment 6	
Change No.	Temp	Longitudinal	Transverse
a	7.2	12.0	7.0
b	-8.6	-21.0	-4.0
c	5.6	20.0	7.0
d	-9.0	-14.0	-8.0
e	7.9	13.0	7.0

E6.2 Summer 2003

Table E6.8. Summer strain changes with corresponding temperature change for top flange, Cogan Viaduct

		Segment 1		Segment 6		Segment 12	
Change No.	Temp (°C)	Corner	Centre	Corner	Centre	Cantilever	Corner
a	12.2	17.0	25.0	16.0	6.0	24.0	17.0
b	-11.6	-18.0	-30.0	-14.0	-7.0	-20.0	-15.0
c	12.3	23.0	32.0	18.0	10.0	26.0	19.0
d	8.3	21.0	21.0	14.0	9.0	17.0	16.0
e	-12.6	-18.0	-27.0	-17.0	-7.0	-25.0	-17.0

Table E6.9. Summer strain changes with corresponding temperature change for bottom flange, Cogan Viaduct

		Segment 1		Segment 6		Segment 12	
Change No.	Temp (°C)	Corner	Centre	Corner	Centre	Corner	Centre
a	12.2	18.0	14.0	8.0	11.0	8.0	-
b	-11.6	-19.0	-18.0	-8.0	-13.0	-7.0	-
c	12.3	20.0	21.0	9.0	14.0	10.0	-
d	8.3	11.0	18.0	6.0	12.0	7.0	-
e	-12.6	-17.0	-14.0	-6.0	-8.0	-4.0	-

Table E6.10. Summer strain changes with corresponding temperature change for webs, Cogan Viaduct

		Segment 12	
Change No.	**Temp**	**Longitudinal**	**Transverse**
a	12.2	15.0	6.0
b	-11.6	-15.0	-5.0
c	12.3	18.0	7.0
d	8.3	16.0	6.0
e	-12.6	-13.0	-7.0

Table E6.11. Summer strain changes with corresponding temperature change for top flange, Grangetown Viaduct

		Segment 1		Segment 6		Segment 11	
Change No.	**Temp (°C)**	**Corner**	**Centre**	**Corner**	**Centre**	**Cantilever**	**Centre**
a	12.2	22.0	22.0	16.0	21.0	22.0	25.0
b	-11.6	-22.0	-22.0	-16.0	-21.0	-20.0	-26.0
c	12.3	26.0	24.0	18.0	23.0	26.0	29.0
d	8.3	21.0	17.0	11.0	15.0	16.0	19.0
e	-12.6	-24.0	-23.0	-14.0	-22.0	-24.0	-27.0

Table E6.12. Summer strain changes with corresponding temperature change for bottom flange, Grangetown Viaduct

		Segment 1		Segment 6		Segment 11	
Change No.	**Temp (°C)**	**Corner**	**Centre**	**Corner**	**Corner**	**Centre**	**Corner**
a	12.2	11.0	12.0	17.0	11.0	15.0	14.0
b	-11.6	-12.0	-13.0	-17.0	-10.0	-15.0	-13.0
c	12.3	14.0	15.0	16.0	8.0	14.0	13.0
d	8.3	11.0	13.0	17.0	8.0	12.0	12.0
e	-12.6	-13.0	-12.0	-14.0	-8.0	-11.0	-12.0

Table E6.13. Summer strain changes with corresponding temperature change for webs, Grangetown Viaduct

		Segment 6	
Change No.	**Temp**	**Longitudinal**	**Transverse**
a	12.2	18.0	5.0
b	-11.6	-19.0	-5.0
c	12.3	19.0	6.0
d	8.3	17.0	4.0
e	-12.6	-15.0	-7.0

E6.3 Autumn 2003

Table E6.14. Autumn strain changes with corresponding temperature change for top flange, Cogan Viaduct

		Segment 1		Segment 6		Segment 12	
Change No.	Temp (°C)	Corner	Centre	Corner	Centre	Cantilever	Corner
a	6.2	5.0	8.0	8.0	2.0	19.0	7.0
b	8.2	5.0	7.0	4.0	3.0	6.0	6.0
c	-6.6	-9.0	-3.0	-4.0	-3.0	-6.0	-7.0
d	3.9	13.0	5.0	6.0	3.0	7.0	9.0
e	-6.7	-2.0	-3.0	-5.0	-3.0	-12.0	-3.0

Table E6.15. Autumn strain changes with corresponding temperature change for bottom flange, Cogan Viaduct

		Segment 1		Segment 6		Segment 12	
Change No.	Temp (°C)	Corner	Centre	Corner	Centre	Corner	Centre
a	6.2	11.0	6.0	4.0	2.0	5.0	-
b	8.2	5.0	4.0	3.0	2.0	5.0	-
c	-6.6	-7.0	-5.0	-3.0	-4.0	-3.0	-
d	3.9	6.0	9.0	4.0	2.0	3.0	-
e	-6.7	-2.0	0.0	-3.0	-2.0	-3.0	-

Table E6.16. Autumn strain changes with corresponding temperature change for webs, Cogan Viaduct

		Segment 12	
Change No.	Temp	Longitudinal	Transverse
a	6.2	4.0	5.0
b	8.2	2.0	2.0
c	-6.6	-1.0	-3.0
d	3.9	6.0	6.0
e	-6.7	0.0	-2.0

Table E6.17. Autumn strain changes with corresponding temperature change for top flange, Grangetown Viaduct

		Segment 1		Segment 6		Segment 11	
Change No.	Temp (°C)	Corner	Centre	Corner	Centre	Cantilever	Centre
a	6.2	6.0	5.0	6.0	7.0	20.0	10.0
b	8.2	3.0	6.0	5.0	7.0	5.0	8.0
c	-6.6	-9.0	-6.0	-6.0	-5.0	-6.0	-6.0
d	3.9	12.0	6.0	8.0	6.0	6.0	6.0
e	-6.7	-4.0	-6.0	-3.0	-5.0	-16.0	-7.0

Table E6.18. Autumn strain changes with corresponding temperature change for bottom flange, Grangetown Viaduct

		Segment 1		Segment 6		Segment 11	
Change No.	Temp (°C)	Corner	Centre	Corner	Corner	Centre	Corner
a	6.2	3.0	3.0	1.0	5.0	1.0	2.0
b	8.2	2.0	2.0	1.0	2.0	3.0	2.0
c	-6.6	-5.0	-8.0	-5.0	-4.0	-3.0	-4.0
d	3.9	6.0	8.0	3.0	3.0	4.0	3.0
e	-6.7	-4.0	-3.0	-2.0	-7.0	0.0	-2.0

Table E6.19. Autumn strain changes with corresponding temperature change for webs, Grangetown Viaduct

		Segment 6	
Change No.	Temp	Longitudinal	Transverse
a	6.2	3.0	5.0
b	8.2	1.0	2.0
c	-6.6	-8.0	-3.0
d	3.9	5.0	4.0
e	-6.7	-1.0	-3.0

E6.4 Winter 2003

Table E6.20. Winter strain changes with corresponding temperature change for top flange, Cogan Viaduct

		Segment 1		Segment 6		Segment 12	
Change No.	Temp (°C)	Corner	Centre	Corner	Centre	Cantilever	Corner
a	-5.4	8.0	7.0	5.0	4.0	4.0	7.0
b	4.9	-7.0	-12.0	-8.0	-4.0	-16.0	-8.0
c	-7.4	1.0	11.0	3.0	2.0	5.0	2.0
d	-5.4	-10.0	-11.0	-7.0	-7.0	-9.0	-10.0
e	5.5	10.0	8.0	7.0	6.0	11.0	8.0

Table E6.21. Winter strain changes with corresponding temperature change for bottom flange, Cogan Viaduct

		Segment 1		Segment 6		Segment 12	
Change No.	Temp (°C)	Corner	Centre	Corner	Centre	Corner	Centre
a	-5.4	5.0	8.0	3.0	5.0	4.0	-
b	4.9	-9.0	-7.0	-4.0	-4.0	-5.0	-
c	-7.4	2.0	0.0	0.0	0.0	-1.0	-
d	-5.4	-7.0	-8.0	-3.0	-4.0	-4.0	-
e	5.5	6.0	7.0	5.0	4.0	7.0	-

Table E6.22. Winter strain changes with corresponding temperature change for webs, Cogan Viaduct

		Segment 12	
Change No.	**Temp**	**Longitudinal**	**Transverse**
a	-5.4	7.0	2.0
b	4.9	-6.0	-5.0
c	-7.4	-3.0	-1.0
d	-5.4	-6.0	-5.0
e	5.5	5.0	4.0

Table E6.23. Winter strain changes with corresponding temperature change for top flange, Grangetown Viaduct

		Segment 1		Segment 6		Segment 11	
Change No.	**Temp (°C)**	**Corner**	**Centre**	**Corner**	**Centre**	**Cantilever**	**Centre**
a	-5.4	4.0	5.0	4.0	6.0	5.0	7.0
b	4.9	-9.0	-12.0	-8.0	-11.0	-17.0	-15.0
c	-7.4	-1.0	8.0	4.0	7.0	-	-
d	-5.4	-8.0	-10.0	-8.0	-8.0	-	-
e	5.5	-	-	-	-	-	-

Table E6.24. Winter strain changes with corresponding temperature change for bottom flange, Grangetown Viaduct

		Segment 1		Segment 6		Segment 11	
Change No.	**Temp (°C)**	**Corner**	**Centre**	**Corner**	**Corner**	**Centre**	**Corner**
a	-5.4	2.0	5.0	5.0	3.0	4.0	3.0
b	4.9	-6.0	-7.0	-7.0	-3.0	-8.0	-7.0
c	-7.4	-2.0	-	-	-	-	-
d	-5.4	-3.0	-	-	-	-	-
e	5.5	-	-	-	-	-	-

Table E6.25. Winter strain changes with corresponding temperature change for webs, Grangetown Viaduct

		Segment 6	
Change No.	**Temp**	**Longitudinal**	**Transverse**
a	-5.4	6.0	1.0
b	4.9	-7.0	-4.0
c	-7.4	-	-
d	-5.4	-	-
e	5.5	-	-

Appendix F

Additional Information For Chapter 7

Contents

F1.0 Comparisons between Measured and Standard Prediction Model Strains – Cogan Viaduct

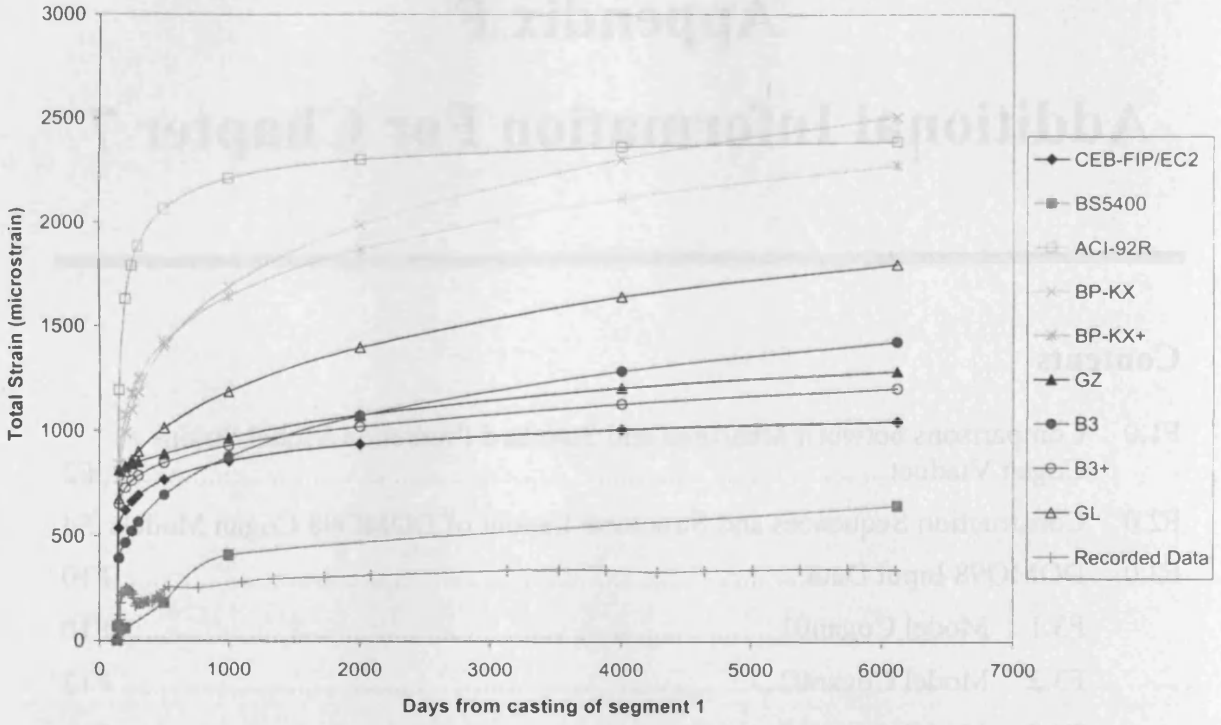

Figure F1.1. Comparison between recorded and predicted strain behaviour in the bottom flange of segment 1, Cogan Viaduct, using standard prediction models.

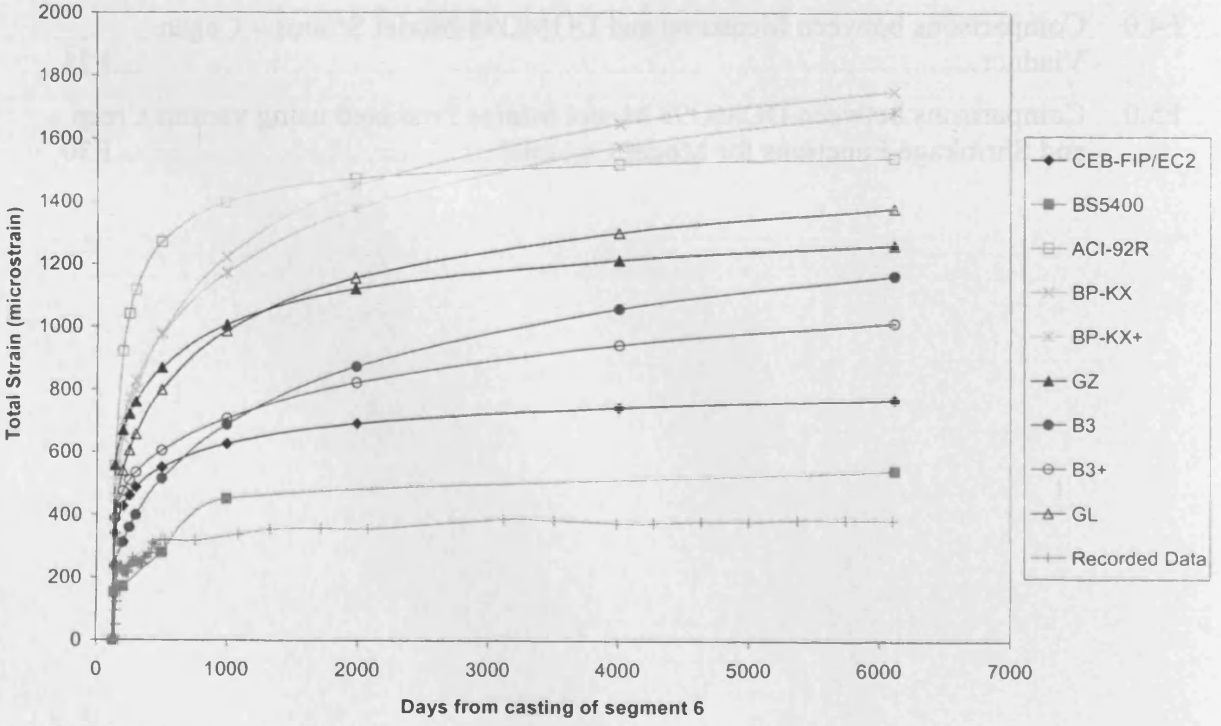

Figure F1.2. Comparison between recorded and predicted strain behaviour in the top flange of segment 6, Cogan Viaduct, using standard prediction models.

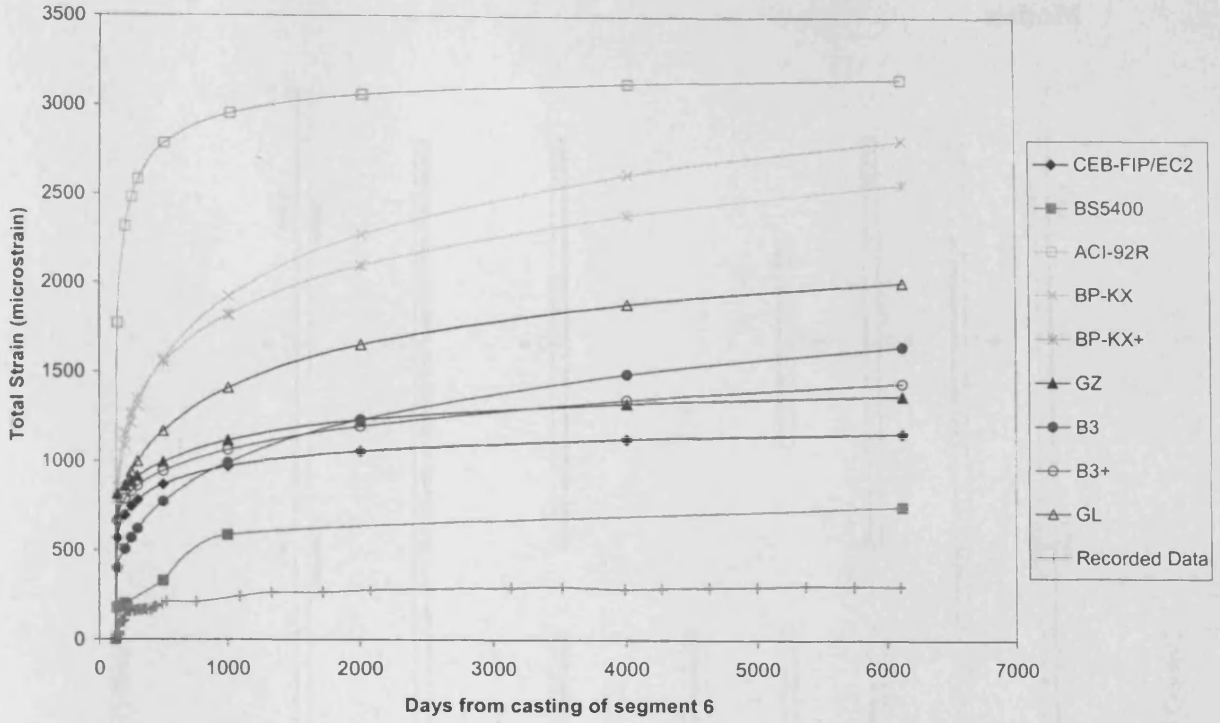

Figure F1.3. Comparison between recorded and predicted strain behaviour in the bottom flange of segment 6, Cogan Viaduct, using standard prediction models.

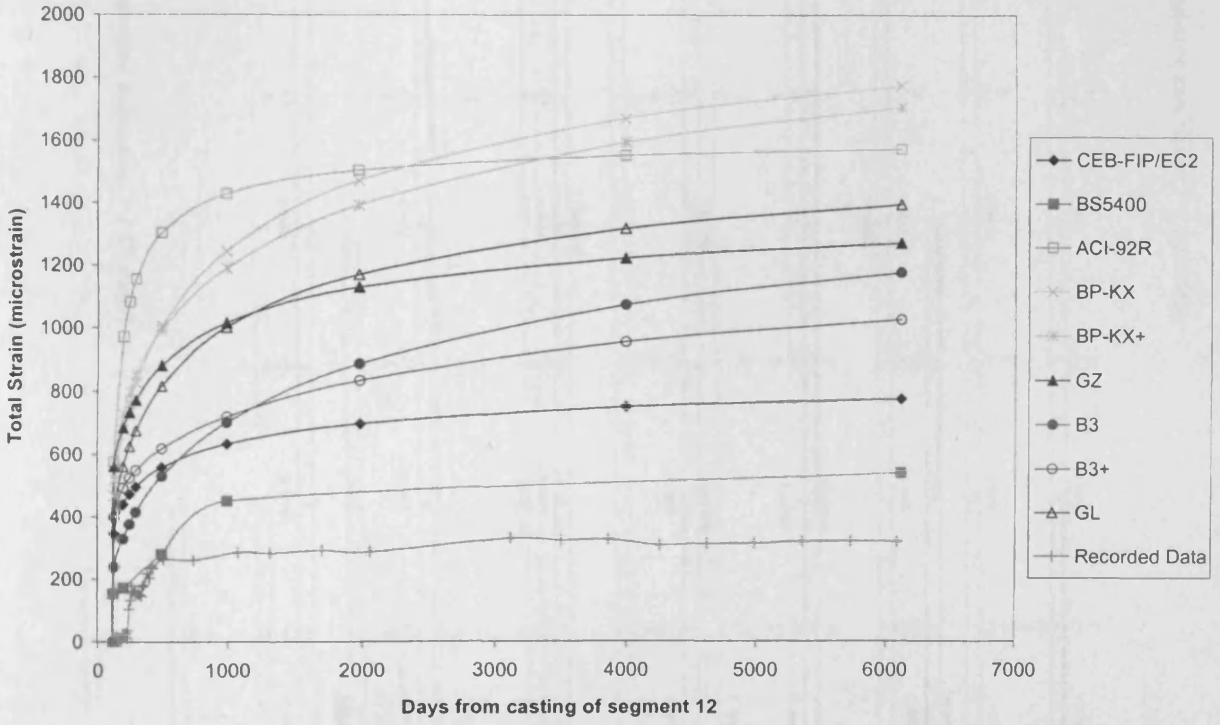

Figure F1.4. Comparison between recorded and predicted strain behaviour in the top flange of segment 12, Cogan Viaduct, using standard prediction models.

F2.0 Construction Sequences and Structural Layout of DOMO98 Cogan Models

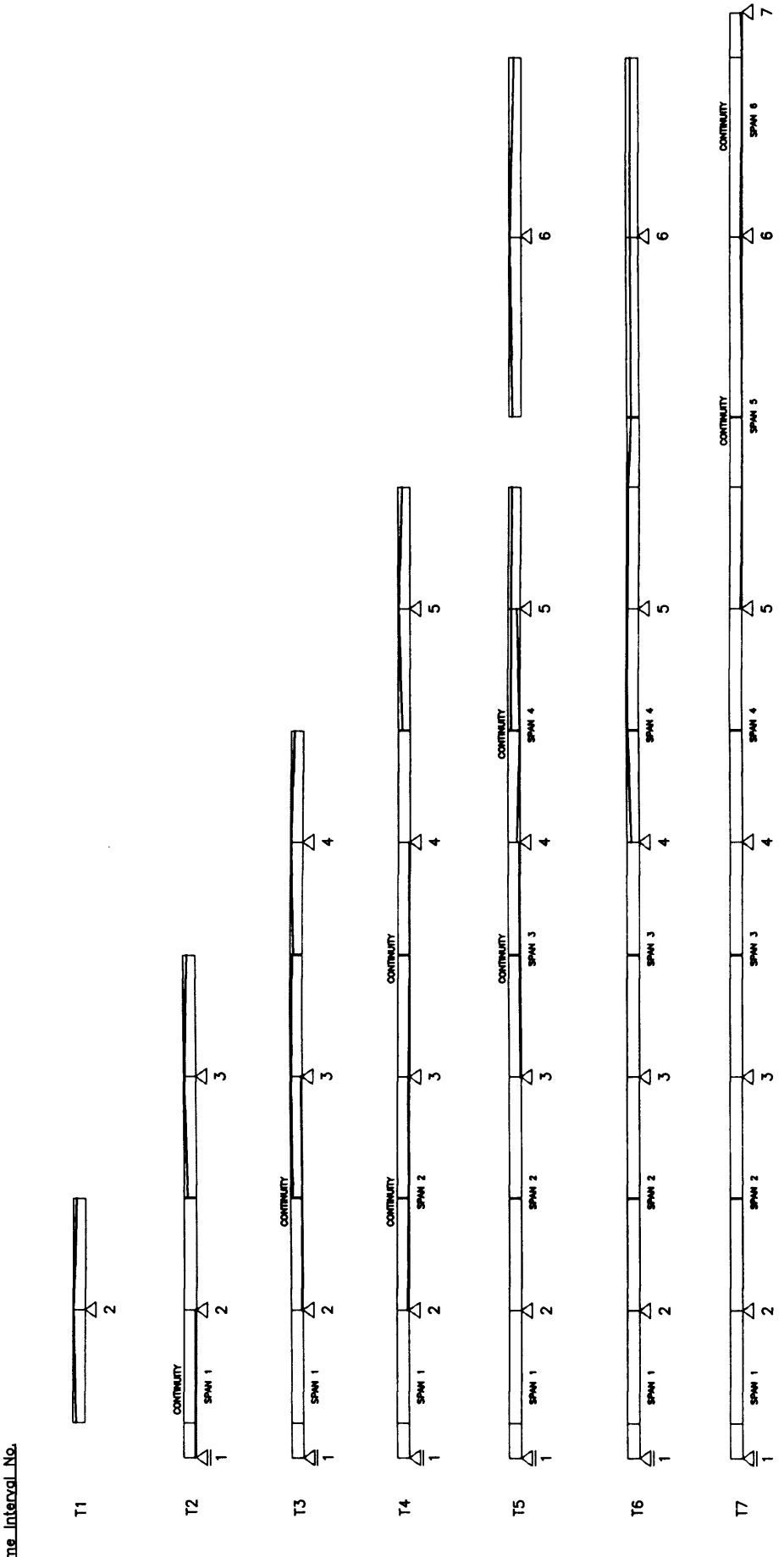

Figure F2.1. Construction Sequence for DOMO98 Model Cogan01.

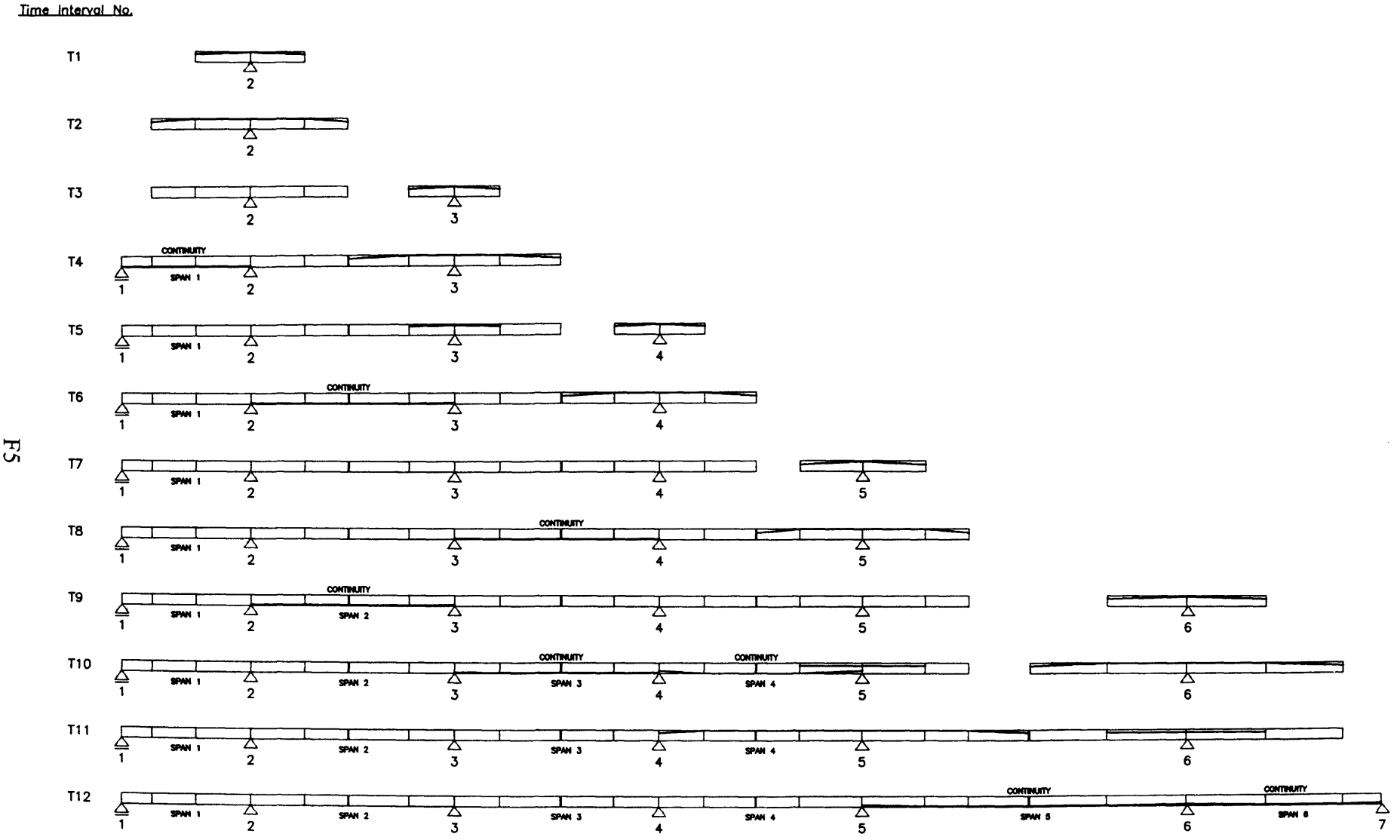

Figure F2.2. Construction Sequence for DOMO98 Model Cogan02.

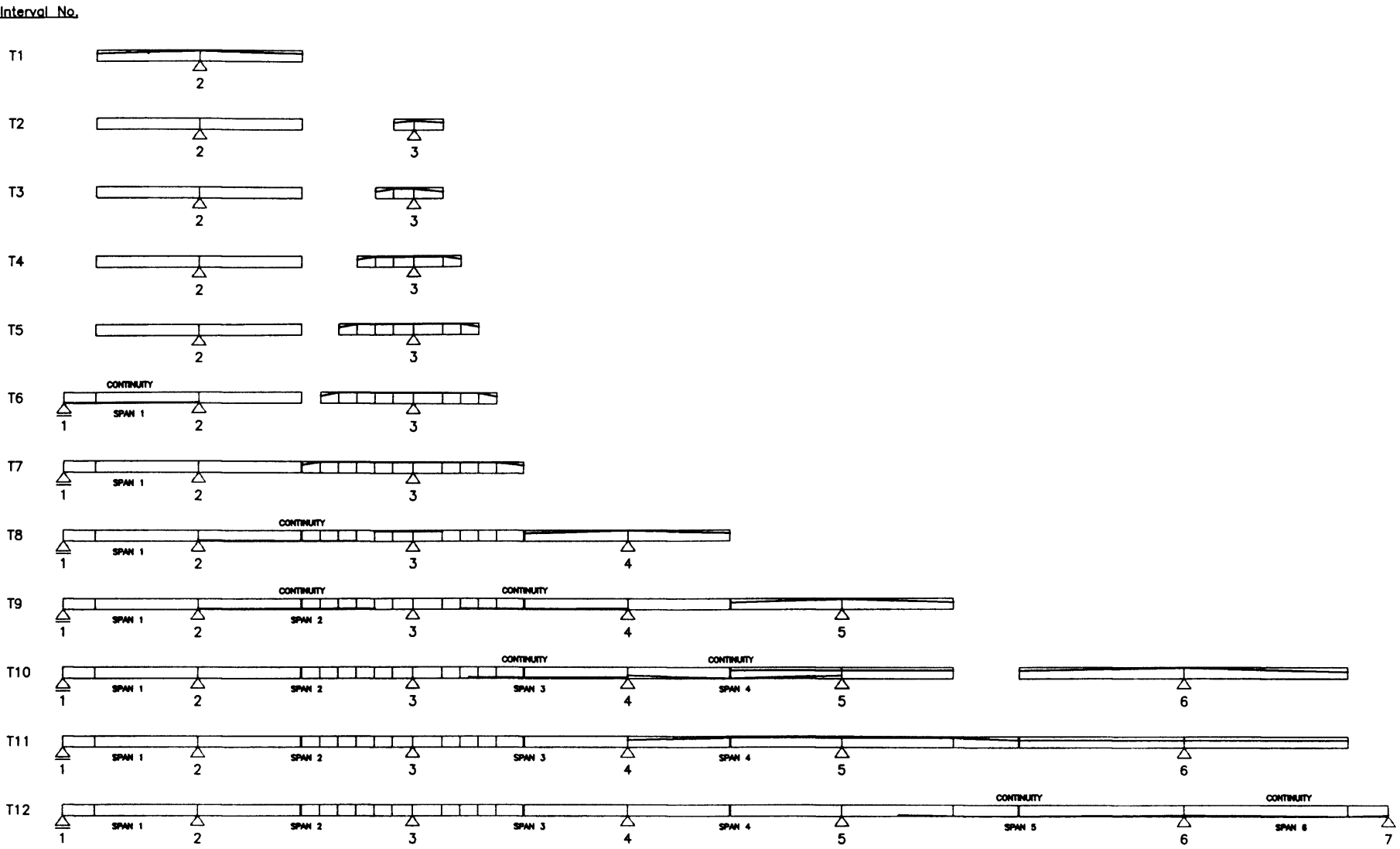

Figure F2.3. Construction Sequence for DOMO98 Model Cogan03.

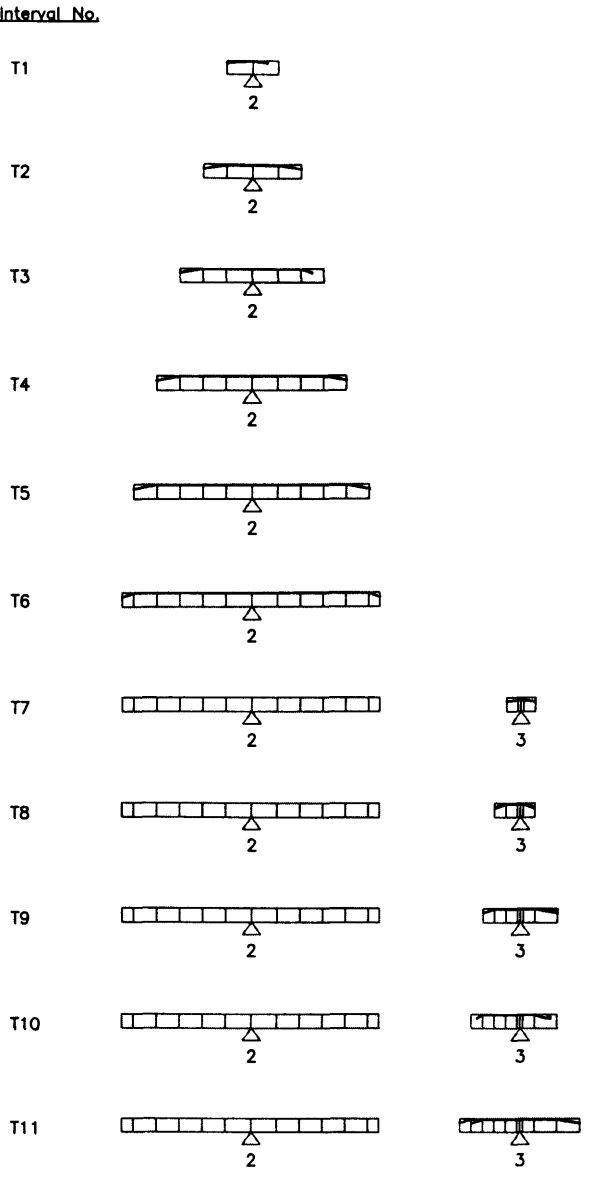

Figure F2.4a. Construction Sequence for DOMO98 Model Cogan04.

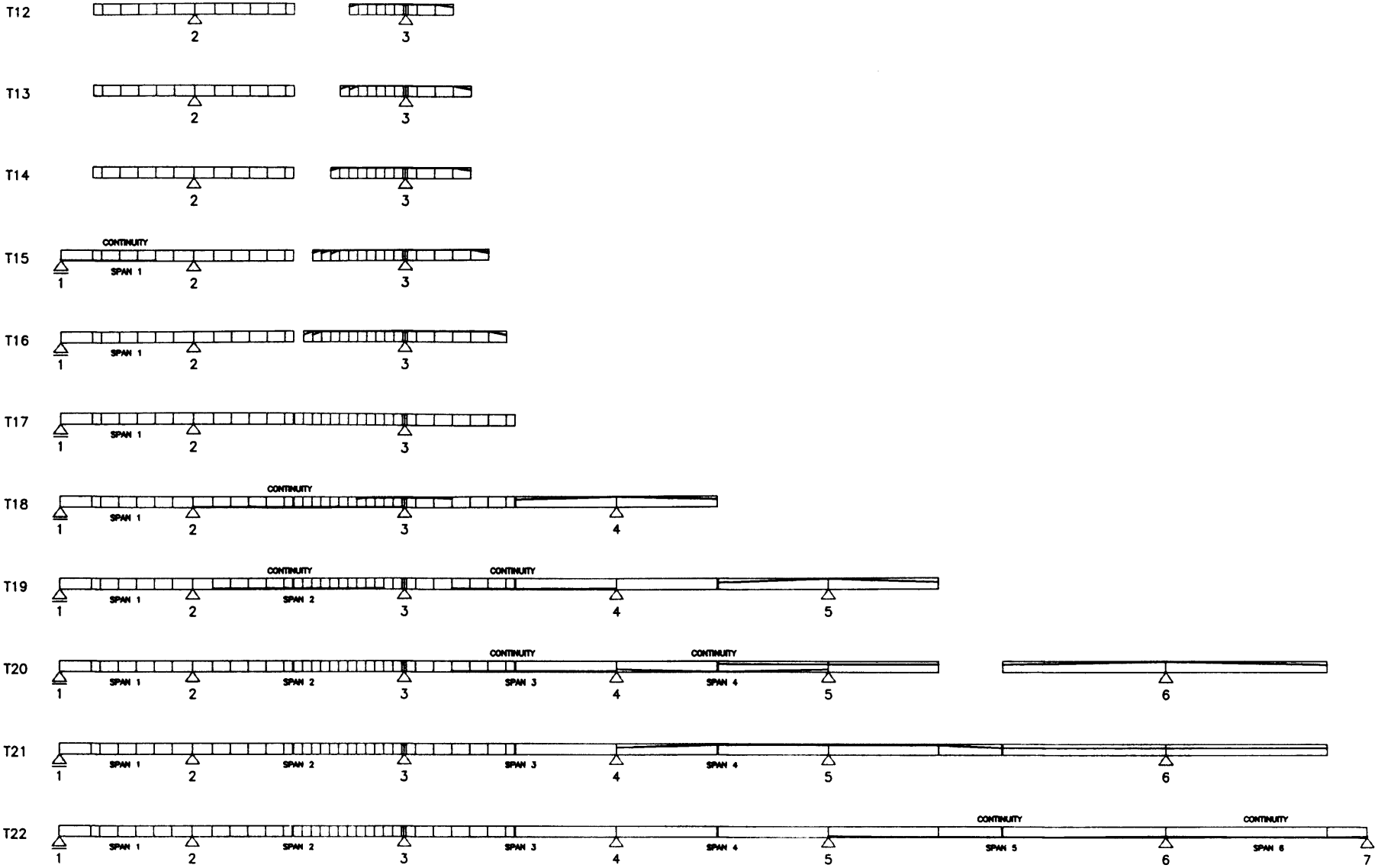

Figure F2.4b. Construction Sequence for DOMO98 Model Cogan04.

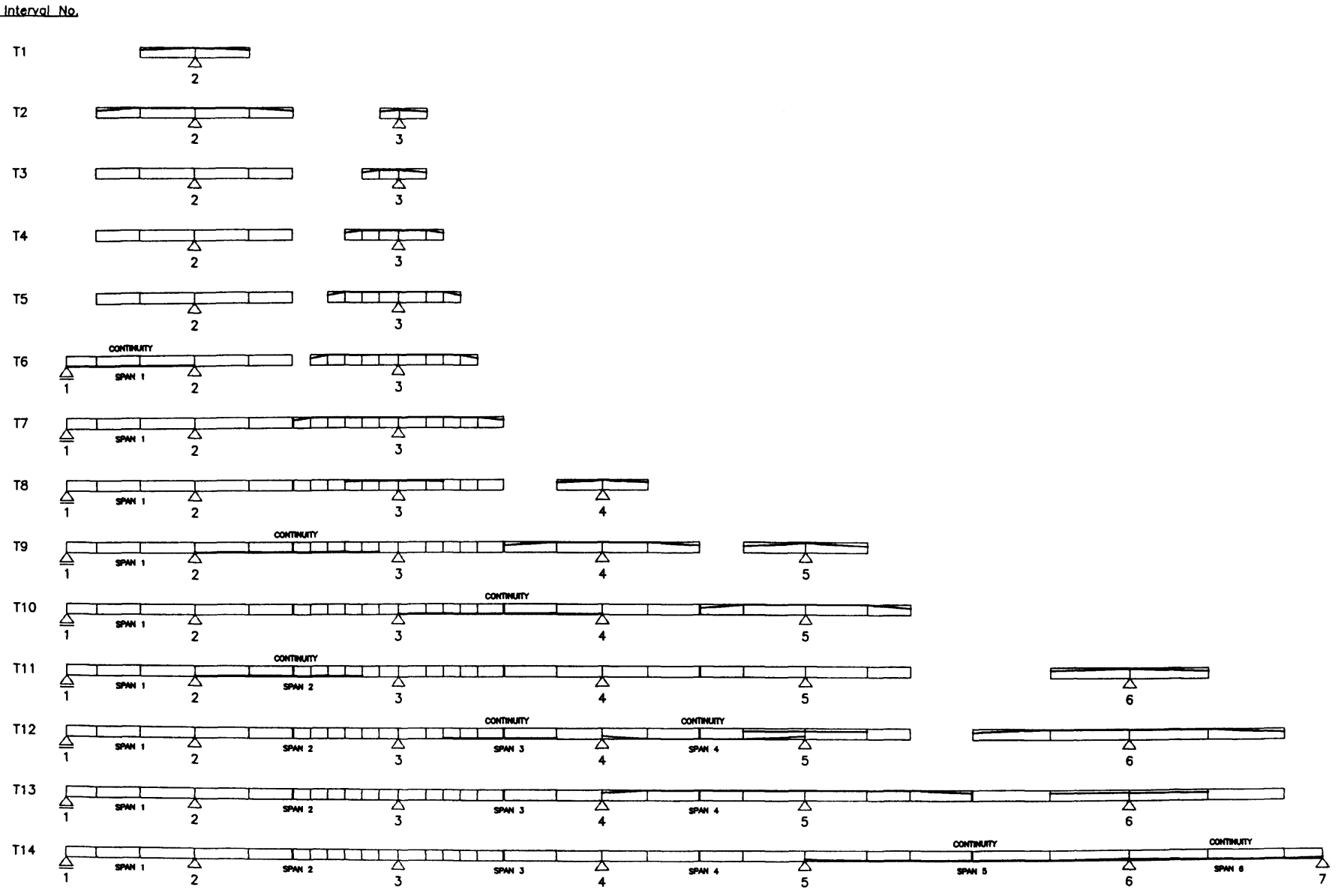

Figure F2.5. Construction Sequence for DOMO98 Model Cogan05.

F3.0 DOMO98 Input Data

F3.1 Model Cogan01

Table F3.1.1. New Prestressing Data for input and use with the DOMO98 Computer Code.

New Domo Cable No.	Prestressing Force (MN)	Cable Cross-Sectional Area (mm^2)	New Eccentricity x_i (m)	New Eccentricity x_j (m)	Cable Start Element	Cable End Element
1	41.588	784.960	0.992	0.353	1	2
2	36.972	784.960	0.966	0.297	4	5
3	18.954	356.800	1.534	1.534	3	1
4	41.181	784.960	0.979	0.353	7	8
5	3.120	71.360	0.836	0.650	4	5
6	11.174	178.400	1.597	1.473	2	4
7	9.837	178.400	1.597	1.473	5	7
8	22.220	463.840	0.942	0.157	10	11
9	14.623	428.160	1.537	1.445	2	4
10	13.864	428.160	1.535	1.459	5	7
11	2.948	107.040	0.370	0.370	10	11
12	9.965	142.720	1.713	0.969	8	10
13	49.271	892.000	0.952	0.291	13	14
14	29.434	428.160	0.979	0.370	8	15
15	1.992	107.040	0.370	0.370	13	14
16	20.373	392.480	1.531	1.221	14	16
17	32.740	749.280	1.530	1.261	11	13

Table F3.1.2. New Time Intervals for input and use with the DOMO98 Computer Code.

Interval No.	Start Time T1	End Time T2	Original Elements Assembled	New Elements Assembled	Continuity Stressing	Cables Stressed
1	329	367	1 - 14	1, 2	Pier 2	1
2	367	386	15, 16, 17 - 37	3, 4, 5	Span 1	2, 3
3	386	423	38 - 51	6, 7, 8	Span 2 - Stage 1	4, 5, 6
4	423	477	52 - 67	9, 10, 11	Span 2 - Stage 2, Span 3 - Stage 1	7, 8, 9
5	477	529	68 - 89	12, 13, 14	Span 3 - Stage 2, Span 4, Pier 5	10, 11, 12, 13
6	529	547	90 - 93	15	Pier 6	14, 15
7	547	650	94 - 96	16, 17	Span 5, Span 6	16, 17
8	650	752	-	-	Dead Load	-
9	752	983	-	-	-	-
10	983	1320	-	-	-	-
11	1320	1575	-	-	-	-
12	1575	1957	-	-	-	-
13	1957	2313	-	-	-	-
14	2313	3528	-	-	-	-
15	3528	6100	-	-	-	-

Table F3.1.3. New Segment Data for input and use with the DOMO98 Computer Code.

New Element No.	Node i	Node j	Element Type	Second Moment of Area, I (mm^4)	Cross-Sectional Area, A (mm^2)	Shear Area A_s (mm^2)	Coefficient of Shear SHE	Eccentricity, y (mm)	Length (m)	Time Cast (days)	Time Erected (days)	Time Interval in which the element becomes active	Element Order (from node 1)
1	2	3	1	8.396	6.876	2.275	3.022	1.142	28.75	131	340	1	3
2	3	4	1	8.396	6.876	2.275	3.022	1.142	28.75	182	340	1	1
3	2	1	1	8.396	6.876	2.275	3.022	1.142	8.75	157	378	2	2
4	5	6	1	8.396	6.876	2.275	3.022	1.142	31.25	228	374	2	6
5	6	7	1	8.396	6.876	2.275	3.022	1.142	31.25	251	375	2	4
6	4	5	1	8.396	6.876	2.275	3.022	1.142	0.3	423	423	3	5
7	8	9	1	8.396	6.876	2.275	3.022	1.142	28.75	305	398	3	9
8	9	10	1	8.396	6.876	2.275	3.022	1.142	28.75	287	398	3	7
9	7	8	1	8.396	6.876	2.275	3.022	1.142	0.3	460	460	4	8
10	11	12	1	8.396	6.876	2.275	3.022	1.142	31.25	365	455	4	12
11	12	13	1	8.396	6.876	2.275	3.022	1.142	31.25	323	455	4	10
12	10	11	1	8.396	6.876	2.275	3.022	1.142	0.3	498	498	5	11
13	15	16	1	8.396	6.876	2.275	3.022	1.142	46.25	401	493	5	15
14	16	17	1	8.396	6.876	2.275	3.022	1.142	46.25	436	493	5	17
15	13	14	1	8.396	6.876	2.275	3.022	1.142	17.5	347	532	6	13
16	17	18	1	8.396	6.876	2.275	3.022	1.142	11.25	471	564	7	14
17	14	15	1	8.396	6.876	2.275	3.022	1.142	0.3	596	596	7	16

F3.2 Model Cogan02

Table F3.2.1. New Prestressing Data for input and use with the DOMO98 Computer Code.

New Domo Cable No.	Prestressing Force (MN)	Cable Cross-Sectional Area (mm^2)	New Eccentricity x_i (m)	New Eccentricity x_j (m)	Cable Start Element	Cable End Element
1	28.920	463.840	1.183	0.648	1	2
2	25.242	321.120	1.022	0.246	3	4
3	22.031	356.800	1.117	0.569	5	6
4	27.279	428.160	1.022	0.246	7	8
5	18.954	356.800	1.320	1.320	9	1
6	24.978	392.480	1.160	0.648	10	11
7	7.090	71.360	1.050	0.864	5	6
8	29.235	392.480	1.022	0.246	12	13
9	10.710	178.400	1.383	1.259	2	5
10	16.151	303.280	1.124	0.385	15	16
11	12.530	160.560	1.022	0.121	17	18
12	9.837	178.400	1.383	1.259	6	10
13	14.017	428.160	1.323	1.231	2	5
14	19.386	374.640	1.108	0.523	20	21
15	13.864	428.160	1.321	1.245	6	10
16	9.965	142.720	1.499	0.755	11	15
17	4.914	107.040	0.584	0.584	15	16
18	39.316	428.160	1.022	0.271	22	23
19	29.434	428.160	0.979	0.370	11	25
20	3.879	107.040	0.584	0.584	20	21
21	20.373	392.480	1.317	1.007	21	26
22	32.740	749.280	1.316	1.047	16	20

Table F3.2.2. New Time Intervals for input and use with the DOMO98 Computer Code.

Interval No.	Start Time T1	End Time T2	Original Elements Assembled	New Elements Assembled	Continuity Stressing	Cables Stressed
1	329	343	1 - 8	1, 2	-	1
2	343	367	9 - 14	3, 4	-	2
3	367	372	17 - 26	5, 6	-	3
4	372	386	15, 16, 27 - 37	7, 8, 9	Span 1	4, 5
5	386	401	38 - 45	10, 11	Pier 3	6, 7
6	401	448	46 - 51	12, 13, 14	Span 2 - Stage 1	8, 9
7	448	457	52 - 61	15, 16	-	10
8	457	477	62 - 67	17, 18, 19	Span 3 - Stage 1	11, 12
9	477	490	68 - 79	20, 21	Span 2 - Stage 2	13, 14
10	490	529	80 - 89	22, 23, 24	Span 3 - Stage 2, Span 4, Pier 5	15, 16, 17, 18
11	529	547	90 - 93	25	-	19
12	547	650	94 - 96	26, 27	Pier 6, Span 5, Span 6	20, 21, 22
13	650	752	-	-	Dead Load	-
14	752	983	-	-	-	-
15	983	1320	-	-	-	-
16	1320	1575	-	-	-	-
17	1575	1957	-	-	-	-
18	1957	2313	-	-	-	-
19	2313	3528	-	-	-	-
20	3528	6100	-	-	-	-

Table F3.2.3a. New Segment Data for input and use with the DOMO98 Computer Code.

New Element No.	Node i	Node j	Element Type	Second Moment of Area, I (mm^4)	Cross-Sectional Area, A (mm^2)	Shear Area A_s (mm^2)	Coefficient of Shear SHE	Eccentricity, y (mm)	Length (m)	Time Cast (days)	Time Erected (days)	Time Interval in which the element becomes active	Element Order (from node 1)
1	3	4	2	10.618	8.743	2.53	3.456	1.356	16.25	102	333	1	9
2	5	4	2	10.618	8.743	2.53	3.456	1.356	16.25	141	333	1	3
3	2	3	1	8.396	6.876	2.275	3.022	1.142	12.5	135	346	2	1
4	6	5	1	8.396	6.876	2.275	3.022	1.142	12.5	187	346	2	2
5	8	9	2	10.618	8.743	2.53	3.456	1.356	13.75	188	369	3	4
6	10	9	2	10.618	8.743	2.53	3.456	1.356	13.75	189	369	3	14
7	7	8	1	8.396	6.876	2.275	3.022	1.142	17.5	232	377	4	7
8	11	10	1	8.396	6.876	2.275	3.022	1.142	17.5	248	378	4	5
9	1	2	2	10.618	8.743	2.53	3.456	1.356	8.75	157	378	4	6
10	13	14	2	10.618	8.743	2.53	3.456	1.356	13.75	229	390	5	8
11	15	14	2	10.618	8.743	2.53	3.456	1.356	13.75	215	390	5	19
12	12	13	1	8.396	6.876	2.275	3.022	1.142	15	309	405	6	12
13	16	15	1	8.396	6.876	2.275	3.022	1.142	15	290	405	6	10
14	6	7	1	8.396	6.876	2.275	3.022	1.142	0.3	423	424	6	11
15	18	19	2	10.618	8.743	2.53	3.456	1.356	18.75	288	451	7	13
16	20	19	2	10.618	8.743	2.53	3.456	1.356	18.75	259	451	7	24
17	17	18	1	8.396	6.876	2.275	3.022	1.142	12.5	384	460	8	17
18	21	20	1	8.396	6.876	2.275	3.022	1.142	12.5	334	460	8	15
19	11	12	1	8.396	6.876	2.275	3.022	1.142	0.3	460	461	8	16
20	24	25	2	10.618	8.743	2.53	3.456	1.356	23.75	325	481	9	18
21	26	25	2	10.618	8.743	2.53	3.456	1.356	23.75	351	481	9	25

Table F3.2.3b. New Segment Data for input and use with the DOMO98 Computer Code.

New Element No.	Node i	Node j	Element Type	Second Moment of Area, I (mm^4)	Cross-Sectional Area, A (mm^2)	Shear Area As (mm^2)	Coefficient of Shear SHE	Eccentricity, y (mm)	Length (m)	Time Cast (days)	Time Erected (days)	Time Interval in which the element becomes active	Element Order (from node 1)
22	23	24	1	8.396	6.876	2.275	3.022	1.142	22.5	423	504	10	27
23	27	26	1	8.396	6.876	2.275	3.022	1.142	22.5	462	504	10	22
24	16	17	1	8.396	6.876	2.275	3.022	1.142	0.3	498	499	10	20
25	22	21	1	8.396	6.876	2.275	3.022	1.142	17.5	347	532	11	21
26	28	27	2	10.618	8.743	2.53	3.456	1.356	11.25	471	564	12	23
27	22	23	1	8.396	6.876	2.275	3.022	1.142	0.3	596	597	12	26

F3.3 Model Cogan03

Table F3.3.1. New Prestressing Data for input and use with the DOMO98 Computer Code.

New Domo Cable No.	Prestressing Force (MN)	Cable Cross-Sectional Area (mm^2)	New Eccentricity x_i (m)	New Eccentricity x_j (m)	Cable Start Element	Cable End Element
1	41.588	784.960	0.992	0.353	1	2
2	9.047	142.720	1.090	0.679	3	4
3	9.870	107.040	1.190	0.522	5	4
4	12.382	142.720	0.929	0.246	7	6
5	12.313	142.720	1.022	0.246	9	8
6	11.809	142.720	1.022	0.163	11	10
7	18.954	356.800	1.534	1.534	12	1
8	8.372	107.040	1.022	0.308	14	13
9	41.181	784.960	0.979	0.353	16	17
10	6.499	71.360	0.836	0.650	7	6
11	13.167	178.400	1.597	1.473	2	7
12	12.743	178.400	1.597	1.473	8	16
13	22.220	463.840	0.916	0.121	19	20
14	6.756	249.760	1.544	1.391	2	11
15	10.820	142.720	1.527	1.527	2	15
16	17.959	428.160	1.513	1.482	8	16
17	2.948	107.040	0.370	0.370	19	20
18	9.965	142.720	1.713	0.969	17	19
19	23.038	892.000	0.952	0.291	22	23
20	14.020	428.160	0.979	0.370	17	24
21	9.961	107.040	0.370	0.370	22	23
22	55.714	392.480	1.531	1.221	23	25
23	27.426	749.280	1.530	1.261	20	22

Table F3.3.2. New Time Intervals for input and use with the DOMO98 Computer Code.

Interval No.	Start Time T1	End Time T2	Original Elements Assembled	New Elements Assembled	Continuity Stressing	Cables Stressed
1	329	367	1 - 14	1, 2	-	1
2	367	369	17 - 22	3, 4	-	2
3	369	371	23, 24	5	-	3
4	371	376	25 - 27	6, 7	-	4
5	376	378	28 - 30	8, 9	-	5
6	378	379	15, 16, 31 - 33	10, 11, 12	Span 1	6, 7
7	379	386	34 - 37	13, 14	-	8
8	386	423	38 - 51	15, 16, 17	Span 2 - Stage 1	9, 10, 11
9	423	477	52 - 67	18, 19, 20	Span 2 - Stage 2, Span 3 - Stage 1	12, 13, 14, 15
10	477	529	68 - 89	21, 22, 23	Span 3 - Stage 2, Span 4, Pier 5	16, 17, 18, 19
11	529	547	90 - 93	24	Pier 6	20, 21
12	547	650	94 - 96	25, 26	Span 5, Span 6	22, 23
13	650	752	-	-	Dead Load	-
14	752	983	-	-		-
15	983	1320	-	-	-	-
16	1320	1500	-	-	-	-
17	1575	1957	-	-	-	-
18	1957	2313	-	-	-	-
19	2313	3528	-	-	-	-
20	3528	6100	-	-	-	-

Table F3.3.3a. New Segment Data for input and use with the DOMO98 Computer Code.

New Element No.	Node i	Node j	Element Type	Second Moment of Area, I (mm^4)	Cross-Sectional Area, A (mm^2)	Shear Area A_s (mm^2)	Coefficient of Shear SHE	Eccentricity, y (mm)	Length (m)	Time Cast (days)	Time Erected (days)	Time Interval in which the element becomes active	Element Order (from node 1)
1	2	3	1	8.396	6.876	2.275	3.022	1.142	28.75	116	339	1	12
2	4	3	1	8.396	6.876	2.275	3.022	1.142	28.75	160	339	1	1
3	10	11	2	10.618	8.743	2.53	3.456	1.356	6.25	19	367	2	2
4	12	11	2	10.618	8.743	2.53	3.456	1.356	8.75	19	368	2	15
5	9	10	2	10.618	8.743	2.53	3.456	1.356	5	19	370	3	14
6	13	12	1	8.396	6.876	2.275	3.022	1.142	5	19	371	4	11
7	8	9	1	8.396	6.876	2.275	3.022	1.142	5	123	372	4	9
8	14	13	1	8.396	6.876	2.275	3.022	1.142	5	251	376	5	7
9	7	8	1	8.396	6.876	2.275	3.022	1.142	5	231	377	5	5
10	15	14	1	8.396	6.876	2.275	3.022	1.142	5	253	378	6	3
11	6	7	1	8.396	6.876	2.275	3.022	1.142	5	234	378	6	4
12	1	2	1	8.396	6.876	2.275	3.022	1.142	8.75	157	378	6	6
13	16	15	1	8.396	6.876	2.275	3.022	1.142	7.5	257	381	7	8
14	5	6	1	8.396	6.876	2.275	3.022	1.142	5	237	381	7	10
15	4	5	1	8.396	6.876	2.275	3.022	1.142	0.3	0	0	8	13
16	17	18	1	8.396	6.876	2.275	3.022	1.142	28.75	263	396	8	18
17	19	18	1	8.396	6.876	2.275	3.022	1.142	28.75	247	396	8	16
18	16	17	1	8.396	6.876	2.275	3.022	1.142	0.3	0	0	9	17
19	20	21	1	8.396	6.876	2.275	3.022	1.142	31.25	286	454	9	21
20	22	21	1	8.396	6.876	2.275	3.022	1.142	31.25	325	454	9	19
21	19	20	1	8.396	6.876	2.275	3.022	1.142	0.3	0	0	10	20

Table F3.3.3b. New Segment Data for input and use with the DOMO98 Computer Code.

New Element No.	Node i	Node j	Element Type	Second Moment of Area, I (mm^4)	Cross-Sectional Area, A (mm^2)	Shear Area As (mm^2)	Coefficient of Shear SHE	Eccentricity, y (mm)	Length (m)	Time Cast (days)	Time Erected (days)	Time Interval in which the element becomes active	Element Order (from node 1)
22	24	25	1	8.396	6.876	2.275	3.022	1.142	46.25	370	492	10	24
23	26	25	1	8.396	6.876	2.275	3.022	1.142	46.25	401	492	10	26
24	23	22	1	8.396	6.876	2.275	3.022	1.142	17.5	347	532	11	22
25	27	26	1	8.396	6.876	2.275	3.022	1.142	11.25	471	564	12	23
26	23	24	1	8.396	6.876	2.275	3.022	1.142	0.3	0	0	12	25

F3.4 Model Cogan04

Table F3.4.1a. New Prestressing Data for input and use with the DOMO98 Computer Code.

New Domo Cable No.	Prestressing Force (MN)	Cable Cross-Sectional Area (mm^2)	New Eccentricity x_i (m)	New Eccentricity x_j (m)	Cable Start Element	Cable End Element
1	15.210	178.400	0.963	0.622	1	2
2	14.040	142.720	0.929	0.246	3	4
3	13.350	142.720	1.022	0.246	5	6
4	13.120	142.720	1.022	0.246	7	8
5	9.840	107.040	1.022	0.246	9	10
6	6.560	71.360	1.022	0.246	11	12
7	3.920	35.680	0.864	0.584	16	17
8	0.900	35.680	1.050	0.335	18	17
9	3.790	35.680	1.236	0.584	18	17
10	3.960	35.680	1.211	1.211	18	19
11	7.440	71.360	0.929	0.246	20	19
12	3.360	35.680	1.022	0.370	21	19
13	3.430	35.680	0.836	0.121	21	22
14	6.679	71.360	0.929	0.246	23	22
15	3.290	35.680	1.022	0.370	24	22
16	3.330	35.680	1.022	0.121	24	25
17	6.484	71.360	1.022	0.246	26	25
18	3.240	35.680	1.022	0.370	27	25
19	3.190	35.680	1.022	0.121	27	28
20	6.240	71.360	1.022	0.246	29	28
21	3.010	35.680	1.022	0.370	30	28
22	27.077	392.480	1.534	1.534	13	5
23	2.990	35.680	1.022	0.121	30	31
24	6.240	71.360	1.022	0.246	32	31
25	7.090	71.360	0.836	0.650	23	22
26	41.181	784.960	0.979	0.353	36	37
27	7.020	71.360	1.738	1.366	8	27
28	3.472	35.680	1.527	1.527	2	16
29	7.020	71.360	1.527	1.527	6	23
30	22.220	463.840	0.942	0.157	39	40
31	12.743	178.400	1.597	1.473	25	36
32	7.020	71.360	1.552	1.366	10	30
33	10.530	107.040	1.552	1.366	12	32
34	7.020	71.360	1.552	1.366	4	20
35	7.020	71.360	1.552	1.366	8	26
36	7.020	71.360	1.527	1.527	10	29
37	17.959	428.160	1.535	1.459	25	36
38	2.948	107.040	0.370	0.370	39	40
39	9.965	142.720	1.713	0.969	37	39

Table F3.4.1b. New Prestressing Data for input and use with the DOMO98 Computer Code.

New Domo Cable No.	Prestressing Force (MN)	Cable Cross-Sectional Area (mm^2)	New Eccentricity x_i (m)	New Eccentricity x_j (m)	Cable Start Element	Cable End Element
40	49.271	892.000	0.952	0.291	42	43
41	29.354	428.160	0.979	0.370	37	44
42	1.992	107.040	0.370	0.370	42	43
43	20.373	392.480	0.815	0.505	43	45
44	48.020	749.280	0.814	0.545	40	42

Table F3.4.2. New Time Intervals for input and use with the DOMO98 Computer Code.

Interval No.	Start Time T1	End Time T2	Original Elements Assembled	New Elements Assembled	Continuity Stressing	Cables Stressed
1	329	335	1 - 4	1, 2	-	1
2	335	339	5, 6	3, 4	-	2
3	339	343	7, 8	5, 6	-	3
4	343	346	9, 10	7, 8	-	4
5	346	349	11, 12	9, 10	-	5
6	349	367	13, 14	11, 12	-	6
7	367	368	17 - 20	14 - 17	-	7
8	368	369	21	18	-	8, 9
9	369	370	22, 23	19, 20	-	10, 11
10	370	371	24	21	-	12
11	371	372	25, 26	22, 23	-	13, 14
12	372	376	27	24	-	15
13	376	377	28, 29	25, 26	-	16, 17
14	377	378	30	27	-	18
15	378	379	15, 16, 31 - 33	13, 28 - 30	Span 1	19 - 22
16	379	382	34, 35	31, 32	-	23, 24
17	382	386	36, 37	33, 34	-	-
18	386	423	38 - 51	35 - 37	Span 2 - Stage 1, Pier 3	25 - 29
19	423	477	52 - 67	38 - 40	Span 2 - Stage 2, Span 3 - Stage 1	30 - 36
20	477	529	68 - 89	41 - 43	Span 3 - Stage 2, Span 4, Pier 5	37 - 40
21	529	547	90 - 93	44	Pier 6	41, 42
22	547	650	94 - 96	45, 46	Span 5, Span 6	43, 44
23	650	752	-	-	Dead Load	-
24	752	983	-	-	-	-
25	983	1320	-	-	-	-
26	1320	1500	-	-	-	-
27	1575	1957	-	-	-	-
28	1957	2313	-	-	-	-
29	2313	3528	-	-	-	-
30	3528	7528	-	-	-	-

Table F3.4.3a. New Segment Data for input and use with the DOMO98 Computer Code.

New Element No.	Node i	Node j	Element Type	Second Moment of Area, I (mm^4)	Cross-Sectional Area, A (mm^2)	Shear Area A_s (mm^2)	Coefficient of Shear SHE	Eccentricity, y (mm)	Length (m)	Time Cast (days)	Time Erected (days)	Time Interval in which the element becomes active	Element Order (from node 1)
1	7	8	1	8.396	6.876	2.275	3.022	1.142	6.25	76	329	1	13
2	9	8	1	8.396	6.876	2.275	3.022	1.142	6.25	102	329	1	11
3	6	7	1	8.396	6.876	2.275	3.022	1.142	5	126	335	2	9
4	10	9	1	8.396	6.876	2.275	3.022	1.142	5	178	335	2	7
5	5	6	1	8.396	6.876	2.275	3.022	1.142	5	130	339	3	5
6	11	10	1	8.396	6.876	2.275	3.022	1.142	5	181	339	3	3
7	4	5	1	8.396	6.876	2.275	3.022	1.142	5	132	343	4	1
8	12	11	1	8.396	6.876	2.275	3.022	1.142	5	185	343	4	2
9	3	4	1	8.396	6.876	2.275	3.022	1.142	5	136	346	5	4
10	13	12	1	8.396	6.876	2.275	3.022	1.142	5	187	346	5	6
11	2	3	1	8.396	6.876	2.275	3.022	1.142	2.5	138	349	6	8
12	14	13	1	8.396	6.876	2.275	3.022	1.142	2.5	189	349	6	10
13	1	2	1	8.396	6.876	2.275	3.022	1.142	8.75	157	378	15	12
14	27	28	2	10.618	8.743	2.530	3.456	1.356	1.25	19	367	7	35
15	29	28	2	10.618	8.743	2.530	3.456	1.356	1.25	19	367	7	33
16	26	27	2	10.618	8.743	2.530	3.456	1.356	2.5	19	367	7	32
17	30	29	2	10.618	8.743	2.530	3.456	1.356	2.5	19	367	7	30
18	25	26	2	10.618	8.743	2.530	3.456	1.356	2.5	19	368	8	29
19	31	30	2	10.618	8.743	2.530	3.456	1.356	5	19	369	9	27
20	24	25	2	10.618	8.743	2.530	3.456	1.356	2.5	19	369	9	26
21	23	24	1	8.396	6.876	2.275	3.022	1.142	2.5	19	370	10	24
22	32	31	1	8.396	6.876	2.275	3.022	1.142	5	19	371	11	23
23	22	23	1	8.396	6.876	2.275	3.022	1.142	2.5	19	371	11	21

Table F3.4.3b. New Segment Data for input and use with the DOMO98 Computer Code.

New Element No.	Node i	Node j	Element Type	Second Moment of Area, I (mm^4)	Cross-Sectional Area, A (mm^2)	Shear Area As (mm^2)	Coefficient of Shear SHE	Eccentricity, y (mm)	Length (m)	Time Cast (days)	Time Erected (days)	Time Interval in which the element becomes active	Element Order (from node 1)
24	21	22	1	8.396	6.876	2.275	3.022	1.142	2.5	226	372	12	20
25	33	32	1	8.396	6.876	2.275	3.022	1.142	5	251	376	13	18
26	20	21	1	8.396	6.876	2.275	3.022	1.142	2.5	230	376	13	16
27	19	20	1	8.396	6.876	2.275	3.022	1.142	2.5	231	377	14	14
28	34	33	1	8.396	6.876	2.275	3.022	1.142	5	253	378	15	15
29	18	19	1	8.396	6.876	2.275	3.022	1.142	2.5	232	378	15	17
30	17	18	1	8.396	6.876	2.275	3.022	1.142	2.5	235	378	15	19
31	35	34	1	8.396	6.876	2.275	3.022	1.142	5	256	379	16	22
32	16	17	1	8.396	6.876	2.275	3.022	1.142	2.5	236	379	16	25
33	15	16	1	8.396	6.876	2.275	3.022	1.142	2.5	237	382	17	28
34	36	35	1	8.396	6.876	2.275	3.022	1.142	2.5	258	382	17	31
35	14	15	1	8.396	6.876	2.275	3.022	1.142	0.3	0	0	18	34
36	37	38	1	8.396	6.876	2.275	3.022	1.142	28.75	263	396	18	38
37	39	38	1	8.396	6.876	2.275	3.022	1.142	28.75	247	396	18	36
38	36	37	1	8.396	6.876	2.275	3.022	1.142	0.3	0	0	19	37
39	40	41	1	8.396	6.876	2.275	3.022	1.142	31.25	286	454	19	41
40	42	41	1	8.396	6.876	2.275	3.022	1.142	31.25	325	454	19	39
41	39	40	1	8.396	6.876	2.275	3.022	1.142	0.3	0	0	20	40
42	44	45	1	8.396	6.876	2.275	3.022	1.142	46.25	370	492	20	44
43	46	45	1	8.396	6.876	2.275	3.022	1.142	46.25	401	492	20	46
44	42	43	1	8.396	6.876	2.275	3.022	1.142	17.5	347	532	21	42
45	47	46	1	8.396	6.876	2.275	3.022	1.142	11.25	471	564	22	43

F3.5 Model Cogan05

Table F3.5.1. New Prestressing Data for input and use with the DOMO98 Computer Code.

New Domo Cable No.	Prestressing Force (MN)	Cable Cross-Sectional Area (mm^2)	New Eccentricity x_i (m)	New Eccentricity x_j (m)	Cable Start Element	Cable End Element
1	42.600	463.840	0.969	0.434	1.000	2.000
2	29.520	321.120	1.022	0.246	3.000	4.000
3	12.570	142.720	1.090	0.679	5.000	6.000
4	10.800	107.040	0.976	0.308	7.000	6.000
5	13.399	142.720	0.929	0.246	9.000	8.000
6	13.054	142.720	1.022	0.246	11.000	10.000
7	12.440	142.720	1.022	0.246	13.000	12.000
8	27.077	392.480	1.534	1.534	14.000	1.000
9	9.230	107.040	1.022	0.184	16.000	15.000
10	11.946	392.480	0.946	0.434	17.000	18.000
11	7.090	71.360	0.836	0.650	9.000	8.000
12	29.235	392.480	1.022	0.246	19.000	20.000
13	14.040	142.720	1.633	1.447	4.000	11.000
14	3.472	35.680	1.527	1.527	2.000	7.000
15	9.691	303.280	0.910	0.171	22.000	23.000
16	12.530	160.560	1.022	0.121	24.000	25.000
17	8.385	142.720	1.633	1.447	10.000	19.000
18	4.358	35.680	1.527	1.527	6.000	17.000
19	24.570	249.760	1.544	1.420	4.000	13.000
20	14.040	142.720	1.552	1.366	2.000	9.000
21	9.955	374.640	0.894	0.309	27.000	28.000
22	17.959	428.160	1.535	1.459	10.000	19.000
23	9.965	142.720	1.713	0.969	18.000	22.000
24	2.948	107.040	0.370	0.370	22.000	23.000
25	39.316	517.360	1.022	0.271	29.000	30.000
26	29.354	428.160	0.979	0.370	18.000	32.000
27	1.992	107.040	0.370	0.370	27.000	28.000
28	20.373	392.480	0.815	0.505	28.000	33.000
29	48.020	749.280	0.814	0.545	23.000	27.000

Table F3.5.2. New Time Intervals for input and use with the DOMO98 Computer Code.

Interval No.	Start Time T1	End Time T2	Original Elements Assembled	New Elements Assembled	Continuity Stressing	Cables Stressed
1	329	343	1 - 8	1, 2	-	1
2	343	369	9 - 14, 17 - 21	3 - 6	-	2, 3
3	369	371	22 - 24	7	-	4
4	371	376	25 - 27	8, 9	-	5
5	376	378	28 - 30	10, 11	-	6
6	378	379	31 - 33, 15, 16	12 - 14	Span 1	7, 8
7	379	386	34 - 37	15, 16	-	9
8	386	401	38 - 45	17, 18	-	10, 11
9	401	457	46 - 61	19 - 23	Span 2 - Stage 1	12 - 15
10	457	477	62 - 67	24 - 26	Span 3 - Stage 1	16 - 18
11	477	490	68 - 79	27, 28	Span 2 - Stage 2, Pier 6	19 - 21
12	490	529	80 - 89	29 - 31	Span 3 - Stage 2, Span 4, Pier 5	22 - 25
13	529	564	90 - 93	32	-	26, 27
14	564	650	94 - 96	33, 34	Span 5, Span 6	28, 29
15	650	752	-	-	Dead Load	-
16	752	983	-	-	-	-
17	983	1320	-	-	-	-
18	1320	1575	-	-	-	-
19	1575	1957	-	-	-	-
20	1957	2313	-	-	-	-
21	2313	3528	-	-	-	-
22	3528	7528	-	-	-	-

Table F3.5.3a. New Segment Data for input and use with the DOMO98 Computer Code.

New Element No.	Node i	Node j	Element Type	Second Moment of Area, I (mm^4)	Cross-Sectional Area, A (mm^2)	Shear Area A_s (mm^2)	Coefficient of Shear SHE	Eccentricity, y (mm)	Length (m)	Time Cast (days)	Time Erected (days)	Time Interval in which the element becomes active	Element Order (from node 1)
1	3	4	2	10.618	8.743	2.530	3.456	1.356	16.25	102	333	1	14
2	5	4	2	10.618	8.743	2.530	3.456	1.356	16.25	141	333	1	3
3	2	3	1	8.396	6.876	2.275	3.022	1.142	12.5	135	346	2	1
4	6	5	1	8.396	6.876	2.275	3.022	1.142	12.5	187	346	2	2
5	12	13	2	10.618	8.743	2.530	3.456	1.356	6.25	19	367	2	4
6	14	13	2	10.618	8.743	2.530	3.456	1.356	8.75	19	368	2	21
7	11	12	2	10.618	8.743	2.530	3.456	1.356	5	19	370	3	16
8	15	14	2	10.618	8.743	2.530	3.456	1.356	5	19	371	4	13
9	10	11	1	8.396	6.876	2.275	3.022	1.142	5	123	372	4	11
10	16	15	1	8.396	6.876	2.275	3.022	1.142	5	251	376	5	9
11	9	10	1	8.396	6.876	2.275	3.022	1.142	5	231	377	5	7
12	17	16	1	8.396	6.876	2.275	3.022	1.142	5	253	378	6	5
13	8	9	1	8.396	6.876	2.275	3.022	1.142	5	234	378	6	6
14	1	2	1	8.396	6.876	2.275	3.022	1.142	8.75	157	378	6	8
15	18	17	1	8.396	6.876	2.275	3.022	1.142	7.5	257	381	7	10
16	7	8	1	8.396	6.876	2.275	3.022	1.142	5	237	381	7	12
17	20	21	2	10.618	8.743	2.530	3.456	1.356	13.75	229	390	8	15
18	22	21	2	10.618	8.743	2.530	3.456	1.356	13.75	215	390	8	26
19	19	20	1	8.396	6.876	2.275	3.022	1.142	15	309	405	9	19
20	23	22	1	8.396	6.876	2.275	3.022	1.142	15	290	405	9	17
21	7	6	1	8.396	6.876	2.275	3.022	1.142	0.3	0	0	9	18

Table F3.5.3b. New Segment Data for input and use with the DOMO98 Computer Code.

New Element No.	Node i	Node j	Element Type	Second Moment of Area, I (mm^4)	Cross-Sectional Area, A (mm^2)	Shear Area As (mm^2)	Coefficient of Shear SHE	Eccentricity, y (mm)	Length (m)	Time Cast (days)	Time Erected (days)	Time Interval in which the element becomes active	Element Order (from node 1)
22	25	26	2	10.618	8.743	2.530	3.456	1.356	18.75	288	451	9	20
23	27	26	2	10.618	8.743	2.530	3.456	1.356	18.75	259	451	9	31
24	24	25	1	8.396	6.876	2.275	3.022	1.142	12.5	384	460	10	24
25	28	27	1	8.396	6.876	2.275	3.022	1.142	12.5	334	460	10	22
26	19	18	1	8.396	6.876	2.275	3.022	1.142	0.3	0	0	10	23
27	31	32	2	10.618	8.743	2.530	3.456	1.356	23.75	325	481	11	25
28	33	32	2	10.618	8.743	2.530	3.456	1.356	23.75	351	481	11	32
29	30	31	1	8.396	6.876	2.275	3.022	1.142	22.5	423	504	12	34
30	34	33	1	8.396	6.876	2.275	3.022	1.142	22.5	462	504	12	29
31	24	23	1	8.396	6.876	2.275	3.022	1.142	0.3	0	0	12	27
32	29	28	1	8.396	6.876	2.275	3.022	1.142	17.5	347	532	13	28
33	35	34	1	8.396	6.876	2.275	3.022	1.142	11.25	471	564	14	30
34	30	29	1	8.396	6.876	2.275	3.022	1.142	0.3	0	0	14	33

F4.0 Comparisons between Measured and DOMO98 Model Strains – Cogan Viaduct

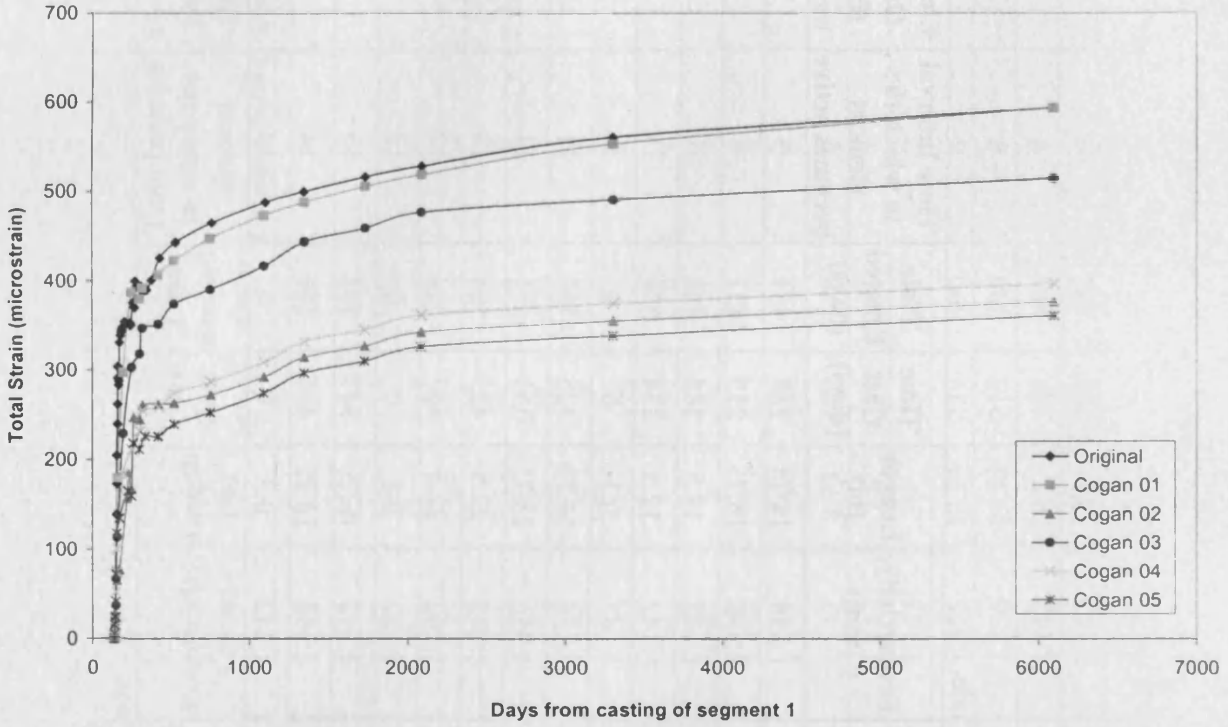

Figure F4.1. Comparison of predicted strains made with different models using the DOMO98 computer code in the top flange of segment 1, Cogan Viaduct.

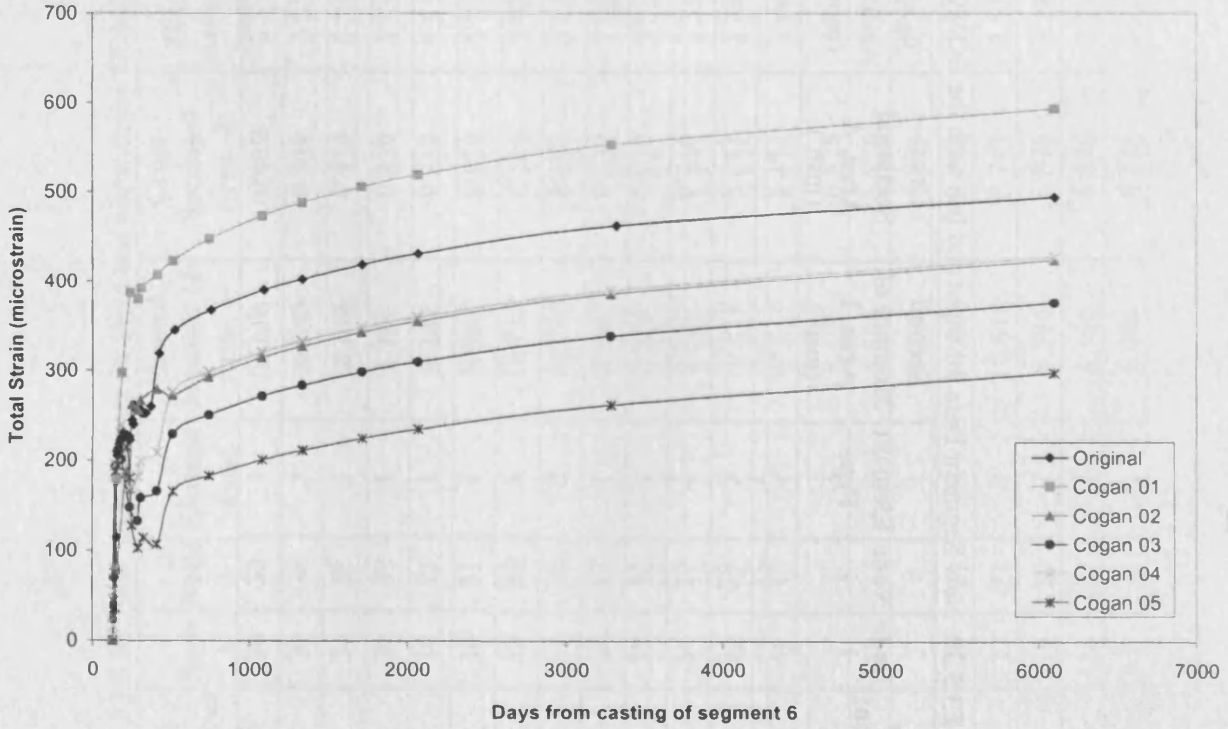

Figure F4.2. Comparison of predicted strains made with different models using the DOMO98 computer code in the top flange of segment 6, Cogan Viaduct.

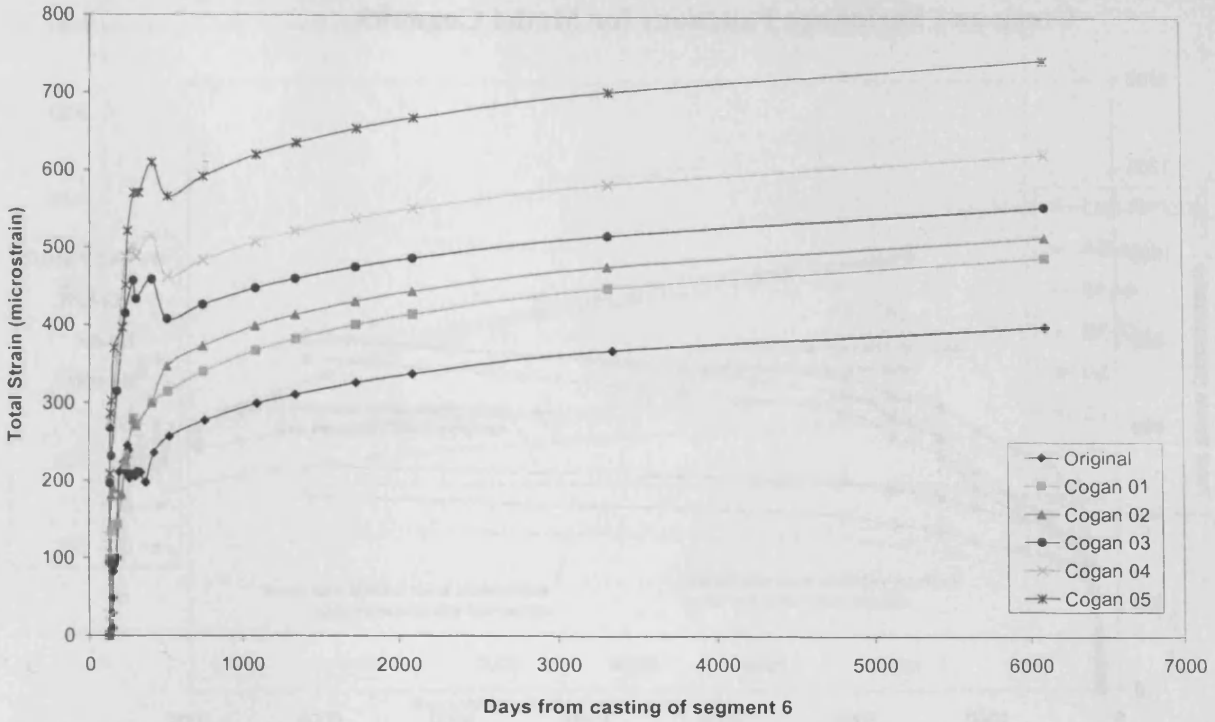

Figure F4.3. Comparison of predicted strains made with different models using the DOMO98 computer code in the bottom flange of segment 6, Cogan Viaduct.

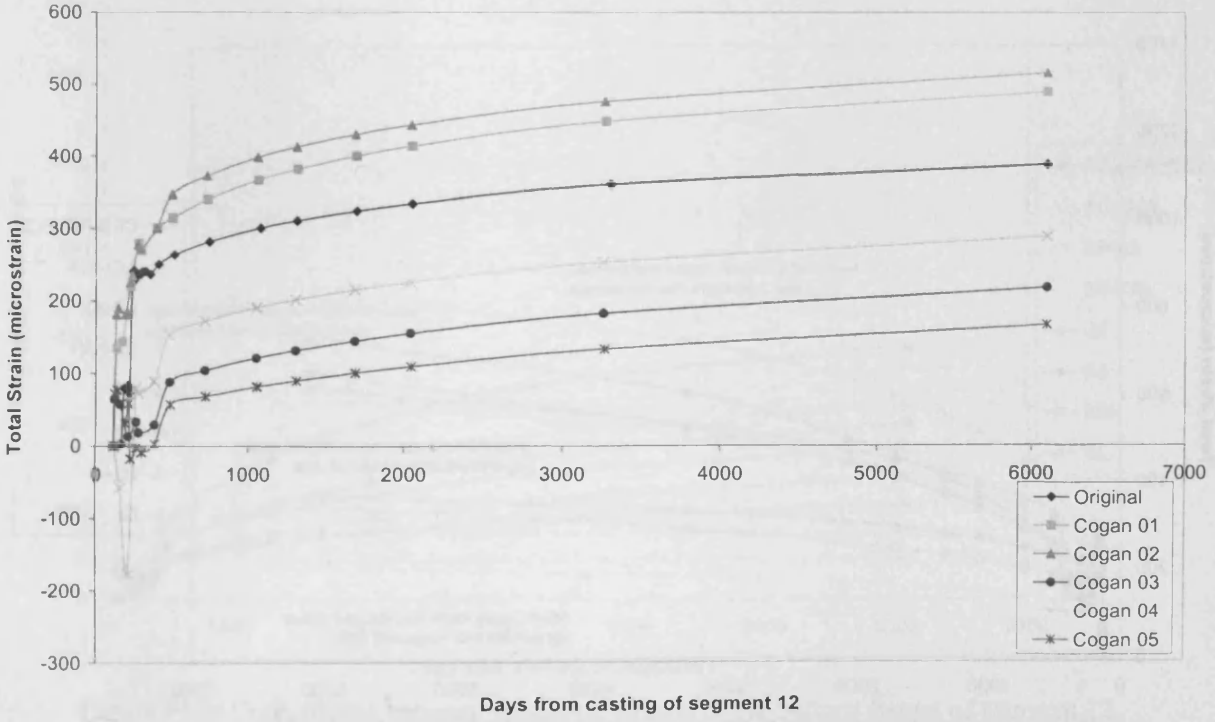

Figure F4.4. Comparison of predicted strains made with different models using the DOMO98 computer code in the bottom flange of segment 12, Cogan Viaduct.

F5.0 Comparisons between DOMO98 Model Strains Predicted using various Creep and Shrinkage Functions for Model Cogan03

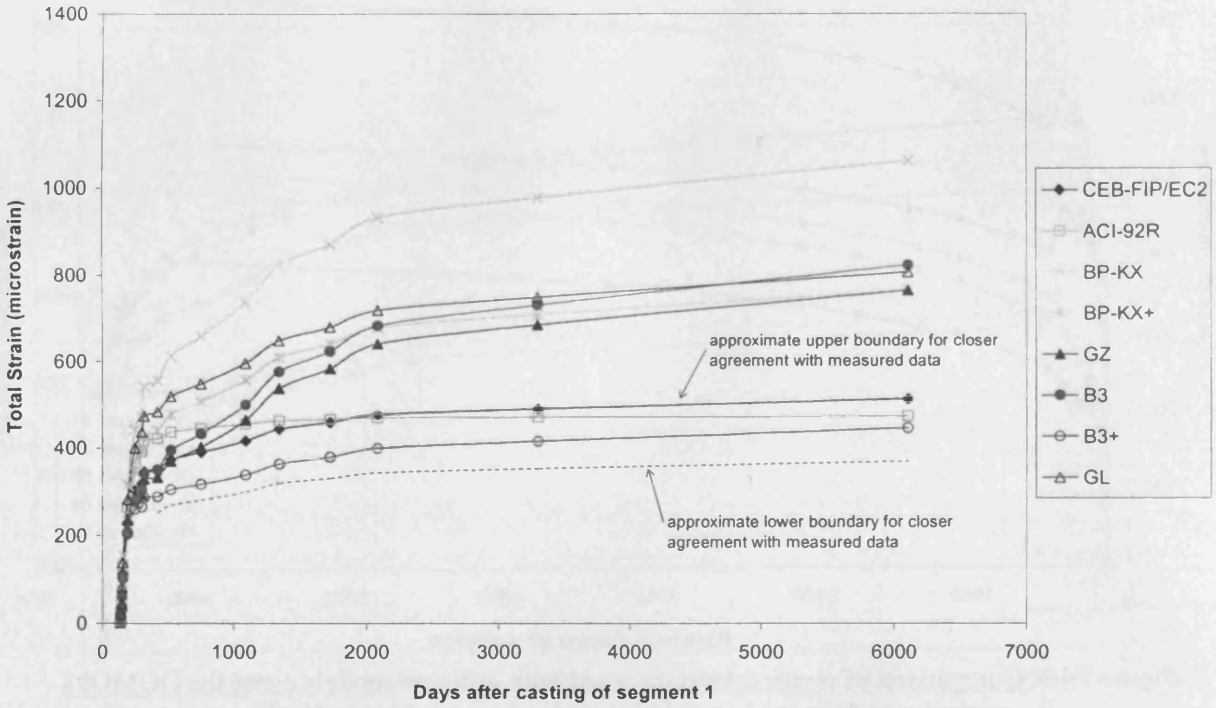

Figure F5.1. Comparison between predicted strains in the top flange of segment 1, Cogan Viaduct, using creep and shrinkage prediction models incorporated into the DOMO98 computer code.

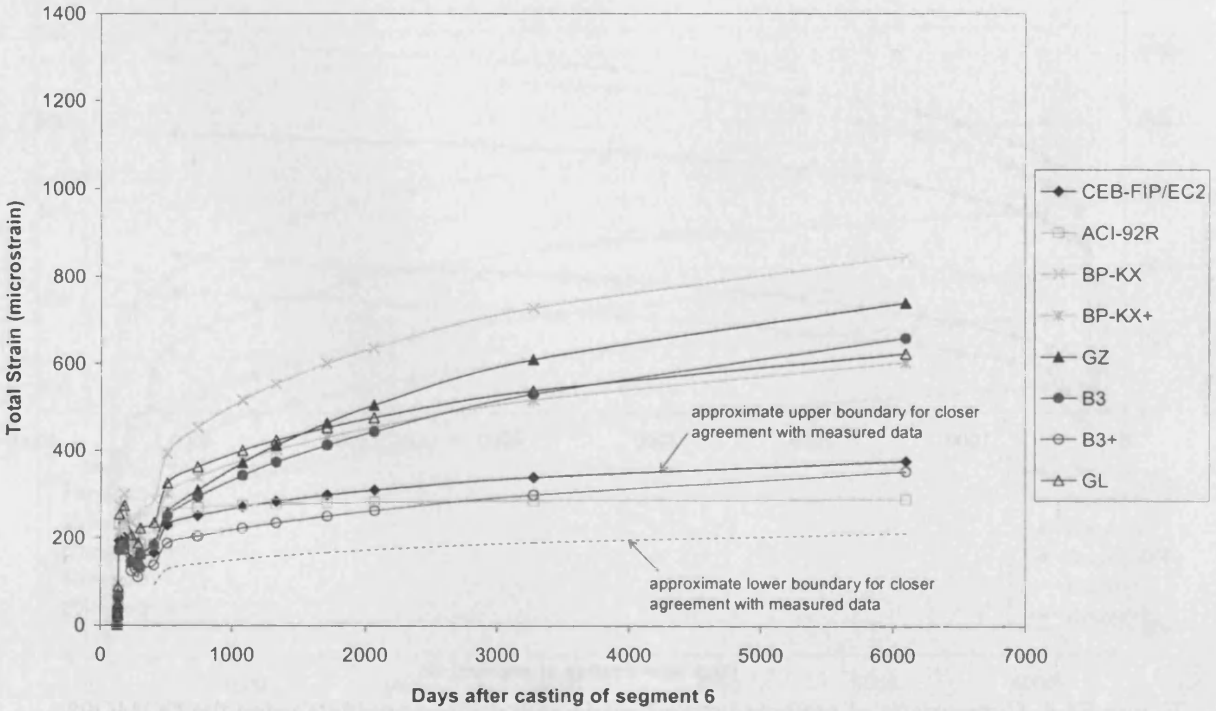

Figure F5.2. Comparison between predicted strains in the top flange of segment 6, Cogan Viaduct, using creep and shrinkage prediction models incorporated into the DOMO98 computer code.

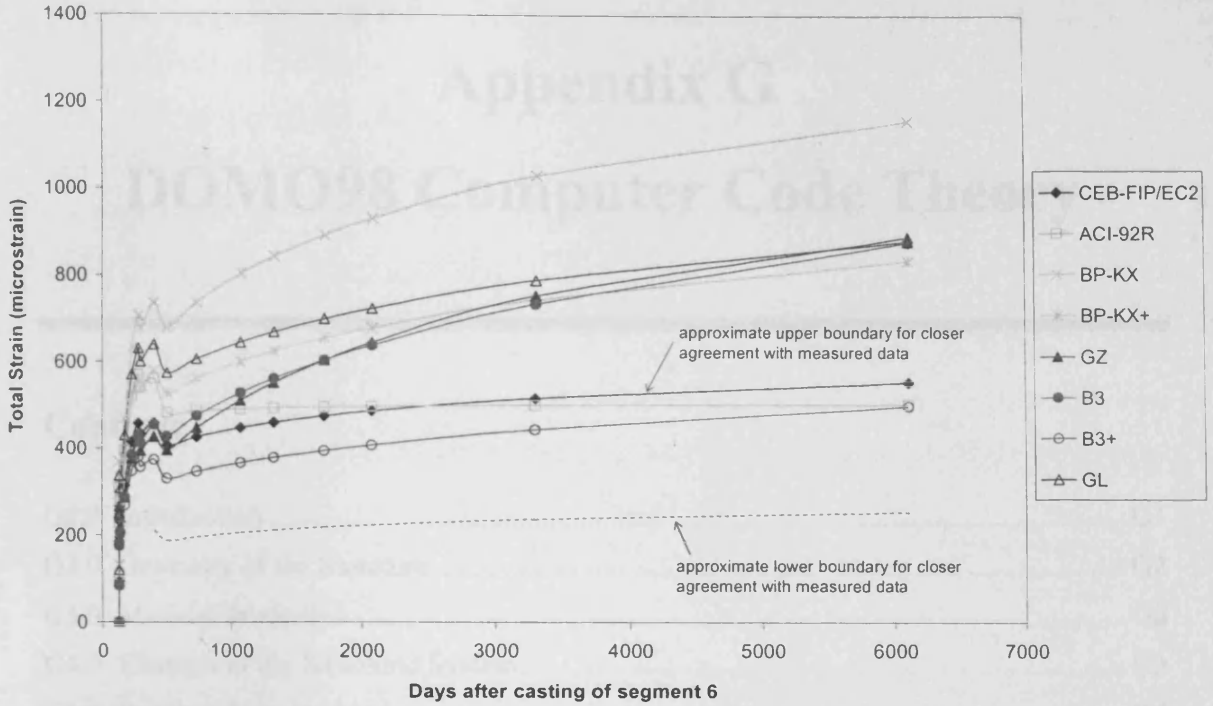

Figure F5.3. Comparison between predicted strains in the bottom flange of segment 6, Cogan Viaduct, using creep and shrinkage prediction models incorporated into the DOMO98 computer code.

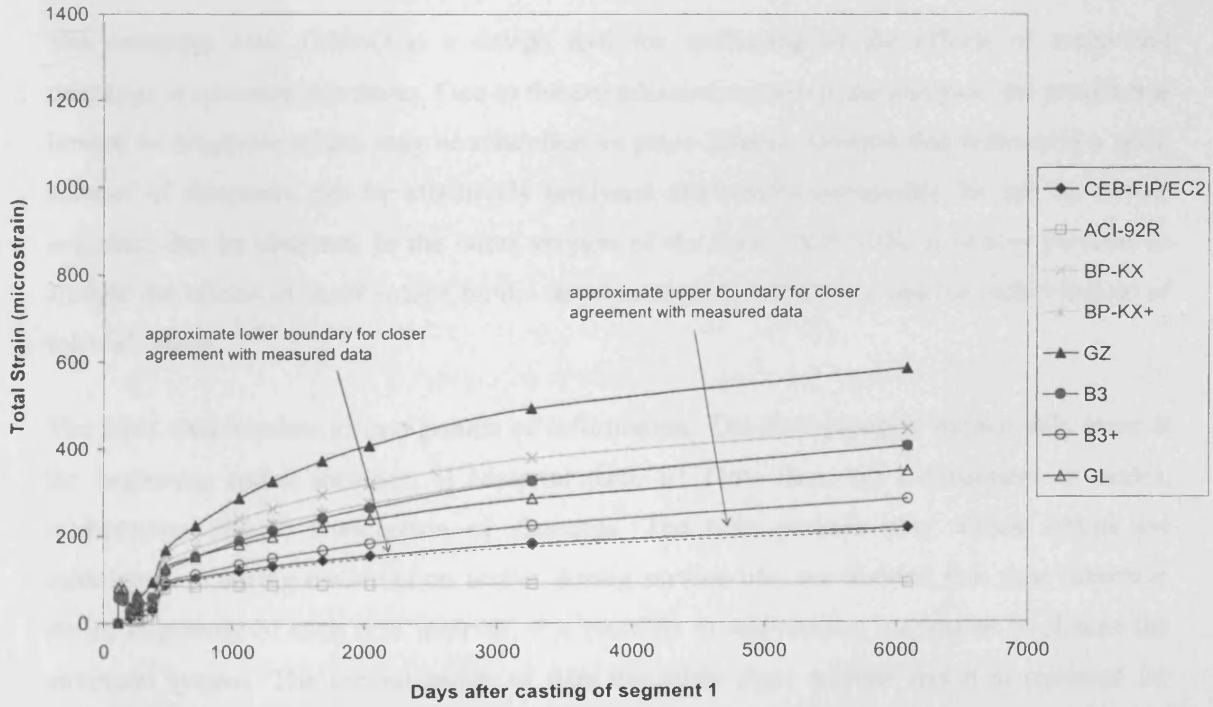

Figure F5.4. Comparison between predicted strains in the bottom flange of segment 12, Cogan Viaduct, using creep and shrinkage prediction models incorporated into the DOMO98 computer code.

Appendix G

DOMO98 Computer Code Theory

Contents

G1.0 Introduction

The computer code DOMO is a design tool for evaluating of the effects of creep and shrinkage in concrete structures. Due to the complicated nature of the analysis, the program is limited to structures which may be modelled as plane frames. Despite this restriction a great number of structures can be effectively analysed and results acceptable for use by design engineers can be obtained. In the latest version of the code, DOMO98, it is now possible to analyse the effects of shear strains on the development of deflections and the redistribution of internal forces.

The input data consists of two groups of information. The first group is written only once at the beginning and it includes: i) Material data, ii) Time data, iii) Coordinates of nodes, iv) Elements and v) Connection of elements. The time periods over which strains are calculated i.e. during construction and/or during service life, are divided into time intervals. At the beginning of each time interval, it is possible to add/remove loading or to change the structural system. The second group of data describes these actions and it is repeated for every time interval.

G2.0 Geometry of the Structure

The structure is described by the central line of the individual beam elements, which are connected in nodes. Positions of nodes are prescribed by the x and y coordinate system, while elements are defined by their geometry (area of their cross-section and moment of inertia) and by a material number, which defines the material properties. The time of casting and the number of the time interval in which the element begins to be active in the structure, supplement the element data and make it possible to model the construction process of the structure.

G3.0 Material Properties

The material properties are given by a compliance function. A number of compliance functions may be used. The original functions followed the recommendations of CEB-FIP Model Code 1990[121] (Eurocode 2[131] – Concrete elements and structures, 1992), the BP Model[124] from 1980 and a variation on the BP-KX Model from 1994. The program code was updated as part of this study to include creep and shrinkage functions from the following models: the ACI Model[117] from 1992, the original BP-KX Model[125] from 1991 and its short-form BP-KX+ Model[126] from 1993, the most recent of the RILEM models, the B3 Model[114] 1995 and its short-form B3+ Model[127] from 1996, and finally two independent models published in the ACI Materials Journal, the GZ Model[128] from 1993 and the GL Model[129] from 2001.

The creep analysis used in this study is based on the following approach. Each time interval is divided into a number of time steps. In each time step the elastic analysis is executed, however, a modulus of elasticity is replaced by a pseudoelastic modulus and an additional strain increment is added (creep shrinkage, temperature effects or the effect of the history of loading). The conventional stress-strain law is modified as follows:

$$\Delta\varepsilon_i = \frac{\Delta\sigma_i}{E_p} + \Delta\varepsilon_h \qquad \text{(G1)}$$

where:

$\Delta\varepsilon_i$ = strain increment,

$\Delta\sigma_i$ = stress increment,

$\Delta\varepsilon_h$ = strain increment due to time-dependent effects, effect of the history of loading, etc., and

E_p = pseudoelastic modulus.

The compliance function representing the time-dependent behaviour is calculated from the creep and shrinkage prediction model formulae and then expanded into a Dirichlet series approximation describing the behaviour of the Kelvin chain rheological model. Then the parameters E_p and $\Delta\varepsilon_h$ are calculated in each time step. Only the subroutine which calculates the constants of the Kelvin chain model has to be modified and stored, the rest of the program remains unchanged. Since this analysis does not need to store the complete loading history, the speed of analysis is not dependent on the number of time steps. This efficient procedure makes it possible to analyse extensive structures during a complex construction process.

The structure may be composed of different types of concrete. Each type can have a different compliance function or the individual elements may be cast of concrete of a different age. This provides a variety of possibilities which may fit the actual behaviour of structures.

G4.0 Changes of the Structural System

The structure may be subjected to several changes of the structural system. The subsequent growth of the structure is modelled if individual elements are added to the existing parts of the structure. If the structure is cast in situ the elements become active early after casting. If prefabricated elements are added, they may be of arbitrary age and become active at the beginning of the time interval specified in the input data. The added element can be attached in various positions, e.g. in the designed position (i.e. position given in design drawings), at one end of the already deformed structure, or at both ends between the existing (and deformed) elements. Also it is possible to attach an element at some angle in order to model any rectification during the construction process. Elements may be removed e.g. if the temporary parts of the structure are modelled, and the opposite action applies in order to achieve this.

The supporting conditions may be changed at the beginning of each time interval. Thus different assembly procedures may be considered in structures. Not only is it possible to add or remove supports, it is also possible to change the kind of support (e.g. hinge, fixed end, one direction support).

Individual parts of a structure, built separately, may be connected in order to form a single, continuous structure. This connection may only be in one direction (e.g. the vertical displacements are considered identical after a certain time) or a hinge or fixed connection may be formed. Such connections of nodes also improve the code's ability to model real structures.

The analysed structure may also be prestressed. Prestressing units are modelled in a polygonal shape. The initial prestressing force is given in the input data at individual elements within the structure. The long term prestress losses due to subsequent prestressing, creep, shrinkage and due to the deformation of the structure are calculated. The prestressing units may be added or removed at any time interval during the construction process.

G5.0 Results of the Analysis

During the analysis, the individual increments of displacements and forces are summed and the whole history of the structural response can be traced. The results from the analysis are printed to an output file, usually at the beginning and at the end of each time interval. The internal forces (bending moments, shear and axial forces) are included while the forces in prestressing tendons may be also printed.